

Jorge Guardia Valenzuela

Optimisation of graphite-matrix composites for collimators in the LHC upgrade

Director/es

Arenal de la Concha, Raúl

<http://zaguan.unizar.es/collection/Tesis>



Universidad
Zaragoza

Tesis Doctoral

OPTIMISATION OF GRAPHITE-MATRIX
COMPOSITES FOR COLLIMATORS IN THE LHC
UPGRADE

Autor

Jorge Guardia Valenzuela

Director/es

Arenal de la Concha, Raúl

UNIVERSIDAD DE ZARAGOZA
Escuela de Doctorado

2019



OPTIMISATION OF GRAPHITE-MATRIX COMPOSITES FOR COLLIMATORS IN THE LHC UPGRADE

INSTITUTE OF NANOSCIENCE OF ARAGÓN (INA)
UNIVERSITY OF ZARAGOZA, SPAIN



PHD THESIS
DOCTORAL PROGRAM IN PHYSICS
CONDENSED MATTER PHYSICS

Author:
Jorge Guardia Valenzuela

CERN Supervisor:
Alessandro Bertarelli

Academic Supervisor:
Dr. Raul Arenal

June 28, 2019

Summary

The present PhD Thesis has been carried out at the European Organization for Nuclear Research (CERN), located in Geneva (Switzerland).

At CERN the structure and physics of matter are studied with the aid of high energy particle beams; "Large Hadron Collider" (LHC) produces the world highest energy particle beam. The beam total energy is equivalent to the energy of a full Airbus A320 (66 t) plane travelling at 380 km/h , but concentrated in the diameter of a pencil lead. Beam intercepting devices, in particular collimators, are required as safety protection devices for using these high energy particle beams. Therefore, collimator absorber materials have to withstand one of the hardest man-made environments. On top of that, they must not disturb the normal particle accelerator operation, introducing additional requirements such as high electrical conductivity and ultra-high vacuum compatibility. Finally, the materials have to be produced industrially, therefore reliable and cost-efficient processes are required.

In the coming years, an important upgrade, known as High Luminosity LHC (HL-LHC), is foreseen, requiring more performing collimator materials. This calls for the development of novel advanced materials.

The uncommon combination of properties required can be met by certain graphite-matrix composites, particularly those including the advantages of liquid phase sintering. Apart from high densification through void infiltration, an adequate liquid phase induces catalytic graphitisation by dissolution of individual carbon atoms and precipitation of "fresh" graphite.

The research in this thesis aimed at significantly extending the knowledge of the physical mechanisms — such as catalytic graphitisation — that govern the behaviour of these materials. One of the main goals of this research was to find new production routes reducing the material cost and facilitating the sintering control, therefore increasing the market dissemination potential. A broad spectrum of candidate elements to replace molybdenum has been explored and chromium was selected for the study.

Four chromium carbide - graphite (CrGr) grades were produced and extensively characterised. Thermo-physical characterisation results have been presented for all the grades produced. Microstructural and phase analysis have been performed. The thermal expansion behaviour and stability of all relevant phases have been characterised by in-situ X-ray diffraction (XRD) up to $600\text{ }^\circ\text{C}$. The results have been compared with two high quality commercial graphites: pyrolytic graphite (PG) and fine-grained nuclear isotropic graphite.

The investigated carbide-graphite composites are mainly composed of oriented graphite, therefore they exhibit a transversely isotropic behaviour with in-plane properties comparable to those of pure ordered graphites. However, unlike the latter, which are extremely anisotropic, the composites keep reasonable thermo-physical and mechanical properties also in the direction perpendicular to the basal planes.

Besides high energy physics, the combination of properties of these carbide - graphite composites is appealing for a broad range of thermal management applications, particularly in aerospace and electronics, where reduced thermal expansion and low density are required along with high thermal conductivity.

Resumen

Esta tesis doctoral se ha realizado en la Organización Europea para la Investigación Nuclear (CERN), ubicada en Ginebra (Suiza).

En el CERN se estudia la estructura y la física de la materia, con ayuda de haces de partículas de alta energía. El acelerador "Gran Colisionador de Hadrones" (LHC) produce el haz de partículas con la mayor energía del mundo. La energía total contenida en el haz equivale a la energía de un avión Airbus A320 lleno (66 t) viajando a 380 km/h, pero concentrada en el diámetro de la mina de un lápiz. Son necesarios equipos de protección e interceptación del haz, particularmente los colimadores, para trabajar con esos haces de alta energía. Por lo tanto, los materiales absorbedores de los colimadores tienen que resistir uno de los más duros entornos creados por el hombre. Además de eso, no pueden alterar el funcionamiento normal del acelerador, lo que introduce requisitos adicionales como alta conductividad eléctrica o compatibilidad con ultra alto vacío. Finalmente, tiene que ser posible producir estos materiales industrialmente, por lo que se necesitan procesos fiables y económicamente viables.

En los próximos años, está prevista una importante serie de mejoras llamada "LHC de alta luminosidad" (HL-LHC upgrade), que requiere materiales absorbedores de colimadores con mejores prestaciones. Esto plantea el desarrollo de nuevos materiales.

Los materiales compuestos de matriz grafitica, en concreto los que incluyen las ventajas del sinterizado en fase líquida, pueden cumplir con la inusual combinación de propiedades. Aparte de alta densificación por infiltración de poros, una fase líquida adecuada induce grafitización catalizada por medio de la disolución de átomos individuales de carbono y precipitación de grafito "fresco".

Esta tesis busca ampliar significativamente el conocimiento de los mecanismos físicos — como la grafitización catalizada — que controlan el comportamiento de estos materiales. Uno de los objetivos principales de esta investigación es encontrar nuevas rutas de producción que reduzcan el coste y faciliten el control del sinterizado, por lo tanto que consigan aumentar su aplicación y uso en el mercado. Un gran abanico de elementos han sido explorados, de los cuales el cromo fue seleccionado.

Cuatro grados de material carburo de cromo - grafito (CrGr) fueron producidos y caracterizados en profundidad. Se han presentado resultados de la caracterización termofísica de todos los grados desarrollados. Los ensayos incluyen caracterización de la microestructura e identificación de las fases cristalinas. Los coeficientes de expansión térmica y la estabilidad de las fases se han caracterizado con difracción de rayos X in-situ hasta 600 °C. Los resultados se han comparado con dos grados comerciales de grafito también caracterizados: grafito pirolítico y grafito isotrópico de grano fino (grado nuclear).

Los composites de carburo-grafito investigados están mayoritariamente compuestos de grafito orientado, por lo que muestran un comportamiento transversalmente isotropo con propiedades en la dirección de los planos basales comparables a las de grafitos orientados puros. Sin embargo, a diferencia de éstos últimos, que son extremadamente anisotrópicos, los composites mantienen propiedades termofísicas y mecánicas razonables en la dirección perpendicular a los planos basales.

Además de en física de altas energías, la combinación de propiedades de estos composites es atractiva para un amplio catálogo de aplicaciones de transferencia de calor, particularmente aeroespaciales y electrónicas, donde se necesitan bajos coeficientes de expansión, bajas densidades y altas conductividades térmicas.

Acknowledgements

When I started working on the subject of graphite-based materials for particle accelerators, I did not know how complex is to collide particles and in particular nor did I know how complex is graphite itself.

I would have never thought to have the great chance to work for this prestigious and world renowned scientific institution, the European Organization for Nuclear Research (CERN), in Geneva. Despite the gratification, it was a hard challenge.

I owe to all those people who I encountered along the way, for their support and contribution to my present experience.

First of all, thanks to my supervisor at CERN Alessandro Bertarelli, who has thoroughly guided me through the mysteries of the investigated materials, for trusting me to do this research and related interesting activities. Second, to my academic supervisor Raul Arenal, for his continued advice and availability to improve the research.

I also want to thank Stefano Redaelli, LHC collimation project leader, for the support given to this research.

This work would have not been possible without the constant support from the Mechanical Measurements and the Metallurgy laboratories at CERN, thanks to their respective leaders M. Guinchard and S. Sgobba, and thanks to their members.

Thanks to G. Antorrena from INA laboratory, for sharing his expertise with me and constantly doing his best to perform successful experiments.

Thanks also to S. Bizzaro from Brevetti Bizz for the useful discussions and the successful execution of the production processes.

Then, I would like to thank my colleagues at CERN, not only for their disinterested support, but also for the good moments shared together during these years: Fede, Carlotta, Claudio, Giorgia, Alex, Przemysław, Michele, Óscar, Sophia, Konstantina, Antonio, Josep, Elisa, Anité, Enrique, Pilar, Adrià, Nacho, Iñigo and many others.

Special thanks to my parents, my family and friends in Spain, no words are needed to explain why. Thanks to Marta for always being there. *Soy quien soy gracias a vosotros.*

Finally, thanks to life, without which nothing else is possible. The pace of technological progress has never been as accelerated as now. It is a great chance to be part of this particular time, surfing on the wave of science and innovation while exercising the professional activity.

The research leading to these results has received funding from the European Commission under the FP7 Research Infrastructures project EuCARD-2, grant agreement No 312453. This project has received funding from the European Union's Horizon 2020 Research and Innovation programme under Grant Agreement No 730871. Research supported by the High Luminosity LHC project.

Contents

1	Introduction	5
1.1	The upgrade of the Large Hadron Collider (LHC)	5
1.1.1	History of CERN	5
1.1.2	CERN's mission	7
1.1.3	Particle collisions, energy and luminosity	7
1.1.4	HiLumi upgrade (HL-LHC) and future plans	12
1.2	The collimation system	16
1.2.1	Functions of the collimators	18
1.2.2	Design of LHC collimators	19
1.2.3	Design of HL-LHC collimators	20
1.3	Materials for collimators	22
1.3.1	Requirements of materials for collimators	22
1.3.2	Figures of merit	25
1.3.3	State of the art of materials for collimators	26
1.3.4	Benchmarking of the state-of-the-art materials	34
1.4	Motivations and objectives of this thesis	35
2	Liquid phase sintering of graphite-matrix composites	41
2.1	Physical mechanisms	41
2.1.1	Graphitisation	41
2.1.2	Catalytic graphitisation	42
2.1.3	Diffusion of carbon atoms	43
2.1.4	Dissolution of carbon atoms	47
2.1.5	Wetting of graphite	49
2.2	Practical application	51
2.3	Carbon solvent selection	54
2.3.1	Minimum liquid phase temperature	54
2.3.2	Volumetric carbon-solvent efficiency	55
2.3.3	Volumetric efficiency in carbon precipitation	56
2.3.4	Cost and solidified product functionality	57
2.3.5	Examples of relevant phase diagrams	58
2.3.6	Carbon solvent survey	61
2.4	Summary of the chapter	65
3	Characterisation techniques	67
3.1	Thermo-physical characterisation	67
3.1.1	Density	68
3.1.2	Thermal diffusivity and conductivity	68
3.1.3	Specific heat	69
3.1.4	Coefficient of thermal expansion	70
3.2	Mechanical characterisation	71
3.3	Elastic constants	72
3.3.1	Theory of vibration: natural frequencies	73
3.3.2	Methodology	74
3.4	Electrical characterisation	75
3.5	X-Ray Diffraction (XRD)	77

3.5.1	Phase identification and crystallite-size analysis	79
3.5.2	Thermal expansion studies	81
3.6	Electron microscopy	89
3.6.1	Scanning Electron Microscopy (SEM)	89
3.6.2	Ion-milling	90
3.6.3	Scanning Transmission Electron Microscopy (STEM)	91
3.6.4	Focused Ion Beam (FIB)	92
3.7	Nanoindentation	92
4	Production routes	93
4.1	Initial powders	93
4.1.1	Asbury 3260 graphite	93
4.1.2	Asbury 3763 graphite	99
4.1.3	Granoc carbon fibres	102
4.1.4	Cytec carbon fibres	104
4.1.5	Molybdenum	106
4.1.6	Titanium	108
4.1.7	Chromium carbide powder	109
4.2	Powders mixing	112
4.3	Green body compaction	112
4.4	Sintering	112
4.5	Post-sintering thermal treatment	114
4.6	Summary of production parameters	114
4.6.1	Molybdenum carbide - graphite (MoGr)	114
4.6.2	Chromium carbide - graphite (CrGr)	115
4.7	Machinability	115
4.7.1	Conventional machining	116
4.7.2	Electrical discharge machining (EDM)	118
5	Characterisation results	119
5.1	Pyrolytic Graphite (PG)	119
5.1.1	Microstructure	119
5.1.2	Crystallography and lattice expansion	120
5.1.3	Electrical conductivity	125
5.1.4	Thermophysical properties	126
5.1.5	Mechanical properties	130
5.2	Graphite R4550	131
5.2.1	Microstructure	131
5.2.2	Crystallography and lattice expansion	131
5.2.3	Electrical conductivity	133
5.2.4	Thermophysical properties	134
5.2.5	Mechanical properties	136
5.3	Molybdenum carbide - graphite MG-6541Fc	137
5.3.1	Microstructure	137
5.3.2	Crystallography and lattice expansion	138
5.3.3	Electrical conductivity	141
5.3.4	Thermophysical properties	142
5.3.5	Mechanical properties	145
5.4	Chromium carbide - graphite CG-1100Ba	146
5.4.1	Microstructure	147

5.4.2	Crystallography and lattice expansion	148
5.4.3	Electrical properties	153
5.4.4	Thermophysical properties	155
5.4.5	Mechanical properties	159
5.5	Chromium carbide - graphite CG-1100A0	160
5.5.1	Microstructure	161
5.5.2	Crystallography	162
5.5.3	Thermophysical properties	163
5.6	Chromium carbide - graphite CG-1100B0	167
5.6.1	Microstructure	169
5.6.2	Crystallography	171
5.6.3	Electrical properties	172
5.6.4	Thermophysical properties	173
5.6.5	Mechanical properties	178
5.7	Chromium carbide - graphite CG-1240X	180
5.7.1	Microstructure	181
5.7.2	Crystallography and lattice thermal expansion	182
5.7.3	Electrical conductivity	186
5.7.4	Thermophysical properties	186
5.7.5	Mechanical properties	190
6	Discussion	192
6.1	Microstructure	192
6.1.1	Carbide particles	192
6.1.2	Graphite	198
6.1.3	Superficial features of the graphite-based materials	201
6.2	Macroscopic properties	208
6.2.1	Thermal conductivity	208
6.2.2	Specific heat	210
6.2.3	Mechanical properties	211
6.2.4	Overall comparison	213
6.3	Carbon fibres	216
6.4	Titanium addition to molybdenum carbide	217
6.5	Processing temperature and outgassing behaviour	218
6.6	Catalytic graphitisation	218
7	Conclusions and perspectives. Conclusiones y perspectivas	226
	APPENDICES	232
A	LHC operation and some of its engineering challenges	233
B	Knowledge Transfer at CERN	239
C	Advanced collimation techniques	241
D	Radiation damage	243
E	Elastic constants derivation	249
F	Uncertainty calculation for the electrical conductivity measurements	265

G High temperature X-ray diffraction data tables	267
Bibliography	270
Glossary	283

1 | Introduction

1.1 The upgrade of the Large Hadron Collider (LHC)

1.1.1 History of CERN

At the end of the Second World War, European science was no longer world-class. Following the example of other international organizations, a handful of visionary scientists imagined creating a European atomic physics laboratory. Raoul Dautry, Pierre Auger and Lew Kowarski from France, Edoardo Amaldi from Italy and Niels Bohr from Denmark were among these pioneers. Such a laboratory would not only unite European scientists but also allow them to share the increasing costs of nuclear physics facilities [1].

The "Conseil Européen pour la Recherche Nucléaire" (CERN) was established in 1954, nine years after the end of the Second World War, when the economical situation allowed an agreement between the 12 founding Member States: Belgium, Denmark, France, the Federal Republic of Germany, Greece, Italy, the Netherlands, Norway, Sweden, Switzerland, the United Kingdom and Yugoslavia.

CERN was founded with the principles of non-military, and non-secretive international institution, as its convention [2] states in Article II:

"The Organization shall have no concern with work for military requirements and the results of its experimental and theoretical work shall be published or otherwise made generally available."

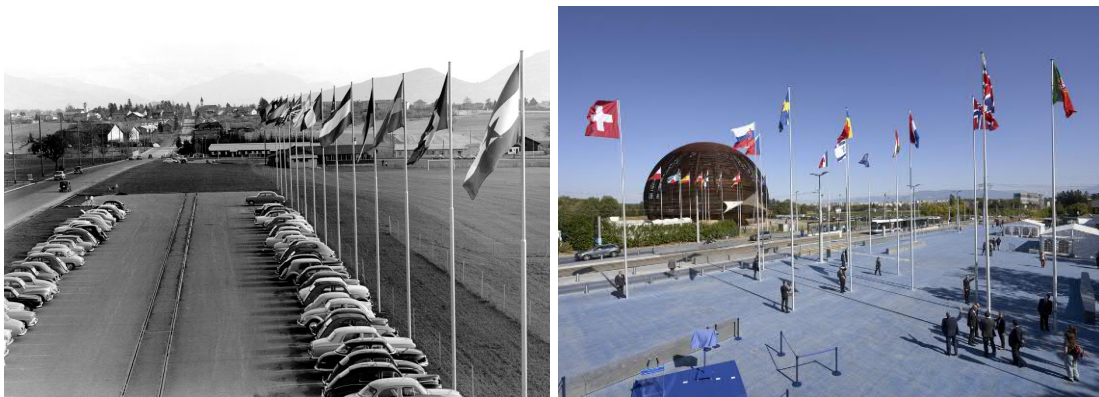


Figure 1.1: Flags of member states at CERN's main entrance, Nov. 1960 and Sep. 2018.

Today CERN has 23 member states: Austria (1959), Spain (1961-1969, re-joined 1983), Portugal (1985), Finland (1991), Poland (1991), Czechoslovak Republic (1992), Hungary (1992), Bulgaria (1999), Israel (2014), Romania (2016) and Serbia (2019). The Czech Republic and Slovak Republic re-joined CERN after their mutual independence in 1993. Yugoslavia left CERN in 1961.

"Member" states have special duties and all privileges of participation in CERN. They contribute to the capital and operating costs of CERN's programmes in proportion to their Net National Income (NNI), and they are represented in the council, responsible for all important decisions about the organization and its activities. The Member states' contribution for 2017 was almost 1,120 million Swiss francs (around a billion euros). The five biggest contributors to the 2017 budget were Germany (20.4%), United Kingdom (15.1%), France (14.3%), Italy (10.6%) and Spain (7.2%) [3].

The contributions to CERN are returned to the member states with dedicated balancing regulations. The return goes to people, companies and institutes from the Members states, having access to staff employment, to student and training programmes, and to contracts for services and supplies of goods.

”Associate” Members states pay a reduced contribution to the CERN budget and enjoy benefits that are reduced accordingly. They are represented at the CERN Council, except at Closed Sessions, and do not have voting rights. Cyprus and Slovenia are Associate Members States in the pre-stage to membership, and India, Lithuania, Pakistan, Turkey and Ukraine are Associate Members States.

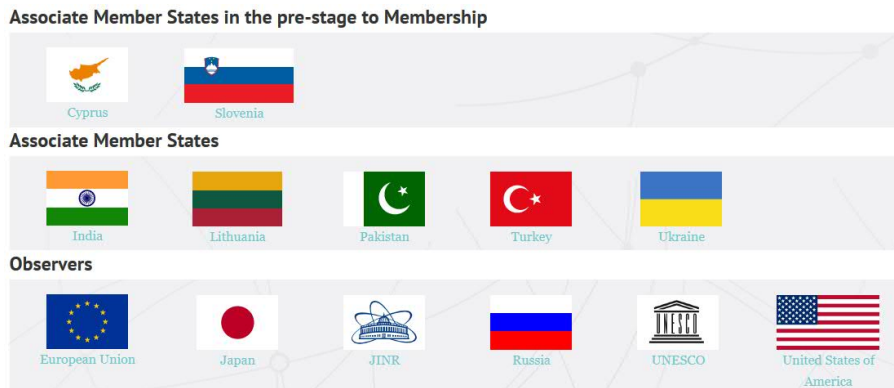


Figure 1.2: Other states and institutions linked to CERN

”Observer” status allows non-member states that have made significant contributions to the CERN infrastructure to attend council meetings and to receive council documents, without taking part in the decision-making procedures of the organization. Observer States and organisations currently involved in CERN programmes include: Japan, the Russian Federation, the United States of America, the European Union, the Joint Institute for Nuclear Research (JINR), and UNESCO, see Figure 1.2.

”Non-member” states with co-operation agreements with CERN include Albania, Algeria, Argentina, Armenia, Australia, Azerbaijan, Bangladesh, Belarus, Bolivia, Brazil, Canada, Chile, China, Colombia, Costa Rica, Croatia, Ecuador, Egypt, Estonia, Georgia, Iceland, Iran, Jordan, Korea, Malta, Mexico, Mongolia, Montenegro, Morocco, New Zealand, North Macedonia, Peru, Saudi Arabia, South Africa, United Arab Emirates and Vietnam. CERN also has scientific contacts with Cuba, Ghana, Ireland, Latvia, Lebanon, Madagascar, Malaysia, Mozambique, Palestinian Authority, Philippines, Qatar, Rwanda, Singapore, Sri Lanka, Taiwan, Thailand, Tunisia, Uzbekistan.

In 2017, there were almost 5,300 members of personnel working at CERN, including 204 doctoral students, 182 undergraduate students in Applied Physics, Engineering or Computing carrying out a project for their Master’s thesis (”technical students”). Besides, there were 342 University students doing 2-3 month internships in summer (”summer students”).

Associate members of CERN personnel also include over 12,000 Users, mainly research physicists, from all over the world, collaborating most of the time from their home institutions [4].

1.1.2 CERN's mission

Four themes encapsulate CERN's mission:

- **Research:** The "core business" of the Organization is to gain understanding of the most fundamental particles and laws of the Universe. This statement underscores the fact that CERN is first and foremost a research laboratory for fundamental physics.
- **Technology:** CERN develops new technologies for high-energy accelerators, detectors and computing. CERN-based innovation have applications in other domains, advancing the frontiers of technology. Knowledge transfer produces important economic return for the industrial sector and drives the creation of start-ups.
- **Collaborating:** Peaceful collaboration and diversity are intrinsic to CERN, bringing nations together through science. People of more than 100 nationalities from across the globe work at CERN, with extremely diverse cultural, academic and professional backgrounds (science, engineering, computing and others).
- **Education:** The scientists, engineers and technicians of tomorrow are trained through diverse employment and internship programmes, with hundreds of new places available each year. CERN motivates school students to pursue the study of science and inspires scientifically aware citizens.

1.1.3 Particle collisions, energy and luminosity

Collisions

In order to accomplish the main goal of the organization, fundamental physics research, particle accelerators are designed and built to collide particles at high energies. Einstein's famous formula $E = mc^2$ (the mass-energy equivalence) states that mass can transform into energy and vice versa, with c the speed of light in vacuum ($2.9979 \times 10^8 \text{ m s}^{-1}$). This transformation is possible by colliding particles.

Annex A describes how the Large Hadron Collider (LHC) is operated, from the source of beam particles to the detection of the collision products.

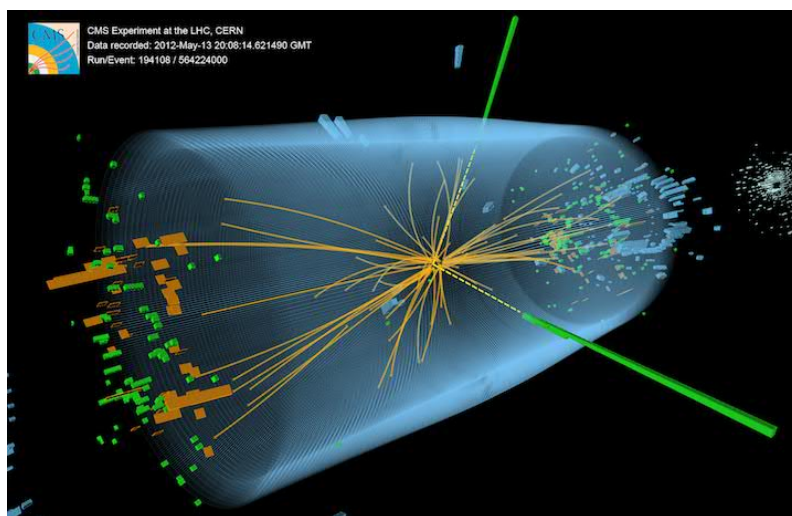


Figure 1.3: Candidate Higgs boson event from collisions between protons in the LHC. The different layers of sensors in the detector show the decay into two photons (dashed yellow lines and green towers).

Energy

At each collision, the energy that has been put into the centre-of-mass (E_{cm}) partially transforms into any of a range of new particles (mass), see Figure 1.5.

The particle energy is usually measured in electron-volt (eV), which is defined as the amount of energy gained (or lost) by a particle of elementary charge moving across an electric potential difference of one volt. One eV equals to approximately $1.6 \times 10^{-19} J$.

Electron-volt is commonly used with the metric prefixes kilo- ($\times 10^3$), mega- ($\times 10^6$), giga- ($\times 10^9$) or tera- ($\times 10^{12}$) (keV, MeV, GeV, TeV respectively). To make a proton gain $7 TeV$ is thus required an electrical potential of 7,000,000,000,000 V , as comparison, the highest voltage electric power transmission lines in the world (China) work at 1,100,000 V . By virtue of the mass-energy equivalence, the electronvolt is also a unit of mass (eV/c^2), which equals to $1.783 \times 10^{-36} kg$.

No particle can move at a velocity higher than the speed of light in a vacuum; however, there is no limit to the energy a particle can attain. In high-energy accelerators, particles normally travel very close to the speed of light. In these conditions, as more energy is given, the increase in speed is minimal (Figure 1.4).

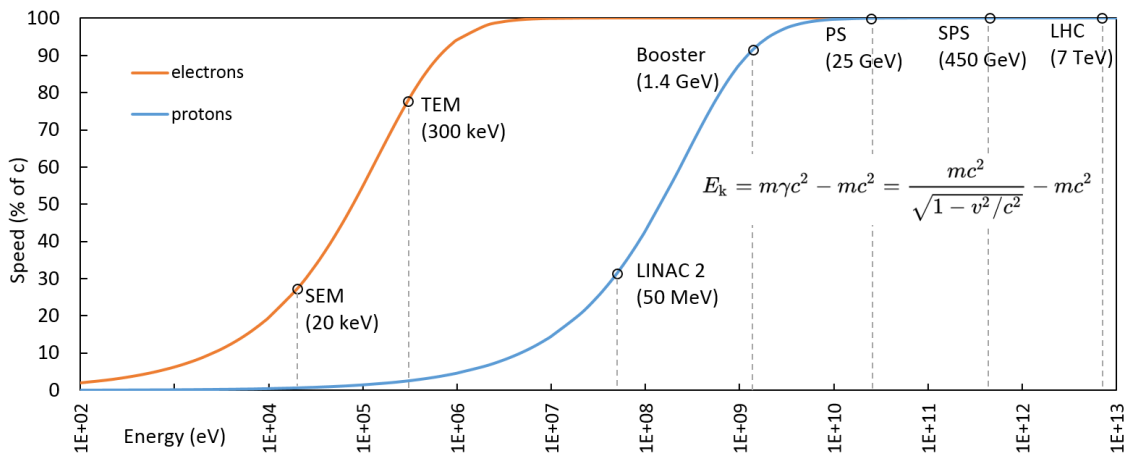


Figure 1.4: Relationship between kinetic energy and speed for relativistic particles.

Einstein never derived an equation for 'relativistic mass', and in later years he expressed his dislike of the idea: *"It is not good to introduce the concept of the mass $M = m/\sqrt{1-v^2/c^2}$ of a moving body for which no clear definition can be given. It is better to introduce no other mass concept than the 'rest mass' m . Instead of introducing M it is better to mention the expression for the momentum and energy of a body in motion."* Albert Einstein in letter to Lincoln Barnett, 19 June 1948 (quote from L.B. Okun (1989), p. 42).

Nevertheless, just to show what would be its effect, if the concept 'relativistic mass' M could be introduced, the mass of the particle would increase as shown in Table 1.1.

Table 1.1: Comparison of the speed and energy of a proton (rest mass $m = 0.938 \text{ GeV}/c^2$) [5]

Accelerator	Kinetic energy of a proton	Speed ($\%c$)	M/m^*
At rest	0	0	1
Linac 2	50 MeV	31.4	1.05
Booster	1.4 GeV	91.6	2.49
PS	25 GeV	99.93	26.73
SPS	450 GeV	99.9998	500.00
LHC	7 TeV	99.9999991	7453.56

*see text

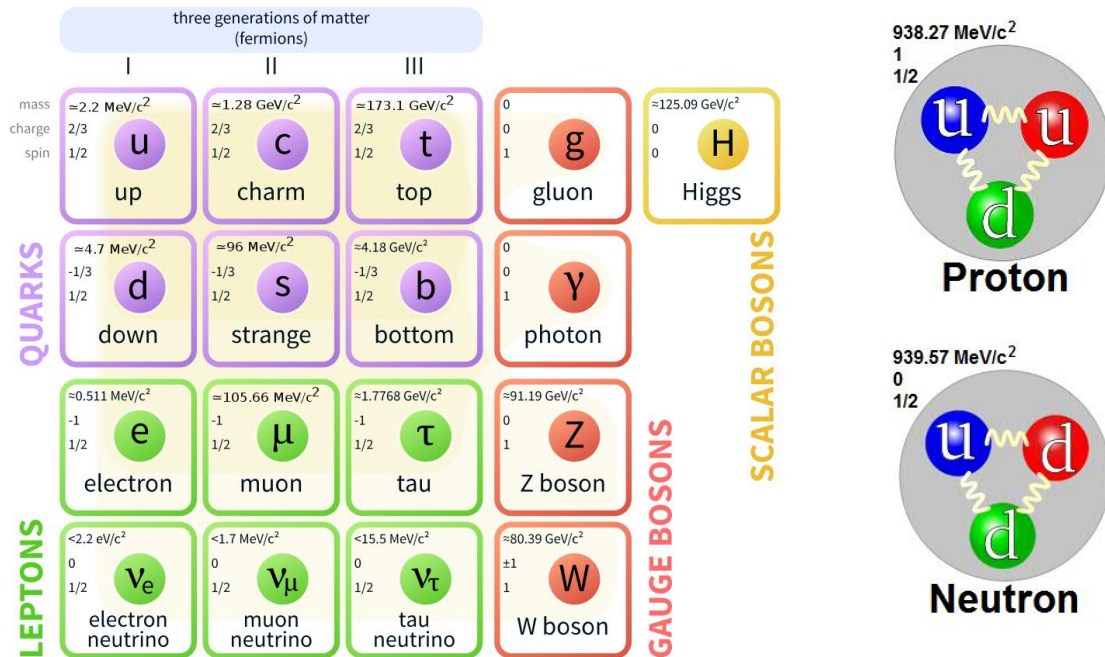


Figure 1.5: (Left) Standard model of elementary particles. The Higgs boson is the only scalar particle: all of its quantum numbers are zero, its only property is mass. Image by Cush / CC0. (Right) Protons are composed of two up quarks and one down quark, held together by the strong force, mediated by gluons. Neutrons are made of two down quarks and one up quark. Modified from original and original by Arpad Horvath / CC-BY-SA-2.5.

The first accelerator built at CERN, the 600 MeV Synchrocyclotron (SC), started working in 1957. It provided beams for CERN's first experiments in particle and nuclear physics by using a single beam and a fixed target.

The Proton Synchrotron (PS), see Figure 1.6, a much bigger machine with 628 m circumference, accelerated protons for the first time on 24 November 1959, becoming for a brief period the world's highest energy particle accelerator. The next morning John Adams announced the achievement in the main auditorium, see Picture 1.6. In his hand is an empty vodka bottle, which he had received from Dubna with the message that it was to be drunk when CERN passed the Russian Synchrophasotron's world-record energy of 10 GeV. The bottle contains a polaroid photograph of the 24 GeV pulse ready to be sent back to Dubna. Today, this figure is a factor 300 larger in the LHC.

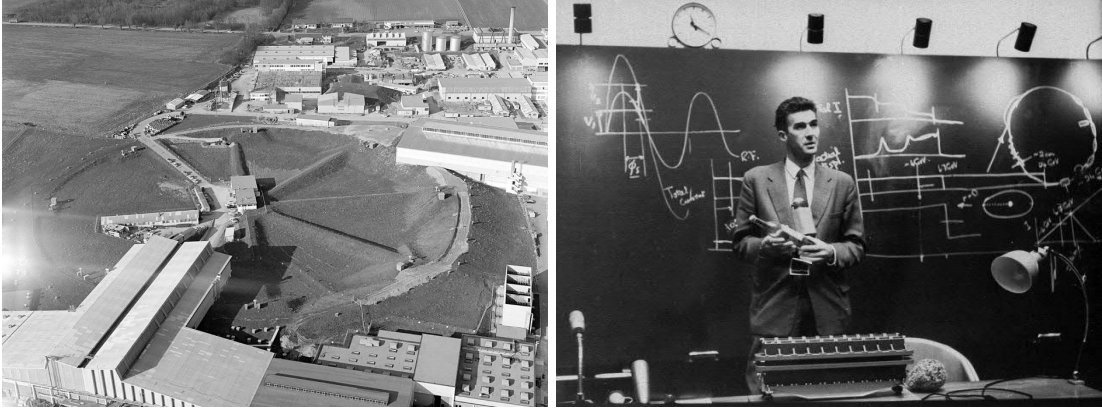


Figure 1.6: (Left) Aerial view of the underground PS ring in 1965. (Right) John Adams in the main auditorium at CERN, 25-Nov-1959.

By the late 1950s, physicists knew that a huge gain in collision energy would come from colliding particle beams head on, rather than by sending a single beam on a stationary target. In the case of a collider of two opposite beams with energies E_1 and E_2 , where the collision point is at rest in the laboratory frame, the centre-of-mass energy (E_{cm}) is [6]:

$$E_{cm}^2 = (E_1 + E_2)^2 \quad (1.1)$$

The world's first interactions from colliding protons were recorded for the first time in 1971, in the Intersecting Storage Rings (ISR).

Since then, several other accelerators, detectors and experiments have been built at CERN with the goal of increasing the energy of the collisions. As of today, the Large Hadron Collider (LHC) at CERN, see Figure 1.7, reached a maximum proton beam energy of 7 TeV, resulting in a world record E_{cm} of 14 TeV.

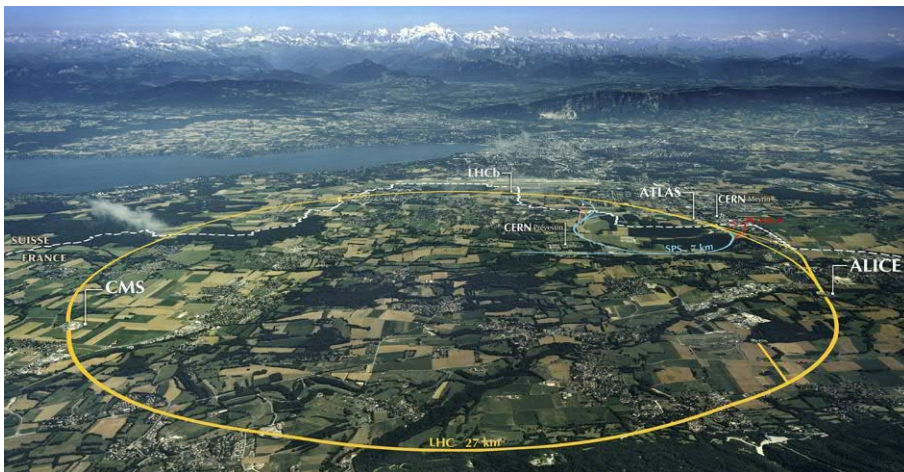


Figure 1.7: Real size footprint of the 27km-long LHC on the Geneva region.

Luminosity

Only particles with, at most, the corresponding mass of the collision energy (E_{cm}) can be created, though not always, as some physical events are more likely than others. Besides, some physical processes require other primary reactions to occur, increasing the difficulty

of taking place.

The probability that an event occurs can be measured by the cross section (σ), with unit 'barn' ($1b = 10^{-24}cm^2$). The number of events per second (N_{ev}) for a specific process is given by the product of the luminosity (L) and the cross section:

$$N_{ev} = L \cdot \sigma_{ev} \quad (1.2)$$

The Luminosity (L) is defined as the measurement of the number of events (collisions) that can be produced per unit of area and per second, therefore it has the units $cm^{-2}s^{-1}$ [6]. It measures how many particles can be squeezed through a given area in a given time. Equation 1.3 is the well-known expression for the luminosity of two Gaussian beams colliding almost head-on, with a small crossing angle. It shows how the luminosity depends on the number of particles crossing the collision point per unit of time, the beam sizes and the luminosity reduction factor S .

$$L = \frac{N_1 N_2 f N_b}{4\pi\sigma_x\sigma_y} \cdot S \quad (1.3)$$

With N_1 and N_2 the number of particles per bunch, f the revolution frequency, N_b the number of bunches per beam, and σ_x and σ_y the beam size in the two directions of its cross-section.

$$S \approx \frac{1}{\sqrt{1 + \left(\frac{\sigma_s \phi}{\sigma_x}\right)^2}} \quad (1.4)$$

With σ_s the bunch length and ϕ the crossing angle. For the LHC parameters S results in 0.835 [6].

The LHC luminosity is therefore [6]:

$$L_{LHC} = \frac{(1.15 \times 10^{11})^2 \cdot 11245 \cdot 2808}{4\pi \cdot (16.7 \times 10^{-3})^2} \cdot 0.835 = 1 \times 10^{34} cm^{-2}s^{-1} \quad (1.5)$$

The total proton-proton cross-section at the LHC includes both elastic and inelastic processes. Furthermore, inelastic processes contain different kinds of soft interactions known as non-diffractive, single-diffractive and double-diffractive processes [7]. The total proton-proton cross-section in the LHC operating with 6.5 TeV beams is around 111 millibarn, broken down in inelastic (80 mb) and elastic (31 mb) scatterings [8]. It is only in inelastic reactions where new particles are produced and/or the internal structure of the initial particles is changed [9], so only them are potentially interesting collisions.

$$N_{collisions} = 1 \times 10^{34} \cdot 8 \times 10^{-26} (80 mb) = 800 \times 10^6 col. per second \quad (1.6)$$

In other words:

$$N_{collisions} = 800 \times 10^6 / (11245 \cdot 2808) = 25 col. per crossing \quad (1.7)$$

On the other hand, the cross-section for producing a Higgs boson (7 TeV beams) at the LHC is in the order of 10 picobarn [10] (by gluon-gluon fusion mechanism).

With nominal luminosity:

$$N_{Higgs} = 1 \times 10^{34} \cdot 1 \times 10^{-35} (10 pb) = 0.1 Higgs per second \quad (1.8)$$

Which is equal to 1 Higgs every 10 seconds. The ratio is only 1 Higgs boson produced per 10 billion collisions in the LHC (0.00000001%). Only after complex statistical analysis of data collected over several years, it was possible to determine at CERN the presence of the Higgs boson. This simple example shows the importance of maximizing the luminosity of the collider.

1.1.4 HiLumi upgrade (HL-LHC) and future plans

In the previous section it was shown why the luminosity of the collisions has to be maximized in order to discover and prove the existence of new particles produced in rare events. This section shows the main accelerator parameters that will be changed during High Luminosity upgrade (HiLumi or HL-LHC) in order to increase its luminosity [11]. One of them in particular, the beam intensity, is critical to the collimation system.

LHC nominal parameters, compared with high HL-LHC upgrade, and with high energy LHC (HE-LHC) and hadron-hadron Future Circular Collider (FCC-hh) [12] proposals are presented in Table 1.2.

The design luminosity of HL-LHC will be improved in a factor 5. As consequence, in the following 12 years of operation, it is expected to gather 10 times more data than the 12 years of operation of LHC (2014-2026).

Table 1.2: Comparison of collider parameters [13]

Parameter	LHC	HL-LHC	HE-LHC	FCC-hh
Collision energy [TeV]	14	14	27	100
Magnetic dipole field [T]	8.33	8.33	16	16
Dipole operating temperature [K]	1.9	1.9	1.9	1.9
Circumference [m]	26.659	26.659	26.659	$\approx 100km$
Injection energy [GeV]	450	450	1300	3300
Total Synchr. radiation power [kW]	3.6	7.3	101	2400
Energy loss ΔE /turn [keV]	6.7	6.7	93	4600
Revolution freq. [Turns per second]	11245	11245	11245	11245
Bunches per proton beam	2808	2808	2808	10400
Protons per bunch [$\times 10^{11}$]	1.15	2.2	0.44-2.2	0.2-1
RMS bunch length [cm]	7.55	8.1	7.55	7.55
Bunch spacing [ns]	25	25	25	25
Beam current [A]	0.58	1.12	1.12	0.5
Stored energy/beam [MJ]	362	700	1300	8400
RMS beam size at int. point [μm]	16.7	8.2	3-6.6	1.5-6.7
Peak luminosity [$\times 10^{34} cm^{-2} s^{-1}$]	1	5	25	5-30
Total inelastic cross section [mbarn]	82	112	91-125	109-156

Crossing angle

One way of increasing the luminosity is to reduce the crossing angle ϕ ($285 \mu rad$ in the LHC). This is planned for the HL-LHC upgrade by installing 16 novel radio-frequency cavities (called Crab Cavities), made of superconducting bulk niobium through a complex forming process. They will rotate the bunches ("crabbing") at the collision points in order

to reach optimal head-on collisions, Figure 1.8. This will make the Luminosity reduction factor S of Equation 1.3 to increase from 0.835 to around 1.

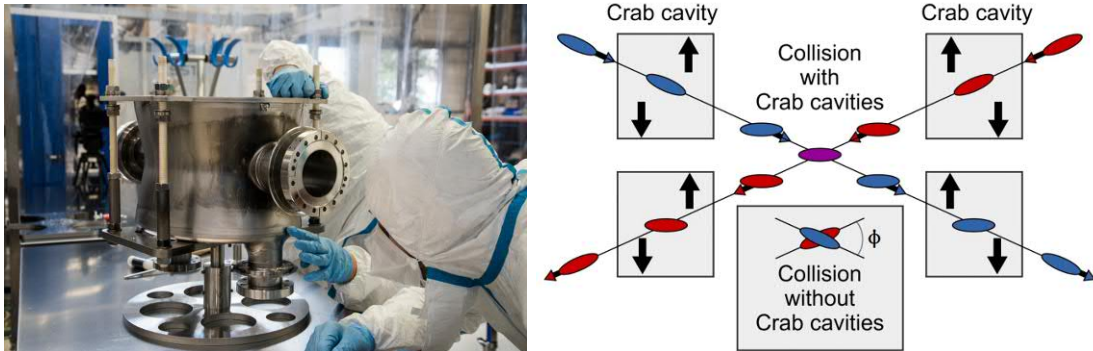


Figure 1.8: (Left) Niobium Crab cavity under construction in a clean room at CERN. (Right) Comparison of the collision crossing angle with and without Crab cavities.

Beam size

The second possible approach is to reduce the size of the beam, in this way the particles are concentrated in a smaller area. The HL-LHC upgrade will comprise 24 new quadrupole magnets that further increase the beam focusing at the collision points (Figure 1.9) to enhance the luminosity. The beam size will be reduced from 16.7 to $8.2 \mu\text{m}$, see Table 1.2.

The new quadrupole magnets, called MQXF, use special engineering techniques to withstand the enormous forces generated by the magnetic field (up to 13 T) in the Nb_3Sn coils. For example, they feature a thick aluminium external ring to profit from its higher thermal contraction with respect to steel, and compress the set-up while being cooled down to operating temperature (1.9 K). This is very important to keep the coils in place and to avoid movements that could generate heat compromising the superconducting state. The new quadrupole magnets are being developed in the framework of a collaboration between CERN and the LHC-AUP (LHC Accelerator Upgrade Project) consortium, which involves three US laboratories.

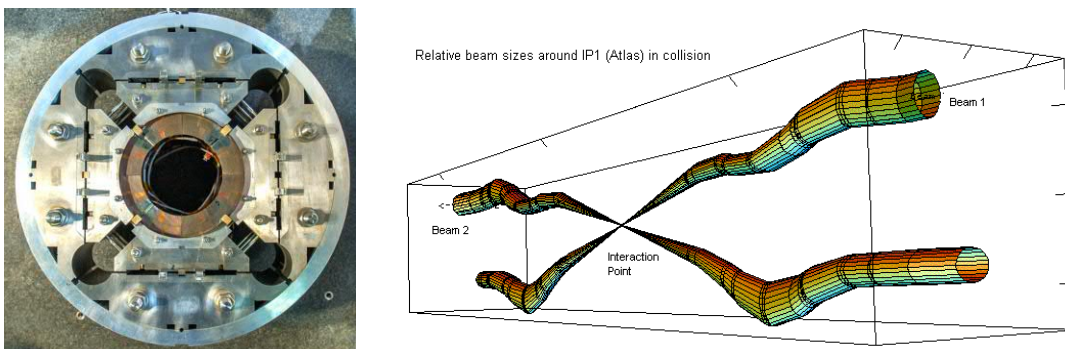


Figure 1.9: (Left) Cross section of the new MQXF quadrupole. (Right) Relative LHC beam sizes around ATLAS interaction point, showing the effect of the quadrupole focusing magnets.

Beam intensity

Another planned upgrade for the HL-LHC is the increase of the intensity of the beams, i.e. the total number of protons in each beam.

As the beam is made of charged particles, it is in fact an electric current flow. Therefore, the beam intensity translates into a circulating electric current (I), measured in Amperes.

The electric current is the rate at which the charge Q flows through a given surface over a time t :

$$I = \frac{dQ}{dt} \quad (1.9)$$

With $q_{proton} = 1.602 \times 10^{-19} C$ and LHC beam parameters (Table 1.2) the charge of a full LHC beam is:

$$2808 \cdot 1.15 \times 10^{11} \cdot 1.602 \times 10^{-19} = 5.17 \times 10^{-5} C \quad (1.10)$$

As it circulates 11245 times per second:

$$5.17 \times 10^{-5} \cdot 11245 = 0.58 C s^{-1} = 0.58 A \quad (1.11)$$

In fact, the actual beam intensity is measured by LHC operators from the beam current through dedicated current transformers, see Figure 1.10.

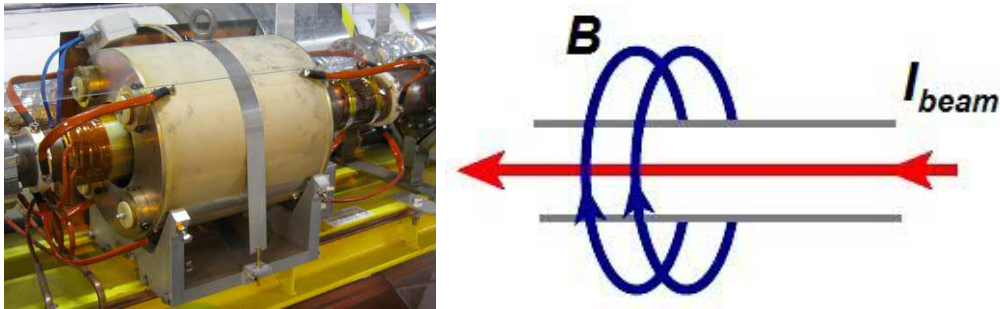


Figure 1.10: LHC Beam current transformer and physical mechanism (Ampère's law) [14]

The beam intensity in the HL-LHC will be almost twice that of the LHC, see Table 1.2. To reach this goal, extensive upgrades are needed in the LHC injector chain (SPS, PS, LINAC and proton source).

The increase in beam intensity involves a growth of the energy stored in each beam from 362 to 692 MJ at 7 TeV (Table 1.2). This design energy is equivalent to the energy of an Airbus A320 (66 ton) airplane travelling at 520 km/h concentrated in the diameter of a lead pencil.

The intensity of the beam has direct consequences on the collimation system, which will be exposed to loads in operation proportionally increasing.

HL-LHC project planning

The first HL-LHC upgrade, including part of the collimation system upgrade, will be installed during the "long shutdown 2" (LS2), starting in December 2019, see Figure 1.11. The full upgrade is foreseen to be completed by 2026.

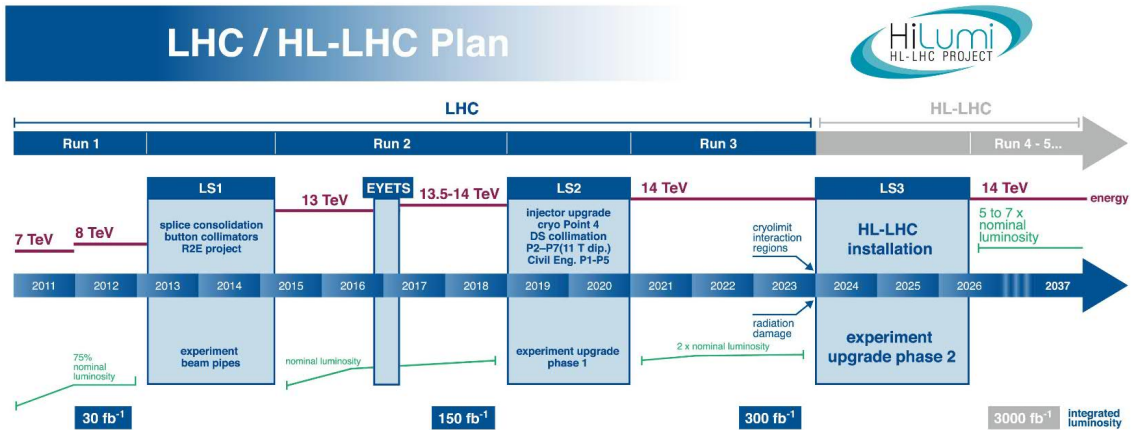


Figure 1.11: Long term plan for LHC

Future plans

The trend towards higher energies is set to continue in future studies such as the 100 km long *Future Circular Collider* (FCC), which has a projected stored energy of 8.4 GJ (Table 1.2).

In fact, after HL-LHC era, several projects to continue performing state-of-the-art physics experiments have been proposed.

High Energy LHC (HE-LHC) would require new and more powerful set of dipole magnets, in order to be able to increase the energy while using the tunnel already built for LHC (27km). The superconducting dipoles were the main budget item and a serious technological challenge of the LHC. To illustrate what the challenge was, 1232 dipoles with a cost of around 0.5 million CHF each were installed in the LHC in one year, see Figure 1.12. Annex A presents some of the technological details of the LHC dipole magnets.



Figure 1.12: The challenge of lowering 1232 dipole magnets to the LHC tunnel. Each dipole weighs 34 tonnes and is 15m-long. Technicians and engineers worked days and nights, carefully installing 20 magnets a week between March 2005 and April 2006. Once they have been lowered down through a single specially constructed shaft, they begin a slow progression to their final destinations in the LHC tunnel, taking about 10 hours to arrive at the furthest point on the LHC ring.

During the current HL-LHC upgrade, 4 new dipole magnets with a novel superconducting material (Nb_3Sn) will be installed for testing purposes. Nb_3Sn is an intermetallic material much more brittle than the current Nb-Ti metallic superconducting cables, requiring a very complex production process to fabricate the coils (5 times more expensive), but will allow to obtain higher magnetic field in the magnets, see Table 1.2.

Future Circular Collider (FCC) proposal, which is even more challenging, would require a new tunnel, much larger than the LHC (100 km), as well as all new accelerator equipment. The tunnel would surround the Salève mountain and would pass under the Lake Geneva, see Figure 1.13. FCC operating conditions, shown in Table 1.2, will cause even higher loads on accelerator equipment, particularly in the collimation system.

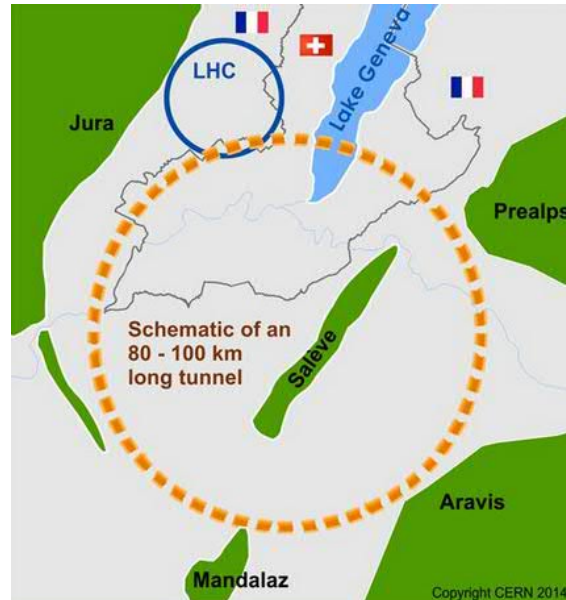


Figure 1.13: Schematic of the 100 km long tunnel for FCC proposal.

1.2 The collimation system

Collimation systems in particle accelerators are designed to absorb losses of highly energetic particles safely and efficiently during beam operation. This is done by intercepting stray particles in the absorber material of the collimator jaw; for this reason collimators are part of the so-called *beam intercepting devices* (BID) family. Other advanced technologies are being investigated to substitute or complement current collimation systems in the future, as described in Annex C.

A complex, multi-stage collimation system was designed to maximize robustness and cleaning efficiency, see Figure 1.14. Several types of collimators exist, using different absorbing materials, at varying proximity to the beam. Primary collimators, the closest to the beam, intercept the so-called primary halo particles, producing a shower of secondary particles and scattered protons which will eventually be absorbed by downstream collimators.

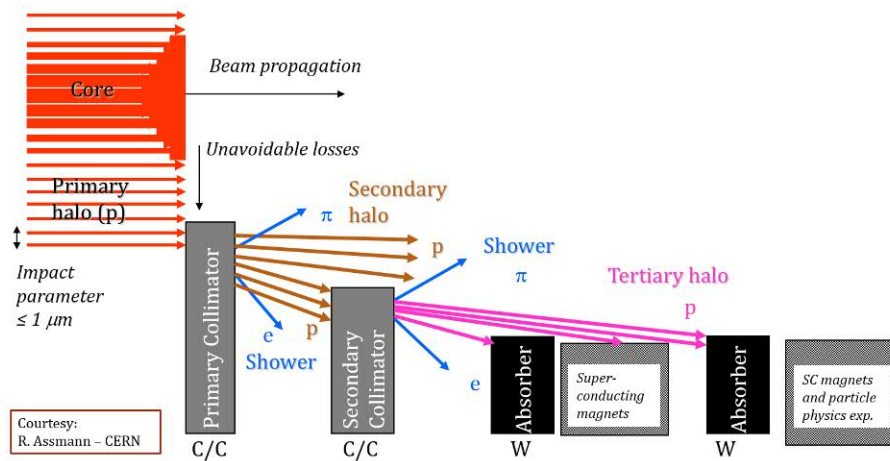


Figure 1.14: Schematic of the types and working principle of collimators

An important concept to understand the main functions of the collimators is the beam halo.

Beam halo

The spatial distribution of particles in a typical LHC particle beam fairly fits a Gaussian distribution, see Figure 1.15. The X-Y plane in this plot represents the cross-section of the beam bunch, while Z axis would be its travelling direction. The halo particles are typically defined as those with amplitudes above three standard deviations ($3\sigma_{RMS}$) of the Gaussian distribution, and the beam core is formed by the particles positioned less than $3\sigma_{RMS}$ away from the mean position, see Figure 1.16. Therefore, for a perfect two-dimensional Gaussian beam, the core accounts for 98.9% of the particle bunch and the halo for the 1.1%.

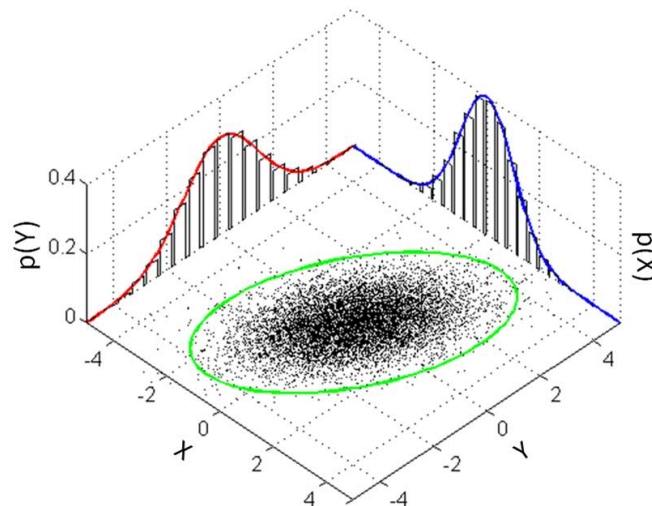


Figure 1.15: Example of multivariate Gaussian distribution, shown along with the 3-sigma ellipse.

The beam size (σ_{RMS}) depends on a number of factors, including the accelerator configuration (injection, top energy before and after squeeze, collision) and varies along the ring. It can be as small as $200\ \mu\text{m}$. The smallest collimator clearance at 7 TeV is 2.1 mm, see Figure 1.16 [16]. For a LHC beam with $\sigma_{RMS}=0.3\ \text{mm}$, the beam core, defined as $3\sigma_{RMS}$, would be within a diameter of 1.8 mm.

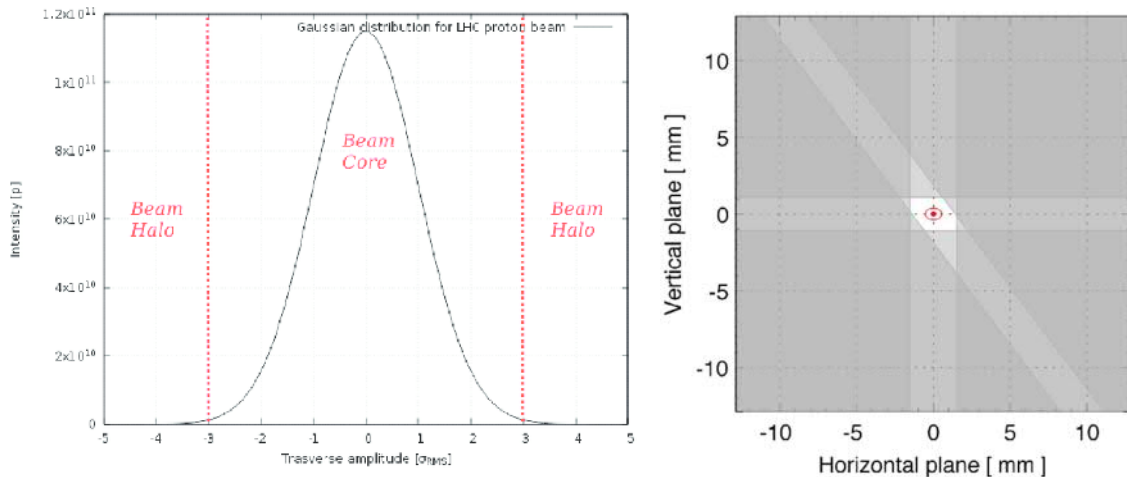


Figure 1.16: (Left) Core and halo definition for a particle beam with Gaussian transverse particle distribution. The intensity is defined as the number of particles (protons) [15]. (Right) Beam clearance for the LHC beams as defined by the primary collimator (vertical, horizontal and skew) gaps [16].

The primary collimators are designed to receive the impact of part of the beam halo in nominal operating conditions. In order to ensure optimum performance, the collimators' jaws need to be movable. The clearance of each collimator is actively adjusted with complex beam-based alignment procedures.

1.2.1 Functions of the collimators

The typical functions of collimator systems are [16]:

- **Cleaning of betatron and off-momentum beam halos:** halo particles must be intercepted and safely disposed of before they reach sensitive equipment, such as superconducting magnets.
- **Passive machine protection:** Collimators are the closest elements to the circulating beam and are the protection system in various possible accidental scenarios due to loss of control of the beam.
- **Cleaning of collision products:** In colliders, this is achieved with dedicated movable collimators located in the outgoing beam paths of each high-luminosity experiment, to catch the products of collisions.
- **Concentration of radiation doses:** in order to reduce radiation exposure personnel during maintenance, it is preferred to localize beam losses in confined and optimized 'hot' areas rather than having a distribution of many activated regions along the machine.
- **Local protection of equipment for improved lifetime against radiation effects:** The exposure of equipment to ionizing radiation might not pose immediate limitations to the operation of a machine but its optimisation is crucial to ensure long-term reliability.
- **Beam halo scraping and halo diagnostics:** Thanks to their robustness, the LHC primary collimators can be efficiently used to scrape and shape the beams. Full beam scraping also provides precise, though destructive, measurements of beam sizes.

Cleaning requirements

An ideal beam collimation would provide perfect cleaning, i.e., no beam losses would reach sensitive equipment. In reality, the *cleaning inefficiency* (η_c), can be introduced as the

relative fraction of beam that 'leaks' to other accelerator components (A_{lost}), compared with what is intercepted and safely disposed of by the collimators (A_{coll}) [16]:

$$\eta_c = \frac{A_{lost}}{A_{col}} \quad (1.12)$$

One of the most important tasks of the collimation system, as explained above, is to protect superconducting magnets. The magnet coils carry large currents, in the order of 12 kA, thanks to their superconducting state. If this superconducting state is lost, the coil becomes resistive and the large current suddenly produces an intense heating by Joule effect that could damage the coil. This is called a superconducting "quench". Safety systems are implemented to properly dispose of the electric current in case of quenches, however, they imply other issues. The loss of magnetic field produces undesirable deviations of the beam trajectory, and the Joule heating can produce boiling of the liquid helium bath. Quenches should therefore be avoided during operation with beams.

The superconducting magnets operating in the LHC at 7 TeV would quench if small amount of heat, on the level of $5 mWcm^3$, is generated inside the coils. This can be induced by a continuous loss of 700 protons per meter and per LHC turn [17]. Equation 1.13 presents the quench limits in units of proton lost per unit length (R_q) at 7 TeV [17].

$$R_q = 7.8 \times 10^6 p \cdot m^{-1} \cdot s^{-1} = 7 \times 10^2 p \cdot m^{-1} \cdot turn^{-1} \quad (1.13)$$

By expressing the quench limits in the approximate formulation of eq. 1.12, one can derive a specification for the local cleaning inefficiency as:

$$\eta_c \leq \frac{1}{10000} = 0.01\% \quad (1.14)$$

Therefore a cleaning efficiency better than 99.99% is required in the LHC collimation system [16].

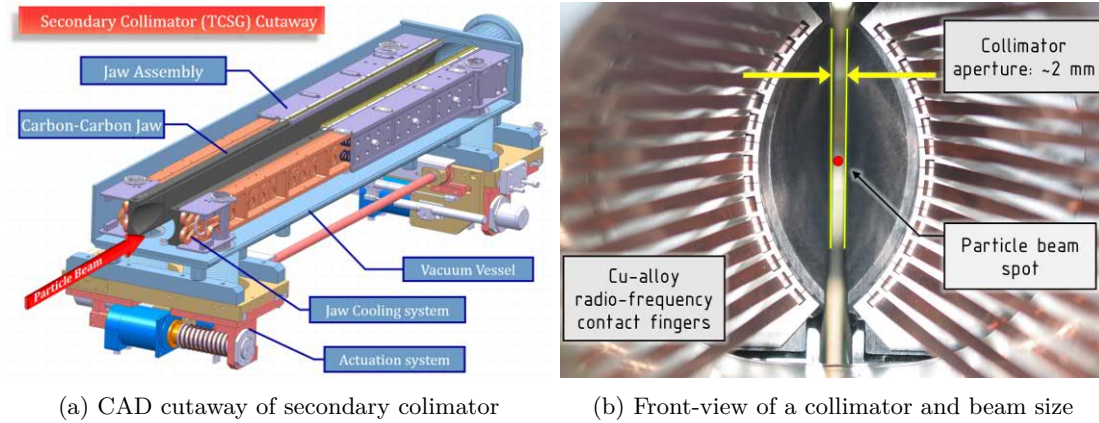
1.2.2 Design of LHC collimators

Collimators must fulfil all the functions described in section 1.2.1. In order to do that, they rely on different collimator absorber materials, depending on their function and loading conditions.

The design of the LHC collimators relies on two movable girders, known as jaws, hosting the absorber material. The jaws have to maintain the required tight tolerances and straightness, and they also include the cooling system for the absorber materials. The absorber material housings are typically made in Glidcop[®] Al-15 alloy [18]. It consists in a copper alloy strengthened with dispersed fine alumina particles, having thermal properties similar to copper, while, unlike copper, maintaining most of its mechanical properties at high temperatures. Water cooling pipes are brazed with a silver-based alloy to this structure at $\sim 800^\circ\text{C}$ to ensure very good thermal conductance.

Figure 1.17a presents a 3D sectioned CAD model of a LHC secondary collimator with Carbon Fibre-reinforced Carbon (CFC) absorbers. Figure 1.17b depicts the front view of a collimator illustrating the beam size and figure 1.18 presents an actual collimator in LHC tunnel. There are also collimators that clean the beam in other directions, such as vertical or skew collimators, see Figure 1.16.

Figure 1.17



The LHC collimators were designed to withstand the highest possible loading conditions, corresponding to an energy deposition in the order of 25 kW over several seconds [19].

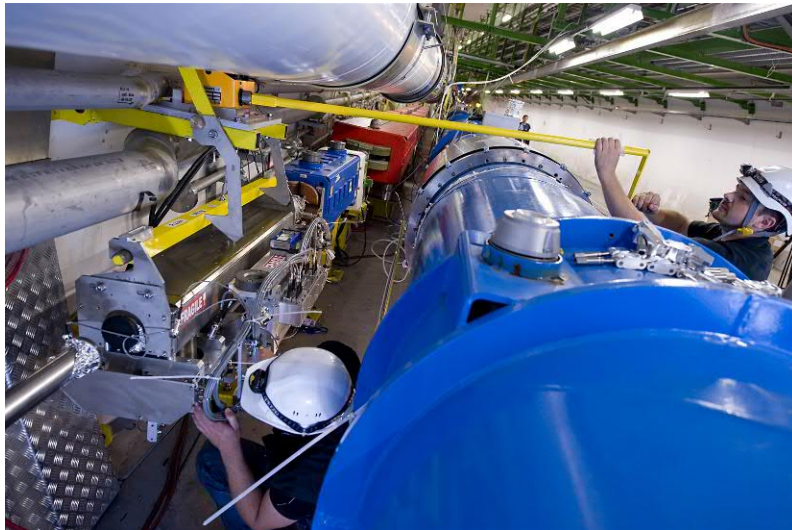


Figure 1.18: Installation of a collimator in a LHC injection line (23 June 2009).

1.2.3 Design of HL-LHC collimators

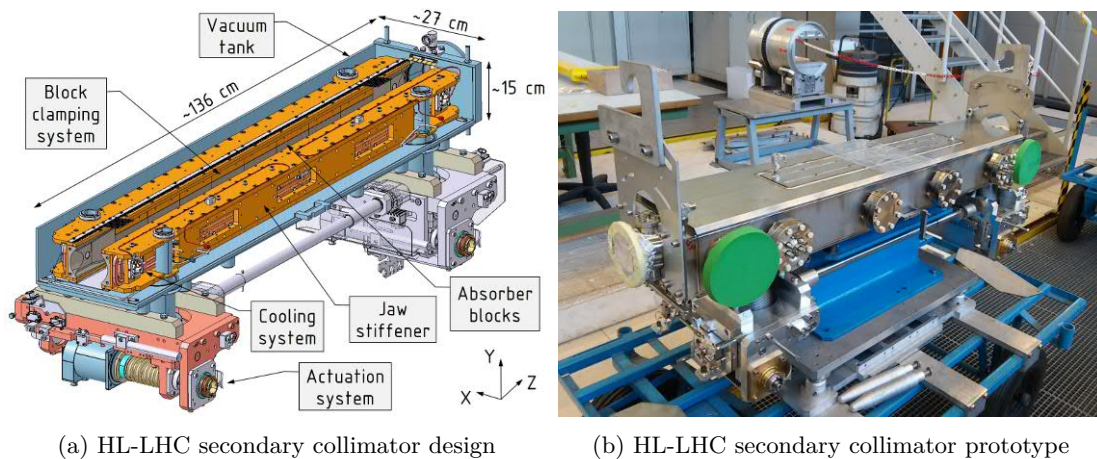
The HiLumi Upgrade (HL-LHC), in particular the increase in beam intensity, will compromise the correct operation of the collimators presently installed in the LHC, see section 1.1.4. For this reason, several units are being replaced by new and more performing devices.

The design of the new HL-LHC collimators is based on the successful design of LHC collimators. Absorbers for the new primary and secondary collimators are made of composite materials produced by hot-pressing techniques. Unlike CFC absorber blocks, which were produced in the form of long bars (around 1.2 m), the new materials cannot be produced in such long pieces. The 1 m active jaws is made of 8 separate absorber blocks. Due to the brittleness of ceramic composites, the blocks cannot be screwed to the GLIDCOP[®] AL-15 housing: a clamping system was therefore integrated [20].

In comparison with the present collimator design, the main differences are [20]:

- The clamping force is now provided by screws instead of springs, with higher contact pressure at the GLIDCOP[®]/MoGr interface (18 bar vs. 3 bar).
- A modified back-stiffener is increasing the rigidity of the jaw.
- The brazing between cooling pipes and stiffener is no more foreseen, simplifying manufacturing.
- Stand-alone, taperings that can be made of MoGr are used to decrease the energy absorption compared to the Cu ones.
- Beam Position Monitors (BPM) are embedded, to speed up the alignment procedure and improve the efficiency of the machine.
- A number of thermal probes is added to the cooling circuit, to better monitor water heating in case of abnormal operation.

Figure 1.19



3D maps of the energy deposited in every location of the collimator were calculated for every impact scenario, relying on the FLUKA Monte Carlo code. With the energy deposition map, one can perform Finite Element Method (FEM) thermo-mechanical calculations to understand how the device will behave, in order to validate or to modify the design (Figure 1.20) [21].

The beam impact duration varies with the different scenarios, inducing different effects in the collimator. In fast accidental impacts ($< 50\mu s$), the heat diffusion time within the structure is significantly longer than the energy deposition duration. Accidental impacts on the absorber material, such as the beam injection error [22], generate a rapid temperature increase which can induce dynamic stresses potentially harmful for the material core and for the bulk/coating interface. [16, 23, 24].

The knowledge of the material properties and their temperature-dependence is needed to perform the FEM simulations. For this reason, collimator absorber materials require comprehensive characterisation campaigns.

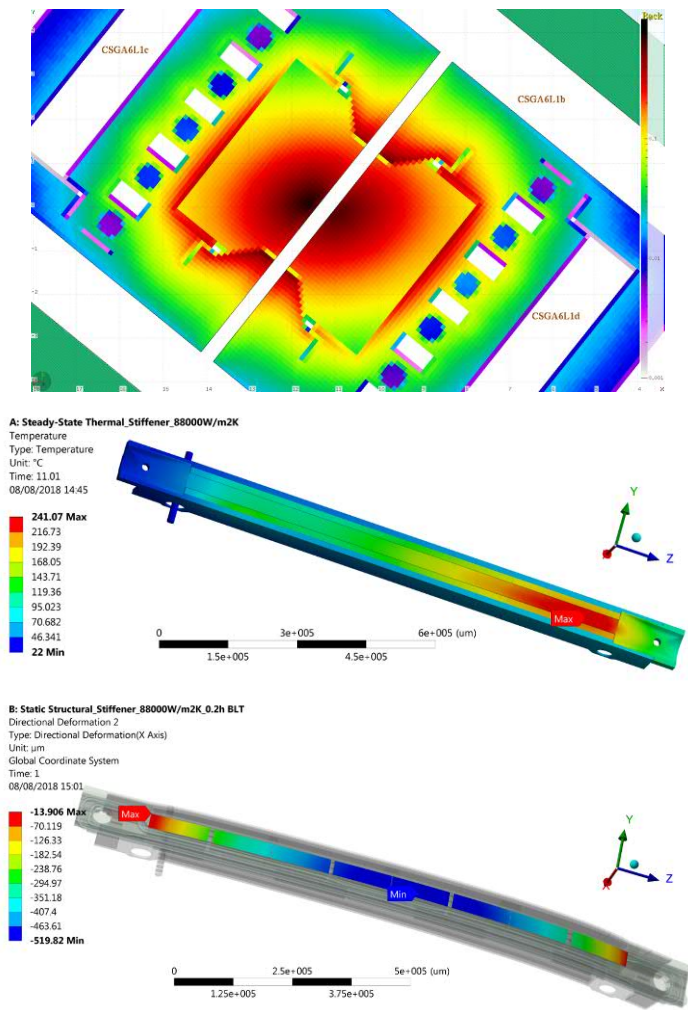


Figure 1.20: Example of collimator design validation iteration.

1- The 3D map of energy deposition is calculated with FLUKA for a particular collimator design and impact scenario. The FLUKA map needs to be recalculated if there are changes in the materials or in the design. This map is the input for the next step.

2- The FEM thermal calculation performed with ANSYS software identifies the maximum temperature reached at every point. This requires good knowledge of the material properties, the cooling system conditions and the thermal conductance between the different pieces. In this example, the peak of 241°C occurs in the last absorber blocks, as the beam enters from the left side.

3- The temperature map is used to obtain the deformation map. Again, this requires the material properties of all involved parts, specially thermal expansion coefficient and elastic modulus. In this example, the jaw deflects around $500\mu\text{m}$ towards the beam, exceeding the specification ($150\mu\text{m}$), so the design needed to be revised.

1.3 Materials for collimators

This section describes each of the individual requirements that materials must fulfil to be qualified as absorbers in collimators. At the end of the section, figures of merit are introduced in order to facilitate the comparison of different materials.

1.3.1 Requirements of materials for collimators

The following set of parameters should be optimized in materials to be used in collimator absorbers:

- Maximize electrical conductivity
- Maximize thermal conductivity
- Minimize thermal expansion coefficient
- Maximize melting/degradation temperature
- Maximize specific heat
- Maximize strength and strain to rupture
- Minimize elastic modulus

- Select adequate density (stopping power)
- Maximize radiation hardness
- Minimize outgassing rate
- Ensure industrial feasibility

Electrical conductivity

Each charged particle in a beam creates in its surroundings an electromagnetic (EM) field that will affect other particles. When the beam passes in the vicinity of physical components such as collimator jaws, those self-generated fields couple with the structure and give rise to the so-called *beam-coupling impedance*, which can be seen as the response function, in the frequency domain, of the structure to a travelling point-like particle. In time domain we rather speak about wake functions or potentials. One can usually distinguish two parts in the beam-coupling impedance, that can be computed independently most of the time. One part is due to geometric features around the beam, such as edges, tapering, or cavities. These create a contribution of two different kinds depending on the type of geometric feature: smooth geometric features (such as jaw tapering) typically create a broad-band impedance; cavity-like geometries can create some resonant peaks due to so-called trapped modes which are typically waves reflected back and forth, giving rise to long-ranged wake fields in time domain. Both contributions can be cured or at least attenuated (small angle tapering in the first case, lossy materials, such as ferrite, adequately placed in a cavity for the second case). The second part of the beam-coupling impedance is due to the electrical resistivity of the materials and to their distance from the beam. This part, when omitting its perfectly conducting part, is usually called *resistive-wall impedance* [15, 25].

Collimators are the closest devices to the beam: in fact, they represent the main source of beam-coupling impedance in the accelerator. Since their distance from the beam cannot be increased, the only possibility to reduce their contribution to the total resistive-wall impedance is to choose materials with the highest possible electrical conductivity.

Radio-frequency (RF) interactions between the beam and the surrounding materials are typically confined in a (relatively) thin material layer below its surface, called skin depth: this is the region where high electrical conductivity is mostly needed. The skin depth is inversely proportional to the square root of the EM frequency. The frequency of the electromagnetic fields generated by the beam in the LHC are in the order of 1 GHz. It is thus possible to apply a highly conductive thin-film to the collimator jaw materials to further reduce their resistive-wall impedance. However, thin-film materials must be selected carefully, as the same requirements of the substrate apply.

Thermal conductivity

High thermal conductivity is required to minimize temperature gradients, which may lead to unacceptable thermal deformations and to limit temperature peaks which may cause material degradation or excessive outgassing rates.

Thermal expansion

Low thermal expansion coefficients are required to limit thermal deformations and to reduce the effects of thermal shocks.

Mechanical properties

High strength and strain to rupture are desired to prevent the failure of the component under extreme loading conditions, including thermal shocks.

Industrial feasibility

The LHC collimation system is composed of hundreds of collimators. It is therefore required to ensure the feasibility of the industrial production process, at a reasonable cost.

Outgassing rate

The collimators jaws are placed in direct vicinity of the particle beam, which require ultra-high vacuum (UHV) conditions (down to 10^{-10} mbar) in order to avoid undesired collisions between beam particles and gas molecules, so that the lifetime of the beam at the available pumping speed does not fall below 100 hours [26]. This level of vacuum imposes that each collimator unit maintains a maximum outgassing rate of $2 \cdot 10^{-7}$ mbar l s⁻¹. For the collimator absorber materials, this translates in outgassing rates lower than 10^{-12} mbar l s⁻¹ cm⁻² at room temperatures.

Radiation resistance

The term *radiation hardness* refers to a material or device that is able to withstand certain dose of (ionizing) radiation without major degradation of its pristine properties.

Annex D describes in detail the different types of radiation and the mechanisms of radiation damage. The different macroscopic radiation damage effects include hardening, changes in physical properties, swelling, release of elastic stress, increased corrosion rates, radiolysis, phase transformations and thermal fatigue.

All the materials present in BIDs, including collimator absorber blocks, are intrinsically subjected to radiation because of their proximity with high energy particle beams, with the risk of suffering these radiation damage effects. For this reason, they are required to be radiation resistant, at least for the radiation type and doses that they will receive during their design life.

Stopping power

Stopping power is defined as the energy loss per unit of length of a particle while interacting with matter. As the main function of the collimators is to dispose losses of particle beams, the absorber blocks must possess sufficient stopping power to do it within the length of the collimation system installed: ensuring the required cleaning efficiency. However, too high stopping power is not beneficial either, as the energy deposition per unit of volume is increased proportionally leading to excessive temperature increase.

Particles and photons deposit energy in the materials while interacting with their atoms. The mechanism in particle radiation is mainly due to the elastic interactions described in annex D. Once the kicked nuclei stop moving in the lattice, the excess energy is kept as vibration energy (thermal energy), producing a local temperature increase. With high energy particle irradiation, this temperature can reach several thousands of degrees around the affected atoms, which is then dissipated macroscopically through the lattice by thermal conduction mechanisms. These extremely high temperatures are often above the melting or vaporization temperature of the material. The affected atoms thus form

nano-areas in fluid state which then can reattach to the lattice once the temperature peak is dissipated.

The amount of deposited energy per unit of volume mainly depends on the material stopping power for the specific radiation type and the irradiation energy. It is important to note that is not possible to analytically calculate the stopping power of a material for particle beams with TeV energies. This is because the beam is composed of billions of energetic particles that produce many physical reactions such as displaced atoms, elastic and inelastic interactions, showers of subatomic particles, etc, including physical processes that are not deterministic. The sum of all these effects in terms of deposited energy, can be obtained using Monte Carlo simulation codes that model all the relevant interactions (such as FLUKA), an example is presented in Figure 1.20.

The stopping power of materials can be benchmarked with the *geometrical radiation length* X_g , see equation 1.15, where A is the atomic mass, Z is the atomic number and ρ is the density. This gives an indication of the penetration depth of the energetic particle. The radiation length X_0 figure is a characteristic of materials related to the energy loss of high energy (charged) particles electromagnetically interacting with it. Besides, the denser is the material, less free space there is between the atoms, therefore collisions with particle radiation are more likely. Density thus plays a major role in the stopping power.

$$X_0 = \frac{716.4 \cdot A}{Z(Z+1)\ln\frac{287}{\sqrt{Z}}} g \cdot cm^{-2} \quad X_g = \frac{X_0}{\rho} cm \quad (1.15)$$

The values of radiation length for several relevant materials are shown in table 1.4.

1.3.2 Figures of merit

To classify and rank potential collimator absorber materials against the large number of requirements, it is useful to define *figures of merit*. They permit several material properties related to the specific requirements to be condensed into a single indicator: the higher the figure of merit, the better the performance [27].

However, one must be aware of the fact that these figures of merit rely on simplified, constant, linearised, temperature-independent material properties and on approximations of certain factors, such as the energy deposition or the effect of the anisotropy. Hence, they should be used only as indicative, comparative tools and not for quantitative assessment of material or component performance.

The three most relevant figures of merit for materials for collimators are related to:

- Thermomechanical robustness
- Thermal stability
- Radio-frequency impedance

Thermomechanical robustness index

The thermomechanical robustness index (TRI), is proposed to assess the material robustness against rapid localised thermal deposition (particle beam impacts) [27]. Given that thermal shock problems are, to a large extent, governed by the thermal deformation induced by a sudden temperature change, it appears reasonable to base this index on the ratio between material admissible strain (which for brittle materials one can take as the strain to failure) ε_{adm} and the actual strain.

The temperature increase ΔT_q can be assumed to be equal to a reference quasi-instantaneous energy deposition q_d , assumed to depend on the geometric radiation length

X_g and the material density ρ , divided by the specific heat c_p . T_m is the melting temperature, R_M is the failure strength, C_R an arbitrary scaling factor and m a coefficient related to the material loss of strength with temperature increase.

$$\Delta T_q = \frac{q_d}{c_p} = \frac{C_R \rho}{c_p X_g} \quad (1.16)$$

$$TRI = \frac{\varepsilon_{adm}}{\varepsilon_{ref}} \left(\frac{T_m}{\Delta T_q} - 1 \right)^m = \frac{R_M c_p X_g}{E(1-\nu)\alpha C_R \rho} \left(\frac{T_m c_p X_g}{C_R \rho} - 1 \right)^m \quad (1.17)$$

The TRI is similar to the well known *thermal shock resistance* index (TSR), but specific to beam impact scenarios, see equation 1.18, where k is the thermal conductivity, R_M is the strength to failure, α is the Coefficient of Thermal Expansion (or CTE) and E is the elastic modulus. However, note that in the TRI k is not relevant, as there is no time for thermal conduction in the rapid beam impacts.

$$TSR = \frac{k R_M}{\alpha E} \quad (1.18)$$

Thermal stability index

The thermal stability index (TSI) gives an indication of the ability of the material to maintain the geometrical stability under steady-state thermal loading (particle losses) [27]. This is particularly important for components such as collimators, which are required to interact precisely with the halo of the beam, maintaining a tight longitudinal straightness tolerance.

$$TSI = \frac{k X_g}{\alpha C_s \rho} \quad (1.19)$$

Radio-frequency impedance index

The last index is the radio-frequency impedance (RFI) index [27], which relates to the material contribution to the accelerator resistive-wall impedance, see section 1.3.1.

$$RFI = \sqrt{\frac{\gamma_e}{\mu_r}} \quad (1.20)$$

where γ_e is the electrical conductivity and μ_r the relative magnetic permeability.

1.3.3 State of the art of materials for collimators

As described in previous sections, the set of loads on collimator absorber blocks challenges the selection of adequate materials. Primary and secondary collimators, the ones that operate closer to the high energy particle beam, use graphite-based absorber materials. Graphite features a unique set of properties that fits this application: low density, good electrical and thermal properties, low thermal expansion, excellent thermal and chemical stability, good thermal shock resistance, and decent mechanical properties. Depending on the microstructure, its anisotropy complicates its engineering integration, but still, no other element in the periodic table surpasses the convenience of the graphitic form of carbon for the most loaded collimators.

In this section, the materials presently employed in LHC collimators and the materials that are under consideration for the HL-LHC upgrade are introduced. At the end, the Figures of Merit are used to benchmark the materials.

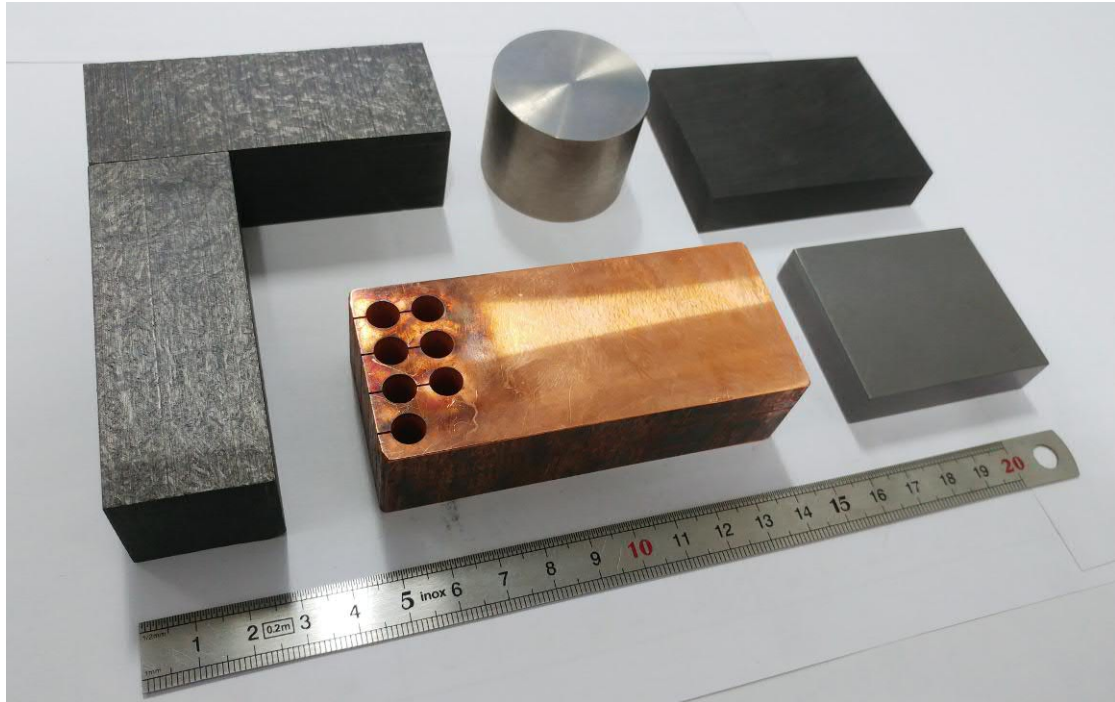


Figure 1.21: Materials currently used in collimator absorber blocks: (left) CFC AC150K, INERMET®180 cylinder (W-alloy), (top right) Graphite R4550 , GLIDCOP® Al-15 (Cu-alloy), MoGr (bottom right).

Isotropic graphite

Several BID at CERN, like the beam dump, see annex A, use isotropic polycrystalline graphite blocks, often called simply *graphite*.

Artificial graphite is made with carbon fillers and binders. The typical filler is powder of grounded natural graphite. The binders are usually forms of carbon pitch, extracted from distillation of crude oil or coal. The two components are mixed together, and heated above pitch softening point (around 200-300 °C). Then the preforms are shaped with different techniques; this forming step defines the final properties. Isostatic compaction results in isotropic properties, while extrusion forming gives a preferred orientation to the grains, leading to anisotropy. The compacts are then heat treated above carbonization temperature (around 1000 °C), which decomposes organic compounds of the pitch into carbon by releasing volatiles through the pores. This process is made slowly, as the internal gas pressure can crack the material.

The last production step is typically the graphitisation treatment. The piece is graphitised at high temperature (2200 °C, typically more than 2600 °C) to transform the disordered carbon into graphite. Nuclear grade graphite has a further purification thermal treatment in chlorine atmosphere to remove impurities.

Isotropic graphite grades used at CERN are R4550 and R7550 from SGL (Germany). Grade R4550 is a fine-grained isotropic nuclear graphite grade with an apparent density of 1.83 g/cm^3 , so its volumetric porosity is around 19%. Figure 1.22 shows Scanning Electron Microscopy (SEM) observations of R4550 grade, with visible randomly oriented graphite flakes. The sample surface is milled and cleaned with sonication in ethanol. Note also

the porosity, with pore size up to $50\ \mu\text{m}$. This material is characterised for comparison purposes, see Section 5.2.

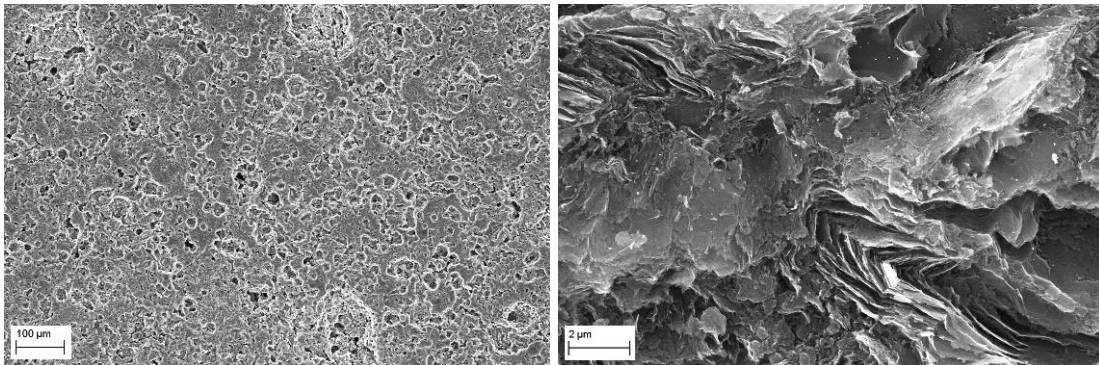


Figure 1.22: SEM of graphite R4550 at different magnifications (milled + sonicated surface).

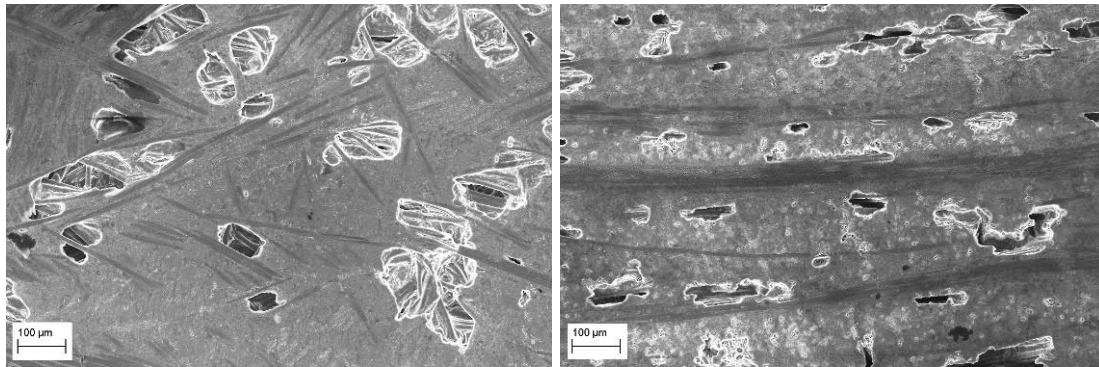
Carbon-fibre Carbon (CFC)

LHC primary and secondary collimators are made of Carbon fibre-Carbon (CFC) absorber material. CFC is a composite material entirely made out of carbon. It consists of a graphite matrix reinforced with carbon fibres, so it features the same extraordinary thermal and chemical stabilities of graphite, but with improved mechanical properties thanks to the fibres. In gross, CFC is made as artificial graphite with the inclusion of carbon fibres.

The CFC grade AC150K was produced by Tatsuno Co., Ltd (Japan) with carbon fibres roughly $5\ \text{mm}$ long randomly oriented in 2D stacked layers. Figure 1.23 shows the SEM observation of the material in two perpendicular orientations. Note the randomly oriented carbon fibres in the in-plane surface, and the pore size of up to $200\ \mu\text{m}$. This material had a rolling production step and was heat treated at very high temperature ($2800\ ^\circ\text{C}$) for graphitisation. This treatment is made to develop a high quality graphitic structure, which enhances the thermal and electrical properties. Typical 2D CFC's have transversely isotropic properties, but, due to the rolling process, AC150K grade has slightly better properties in the rolling direction, thus having orthotropic properties different in the 3 directions.

This material withstands beam impacts without significant permanent damage for the worst LHC failure cases, such as impacts of a full injection batch of $288 \cdot 1.15 \times 10^{11}$ protons at 450 GeV (Beam injection error) and of up to 8 bunches of 1.15×10^{11} protons at 7 TeV (Asynchronous beam dump) [18].

Figure 1.23: SEM of CFC AC150K (polished surface).



(a) In-plane surface

(b) Through-plane surface

Metals and alloys

Metallic absorbers are used only in tertiary collimators. Tertiary collimators are further away from the beam, complementing the work of primaries and secondaries. This thesis is focused in the materials for the latter, so metals and alloys are not investigated. The only metal having properties appealing for the first-stage collimators is beryllium [27]. Unfortunately, extensive use of this light metal is severely limited by its toxicity.

Tertiary absorber blocks are made of dense tungsten alloy (INERMET[®]180) or Al_2O_3 -dispersion strengthened copper (GLIDCOP[®]Al-15), in order to maximize stopping power. At the same time, they do not have high beam impact robustness, so they can work only after the primaries and secondaries have filtered out most of the particle losses.

Figure 1.25 shows the sample holder after beam irradiation, as part of an experiment performed in 2012 at CERN HiRadMat facility [28]. In that experiment, named HRMT-14 [29], samples of different materials were impacted with 440 GeV proton beams of various intensities to benchmark material response against simulations. The densest material used at CERN in collimators, also tested in HRMT14 experiment, is INERMET[®]180, with a density of $18 g/cm^3$, see Figure 1.24. It is composed of 95 wt% W, 3.5 wt% Ni and 1.5 wt% Cu. The Cu-Ni matrix increases by a factor of 10 the strain to rupture (ductility), from 0.2% in pure tungsten to around 2-3%. The W-grains are partially sintered, which allows keeping high elastic modulus and strength. Relatively low intensity beam impacts in INERMET[®]180 were enough for creating a 1 cm diameter hole by extensive melting of the Cu-Ni matrix.

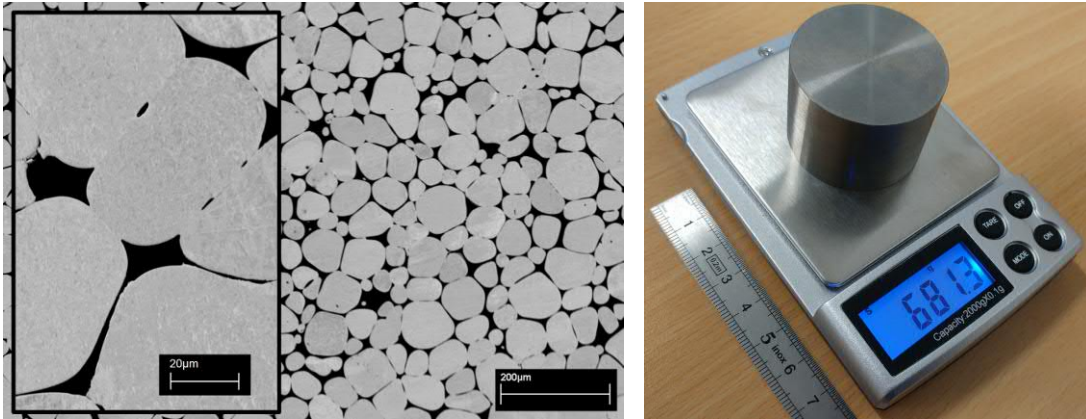


Figure 1.24: (Left) Microstructure of INERMET[®]180 by SEM backscattered electron detector: bright grains are tungsten and dark areas are the Cu-Ni matrix [29]. (Right) Weight of a cylinder of INERMET[®]180 alloy with size $\varnothing 40 \times 30 \text{ mm}$: 681 g.

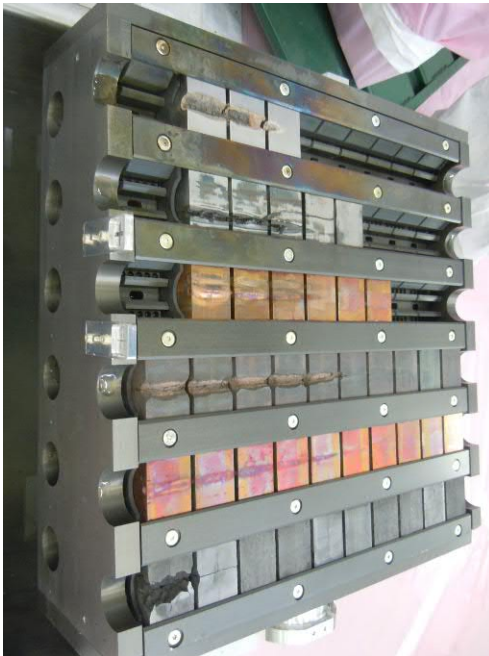


Figure 1.25: HRMT14 sample holder, extracted from the containment tank about two years after the experiment, to allow radiation cooling-down. The samples were half-cylinders of $\varnothing 40 \text{ mm}$ and 30 mm height. From top to bottom: INERMET[®]180, Molybdenum, GLIDCOP[®] Al-15, Molybdenum-Copper-Diamond, Copper-Diamond, and Molybdenum-Graphite (three early grades). The densities are respectively: 18, 10.2, 8.9, 7.15, 5.25, 3.6-5.4 g/cm^3 . Note that the beam was coming from the right side of the picture; the shower of particles and scattered protons produces more damage in forward sections, up to certain distance where damage starts decreasing according to the stopping power of the material.

Coated graphite-based materials

The graphite-based materials that were used in the LHC for many years have as main limitation their low electrical conductivity. As explained in section 1.3.1, good electrical conductivity is mostly needed at the surface of the absorber blocks. This would allow the use of deposited thin-films with good electrical conductivity on top of isotropic graphite or CFC. This option is under investigation, with four material candidates for the coating: copper, molybdenum, titanium nitride (TiN) and titanium diboride (TiB_2). The last two are hard ceramic compounds, which are mainly used in the industry for protecting tools against wear, but at the same time exhibit good values of electrical conductivity, see Table 1.3. Figure 1.26 shows TiN coating tests.

Table 1.3: Physical properties of the coatings

	Cu	Mo	TiN	TiB_2
Deposition technique	Sputtering	Sputtering	CVD ($Ti + N_2$)	Sputtering
T_m ($^{\circ}C$)	1084.6	2623	2950 [30]	2980 [30]
ρ (bulk) g/cm^3	8.89	10.22	5.4 [30]	4.52 [30]
ρ_e (bulk) $\mu\Omega cm$	1.7	5	40 [30]	9.0 [30]
γ_e (bulk) MS/m	58.8	20	2.5 [30]	11.1 [30]
γ_e (coating) MS/m		4-16	≈ 2	0.2-0.6

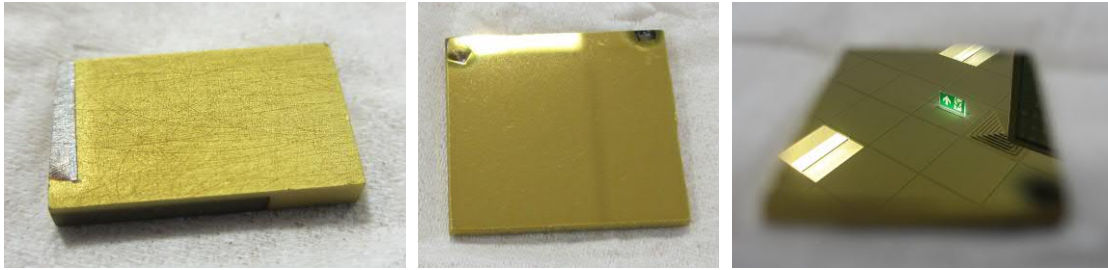


Figure 1.26: Coating tests of TiN ($5\ \mu m$) on (left) MoGr MG-6530Aa (10x15 mm), and (centre/right) glass (25x25 mm). Note how the substrate roughness defines that of the coating; the smooth surface of glass produces a perfect TiN mirror that allows to see the roof, while the sanding scratches on MoGr are still visible on the coating.

In general, the presence of an interface between different materials is a weak point. Adhesion tests have to be performed to assess the quality of the thin-film. Grazing beam impact tests have shown that the coating can locally peel-off due to the intense shock-wave generated [31]. For this reason, a substrate having high electrical conductivity is preferred in order to maintain adequate performance in that scenario.

The deposition parameters play a big role in the final properties of the coating, such as electrical conductivity. The grain boundaries obstruct the conduction of electrons, so small grains result in higher electrical resistivity. Impurities typically also increase the resistivity. It has been found from coating tests done at CERN that the roughness of graphite-based substrates affects the way the grains grow in the film, largely influencing the grain shape and the electrical properties. For these reasons the electrical properties of the thin-films are typically worse than those of bulk materials. The experimental values of electrical conductivity of Mo and TiB_2 coatings (7 and $2\ \mu m$ -thick respectively) in table 1.3 correspond to tests performed at CERN coating laboratory. TiN coating ($5\ \mu m$ -thick), see Figure 1.26 was performed by DTI (Denmark).

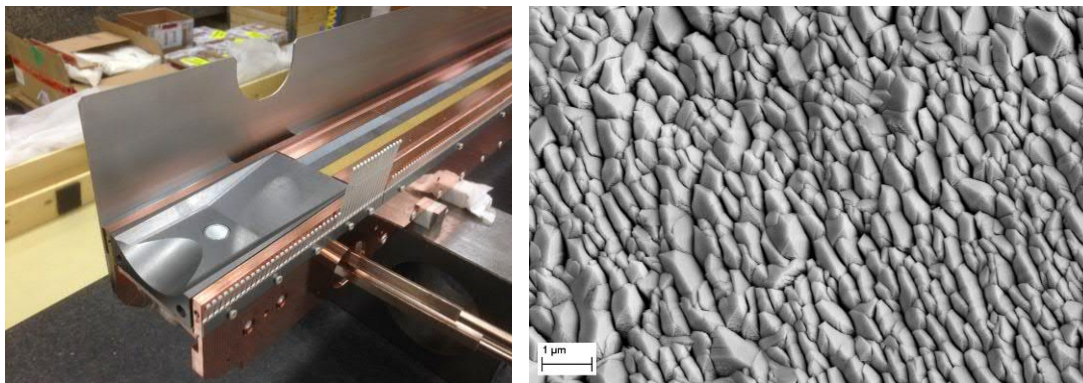


Figure 1.27: (Left) TCSPM collimator prototype before installation in the LHC. The jaw is made of MoGr absorber blocks coated with a strip of Mo and another of TiN for testing purposes. (Right) SEM observation of the surface of Mo film ($7\ \mu\text{m}$) deposited at CERN on MoGr MG-6403Fc.

Pyrolytic graphite (PG)

Other pure graphite-based materials such as forms of *Highly Oriented Pyrolytic Graphite* (HOPG) and *Pyrolytic Graphite* (PG) have been considered for the upgrade.

PG is obtained by thermal cracking of a hydrocarbon gas on a heated substrate, followed by a graphitisation process consisting of a very-high-temperature annealing [32]. The degree of crystalline alignment can be assessed by the *mosaic spread* (MS) or "c-axis orientation dispersion", which is measured with diffraction techniques [32, 33]. The term HOPG refers to PG with a mosaic spread lower than 1° that is obtained mainly by compression annealing [32, 34]. HOPG with mosaic spread as low as 0.2° can be achieved by uniaxial compression along the c-axis (up to 50 MPa) at about 3000°C [32]. The most aligned HOPGs are used in X-ray and neutron monochromators in diffractometers. Monochromators diffract a range of wavelength which is narrower as their mosaic spread diminishes, allowing to produce monochromatic beams.

Basal plane properties are extremely sensitive to structural defects. Accordingly, many properties of HOPG are scarcely affected by mosaic spreads variation in the range 0.2 to 5° , whereas other properties differ markedly from sample to sample, even in specimens with the same mosaic spread [34].

TPG (Thermal pyrolytic Graphite) is a commercial material, produced by Momentive Performance Materials, Inc. (US). It is produced by CVD by decomposition of methane gas at high temperature. TPG is a form of PG, therefore it is not expected to be as aligned as HOPG. However, the thermo-physical properties of TPG are very close to the best known oriented graphites, while being much more affordable. HOPG cost is in the order of hundreds of Euro per cm^3 , while TPG is close to $10\ \text{€}/\text{cm}^3$. As it is made by CVD process, its cost increases with the thickness of the sample in the graphite c-direction.

TPG was characterised for benchmarking purposes, see section 5.1. The samples analysed had thicknesses in the c-direction up to 10 mm.

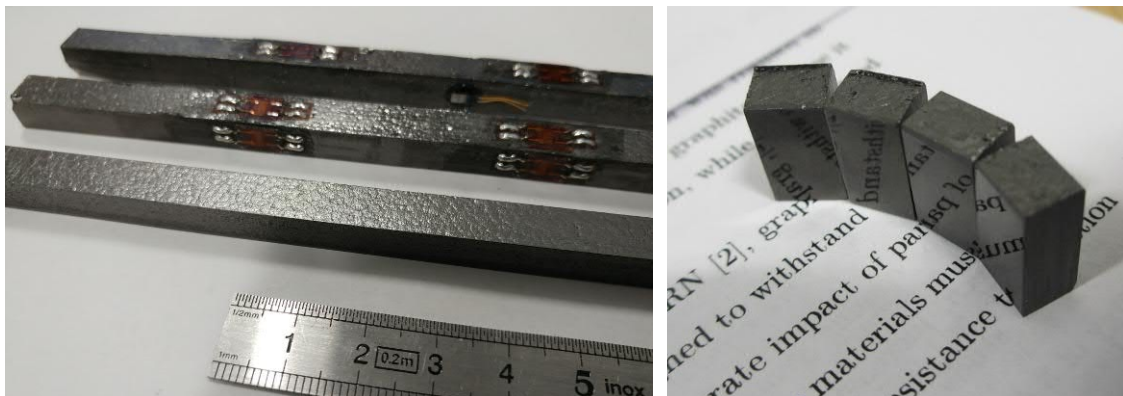


Figure 1.28: TPG samples. (Left) Samples instrumented for HRMT36 beam impact experiment ($247 \times 7 \times 5 \text{ mm}$). (Right) Polished through-plane surface, 10 mm-high samples, horizontal basal planes.

These materials have thermo-physical properties that exceed the requirements of collimator absorbers in the direction parallel to the basal planes; however, their poor intrinsic performance in the through-plane direction make them unfit for the HL-LHC collimators.

Graphite-carbide composites: MoGr

None of the graphite-based materials currently employed in the primary and secondary LHC collimators is predicted to fulfil all the requirements posed by the more severe working conditions expected in the HL-LHC: in particular, numerical simulations indicate that the limited electrical conductivity of graphite and CFC may induce electro-magnetic instabilities in the particle beam [35]. The uncommon combination of properties required may be potentially met by certain graphite-matrix composites, particularly those relying on *liquid phase* (LP) sintering.

In this context, an R&D program to develop materials fitting the requirements of HL-LHC collimator absorbers started in 2012 [29]. A family of graphite-matrix composites reinforced with molybdenum carbides (Molybdenum Carbide – Graphite, *MoGr*) was eventually co-developed by CERN and the Italian company Brevetti Bizz [36], partly within the EuCARD, EuCARD-2¹ and ARIES² collaborations, with the goal of increasing the electrical conductivity of collimator absorber materials, while maintaining or improving the beam impact robustness of currently adopted CFC jaws [29, 37].

A beam-impact experiment, named HRMT-23 (July 2015), see Figure 1.29, demonstrated the validity of the design of HL-LHC collimators with MoGr absorber blocks [20, 23, 38]. A collimator prototype using this novel composite material was manufactured and installed in the LHC ring in 2017. The replacement of 8 secondary and 4 primary collimators with new units having MoGr absorbers is on-going in 2019. Besides, 3 spare collimators will be produced. Each new collimator requires 20 blocks precisely machined, totalling 300 MoGr blocks.

¹<http://eucard2.web.cern.ch/>

²<http://aries.web.cern.ch/>



Figure 1.29: The three collimator jaws and the vacuum tank of the HRMT23 experiment. The top jaw is made of a single piece of CFC AC150K and GLIDCOP[®] Al-15 taperings, the middle one is made of MoGr blocks and taperings and the bottom one has copper-diamond blocks and MoGr taperings.

1.3.4 Benchmarking of the state-of-the-art materials

Table 1.4 shows the comparison of the figures of merit for several materials currently used at CERN in collimation systems. Stainless steel 316L is added for comparison purposes. Metallic alloys having densities larger than 7 g/cm^3 , such as GLIDCOP[®] Al-15 (Cu-alloy) or INERMET[®] 180 (W-alloy), have poor TRI and TSI, mainly due to their large stopping power and large CTE. For these reasons they are not compatible with primary collimators. On the contrary, they have high values of electrical conductivity, hence large RFI values.

CFC (AC150K) and graphite (R4550) have large values of TRI and TSI compared with metals. The composite material MoGr that has been developed specifically for collimators has slightly worse TRI than CFC or graphite. The TSI of MoGr is comparable to that of CFC. The biggest advantage of MoGr over the other two C-based commercial materials is its larger electrical conductivity, which almost reaches that of stainless steel.

Table 1.4: Figures of merit of several collimator materials. The relevant properties needed for their calculation are also shown.

	MoGr		CFC AC150K		R4550	GLIDCOP	INERMET	SS-316L
		⊥		⊥	Isotr.	Isotr.	Isotr.	Isotr.
ρ [$g\,cm^{-3}$]	2.5–2.6		1.89	1.86	8.75	17.94	7.95	
T_m [$^{\circ}C$]	2589		3650	3650	1083	1350	1400	
c_p [$J\,g^{-1}K^{-1}$]	0.6–0.65		0.71	0.71	0.39	0.15	0.45	
Z	6.6–6.8		6	6	28.96	67.66	25.5	
A	13.5–13.8		12.01	12.01	63.62	166.67	54.7	
γ_e [$MS\,m^{-1}$]	0.9–1.2	0.05–0.07	0.24–0.18	0.03	0.08	53.8	8.7	1.35
a [$mm^2\,s^{-1}$]	430–530	28–37	174–227	40	73	106	34	4
k [$W\,m^{-1}K^{-1}$]	650–900	45–65	233–304	54	100	365	91	14
α [$10^{-6}K^{-1}$]	1.7–2.7	8–12	-0.8	11	4.2	18.5	5.3	15
R_M [MPa]	60–80	10–12	105–140	10	60	375 (T)	683 (T)	515 (T)
E [GPa]	60–85	4–5	≈ 50	5	11.5	128	360	195
ε_{adm} [%]	0.18–0.26	0.45–0.72	0.14–0.2	0.43	0.7	10	3	40
X_0 [$g\,cm^{-2}$]	39–42		43.0	43.0	13.2	7.2	14.4	
X_g [m]	15–17		22.8	23.1	1.5	0.4	1.8	
ΔT_q [K]	2.4–2.9		1.5	1.5	57.1	646	40.6	
TRI	141–367		1362	3445	6.3	0.6	10.9	
TSI	43–73		47	23	0.9	0.1	0.1	
RFI	0.9–1.1		0.4	0.3	7.3	2.9	1.2	

1.4 Motivations and objectives of this thesis

Although MoGr materials have been sufficiently developed so far to meet the requirements of the new primary and secondary collimators for the first stage of the HL-LHC upgrade, there is an interest to reach even better properties. In fact, future accelerators that are expected to use particle beams with even higher energies and intensities, see section 1.1.4, will require even more performing materials.

The main objective of the thesis is to better understand the structure, the roles of the components and their influence on the properties of MoGr composite materials. It also aims at improving the understanding of the physical mechanisms at play in the production of graphite-matrix materials, particularly during sintering in presence of liquid phase.

Chapter 2 describes all the physical mechanisms involved in the production of graphite-matrix composites sintered in presence of liquid phase.

A correct understanding of these mechanism and effects is crucial for improving the performance of present and future composites. The most important properties of MoGr that should be further improved are described below:

Electrical conductivity

Graphite is a semimetal with equal numbers of electrons and holes. Electrical transport is caused by the diffusive motion of those charge carriers. They are accelerated by the applied electric field, within a certain distance, the mean free path, and after experiencing a collision with a scattering centre, are again accelerated by the electric field, and so on. The mean free path, a few interatomic distances for metals at room temperature (much shorter than the sample dimensions), prevents a single electron to travel from one side of

the sample to the other, as is the case for ballistic motion. The electrical conductivity γ_e (equations 1.21 and 1.22) is given by the sum of the partial conductivities of each group of charge carriers [39].

$$\gamma_e = qN\mu \quad \mu = (q\tau)/m^* \quad l = v\tau \quad (1.21)$$

where q is the elementary charge ($1.602 \cdot 10^{-19}$ C), N is the charge carrier density, μ the mobility (related to the relaxation time τ and the carrier effective mass m^*), l is the carrier mean free path and v the velocity of the charge carriers [40]. The conductivity can alternatively be written as:

$$\gamma_e = \frac{q^2 N l}{m^* v} \quad (1.22)$$

The carrier concentration at room temperature (RT) is $N_e = N_h \approx 1 \times 10^{25} m^{-3}$ [41] (3×10^{-5} per carbon atom [42]). Although the carrier concentration in graphite is so much smaller than that in metals, the electrical conductivity is relatively not so low because effective masses of the carriers in graphite are small in comparison to other semi-metals, the carriers being easily accelerated by an external electric field [42]. Carrier mobilities are presumably limited by impurities and by structural disorder (corrugation of basal sheets) [41].

The RT basal plane electrical conductivity in perfect graphite crystals is limited by acoustic phonon scattering. Real specimens contain also static lattice defects, which produce carrier scattering and reduce the mobility. The carrier mobility increases with decreasing temperature due to the freezing of phonons, both in metals and in graphite. However, carrier densities in metals are large and temperature insensitive, opposite to semimetallic graphite, where the carrier density (which depends on thermal activation) decreases at low temperatures. Besides, because of the very small values, carrier densities in graphite are also very sensitive to defects [39]. The mean free path of carriers in graphite, which is the distance between two scattering centres, may be directly related to the size of large scale defects (boundary scattering) [40].

The electronic properties of ideal graphite are actually not well known simply because defect-free graphite samples do not exist [43]. However, the typical resistivity value for high quality graphite crystals is $\rho_e \approx 40 \mu\Omega cm$ ($\gamma_e \approx 2.5 MSm^{-1}$) [41, 44, 45]. On the other hand, ideal graphene shows higher values due to the absence of interactions between basal planes, see Table 1.5. In fact, TPG (see section 1.3) has been measured by the author and found having an electrical conductivity of $2.4 MSm^{-1}$, see section 6.1.2.

Table 1.5: Electrical properties of graphite and single-layer graphene (thickness $0.33553 nm$), see equation 1.21. Graphene experimental results are limited by the (phonon) interactions with the substrate and by the impurities [45].

	Carrier mobility $\mu [cm^2 V^{-1} s^{-1}]$	Carrier density n cm^{-2}	cm^{-3}	Conductivity MSm^{-1}
Graphite, HOPG (298 K) [46]	11740	-	$1.35 \cdot 10^{19}$	2.54
Graphite, HOPG (77.4 K) [46]	63450	-	$4.25 \cdot 10^{18}$	4.3
Graphite, HOPG (4.2 K) [46]	1076000	-	$2.36 \cdot 10^{18}$	40.6
Graphene on SiO ₂ (298 K) [45]	10000	$1 \cdot 10^{12}$	$3 \cdot 10^{19}$	4.8
Graphene on SiO ₂ (77 K) [45]	10200	$1 \cdot 10^{12}$	$3 \cdot 10^{19}$	4.9
Suspended graphene (5 K) [47]	230000	$2 \cdot 10^{11}$	$5.96 \cdot 10^{18}$	22.0
Graphene theoretical limit (RT) [45]	~ 200000	$1 \cdot 10^{12}$	$3 \cdot 10^{19}$	≈ 100

It is important to note that the proximity of the RT mobility values for graphene and bulk graphite is a coincidence. Removing impurity scattering in graphene will greatly increase the low-temperature mobility as well as the RT mobility [45]. The fact that the mobilities in graphene coincide at RT and 77 K is proving that static defect scattering is the limiting factor.

Because of this, the Residual Resistivity Ratio (RRR) is often used to characterise the purity of a conductor material. The RRR is the ratio between resistivities at RT and at ≈ 0 K; the value $RRR = \rho_{e,298K} / \rho_{e,4.2K}$ is often used for practical reasons. As stated above, metals with no defects will have as limiting factor the phonon-carrier scattering, which tends to zero with decreasing temperatures. Therefore they possess high RRR. In metals for which widespread defects are the limiting factor, the RRR tends to unity, since this type of carrier scattering is temperature-independent. In graphite, the dependence is somehow more complex, because the carrier density slightly decreases with temperature, but the RRR is still a very good indirect method to quantify lattice defects. The very high quality HOPG presented in Table 1.5 shows RRR=16.

In fact, the graphite crystallite size can be estimated from the low temperature mobility, assuming that the crystallite boundaries are the main static defects. Graphite specimens presented in table 1.5 have basal crystallite size of $\sim 5 \mu m$ (average carrier velocity of $2 \cdot 10^5 m s^{-1}$ and effective mass of $0.04m_0$ were assumed) [46]. This is unusually large for HOPG, but in accordance with the annealing treatment ($\geq 3300^\circ C$), and the c-axis mosaic spread ($0.2-0.3^\circ$) measured with XRD.

Kish graphite shows even larger values of RRR, up to 106 [48]. This type of graphite is obtained by recrystallization from iron-carbon melts, having large lattice perfection but some metal impurities. Hishiyama and Kaburagi studied the electrical resistivity of three kish graphite specimens between 1.28 and 300 K. They reported RRR values of 16.7, 56 and 106 ($\rho_{e,300K}$: 0.407, 0.390 and $0.386 \mu\Omega cm$), which correspond to conductivities at 4.2 K of 41.0, 143.4 and $274.6 MSm^{-1}$ respectively [48]. The two best specimens were kish flakes not machined to prevent introductions of defects, while the one with RRR=16.7 was previously cut to facilitate the 4-wire electrical measurement.

Up to date, the highest electrical conductivity experimentally measured in graphite at RT is $2.5-2.6 MSm^{-1}$, shown above. This corresponds to the most probable limit that the graphite matrix could reach in the best conditions. It is a factor ≈ 2.5 larger than MoGr [37]. This leaves room for improvement in MoGr materials.

Thermal conductivity

Heat may be carried in solids either by the charge carriers or by lattice waves, the phonons. In pure metals it is mainly carried by the charge carriers. In graphite, owing to the small density of charge carriers, associated with strong covalent bonds and light lattice atoms, heat at RT is almost exclusively carried by the phonons [39, 49]. The large spacing in the c-crystallographic direction and the weak binding forces between basal planes lead to an almost two-dimensional character of the phonon dispersion curves. The thermal conductivity k in the basal plane of a single crystal is larger by a factor of 300, than in the c-axis direction. Null et al. studied the thermal conductivity between 300 and 2700 K and the mosaic spread (MS) of several pyrolytic graphites [50]. The results are shown in table 1.6. Note that despite the different levels of crystallite misalignment in the treated PG's, k does not change much (experimental error $\approx 5\%$). However, the crystallite conductivity is larger in the PG annealed at higher temperature, as shown by the larger macroscopic

values even with larger misalignment.

Table 1.6: Density, mosaic spread (MS), thermal diffusivity (a) and conductivity (k) of PG and HOPG at 300 K [50].

Material	ρ	MS [°]	a_{\parallel}	k_{\parallel}	a_{\perp}	k_{\perp}
PG, as-deposited at 2200 °C	~ 2.19	~ 45	194	306	1.5	2.4
PG annealed above 3200 °C	~ 2.25	~ 5	1135	1840	3.8	6.2
HOPG, stress-annealed above 3000 °C	~ 2.25	~ 0.4	~ 954	~ 1840	5.4	8.7

ρ in $g\,cm^{-3}$, a in mm^2s^{-1} and k in $W\,m^{-1}K^{-1}$

At room temperature, the highest predicted conductivity for graphite and graphene, for natural occurring carbon and for the isotopically pure case, are shown in table 1.7. Imperfections such as point defects (vacancies, substitutional and interstitial impurities, etc.) and boundaries (grain boundaries, porosity, specimen surfaces) produce phonon scattering and they are responsible for not reaching experimentally the ideal values of Table 1.7.

Fugallo et al. showed that the crystalline-domain size in a polycrystalline sample corresponds to the *extrinsic scattering length* (named L) for the heat carriers [51]. For grains without defects in their atomic lattice, the crystalline-domain size corresponds to the grain size (a more detailed explanation is presented in section 3.5.1). Their study also shows the longest mean free path of the heat carriers (L_{diff}), see Table 1.7. If $L > L_{diff}$, the intrinsic thermal conductivity reaches its thermodynamic limit. In other words, bigger crystalline-domain sizes than L_{diff} do not improve the thermal conductivity.

Table 1.7: Highest theoretical limit, at 300 K, of the lattice conductivity of graphite and graphene ($W\,m^{-1}K^{-1}$). Longest mean free path of the heat carriers L_{diff} [51]

	Graphite (\parallel)	Graphite (\perp)	Bilayer graphene	Single layer graphene
1.1% ^{13}C	2000	6.6	2200	3600
0% ^{13}C	2200	6.6	2500	4300
L_{diff} [μm]	10-100	1-10	10-100	100-1000

Although in metals, electrical and thermal conductivities are both governed by electron conduction, in graphite it is not the case. Therefore, it is in theory possible to tune them independently. For instance, the isotope concentration does not alter the electronic transport [51], but greatly affects the phonon conduction (see Table 1.7) due to the presence of different masses that vibrate in the same lattice. Nevertheless, it has been shown above that electrical conductivity is very much affected by phonon scattering, so the two properties are in practice related to each other.

Another factor to take into account is the anisotropy of the graphite crystals. A material with very aligned graphite grains is desirable if the maximum possible conductivity is required only in two directions. However, if isotropic properties are required, the graphite grains must be randomly oriented, which, using Table 1.7 values, would result in a theoretical maximum of:

$$k_{av} = \frac{2 \times k_{\parallel} + k_{\perp}}{3} = \frac{2 \times 2000 + 6.6}{3} = 1340\,W\,m^{-1}K^{-1} \quad (1.23)$$

This would require a fully compact body made of randomly oriented graphite grains,

big enough and defect-free to reach the conductivity limit. This is probably not realisable, because graphite only forms strong bonds at the edges of its basal planes. Furthermore, even if the bonds could be perfect, the ratio between in-plane and through-plane conductivities inside the crystallites can limit the macroscopic transport [52].

In any case, those figures show that graphite-matrix composites such as MoGr could, in the best conditions, be improved by a factor of two or more in terms of thermal conductivity, depending on the acceptable anisotropy level. The graphite matrix in MoGr represents more than 95 vol %, so the presence of other components can be neglected for this rough estimation.

Mechanical properties

Highly oriented and pure graphites, such as TPG material, in spite of the very strong atomic bond within graphite basal planes, possess mediocre in-plane mechanical properties. This is probably caused by delamination of the basal planes by shear stresses. The basal planes are kept together only by van der Waals forces, hence the strength in the through-plane direction is expected to be negligible.

However, MoGr composites show, with respect to TPG, a factor 2-3 improvement in the in-plane strength thanks to the presence of carbides within the graphite matrix [37]. Still, high-quality CFCs exhibit slightly larger overall strength to rupture thanks to their carbon fibre reinforcement. Besides, those CFCs have non-negligible porosity content (~ 15 vol%), much larger than MoGr. These facts demonstrate that the strength limit in MoGr composites has not been reached yet, and there is room for optimisation.

Most of the typical loads in beam intercepting devices are governed by thermally-induced deformations. Therefore, the strain to rupture of the absorber material is to some extent more relevant than the strength to rupture. The former property has to be maximized in this application.

Vacuum compatibility

Certain MoGr grades have shown limited ultra-high vacuum compatibility because of air outgassing rates above the specification for the LHC. To date, it seems that the presence of open porosity helps to have the required UHV compatibility [26]. However, porosity is detrimental for mechanical, thermal and electrical properties.

Production cost

MoGr is a material relatively expensive to produce, as it has to be manufactured by a hot-pressing technique at more than 2600°C, see Section 4.4. This is of paramount importance in case mass production is required. Smaller production costs may also imply better production control, because the complexity and duration of the process is reduced.

Other industrial applications

MoGr properties are very appealing also for applications beyond particle physics, such as thermal management in demanding environments as aerospace. However, some properties are overkill for most industrial applications, such as the melting temperature or the UHV compatibility. Other applications might require more isotropic properties or could tolerate denser composites. The detailed knowledge of the production process is fundamental for

an effective tailoring process.

Knowledge transfer is an important mission of CERN as an international organisation. The member states encourage CERN knowledge transfer activities, see Appendix B, as it returns the financial investment in the form of new technologies to the industries and eventually to the society. Most of the technological developments for physics applications find uses in the industry, in laboratories or in commercial devices. The materials for collimators are, due to their particular combination of properties, certainly appealing for other applications.

2 | Liquid phase sintering of graphite-matrix composites

This chapter describes the physical mechanisms involved in the production of graphite-matrix composites sintered in the presence of liquid phase (LP). The roles of the filler particles during production of the composites are described, the most important being the ability to dissolve carbon in liquid state. The practical application of these mechanisms in the LP production process is discussed. A survey is presented to select the optimal carbon solvent for producing successful composites. At the end, a summary is provided.

2.1 Physical mechanisms

2.1.1 Graphitisation

At pressures lower than 2 GPa, graphite is the most thermodynamically stable solid form of carbon, see carbon phase diagram (Figure 2.1).

Graphitisation is defined as the process in which carbon transforms into graphite, for thermodynamical reasons, see Figure 2.2. The distance between basal planes in graphite is an indicator of its graphitisation level. The ideal graphite crystalline structure exhibits an interplanar spacing d_{002} of 3.3553 Å ($c = 6.7106$ Å) [53]. Defects such as intercalated foreign atoms or corrugation of basal planes (turbostratic structure) enlarge d_{002} . The higher the graphite quality, the smaller the d_{002} . d_{002} smaller than 3.3553 Å are not thermodynamically stable.

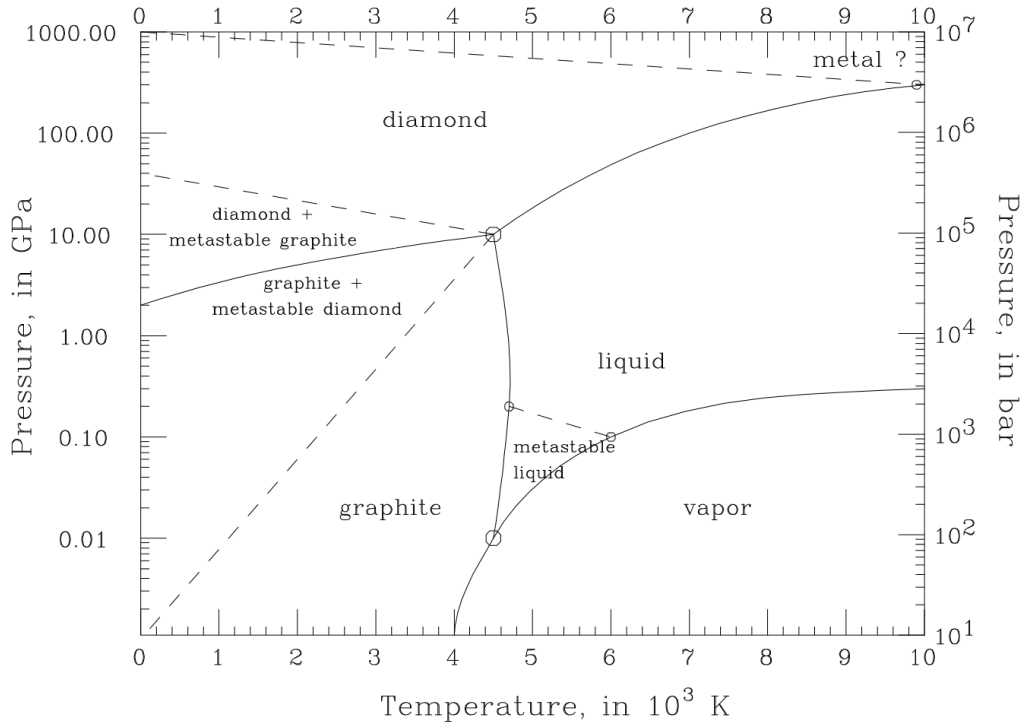


Figure 2.1: Phase diagram of carbon. From [54].

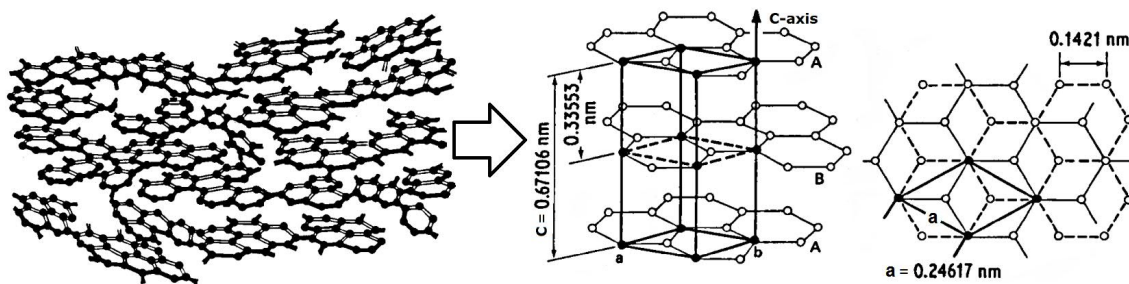


Figure 2.2: Graphitisation: conversion from disordered carbon to the ideal graphite crystal [55].

The graphitisation process occurs thanks to the high mobility of defects within the graphitic structure at high temperatures. This effect progressively brings the lattice closer to the ideal one.

Graphitisation is a temperature-dependent process which begins at temperatures close to 2300 K at ambient pressure. The strongest temperature-dependent structural changes by the graphitisation process occur at around 2550 K , the so-called graphitisation threshold which is the minimal heat treatment temperature for the development of true graphitic ordering [56]. For practical reasons, highly graphitised commercial products typically receive thermal treatments at temperatures above 3000 K to ensure the efficient development of the graphitic structure [57].

2.1.2 Catalytic graphitisation

By adding selected catalysts, graphitisation can occur at lower temperatures, with significantly shorter durations. Catalytic graphitisation does so by modifying the energetic pathways of graphitisation.

The first written words about the production of artificial graphite by catalytic graphitisation were registered in the end of the 19th century [58]. G.E. Acheson (U.S.A.) invented an oven to produce graphite, and he registered several patents. The oven was designed to withstand very high temperatures, enough for decomposing sand (SiO_2) and other compounds. In the centre of the oven he put a mixture of coke powder with several additions and a graphite rod crossing all the mixture. The rod was connected to an electric generator and the current through it produced heat by resistive losses. Initially he produced what he named "carborundum", of which the pure formula was according to him "SiC, silicide of carbon or carbide of silicon". He tested several mixtures and in the last patents he started to mention the effect of catalytic additions and the catalytic graphitisation. His idea was to add metallic compounds (such as iron, silicon, titanium, aluminium, boron or compounds thereof) to the mixture, which volatilize at high temperatures and permeate the mass of carbon. He found the best effect adding iron oxide to amorphous carbon obtained from the distillation of petroleum-oil. The iron was first reduced to metallic state by the effect of the temperature and it either held in the cavities and interstices of the carbon mass or it dropped to the bottom of the furnace; after that, he reported that with temperature rising it was volatilized *converting the amorphous carbon in to graphite*.

Reactions known to give rise to highly crystalline graphite at temperatures far below that of thermal recrystallization (graphitisation) involve the liberation of individual carbon atoms [59].

Catalytic graphitisation occurs by dissolution of individual carbon atoms, eventually connecting between them to form solid graphite. This continuous dynamic dissolution-

precipitation process dissolves the most disordered and hence most reactive carbon structures – such as amorphous regions or edges of basal planes – and precipitates "fresh" graphite that grows and bonds together the initial graphite crystallites [55, 60–62]. The most perfect graphite structures are thermodynamically the less prone to be dissolved, therefore the high-quality precipitated graphite can continue growing.

The diffusion rate of carbon inside the catalyst is expected to play an important role in the dynamics of this process. Baraniecki et al. reported that the rapid transport of carbon atoms through liquid Fe or Fe-Si is responsible for the accelerated graphitisation [62].

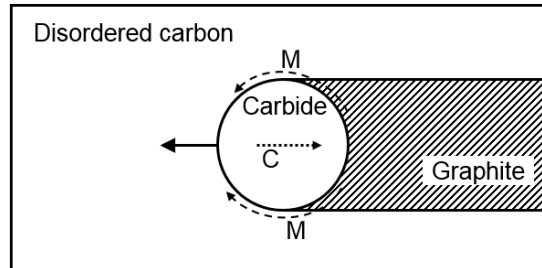


Figure 2.3: Schematic of a molten carbide particle forming graphite from disordered carbon (catalytic graphitisation). Metal (M), carbon (C). [55].

2.1.3 Diffusion of carbon atoms

Diffusion is defined as the transfer of mass within a specific solid, liquid or gas, or between two phases in different states of matter.

In solids, two diffusion mechanisms are proposed:

- **Vacancy diffusion:** It involves the interchange of an atom from a specific lattice position to an adjacent vacant lattice site. In general, it is called self-diffusion, as the own atoms of the lattice crystal are the ones moving.

Grain boundaries (GB) are two dimensional defects between grains having different crystallographic orientations. There, the atoms are bonded less regularly and consequently they are in a higher energy state than atoms in at interior positions, see Figure 2.4. In these areas diffusion and precipitation processes are more likely to occur.

Thermodynamic principles explain that all crystalline solids contain vacancies; in essence, the presence of vacancies increases the entropy of the crystal. The equilibrium number of vacancies N_v for a given quantity of material is $N_v = N \exp(-Q_v/k_B T)$, where N is the total number of atomic sites, Q_v is the energy required for the vacancy formation, T is the absolute temperature and k_B is the Boltzmann's constant ($8.62 \times 10^{-5} \text{ eV atom}^{-1} \text{ K}^{-1}$ or $1.38 \times 10^{-23} \text{ J atom}^{-1} \text{ K}^{-1}$). For example, in copper N is $8.42 \times 10^{23} \text{ atoms/cm}^3$, and the vacancy formation energy is 0.9 eV/atom, resulting in 28.7 million vacancies per cm^3 at room temperature [63]. However, in graphite ($1.13 \times 10^{23} \text{ atoms/cm}^3$), Q_v is 7.3 eV/atom [64], resulting in virtually zero vacancies at RT. Only above 1900 °C defects become sufficiently mobile and graphite starts to have more than 1 million vacancies per cm^3 . Figure 2.5 shows the comparison of the vacancies in these two solids.

- **Interstitial diffusion:** It involves impurity atoms migrating from an interstitial position to a neighbouring one that is empty, see Figure 2.6. This mechanism is found

for diffusion of impurities with smaller atomic radius compared to the host lattice. In most metals the typical interstitial impurities are hydrogen, carbon, nitrogen and oxygen. This type of diffusion occurs much more rapidly than vacancy diffusion, due to the more mobile nature of the small atoms. [63].

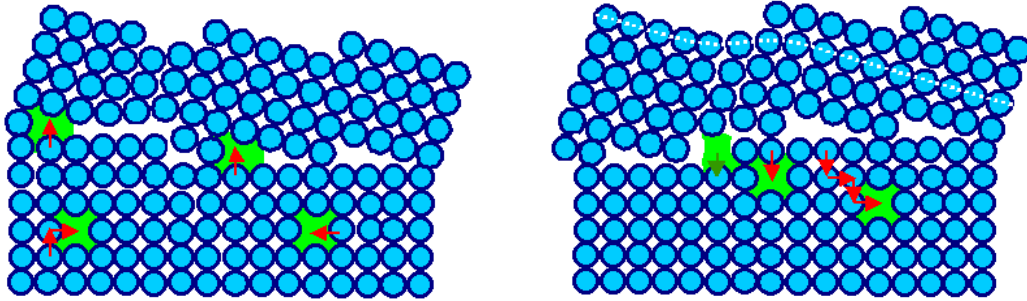


Figure 2.4: Visualisation of how grain boundaries are a source for vacancy diffusion (emitting and absorbing vacancies). [65]

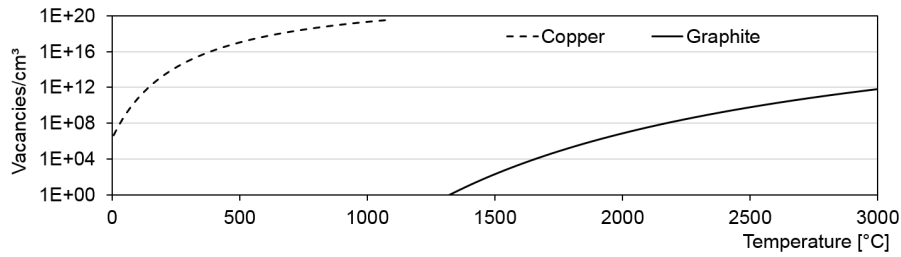


Figure 2.5: Comparison of the number of vacancies per unit of volume.

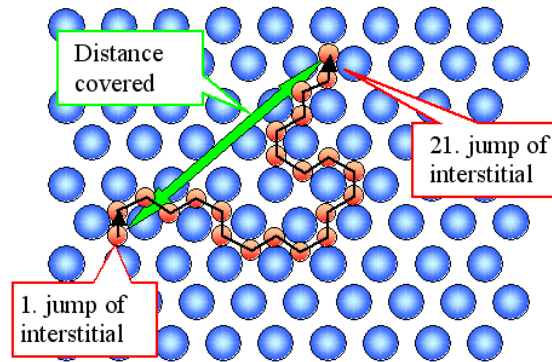


Figure 2.6: Schematic of the interstitial diffusion, showing the difference between distance covered (diffusion length) and the path length. [65]

Diffusion is a time-dependent process. The diffusion flux J is defined as the mass M diffusing through and perpendicular to a unit cross-sectional area A of solid per unit of time.

$$J = \frac{1}{A} \frac{dM}{dt} \quad (2.1)$$

One common case of steady-state diffusion is between two zones with different constant concentrations C , where D is the diffusion coefficient with units m^2/s .

$$J = -D \frac{dC}{dx} \quad (2.2)$$

Temperature has a large influence in D , increasing the diffusion rate with increasing temperature, see equation 2.3, where D_0 is a temperature-independent pre-exponential factor (m^2/s), Q_d is the activation energy for diffusion (J/mol or $eV/atom$), k_B the Boltzmann constant and T the absolute temperature.

$$D = D_0 \exp\left(-\frac{Q_d}{k_B T}\right) \quad (2.3)$$

Table 2.1: Comparison of diffusion coefficients. In bold, diffusion in liquid media.

Diffusing species	Host medium	T [°C]	D [$cm^2 s^{-1}$]	Diffusing species	Host medium	T [°C]	D [$cm^2 s^{-1}$]
Fe	α -Fe	900	$1.8 \cdot 10^{-11}$	H_3O^+	H_2O	20	$9.3 \cdot 10^{-5}$
Fe	γ -Fe	900	$1.1 \cdot 10^{-13}$	K^+	H_2O	20	$2.0 \cdot 10^{-5}$
C	α -Fe	900	$1.7 \cdot 10^{-6}$	Na^+	H_2O	20	$1.3 \cdot 10^{-5}$
C	γ -Fe	900	$5.9 \cdot 10^{-8}$	OH^-	H_2O	20	$5.3 \cdot 10^{-5}$
Cu	Cu	500	$4.2 \cdot 10^{-15}$	Cl^-	H_2O	20	$2.0 \cdot 10^{-5}$
Al	Al	500	$4.2 \cdot 10^{-10}$	Si	Fe pure	1550	$3.0 \cdot 10^{-5}$
Cu	Al	500	$4.1 \cdot 10^{-10}$	Si	C-saturated Fe	1550	$2.5 \cdot 10^{-5}$
Ti	Al	900	$5.0 \cdot 10^{-5}$	S	Fe pure	1550	$4.5 \cdot 10^{-5}$
V	Al	900	$2.0 \cdot 10^{-5}$	S	C-saturated Fe	1550	$3.5 \cdot 10^{-5}$
Co	Al	900	$3.7 \cdot 10^{-5}$	Fe	2.5%C-Fe	1550	$1.3 \cdot 10^{-4}$
Fe	Al	900	$5.1 \cdot 10^{-5}$	C	2.1-3.5%C-Fe	1550	$6.0 \cdot 10^{-5}$
Ni	Al	900	$8.0 \cdot 10^{-5}$	C	0.5-1.5%C-Fe	1550	$3.4 \cdot 10^{-4}$
Glucose	H_2O	20	$6.8 \cdot 10^{-6}$	Ni	C-saturated Fe	1550	$3.1 \cdot 10^{-5}$
Sucrose	H_2O	20	$5.2 \cdot 10^{-6}$	Ti	C-saturated Fe	1550	$5.5 \cdot 10^{-5}$
Sucrose	H_2O	45	$9.2 \cdot 10^{-6}$	Mn	C-saturated Fe	1550	$3.9 \cdot 10^{-5}$

Melting temperatures: Al 660 °C, Fe pure 1536 °C, eutectic Fe-C 1153 °C. All data of diffusion in H_2O is at infinite dilution. References: in solid metals [63], in molten Al [66], in molten Fe [67], and carbohydrates [68] and ions [69] in H_2O .

Table 2.1 shows an overview of how D varies in different solids or liquids, depending on the diffused species and the host mediums, at different temperatures. Figure 2.8 shows the same but specifically for carbon on different solids. In a liquid, the atoms of molecules do not have sufficient kinetic energy to separate completely between them (like in gaseous state), yet they can move independently and they do not form a crystalline lattice. In this high mobility medium, diffusion coefficients D are at least 5 orders of magnitude larger than in solids.

Thermal agitation of atoms and molecules result in Brownian motion of particles in solution. Brownian motion¹ or pedesis (from ancient Greek: $\pi\acute{\eta}\delta\eta\sigma\iota\varsigma$ "jumping") is the random movement of particles inside a fluid as they constantly collide with their molecules or atoms. Albert Einstein, in 1905, brought the solution of the problem to the attention of physicists, presenting this motion as the result of the atoms and molecules constituting matter colliding with the pollen molecules. Jean Perrin verified experimentally the theory in 1908.

The Brownian motion is observed in particles smaller than 1 μm immersed in liquids, with decreasing amplitude as particles become larger. The Brownian movement is responsible of the stability of colloidal solutions (particles between 1 nm - 100 nm), because it

¹This motion is named after the botanist Robert Brown, in 1827, observed how certain pollen particles moved in water in a random fashion, executing a jittery motion.

does not permit the particles to settle. This motion is independent of the nature of the colloid but depends on the size of particles and the viscosity of the solution. The smaller the particle size and the lower the viscosity, the faster the motion.

Brownian motion can be adopted also for modelling diffusion in solid media, such as interstitial diffusion, as illustrated in Figure 2.6.

If the solution is in equilibrium, the random motion results in zero net movement (no mass transport). However, when concentration gradients exist, the Brownian motion results in the net movement of the solute (diffusion) towards the region with lower concentration.

The mean squared displacement (net movement, or diffusion length) of species experiencing Brownian motion is expressed in terms of the time elapsed and the diffusion coefficient, see equation 2.4 [70]. From this expression Einstein argued that the displacement of a Brownian particle is not proportional to the elapsed time, but rather to its square root.

$$\overline{x^2} = 2Dt \quad (2.4)$$

Figure 2.7 represents the diffusion times of different combinations of D and \bar{x} . Table 2.2 gathers also the data of the cases $\bar{x} = 50 \mu\text{m}$ and $t = 1 \text{ min}$.

A reasonable distance between non-sintered graphite particles in the green body would be in the order of $50 \mu\text{m}$. Note that the D required to diffuse those $50 \mu\text{m}$ in reasonable times (few seconds) is in the order of $1 \cdot 10^{-6} \text{cm}^2 \text{s}^{-1}$. These values of D are observed in the cases of diffusion in liquid media.

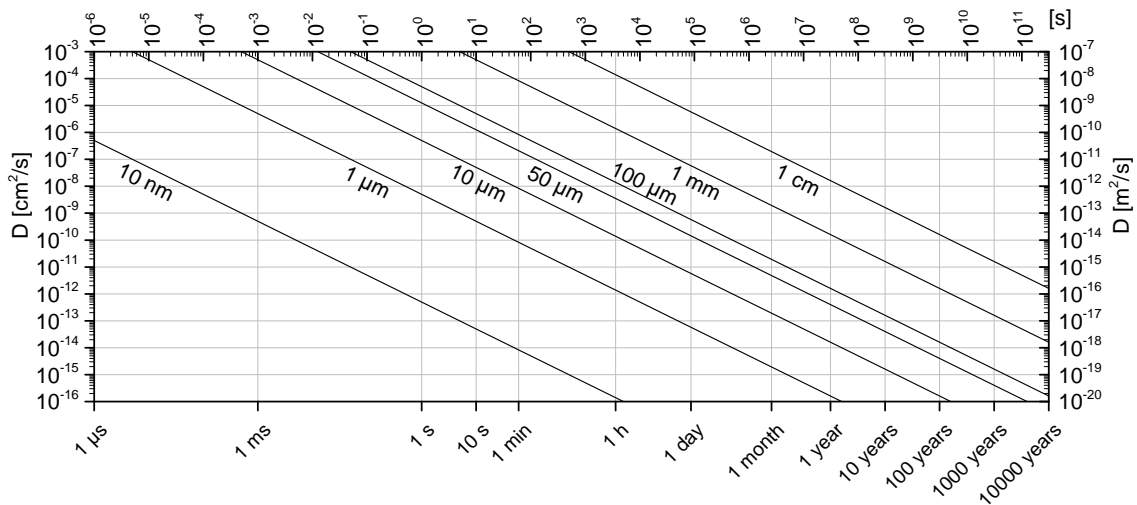
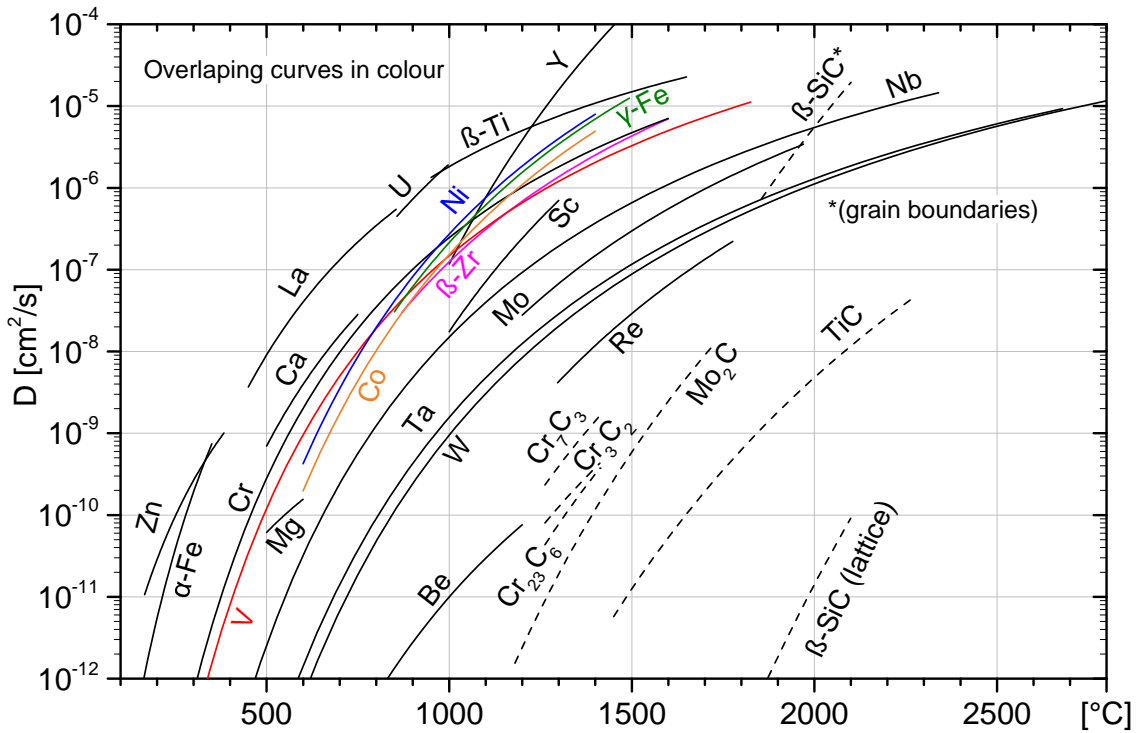


Figure 2.7: Diffusion time t for different D , each line represents a constant diffusion length \bar{x} .

Table 2.2: Comparison of the diffusion length \bar{x} and diffusion time t for different D

D		t for	\bar{x} for
cm^2s^{-1}	m^2s^{-1}	$\bar{x} = 50 \mu\text{m}$	$t = 1 \text{ min}$
$1 \cdot 10^{-3}$	$1 \cdot 10^{-7}$	12.5 μs	3.5 mm
$1 \cdot 10^{-4}$	$1 \cdot 10^{-8}$	0.13 s	1.1 mm
$1 \cdot 10^{-5}$	$1 \cdot 10^{-9}$	1.25 s	0.3 mm
$1 \cdot 10^{-6}$	$1 \cdot 10^{-10}$	12.5 s	0.1 mm
$1 \cdot 10^{-7}$	$1 \cdot 10^{-11}$	2.1 min	35 μm
$1 \cdot 10^{-8}$	$1 \cdot 10^{-12}$	20.8 min	11 μm
$1 \cdot 10^{-9}$	$1 \cdot 10^{-13}$	3.5 h	3.5 μm
$1 \cdot 10^{-10}$	$1 \cdot 10^{-14}$	1.4 days	1.1 μm
$1 \cdot 10^{-11}$	$1 \cdot 10^{-15}$	14.5 days	0.3 μm
$1 \cdot 10^{-12}$	$1 \cdot 10^{-16}$	145 days	0.1 μm
$1 \cdot 10^{-13}$	$1 \cdot 10^{-17}$	4 years	35 nm
$1 \cdot 10^{-14}$	$1 \cdot 10^{-18}$	40 years	11 nm
$1 \cdot 10^{-15}$	$1 \cdot 10^{-19}$	402 years	3.5 nm
$1 \cdot 10^{-16}$	$1 \cdot 10^{-20}$	4019 years	1.1 nm

Figure 2.8: Diffusion coefficients of carbon in different metals and carbides, in solid state. References: metals [71], SiC [72], Cr-carbides [73], Mo₂C and TiC [30].

2.1.4 Dissolution of carbon atoms

Catalytic graphitisation is based in the dissolution-precipitation mechanism. Therefore, the catalyst has to dissolve enough carbon atoms to sustain the process.

It has been shown above that higher diffusion rates should be beneficial for the dissolution-precipitation, making liquid catalysts more appealing than solids. White and Pontelandolfo observed indeed better results when the catalyst were molten [74], see section 2.2.

For these reasons, the processing conditions analysed below are those of the liquid phase. Several elements are surveyed in section 2.3. Figures 2.9 and 2.10 depict the different solubilities of carbon in the liquid phases of these elements.

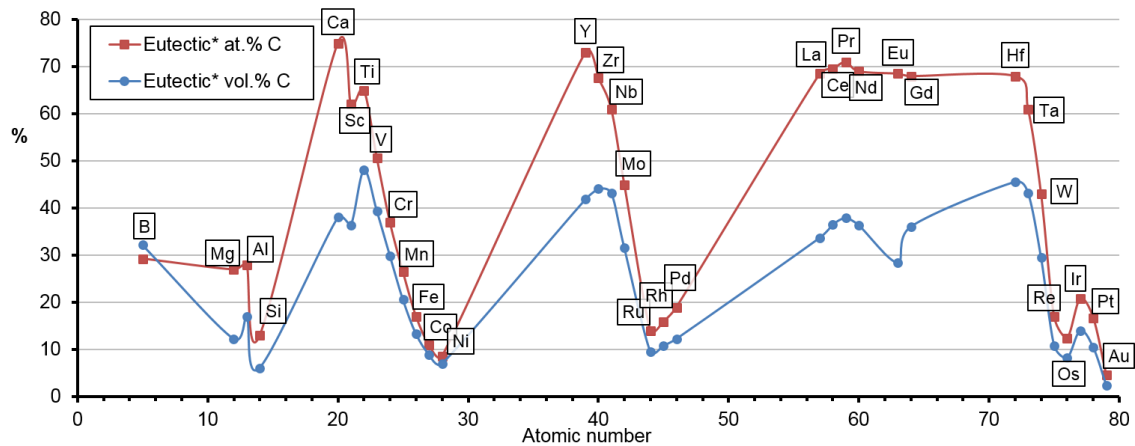


Figure 2.9: Carbon solubility in 100% liquid phase of several elements. (*)In systems without eutectic reaction, peritectic-liquid composition is used; for complete description of the liquid phase in equilibrium with excess carbon see Section 2.3.6.

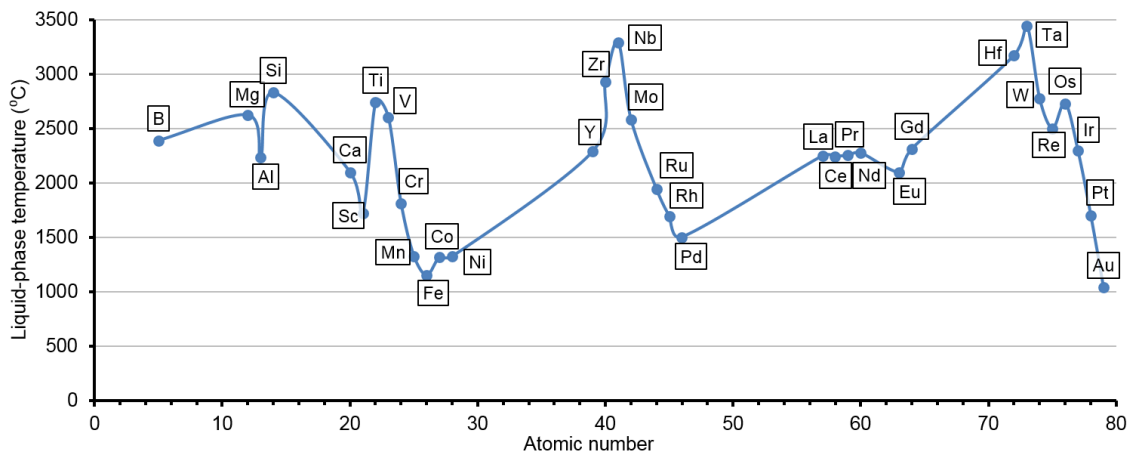


Figure 2.10: Liquid phase temperature of several elements in equilibrium with carbon (100% liquid).

The interaction of molten Ag-Sn alloys with graphite was studied in reference [75] up to 1200 °C. It was shown by XRD and SEM-EDS that no dissolution of carbon or chemical reaction takes place in the system. Conversely, in another study, amorphous carbon films deposited on cobalt polycrystalline foils converted into graphite at temperatures as low as 800 °C [76]. Jackson [77] showed that carbon fibres completely dissolve and recrystallize in a nickel matrix at 1100 °C (4-days treatment). At 1000 °C (same duration) the recrystallization was partial. This comparison of studies between Ag-Sn, Co and Ni demonstrates that the dissociation of carbon from the graphite lattice followed by dissolution in the solvent medium is not only dependent on thermally activated reactions. It is thus reasonable to assume that the electronic structure (reactivity with carbon) and the interatomic distances of the host atoms are the main actors in the process.

2.1.5 Wetting of graphite

The dissolution-precipitation mechanism requires intimate contact between the LP and the solid graphite particles.

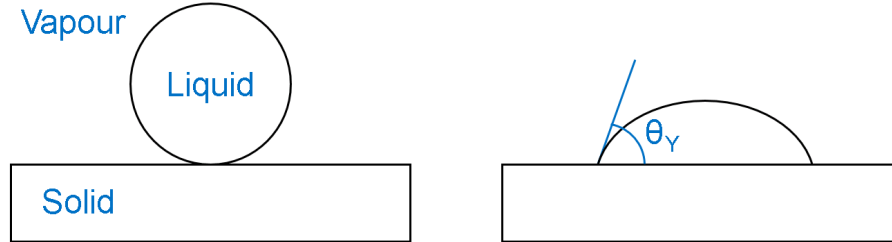


Figure 2.11: Sessile drop technique. The macroscopic contact angle θ_Y of a liquid drop on a solid surface depends on solid and liquid surface energies.

The strength of the contact between different liquids and graphite can be assessed with sessile drop tests (Figure 2.11) [78, 79]. The theoretical description of this type of contact arises from the consideration of a thermodynamic equilibrium between the three phases involved: the liquid phase L , the solid phase S , and the gas or vapour phase V . The latter can be a mixture of ambient atmosphere and an equilibrium concentration of the liquid vapour. The cases in which two immiscible liquids and a solid phase coexist are treated equally. The equilibrium contact angle θ_Y is determined by the Young equation:

$$\gamma_{SV} - \gamma_{SL} - \gamma_{LV}\cos\theta_Y = 0 \quad (2.5)$$

with γ_{SV} the solid-vapour interfacial energy, γ_{SL} the solid-liquid interfacial energy, and γ_{LV} the liquid-vapour interfacial energy (i.e. the surface tension). Contact angles of $\theta_Y > 90^\circ$ are considered "non-wetting", see Figure 2.11. The best wetting occurs when $\theta_Y = 0^\circ$, indicating that the liquid completely spreads over the solid.

Wetting by liquid metals at high temperatures is determined by the chemical interaction of the metal and the solid surface. However, the intensity of chemical reaction at high temperatures depends more on the nature of the reacting atoms than on the lattice structure [80]. The excellent wetting and spreadability of molten metals (materials with high surface energy) relative to various solid bodies is due to the formation at the interface of bonds, the energy of which is comparable with the liquid phase surface energy and which can only be achieved via interatomic chemical forces [81].

It is worth noting that the general behaviour of graphite and diamond during wetting is generally similar, as indicated by the similarity of their heats of combustion (385.5 and $387.3 \text{ kJ mole}^{-1}$, respectively), related to the lattice bond energy [80]. However, the different crystallographic faces of graphite or diamond crystallites possess dissimilar surface energies.

It is well known that the unsatisfied bonds on edges of basal planes result in much more active surfaces than basal planes themselves [61]. The basal plane surface energy of graphite is only 63 mJ m^{-2} ; graphene has shown similar values (61 mJ m^{-2}) [82]. For comparison, polytetrafluoroethylene (PTFE) polymer (Teflon[®]) has one of the lowest values with 19 mJ m^{-2} [83], while metals have surface energies in the order of 2000 mJ m^{-2} [84]. Graphite edge (through-plane) surfaces produce stronger bonding than the van der Waals interactions expected for interfacial basal planes [85]. For this reason, polycrystalline graphite has local differences in the wetting properties. Besides, atomic density is an important factor influencing surface energy, for example, between vitreous carbon ($\rho = 1.5 \text{ g cm}^{-3}$) and pseudomonocrystalline graphite ($\rho = 2.26 \text{ g cm}^{-3}$), the latter shows

smaller contact angles [85].

In the wetting studies of metal melts on graphite, three groups are considered [85]:

- Non-reactive elements: those in which the maximum solubility of carbon is lower than 1 ppm (such as Cu).
- Elements that form stable carbides (such as Si or Ti).
- Metals dissolving large amounts of carbon without forming stable carbides (such as Ni).

Non-reactive elements

Non-transition metals and other elements, which do not form stable compounds with carbon, cannot be expected to wet the surface of graphite and diamond. These conclusions were confirmed by experimental results: the metals Cu, Ag, Au, Ge, Sn, In, Sb, and Pb do not wet diamond [80]. Other studies performed on graphite confirm the same behaviour, see table 2.3.

Carbide-forming elements

Graphite may be expected to be wetted by those metals which intensively react chemically with carbon.

Strong bonds of a metal-like character are formed with carbon by most transition metals (elements with a defect in the d- or f- electron shells). Relatively strong compounds with > 50% ionic bond component are formed with carbon by the most electropositive elements, found in Groups I, II and III to the left of the Periodic table. They form generally transparent and insulator carbides, with high melting point, although they are decomposed by water at ordinary temperatures. Some contain C^{4-} ions such as Al_4C_3 or Be_2C , others contain C_2^{2-} ions (corresponding to carbon *sp* hybridization with triple bond, $[C\equiv C]^{2-}$) such as CaC_2 . Carbides having C^{4-} ions release methane when hydrolized (methanides), while those having C_2^{2-} yield acetylene (acetylides). Elements such as Si and B have similar electronegativity and atomic size than C, therefore they form carbides with strong covalent bonds [86].

It may be expected that transition elements, as well as strongly electropositive metals and other elements forming strong covalent bonds with carbon, will show intensive adhesion and wetting [80].

It was proposed that the formation of Al_4C_3 at the triple line could be controlled by the rupture of C-C covalent bonds at the substrate surface. This process will be strongly affected by atomic defects in carbon, which are much more numerous in vitreous carbon than in monocrystalline graphite or pyrocarbon [85].

Pure Cr and Ti react with C to form carbides that are metallic conductors. It has been found that molten Cr in argon atmosphere wets well both graphite ($\theta_Y = 40^\circ$) and vitreous carbon ($\theta_Y = 35^\circ$). Similar results have been obtained at 1740 °C in Ar using pure Ti for which the angles were 60° on polycrystalline graphite and 50° on vitreous carbon [85].

Elements forming stable carbides typically produce a solid carbide layer between the graphite and the liquid, and this layer may be a diffusion barrier for carbon. This would impede catalytic graphitisation from progressing, however, this does not occur if the carbide is molten [87].

Non-carbide forming but wetting transition metals

The ferrous metals Fe, Ni, Co, etc. dissolve relatively large amounts of carbon, but do not form stable carbides (Fe_3C , Ni_3C , etc. are metastable). It is interesting to note that these elements do wet graphite well. The resultant wetting behaviour is very complex and not yet understood [85]. The transition metals Ru, Rh, Pd, Re, Os, Ir, Pt and Au also dissolve carbon and do not form stable carbides (see Table 2.4). Cu, Ag and Au, all part of Group XI transition metals (defect of one electron in the d- sub-shell), belong to the first wetting group (carbon non-reacting elements) because they have shown non-wetting behaviour in the studies. However, as an exception, the solubility of C in liquid Au at its melting point is significant (≈ 4.7 at%) [88].

The high degree of wetting of graphite by nickel is attributable to the dissolution of carbon in liquid nickel under the action of the difference in the chemical potentials of carbon in the solid and liquid phases [89].

The equilibrium of these system is reached when the carbon concentration in the liquid reaches the solubility limit. In a non-equilibrium contact system, wetting is much more effective than in an equilibrium system [89, 90]. This effect is shown in the contact angles of carbon-saturated molten metals, in Table 2.3. The effect of carbon on the surface tension of nickel can be neglected (carbon on nickel does not act as a surface-active element) [89, 90]. Therefore, the effect of carbon additions to the liquid in the contact angle is attributed to an increasing liquid-solid interface energy [90].

Modification of behaviour in non-reactive systems

The wetting behaviour of non-reactive elements can be improved by alloying with carbide-forming elements such as Al, Si, Ti, V and Cr [85].

Carbide-forming elements are adsorbed out of the melt at the graphite interface and form there a layer of an intermediate carbide phase, which sharply increases the degree of wetting of graphite by the alloy [85, 91]. These elements, if dissolved in inert elements, also form the carbide layer, improving the wetting with respect to the inert element alone.

In some cases, metals of the second wetting group such as Ni, have also shown wetting improvements in non-reacting elements. For example, a substantial θ_Y decrease from 117° to 100° was observed at 285°C for small Pb crystallites on graphite, by adding 0.5 at.% Ni to Pb. Ni carbide (Ni_3C) is not stable and the solubility of C in Pb-Ni alloys is expected to be extremely low. The effects of Ni on the wetting behaviour were due to strong adsorption of Ni at the Pb-graphite interface [85].

2.2 Practical application

In the industry, components made of materials such as technical ceramics, cermets and refractory metals are typically produced by powder sintering techniques, in particular hot-pressing in solid state. The absence of liquid phase facilitates the process, as there is no molten material that can escape the pressed volume. The tools used for the solid-state hot-pressing can be readily reused. In sintered metals, the use of temperatures close to the recrystallisation point (normally 1/3 of the melting temperature in pure metals) is more convenient than reaching the melting temperature. The grain growth can also be minimized using short sintering times (often less than 1 minute), producing strong metallic bodies.

Table 2.3: Contact angles of molten metals and alloys on graphite [79].

	T [°C]	θ_Y [°]	θ_Y^* [°]	(*)	Other conditions:
Cu	1100	140	0	1150 °C	10%Ti in Cu
			18	1250 °C	5%Cr in Cu
			53	1200 °C	5%V in Cu
			71	1200 °C	5%Nb in Cu
			140	1300 °C	5%Ni in Cu
			138	1300 °C	5%Co in Cu
Ag	980	136			
Ge	1100	148			
Sn	900	156	5	1150 °C	3%Ti in Sn
"	1150	150 [87]			
In	800	142			
Sb	900	140			
Bi	800	136			
Pb	800	138			
Al	800	157			
"	1200	38			
Si	1450	0			
Fe	1550	50	107	1550 °C	C-sat. Fe
"	1425	60 [87]			
Ni	1550	57	115	1550 °C	C-sat. Ni
"	1425	60 [87]			
Co	1550	68	120	1550 °C	C-sat. Co
"	1425	82 [87]			
Pd	1560	48	118	1550 °C	C-sat. Pd
Mo	2625	53			
"	2730	48 [61]			

C-sat.= carbon-saturated

Nonetheless, the type of materials investigated in this research (graphite-matrix composites) and the advantages provided by the liquid phase led to the adoption of liquid phase sintering for the production of the materials.

Liquid phase sintering provides an alternative densification route especially useful for systems where solid state sintering is difficult or requires very high temperatures. The liquid phase is produced by reaching the melting temperature of at least one of the initial components, or by exceeding the solidus temperature of the phases formed during the process. The liquid phase can flow between the solid particles, infiltrating the inter-particle pores and enhancing densification [92]. For optimum densification, the liquid should wet the solid, and the latter should have low solubility for the elements present in the liquid phase. This last condition is needed to prevent the complete dissolution of the liquid phase inside the solid. Graphite exhibits negligible solubility for most metals, except in some cases such as lithium, which fits between basal planes, forming *intercalation compounds*.

Normally there is a significant increase in density upon solidification of the liquid phase. This effect may distort the body or produce flaws such as pores or cracks in the matrix, therefore the liquid and solid phases must be carefully chosen.

One of the first published attempts at producing metal (carbide) – graphite composites sintered with metals in liquid form was that by Humenik and colleagues [90, 93], targeting use in electrical brushes for motors. The green bodies containing Fe, Co, Ni, Cu, Ag or Al were pressed at RT at more than 340 MPa and then were pressure-less sintered up to 1371 °C. They found that using metals or alloys with $\theta_Y < 90^\circ$ did not produce metal loss due to sweating.

Graphitic materials produced by hot-working with a dispersed liquid carbide phase (termed HWLC) were firstly investigated by White and Pontelandolfo in 1966 [74, 94] for the purpose of developing graphite-based materials with improved properties for high-temperature nuclear and aerospace applications. They investigated bodies containing Mo or Zr. In the same years, Harada prepared a technical report for NASA where similar composite materials were described [95]. The elements investigated in this report include Nb, Hf, Mo, Zr, Ti, Ta, Be, B, Th and U, hot-worked with graphite up to $\sim 3000^\circ\text{C}$, so most of them produced LP. The highest flexural strengths were obtained for Nb and Mo composites (50 wt% metal), with 111 and 99 MPa respectively, resulting in densities of 3.38 and 2.96 g cm^{-3} . The observed strengthening effect with the HWLC method was in sharp contrast with bodies hot worked in similar conditions but without the carbide additives [96], and to bodies including the carbide phase but hot worked at temperature below the carbide melting point [74]. The strengthening effect of the carbide inclusions was also demonstrated in [97], in comparison with bodies without the inclusions hot-worked in the same conditions (2700 °C). R.B. Matthews [60] presented a very comprehensive study of the HWLC materials, comparing different additions, treatments and studying the strengthening mechanism in detail, especially the interactions between molten molybdenum carbide and carbon [61]. It was shown that besides high densification through void infiltration, the LP induces catalytic graphitisation helping to improve the graphite matrix.

In metal carbide - graphite compounds, the liquid phase is constituted by the molten catalyst that, by dissolving carbon atoms, forms a fully liquid mix of catalyst and carbon. As explained above, the catalyst also serves as a diffusion medium for carbon atoms, so catalysing graphitisation. The process is faster if the solubility limit and the diffusion coefficient are increased. The diffusion coefficients of carbon in different liquid phases are

probably comparable, however the solubility limits are quite different, see section 2.3.6. The most important requirement for a catalyst is thus to be a good **carbon solvent** when liquid.

Even if the graphite precursors are already crystalline and of high quality, catalytic graphitisation is fundamental for the final properties of the composites. The graphite particles from the initial powder need to be sintered together to form a solid matrix. Carbon atoms must be in a state of high mobility to form strong bonds between grains. This is accomplished by the aforementioned dissolution-precipitation mechanism, see Figure 2.12.

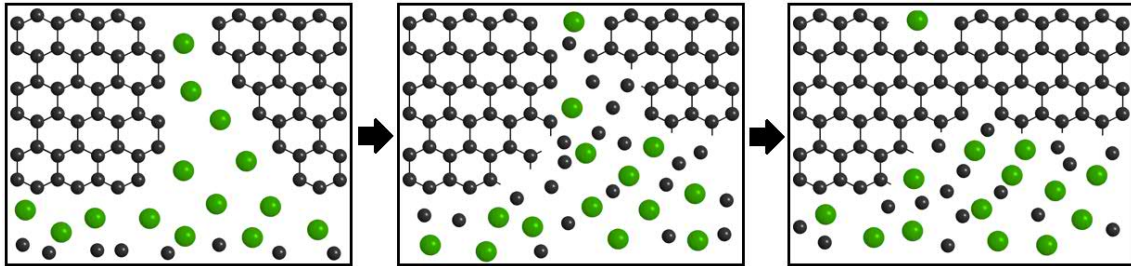


Figure 2.12: Schematic of the dissolution-precipitation mechanism bonding two graphite crystallites. The molten catalyst is represented by the green atoms.

While the catalytic graphitisation process is in general favoured by higher temperatures and longer sintering times, an optimal particle size of the catalyst and of the carbon-based precursors, as well as their homogeneous distribution, are necessary to reach a satisfactory final material structure. The use of very fine catalyst particles is believed to be beneficial for the process, because for the same volume, larger graphite surface area can be catalysed. Besides, the amount of LP has to be sufficient to completely fill the voids between the graphite particles inside the green body.

2.3 Carbon solvent selection

In order to rank the candidate carbon-solvent elements, the following parameters must be assessed:

- *Minimum liquid phase temperature*
- *Volumetric carbon-solvent efficiency*
- *Volumetric efficiency in carbon precipitation*
- *Cost and solidified product functionality*

These are described underneath.

2.3.1 Minimum liquid phase temperature

The catalyst, or carbon-solvent, is normally solid at room temperature. In order to enhance the dissolution-precipitation mechanism, it must reach the liquid state.

The minimum liquid phase temperature of candidate solvents represents, as the name says, the threshold of solid to liquid phase change for the solvent, while being in equilibrium with excess solid carbon.

- In general, the minimum liquid phase temperature corresponds to the **eutectic point** including solid carbon (graphite) in the equilibrium reaction $L \leftrightarrow X(\text{solid}) + C(\text{solid})$, see the example (Mo-C) in Figure 2.14. In those cases, the composition of the liquid phase is that of the eutectic point described above.
- In systems without eutectic reaction, peritectic temperature is considered instead. The composition of the liquid phase is that of the peritectic liquid (100% liquid), see the example (Si-C) in Figure 2.15.

It is important to clarify that the melting point of the metal does not necessarily match the LP temperature; in fact, for the analysed systems, it never does so, see Table 2.4. The composites are typically made with excess of carbon (graphite). For example, a mix of powders could correspond to an overall composition of 10at% of pure metal and balance of graphite. Upon heating, this mixture will tend to the equilibrium by diffusion of carbon into the metal. In particular, for the Mo-C system (Fig. 2.14), Mo metal melts at 2619 °C, but with 17at.%C it forms an eutectic at 2200 °C, with 42at.%C it would be solid ($\alpha\text{-MoC}_{1-x}$) up to 2600 °C and when being in equilibrium with excess carbon it forms an eutectic at 2584 °C. However, if the formation of the carbides occurs at a temperature below the first eutectic, and enough C is able to diffuse into the metal to complete the reaction, the particles will not experience the first eutectic reaction (2200 °C). This is actually the case, as Mo and C (graphite) fully react between 800 and 1000 °C [98]. In the Si-C system (Fig.2.15), pure Si melts at 1414 °C, but if enough C diffuses to reach $\text{Si}_{50}\text{C}_{50}$, SiC is formed and no liquid appears below 2830 °C.

The LP temperature parameter has significant importance in the production cost, as reaching higher temperatures involves more expensive equipment and higher energy consumption. The LP temperature cannot be too low either, as the final solid products of the composite could melt while in operation in collimators.

In fact, beam impacts reproducing HL-LHC accidental cases on MoGr and CFC collimators were experimentally tested in HRMT23 experiment and analysed by Carra [23], notably the *beam injection error*. During the experiment, maximum temperatures of 1025 °C in MoGr ($\rho = 2.5 \text{ g cm}^{-3}$) and 475 °C in CFC ($\rho = 1.9 \text{ g cm}^{-3}$) were reached, which give an idea of the minimum acceptable limits for the melting point of the filler particles in the composites.

2.3.2 Volumetric carbon-solvent efficiency

This parameter measures the maximum volume of carbon which can be dissolved in a volume unit of the solvent. For example, a 75% *volumetric efficiency* means that 1 cm^3 of this element can ideally dissolve 0.75 cm^3 of solid carbon at the liquid phase temperature.

$$\text{vol.\% carbonsolvent efficiency} = 100 \frac{\text{vol. dissolved carbon}}{\text{vol. liquid pure solvent}} \quad (2.6)$$

The information needed is obtained from the available phase diagrams between the solvent element and carbon.

To calculate the vol.% efficiency, the following assumptions are made:

- The composition corresponds to the minimum liquid phase temperature, described above (LP composition is temperature-dependent).

- To convert the information from the phase diagrams, typically expressed in at.% or wt.% units, the densities of solid elements are used. Liquid density data is not available for some of the elements. As the density of metals in molten state is typically lower than in solid state, the vol.% efficiencies shown are approximate.
- The efficiencies are calculated considering the dissolution-precipitation of fully dense graphite. The density of graphite single crystal 2.265 g cm^{-3} [53] is used for graphite. If carbon structures with lower density are dissolved instead, the volumetric carbon-solvent efficiency would be higher.

This parameter is of significant importance for the sintering process employed in the production. Graphite powder in excess (i.e. $>90 \text{ vol.}\%$) is used in the mixture, therefore only a very small part of the graphite powder surface is in contact with the catalyst. The volume of carbon that the catalyst is able to dissolve has to be thus maximized.

2.3.3 Volumetric efficiency in carbon precipitation

Another parameter could also play a role in the production process, named *Volumetric efficiency in carbon precipitation*. This is the volume of carbon which can be precipitated after cooling down per volume of catalyst. It is worth mentioning that not all surveyed C-solvents precipitate graphite. The precipitation occurs when the solution becomes supersaturated, meaning that it contains more solute than in the saturated conditions. This typically occurs due to a change in solubility limit.

$$\text{vol.\% efficiency carbon precip.} = 100 \frac{\text{vol. precipitated carbon at } RT}{\text{vol. dissolved carbon at LP temp.}} \quad (2.7)$$

There are substantial differences between systems with eutectic and peritectic reactions. In order to compare those type of reactions, an example of two hypothetical systems, with the same LP temperature and same LP composition is presented in Figure 2.13 and equation 2.8. In the eutectic system, the eutectic point is "E". In the peritectic system, "P" is the peritectic point and "P_L" the peritectic liquid. Both "E" and "P_L" are 100% liquid, therefore they are considered to be the LP.

The exercise starts for both systems with an overall composition of 90 at.% C and 10 at.% of the catalyst element (dashed vertical line). The relative phase amounts W are determined for four different temperatures: T_1 is much above minimum LP temperature, T_2 just above, T_3 just below and T_4 much below. The results of the relative amounts of the phases present at equilibrium are calculated with the lever rule and presented in equation 2.8.

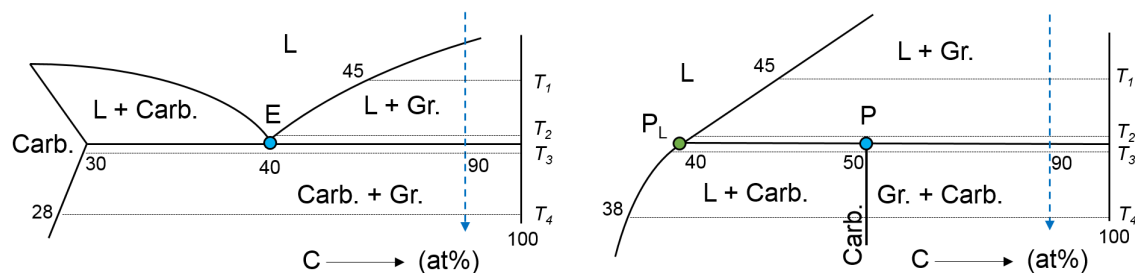


Figure 2.13: (Left) Eutectic system. (Right) Peritectic system.

<i>Eutectic system</i>	<i>Peritectic system</i>
$T_1 : \quad W_L = \frac{100-90}{100-45} = 0.182 \text{ (45\%C)}$ $W_{Gr.} = 0.818$	$W_L = \frac{100-90}{100-45} = 0.182 \text{ (45\%C)}$ $W_{Gr.} = 0.818$
$T_2 : \quad W_L = \frac{100-90}{100-40} = 0.167 \text{ (40\%C)}$ $W_{Gr.} = 0.818 + \downarrow 0.015 = 0.833$	$W_L = \frac{100-90}{100-40} = 0.167 \text{ (40\%C)}$ $W_{Gr.} = 0.818 + \downarrow 0.015 = 0.833$ (2.8)
$T_3 : \quad W_{Carb.} = \frac{100-90}{100-30} = 0.143 \text{ (30\%C)}$ $W_{Gr.} = 0.833 + \downarrow 0.024 = 0.857$	$W_{Carb.} = \frac{100-90}{100-50} = 0.200 \text{ (50\%C)}$ $W_{Gr.} = 0.833 - \uparrow 0.033 = 0.800$
$T_4 : \quad W_{Carb.} = \frac{100-90}{100-28} = 0.139 \text{ (28\%C)}$ $W_{Gr.} = 0.857 + \downarrow 0.004 = 0.861$	$W_{Carb.} = \frac{100-90}{100-50} = 0.200 \text{ (50\%C)}$ $W_{Gr.} = 0.800$

The conclusions of this exercise are:

- The liquidus lines of both systems show increasing C-content with increasing temperature. This produces precipitation of carbon during cooling down (from T_1 to T_2), and the opposite (carbon dissolution) during heating up.
- The solidification of the eutectic liquid precipitates graphite, while the solidification of the peritectic liquid absorbs graphite (from T_2 to T_3).
- The carbide which shows a decreasing solubility line (in this example, in the eutectic system), produces further precipitation of carbon in solid state (from T_3 to T_4).
On the other hand, the carbide vertical solvus line in the peritectic system, implies no precipitation nor absorption of carbon (from T_3 to T_4).

The systems absorbing graphite during cooling down, due to the formation of carbides with larger C-content than the liquid phase (such as in the peritectic reaction shown above) are assumed to have zero "volumetric efficiency in precipitating carbon".

In reality, limited diffusion coefficients and short cooling down times produce further differences between eutectic and peritectic solidification. For an eutectic solidification, $L \rightarrow \alpha + \beta$, both solid phases form directly from the liquid; that is, locally $L \rightarrow \alpha$ and $L \rightarrow \beta$. Thus, the necessary solute redistribution occurs in the liquid ahead of the individual interfaces [99]. On the other hand, the peritectic reaction, $L + \alpha \rightarrow \beta$, requires the complete disappearance of the α phase (graphite), a process that involves solute diffusion in two solid phases at the peritectic temperature. The kinetics are therefore quite different for eutectic and peritectic reactions because of the extremely different rates of diffusion in liquids and substitutional/interstitial solids [99].

If one assumes the extreme case, where no diffusion occurs in the solid upon cooling, solidification merely switches from the freezing of the high temperature phase ($L \rightarrow \alpha$) to freezing of the low temperature phase ($L \rightarrow \beta$) at the peritectic temperature and below. Then, the β phase (carbide) usually surrounds the α phase (graphite) in the microstructure [99].

2.3.4 Cost and solidified product functionality

The amount of metal that is used to produce the composites is typically less than 10 vol% and the rest is relatively inexpensive graphite powder. In fact, the cost of the raw materials is small compared with the sintering and manual labour operations. Still, the powders

have some impact in the final cost, specially if mass production is envisaged. For this reason, metals with very high cost, such as noble metals should be avoided.

Another important element is that the chosen catalyst remains in the composite, either as pure element or as carbide. As explained in section 1.3.3, the solidified metal or carbide particles serve as reinforcement in the composite, improving its properties. They must help meeting the requirements and not being a weak point in the composite.

For example, calcium carbide reacts with water or moisture at room temperature producing acetylene gas and calcium hydroxide ($\text{CaC}_2 + 2\text{H}_2\text{O} \rightarrow \text{C}_2\text{H}_2 + \text{Ca}(\text{OH})_2$). Because of this, it was used to produce a flame as source of light in lamps for mines and early automobiles. The reactivity of CaC_2 is obviously not desirable in graphite-matrix composites, which can be exposed to moisture from air.

2.3.5 Examples of relevant phase diagrams

The Mo-C, Si-C, Fe-C and Cr-C phase diagrams are shown in Figures 2.14, 2.15, 2.16 and 2.17 respectively. Mo-C and Cr-C diagrams are directly related to the investigated materials, while Si-C and Fe-C are shown to illustrate the different types of metal-carbon systems.

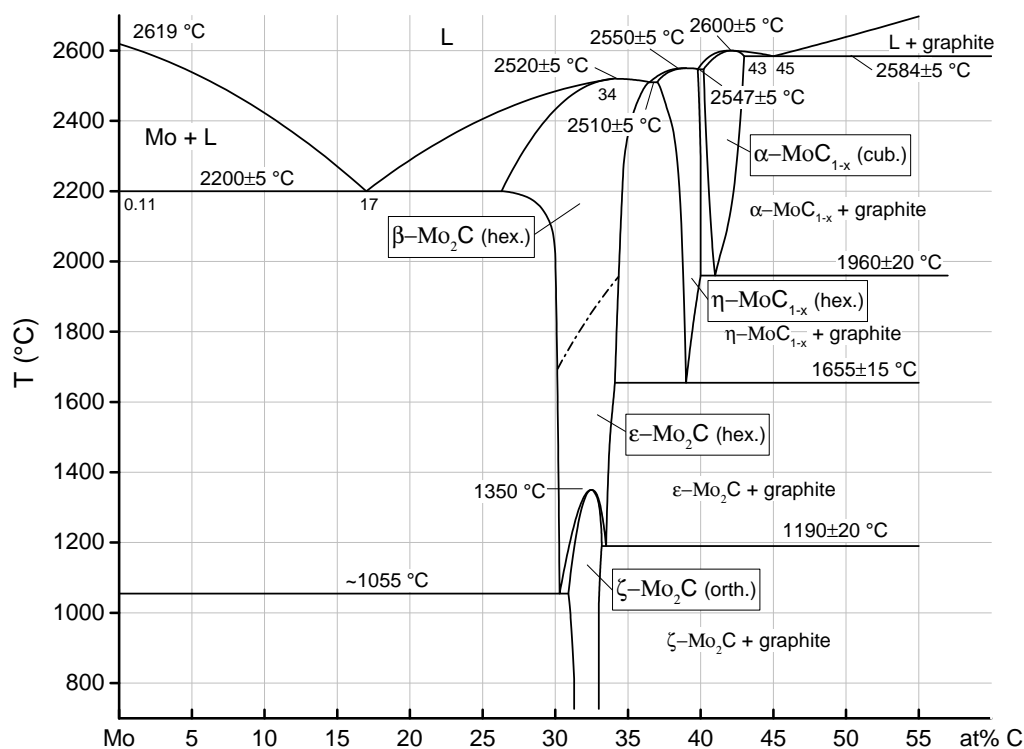


Figure 2.14: Phase diagram of the molybdenum-carbon system [100]. At least two eutectic reactions $L(\text{liquid}) \leftrightarrow A(\text{solid}) + B(\text{solid})$ exist: $\text{Mo}_{83}\text{C}_{17}$ (2200 °C) and $\text{Mo}_{55}\text{C}_{45}$ (2584 °C). The latter is in equilibrium with solid carbon (graphite), thus it is the one of interest for this survey.

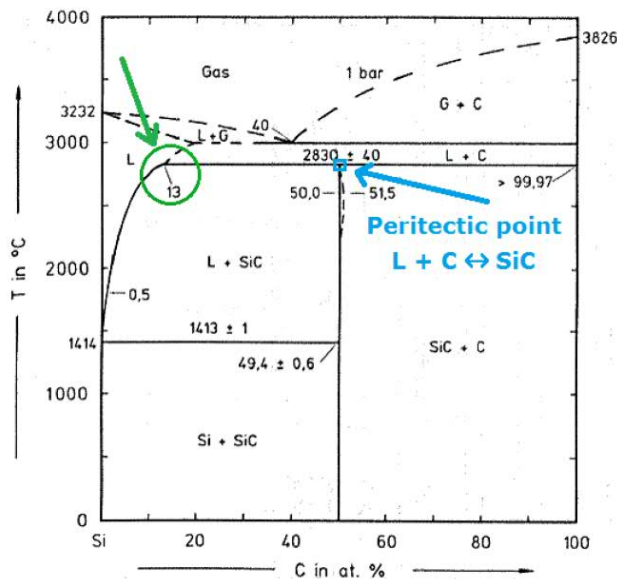


Figure 2.15: Phase diagram of the silicon-carbon system at 1 bar total pressure [101]. This system does not have eutectic reactions, however there is one peritectic reaction $L(\text{liquid}) + A(\text{solid}) \leftrightarrow B(\text{solid})$ at $\text{Si}_{50}\text{C}_{50}$ (2830°C) indicated by the blue square. It involves solid carbon (graphite) in the equilibrium. The green circle is the peritectic liquid at $\text{Si}_{87}\text{C}_{13}$ (2830°C), whose composition is used for this survey.

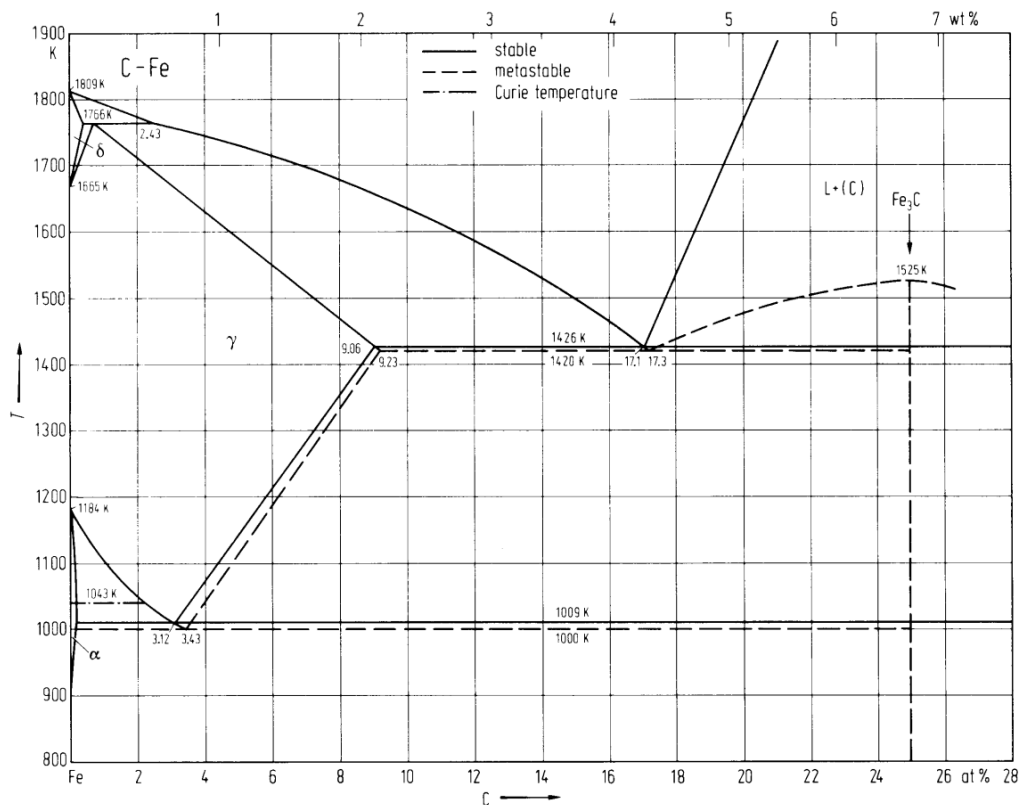


Figure 2.16: Phase diagram of the iron-carbon system [102]. There is one eutectic reaction (LP) at $\text{Fe}_{82.9}\text{C}_{17.1}$ (1153°C), in equilibrium with solid C (stable system). With excess carbon, if cementite is formed (metastable system), its composition presents larger C-content ($\text{Fe}_{75}\text{C}_{25}$, Fe_3C) than the LP. However if cementite is not formed, the LP moves to lower C-content ($\text{Fe}_{90.94}\text{C}_{9.06}$, then to $\text{Fe}_{96.88}\text{C}_{3.12}$, and then to even less C in $\alpha\text{-Fe}$), precipitating carbon.

The carbon precipitation, taking into account excess-carbon composition, in the systems presented above is as follows:

- In Fe-C system, if cementite (Fe_3C) is not formed, the LP precipitates carbon ($\text{Fe}_{82.9}\text{C}_{17.1} \rightarrow \text{Fe}_{90.94}\text{C}_{9.06}$) when solidifying. Austenite ($\gamma\text{-Fe}$) is formed and shows

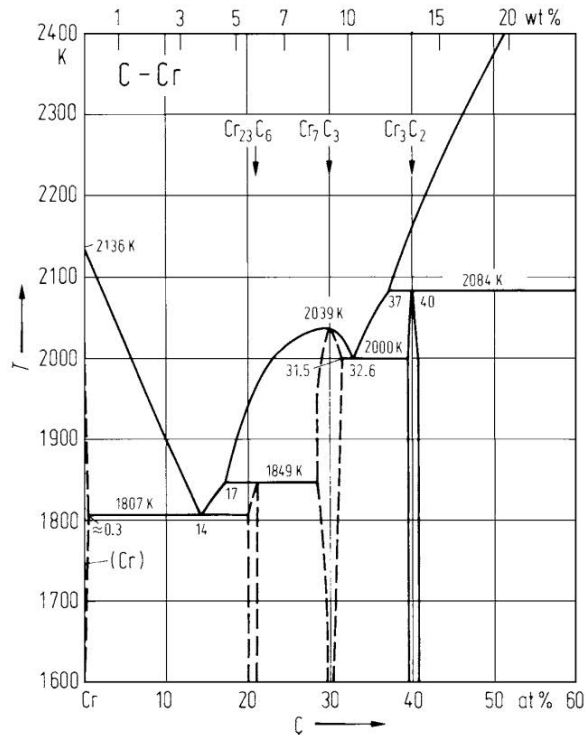


Figure 2.17: Phase diagram of the chromium-carbon system [103]. There is one peritectic reaction at Cr₆₀C₄₀ (1811 °C), in equilibrium with solid C. The peritectic liquid (100% liquid) has Cr₆₃C₃₇; during cool down, it forms Cr₃C₂ and the liquid moves to the eutectic reaction L(Cr_{67.4}C_{32.6}) ↔ Cr₇C₃ + Cr₃C₂, which is not in equilibrium with solid C. However, with excess carbon, only Cr₃C₂ is formed from the LP, solidifying completely at 1811 °C.

a decreasing solubility line, so it also precipitates carbon in solid state during cooling down, see Figure 2.16. On the other hand, if cementite is formed, carbon is absorbed during solidification.

- In Mo-C system, the solidification of the LP precipitates carbon (Mo₅₅C₄₅ → Mo₅₇C₄₃). Carbon is also precipitated in solid state, as α-MoC_{1-x} and the rest of carbides show a decreasing solubility lines, see Figure 2.14.
- In Si-C system (peritectic reaction), carbon is absorbed to form the carbide when the liquid phase solidifies, see Figure 2.15. The LP solidifies into Si+SiC, but with excess carbon composition and unimpeded carbon diffusion, the system would move to the SiC+C zone.
- In Cr-C system (peritectic reaction), carbon is absorbed to form the carbide when the liquid phase solidifies, see Figure 2.17. However, the difference in carbon content between the LP and the carbide is much smaller than in Si-C system. The LP solidifies into Cr₇C₃+Cr₃C₂, but with excess carbon composition and unimpeded carbon diffusion, the system would move to the Cr₃C₂+C zone.

In Mo-C system, the undoped molybdenum carbides, formed upon solidification of the eutectic mixture, experience three changes of phase until complete cool-down at RT, as shown in the Mo-C binary diagram (Figure 2.14).

The occurrence of solid phase changes in carbides is believed to be detrimental for colimator materials, since, during beam impact scenarios, temperatures may locally exceed 1000 °C: if changes of phase occur, the carbide specific volume would also vary, leading to internal stresses and potentially voids or cracks. Additionally, the presence of strongly stabilised phases usually improves the radiation resistance by preventing those phase changes.

Small additions of elements with affinity for carbon higher than molybdenum, such as hafnium and boron, stabilize the FCC α-MoC_{1-x} carbide [104]. The *face centred cubic*

(FCC) $\alpha\text{-MoC}_{1-x}$ phase is normally not stable under 1960°C (Figure 2.14). In the course of this study, we have found that the effect of small quantities of titanium in MoGr, around one titanium atom every 10 molybdenum atoms, seems sufficient to turn all molybdenum carbide into the FCC phase ($\alpha\text{-MoC}_{1-x}$), over the full range of temperatures of interest [37].

2.3.6 Carbon solvent survey

Table 2.4 presents the information of all the candidate C-solvents, obtained from their respective binary phase diagrams with carbon [102]. Some phase diagrams were not available, such as those of alkali metals. Other elements such as Cu, Zn, Ge, Ag, Sn, Pb or Bi have negligible solubility of carbon in molten state, so they are not considered.

Figure 2.18 shows the comparison of all candidate C-solvents, in terms of minimum liquid phase temperature and volumetric C-solvent efficiency.

Figure 2.19 shows the comparison of all candidate C-solvents, in terms of minimum liquid phase temperature and volumetric efficiency in carbon precipitation.

Table 2.4: Results of the survey.

Atomic number	Element	Pure element melting point [°C]	LP temp. [°C]	LP at.%C	LP vol.% C	Vol. C-solvent efficiency	% of dissolved C that precipitates	Vol. efficiency in C precipitation	Solid products from the LP
5	B	2075	2390	29.3	32.2	47.5	39.7	18.9	B ₄ C + C
12	Mg	650	2625	27.0	12.3	14.0	0.0	0.0	Mg + MgC
13	Al	660	2235	28.0	17.1	20.6	0.0	0.0	Al + Al ₄ C ₃
14	Si	1410	2830	13.0	6.2	6.6	0.0	0.0	Si + SiC
20	Ca	842	2100	75.0	38.1	61.5	33.3	20.5	CaC ₂ + C
21	Sc	1541	1722	62.0	36.5	57.4	22.4	12.8	Sc ₁₅ C ₁₉ + C
22	Ti	1668	2740	65.0	48.1	92.6	50.3	46.6	TiC + C
23	V	1902	2605	50.6	39.4	65.1	9.9	6.4	VC + C
24	Cr	1857	1811	37.0	29.9	42.7	0.0	0.0	Cr ₇ C ₃ +Cr ₃ C ₂
25	Mn	1244	1330	26.5	20.6	26.0	0.0	0.0	Mn carbides
26	Fe	1535	1153	17.1	13.3	15.4	0.0	0.0	Fe + Fe ₃ C
27	Co	1500	1320	11.0	9.0	9.9	100.0	9.9	Co + C
28	Ni	1455	1325	8.6	7.0	7.6	100.0	7.6	Ni + C
39	Y	1526	2290	73.0	41.9	72.0	26.0	18.8	YC ₂ + C
40	Zr	1881	2927	67.6	44.1	78.9	52.1	41.1	ZrC + C
41	Nb	2477	3290	60.9	43.2	76.1	35.8	27.2	NbC + C
42	Mo	2623	2584	45.0	31.6	46.2	38.9	17.9	Mo ₂ C + C
44	Ru	2334	1942	14.0	9.5	10.6	100.0	10.6	Ru + C
45	Rh	1963	1694	16.0	10.9	12.2	100.0	12.2	Rh + C
46	Pd	1555	1504	19.0	12.3	14.0	100.0	14.0	Pd + C
57	La	920	2250	68.5	33.8	51.0	8.0	4.1	LaC ₂ + C
58	Ce	798	2246	69.5	36.6	57.6	0.0	0.0	CeC ₂ +CeC ₆
59	Pr	931	2254	71.0	37.9	61.1	18.3	11.2	PrC ₂ + C
60	Nd	1024	2275	69.0	36.4	57.3	0.0	0.0	NdC ₂ +NdC ₆
63	Eu	826	2100	68.5	28.4	39.8	0.0	0.0	EuC ₂ +EuC ₆
64	Gd	1312	2315	68.0	36.1	56.6	0.0	0.0	GdC ₂ +GdC ₆
72	Hf	2233	3173	68.0	45.6	83.9	52.9	44.4	HfC + C
73	Ta	3017	3445	61.0	43.3	76.2	36.1	27.5	TaC + C
74	W	3422	2774	43.0	29.5	41.8	0.0	0.0	W + WC
75	Re	3186	2500	17.0	10.9	12.2	100.0	12.2	Re + C
76	Os	3050	2732	12.5	8.2	9.0	100.0	9.0	Os + C
77	Ir	2466	2296	20.8	14.0	16.3	100.0	16.3	Ir + C
78	Pt	1772	1705	16.8	10.5	11.8	100.0	11.8	Pt + C
79	Au	1064	1041	4.7	2.5	2.6	100.0	2.6	Au + C

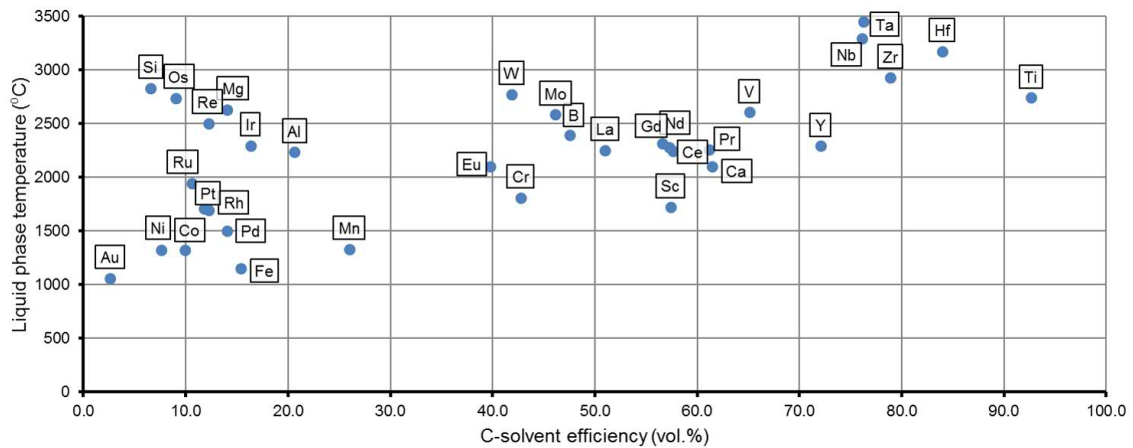


Figure 2.18: Carbon solvent efficiency versus (minimum) liquid phase temperature.

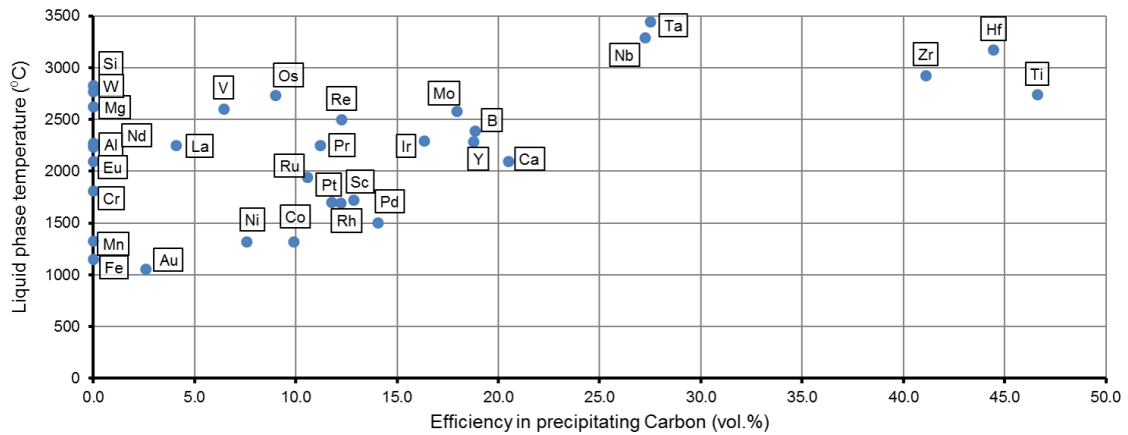


Figure 2.19: Efficiency in carbon precipitation versus (minimum) liquid phase temperature

The elements with minimum LP temperature lower than 2000 °C are: Sc, Cr, Mn, Fe, Co, Ni, Ru, Rh, Pd, Pt and Au. For cost reasons noble metals and Scandium are discarded. Table 2.5 presents their prices per gram (powders and market prices), including molybdenum for comparison purposes. For cost reasons, only Cr, Mn, Fe, Co, and Ni remain eligible. The C-solvent efficiency is from highest to lowest: Cr, Mn, Fe, Co and Ni.

The efficiency in carbon precipitation is from highest to lowest: Co and Ni. Cr, Mn, and Fe do not precipitate carbon. Both Co and Ni do not form stable carbides during slow cooling down of the LP, resulting in the metallic element plus carbon. In these cases, the amount of precipitated carbon is the same as the amount of dissolved carbon.

Between Co and Ni, the latter was chosen and tested in [106] with the goal of developing a new material similar to MoGr for applications other than high energy physics. "NiGr2" composite features an IP thermal conductivity of $368 \text{ W m}^{-1} \text{ K}^{-1}$, an electrical conductivity of $0.71 \text{ MS} \cdot \text{ m}^{-1}$, and a coefficient of thermal expansion of $1.8 \cdot 10^{-6} \text{ K}^{-1}$ (20-200 °C); all properties at 20 °C. The metallographic observations revealed signs of the dissolution-precipitation mechanism actually taking place at $\sim 1400 \text{ }^\circ\text{C}$ and $\sim 1800 \text{ }^\circ\text{C}$. Its thermal conductivity is slightly lower than that of copper, but its very low coefficient of thermal expansion (IP) and very low density ($2.36 \text{ g} \cdot \text{ cm}^{-3}$) make the material very appealing for certain thermal management applications, such as heat spreader for semi-

Table 2.5: Range of price of metal powders per gram from a German supplier, depending on particle size and purity ($< 45 \mu\text{m}$, $>99.0\%$ purity). Market price of the bulk metals (commodities, 11-Apr-2019 [105]). [€/g].

	Min.	Max.	Market [€/g]
Sc	652	804	5-13*
Cr	0.4	2.2	
Mn	1.0	4.3	
Fe	0.04	0.06	0.08 (1 kg)
Co	1.1	7	29.71 (1 kg)
Ni	1.0	6.6	11.67 (1 kg)
Ru	65.4	65.4	7.50
Rh	528	528	86.38
Pd	89	264	38.8
Pt	181	609	25.86
Au	394	529	37.15
Mo	0.5	15	

* U.S.A. supplier, metal lump

conductor materials.

The overall performance of NiGr2 is not adequate for HL-LHC collimator absorber blocks because of its large CTE in the TP direction ($17.5 \cdot 10^{-6} K^{-1}$, 20-200 °C), and its limited IP γ_e . Besides, Ni is ferromagnetic, fact that prevents its integration close to the particle beam.

In this thesis, the C-solvent efficiency has been prioritized over the precipitation of carbon. The author considers that the former parameter has more importance in the dissolution-precipitation mechanism, so the final properties are likely to be better if this parameter is maximized.

In fact, John [97] showed that the absence of carbon precipitation in solid state, such as in Ti-C or V-C systems, does not impede good cohesion in the sintered bodies.

It is therefore clear that taking all constraints into account, the best C-solvent alternative to molybdenum is chromium, which exhibits the greatest capability of dissolving carbon at the LP temperature. In fact, its C-solvent efficiency is 92.5% of that of molybdenum, see Table 2.4, but with a LP temperature of 1811 °C instead of 2584 °C.

In addition, the carbide of chromium (Cr_3C_2) has a density of 6.68 g cm^{-3} , compared with $8.92 - 9.39 \text{ g cm}^{-3}$ of the molybdenum carbides [37], this helps to produce lighter composites.

Also, chromium is 3.6 times less prone to activation than molybdenum, see Table 2.6. This helps to reduce the dose to personnel working around the used collimators in the LHC.

Another novelty in this thesis is that the Cr catalyst is added in the form of very small carbide particles ($< 2 \mu\text{m}$). This was chosen because of the following advantages:

- For the same amount of catalyst, smaller particles contact a larger surface area of graphite. Harada reported that finer particles produced improved densification and bonding [95]. The typical metal/carbide particle size in the prior art studies was $45 \mu\text{m}$ or larger [60, 93, 95, 97].
- The carbide is more resistant to oxidation than the metal, therefore the powder is

less prone to contain oxygen.

- Very fine powders of metallic elements are typically dangerous to handle, because they can ignite or explode in air. This is due to their high specific surface area per unit of mass, and their reactivity with oxygen. Carbides are in general much less reactive with oxygen, therefore they are safer to handle.
- The previous characteristic of carbides facilitates the production of very fine particle size powder. In fact, very fine commercial metallic powders are typically not available or they have high cost compared with more stable compounds such as carbides.
- The LP can be formed both from the metal or the carbide. However, as the carbide contains not only the catalyst but also carbon, the required amount has to be calculated accordingly.

Element	Operational	Waste
Ta	27.70	5.73
Co	9.80	66.50
W	3.98	4.72
Ni	3.51	1.17
Mo	3.31	0.47
Cu	1.37	2.93
Fe	1.30	0.61
Cr	0.91	0.62
Ti	0.89	1.10
Al	0.25	0.35
C	0.007	0.29

Table 2.6: Relative radiological hazard factors, per volume unit of elements irradiated with 7 TeV LHC proton beam (irradiation time independent). Operational aspects: dose to personnel, related to the sum of weighted dose rate contributions as function of the cooling time (1 h-20 years). Waste: probability to produce radioactive waste, related to the dose with a cooling time of 20 years. [107]

2.4 Summary of the chapter

Graphite-matrix composite materials have appealing properties for collimator absorber blocks in particle accelerators and for other thermal management applications.

The carbon dissolution-precipitation mechanism is responsible of catalytic graphitisation. This catalytic effect allows production of high quality graphite at lower temperatures than by standalone graphitisation processes.

Liquid phase sintering processes, in presence of adequate catalysts, allow to obtain composites benefiting both from high densification and catalytic graphitisation under fast (liquid state) diffusion media. In this process, dissolving large amounts of carbon in the LP is of great importance, therefore elements with good carbon-solvent characteristics are favoured as catalyst candidates. The temperature at which the LP is formed must be sufficiently low for the viability of the industrial production, but high enough so that the melting point is not reached in operation. In the LP, carbon atoms can dissolve and diffuse, eventually build carbon structures to sinter together the graphite initial powders into solid graphite. Upon cooling down, the solid products of must serve as beneficial features in the composite, for example improving the through-plane graphite properties.

Taking into account all the constraints, chromium is the most promising alternative to molybdenum, as it has nearly the same C-solvent characteristics, but with a LP temperature 773 °C lower. Chromium carbide (Cr_3C_2) powder has some practical advantages

with respect to the metallic form, and virtually no counter-indications. For these reasons, Cr_3C_2 powder is selected as filler material for some composites investigated in this thesis.

3 | Characterisation techniques

This chapter describes all the techniques used to characterise the materials for this thesis. These are both macro- and microscopical. More emphasis is put in the description of the techniques that the author has developed or tailored for the investigated materials, such as the elastic constants optimisation, the electrical characterisation and the X-ray diffraction.

3.1 Thermo-physical characterisation

After production, samples for thermomechanical characterisation were machined by conventional milling methods from the sintered plates. For measuring each property, three samples per direction were tested and the resulting values averaged. In temperature dependent plots, the curve shown corresponds to the best fit of all measurements.

The thermomechanical characterisation was performed at CERN, see Figure 3.1, with the following equipment: Netzsch *Differential Scanning Calorimeter* (DSC) Pegasus 404C, Netzsch *Laser Flash Apparatus* (LFA) LFA427, Archimedes scale, Netzsch horizontal pushrod dilatometer DIL 402E, and Zwick/Roell Z400 Universal Testing Machine. Full details of the measurements can be found in [108–110]. The accuracy of these measurements, as defined in the ISO 5725 standard, is typically within 5%.

The standard dimensions of the specimens for the thermomechanical characterisation are listed in Table 3.1. Anisotropic materials require tests in all different directions. In particular, the investigated transversely isotropic materials require the specimens oriented as shown in Figure 3.2. The reference Cartesian coordinate system for the sintered plates is also shown in Figure 3.2.

Table 3.1: Specimens for thermomechanical characterisation

Short name	Direction	Tests	Standard dimensions (mm)
LFA	IP	LFA	$\emptyset 10 \times 8$ or $10 \times 10 \times 8$
LFA	TP	LFA	$\emptyset 10 \times 2$ or $10 \times 10 \times 2$
DIL	IP	Dilatometry	$\emptyset 6 \times 25$ or $5 \times 5 \times 25$
DIL	TP	Dilatometry	$\emptyset 6 \times 25$ or $5 \times 5 \times 25$
DSC	any	DSC	$\emptyset 5 \times 0.75$
FLEX	IP	IET + Flexural test	$55 \times 10 \times 5$
FLEX	TP	IET + Flexural test	$25 \times 10 \times 5$
ELEC	IP	DC electr. conductivity	$45 \times 5 \times 4$
ELEC	TP	DC electr. conductivity	$25 \times 5 \times 5$



Figure 3.1: Thermo-physical measurements Lab at CERN. Right side: horizontal dilatometer (DIL 402E). Next to the left: vertical Laser Flash machine (LFA427).

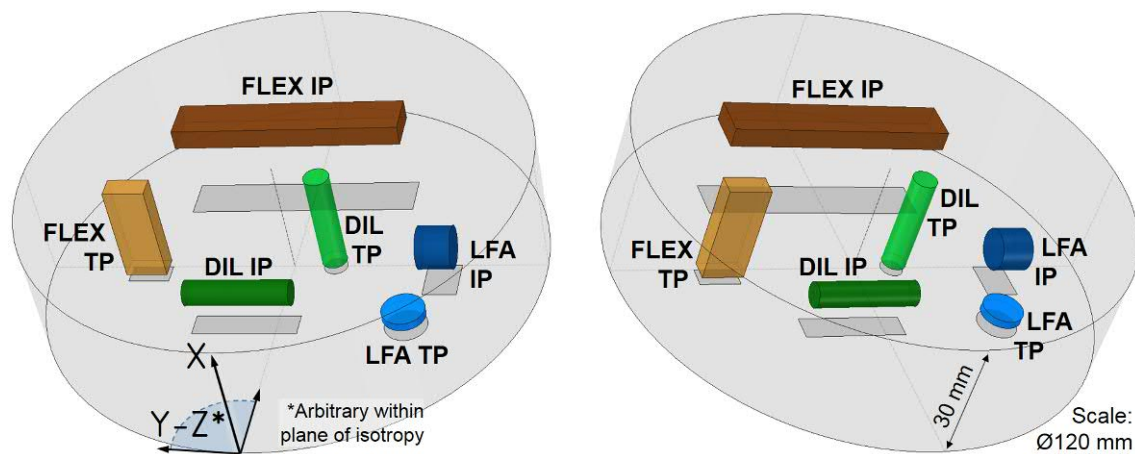


Figure 3.2: Schematic of the orientations of the specimens for characterisation of transversely isotropic materials. IP=In-plane, TP=Through-plane. In the Cartesian coordinate system: IP=Y-Z, TP=X.

3.1.1 Density

All the density values presented are calculated from the apparent solid volume measured with the Archimedes Scale, in calibrated ethanol, therefore taking closed porosity into account. The volume of the open pores is not considered because the liquid can infiltrate them.

The density can also be calculated by dividing the mass of a specimen by its volume, provided it has a simple geometry and dimensions are precisely measured.

The thermal expansion characterisation allows to deduce the variation of density with temperature, see equation 3.4 in section 3.1.4.

3.1.2 Thermal diffusivity and conductivity

Thermal diffusivity indicates how quickly a material reacts to a change in temperature. As opposed to thermal conductivity, which characterises steady heat transport, diffusivity is associated to unsteady heat conduction. Thermal diffusivity $a(T)$ is measured in $[mm^2s^{-1}]$, and thermal conductivity $k(T)$ in $[WK^{-1}m^{-1}]$. These two properties are re-

lated through the specific heat $c_p(T)$ and the density $\rho(T)$, by the following expression:

$$k(T) = \rho(T) \cdot c_p(T) \cdot a(T) \quad (3.1)$$

The thermal diffusivity is measured by the flash method ASTM E2585 with a Laser Flash Analysis (LFA). The furnace of the LFA427 apparatus can reach up to 2000 °C allowing temperature-dependent measurements. The atmosphere in the testing chamber consists in a limited flow of inert gas (100 ml min⁻¹ argon) at atmospheric pressure. This enables convection thermal transfer, improving the accuracy of the temperature reading by the temperature sensor.

Both faces of the sample are sprayed with a thin graphite coating so that the emissivity and absorptivity of the samples is independent of the material and close to 1. During the characterisation campaign of highly conductive MoGr it was found that the standard thickness of LFA samples ($\text{Ø}10 \times 2 \text{ mm}$) may be erroneously assessed by the apparatus, even when using the shortest practical laser pulses (0.6 ms), since the characteristic heat diffusion time is of the same order of magnitude of the laser pulse. This effect was observed when measuring samples of different thicknesses from the same material, in the in-plane direction and at low temperatures (high diffusivity). Thicknesses between 5 – 10 mm were observed to provide more accurate results and were adopted for the in-plane diffusivity measurements [111]. The same issue was described in reference [96], though the availability of a pulsed xenon lamp with peak time of 0.085 ms, made measurements of 1.5 mm-thick samples possible.

3.1.3 Specific heat

The specific heat, or heat capacity, corresponds to the amount of energy that is required to change the temperature of the material. The specific heat can be expressed in different units, like molar, volumetric or mass. Usually the magnitude is per unit of mass and at constant pressure (isobaric): $c_p(T)[J/(g \cdot K)]$, this is the amount of energy in Joules required to increase the temperature of one gram of material by one Kelvin.

The specific heat depends on the atomic bond, the atomic structure, the valence electrons of the atoms and the temperature. The greater the number of degrees of freedom for the atomic structure to oscillate, the larger the specific heat will be. For instance, graphite and diamond have very different heat capacity, despite being both formed by pure carbon (0.71 and 0.42 $J/(g \cdot K)$ respectively).

The apparatus used for the measurement is a Differential Scanning Calorimeter (DSC). This device applies a stable heat flux to both the sample and to a reference specimen at the same time. The specific heat of the reference specimen is known, as well as the masses. The temperatures of both samples are continuously monitored, allowing to obtain the specific heat of the sample of interest.

Generation and absorption of heat around the sample, even in minuscule amounts, can affect these measurements. S.K. Leiva studied the effect of oxygen in the DSC measurements [112]. The presence of traces of oxygen in the furnace gas produce oxidation reactions in the crucibles that contain the sample, eventually providing wrong $c_p(T)$ results. Oxygen levels smaller than 20 ppm are recommended for the device. An oxygen-trapping system consisting in a small zirconium getter helps reducing oxygen above ~ 600 °C. Besides, it was learnt that the use of alumina washers between the graphite crucibles and the platinum holder is required above 1000 °C, in order to prevent chemical reactions between them. Under these two conditions, reliable measurements up to 1200 °C are possible [112].

The furnace of the DSC Pegasus 404C features only air cooling system. This limits the minimum practical temperature of the test to around ~ 40 °C, preventing reliable

measurements of $c_p(T)$ below this temperature. The curves presented in this thesis are therefore extrapolated down to 20 °C, the mathematical functions used are shown.

3.1.4 Coefficient of thermal expansion

The Coefficient of Thermal Expansion (CTE) provides information about the change in length that a material experiences with a given change in its temperature. The dilatometry technique is used to determine the CTE. The Netzsch horizontal pushrod dilatometer DIL 402E consists in a furnace able to operate up to 2000 °C under inert atmosphere, with a pushrod transmitting the changes in length of the sample to a very precise linear variable displacement transducer (LVDT). Key parts of the furnace chamber are made in graphite. The pushrod applies a force of $15 - 45 \cdot 10^{-2}$ N to ensure good contact with the specimen. The LVDT sensor can measure differences in length up to 20 nm, however the global resolution of the device is around $0.1 \mu m$. A small flow of inert gas (100 ml min^{-1} helium) at atmospheric pressure is present in the furnace during the measurements. A reference measurement to a calibrated sample is required to deduct the expansion of the machine parts.

The result of the measurement is a curve dL/L_0 versus temperature, see Figure 3.3. dL/L_0 values are dimensionless, however, if multiplied by 100, they are expressed as percentage. The technical alpha (α), also known as average linear CTE or secant CTE, in the range T_0-T , is calculated with the following expression:

$$\alpha = \frac{1}{L_0} \frac{dL}{dT} = \frac{1}{L_0} \frac{(L(T) - L_0)}{(T - T_0)} = \frac{\frac{dL}{L_0}(T) - \frac{dL}{L_0}(T_0)}{T - T_0} \quad (3.2)$$

Where T_0 is the reference temperature (20 °C).

On the other hand, the physical (tangent) CTE is obtained deriving the dL/L_0 curve with respect to temperature. Figure 3.3 shows an example of dilatometer measurement, including both types of CTE. They are calculated from a 4th degree polynomial fit to the experimental data, which is needed to smooth out the measurement irregularities. Note how the secant CTE is 0 when dL/L_0 matches $dL/L_0(20^\circ C) \approx 0\%$, at around 1000 °C.

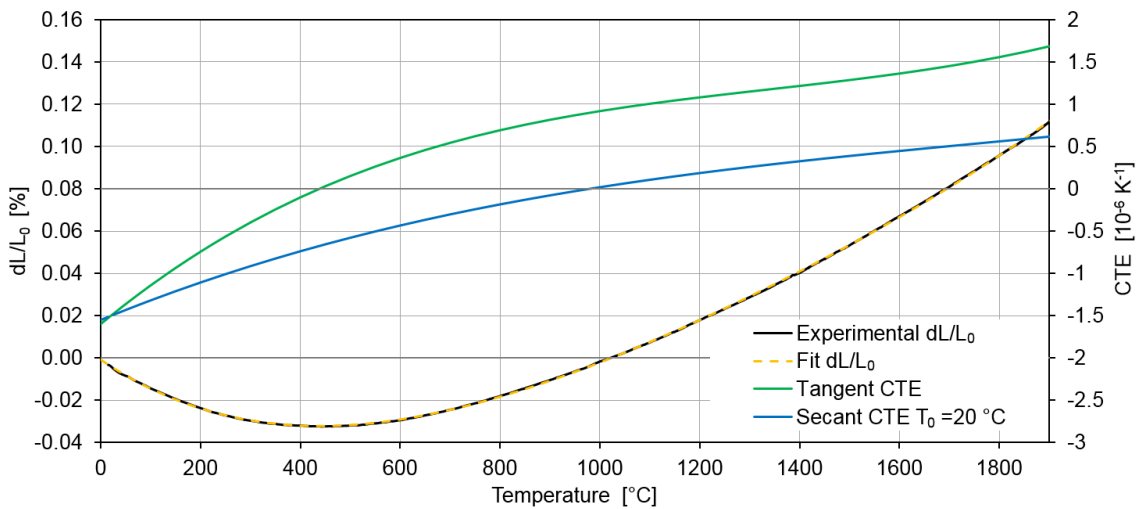


Figure 3.3: Example of dilatometry curve (cooling down ramp of CFC AC150K IP test), including the calculation of the tangent and secant CTE.

For practical reasons, some tests start and/or finish at temperatures slightly above RT

(30–40 °C), in those cases T_0 is set accordingly. This should have negligible effect in the α values.

Non constant heating/cooling rates produce measuring artefacts. They are commonly occurring during the heating up ramp at temperatures close to RT (up to ~ 100 °C). For this reason, the experimental results are typically calculated from the cooling down ramp of the dilatometry test.

The cooling down measurement implies that the sample has received a thermal treatment up to the maximum test temperature, which helps to relax internal stresses. At the end of the measurement, the change in length of the specimen (called "residual strain", in [%] units) gives a hint of the amount of internal stresses.

Volumetric expansion

The volumetric CTE (α_V), in the range T_0 – T , is defined by the following expression:

$$\alpha_V = \frac{1}{V_0} \frac{dV}{dT} = \frac{1}{V_0} \frac{(V(T) - V_0)}{(T - T_0)} = \rho_0 \frac{\frac{1}{\rho(T)} - \frac{1}{\rho_0}}{(T - T_0)} \quad (3.3)$$

The density is expressed as a function of α_V :

$$\rho(T) = \frac{\rho_0}{\alpha_V(T - T_0) + 1} \quad (3.4)$$

Where α_V corresponds to the range T_0 – T . α_V is deduced from the linear CTE α , with the following approximation:

$$V_0 + \Delta V = (L_0 + \Delta L)^3 = L_0^3 + 3 L_0^2 \Delta L + 3 L_0 \Delta L^2 + \Delta L^3 \approx L_0^3 + 3 L_0^2 \Delta L = V_0 + 3 V_0 \frac{\Delta L}{L_0} \quad (3.5)$$

This is valid for isotropic materials. For orthotropic materials the expression is analogous but multiplying the three different $(L_0 + \Delta L)$ instead of one cubed. The outcome from equation 3.5 is that the volumetric thermal expansion of isotropic materials is approximately three times the linear coefficient (equation 3.6).

$$\frac{\Delta V}{V_0} = 3 \frac{\Delta L}{L_0} \quad ; \quad \alpha_V = 3 \alpha \quad (3.6)$$

For orthotropic materials, α_V is approximately three times the average linear coefficient, see equation 3.7. In the particular case of transversely isotropic materials, the in-plane direction corresponds to two of the three orthogonal axes, so the average linear coefficient is calculated accordingly, see equation 3.7.

$$\alpha_V = 3 \alpha_{average} = 3 \frac{(\alpha_X + \alpha_Y + \alpha_Z)}{3} = 3 \frac{(2 \alpha_{IP} + \alpha_{TP})}{3} \quad (3.7)$$

These approximations (equations 3.6 and 3.7), for the investigated materials and ranges of temperature, is conform to the exact formula within less than 1%.

3.2 Mechanical characterisation

The brittleness of graphite and graphite-matrix materials leads to very complicated execution of tensile tests, mainly due to gripping and alignment difficulties. Bending tests are much more convenient in that case. The geometry of the bending test specimens is also much easier to produce, and requires less volume of material, see Table 3.1.

The bending strength was measured according to the standard ASTM C1161-02, with the 4-point flexural test; this configuration, as opposed to the three point flexural test, has the advantage of bringing to maximum stress a much longer portion of the sample (loading span), so limiting the statistical dispersion in results related to internal flaws, typical of brittle materials. Strains were measured with a strain gauge glued to the face under tensile stress. Some tests were performed with a contact-less laser extensometer instead, see Figure 3.4.

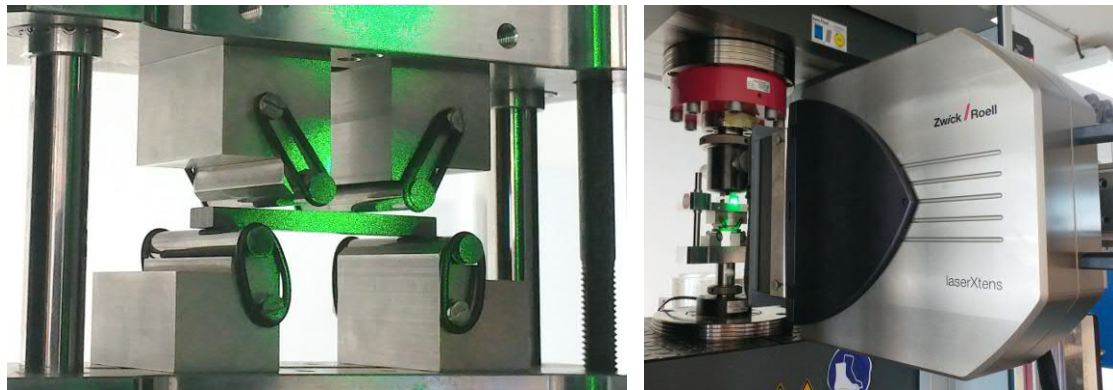


Figure 3.4: Bending test set-up, the pictures show the optional (green) laser extensometer system to do contact-less strain measurements. The specimen in the pictures is 55 mm long.

The flexural stress (σ_f) on the outer fibres of a beam with rectangular cross section is calculated with equation 3.8.

$$\sigma_f = c \frac{F L}{b d^2} \quad (3.8)$$

Where F is the applied load, L is the support span, b is the width of the specimen and d is the thickness. c is 1 for three point bending test, $3/4$ for four point bending test where the loading span is $1/2$ of the support span, and $3/2$ if the loading span is $1/3$.

3.3 Elastic constants

The elastic properties of ductile materials are typically obtained from tensile tests, by measuring the force and the elongation. With the force and the specimen section, the stress is calculated. The elastic modulus is the slope of the stress-strain curve during the linear behaviour (elastic part). As explained in section 3.2, in brittle materials the practical implementation of traction tests is complicated. For this reason, flexural tests are typically performed instead.

The elastic modulus can be obtained from the stress-strain curve in the traction face of bending test specimens. However, the stress-strain relationship in graphitic materials is significantly not linear, as it can be seen in CFC, compared for example with pure silicon (Figure 3.5). For this reason, in order to measure the Young's Modulus of these materials, an Impact Excitation Technique (Impact Excitation Technique (IET), also called resonant bar method) is used. In fact, IET only investigates the part of the curve at very low stresses, where the theory of elasticity (Hooke's law) is still valid. Besides, IET allows to easily obtain the shear modulus. The IET is based on the relationship between the elastic properties and the natural frequencies of a body.

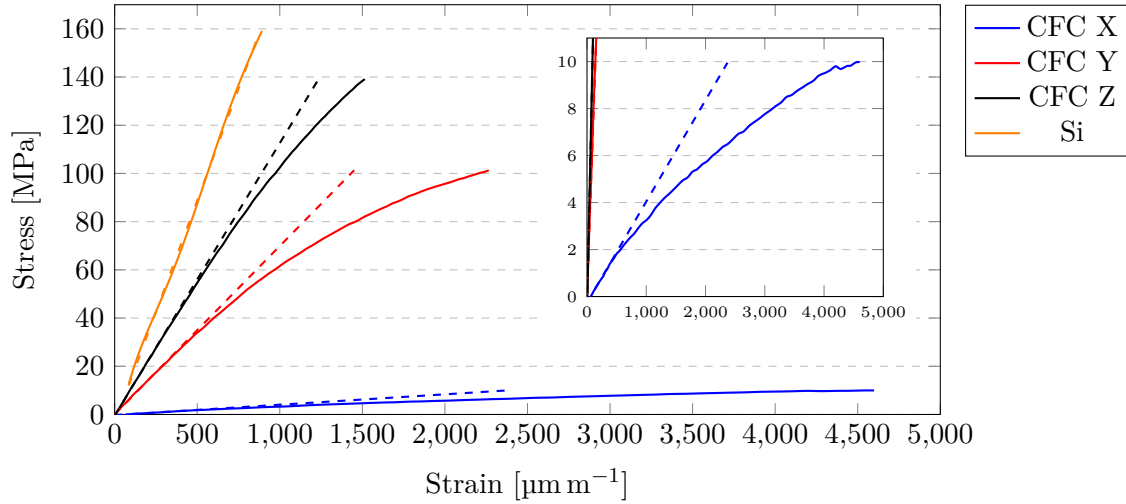


Figure 3.5: Four-point bending test of CFC AC150K (orthotropic) and polycrystalline silicon.

3.3.1 Theory of vibration: natural frequencies

A beam of isotropic and homogeneous material can propagate elastic waves. Those waves can also be described as a superposition of stationary waves (their peak amplitude profile does not move in space). This behaviour can be studied with the theory of beams, which relates the elastic properties, the mass and the dimensions of the beam to its natural frequencies. The interesting vibration modes for this study are the flexural and the torsional (first modes), with boundary conditions similar to a free-standing (unsupported) body.

Bending mode

The simplest approach is to study the bending behaviour of slender "Euler-Bernoulli" beams. A slender beam is typically defined as having a thickness-to-length ratio smaller than $1/50$. The bending behaviour is more complex than the torsional or axial, because two degrees of freedom are involved: the displacement u_x (for bending in the plane xz) and the rotation Φ_y . In general, the expression of the natural bending frequency (in $rad\ s^{-1}$) of the mode i is:

$$\lambda_i = \frac{\beta_{fi}^2}{l^2} \sqrt{\frac{EI_y}{\rho A}} \quad (3.9)$$

With β_{fi} a factor that depends on the supporting conditions (for the first bending mode ($i=1$), $\beta_{fi} = 4.730$ for free-standing or fixed-fixed bar, $\beta_{fi} = \pi$ for hinged-hinged for hinged-hinged and $\beta_{fi} = 1.875$) fixed-free, E is the Young's modulus, I_y the moment of inertia of the section about y -axis ($I_y = bt^3/12$, with t the dimension in y direction), ρ the density and A the cross-section area.

Adding the rotational bending effects, the slenderness factor S is introduced:

$$S = l \sqrt{\frac{A}{I_y}} = \frac{l}{r_i} \quad (3.10)$$

Where $r_i = \sqrt{I_y/A}$ is the radius of gyration of the section A . The frequency then becomes:

$$\lambda = \lambda^* \frac{S}{\sqrt{S^2 + i^2 \pi^2}} \quad (3.11)$$

Where λ^* is the frequency calculated neglecting the rotational bending effects (from eq. 3.9). Finally, considering the effect of the shear deformation and rotational bending effects ("Timoshenko" beam):

$$\left(\frac{\lambda}{\lambda^*}\right)^4 - \left(\frac{\lambda}{\lambda^*}\right)^2 \frac{S^2}{i^2\pi^2\chi^*} \left(1 + \chi^* + \frac{S^2}{i^2\pi^2}\right) + \frac{S^4}{i^4\pi^4\chi^*} = 0 \quad (3.12)$$

With $\chi^* = \chi E/G$, which for isotropic materials is $\chi^* = 2\chi(1 + \nu)$. χ is a shear coefficient depending on the shape of the cross-section [113]. Equations 3.11 and 3.12 are valid only for hinged-supported beams. It is important to note that the considered Timoshenko beam is still an approximation because it is based on the simplified hypotheses of the theory of beams.

More importantly, for anisotropic materials, the stress state cannot be assumed uniaxial as in isotropic materials, but will include triaxial stress states. This makes impossible to develop an analytical formula to calculate the frequency.

Torsional mode

In general, the expression of the natural torsional frequency (in $rad\ s^{-1}$) of the mode i is:

$$\lambda_i = \frac{\beta_{ti}}{l} \sqrt{\frac{G}{\rho}} \quad (3.13)$$

With β_{ti} a factor that depends on the supporting conditions (for free-standing bar $\beta_{ti} = i\pi$), G the shear modulus, ρ the density and l the specimen length.

When applied to anisotropic materials, the presence of triaxial stress states, makes not possible to develop an analytical formula for the calculation, like for the bending mode.

3.3.2 Methodology

In order to derive the elastic properties, IET tests are performed to measure the natural frequencies. The IET tests are performed according to the standard ASTM C1259-01. In transversely isotropic materials, specimens with two different orientations are tested, supported in two different ways to favour the excitation of their flexural and torsional modes, see Figures 3.6 and 3.7. In general, the flexural mode depends on the elastic modulus and the torsional mode on the shear moduli. The dimensions and orientation of the specimens are shown in Table 3.1 and Figure 3.2. Direction X corresponds to TP (trough-plane), and Y-Z to IP (in-plane).

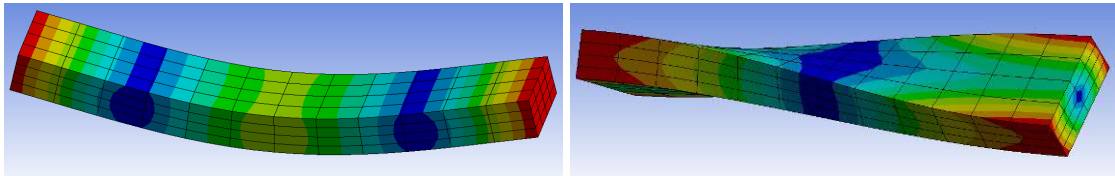


Figure 3.6: Visualisation of the deformations during the bending (left) and torsional (right) modes. The nodes are the imaginary lines with no deformation (blue), while the anti-nodes are the points with largest amplitude (red).

The specimens are excited with a small hammer in one of the points of maximum amplitude of the desired mode (anti-nodes), so exciting the corresponding resonance frequency. The generated sound waves are acquired with a microphone and the spectrum

analysed. The signal is processed with a *fast Fourier transform* (FFT) algorithm that allows to obtain amplitude peaks in the spectrum of frequencies of interest, see Figure 3.8.

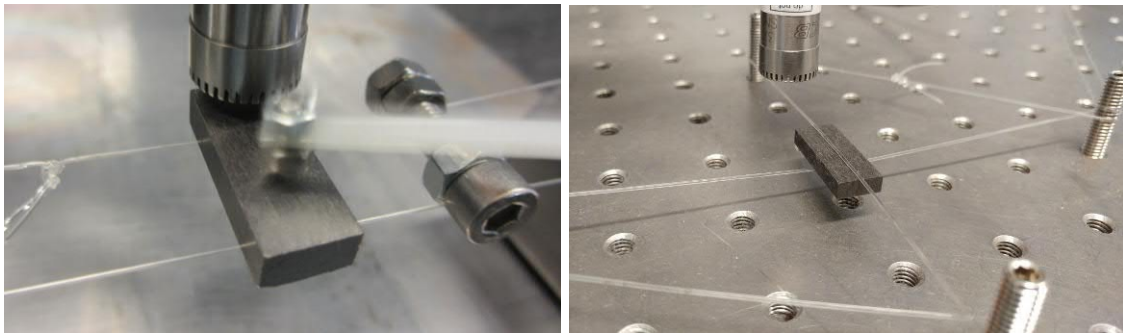


Figure 3.7: IET experimental set-up. Nylon-wire supports for exciting the flexural (left) and torsional (right) frequencies. Left picture shows the specimen being impacted with the excitor. Specimens shown are 25 mm long.

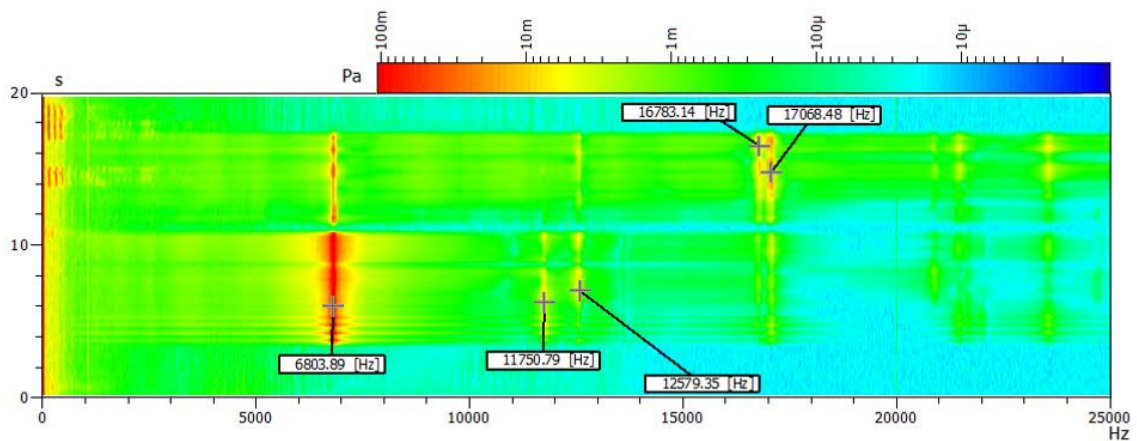


Figure 3.8: Example of the acquired spectrum processed with the FFT algorithm.

As explained in section 3.3.1, it is not possible to analytically calculate the elastic properties from the natural frequencies of anisotropic bodies. Therefore, the formulae from the standard method ASTM C1259-01, which allow to obtain the elastic properties from the resonant frequency, cannot be used.

Instead, a finite element analysis optimisation algorithm is performed to derive the elastic constants by reverse engineering. ANSYS software, in this case version 17.2, was used as FEM code.

The details and limitations of the method to derive the elastic constants are shown in Appendix E.

3.4 Electrical characterisation

Two methods are used to measure the electrical conductivity or its inverse, the electrical resistivity.

Direct current (DC) method

The electrical resistivity ρ_e of parallelepiped specimens is calculated from their dimensions and resistance, which is measured using four-wire sensing in order to make the measurement independent of the electrode-specimen contact resistance. Direct current (DC) is used for the test. The set-up is custom made, analogous to that proposed by the standard ASTM C611-98. The conductivity γ_e , inverse of the resistivity, is measured in $[S m^{-1}]$. The calculation of the uncertainty of this measurements is presented in Appendix F.

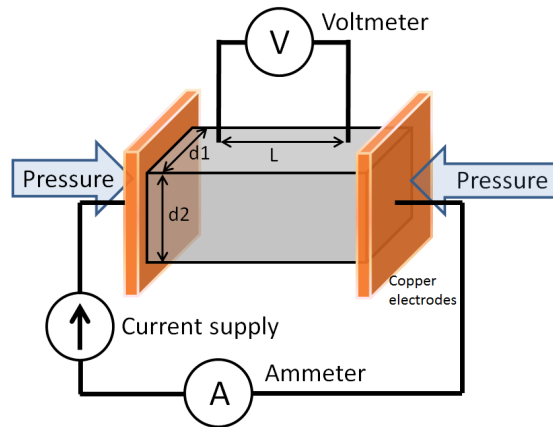


Figure 3.9: Direct method schematic

$$R[\Omega] = \frac{V}{I} \quad ; \quad \rho_e[\Omega m] = R \frac{A}{L} = R \frac{d1 \cdot d2}{L} \quad ; \quad \gamma_e[S m^{-1}] = \frac{1}{\rho_e} \quad (3.14)$$

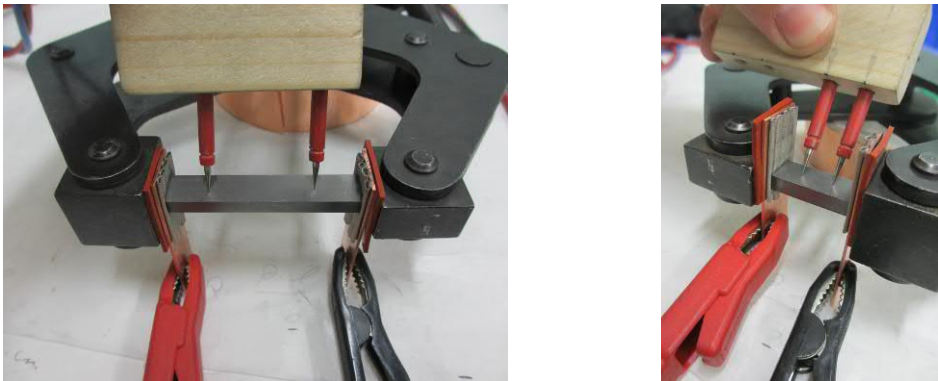


Figure 3.10: Custom-made direct method set-up for measuring electrical conductivity

Superficial electrical conductivity

In the in-plane direction, an eddy-current commercial device *Sigmatest 2.069* from Foerster (in the full frequency range 60 to 960 kHz) provides the electrical conductivity values within $\pm 10\%$ with respect to the DC method. Due to the anisotropy of MoGr, in TP surfaces, somehow averages the TP (x) and IP (y or z) directions, thus not appropriate for obtaining the through-plane conductivity only.

By varying the frequency, the depth of the measured region changes, because of the skin effect.

The skin effect is the tendency of an alternating current in a conductor to distribute nearby the surface. The skin depth δ , see equation 3.15, is defined as the depth below the surface of the conductor at which the current density has fallen to $1/e$ of its value at the surface.

$$\delta = \sqrt{\frac{2\rho_e}{2\pi f \mu_0 \mu_r}} \approx 503 \sqrt{\frac{\rho}{\mu_r f}} = \frac{503}{\sqrt{\gamma_e \mu_r f}} \quad (3.15)$$

where δ is the skin depth (mm), ρ_e and γ_e are respectively the electrical resistivity and conductivity of the material ($\mu\Omega m$ and $MS m^{-1}$), f is the frequency (kHz), μ_0 is the magnetic permeability of vacuum (H/m) and μ_r is the relative magnetic permeability of the material (dimensionless). In paramagnetic and diamagnetic materials: $\mu_r \approx 1$, being respectively slightly higher and smaller than one.

The Sigmatest device requires that the specimen thickness is at least 3 times the skin depth for an accurate measurement.



Figure 3.11: Sigmatest device

3.5 X-Ray Diffraction (XRD)

Historically much of our understanding of the atomic and molecular arrangements in solids has resulted from X-Ray diffraction investigations. Diffraction is a very versatile technique. With the appropriate set-ups, it can be used to measure interplanar distances, strain, thin-films thickness, crystallite size, to identify phases, to characterise texture, etc.

Diffraction occurs when a wave encounters a series of regularly spaced obstacles that are capable of scattering the wave, and have spacings that are comparable to the wavelength. Those obstacles are the atomic planes in a crystalline solid, with interplanar distances d_{hkl} .

The unit cell is the smallest group of particles (atoms or molecules) that constitutes a crystal pattern. The lattice parameters are the dimensions of unit cells. These dimensions are related to the strength of the bonds between particles, therefore they vary due to factors such as changes in the chemical composition (impurities, doping, stoichiometry, etc.), stresses or thermal expansion. The particles arrange themselves in the type of pattern (crystal system) which minimises the energy of the structure, hence factors affecting the structure energy, such as temperature or chemical composition variations, can produce phase changes.

In crystallography, the plane (hkl) intercepts the axes a , b and c at the reciprocal of h , k and l respectively (Miller indices). The intercepts are measured in terms of fractions or

multiples of the lattice parameters. The vector d_{hkl} extends from the origin to the plane (hkl) and is normal to it.

If the Bragg's law is satisfied, see equation 3.16, the interference between two or more waves that have been scattered is constructive, therefore the diffracted beam will have high intensity and can be detected. Diffractometers use x-rays and precise goniometric systems to measure those nanometric d_{hkl} distances.

$$d_{hkl} \text{ from Bragg's law : } \quad d_{hkl} = \frac{\lambda}{2\sin(\theta)} \quad (3.16)$$

Bragg's law is a necessary but not sufficient condition for diffraction by real crystals. Depending on the type of crystal structure, other conditions that define the allowed and forbidden reflections rule the diffraction (known as selection or reflection rules). The allowed reflections are:

- Simple cubic: any h , k and l .
- BCC: $[h + k + l = \text{even}]$.
- FCC: h , k and l all even or all odd.
- Hexagonal: other than $[h + 2k = 3n \text{ and } l = \text{odd}]$.

Equations 3.17 to 3.19 present the interplanar spacing relationships for different crystallographic systems. They relate d_{hkl} with the lattice parameters.

$$\text{Cubic : } \quad \frac{1}{d_{hkl}^2} = \frac{h^2 + k^2 + l^2}{a^2} \quad (3.17)$$

$$\text{Orthorhombic : } \quad \frac{1}{d_{hkl}^2} = \frac{h^2}{a^2} + \frac{k^2}{b^2} + \frac{l^2}{c^2} \quad (3.18)$$

$$\text{Hexagonal : } \quad \frac{1}{d_{hkl}^2} = \frac{4}{3} \left(\frac{h^2 + hk + k^2}{a^2} \right) + \frac{l^2}{c^2} \quad (3.19)$$

Theoretical density

The density of ideal crystal structures is calculated from the unit cell dimensions and the atomic composition.

For example, the theoretical density of the ideal graphite structure, considering the lattice parameters reported in reference [53] ($a = 2.4617 \text{ \AA}$ and $c = 6.7106 \text{ \AA}$), is calculated as follows.

There are a total of 4 carbon atoms per unit cell (2 layers of $[1/6 + 1/3 + 1/6 + 1/3 + 1]$ atoms), see Figure 3.12. Knowing that carbon atoms have a mass of $12.01 \text{ g mole}^{-1}$, the mass of one unit cell is deduced. The theoretical density, calculated from that mass and the volume of the hexagonal unit cell (Figure 3.12 and equation 3.20) results in 2.265 g cm^{-3} .

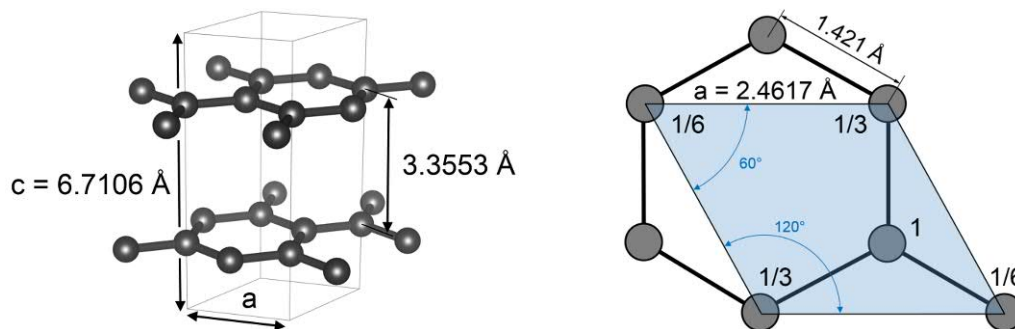


Figure 3.12: (Left) Unit cell of graphite crystal structure. (Right) Number of carbon atoms at each of the two basal layers in the unit cell.

$$V_{hex. \text{ unit cell}} = \frac{\sqrt{3}}{2} a^2 c \quad (3.20)$$

3.5.1 Phase identification and crystallite-size analysis

The reflections visible in the diffraction patterns are a signature of the type and dimensions of the crystalline structures present in the sample. The theoretical peak positions of known phases can be calculated analytically with the rules introduced above. This is an easy process for cubic and hexagonal structures because they have many symmetries, while for more complex systems such as the orthorhombic, it is not practicable. If the experimental peak positions match the calculated ones, it is likely that the phase is present. In that case, Rietveld refinement is performed to the experimental pattern with *Materials Analysis Using Diffraction* (MAUD) software to obtain the real lattice parameters and other information such as crystallite-size [114] [115]. The required CIF files containing the crystallographic information of the known phases are downloaded from Crystallography Open Database (COD) [116].

When facing unknown phases (peaks) in the analysis, the process used is to understand first which elements are present in the sample. A chemical analysis, such as EDS (see SEM) provides this information. With the chemical information, the possible phases are found in the literature and the corresponding peak positions checked for matches in the pattern. The presence of multiple phases complicates the identification, as the peaks of each phase have to be distinguished from the rest.

X-ray diffraction (XRD) phase identification and crystallite-size analyses were performed with a Siemens D5000 diffractometer with Bragg-Brentano θ - 2θ configuration, using Cu $K\text{-}\alpha_1$ radiation ($\lambda = 1.54056 \text{ \AA}$) at room temperature (RT), see Figure 3.13. Its goniometer radius is 250 mm. A nickel foil filter is used before the detector to limit the Cu $K\text{-}\beta_1$ radiation. The resulting X-rays include also Cu $K\text{-}\alpha_2$ radiation ($\lambda = 1.54439 \text{ \AA}$) and Cu $K\text{-}\beta_1$ radiation ($\lambda = 1.39222 \text{ \AA}$), with intensities a factor 0.49 and 0.02 with respect to the Cu $K\text{-}\alpha_1$ intensity. The standard acquisition is done between $2\theta=20$ to 110° , with steps of 0.02° (integrated time of 2 s/step, 150 min. test), with divergence and anti-scatter 0.5° slits and receiving 0.2 mm slit. Longer step times are used for better quality patterns (larger signal-to-noise ratio). The patterns are shown as-acquired, i.e. not corrected for specimen displacement/transparency experimental errors, see section 3.5.2. Two intensity scales are used: linear scale (proportional to the absolute counts) or square root scale (square root of the counts). The latter scale homogenises very different peak heights for better readability.

Some XRD analyses of the bulk materials were performed on perpendicular surfaces, in



Figure 3.13: Siemens D5000 X-ray diffractometer, testing a graphite sample ($\sim 10 \times 10 \times 25$ mm).

this manner the most intense peaks of graphite, mainly the (002) and (004), had reduced intensity due to the texture. Besides that, this orientation favours the diffraction of the set of planes (100) and (110), which allows to obtain the basal plane crystallite size (L_a).

The surface state of the samples for XRD analyses was as-received (AR) from the supplier or sanded with P1200 sandpaper. No relevant differences in the position of the diffraction peaks were found by changing the surface state, for instance after polishing or ultrasonic bath cleaning.

Powders were characterised by pouring a small quantity on the support, which consists in an aluminium cylinder with a threaded plastic base ($\text{Ø}30$ mm) moving along its axis. The base was set to around 1-2 mm depth. The corresponding volume was filled with the powder and levelled with a flat spatula. Some texture in the crystallites is expected due to this necessary last step.

Crystallite-size determination

The author considers important to clarify here the differences between domain, crystallite and grain.

- **Domain:** The term domain is generally used to refer to the diffraction domain, which is each volume of a material with perfectly regular atomic structure (no defects) that produces a coherent diffracted beam. It is also called crystalline-domain. The domains form a substructure that can occur in single crystals and in polycrystalline materials. The individual domains are very slightly misoriented (typically $< 1^\circ$) with respect to each other, and are smaller than the grain size. The separation between domains is called low-angle grain boundary or subgrain boundary [117].
- **Grain:** A grain is each crystal in a material having different crystallographic orientation than its neighbours. This produces surfaces where the atoms are bonded less regularly than in the perfect lattice, which are called grain boundaries.

- **Crystallite:** Crystallite is a more general term that refers to domain if there are domains present and it is the same thing than grain if not [117].

A well-annealed metal does not have domains, but does have grains. A perfect single crystal does not have neither grains nor domains nor other defects.

If the crystallites in the sample are smaller than 500 nm , the diffraction conditions are not ideal and the peaks broaden. An analysis of diffraction peak broadening can be used to determine the crystallite sizes up to 500 nm [117]. Rietveld refinement is done with MAUD to obtain the graphite crystallite size after calibration of the instrumental broadening with a LaB_6 powder reference sample. The broadening effects considered (Delft model) are the crystallite size and the instrumental broadening. The refinements done with MAUD with the calibrated instrumental broadening show crystallite sizes sensitivity up to $\sim 1\ \mu\text{m}$. The best results to fit XRD patterns of graphitic materials with the Rietveld refinement method have been obtained with the following MAUD parameters:

- Size-strain model: in general, the isotropic model is used.
- Texture: Harmonic, with fibre symmetry ($L_{max}=4$), with the two harmonic parameters (H_{211} and H_{411}) refined. If the fit is not good enough, the model "arbitrary texture" is used instead.
- Specimen displacement refined (parameter "_riet_par_spec_displac_z_2R", see section 3.5.2).
- Parameter 2θ -offset equal to zero (calibrated diffractometer). This is a constant shift in 2θ , as opposite to the specimen displacement error, which produces a shift that decreases as 2θ increases.

The combination of those texture and crystallite size parameters usually manages to fit the relative intensities.

Anisotropic crystallite size has been considered, as is the most probable case for flake-like graphite. The model of Popa (spherical harmonics, with expansion degree $L_{max}=6$), with R_0 and R_4 refined (R_1 to R_3 equal to 0), simulates crystals with hexagonal symmetry [118]. However, the peak shape is typically not correctly fitted at high 2θ angles, leading to big errors in size and non-realistic crystallite shapes. This may be due to the low signal-to-noise ratio a high 2θ angles (too short acquisition times). For this reason, the isotropic model is used instead.

The fit quality can be improved, specially to model the shape in some graphite peaks. In particular, the error when fitting (002) graphite peak, is probably due to the distribution of grain sizes. This peak is typically the most intense one in graphite, with enough level of signal. MAUD has an option to model this kind of distributions, but the results were not successful.

For metals or compounds with negligible preferred orientation, the refinement is performed with "no texture" model, with good results.

3.5.2 Thermal expansion studies

Thermal expansion is the macroscopic effect of the change in average distance between atoms at different temperatures. The latter results from the asymmetric curvature of the trough in the interatomic potential energy curve. This process is neither linear nor necessarily monotonic across all temperatures, as demonstrated by many real materials.

As XRD technique is capable of measuring the distance between atomic planes, it can be used to characterise the thermal expansion. With XRD, the thermal expansion of all present phases, in all crystallographic orientations can be measured, while with dilatometry techniques, the macroscopic thermal expansion of the full body is measured.

The thermal expansion measurements were done in a Panalytical X-ray diffractometer with Bragg-Brentano θ - 2θ configuration, using Cu $K\text{-}\alpha_1$ radiation ($\lambda = 1.54056 \text{ \AA}$) at varying temperature. Its goniometer radius is 240 mm. The heated chamber has openings for the X-rays, see Figure 3.14. The tests were done between RT and maximum temperature 600°C , in air at atmospheric pressure. Once the temperature is stabilized, each pattern acquisition $20^\circ < 2\theta < 90^\circ$ lasts 16 min. The duration of the furnace ramps 25-100, 100-200, 200-300, 300-400, 400-500, 500-600 and $600\text{-}500^\circ\text{C}$ until stabilization of the temperature are $8 \pm 1 \text{ min}$, the $500\text{-}300$ and $300\text{-}100^\circ\text{C}$ are $14 \pm 1 \text{ min}$ and the $100\text{-}25^\circ\text{C}$ is around $30 \pm 1 \text{ min}$. The total duration of the full test is around 4.5 h, however some tests were performed with no pattern acquisition during the cooling down ramp.

The bulk specimens, around 1-2 mm thick are supported on the alumina sample holder, see Figure 3.14. Powders are placed on a cylindrical alumina holder, which features an edge all around to level the powder with a flat spatula.



Figure 3.14: (Left) X-ray diffractometer with furnace chamber. (Right) sample holder for the high temperature XRD test. Sample shown on top of it is about $\text{Ø}13 \text{ mm}$.

The calibration of sample height was done for each sample, only at RT, with the X-ray source and detector at $2\theta = 0^\circ$. The sample holder is then moved upwards (machine parameter $+Z$), showing the typical Gaussian beam grazing absorption curve, see Figure 3.15. The specimen surface is at the Z which shows the middle intensity between the maximum and the sample transparency signal, see Figure 3.15.

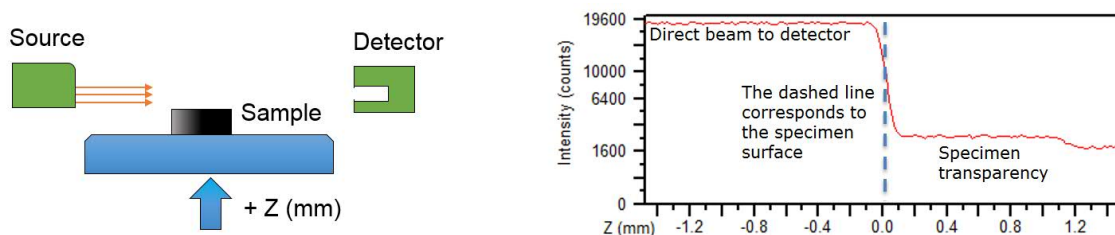


Figure 3.15: Schematic and typical signal of the alignment process.

One specimen was tested doing the alignment at every temperature point. This align-

ment requires a manual change of slits and a different acquisition program, which prevents the execution of an automatic measuring program and requires around twice the time to complete the test. For this reason, the alignment was performed only once, at RT. This requires a correction of the specimen displacement error for each acquired pattern.

The peak positions are manually listed and identified from each diffraction pattern. The identification of the peaks requires previous knowledge of the structure and theoretical lattice parameters of the phases. Afterwards, the experimental lattice parameters are calculated, using the Bragg's law (equation 3.16) and the interplanar spacing relationships (equations 3.17 to 3.19).

The uncertainty in the lattice parameters results, with this method, is estimated to 0.002 Å. This is the reason of presenting only 3 decimals in the results. An uncertainty of 30 μm in the specimen height position seems reasonable, and would result in an error of $\pm 0.06\%$ (0.002 Å) for peaks above $2\theta = 25^\circ$. This uncertainty produces a maximum peak shifting at low angles of $\Delta 2\theta \leq \pm 0.02^\circ$.

Second-order polynomials are fitted to the experimental data using a least-squares procedure. The average linear thermal expansion coefficients (also known as secant CTE) are determined from the relation:

$$\bar{\alpha} = \frac{1}{a_0} \frac{(a - a_0)}{(T - T_0)} \quad (3.21)$$

The function-fitting of the data allows to smooth out experimental errors, and to extrapolate the lattice parameters to 20 °C.

Sample displacement/transparency correction

If the surface of the sample is not exactly at the diffractometer focusing circle, the positions of the diffraction peaks are not correct, they shift. The specimen transparency error, due to the penetration of the x-rays in low-density specimens, produces a peak interaction inside and not on the surface of the sample. It is therefore of the same nature than the displacement error.

In the ideal case of the diffractometer optics aiming only at the point of the diffractometer centre, sample displacements would make the detector to receive no signal. In reality, the beam and optics are not ideal, and those sample displacements produce peak shifting. Figure 3.18 shows graphically how this error is produced.

This error is eliminated using parallel-beam optics. However, this results in less detected intensity and larger peak-broadening, see Figures 3.16 and 3.17. The conventional Bragg-Brentano optics were chosen for the tests, due to the aforementioned disadvantages. Therefore, sample displacement error has to be corrected.

In the used set-up, the increase of temperature provokes an expansion in the specimen and sample holder, moving the surface of the sample upwards from the diffractometer centre. The displacement of the sample due to its own CTE is in the order of 17 μm for a 1 mm-high sample of TPG ($CTE_{\perp} = 28 \times 10^{-6} \text{ m}^{-1} \text{ K}^{-1}$) with 600 °C of thermal excursion, and around 10 μm for a 1.5 mm-high MoGr sample ($CTE_{\perp} = 11 \times 10^{-6} \text{ m}^{-1} \text{ K}^{-1}$). On the other hand, the sample holder expansion is much larger, see Table 3.2, making the specimen expansion negligible.

The error in the peak position induced by the change in height is ruled by the following

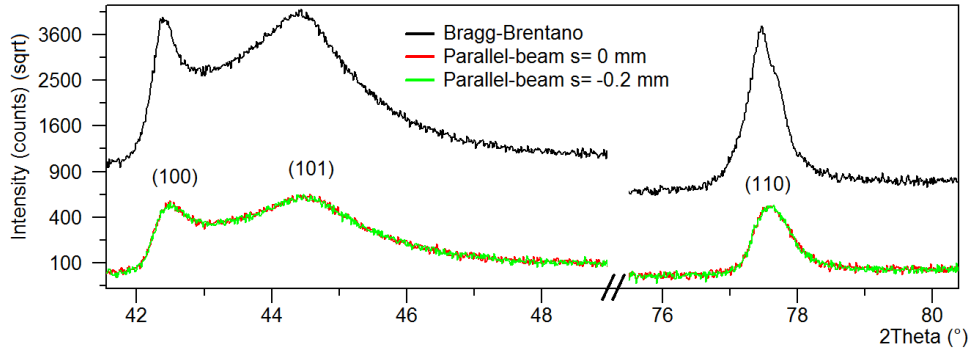


Figure 3.16: XRD patterns of the same graphite R4550 specimen: $\theta - 2\theta$ Bragg-Brentano geometry and parallel-beam configuration. Parallel-beam optics result in lower intensity and broader peaks, but sample displacement errors (s) do not produce peak shifting.

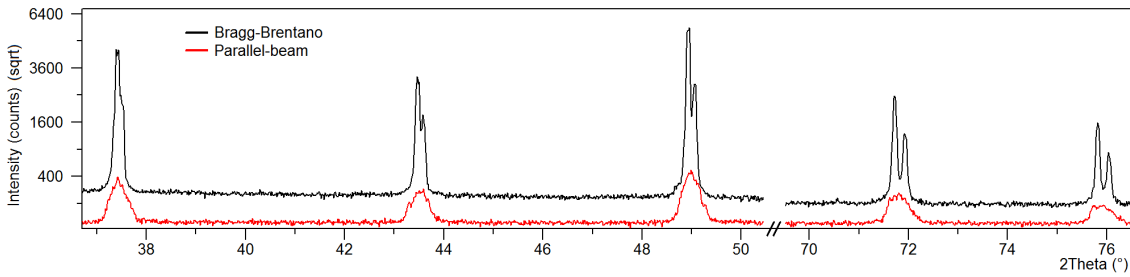


Figure 3.17: Extreme peak broadening visible in LaB_6 powder with the parallel-beam optics. The double peaks ($\text{Cu-K}\alpha_1$, $\text{Cu-K}\alpha_2$) merge in broad single peaks with the parallel-beam optics, making difficult to determine their positions.

expression:

$$\Delta 2\theta = -\frac{2s \cos(\theta)}{R} \text{ (in radians)} \quad (3.22)$$

The $\Delta 2\theta$ generates an error in d as follows [117]:

$$\frac{\Delta d}{d} = -\frac{s \cos^2(\theta)}{R \sin(\theta)} \quad (3.23)$$

The errors are defined as (idem for d):

$$2\theta_{actual} = 2\theta_{exp} - \Delta 2\theta \quad (3.24)$$

For example, if a given sample should produce a peak at $2\theta = 90^\circ$ using $\text{Cu } K\text{-}\alpha_1$ radiation in perfect aligned conditions, if the sample is lowered down 0.5 mm ($s = +0.5 \text{ mm}$ according to the convention of Fig. 3.18), $\Delta 2\theta$ will be -0.17° , so the machine ($R = 240 \text{ mm}$)

Table 3.2: Sample holder expansion in air (in the direction $+Z$ of Figure 3.15), specification.

T [°C]	[mm]
25	0
100	0.02
200	0.06
300	0.09
400	0.13
500	0.18
600	0.22

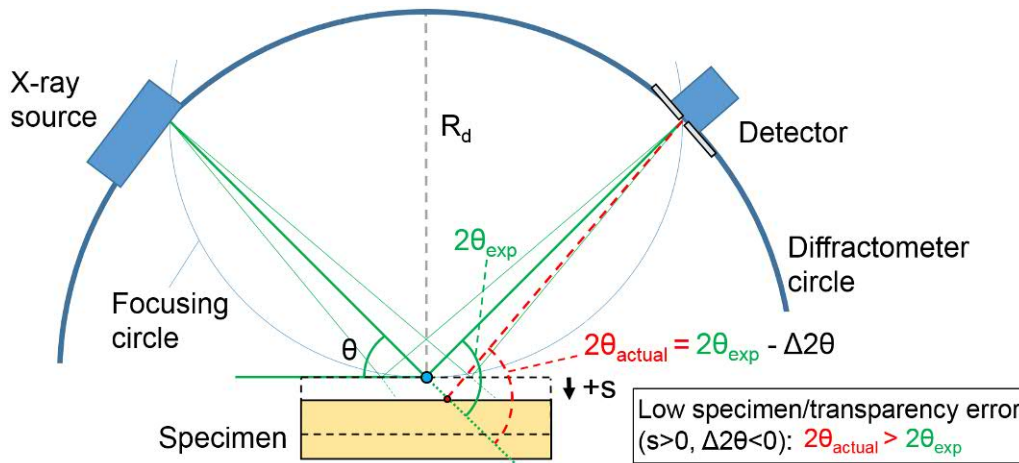
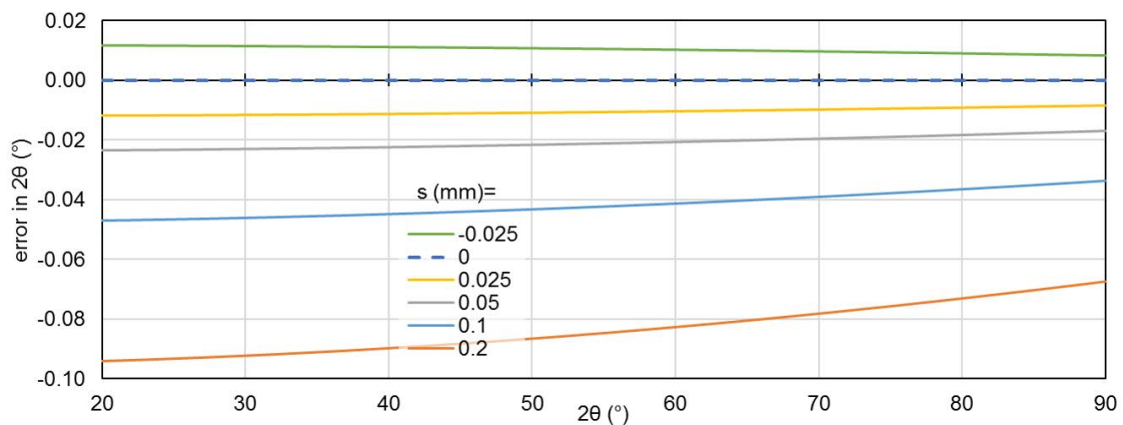


Figure 3.18: XRD specimen displacement error.

will be at $2\theta_{exp} = 89.83^\circ$ when the peak is detected. At this θ , the error corresponds to $\Delta d = -0.002 \text{ \AA}$.

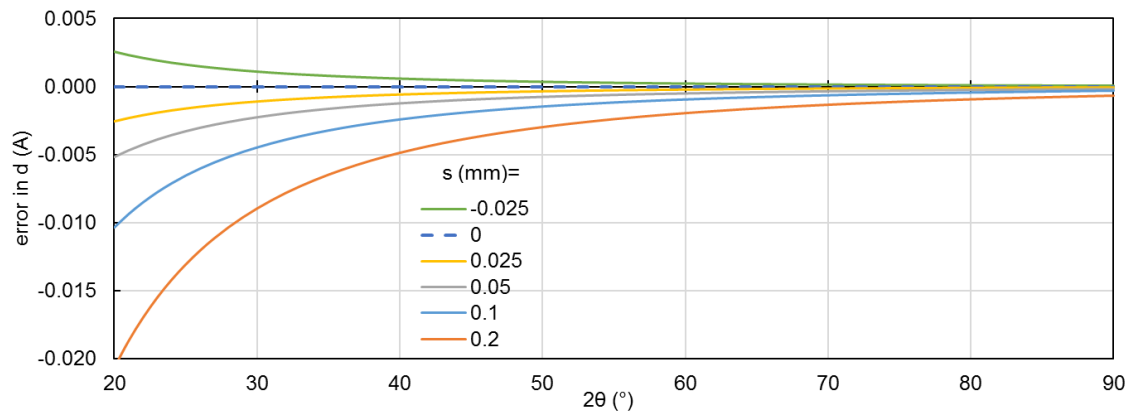
The effect of the error with different displacements s is illustrated in Figures 3.19 and 3.20. A diffraction pattern is considered to have high quality if the average difference between the measured and predicted peak position is $\Delta 2\theta_{av} \leq \pm 0.03^\circ$ and the maximum is $\Delta 2\theta_{max} \leq \pm 0.05^\circ$ [119].

Figure 3.19: $\Delta 2\theta$ (°) due to specimen displacement s .

The specimen displacement produces smaller error in the peak positions with increasing 2θ angle. Apart from that, parallel sets of planes must meet certain known relationships, explained below. All things considered, if the pattern shows different peaks (thus at different angles) of sets of planes that are parallel between them, it is possible to estimate the value s of the actual displacement of the specimen. The same applies for sets of planes that depend on only one lattice parameter, such as all planes in cubic phases or (100)-(110) in hexagonal phases.

First, at least two peaks that correspond to parallel set of planes, such as (002), (004) and (006), are identified. The magnitudes of vectors d_{hkl} of different parallel planes are related between them through the relationship between the intercepts of the planes. For example, in graphite's hexagonal structure, $d_{002} = 2 * d_{004} = 3 * d_{006}$.

With this information, it is possible to obtain the value s that produces the minimum

Figure 3.20: Δd (Å) due to specimen displacement s (Cu $K\text{-}\alpha_1$)

disagreement between d_{hkl} of parallel planes. First, all experimental peak positions of the pattern are identified and tabulated in a spreadsheet. The s are calculated using "Solver" Microsoft Excel add-in, by minimizing a cell containing the desired sum of squared residuals, and letting the cells that contain s vary, see Figure 3.21. The solution process is similar to the one described in reference [120]. The obtained displacement value s allows to correct all the peak positions of the pattern. It is assumed that the displacement error is the only source of peak shifting. For example, the residual strain is neglected.

	A	B	C	D	E	F	G	H	I	J	
1			λ [Å]:	1.54056		R [mm]:	240				
2			Graphite experimental peak positions ($2\theta_{\text{exp}}$)								
3		Temp [°C]	(002)	(100)	(101)	(004)	(110)	(112)			
4		25	26.534	42.356	44.547	54.657	77.473	83.596			
5		100	26.494	42.373	44.554	54.543	77.492	83.59			
6		200	26.435	42.392	44.562	54.389	77.513	83.579			
7		300	26.376	42.409	44.566	54.244	77.533	83.564			
8		400	26.318	42.43	44.575	54.089	77.551	83.541			
9		500	26.262	42.45	44.581	53.95	77.567	83.528			
10		600	26.206	42.471	44.593	53.794	77.583	83.509			
11											
12	s [mm]		Corrected 2θ ($2\theta_{\text{actual}}$) = $2\theta_{\text{exp}} - \Delta 2\theta$						$\Delta 2\theta = \text{DEGREES}(-2*s*\text{COS}(\text{RADIANS}(2\theta_{\text{exp}}/2)))/R$		
13	0.0020	25	26.5350	42.3569	44.5479	54.6579	77.4738	83.5967			
14	-0.0274	100	26.4812	42.3608	44.5419	54.5314	77.4818	83.5802			
15	-0.0608	200	26.4067	42.3649	44.5351	54.3632	77.4904	83.5573			
16	-0.0885	300	26.3349	42.3696	44.5269	54.2064	77.5001	83.5325			
17	-0.1349	400	26.2553	42.3700	44.5154	54.0316	77.5008	83.4930			
18	-0.1811	500	26.1778	42.3694	44.5010	53.8729	77.4996	83.4635			
19	-0.2312	600	26.0985	42.3681	44.4909	53.6956	77.4970	83.4267			
20											
21			Corrected d_{hkl} (from $2\theta_{\text{actual}}$) = $\lambda/(2*\text{SIN}(\text{RADIANS}(2\theta_{\text{actual}}/2)))$						$(d_{002} - 2*d_{004})^2 + (d_{100} - d_{110}*\text{SQRT}(3))^2$		
22		25	3.3564	2.1321	2.0322	1.6778	1.2310	1.1557	5.75E-07	4.61E-17	
23		100	3.3631	2.1319	2.0325	1.6814	1.2309	1.1559	6.58E-08	8.81E-18	
24		200	3.3724	2.1317	2.0328	1.6862	1.2308	1.1561	8.94E-10	4.63E-18	
25		300	3.3814	2.1315	2.0331	1.6907	1.2306	1.1564	4.46E-12	1.18E-17	
26		400	3.3915	2.1315	2.0336	1.6958	1.2306	1.1569	1.99E-09	5.52E-18	
27		500	3.4014	2.1315	2.0342	1.7004	1.2306	1.1572	3.37E-07	1.06E-19	
28		600	3.4115	2.1316	2.0347	1.7056	1.2307	1.1576	1.14E-07	7.00E-18	
29			Sum of Squared Residuals (SSR):						1.09E-06	8.40E-17	

Figure 3.21: Example of s calculation in Excel. In this case, peak (004) was not as sharp as peaks (100) and (110), so the solver was executed to minimize cell J29, by changing variable cells A13:A19 (in yellow). Cell J29 corresponds to the disagreements between d_{100} and d_{110} .

If the conditions to obtain s are met, it is also possible to do it with MAUD software (Rietveld refinement). The MAUD parameter "_riet_par_spec_displac_z_2R" (Datasets, Datafile, Additional parameters, Sample displacement $z/2R$) multiplied by $-R/2 = -120$

equals to s in mm (R diffractometer radius, 240 mm), in MAUD version 2.8. However, this requires very precise fitting in order to correctly capture the real peak positions. If the XRD pattern shows sharp peaks (easy to locate) and the MAUD fitting is not precise, the Excel Solver method gives more consistent results.

Experimental validation

In order to validate the CTE-XRD measurement method, pure niobium was tested both with dilatometry technique and with XRD. The niobium samples were obtained from a 3 mm -thick sheet, fully recrystallized and with $\text{RRR} > 300$ (very low impurity content). The microstructure is shown in Figure 3.22, featuring equiaxed grains with an average size of $7\ \mu\text{m}$. Niobium was chosen because of its cubic structure (BCC), which, if there is no preferred orientation, results in completely isotropic thermal expansion. Besides, the expansion behaviour of the lattice should match the macroscopic thermal expansion measured with the dilatometer, due to the high purity of the sample. The surface for the XRD test was mechanically and chemically polished, resulting in a very reflective mirror-like surface. This was done to remove the superficial texture and oxide layers. The samples for dilatometry were long (25 mm), in order to have the minimum possible measurement uncertainty.

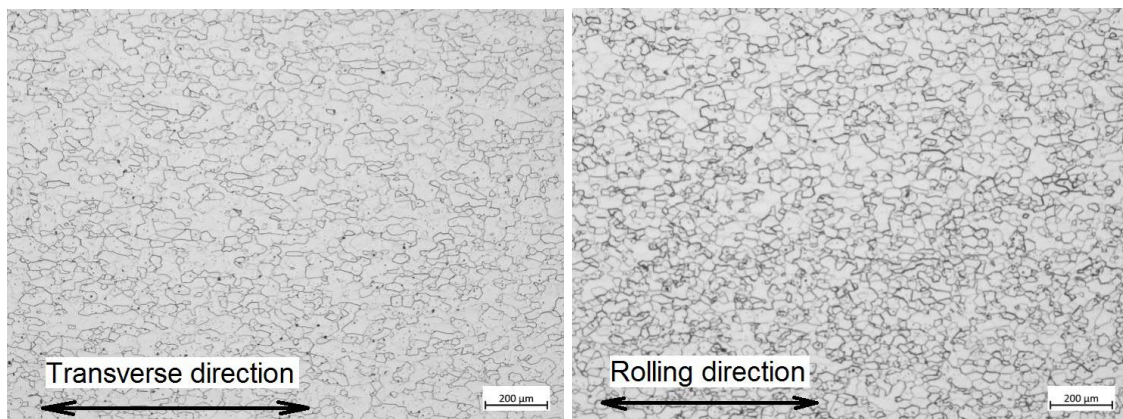


Figure 3.22: Metallography of the niobium sheet (cross-section, mid thickness), A.Gallifa (CERN).

The experimental XRD patterns are shown in Figure 3.23. The three expected peaks of the BCC Nb structure appear between $2\theta = 20$ to 90° . At 300°C , the intensity of the peaks starts to decrease and oxides are formed due to the presence of air. Eventually, the white layer of oxides covers the surface and the Nb signal completely vanishes. Measurements of the lattice parameters were possible up to 300°C , see Table 3.3. The correction of the specimen displacement is shown in the table, calculated with the method described above. The lattice parameters are calculated from the corrected peak positions, using equations 3.16 and 3.17. A second degree polynomial is fitted to the data, and the secant CTE is calculated from the former, see Table 3.4 and Figure 3.24. This allows to smooth out the data, reducing experimental errors, and to extrapolate the CTE up to 600°C .

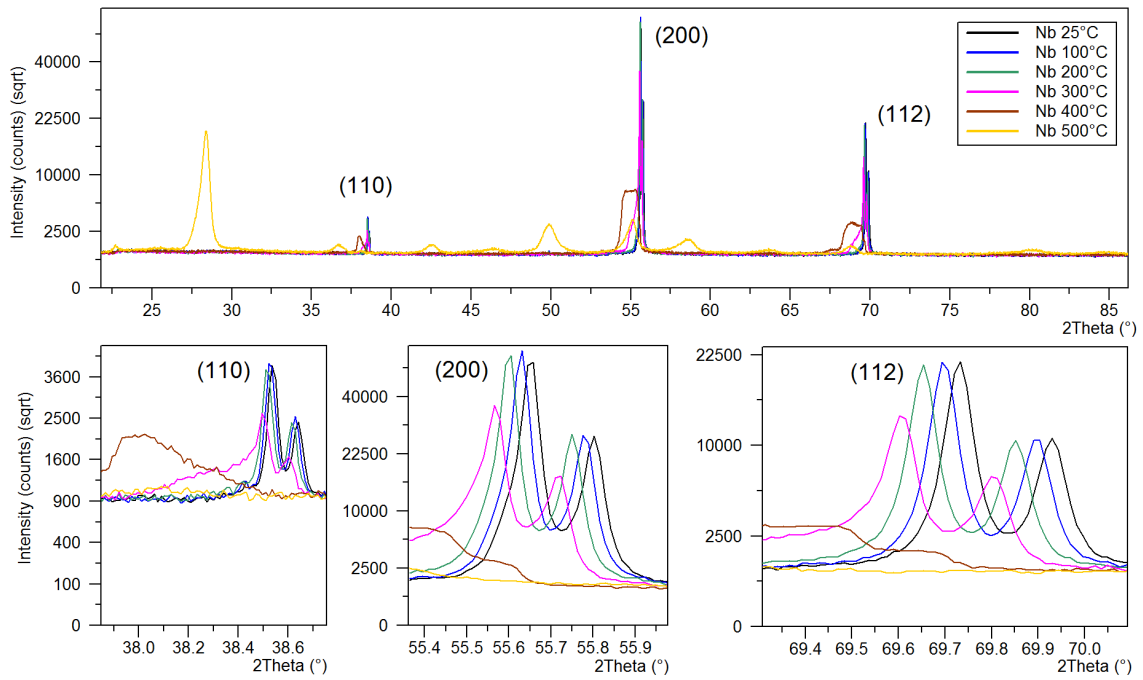
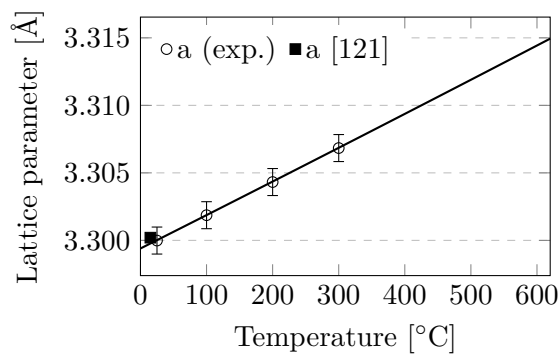


Figure 3.23: Niobium experimental XRD patterns.

Table 3.3: BCC Nb 2θ experimental and corrected peak positions [°]. Resulting lattice parameters.

T [°C]	s [mm]	(110)		(200)		(112)		a [Å]	
		Exp.	Corr.	Exp.	Corr.	Exp.	Corr.		
Heating up	25	0.027	38.537	38.549	55.652	55.663	69.731	69.742	3.300
	100	-0.001	38.527	38.527	55.629	55.629	69.697	69.697	3.302
	200	-0.040	38.515	38.497	55.601	55.584	69.653	69.637	3.304
	300	-0.070	38.498	38.467	55.566	55.537	69.605	69.578	3.307

Figure 3.24: Niobium lattice parameter versus temperature, matching $a_{15^\circ\text{C}} = 3.3002 \text{ \AA}$ [121].Table 3.4: Fitting equation for the lattice parameter variation ($d = AT^2 + BT + C$, T in °C, d in Å). From the heating-up curve.

	A	B	C	Value at 20°C
a (Nb)	$6.6783 \cdot 10^{-10}$	$2.4654 \cdot 10^{-5}$	3.2994	3.300

Table 3.5: Comparison of secant CTE 20-T ($^{\circ}\text{C}$) [K^{-1}]. Four samples tested with dilatometry (RD: Rolling direction, TD: Transverse direction), one sample tested with XRD technique.

T [$^{\circ}\text{C}$]	DIL Heating-up (H)				DIL Cooling-down (C)				Average		Diff. [%]
	RD1	RD2	TD1	TD2	RD1	RD2	TD1	TD2	(C) DIL	XRD	
50	7.30	7.27	7.23	7.36	7.33	7.44	7.36	7.35	7.37	7.49	1.6
100	7.36	7.34	7.30	7.41	7.40	7.49	7.42	7.42	7.43	7.50	0.8
200	7.47	7.47	7.44	7.51	7.53	7.58	7.52	7.54	7.54	7.52	-0.4
300	7.59	7.59	7.57	7.62	7.62	7.66	7.61	7.64	7.63	7.54	-1.3
400	7.71	7.71	7.69	7.73	7.69	7.71	7.68	7.70	7.70	7.56	-1.8
500	7.82	7.82	7.79	7.84	7.73	7.75	7.73	7.74	7.74	7.58	-2.1
600	7.94	7.92	7.89	7.96	7.74	7.76	7.77	7.75	7.75	7.60	-2.0

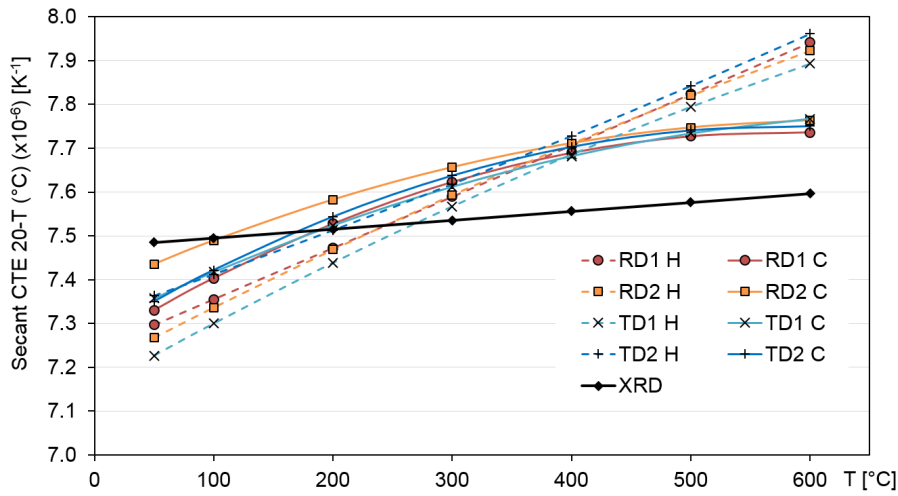


Figure 3.25: Comparison of niobium secant CTE 20-T ($^{\circ}\text{C}$) [K^{-1}], from XRD and dilatometry techniques.

The result of the CTE obtained from the XRD measurements is compared with the dilatometer measurements, the results of all the samples are shown in Table 3.5 and Figure 3.25. There is no difference between the CTE in the rolling and the transverse direction, measured with the dilatometer. The results show that the difference between the results from the two methods to measure the CTE is very small, less than 2.1%. Straumanis and Zyszczyński reported a linear (secant) thermal expansion coefficient between 15-65 $^{\circ}\text{C}$, measured by XRD, of $7.6 \cdot 10^{-6} \text{ K}^{-1}$ [121], matching the present measurements.

These results demonstrate the validity of the method to measure the CTE, by XRD technique.

3.6 Electron microscopy

3.6.1 Scanning Electron Microscopy (SEM)

Microstructural analyses were performed using a Zeiss Sigma field emission *scanning electron microscope* (SEM), see Figure 3.26. Samples prepared for SEM observation were progressively polished with silicon carbide polishing discs under water flow (up to grit size P1200), and finally with two steps of diamond polishing paste on polishing soft cloth.

Last step applied was using $1\ \mu\text{m}$ diamond paste, after a step with $6\ \mu\text{m}$ diamond paste. To facilitate the polishing process, the samples are embedded in a resin cylinder, made of a special charged polymer that has enough electrical conductivity to be compatible with SEM, see Figure 3.26.

The typical SEM working parameters are: accelerating voltage 5-20 kV, aperture size 30-120 μm , working distance 4-15 mm. Secondary electron (SE) image gives topological information, while backscattered electron BE image provides information about the chemical composition (the higher the atomic number, the brighter the signal).

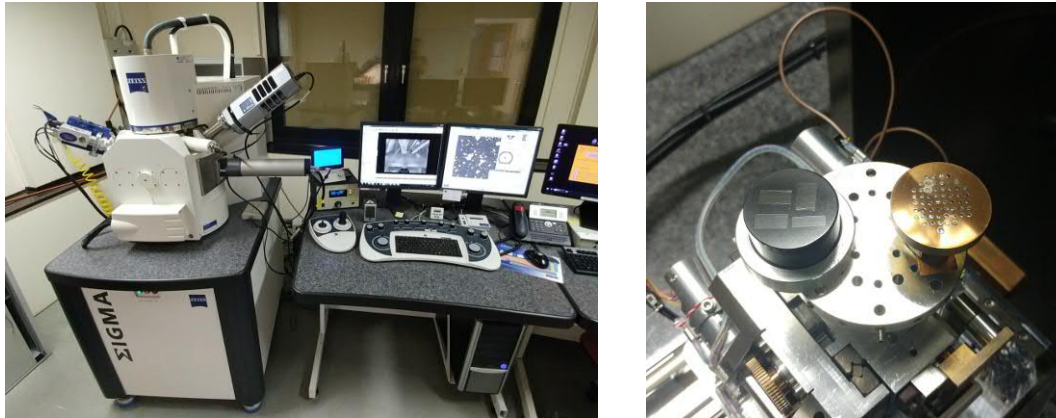


Figure 3.26: (Left) SEM Zeiss Sigma. (Right) MoGr specimens mounted in a black resin cylinder on the SEM sample holder, together with a piece containing several reference samples for EDS analysis.

3.6.2 Ion-milling

Mechanical polishing can produce local plastic deformation at the surface of the sample. This effect has been observed in the graphite-based materials investigated in this thesis. Some small features of the materials, such as pore walls can be deformed during mechanical polishing, leading to wrong image analysis. In order to have a precise estimation of the porosity, ion-polishing was performed on some specimens, with a Gatan Iliion II argon milling system.

The specimens are glued with silver-based adhesive on a titanium blade. The sample is placed so that it stands above the blade some microns, see Figure 3.27. The ion beam is grazed towards the sample at the level of the blade surface, so the blade shapes the beam by partly blocking it. This leaves a flat polished area on the specimen, with a characteristic Gaussian shape, see Figure 3.27. The plastic deformation is minimal, because the beam ablation process occurs at the atomic scale.

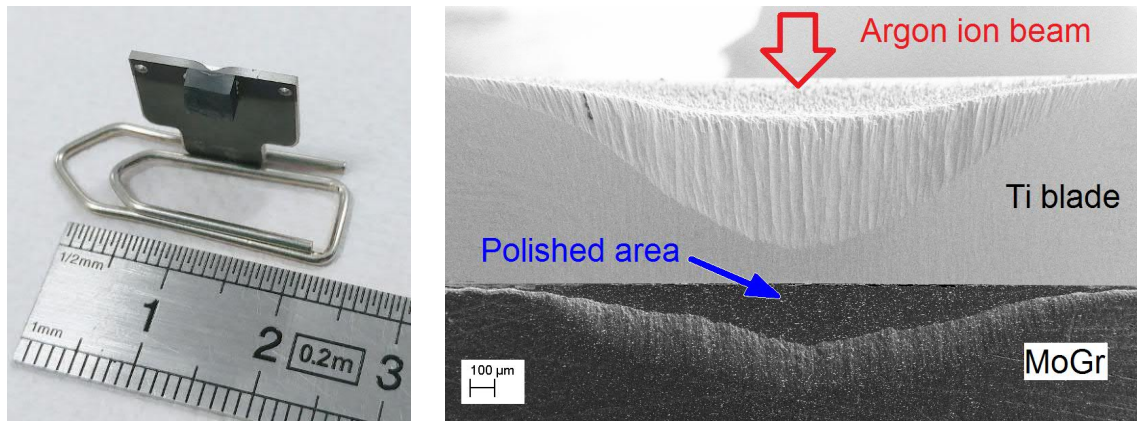


Figure 3.27: (Left) MoGr sample ($\sim 4 \times 4 \times 2 \text{ mm}$) mounted on the blade. (Right) SEM image of the finished ion-polishing process.

3.6.3 Scanning Transmission Electron Microscopy (STEM)

Transmission Electron Microscopy (TEM) is a technique that provides information on the atomic arrangement of materials due to its high spatial resolution [122, 123]. In TEM, the sample is illuminated with an electron plane wave and a following lens system magnifies the image onto a camera. An aberration corrector allows cancelling the imperfections of the electromagnetic lenses to improve the spatial resolution (even less than 0.1 nm). Instead of illuminating the sample with a plane wave, the sample can also be scanned with a focused electron beam (Scanning (S)TEM) while collecting scattered electrons to obtain an image. Different STEM detectors collect the electrons scattered at different angles. For these measurements, we have employed the high angle annular dark field (HAADF) detector, as this one provides the highest image contrast. This HAADF detector collects incoherent electrons scattered at angles higher than 50 mrad. It is also called Z-contrast STEM technique, owing high Z atoms scatter electrons to higher angles more strongly than lighter atoms. Indeed, the intensity of HAADF image is proportional to $Z^{1.7}$ [124, 125]. STEM measurements were performed on a FEI Titan Low-Base microscope (see Figure 3.28) working at 200 kV, equipped with a Cs probe corrector, a monochromator and an ultrabright X-FEG electron source. The convergence angle was 25 mrad and the inner and outer angles for HAADF imaging were 70 and 200 mrad, respectively.

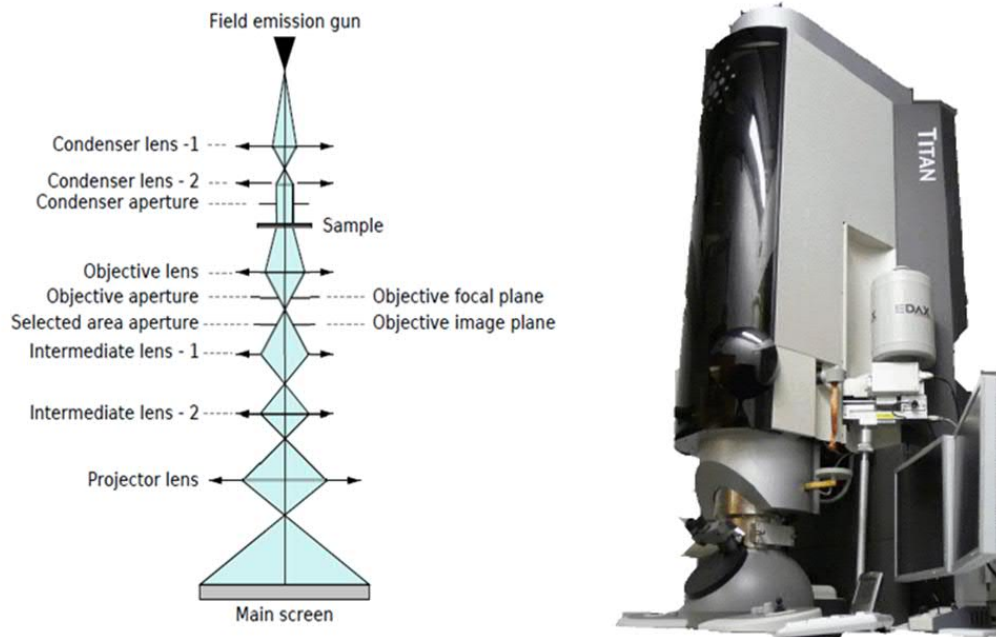


Figure 3.28: Schematic of a conventional TEM microscope and the TEM microscope used in this study (FEI Titan Low Base at the LMA-INA-U, Zaragoza facility).

3.6.4 Focused Ion Beam (FIB)

Focused ion beam (FIB) is an appropriate technique for preparing electron transparent samples (lamellas) for transmission electron microscopy (TEM). FIB equipment consists of a column of Ga^+ ions used for imaging or for milling the specimen, and a column of electrons to obtain images. The well controlled Ga^+ beam can be used to thin the material (preparing a TEM lamella) while the electron beam facilitates the observation of the specimen [126].

3.7 Nanoindentation

Nanoindentation tests were performed on several MoGr grades, pointing at the carbide particles. The aim of this test is to assess possible differences in hardness between the different carbide phases. The surface of the samples was polished with diamond paste down to $1\ \mu\text{m}$.

The tests were performed with an Agilent G200 Nanoindenter, featuring a thermal shield enclosure. The device characteristics are:

- Positioning accuracy (X-Y): $1\ \mu\text{m}$.
- Load resolution: 50 nN.
- Displacement resolution (Z): $< 0.01\ \text{nm}$.
- Contact force: $< 1\ \mu\text{N}$.

4 | Production routes

This chapter details the production processes employed for the investigated composite materials. First, the raw materials (powders) are characterised and the results reported. Then, each part of the process and its corresponding variables are described in separate sections. The production parameters used for each material grade are reported. At the end, the methods used to obtain specimens from the sintered plates are described.

4.1 Initial powders

The characterisation of the raw materials is based in SEM and XRD techniques. SEM images allow to characterise the average particle size and the particle shape. Energy Dispersive X-ray spectroscopy (EDS) analyses provide information about the elements present in the powder, which in turn shows the impurity content. XRD analyses provide crystallographic information on the present phases. Besides, if performed with varying temperature, the thermal expansion behaviour of the phases, in all crystallographic orientations, can also be determined.

4.1.1 Asbury 3260 graphite

The graphite powder used for most of the investigated materials is grade 3260 from Asbury Carbons company, consisting of crystalline natural graphite. The carbon content was measured by the powder manufacturer with loss on ignition (LOI) technique, resulting in 99.01 *wt%*. The typical results of the sieving test done by the powder supplier are shown in table 4.1.

Table 4.1: Sieving test of Asbury 3260 powder (U.S. Standard test sieves)

Mesh size	%
+80 Mesh (180 μm)	0.05
+100 Mesh (150 μm)	0.08
+200 Mesh (75 μm)	6.95
+325 Mesh (44 μm)	30.06
-325 Mesh (44 μm)	62.86

Morphology

The SEM observations of Asbury 3260 graphite powder are presented in figures 4.1 to 4.8. These powders contain two different morphologies: flakes and spheroidal-flakes.

Flakes are flat and typically round; on the other hand, spheroidal-flakes are agglomerations of small flakes displaying a spheroidal shape. Figure 4.3a shows one particle with large spheroidicity. Therefore, spheroidal-flakes contain graphite crystallites in many different orientations. This morphology was chosen to limit the anisotropy of the composites, as well as to facilitate compactness [29]. A possible disadvantage of this morphology is the fact that the final material is prone to contain many folded basal planes, already visible in the non-compacted powder, in figures 4.5b and 4.8b.

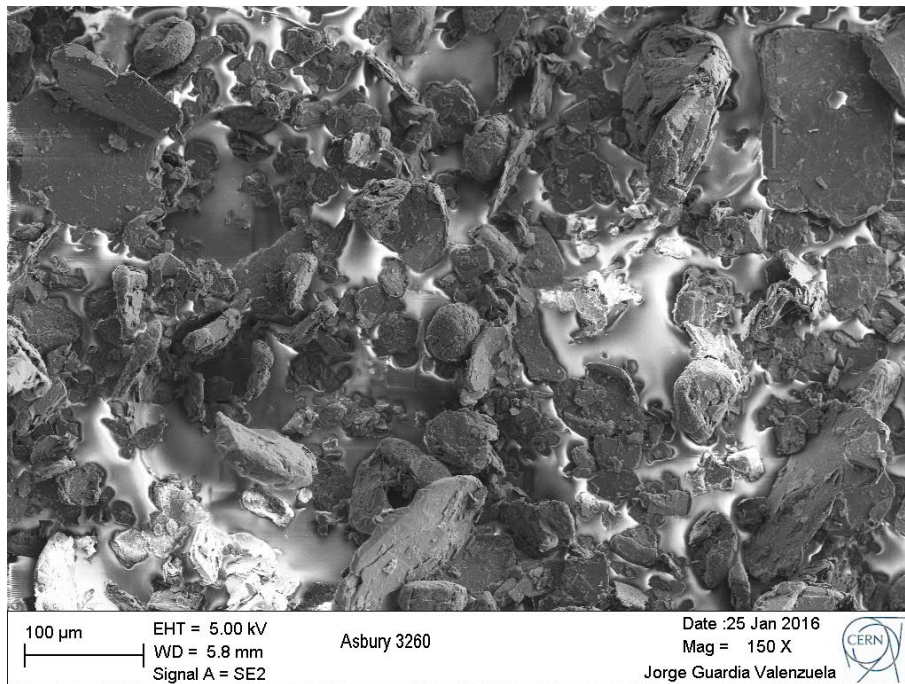


Figure 4.1: General view. Bright areas are due to charging effect.

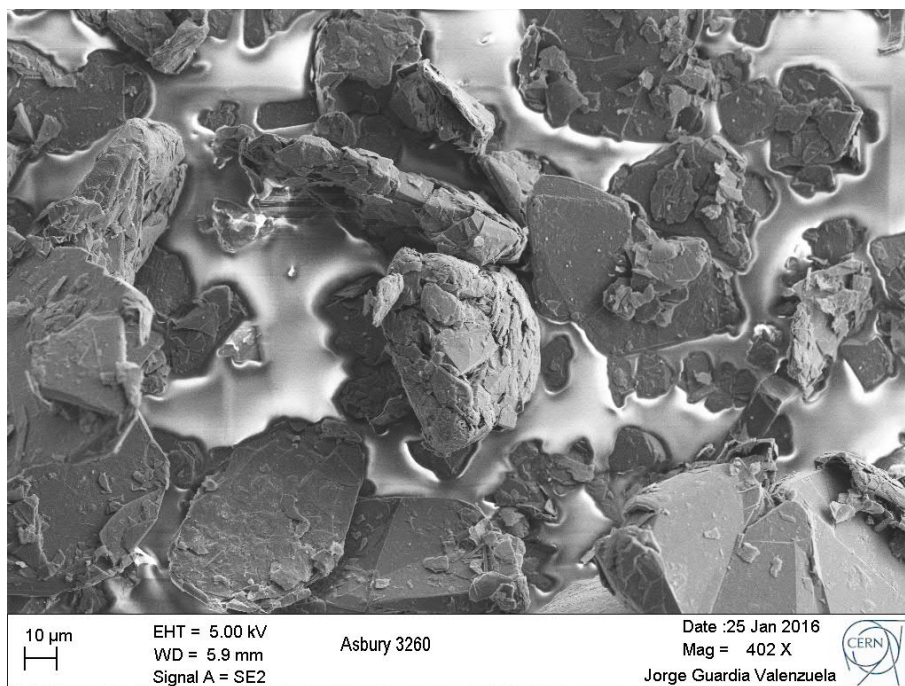
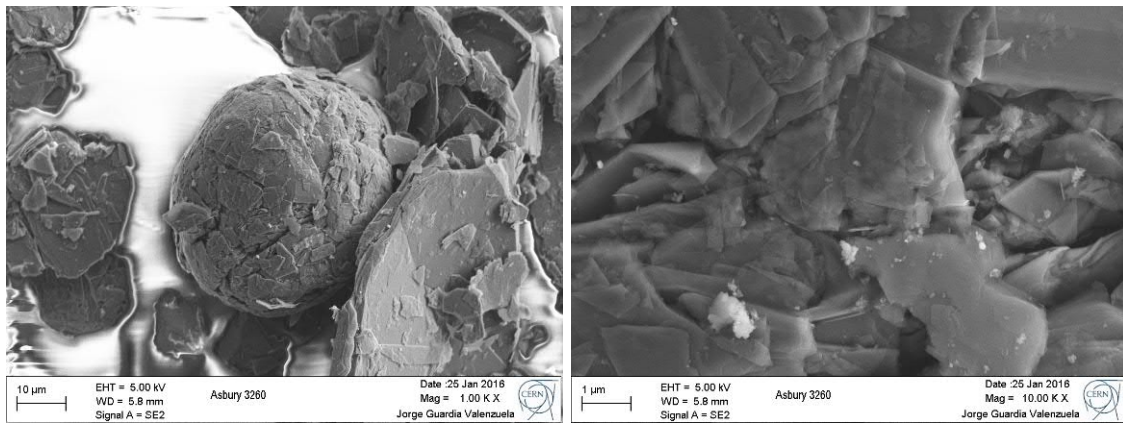


Figure 4.2: General view.

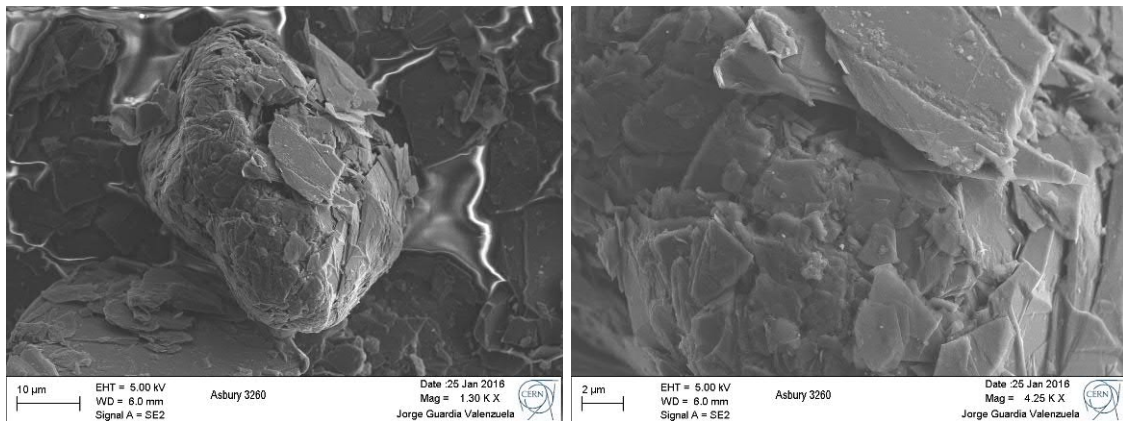
Figure 4.3



(a) Spheroidal particle and...

(b) ...its surface close-up view.

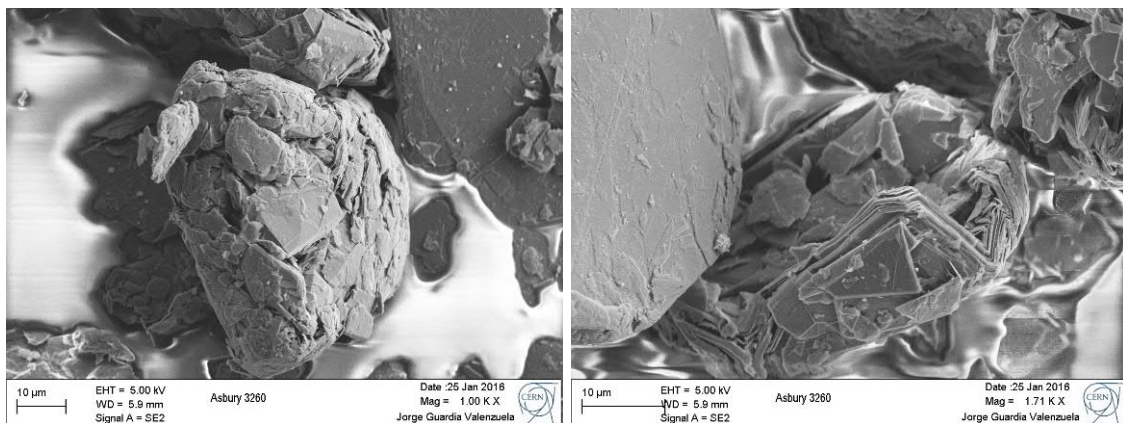
Figure 4.4



(a) Spheroidal particle and...

(b) ...its surface close-up view.

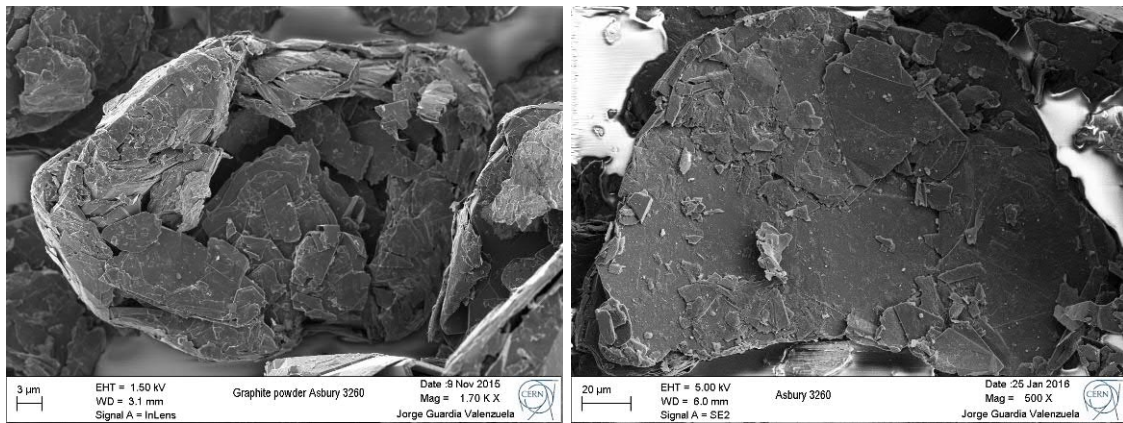
Figure 4.5



(a) Spheroidal particle.

(b) Folded basal planes in a spheroidal particle.

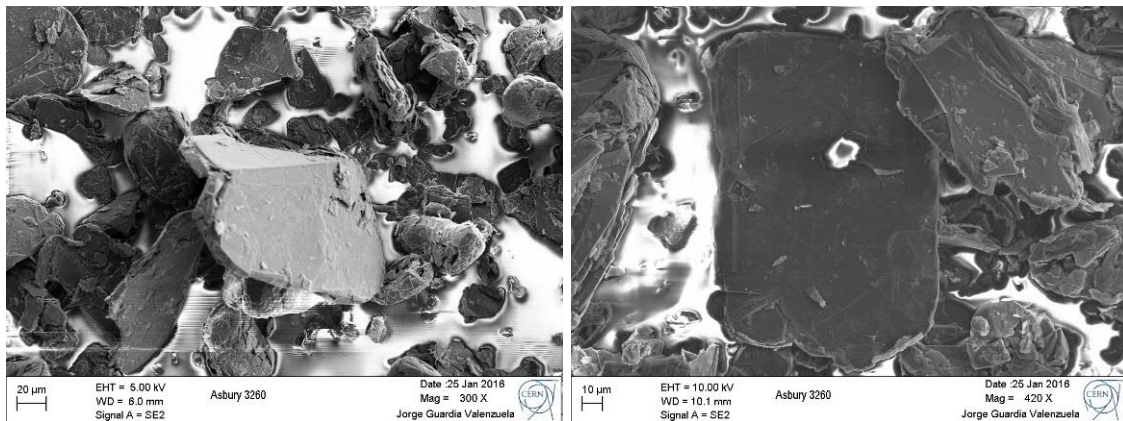
Figure 4.6



(a) Flake-like particle.

(b) Flake-like particle.

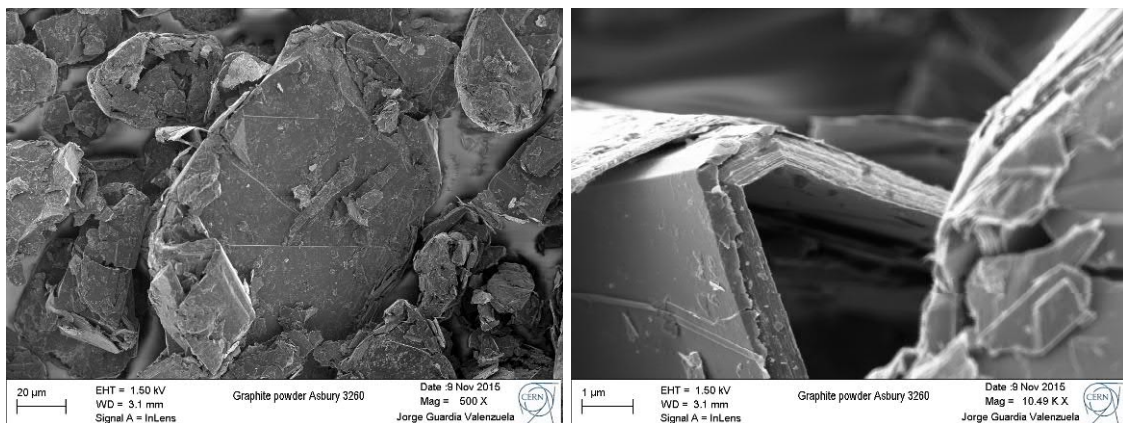
Figure 4.7



(a) Flake-like particle.

(b) Flake-like particle.

Figure 4.8



(a) Flake-like particle.

(b) Folded basal planes in a flake.

The bright small particles visible on the surface of the graphite powder, more noticeable in images 4.3b and 4.3b, show high content of iron. The inclusion visible in flake of

image 4.7b shows strong signal of Si and O, thus being most likely silicon oxide. It is also showing charging effect, confirming electrical insulating properties. These impurities are compatible with natural graphite ores.

The supplier certifies a minimum carbon content of 98%, and the batch analysis resulted in a 99.01% content. A quantitative EDS analysis could not be performed due to the visible adhesive tape around the powder particles. However, the small volume of visible impurities is compatible with the carbon content specification.

The mean observed particle size is around 30 μm , with at least 90% of the particles between 10 and 80 μm , matching the supplier's specification.

Crystallography

Figure 4.9 presents the XRD pattern of Asbury 3260 powder. The experimental lattice parameters of the hexagonal graphite phase are reported in the next section (Thermal expansion). The peaks not related to the thermodynamically stable phase of graphite (hexagonal) are likely to be rhombohedral graphite. The rhombohedral structure of graphite is known to form by applying shearing forces, for example, by grinding. This introduces stacking faults in the crystallites having the hexagonal stacking regularity (ABAB...), leading to sequence ABCABC... of the rhombohedral phase [127] ($a = 3.635 \text{ \AA}$ and $\alpha = 39.49^\circ$). The corresponding lattice parameters of this phase in the hexagonal system are $a = 2.462 \text{ \AA}$ and $c = 10.062 \text{ \AA}$ [127]. The stable ABAB stacking is recovered progressively on heating above 1300 $^\circ\text{C}$ [128, 129].

The asymmetric shape of the 002 graphite peak, see Figure 4.10, indicates that there is a distribution of crystallites with different interplanar d_{002} distances. The right side of the peak (higher 2θ angles) corresponds to the smallest d_{002} , corresponding to the highest graphitisation level. At the left side, the peak broadens, indicating presence of crystallites with larger d_{002} , but with decreasing amount as d increases (lower intensity).

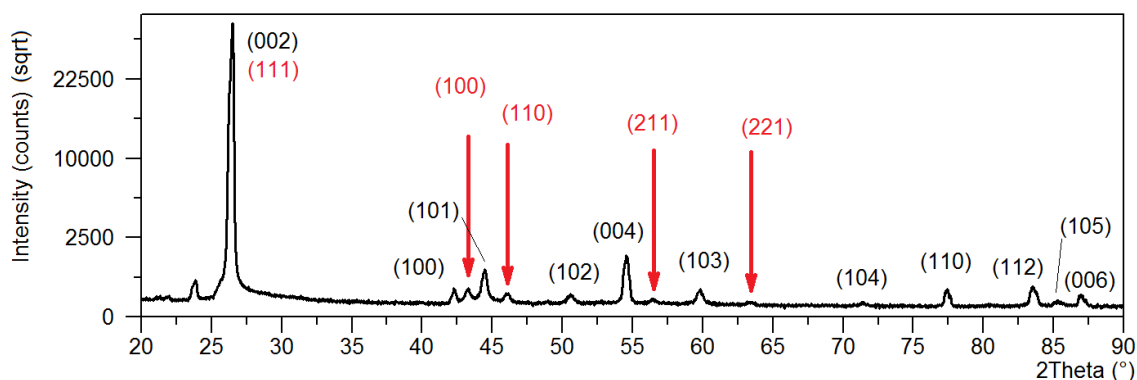


Figure 4.9: XRD pattern of Asbury 3260 powder (Siemens D5000, as-acquired pattern¹). Red arrows indicate rhombohedral graphite peaks.

¹Specimen displacement/transparency correction not applied, see section 3.5.2.

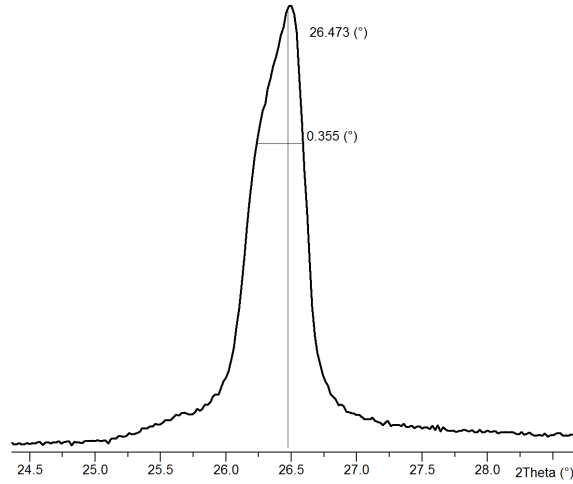


Figure 4.10: Close-up view of the 002 peak from the XRD pattern of figure 4.9.

Thermal expansion

The thermal expansion behaviour of graphite Asbury 3260 was characterised by performing XRD analysis to a mixture (obtained by dry mixing, see section 4.2) of 4.5vol% molybdenum powder and balance Asbury 3260. The test was performed in air at 25-100-200-300-400-500 °C, in the Panalytical diffractometer, with parallel beam configuration to remove sample displacement and sample transparency errors. The experimental points with the fitting function are shown in Figure 4.11. The lattice parameters at RT match those of the ideal graphite structure [53]. The coefficients of the second degree polynomial fitting are presented in Table 4.2.

Table 4.2: Asbury 3260. Fitting coefficients of graphite lattice parameters [Å].

Param.	$\cdot x^2$	$\cdot x$	<i>ind.</i>	Value at 20 °C
a	$5.6085 \cdot 10^{-9}$	$-4.5209 \cdot 10^{-6}$	2.4620	2.4619
c	$1.6396 \cdot 10^{-8}$	$1.8428 \cdot 10^{-4}$	6.7091	6.7128

The average linear thermal expansion coefficients are calculated with equation 3.21, using the polynomial fits of Table 4.2. The results are shown in table 4.3.

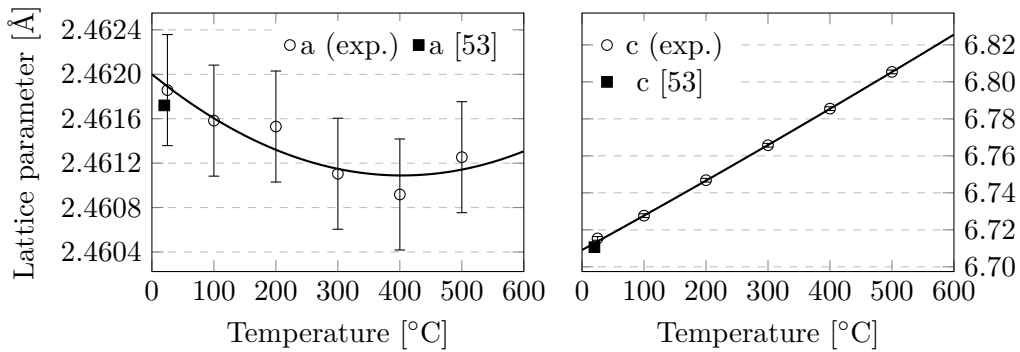


Figure 4.11: Lattice parameters versus temperature of graphite in Asbury 3260.

Table 4.3: Secant CTE $20-T^{\circ}\text{C}$ of graphite in Asbury 3260, a and c parameters ($\times 10^{-6}$) [K^{-1}]

	T= 50	100	200	300	400	500	600 °C
a	-1.7	-1.6	-1.3	-1.1	-0.9	-0.7	-0.4
c	27.6	27.7	28.0	28.2	28.5	28.7	29.0

4.1.2 Asbury 3763 graphite

Another graphite powder, Asbury 3763, was investigated. It consists in high purity crystalline natural graphite flakes, with very large particle size, see Figures 4.12 and 4.13. These large flakes should in theory be optimal for the best possible IP thermal and electrical conduction. The composites produced with this powder are likely to be highly textured, similarly to pure ordered graphites. In the negative side, this may produce a very high degree of anisotropy, resulting in too weak properties in the TP direction.

The process to produce big particle size powder is typically less aggressive and introduces less defects than milling operations required in small-sized particles. The carbon content was measured by the powder manufacturer with loss on ignition (LOI) technique, resulting in 99.59 wt.%. The moisture content was 0.16 wt.%. The typical results of the sieving test done by the powder supplier are shown in table 4.4.

Table 4.4: Sieving test of Asbury 3763 powder (U.S. Standard test sieves)

Mesh size	wt. %
+10 Mesh (2.00 mm)	0
+20 Mesh (850 μm)	6.13
+35 Mesh (500 μm)	78.64
+40 Mesh (425 μm)	7.81
+50 Mesh (300 μm)	4.53
+60 Mesh (250 μm)	0.82
-60 Mesh (250 μm)	2.07

Morphology

The mean observed particle size is around 750 μm , in agreement with the specification. The SEM characterisation is presented in Figures 4.14, 4.15 and 4.16. The flakes show some basal plane wrinkles and micron-sized graphitic platelets at the surface. The thickness of the observed flakes is around 30 μm , as shown in Figure 4.16.



Figure 4.12: Asbury 3763 graphite powder on adhesive tape.

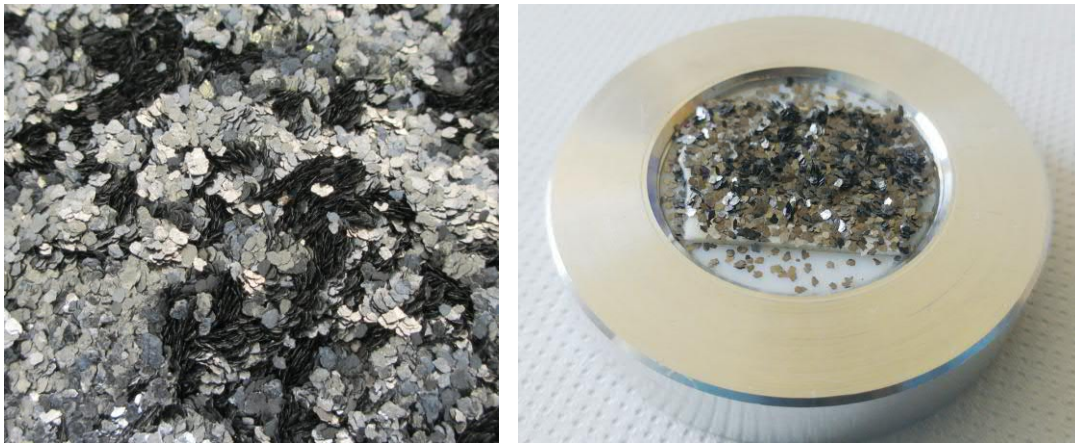


Figure 4.13: Photographies of the Asbury 3763 powder. The right one corresponds to the specimen for XRD test.

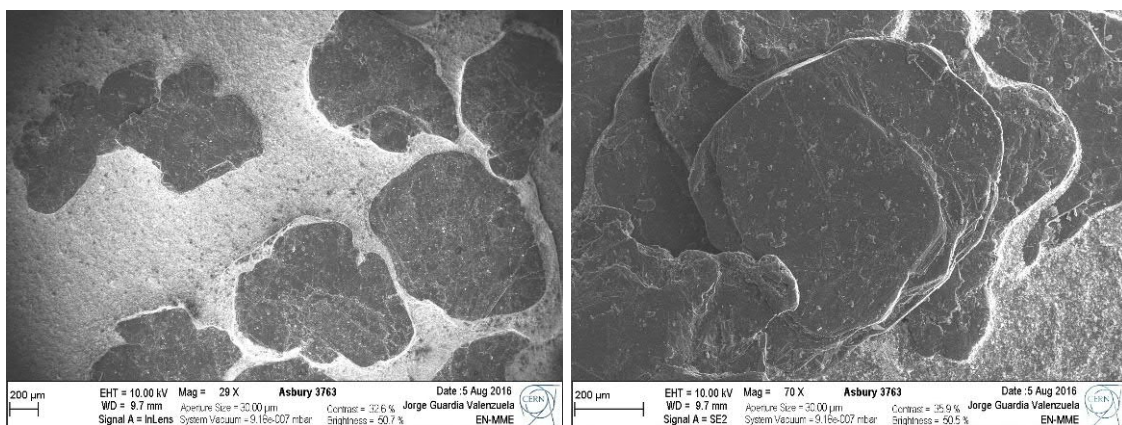


Figure 4.14: SEM secondary electron images of Asbury 3763 graphite powder.

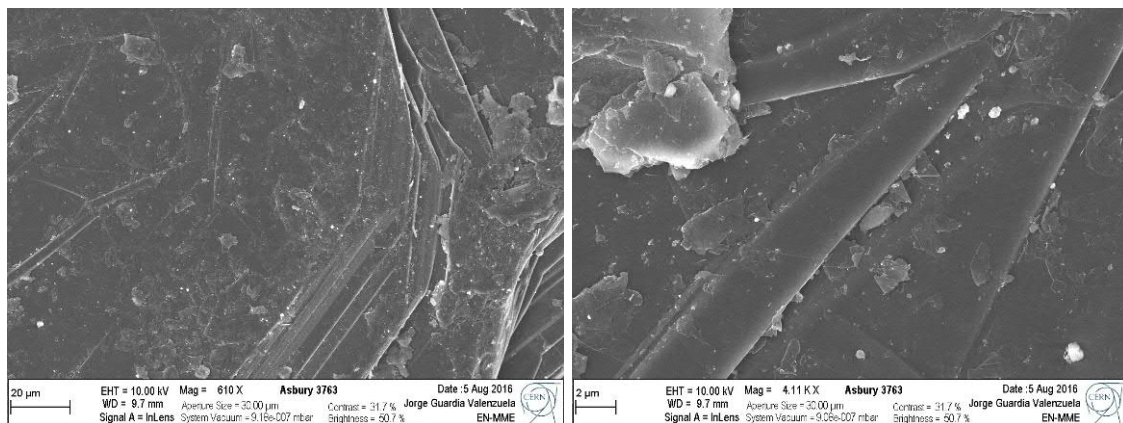


Figure 4.15: SEM secondary electron images of Asbury 3763 graphite powder. Close view of the surface, showing some wrinkles and small adhered flakes.

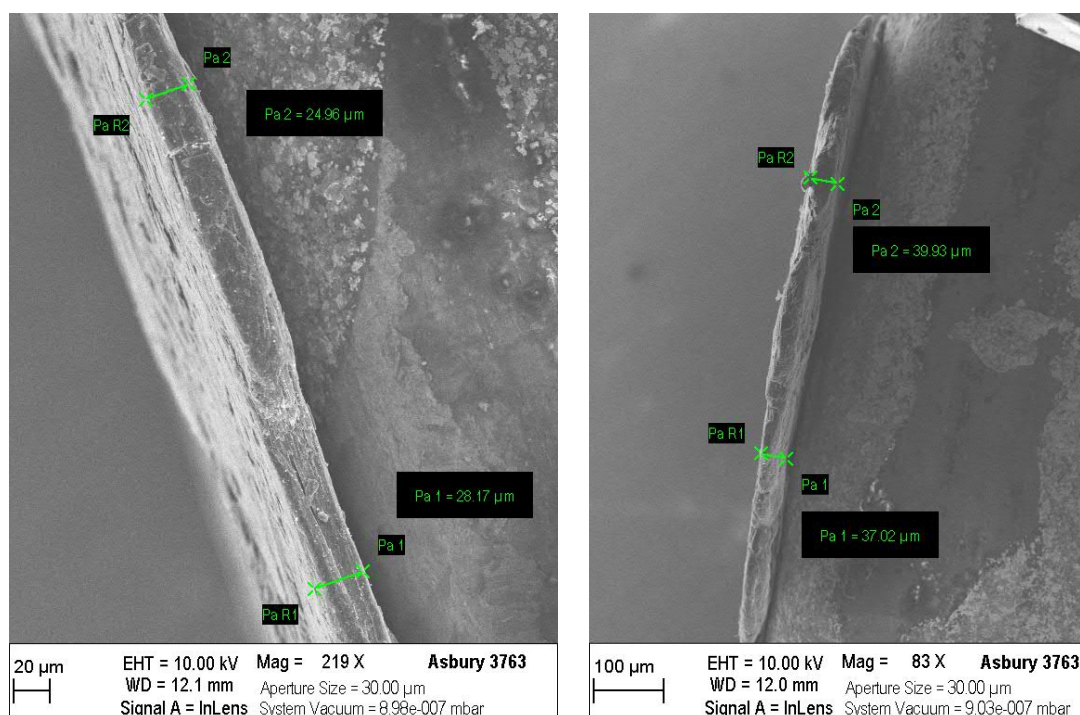


Figure 4.16: SEM secondary electron images of two Asbury 3763 graphite flakes, thickness view: $\sim 25.5 \mu\text{m}$ (left) and $\sim 38 \mu\text{m}$ (right).

Crystallography

The XRD analysis shows very strong and sharp peaks related to the interplanar distance, see Figure 4.17. This type of flakes shows a very slippery nature, so the powder was supported with double-sided adhesive tape to keep it in place during the test (the sample holder is tilted by the goniometer). This helped to have some flakes aligned vertically, see Figure 4.13, which in principle allows $hk0$ reflections (related to the atomic planes perpendicular to graphite basal plane). Nevertheless, most of the flakes were oriented with the basal planes parallel to the surface of the sample holder.

The big size of the flakes produces a strong displacement error, which is not constant

²Specimen displacement/transparency correction not applied, see section 3.5.2.

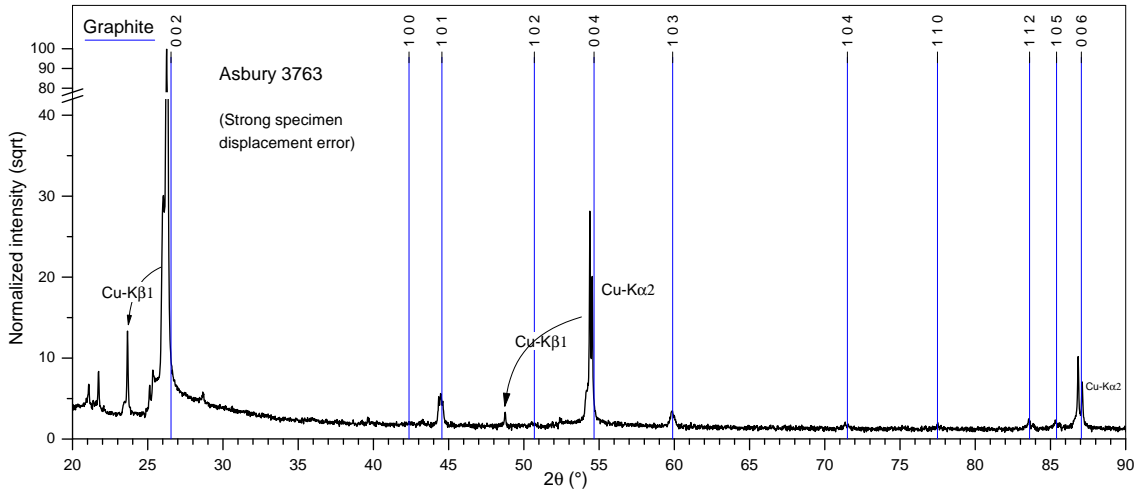


Figure 4.17: XRD pattern of Asbury 3763 (Siemens D5000, as-acquired pattern²). Peak positions of ideal graphite.

for all peaks. The interaction volume is at the top surface of the flakes, referenced to the sample holder surface. The relative height depends on the alignment of the flakes; the horizontal flakes have the interaction volume close to the level of the sample holder, while the vertical ones have it much above, around 0.75 mm higher (flake diameter). This causes that each set of crystallographic planes has a different displacement error, visible in the XRD pattern.

Due to this two combined effects, only the $00l$ peaks can be analysed (c lattice parameter and L_c crystallite size), the results are shown in table 4.5. The sample displacement correction shows $s \approx 0.65$ mm (the interaction volume is at lower height than the diffractometer centre). The value of L_c obtained from the Rietveld refinement (MAUD) is not real, as it would be too large to produce peak broadening, see section 3.5. This indicates that real value is $L_c > 1 \mu\text{m}$. The corrected interplanar distance is matching that of ideal graphite. It is possible to notice in the pattern that the peaks including hk miller indices show much less peak shifting, due to the effect explained above. The 100 and 110 peaks, are almost non-existent, due to the texture of the specimen. Other interesting effects, visible also in other high quality and highly oriented graphites, are the peaks appearing between 2θ 20 and 23° , at around $2\theta = 29^\circ$, and the shape of the left side of 002 peak. They could be due to the strong 002 reflection, which produces these artefacts.

Table 4.5: Results of the XRD analysis for Asbury 3763.

Method	a [\AA]	c [\AA]	L_c [nm]	z_2R	s [mm]
MAUD	-	6.7106	1523*	-0.005428	0.678
Spreadsheet ¹	-	6.7112	-	-	0.624

¹Sample displacement error correction, see section 3.5.2.

4.1.3 Granoc carbon fibres

Nippon Graphite Fibres Granoc XN-100-03Z pitch-based Carbon Fibres (CFs) are present in one of the investigated grades (MG-6530Aa). Their nominal length is 3 mm, therefore they are referred as "long", in contrast to the other Cytec fibres. Typically the compaction of bodies having such long fibres could lead to more porosity content than when using short

fibres.

The specifications of the Granoc XN-100-03Z fibres from the supplier datasheet are:

- Nominal length: 3 mm.
- Electrical conductivity: 0.67 MS m^{-1} .
- Thermal conductivity: $900 \text{ W m}^{-1} \text{ K}^{-1}$.
- Density: 2.22 g cm^{-3} .

Morphology

Figures 4.18 and 4.19 show SEM observations of Granoc CFs. The SE image shows small graphite crystallites on the surface, confirmed by the absence of contrast in the BE image. The presence of oriented graphite produces characteristic straight marks on the surface, conform to a pitch precursor fibre structure. The average diameter of the Granoc fibres is around $10 \mu\text{m}$. Length varies between 2 mm up to 4–5 mm, some fibres are even much shorter (hundreds of microns).

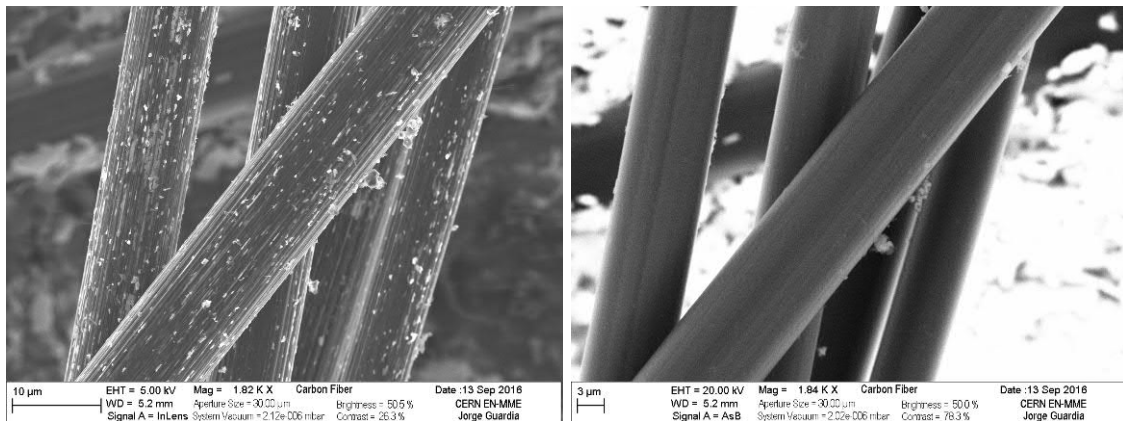


Figure 4.18: SEM image of Granoc carbon fibres with two different detectors: (Left) Secondary electron image. (Right) Backscattered electron image.

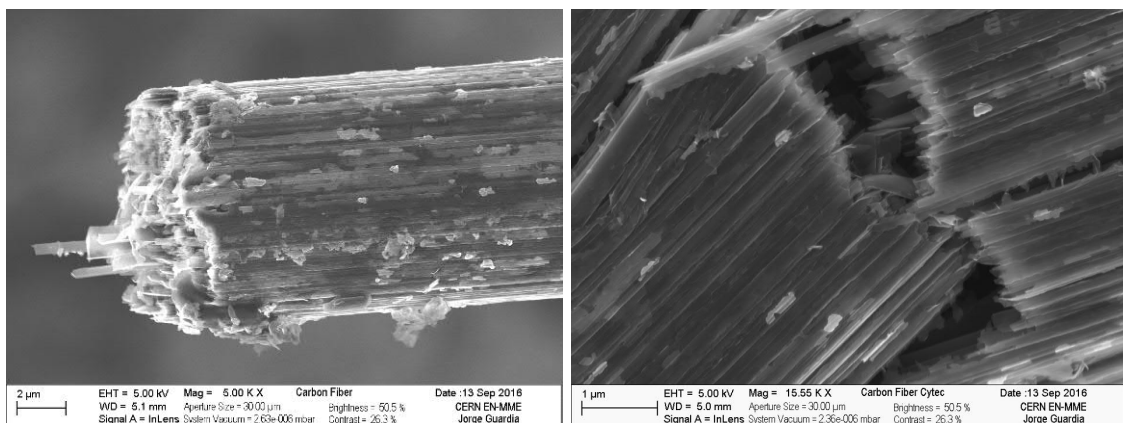


Figure 4.19: SEM secondary electron images of Granoc carbon fibres. (Left) Fibre end. (Right) Broken fibre.

Crystallography

The XRD pattern of Granoc CFs is shown in Figure 4.20. The graphite 002 and 004 peaks are clearly visible, rather broad due to small crystallite size. The Rietveld refinement is performed with isotropic crystallite model, the results are presented in table 4.6. Due to the absence of clear $hk0$ peaks, it is not practicable to get information related to the in-plane direction. The a lattice parameter is obtained from the fitting of the very weak 100 and 110 peaks, so this information is considered not reliable.

The c lattice parameter, 6.741 Å, is relatively large compared with high quality graphite (6.7106 Å [53]), indicating low degree of lattice perfection. The crystallite size, 66 nm, is quite small compared with the diameter of the fibres. The small flakes visible on the surface of the fibres are approximately matching this dimension, confirming the fact that they are part of the fibre structure.

Table 4.6: Granoc (long) and Cytec (short) carbon fibres: graphite lattice parameters [Å], isotropic crystallite size ($L_{isot.}$) [nm], MAUD texture parameters (H_{211} and H_{411}) and sample displacement/transparency correction (see section 3.5.2).

CF type	a^*	c	$L_{isot.}$	H_{211}	H_{411}	Z_2R	s [mm]
Granoc (long)	2.461	6.741	66	3.01	3.47	-0.00210	0.262
Cytec (short)	2.456	6.763	52	1.59	2.39	-0.00149	0.186

(*) see text

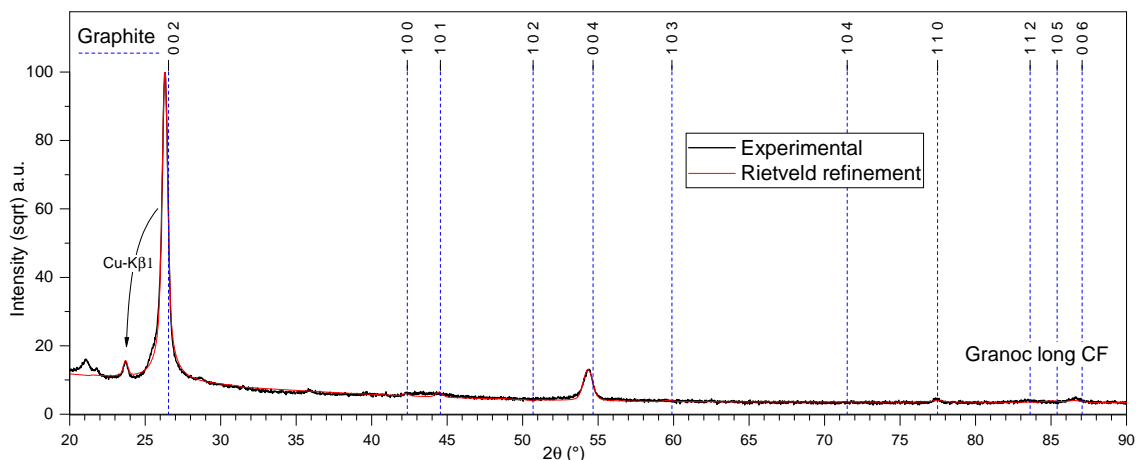


Figure 4.20: XRD pattern of Granoc carbon fibres (Siemens D5000). The peak positions of ideal graphite are shown.

4.1.4 Cytec carbon fibres

Cytec ThermalGraph DKD pitch-based CFs are present in several investigated grades. Their average length is 250 μm , therefore they are referred as "short", in contrast to the Granoc fibres.

The specifications of the ThermalGraph DKD fibres from supplier datasheet are:

- Nominal length: 200 μm , < 20% fibres < 100 μm , < 20% > 300 μm .
- Filament diameter: 10 μm .
- Electrical Conductivity: > 0.33 $MS m^{-1}$.

- Thermal Conductivity: $400\text{--}650\text{ W m}^{-1}\text{K}^{-1}$.
- Density: 2.22 g cm^{-3} .
- Tensile Strength: 200 ksi ($\sim 1380\text{ MPa}$)
- Young's Modulus: 100-120 Msi ($\sim 690\text{--}830\text{ GPa}$).

The fibres nominal properties are lower than those of Granoc XN-100-03Z fibres, however the difference is not dramatic.

Morphology

Figure 4.21 show SEM observations of Cytec CFs. The average fibre length is around $250\text{ }\mu\text{m}$, but it ranges from $50\text{ }\mu\text{m}$ up to 1 mm. The cross-section of the fibre shows its graphitic nature, where some corrugation of basal planes is visible, conform to pitch based fibres.

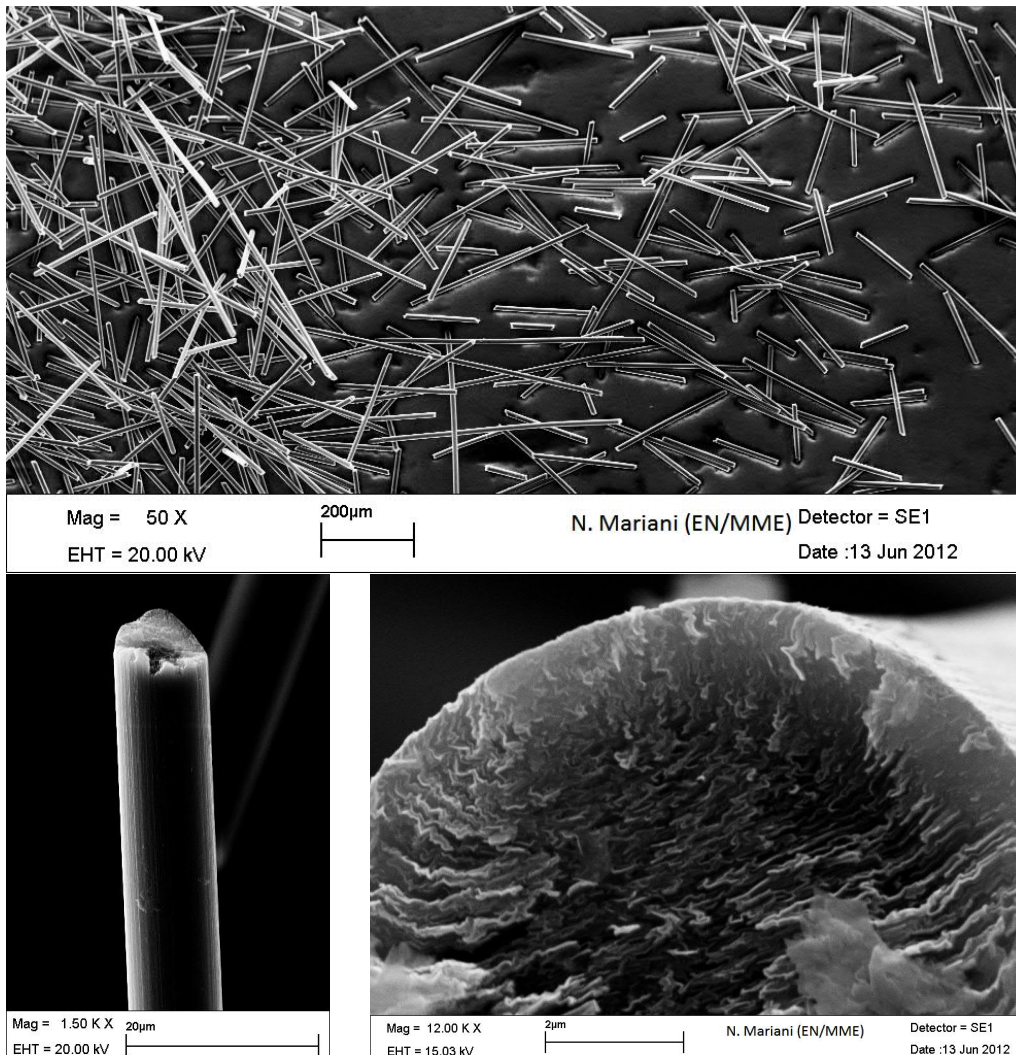


Figure 4.21: SEM image of Cytec carbon fibres [29].

Crystallography

The XRD pattern of Cytec CFs is shown in Figure 4.22. The graphite 002 and 004 peaks are clearly visible, rather broad due to small crystallite size. The Rietveld refinement is performed with isotropic crystallite model, the results are presented in table 4.6. Due to the absence of $hk0$ peaks, it is not practicable to get information related to the in-plane direction. The a lattice parameter is got from the fitting of the very weak 100 and 110 peaks, so this information is considered not reliable.

The c lattice parameter, 6.763 Å, is relatively large compared with high quality graphite (6.7106 Å [53]), indicating a low degree of lattice perfection. The crystallite size, 52 nm, is quite small compared with the diameter of the fibres. The Cytec fibres show crystallographic properties corresponding to slightly worse lattice perfection than Granoc fibres (smaller crystallite size and larger interplanar distance, see table 4.6). This matches the difference in nominal properties between the two type of fibres.

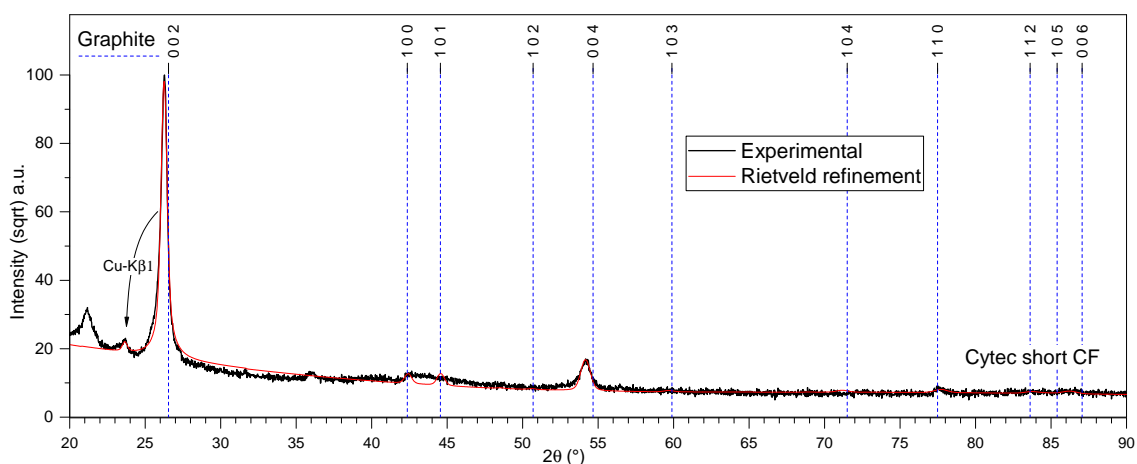


Figure 4.22: XRD pattern of Cytec carbon fibres (Siemens D5000).

4.1.5 Molybdenum

Morphology

The SEM observations of the molybdenum powder used for the investigated materials are shown in Figure 4.23. The particles are composed of aggregates of small spheroidal particles. This indicates that the powder production process involved melting, such as in atomization techniques. The aggregates show sizes smaller than 10 μm , with a mean particle size of around 5 μm . The smallest particles have diameters of less than 1 μm . The metal purity is higher than 99.9%, given nothing else but a very weak signal of oxygen. The phase analysis by XRD performed with the Siemens D5000 diffractometer, see Figure 4.24, shows only four sharp peaks, matching the BCC metallic molybdenum phase. The small peak at $2\theta \sim 36^\circ$ is due to the presence of unfiltered $Cu - k\beta$ radiation. The results of the analysis are shown in Table 4.7. The value of crystallite size L_a given by MAUD is not real, as it would be too large to produce peak broadening, see section 3.5. This indicates that real value is $L_a > 1 \mu m$, therefore the observed particles are probably monocrystalline.

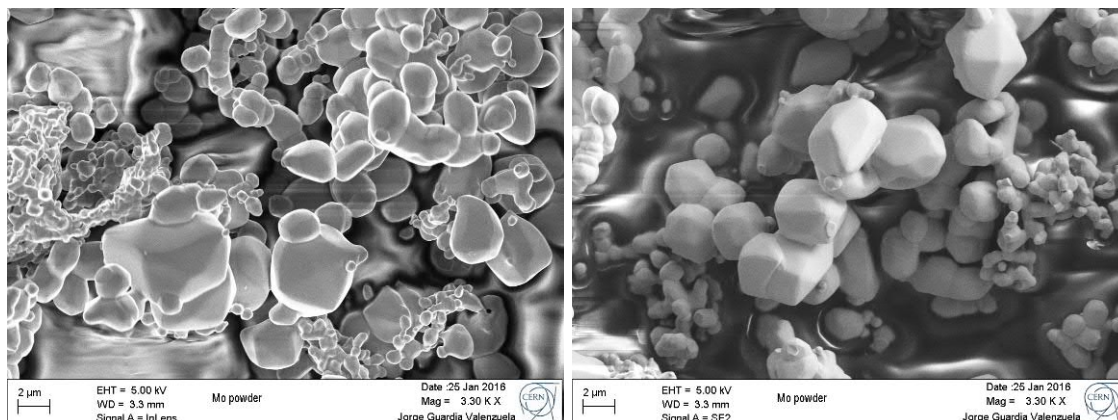


Figure 4.23: Typical morphologies of the molybdenum powder. Images with different secondary electron detectors: ZEISS In-lens (left) and lateral (right).

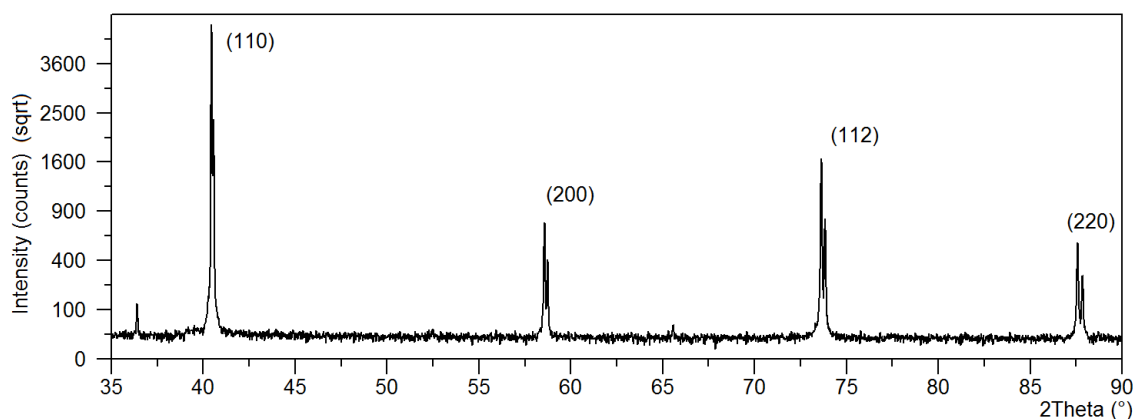


Figure 4.24: XRD pattern of molybdenum powder (Siemens D5000).

Table 4.7: Results of the XRD analysis for Mo powder.

Method	a [Å]	L_a [nm]	z_2R	s [mm]
MAUD	3.1476	1494*	-0.000817	0.10
Spreadsheet ¹	3.1473	-	-	0.11

¹Sample displacement error correction, see section 3.5.2.

Crystallography and thermal expansion

The thermal expansion behaviour of molybdenum powder was characterised by performing XRD analysis to a mixture (obtained by dry mixing, see section 4.2) of 4.5vol% molybdenum powder and balance Asbury 3260. The test was performed in air at 25-100-200-300-400-500 °C, in the Panalytical diffractometer, with parallel beam configuration to remove sample displacement and sample transparency errors. In the acquisition at 500 °C, peaks corresponding to molybdenum oxides are clearly visible and the identification of molybdenum peaks is not possible.

The experimental points with the fitting function are shown in Figure 4.25. The coefficients of the second degree polynomial fitting are presented in Table 4.8.

The average linear thermal expansion coefficients are calculated with equation 3.21,

Table 4.8: Molybdenum powder lattice parameter fitting coefficients [\AA].

Param.	$\cdot x^2$	$\cdot x$	<i>ind.</i>	Value at 20 °C	a_{RT} , from [130]
a	$6.0922 \cdot 10^{-9}$	$1.5390 \cdot 10^{-5}$	3.1475	3.1478	3.14737

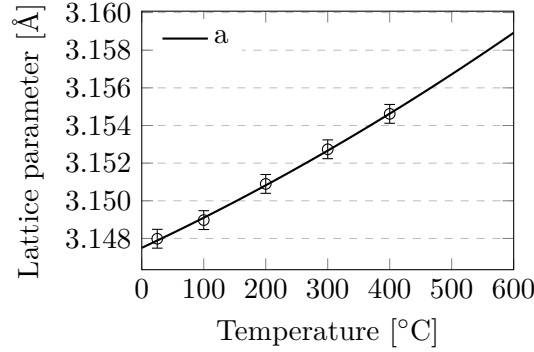


Figure 4.25: Lattice parameter versus temperature of molybdenum powder.

using the polynomial fits of Table 4.2. The results are shown in table 4.9. The CTE matches literature values reported in [131].

Table 4.9: Secant CTE 20–T °C of Mo in the mixed powder, a parameter ($\times 10^{-6}$) [K^{-1}]

	T= 50 100 200 300 400 500 600 °C						
a (this work)	5.0	5.1	5.3	5.5	5.7	5.9	6.1
a ([131])	5.1	5.2	5.2	5.3	5.4	5.5	5.6

4.1.6 Titanium

Morphology

SEM observations of the titanium powder used for some of the investigated materials are shown in Figure 4.26. Titanium particles show sizes smaller than 20 μm , with a mean particle size of around 5 μm . The smallest particles have diameters of around 1 μm . The sharp edges of the particles indicate that the last step of the powder production process did not involve melting, but mechanical milling or crushing techniques. The metal purity is higher than 99.9%.

Crystallography

The XRD phase analysis, see Figure 4.27, shows all peaks matching the hexagonal α -Ti phase ($a = 2.9504 \text{ \AA}$ and $c = 4.6833 \text{ \AA}$ [130]).

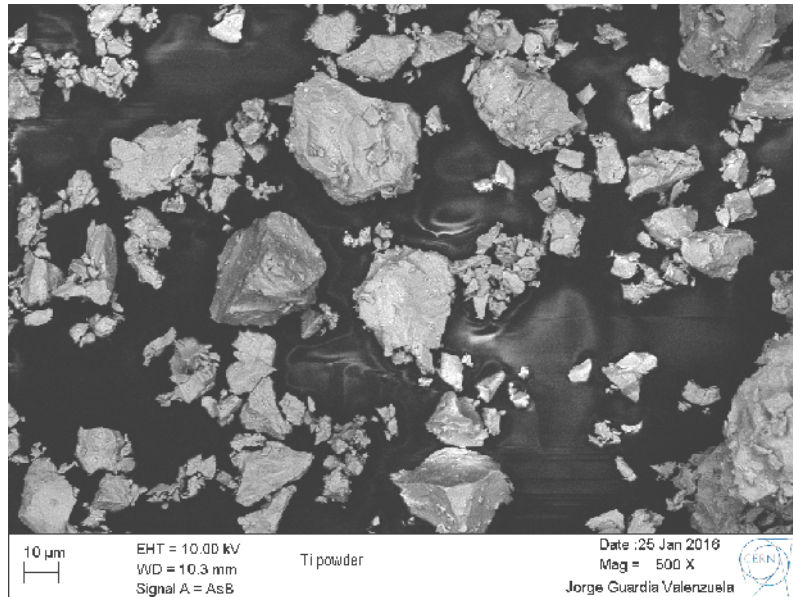


Figure 4.26: Typical morphologies of the titanium powder (SEM). Backscattered electron detector.

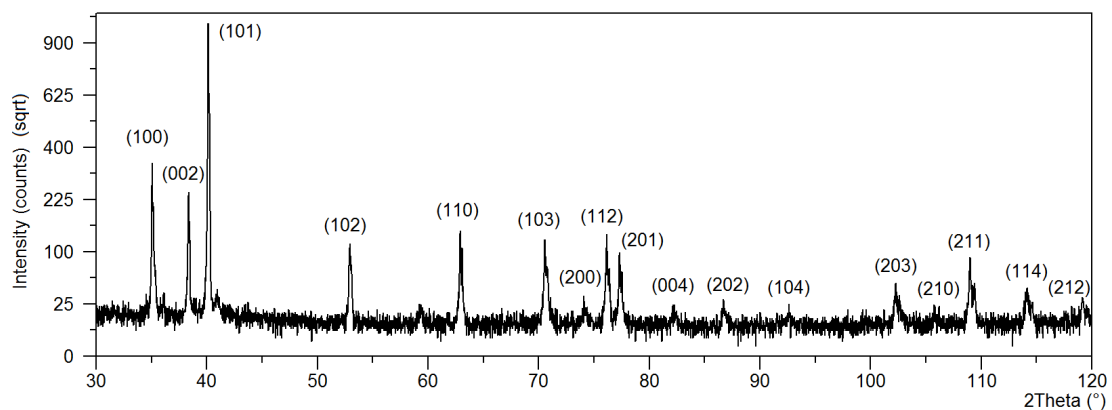


Figure 4.27: XRD pattern of titanium powder (Siemens D5000).

4.1.7 Chromium carbide powder

The powder selected for the tests is chromium carbide grade Cr_3C_2 -160 from the company H.C.Stark (Germany). The main use of this powder in the industry is as grain growth inhibitor of WC-based hard metals for milling tools. The nominal maximum particle size of grade 160 is $1.6 \mu\text{m}$. The chemical analysis reported by the supplier is shown in Table 4.10. Another grade from the same supplier, Cr_3C_2 -300, was also available with nominal size between 2.0 and $4.0 \mu\text{m}$, showing slightly lower contents of oxygen (max. $0.4 \text{ wt}\%$) and iron (max. 1200 ppm), however the size was prioritized for the study over these small impurity content differences.

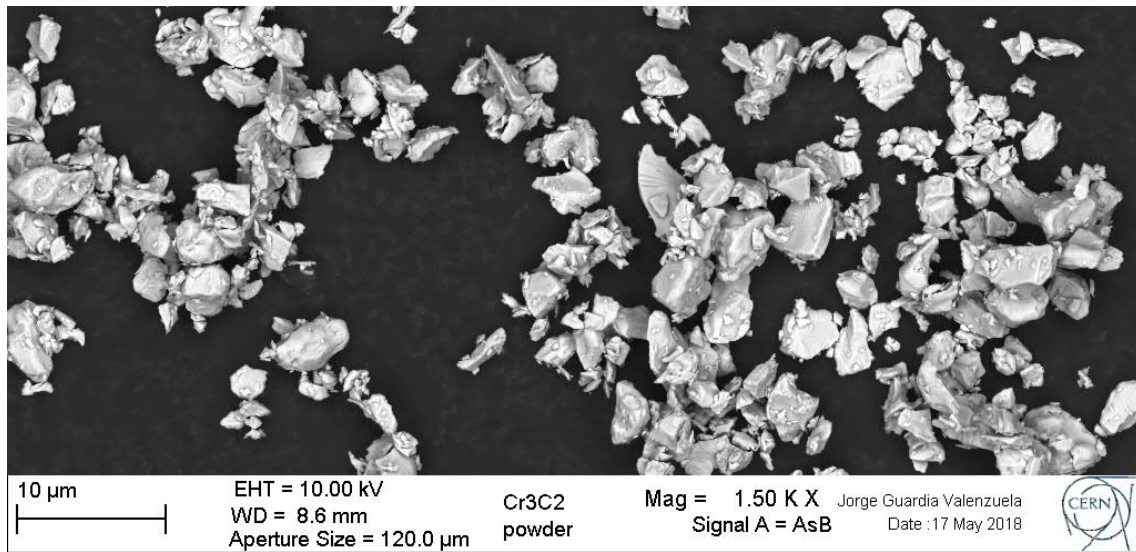
Morphology

SEM observations of the Cr_3C_2 powder used for some of the investigated materials are shown in Figure 4.28. The particles show sizes smaller than $3 \mu\text{m}$, with a mean particle size of around $2 \mu\text{m}$. The smallest particles have diameters of around $0.5 \mu\text{m}$. The sharp

Table 4.10: Cr₃C₂ chemical characteristics (from supplier datasheet).

C _{total}	max 13.3 wt.%
O	max 1.0 wt.%
N	max. 1000 ppm
Fe	max. 1500 ppm
S	max. 200 ppm
Si	max. 200 ppm
Ca	max. 100 ppm

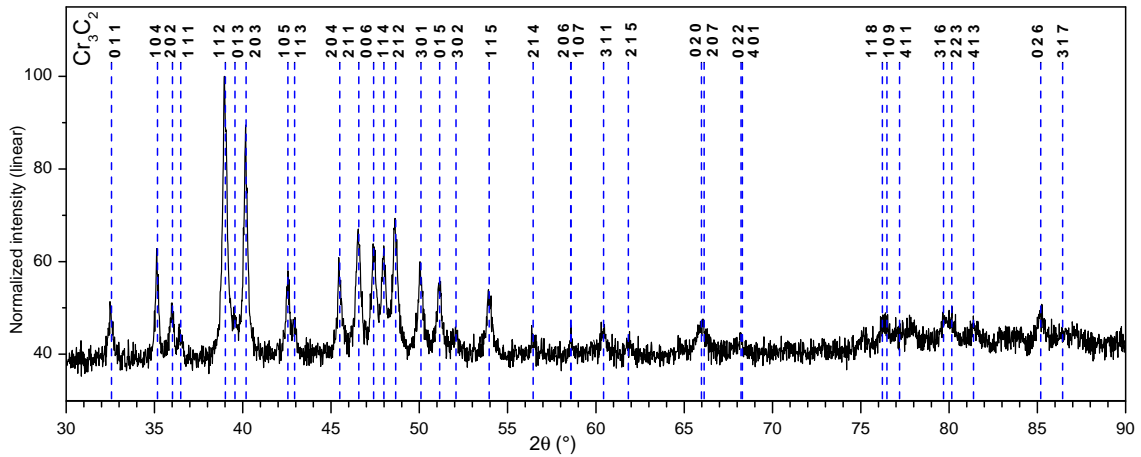
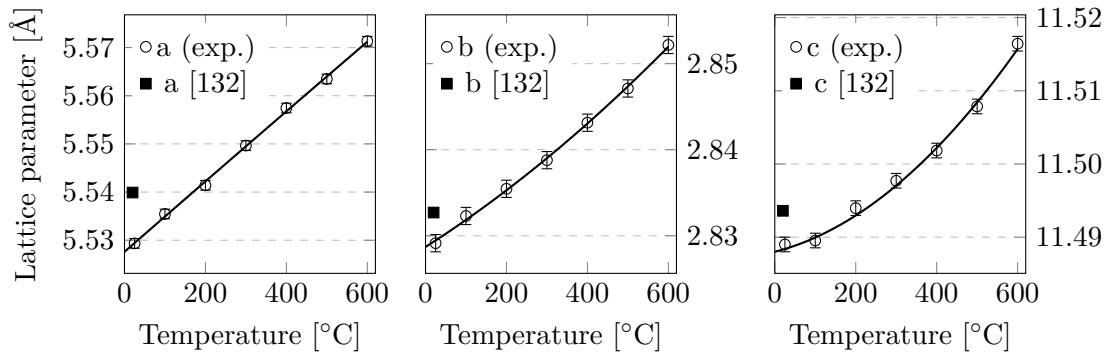
edges of the particles indicate that the last step of the powder production process did not involve melting, but mechanical milling or crushing techniques.

Figure 4.28: Typical morphology of the Cr₃C₂ powder (SEM). Backscattered electron detector.

Crystallography and thermal expansion

The XRD phase analysis, see Figure 4.29, shows all peaks matching the orthorhombic Cr₃C₂ phase, the peak positions are calculated with the lattice parameters resulted from the Rietveld refinement, see Table, ($a = 5.529 \text{ \AA}$, $b = 2.829 \text{ \AA}$ and $c = 11.489 \text{ \AA}$). The acquisition time for this test was 12s per 0.02° step, longer than usual, to improve signal-to-noise ratio. Still, the peaks are relatively weak compared with the strong background ($\sim 40\%$). This is partly due to the fluorescence of Cr under the incident Cu- k_α radiation, and to the low peak intensity due to very small particle size ($\approx 1 \mu\text{m}$). The fluorescence of Cr occurs because the incident energy (Cu- k_α , 8.04 keV) is larger and close to the K absorption edge of Cr (5.99 keV), creating polychromatic radiation [117]. The use of other anode materials in the X-ray tube, or a monochromator in the diffracted beam side, should eliminate the effect of fluorescence.

The experimental points with the fitting function are shown in Figure 4.25. The coefficients of the second degree polynomial fitting are presented in Table 4.8. The average linear thermal expansion coefficients are calculated with equation 3.21, using the polynomial fits of Table 4.11. The results are shown in table 4.12 and Figure 4.31.

Figure 4.29: XRD pattern of Cr_3C_2 powder (Siemens D5000).Figure 4.30: Lattice parameters versus temperature of the Cr_3C_2 phase in the powder.Table 4.11: Fitting equation for the Cr_3C_2 lattice parameters variation ($d = AT^2 + BT + C$, T in $^\circ\text{C}$, d in Å). From the heating-up curves.

	A	B	C	Value at 20°C	idem from [132]
a	$-1.0120 \cdot 10^{-9}$	$7.3285 \cdot 10^{-5}$	5.5276	5.529	5.5399
b	$1.4644 \cdot 10^{-8}$	$2.9994 \cdot 10^{-5}$	2.8287	2.829	2.8327
c	$5.3383 \cdot 10^{-8}$	$1.4128 \cdot 10^{-5}$	11.488	11.489	11.4936

Table 4.12: Secant CTE $20\text{--}T^\circ\text{C}$ of Cr_3C_2 powder; a , b and c parameters ($\times 10^{-6} m^{-1} K^{-1}$). From XRD, heating-up ramp.

	T= 30	100	200	300	400	500	600 $^\circ\text{C}$
a	13.2	13.2	13.2	13.2	13.2	13.2	13.1
b	10.9	11.2	11.7	12.3	12.8	13.3	13.8
c	1.5	1.8	2.3	2.7	3.2	3.6	4.1
Average	8.5	8.7	9.1	9.4	9.7	10.0	10.4

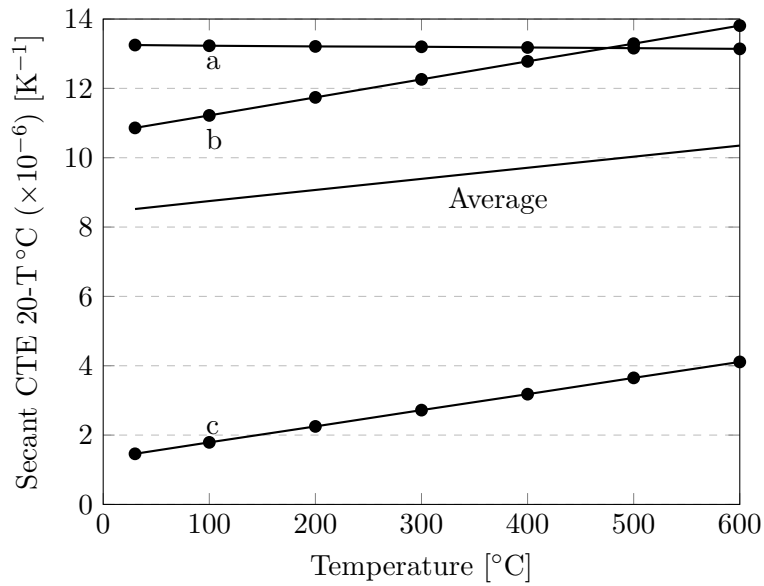


Figure 4.31: Secant CTE 20-T °C of each crystallographic direction in Cr_3C_2 ($\times 10^{-6}$) [K^{-1}]

4.2 Powders mixing

The desired composition of the powders is obtained by calculating the required weight of each component. Afterwards the powders are mixed to ensure a good homogeneity in the sintered plate.

The technique used to mix the powders is called dry-mixing. The powder mixture is prepared in a 3D mixing machine, dry and without any mixing media. This method ensures good homogeneity of the mixture and maintains the original morphology of the graphite flakes.

4.3 Green body compaction

The mixed powders are uniaxially cold pressed into a green body inside a steel mould at up to 300 MPa.

Compression-induced shear stress preferentially orients the graphite crystallites with their basal plane perpendicular to the pressing direction (Figure 4.32). Due to the spheroidal shape of the graphite powder, a minor part of the graphite grains is present in other-than-the preferred orientation. Even if CFs, when present, are dispersed randomly together with the other powders in the mixing machine, they likely have preferred orientation after compaction, with their axis perpendicular to the pressing direction.

4.4 Sintering

The green body is then inserted into a tailor made graphite mould consisting in top and bottom punches and a lateral container (Figure 4.33). This is an additional difference with respect to the HWLC process investigated by White and Pontelandolfo [94] where the lateral surface was free to expand allowing the excess liquid to be squeezed out. John and Jenkins showed that hot-working radial strain is beneficial for strengthening, up to a certain extent when cracks appear and decrease the final properties [97].

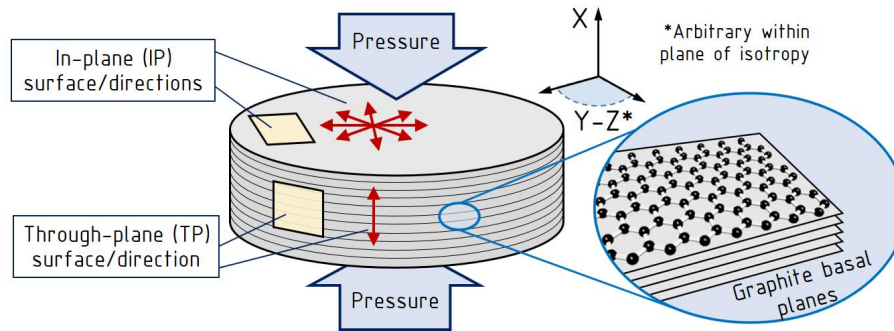


Figure 4.32: Preferred orientation of graphite basal planes with respect to the applied uniaxial pressure. Naming convention for the material directions.

The sintering cycles are performed by Spark Plasma Sintering (SPS) technique. SPS, a variation of hot-pressing, is a powder metallurgy technique that uses the flow of electrical current through the material and the mould as heating source [133]. During the process, temperatures in excess of 2700°C can be reached, while applying a pressure of up to 35 MPa . It is well known that the application of pressure thermodynamically favours graphitisation [134]: sintering pressures are limited by the mechanical strength of the mould.

The direct current through the electrode is typically around 15 kA for plates with an area of 150 cm^2 ($\sim 100\text{ A cm}^{-2}$), which produces a power loss in the order of 100 kW . The morphology of the components and the manufacturing process lead to a transversely isotropic material: the in-plane and perpendicular directions are defined as those parallel and perpendicular to the graphite basal planes, as shown in Figure 4.32.

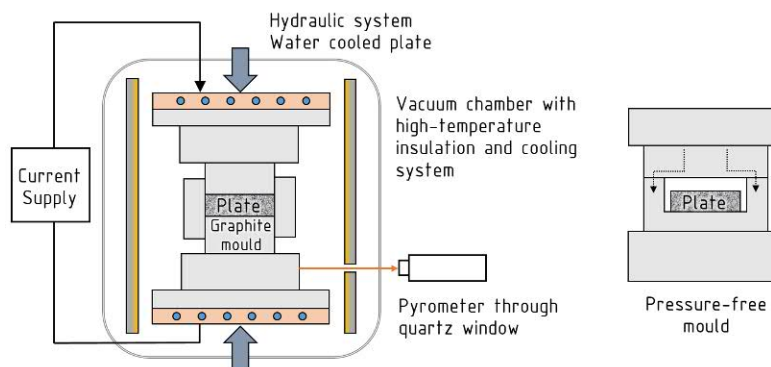


Figure 4.33: Schematic of the sintering machine used. Once sintered, the pressure-free mould is used for the post-sintering cycle

The sintering temperature exceeds the eutectic temperature of molybdenum with carbon (2584°C), forming a LP containing large amounts of dissolved carbon; the eutectic molybdenum-carbon contains $45\text{ at.}\%$ of carbon (Figure 2.14).

Since, during sintering, part of the LP flows out of the plate impregnating the graphite mould, the final composition results in a lower carbide content compared to the theoretical one, based on initial Mo content. This entails difficulties to calculate the actual compaction and the final composition, because the exact measurement of the amount of LP spill is not practicable.

The processing temperature is controlled by means of an optical pyrometer; in the sintering set-up used, the temperature is read on the lower punch, to limit issues related to the very high temperatures achieved (Figure 4.33). Since a non-negligible temperature

gradient exists between the measuring point and the core, the actual temperature during the process can be inferred by recording the temperature at the moment of the eutectic reaction (2584°C), which can be deduced by the change in compression speed due to ongoing melting. The presence of molten material squeezed out of the plates confirms that the eutectic point is reached.

The size of the final plates is $100 \times 150 \text{ mm}$ with a thickness of around 30 mm . Cylindrical plates can also be produced, but the rectangular ones minimize wasted material when collimator blocks are produced. Out of these, specimens for the characterisation as well as full-size collimator blocks were machined, hence ushering in industrial-scale production.

Gas pressure inside the sintering machine is lower than $\sim 0.1 \text{ mbar}$. Due to the closed geometry of the moulds during sintering, the effect of the chamber pressure in material gas content might be negligible.

4.5 Post-sintering thermal treatment

After sintering, the plate is submitted to a pressure-free heat treatment aiming at releasing the internal stresses induced by the sintering cycle. This is performed inside a special set-up allowing the flow of current through the mould walls without the application of pressure to the plate.

The pressure-free set-up used for the post-sintering heat treatment, see Figure 4.33, includes openings in the mould, allowing material outgassing and improving pumping. The chamber atmosphere during this thermal treatment is similar to the sintering conditions described above.

4.6 Summary of production parameters

This section details the initial composition and the parameters of the sintering and the post-sintering cycles. Each material grade is given a technical identifier. The digits of the identifier depend on the initial content of molybdenum (or chromium), graphite, carbon fibres and titanium powders respectively. The two letters tags the different sintering and post-sintering treatments respectively.

4.6.1 Molybdenum carbide - graphite (MoGr)

The different MoGr grades investigated are shown in Table 4.13. The relevant differences between each grade and the previous one are in bold. The main variables are the content of titanium, CFs, and the sintering and post-sintering cycle parameters. T_{est} is the estimated plate temperature. The sintering set-up used (Figure 4.33), as explained above, allows an indirect temperature measurement. The time shown in the tables is the total dwell time, which is the sum of two identical sintering cycles or one single cycle. The post-sintering cycle is always single. The double-cycles are done to flip the plate in order to get more homogeneous properties. This is because one-sided uniaxial compaction creates different distributions of stresses in the two faces of the plate [135] which could lead to different preferred orientations to the graphite crystallites.

Table 4.13: Initial production parameters of the "MG-" MoGr grades.

Vol.%	MG-6530Aa		MG-6541Aa		MG-6403Ga		MG-6403Fc		MG-6541Fc	
Mo	4.5		4.4		4.5		4.5		4.4	
Gr. Asb.3260	90.5		90.1		94.95		94.95		90.1	
Short CF ¹	0		5		0		0		5	
Long CF ¹	5		0		0		0		0	
Ti	0		0.5		0.55		0.55		0.5	
	S	PS	S	PS	S	PS	S	PS	S	PS ²
No. cycles	2	1	2	1	2	1	2	1	2	1
T _{est} [°C]	2600	2100	2600	2100	2600	2100	2600	2600	2600	2600
Time [s]	2400	3000	2400	3000	2400	3000	2400	3000	2400	3000
P [MPa]	35	0	35	0	35	0	35	0	35	0

¹ Short carbon fibres: length of 250 μm , long carbon fibres: 3 mm

² Sintering cycle (S), Post-Sintering thermal treatment (PS)

4.6.2 Chromium carbide - graphite (CrGr)

The grades including chromium as catalyst instead of molybdenum are shown in Table 4.14.

Table 4.14: Initial production parameters of the CG- grades

Vol.%	CG-1100A0		CG-1100B0		CG-1100Ba		CG-1240X	
Cr ₃ C ₂	15		15		15		15	
Gr. Asb.3260	85		85		85		0	
Gr. Asb.3763	0		0		0		80	
Short CF ¹	0		0		0		5	
	S	PS	S	PS	S	PS	S	PS
No. cycles	1	0	2	0	2	1	2*	0
T _{est} . [°C]	2000	0	2000	0	2000	2000	2000	0
Time [s]	1200	0	2400	0	2400	3000	≈1500*	0
P [MPa]	35	0	35	0	35	0	35	0

¹ Short carbon fibres: length of 250 μm , long carbon fibres: 3 mm

Grade CG-1240X suffered a production failure, and time did not permit to repeat the test. However, the broken pieces of the plate were big enough to extract most of the specimens required for characterisation. It is important to note that the sudden pressure release and the breakage itself are likely affecting the final properties. Still, it was decided to characterise this plate to check the influence of the Asbury 3763 big flake graphite powder. The failure happened at the beginning of the second sintering cycle, which was planned to be the same as in the CG-1100B0. For this reason, the sintering time reported is ≈1500 s.

4.7 Machinability

All the characterisation techniques require specific specimen dimensions, therefore the specimens should be extracted from the sintered plates.

4.7.1 Conventional machining

In spite of the limited content of hard molybdenum carbides, the material is mainly composed of graphite. For this reason it can be machined with conventional milling methods, similarly to other graphitic materials. Dry machining is adopted to assure ultra-high vacuum compatibility; a suction system equipped with filters collects the airborne dust generated during milling. Figure 4.34a shows some of the MoGr blocks machined for a full-size collimator test. The blocks, which include features such as functional M8 threaded holes, chamfers or curved surfaces, are machined with a CNC milling machine. Small specimens for mechanical characterisation have also been successfully produced (Figure 4.34b).



(a) MG-6530Aa machined blocks for full-size collimator test. External dimensions of the parts shown are $150 \times 100 \times 25 \text{ mm}$ or $125 \times 45 \times 25 \text{ mm}$



(b) Example of MG-6541Aa specimens for dynamic tests machined by Brevetti Bizz. Length is 30 mm and threads are M6

Figure 4.34



Figure 4.35: Milling specimens from a sintered plate

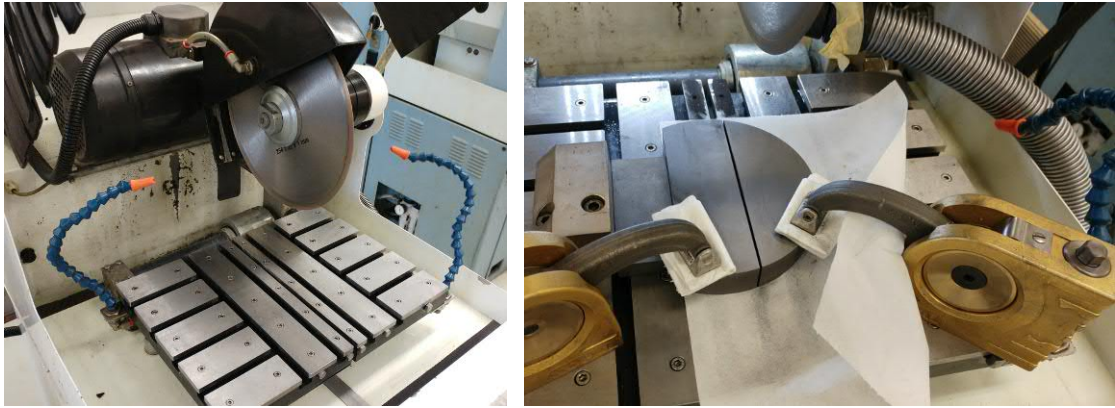


Figure 4.36: Slicing process with circular saw, diamond disk ($\text{Ø}254 \times 1 \text{ mm}$) The conventional SiC disk work also well, but having larger thickness they produce more graphite dust and waste more material.

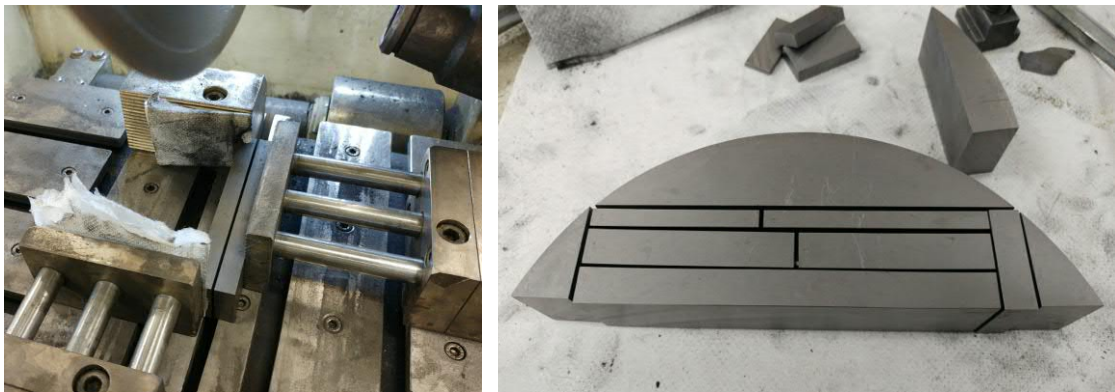


Figure 4.37: Slicing process with circular saw.

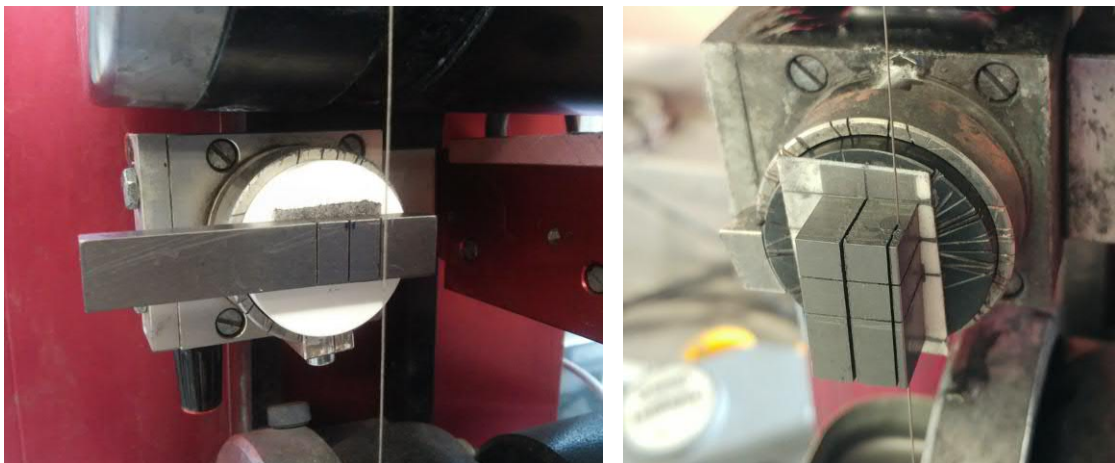


Figure 4.38: Diamond wire saw. Sample holder is $\text{Ø}30 \text{ mm}$ ($\text{Ø}0.3 \text{ mm}$ wire).



Figure 4.39: (Left) Samples extracted with the diamond wire saw. (Right) Samples milled by the supplier.

4.7.2 Electrical discharge machining (EDM)

EDM uses arc discharge created between an electrode or wire and the material to locally melt and cut the piece. The EDM-wire technique was tested in MoGr, giving unsatisfactory results, see Figure 4.40. The EDM-machined surfaces shows delamination marks, in the direction of the preferred orientation of the graphite.

This technique works well for electrically conductive materials, even those having very high melting temperatures, such as tungsten ($T_m = 3422^\circ\text{C}$). Graphite does not melt at ambient pressure, and the sublimation temperature is very high ($\sim 4000\text{ K}$, see C-phase diagram in Figure 2.1). In spite of this characteristic, Cope and Brown showed that graphite-epoxy laminated material can be successfully machined using EDM [136]. However, they reported a volumetric removal rate of only $1\text{ mm}^3\text{min}^{-1}$.

The MoGr unsuccessful EDM machining test could be due to the following reasons:

- The high thermal conductivity of MoGr could prevent reaching high local temperatures with the arc discharge.
- Non-adequate EDM settings (no settings information is available).

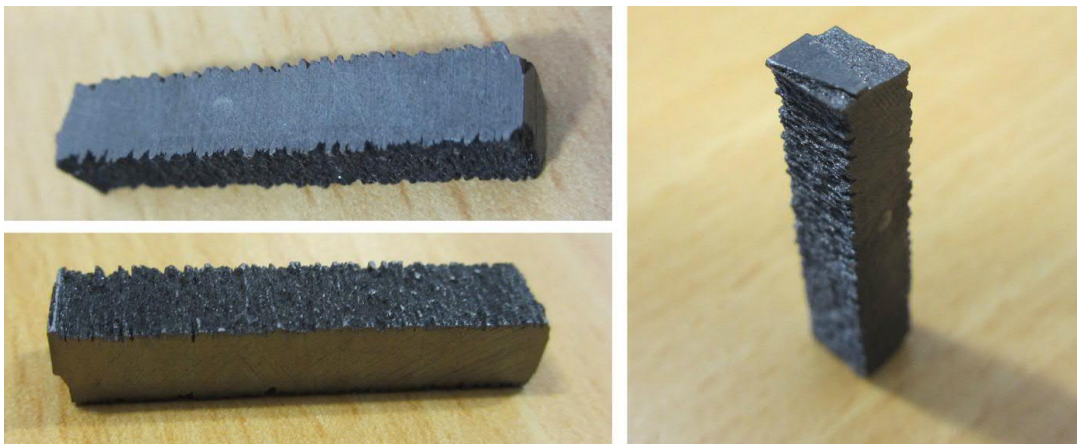


Figure 4.40: MoGr specimen (MG-6403Fc) cut with EDM-wire technique. Dimensions are $5 \times 5 \times 25\text{ mm}$. Pressing direction was parallel to the long side. The smooth surfaces were milled.

5 | Characterisation results

This chapter presents the results of the analyses performed on each of the materials. At the beginning, two pure graphitic materials are presented, to compare with the composites. The tests include both microstructural and macroscopic characterisation results. The discussion of these results is presented in chapter 6.

5.1 Pyrolytic Graphite (PG)

TPG (Thermal Pyrolytic Graphite) has been introduced in section 1.3.3. It is a commercial grade of pyrolytic graphite (PG), made from decomposition of hydrocarbon gas. The material is very anisotropic, showing very high in-plane thermal conductivity. Most of the samples were obtained by diamond wire machining. This technique is possible for TPG with careful sample supporting, in order to prevent delamination between basal planes.

The characterisation results are presented below.

5.1.1 Microstructure

Figures 5.1 to 5.3 depict the SEM observations of TPG (the latter corresponds to through-plane surface). The backscattered electron (BE) images show channeling effect, due to the different scattering efficiencies of the crystallographic orientations. This permits contrast between domains with different orientations.

The in-plane (IP) as-received surface shows large-scale wrinkles, possibly due to fast deposition rates, however, there are areas with sizes up to $\sim 60 \mu m$ with smoothly oriented graphite. Figure 5.2 shows the results of a polishing trial of the IP surface. The combination of texture and lubricating nature of the graphite does not allow good polishing results on this orientation. The same polishing procedure was used successfully to obtain mirror-like aspect in the through-plane (TP) surface.

The TP surface, shows parallel domains corresponding to the oriented graphite.

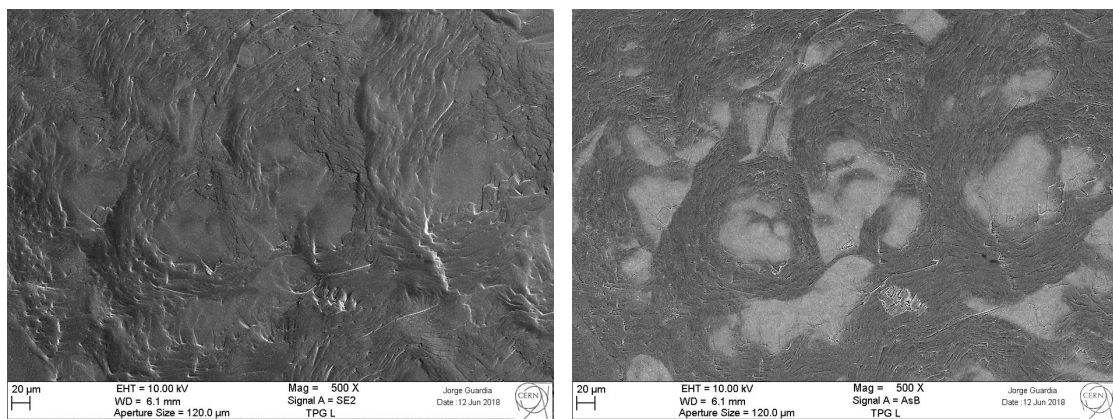


Figure 5.1: SEM observations of IP as-received surface of TPG. (left) SE image, (right) BE image.

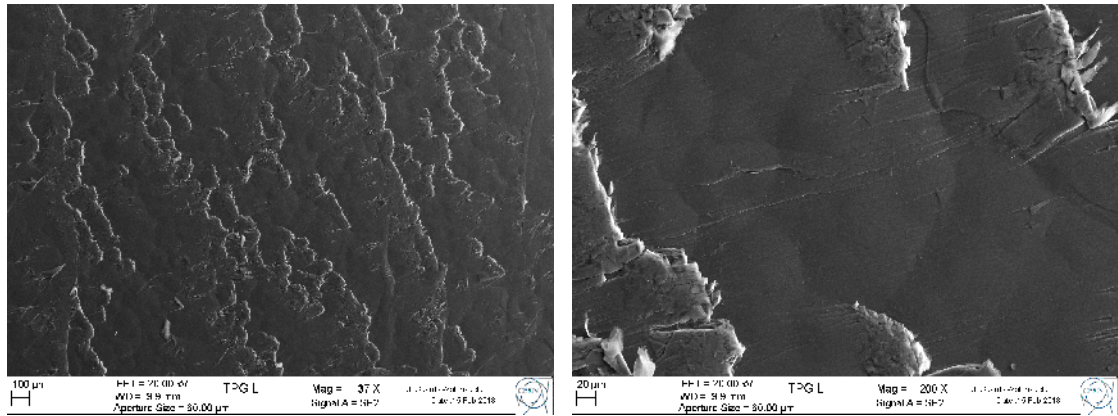


Figure 5.2: SEM observations (SE) of polished IP surface of TPG at different magnifications

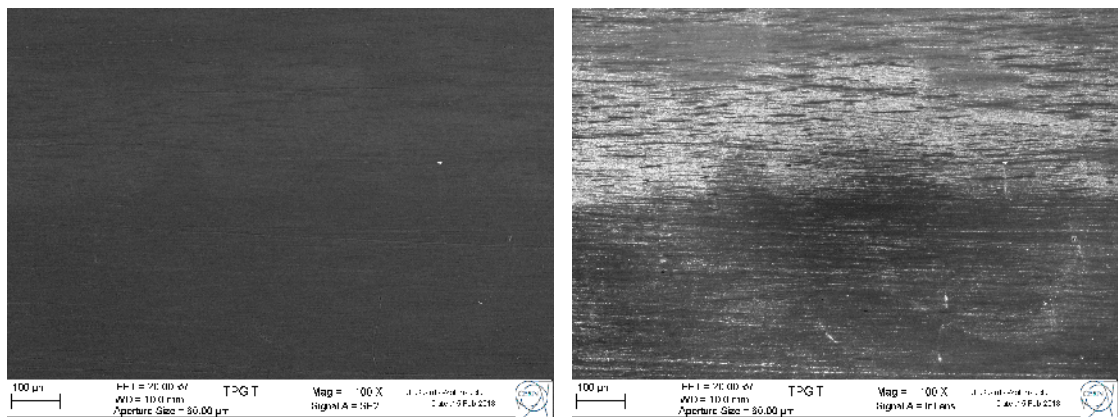


Figure 5.3: SEM observations of polished TP surface of TPG. (left) SE image, (right) BE image.

These observations (SE and BE SEM characterisation) do not allow grain size measurements. Figure 5.1 (right) shows contrast between areas with different curvatures, with average size of around $50\ \mu\text{m}$, which could correspond to high-angle grain boundaries. Other techniques should be implemented to precisely assess the grain size, specially those involving grain boundary revealing (chemical attack or combustion in oxygen atmosphere). As explained in section 2.1.3, grain boundaries are high energy areas due to the presence of unsatisfied bonds, which makes them more prone to chemical reactions than defect-free areas.

5.1.2 Crystallography and lattice expansion

Several XRD analyses were performed at RT on TPG material, see Figure 5.4. The IP surface produces very strong signal of the $00l$ peaks, specially the (002). A special set of slits, much more restrictive than in the usual tests, was required to prevent saturation of the detector. Due to the texture of graphite in TPG, the TP surface should show only peaks related to the $hk0$ planes, however, the (002) and (004) peaks were visible. It was identified that the source of this reflections are the flakes bent on the surface due to the machining. Another test was performed after polishing the TP surface, with mirror finishing (see Figure 1.28). The polishing was performed on the rotating soft cloth disk using as last step $1\ \mu\text{m}$ diamond paste. This treatment considerably reduces the intensity of the $00l$ reflections, but the (002) peak is still visible.

It is demonstrated below (lattice expansion section) that the removal of bent flakes on the surface can be further improved by polishing with manual alternative movements parallel to the basal planes, instead of using randomly rotating movements. This cuts the flakes bent on the surface, exposing to the surface the inner oriented graphitic structure.

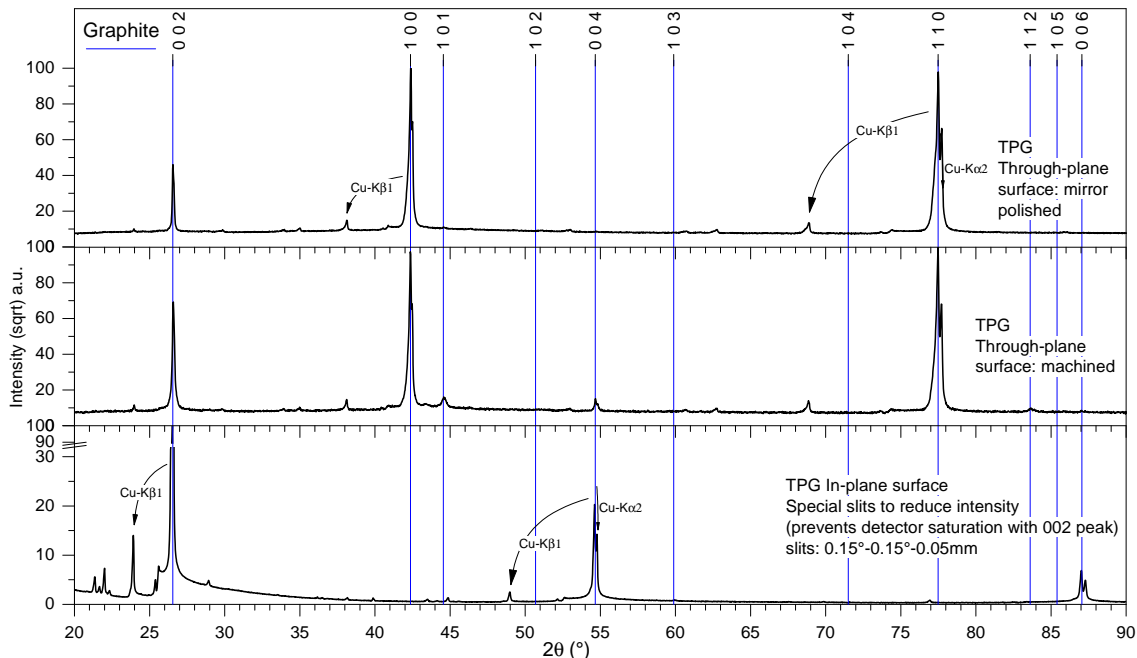


Figure 5.4: TPG XRD patterns at RT.

Lattice expansion

Figure 5.5 shows the acquired XRD patterns on the TPG IP sample. The IP surface was tested as-received. Due to the extreme preferred orientation of the graphite, only peaks related to the basal-plane spacing appear ($00l$). This produces that only the c lattice parameter can be analysed. (006) peak shows smaller absolute intensity when increasing temperature, but this effect is completely reversible. The peak intensities and positions during cooling down match perfectly the ones from the heating up ramp. For this reason, this effect is not related with changes in the surface due to the combustion, it is caused only by the temperature. The effect is likely due to the change in density due to the thermal expansion, which causes that at high angles, the penetration of the X-rays increases, and less intensity escapes the material (increased absorption).

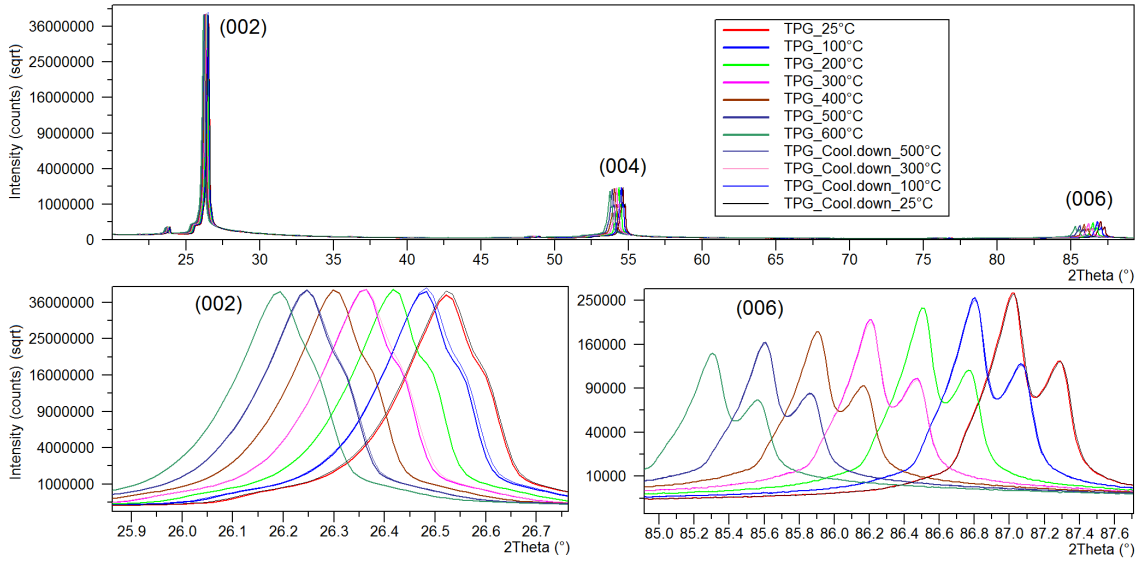


Figure 5.5: TPG IP experimental XRD patterns. The patterns acquired during cooling down (500, 300, 100 and 25 °C) are also showed, matching almost perfectly.

The thickness of the specimen was measured with a micrometer and the mass with a precision scale, before and after the test: 1.031 mm and 1.030 mm respectively; this difference is negligible. The masses are 0.24756 g and 0.24731 g respectively, showing a decrease of 25 μg , which should be due to combustion in the air atmosphere. This shows that high quality graphite oxidises very slowly at the temperatures of the test. In fact, the intensity of the peaks does not decrease after the test.

Table 5.1 lists the experimental peak positions and the results of the specimen displacement correction s , see section 3.5.2. The height correction and the alignment at RT match within 30 μm . This difference probably comes from the specimen transparency error. The cooling-down behaviour is coincident with the heating-up one, within the uncertainty of the measurement. This confirms that for these temperatures the process is fully reversible.

Table 5.1: Graphite 2θ peak positions [°] in TPG IP test. Resulting lattice parameters.

	T [°C]	s [mm]	(002)		(004)		(006)		Lattice param.	
			Exp.	Corr.	Exp.	Corr.	Exp.	Corr.	a [Å]	c [Å]
Heating up	25	0.030	26.520	26.534	54.623	54.636	87.011	87.021	-	6.713
	100	0.006	26.475	26.478	54.509	54.512	86.795	86.797	-	6.727
	200	-0.030	26.415	26.401	54.359	54.346	86.498	86.488	-	6.746
	300	-0.074	26.357	26.323	54.206	54.175	86.199	86.173	-	6.766
	400	-0.117	26.298	26.243	54.052	54.002	85.897	85.856	-	6.786
	500	-0.169	26.242	26.163	53.900	53.828	85.596	85.537	-	6.806
600	-0.228	26.189	26.083	53.749	53.652	85.298	85.218	-	6.827	
Cooling d.	500	-0.177	26.245	26.163	53.901	53.826	85.597	85.535	-	6.807
	300	-0.078	26.359	26.323	54.210	54.177	86.200	86.173	-	6.766
	100	0.005	26.476	26.479	54.512	54.514	86.797	86.799	-	6.727
	25	0.031	26.521	26.536	54.628	54.641	87.016	87.027	-	6.713

Figure 5.6 shows the acquired patterns on the TPG TP sample. The TP surface was mirror-polished by hand, with alternative movements parallel to the basal planes. This prevents that crystallites at the surface bend and produce 002 signal. It is visible in

the pattern that the polishing was very successful, as almost no signal from the basal-plane spacing was acquired. Due to the extreme preferred orientation of the graphite, only peaks related to the a lattice parameter appear ($hk0$). It is required to test this orientation to analyse the a lattice parameter, as explained above. The peaks shift with temperature in the opposite direction than the $00l$ peaks in the IP test, because the lattice parameter decreases this time with increasing temperatures. Besides, the shift is much less in amplitude. In this case, only the heating-up ramp was acquired.

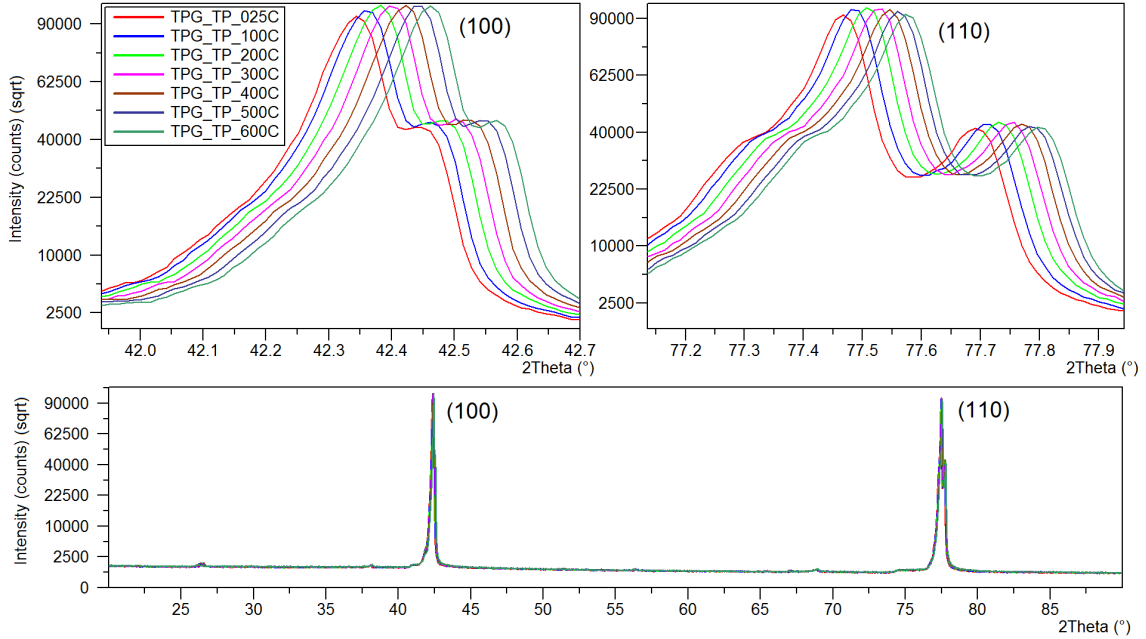


Figure 5.6: TPG TP experimental XRD patterns.

Table 5.2 lists the experimental peak positions and the results of the specimen displacement correction s , see section 3.5.2. The height correction and the alignment at RT match within $42 \mu m$. This difference probably comes from the specimen transparency error.

Table 5.2: Graphite 2θ peak positions [°] in TPG TP test. Resulting lattice parameters.

	T [°C]	s [mm]	(100)		(110)		Lattice param.	
			Exp.	Corr.	Exp.	Corr.	a [Å]	c [Å]
Heating up	25	0.042	42.341	42.360	77.464	77.480	2.4618	-
	100	0.018	42.356	42.364	77.482	77.489	2.4616	-
	200	-0.017	42.376	42.368	77.504	77.498	2.4613	-
	300	-0.061	42.397	42.370	77.523	77.500	2.4613	-
	400	-0.098	42.416	42.372	77.542	77.505	2.4611	-
	500	-0.156	42.439	42.370	77.558	77.500	2.4613	-
	600	-0.204	42.458	42.367	77.571	77.495	2.4614	-

A second degree polynomial is fitted to the data, see Table 5.3. Figure 5.7 shows the experimental lattice parameters in TPG, from the two tested orientations, both the measurements and the fitting curve. The values from the literature are also reported for comparison.

Table 5.3: Fitting equation for the lattice parameters variation ($d = AT^2 + BT + C$, T in °C, d in Å) in TPG. From the heating-up curves.

	A	B	C	Value at 20°C [Å]
a	$4.8532 \cdot 10^{-9}$	$-3.7329 \cdot 10^{-6}$	2.4619	2.4618
c	$1.9528 \cdot 10^{-8}$	$1.8622 \cdot 10^{-4}$	6.7084	6.7121

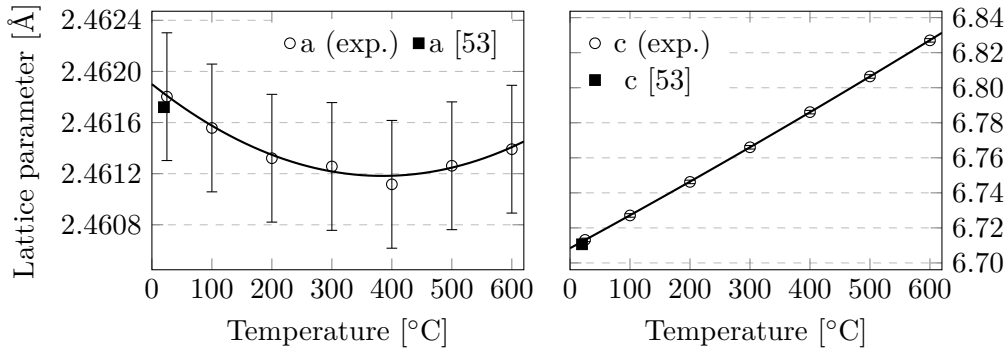


Figure 5.7: Lattice parameters versus temperature of graphite in TPG.

The value of c extrapolated to 20 °C is 6.712 Å. Howe et al. [53] reported a value of 6.7106 Å for the unit cell dimension c of graphite. The difference between the two is smaller than our measurement's uncertainty.

It is well known that the interplanar distance in graphite varies depending on its quality. The highest quality graphite, perfect single crystal, shows the smallest figure (6.7106 Å) and this figure becomes larger as the perfection worsens (due to wrinkles in the basal planes). In this measurement, the result matches the ideal value, meaning that the graphite crystallites in TPG material are of the best possible quality.

The CTE is calculated from the fitting curves, the results are shown in Table 5.4 and Figure 5.8, compared with the dilatometry technique (see section 3.1.4). There is a slight difference between the results of the two techniques, but the overall matching is very good. The results from the dilatometer in the IP direction show unusual high dispersion because of the small change in length and the size of the tested specimens (10 mm). Longer specimens produce lower uncertainty. If one takes the average between heating-up and cooling down curves, the match with the XRD technique is very good.

In the TP direction, the large expansion reduces the uncertainty of the dilatometry technique, and the two techniques match within 5%.

Table 5.4: Result of the secant CTE 20–T °C of graphite in TPG ($\times 10^{-6} m^{-1} K^{-1}$).

T [°C]	XRD (Heating)		Dilatometer			
	a	c	a (H)	a (C)	c (H)	c (C)
50	-1.4	27.9	-1.9	-1.0	29.0	29.3
100	-1.3	28.1	-1.6	-1.0	29.0	29.3
200	-1.1	28.4	-1.3	-0.9	29.1	29.3
300	-0.9	28.7	-1.0	-0.7	29.2	29.3
400	-0.7	29.0	-0.8	-0.5	29.3	29.4
500	-0.5	29.3	-0.6	-0.4	29.4	29.4
600	-0.3	29.5	-0.4	-0.3	29.5	29.4

(H):Heating-up, (C): Cooling-down

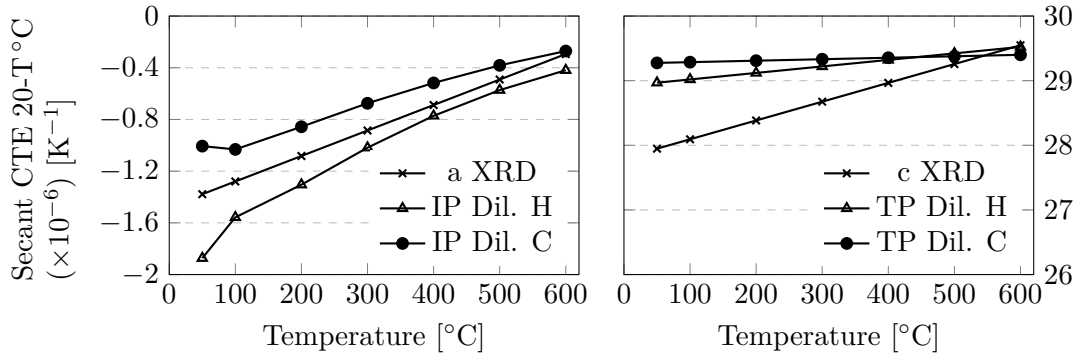


Figure 5.8: Secant CTE 20-T °C of graphite in TPG (XRD), compared with the dilatometer measurement (IP: In-plane, TP:Through-plane, H: heating-up, C:cooling-down).

5.1.3 Electrical conductivity

Bulk electrical conductivity measurements on TPG material are shown in Table 5.5. This method allows to measure the two directions of the material, which are very different due to its anisotropy. Only the results from 2 samples are reported, as the other measurements were unsuccessful due to damage in the specimens while supporting them in the set-up, see Figure 5.9. The distance between voltmeter probes (L) is typically kept constant with a holder (uncertainty 0.5 mm), however for the TP specimen, it was too small and had to be kept manually, increasing the uncertainty to around 1 mm, see Figure 5.9.

Table 5.5: 4-wire DC method electrical measurements on TPG material, see section 3.4.

	IP 1	IP 2	Average IP	TP 1	TP 1	Average TP
d_1 [mm]	1.12	1.13		3.04	3.04	
d_2 [mm]	3.16	3.5		5.13	5.13	
d_3 [mm]	49.5	49.5		10.15	10.15	
L [mm]	30.0	30.0		5	3	
Current [mA]	199.3	199.3		300.1	300.1	
Av. Voltage [μ V]	710	654		99167	67233	
ρ_e [$\mu\Omega$ m]	0.42	0.43	0.43	1030.67	1164.63	1097.65
γ_e [MS m ⁻¹]	2.38	2.31	2.35	0.00097	0.00086	0.00091

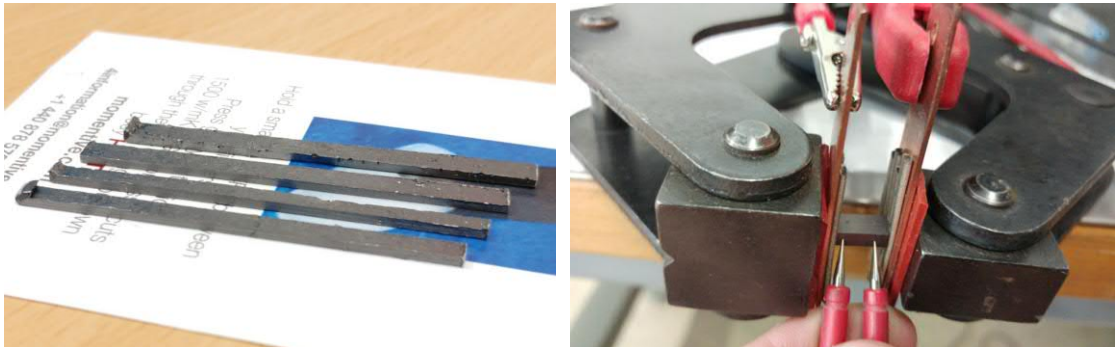


Figure 5.9: (Left) TPG IP specimens tested for bulk electrical resistivity showing damage due to the gripping in the set-up. (Right) Test of the TPG TP specimen.

Superficial electrical conductivity measurements on TPG material are shown in Table

Table 5.6: Superficial electrical conductivity measurements on TPG material [MS m^{-1}]. 6–10 measurement points per test.

Th. [mm]	Sample 1				Sample 2		Sample 3		Average
	~ 10				~ 1		~ 1		-
Surface	IP	IP	TP*	TP*	IP	IP	IP	IP	IP
Freq. [kHz]	60	960	60	960	60	960	60	960	-
1	2.46	2.41	0.96	0.94	1.71	2.6	1.69	2.65	
2	2.48	2.43	1.05	0.89	1.74	2.62	1.75	2.65	
3	2.5	2.45	1.02	0.94	1.73	2.61	1.82	2.63	
4	2.3	2.25	0.96	0.95	1.7	2.6	1.77	2.61	
5	2.36	2.29	1.04	0.92	1.65	2.53	1.78	2.56	
6	2.36	2.28	0.95	0.96	1.72	2.63	1.66	2.57	
7			0.91	0.96	1.73	2.59	1.82	2.65	
8			0.9	0.88	1.72	2.6	1.81	2.65	
9					1.72	2.58	1.73	2.65	
10					1.64	2.6	1.77	2.62	
Average	2.41	2.35	0.97	0.93	1.71	2.60	1.76	2.62	2.50
σ_{RMS}	0.08	0.09	0.06	0.03	0.03	0.03	0.05	0.03	0.13

(*) see text.

5.6. The measuring frequency of 60 kHz is not enough for measuring the 1 mm-thick specimens, see section 3.4 and equation 3.15 (Skin depth δ). The skin depth in 60 kHz measurements is larger than the 1 mm-thick specimens ($\delta = 1.3 \text{ mm}$ for $\gamma_e = 2.4 \text{ MS m}^{-1}$). In the 10 mm-thick specimen, the variation in frequency does not alter the result, within the error of the measurement (5%).

The average of the IP tests, excluding those done at 60 kHz in 1 mm-thick specimens, is 2.50 MS m^{-1} . The results from the 4-wire DC method are compatible within the uncertainty of the measurements.

The average value between the two methods is 2.4 MS m^{-1} and is taken as reference for TPG material. This value is very close to the best reported measurements in PG materials (2.5 MS m^{-1}), see section 1.4.

The TP-surface measurements give a 3D average value of TP and IP directions, hence not practical. However, they are reported for reference because they are measurements on a known anisotropic material.

5.1.4 Thermophysical properties

The density at RT measured with the Archimede's method is 2.261 g cm^{-3} . This is in agreement with the value reported by the supplier (2.25 g cm^{-3}) and is almost as high as the lattice density of graphite (2.265 g cm^{-3} [53], see section 3.5).

The variation of density with respect to temperature, $\rho(T)$, is shown in Figure 5.10. $\rho(T)$ is calculated as explained in section 3.1.4, from the volumetric expansion coefficient (α_V). The latter is three times the average linear CTE ($\alpha_{average}$), which is obtained from the linear coefficients in the two directions. The density variation is small, moving from 2.261 to 2.12 g cm^{-3} in the range 20–2000 °C. This variation does not produce a relevant change in the thermal conductivity calculation (see Figure 5.14). For this reason, for the rest of investigated materials, the density variation with temperature is neglected for k calculation.

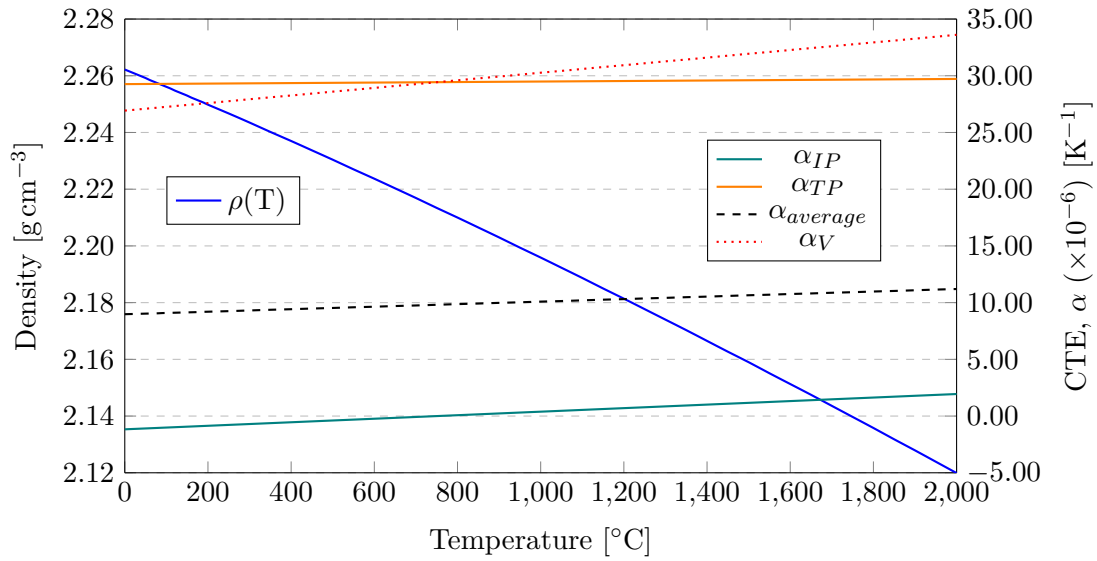


Figure 5.10: Density of TPG versus temperature. α values required for its calculation (α_{IP} and α_{TP} are fitted as linear functions from the experimental data).

The thermal diffusivities and the specific heat of TPG are shown in figures 5.11, 5.12 and 5.13.

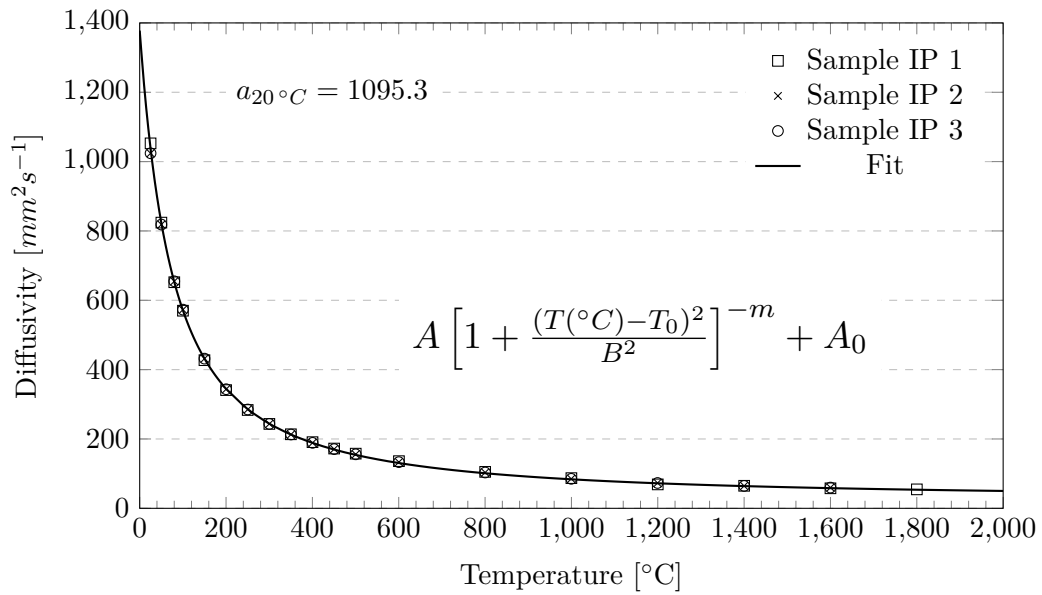


Figure 5.11: Thermal diffusivity of TPG IP direction. Fitting equation constants: $A = 4388$, $B = 36.12$, $T_0 = -84.25$, $m = 0.6313$ and $A_0 = 23.87$. Specimens thicknesses: 12, 10 and 8 mm respectively.

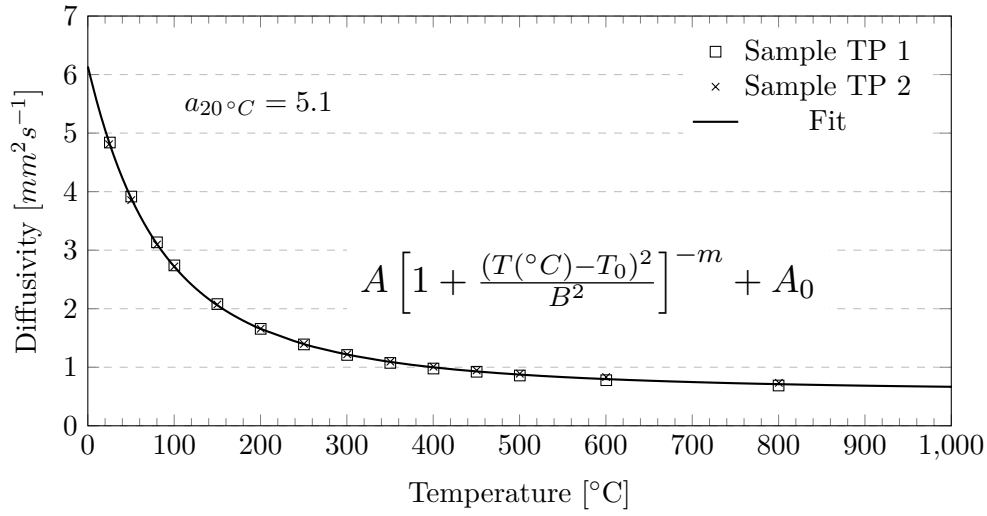


Figure 5.12: Thermal diffusivity of TPG TP direction. Fitting equation constants: $A = 14.62$, $B = 85.60$, $T_0 = -110.9$, $m = 0.9799$ and $A_0 = 0.5703$. All specimens with thickness ≈ 1 mm.

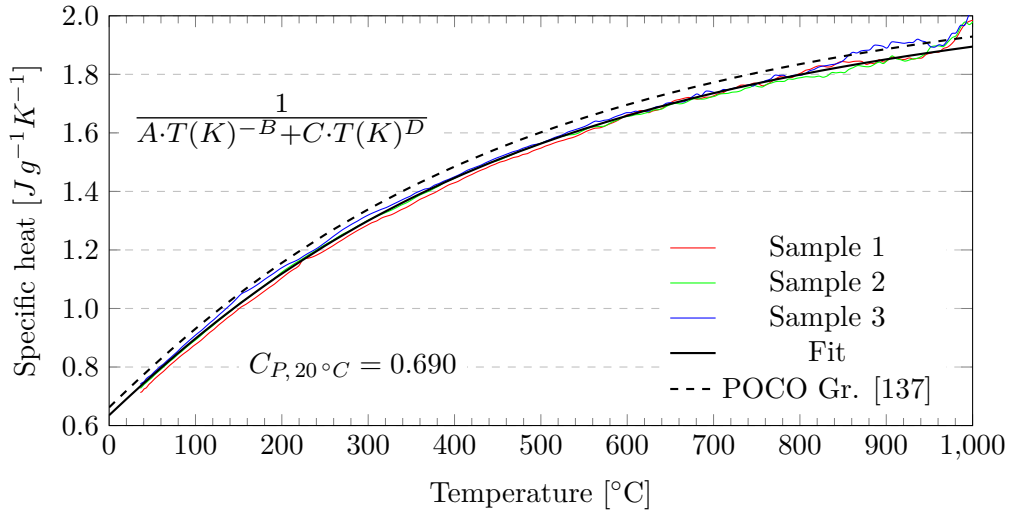


Figure 5.13: Specific heat of TPG. Fitting equation constants: $a = 11.67$, $b = 1.644$, $c = 3.728\text{E-}4$ and $d = 0.02191$.

The specific heat C_p curve is roughly the same than the data reported for POCO AXM-5Q graphite ($a = 11.07$, $b = 1.644$, $c = 3.688\text{E-}4$ and $d = 0.02191$) [137]. The $C_{p,20^\circ\text{C}}$ value is 0.690 , slightly lower than $0.719 \text{ J g}^{-1} \text{ K}^{-1}$ of POCO graphite. The same fitting function is used also for the C_p of the materials investigated in this thesis.

The thermal conductivity k is calculated from the diffusivity, specific heat and density, see Figure 5.14. The IP values reach $1710.0 \text{ W m}^{-1} \text{ K}^{-1}$ at 20°C , while the TP conductivity is only $7.9 \text{ W m}^{-1} \text{ K}^{-1}$.

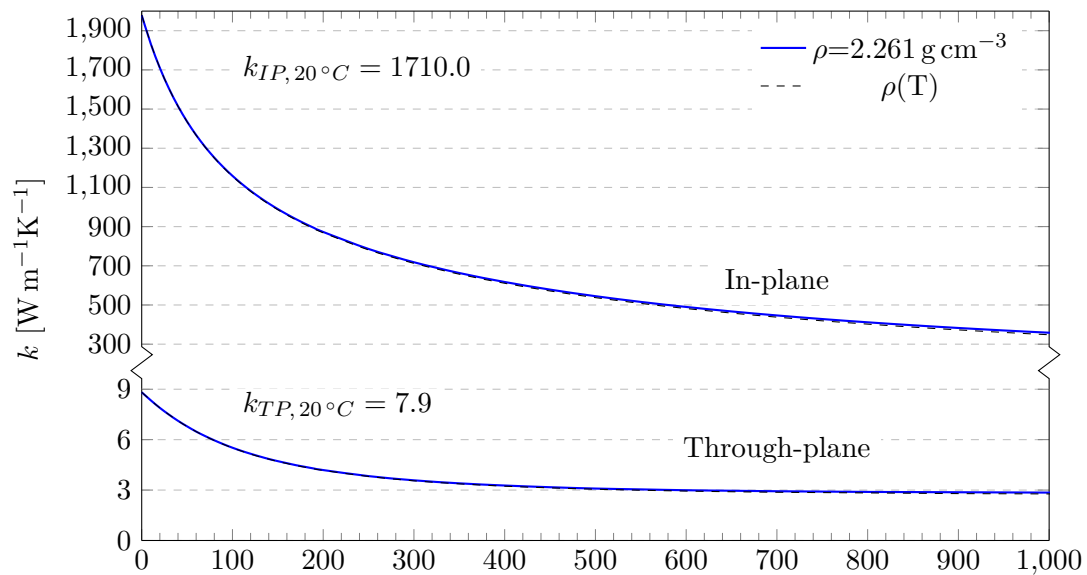


Figure 5.14: Thermal conductivity of TPG in both directions. Calculated both from $\rho(T)$ (see Figure 5.10) and from constant density.

Thermal expansion measurements are shown in Figures 5.15 and 5.15. It is important to note that in the TP direction, only test TP4 is considered. The rest of TP measurements show abnormally high α , reaching $40 \times 10^{-6} \text{ K}^{-1}$, due to experimental errors. The α_{TP} of TPG is thus around $30 \times 10^{-6} \text{ K}^{-1}$ in the range 20–600 °C, which matches quite closely the expansion behaviour characterised by XRD (see Table 5.4).

α_{IP} average values are tabulated in Table 5.4, being $-0.3 \times 10^{-6} \text{ K}^{-1}$ (cooling-down ramp) in the range 20–600 °C.

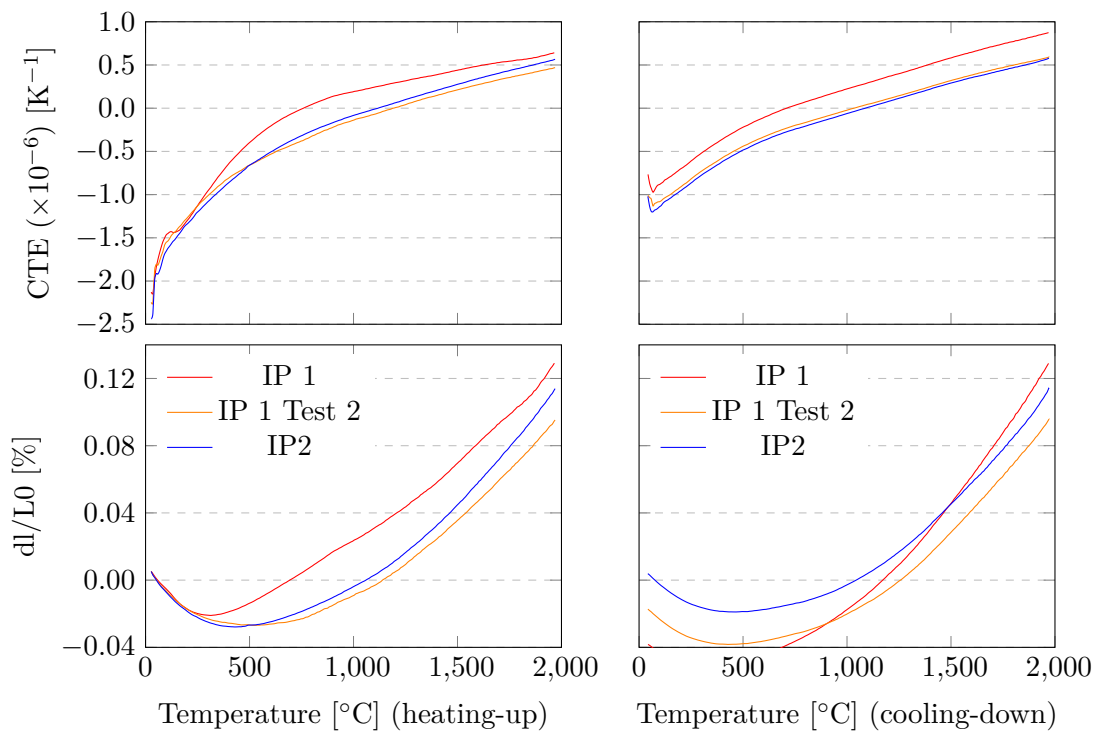
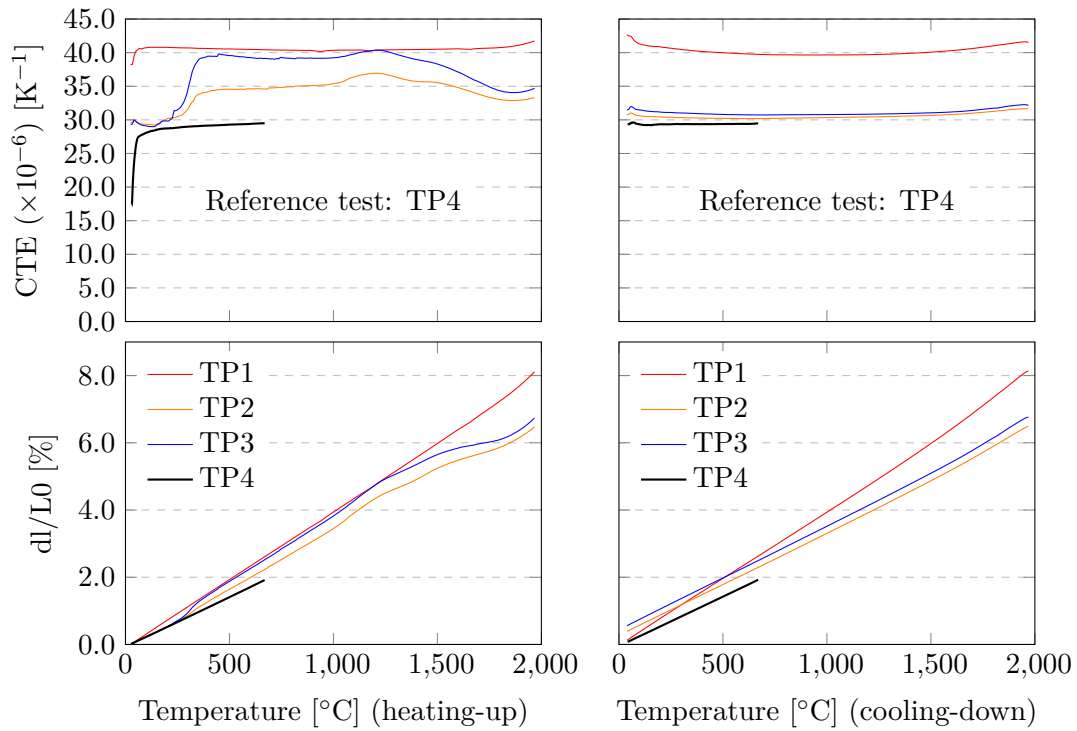


Figure 5.15: CTE TPG IP. All specimens with length ≈ 25 mm.

Figure 5.16: CTE TPG TP. All specimens with length ≈ 10 mm.

5.1.5 Mechanical properties

The IP bending test curves are shown in Figure 5.17. The average maximum strength is $25.5 \pm 0.4 \text{ MPa}$ and the average strain to rupture is $820 \pm 30 \text{ } \mu\text{m m}^{-1}$. The nominal size of the specimens is $5 \times 10 \times 50 \text{ mm}$, being 5 mm the TP direction. The test jig span is $L=40 \text{ mm}$ and the loading span is $L/2$ (four point configuration).

Tests in the TP direction are not available, because the maximum available specimen length was 10 mm, which is too short for conventional testing.

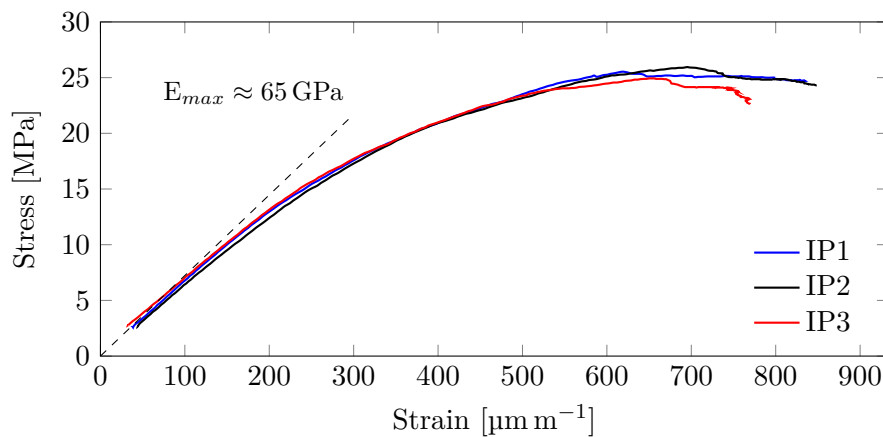


Figure 5.17: Bending test of TPG.

The elastic constants could not be identified with the IET method. Only the flexural frequency (ff) of IP specimens was acquired, the torsional frequency excitation was not successful, see Table 5.7. Therefore, unless most of the elastic constants are arbitrarily

estimated, the elastic matrix cannot be reverse engineered. It is expected that the IP Young's modulus is in the order of 65 GPa, as seen in the bending test (Figure 5.17).

Table 5.7: IET test of TPG.

Specimen	m [g]	L [mm]	b [mm]	t [mm]	ff [kHz]
1	5.8	50.03	10.16	5.10	6713
2	5.9	50.04	10.33	5.08	6765
3	5.92	50.00	10.38	5.11	6741
Average	5.87	50.02	10.29	5.10	6740

5.2 Graphite R4550

Graphite R4550 is introduced in section 1.3.3. It is a commercial artificial graphite, more specifically, it is a fine-grained isotropic nuclear graphite grade. The material processing results in isotropic properties, hence only one direction is characterised. The characterisation results are presented below.

5.2.1 Microstructure

SEM observations of graphite R4550 are shown in Figure 5.18. The image shows homogeneous distribution of pores, with average size of around $10\mu\text{m}$ and maximum size of $20\mu\text{m}$. The pore shape does not show preferred orientation, corresponding to isotropic structure.

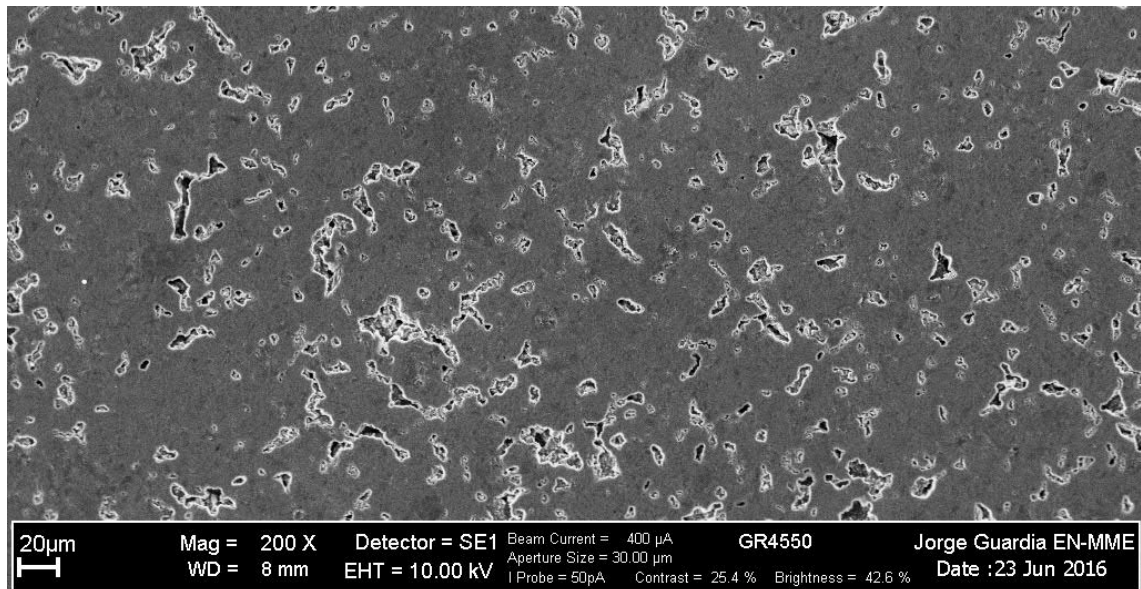


Figure 5.18: SEM observation of polished Graphite R4550 surface

5.2.2 Crystallography and lattice expansion

Figure 5.19 shows the acquired XRD patterns on the graphite R4550 sample. This material is isotropic, therefore no specific orientation was tested. The surface was mirror polished ($1\mu\text{m}$ diamond paste) in order to remove crystallites bent or damaged by the cutting process.

The peaks are broad, making difficult the manual identification of their position. This is due to small crystallite size. For this reason, these XRD patterns were analysed by Rietveld refinement, calibrating the instrumental broadening with LaB₆ powder. The results of the analysis are shown in table 5.8, including the specimen displacement correction s calculated by MAUD (from Z_2R parameter), see section 3.5.2.

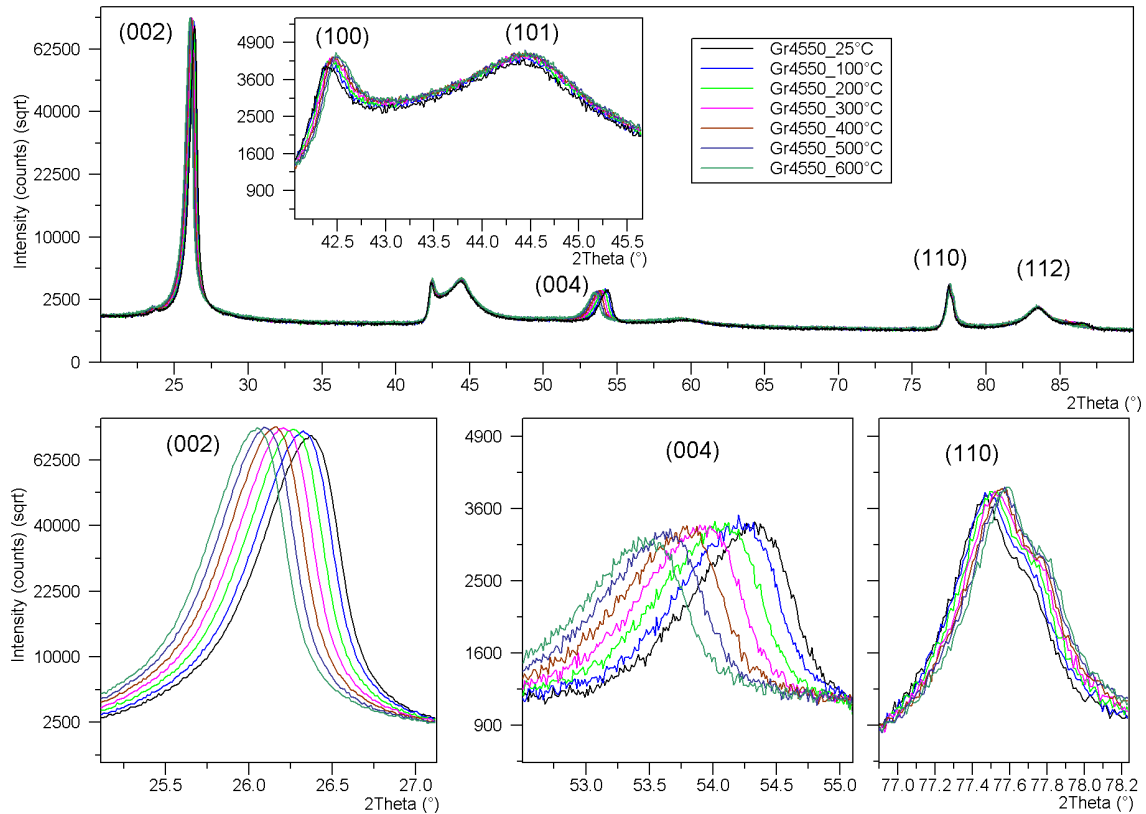


Figure 5.19: Graphite R4550 experimental XRD patterns.

Table 5.8: Result of the lattice parameters of graphite in R4550, from MAUD Rietveld refinement.

	T [°C]	Z_2R	s [mm]	a [Å]	c [Å]
Heating up	25	$-7.03 \cdot 10^{-6}$	0.001	2.4623	6.764
	100	$3.34 \cdot 10^{-4}$	-0.040	2.4622	6.780
	200	$5.37 \cdot 10^{-4}$	-0.064	2.4619	6.797
	300	$8.99 \cdot 10^{-4}$	-0.108	2.4618	6.817
	400	$1.15 \cdot 10^{-3}$	-0.139	2.4616	6.835
	500	$1.59 \cdot 10^{-3}$	-0.191	2.4618	6.855
	600	$2.15 \cdot 10^{-3}$	-0.258	2.4620	6.877

A second degree polynomial is fitted to the data, see Table 5.9. Figure 5.20 shows the graphite experimental lattice parameters in R4550, both the measurements and the fitting curve. The values from the literature are also reported for comparison, indicating incomplete graphitisation level.

Table 5.9: Fitting equation for the lattice parameters variation ($d = AT^2 + BT + C$, T in $^{\circ}\text{C}$, d in \AA) in R4550. From the heating-up curves.

	A	B	C	Value at 20 $^{\circ}\text{C}$ [\AA]
a	$5.4517 \cdot 10^{-9}$	$-4.1409 \cdot 10^{-6}$	2.4625	2.462(4)
c	$2.5768 \cdot 10^{-8}$	$1.7695 \cdot 10^{-4}$	6.7605	6.764

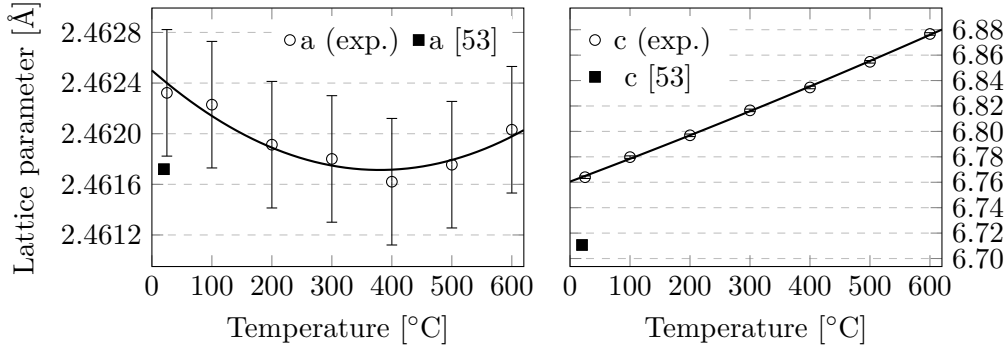


Figure 5.20: Lattice parameters versus temperature of graphite in R4550.

The secant CTE is calculated from the fitting equation, see Table 5.10. The comparison with the macroscopic CTE, measured with the dilatometer, shows that the crystallites must be randomly oriented to show that macroscopic behaviour. The crystallite average $\text{CTE}_{20-50^{\circ}\text{C}}$ is $(2 \times (-1.5) + 26.4)/3 = 7.8$ ($\times 10^{-6} \text{ m}^{-1} \text{ K}^{-1}$), therefore there must be an effect of the porosity, decreasing the CTE. It could also be that the a thermal expansion weighs more due to the stronger atomic bond and so the macroscopic result is lower than the crystallite average.

Table 5.10: Result of the secant CTE 20-T $^{\circ}\text{C}$ of graphite in R4550 ($\times 10^{-6} \text{ m}^{-1} \text{ K}^{-1}$).

T [$^{\circ}\text{C}$]	XRD (H)		Dil. average	
	a	c	(H)	(C)
50	-1.5	26.4	4.5	3.9
100	-1.4	26.6	4.6	4.0
200	-1.2	27.0	4.7	4.1
300	-1.0	27.4	4.8	4.3
400	-0.8	27.8	4.9	4.4
500	-0.5	28.1	4.9	4.5
600	-0.3	28.5	5.0	4.6

(H):Heating-up, (C): cooling-down.

5.2.3 Electrical conductivity

Bulk electrical conductivity measurements on R4550 graphite are shown in Table 5.11. Only two measurements were performed, giving an average resistivity of $12.6 \mu\Omega \text{ m}$ or conductivity 0.08 MS m^{-1} , which match the specification in the supplier's datasheet ($13 \mu\Omega \text{ m}$).

This material has too low conductivity for the Sigmatest device to measure it.

Table 5.11: 4-wire DC method electrical measurements on graphite R4550, see section 3.4.

	Sample 1	Sample 2	Average
d_1 [mm]	13.88	13.91	
d_2 [mm]	3.89	3.10	
d_3 [mm]	26.52	26.51	
L [mm]	9.5	9.5	
Current [mA]	75.1	75.1	
Av. Voltage [μ V]	169.4	205.3	
ρ_e [$\mu\Omega$ m]	12.83	12.42	12.62
γ_e [$MS\ m^{-1}$]	0.078	0.081	0.079

5.2.4 Thermophysical properties

The density of Graphite R4550 measured from the mass and dimensions of several parallelepiped specimens is 1.830 g cm^{-3} , which is the same value than in the material datasheet. The vol.% of porosity, with respect to fully dense graphite is in the order of 18.7%. The Archimede's measurements in this porous material do not count the open porosity, reaching values of 1.9 g cm^{-3} .

The thermal diffusivity a and the specific heat (C_P) of graphite R4550 are shown in figures 5.21 and 5.22. The conductivity (k) is calculated with equation 3.1 assuming constant density (1.830 g cm^{-3}), see Figure 5.23. The k plot shows a maximum between 0 and 20°C . It is important to note that neither $a(T)$ nor $C_P(T)$ fitting functions have a maximum around those temperatures, so the k peak is the result of the multiplication of $a(T)$ and $C_P(T)$ values. No measurements under $\sim 25^\circ\text{C}$ are available to verify this behaviour, therefore it could just be due to the fitting functions.

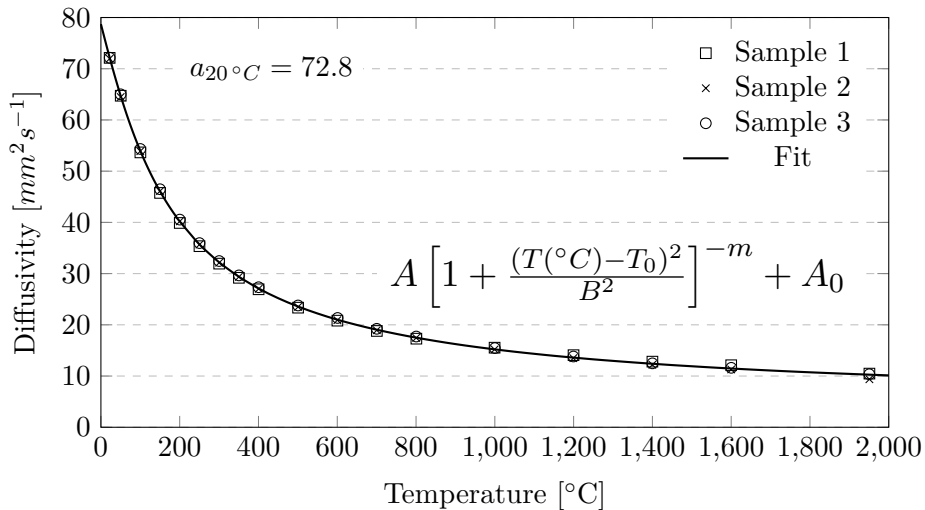


Figure 5.21: Thermal diffusivity of isotropic graphite R4550. Fitting equation constants: $A = 92.10$, $B = 109.1$, $T_0 = -82.84$, $m = 0.4547$ and $A_0 = 3.835$. All specimens with thickness $\approx 3\text{ mm}$.

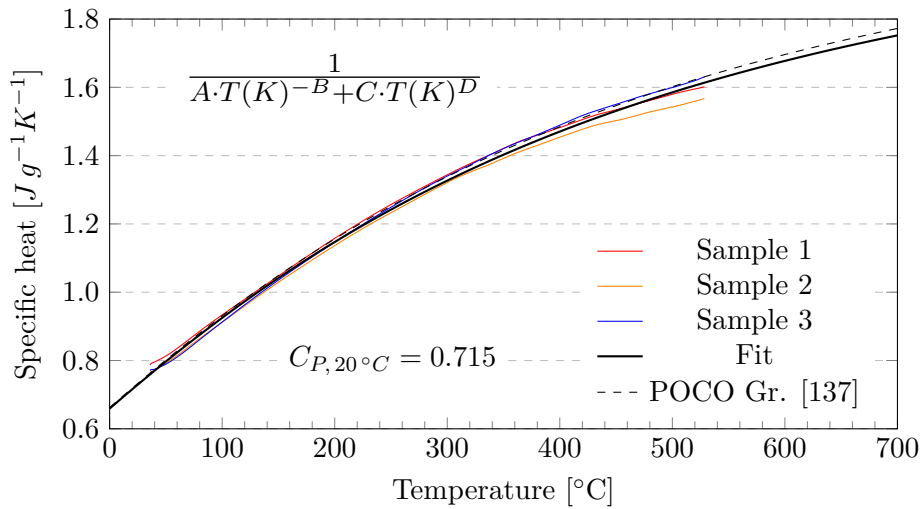


Figure 5.22: Specific heat of R4550. Fitting equation constants: $A = 11.08$, $B = 1.644$, $C = 3.744\text{E-}4$ and $D = 0.02191$.

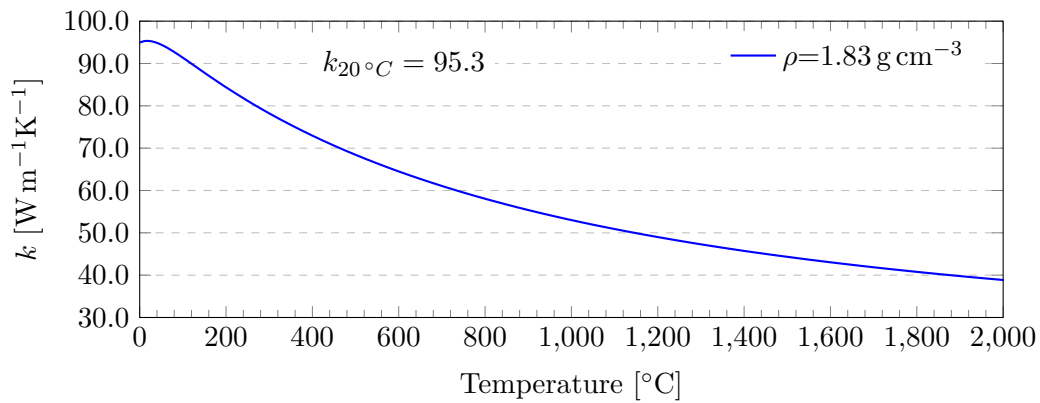
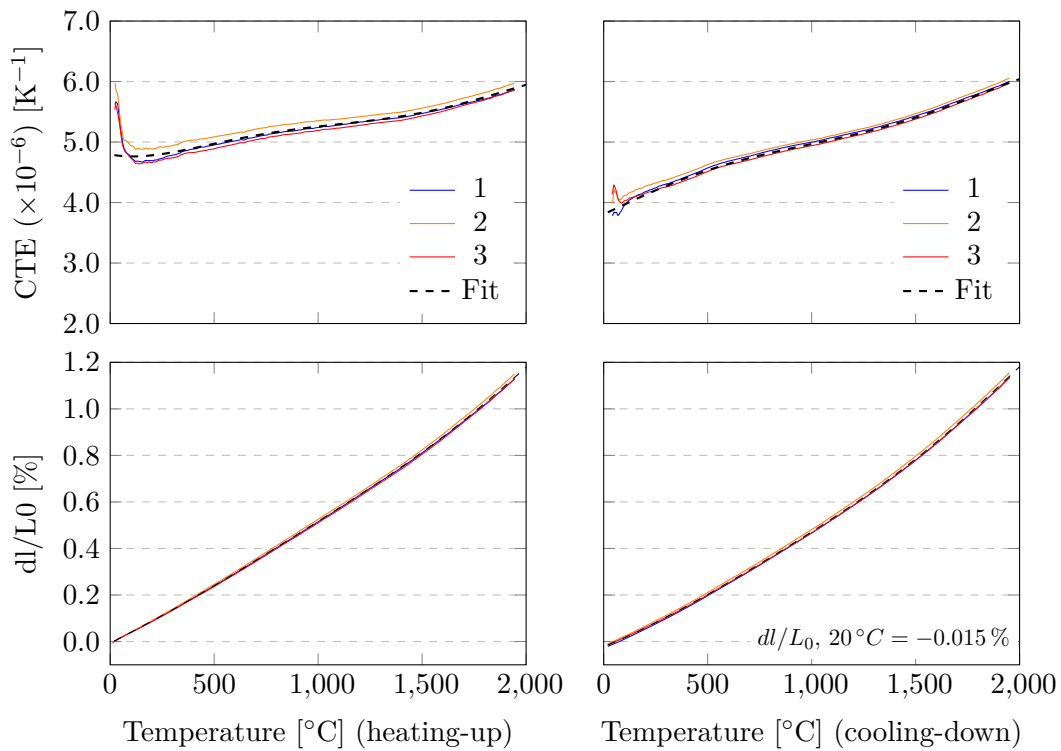


Figure 5.23: Thermal conductivity of isotropic graphite R4550.

Thermal expansion measurements are shown in Figure 5.24. The dl/L_0 curves are fitted with a 6th degree polynomials in order to calculate the average CTE and to smooth out experimental errors close to room temperature. The change in length after the cooling-down ramp (-0.015 %) indicates that the specimens shorten after the 20–1950–20 °C cycle, but the magnitude is negligible.

The behaviour is remarkably similar in the three tested specimens, with little differences between heating-up and cooling-down ramps. α values are tabulated in Table 5.10, being $4.5 \times 10^{-6} \text{ K}^{-1}$ (cooling-down ramp) in the range 20–500 °C.

Figure 5.24: CTE R4550 IP. All specimens with length ≈ 25 mm.

5.2.5 Mechanical properties

The bending test curves are shown in Figure 5.25. The average maximum strength is 61.2 ± 3.0 MPa and the average strain to rupture is $7150 \pm 410 \mu\text{m m}^{-1}$. The supplier specifies a flexural strength of 60 MPa; the results are thus compliant with the datasheet. The nominal size of the specimens is $5 \times 10 \times 25$ mm, the test jig span is $L=20$ mm and the loading span is $L/2$ (four point configuration).

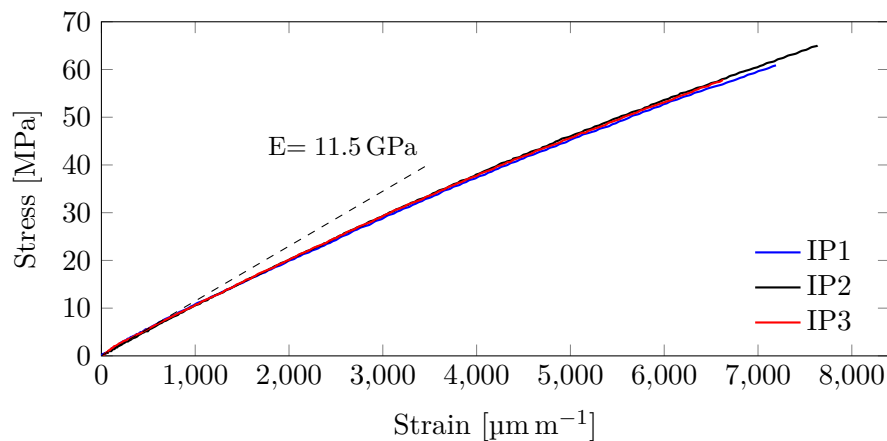


Figure 5.25: Bending test of graphite R4550.

Only the flexural frequency (f_f) of IP specimens was acquired with the IET method, the torsional frequency excitation was not successful, see Table 5.12. As the material is isotropic, the analytical calculation of the Young modulus is feasible, according to the standard ASTM C1259-01. The resulting average Young's modulus is 11.5 GPa, which

matches perfectly the slope in the elastic domain of the bending test plot (Figure 5.25), and the material specification.

Table 5.12: IET test of graphite R4550. Young modulus analytically calculated according to standard ASTM C1259-01.

Specimen	m [g]	L [mm]	b [mm]	t [mm]	ff [kHz]	E [GPa]
1	2.3	24.97	9.99	5.03	18.45	11.50
2	2.32	24.98	10.02	5.05	18.55	11.58
3	2.27	25.01	9.88	5.04	18.46	11.48
4	2.32	24.95	9.98	5.08	18.65	11.54
5	2.3	24.97	10.02	5.04	18.50	11.47
Average						11.51

The rest of elastic properties are estimated thanks to the similarities between this grade and POCO 9Q fine grained graphite grade characterised in reference [138]. With respect to R4550, POCO 9Q has the roughly the same porosity content (18.7%, considering $\rho_{gr.} = 2.25 \text{ g cm}^{-3}$) and very similar Young's modulus (11.35 GPa) [138]. Therefore, it is reasonable to assume that both grades have very similar elastic matrix. The reported Poisson's ratio for POCO 9Q is 0.251 [138]. Using $E=11.5 \text{ GPa}$ and $\nu=0.25$ in formula E.10 results in an estimated shear modulus of $G=4.6 \text{ GPa}$ for R4550 grade.

5.3 Molybdenum carbide - graphite MG-6541Fc

MoGr grade MG-6541Fc is introduced in section 1.3.3. The material processing parameters are detailed in section 4.6. The characterisation results are presented below.

5.3.1 Microstructure

Figure 5.26 shows SEM observations of polished MG-6541Fc TP surfaces. The as-polished surfaces show a connected graphite matrix (dark) with molybdenum carbide particles (bright) having an average size of $5 \mu\text{m}$. It is possible to appreciate how the carbides tend to elongate in the direction orthogonal to the force (pressing force was vertical on figure 5.26), filling the voids between graphite flakes. The observations show good compaction.

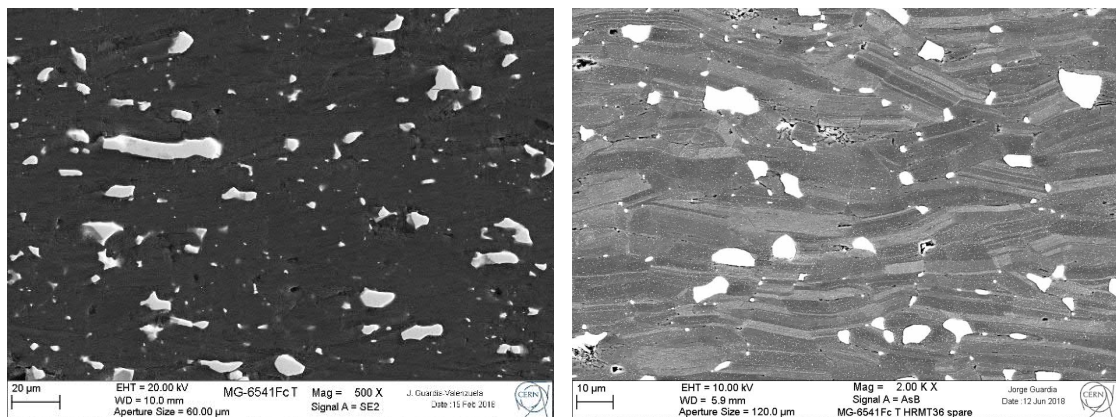


Figure 5.26: SEM observations of MG-6541Fc TP surface, pressing force was vertical. (Left) SE image. (Right) BE image, showing channeling effect. This allows identification of domains where the crystallographic orientation is approximately constant (grains).

Careful Scanning Electron Microscopy examination of the fracture surfaces of bending test specimens revealed no visible trace of CFs. The diameter of the CFs ($10\ \mu\text{m}$) is probably small enough to be dissolved and re-precipitated by the molten Mo-C phase. A similar effect was observed but in solid nickel at much lower temperature (1100°C) in [77], where the dissolution-precipitation mechanism managed to completely dissolve and recrystallize CFs. In early MoGr grades, which were processed below the eutectic temperature, the CFs were not dissolved and were clearly visible in the microstructural examinations as bundles of agglomerated CFs [29]. The dissolution of the carbon fibres is discussed in Chapter 6.3.

5.3.2 Crystallography and lattice expansion

Figure 5.27 shows the XRD analysis of MG-6541Fc, including IP and TP surfaces. The TP surface shows reduced intensity in the $00l$ peaks, such as (002). The carbide peaks correspond to the cubic (FCC) $\alpha\text{-MoC}_{1-x}$ phase, stabilised by the Ti addition.

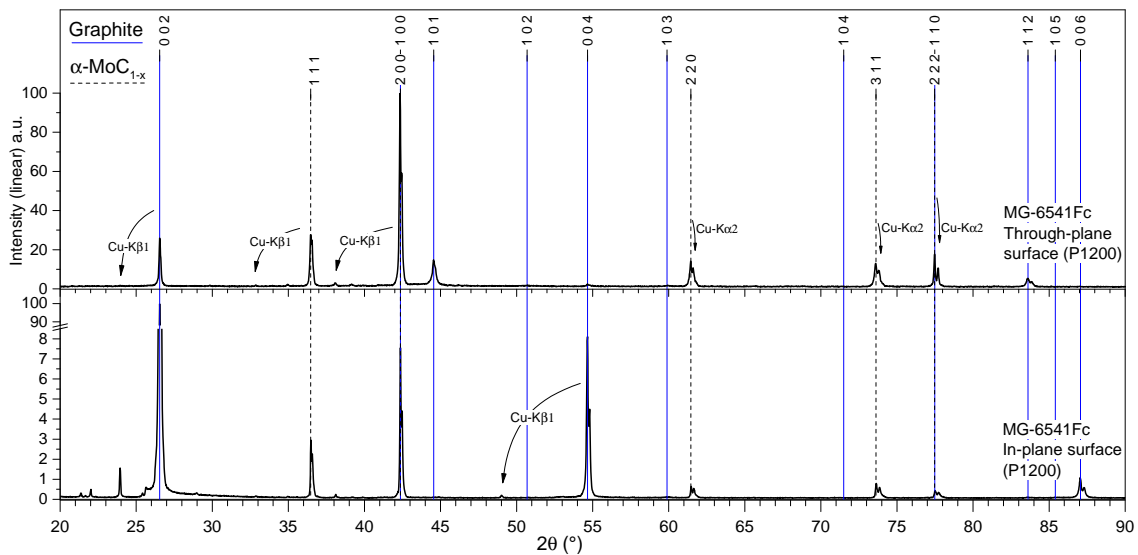


Figure 5.27: MG-6541Fc IP and TP XRD patterns.

Figure 5.28 shows the high temperature diffraction patterns on the MG-6541Fc TP sample. The TP surface was sanded with P1200 sandpaper. The test shows that new peaks appear above 500°C , which correspond to molybdenum oxides. The oxides are not characterised, as they would not form in collimators' normal operation (ultra-high vacuum). The intensity of the carbide peaks decreases as the oxides are formed. The intensity of the oxide peaks continue increasing also during cooling down, down to 500°C when the carbides stop oxidizing. The pattern shows an interesting effect: some overlapping graphite-carbide peaks separate in opposite directions as the temperature increases, due to the negative CTE of graphite a parameter, see Figure 5.29.

It is very important to note that the orientation of this sample implies that the $00l$ planes analysed, such as (002), are those oriented parallel to the surface (TP), and not in the IP direction, see Figure 4.32.

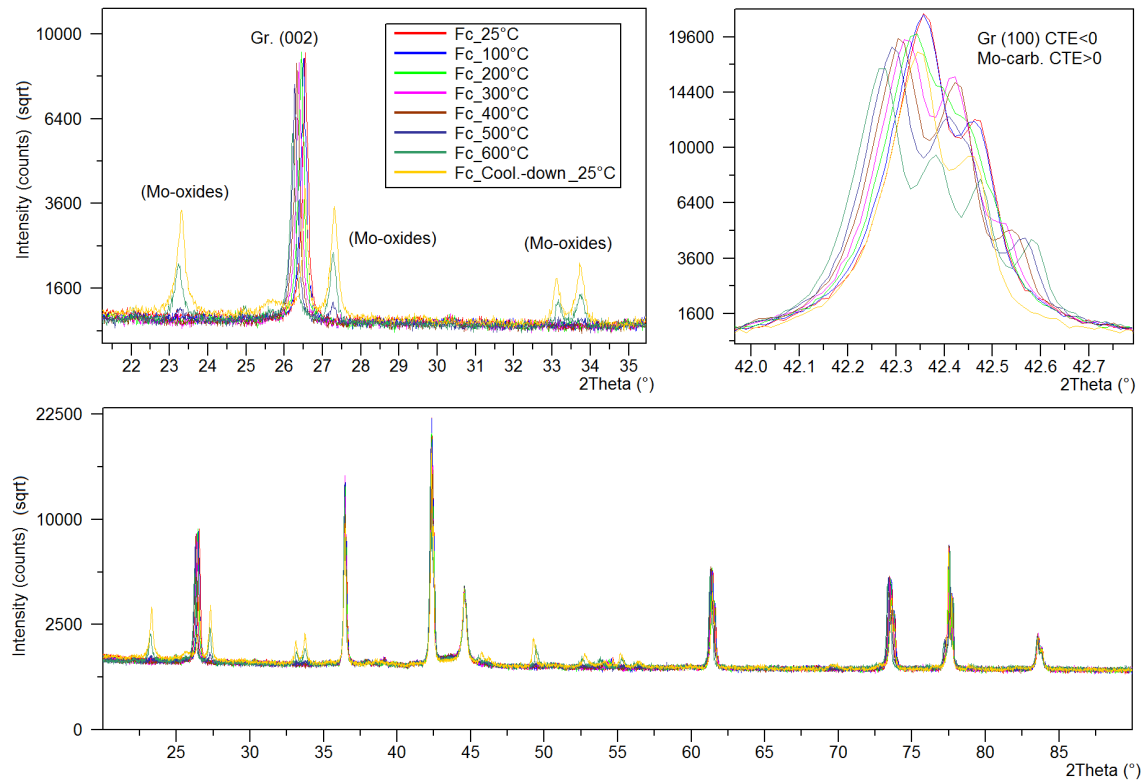


Figure 5.28: MG-6541Fc TP experimental XRD patterns. The patterns acquired during cooling down (500, 300, 100 °C are not showed).

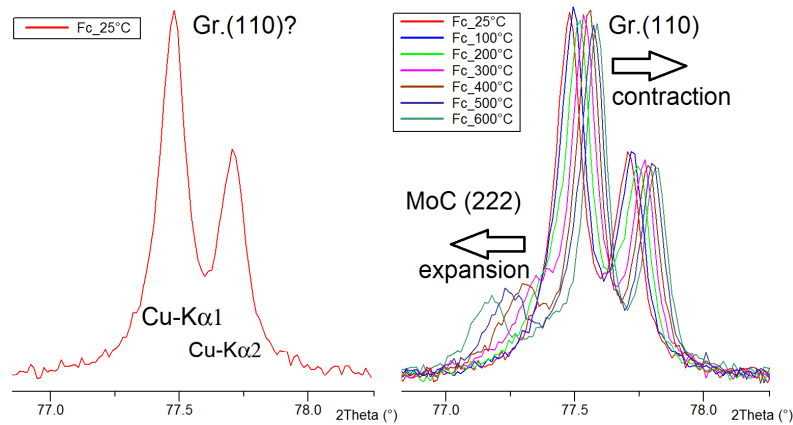


Figure 5.29: Graphite (110) and α - MoC_{1-x} (220) overlapped peaks shifting in opposite directions.

Tables G.1 and G.2 (Appendix G) list the corrected peak positions and the results of the lattice parameters of graphite and α - MoC_{1-x} FCC carbide. The specimen displacement correction s is calculated as explained in section 3.5.2. The matching between heating-up and cooling-down ramps is virtually perfect, which confirms that the phases are stable (except for the oxidation reaction) and that the process is fully reversible for these temperatures.

Second degree polynomials are fitted to the data, see Table 5.13. Figure 5.30 show the graphite experimental lattice parameters in MG-6541Fc, both the measurements and the fitting curve. The values from the literature are also reported for comparison, indicating

complete graphitisation. Figure 5.31 shows the same information but for the α -MoC_{1-x} phase.

Table 5.13: Fitting equation for the lattice parameters variation ($d = AT^2 + BT + C$, T in °C, d in Å) in MG-6541Fc. From the heating-up curves.

	A	B	C	Value at 20°C
a (Graphite)	$2.8333 \cdot 10^{-9}$	$-2.5328 \cdot 10^{-6}$	2.4618	2.461(7)
c (Graphite)	$1.9142 \cdot 10^{-8}$	$1.7959 \cdot 10^{-4}$	6.7071	6.711
a (α -MoC _{1-x})	$1.4885 \cdot 10^{-8}$	$2.2555 \cdot 10^{-5}$	4.2635	4.264

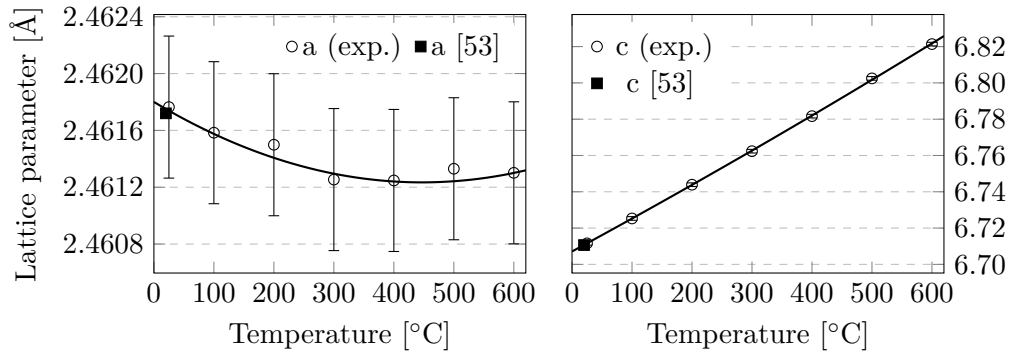


Figure 5.30: Lattice parameters versus temperature of graphite in MG-6541Fc.

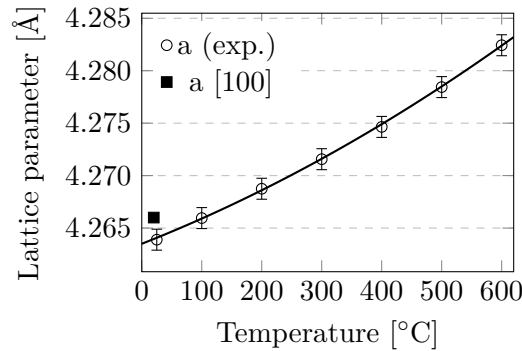
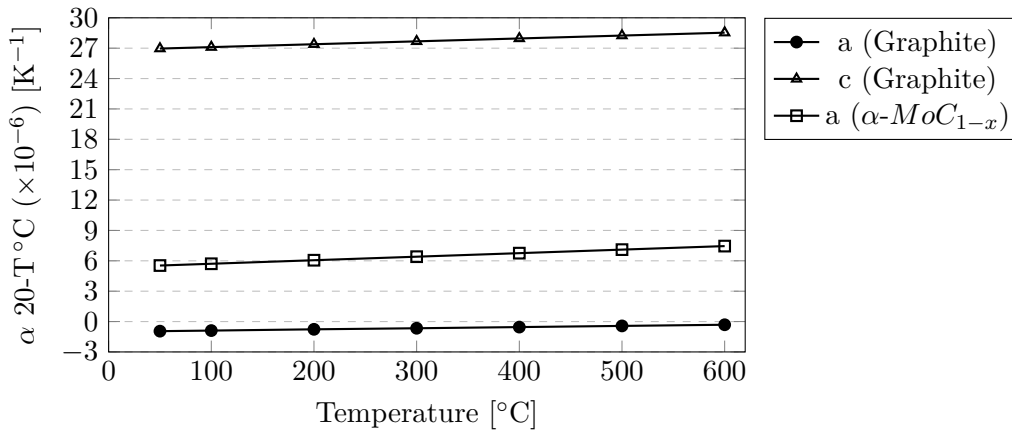


Figure 5.31: Lattice parameters versus temperature of α -MoC_{1-x} in MG-6541Fc.

The CTE is calculated from the fitting curves, the results are shown in Table 5.14 and Figure 5.32.

Table 5.14: Result of the secant CTE $20-T$ °C of graphite and $\alpha\text{-MoC}_{1-x}$ in MG-6541Fc TP ($\times 10^{-6} m^{-1} K^{-1}$). Heating-up ramp.

T [°C]	a (Gr.)	c (Gr.)	a (MoC)
50	-0.9	27.0	5.5
100	-0.9	27.1	5.7
200	-0.8	27.4	6.1
300	-0.7	27.7	6.4
400	-0.5	28.0	6.8
500	-0.4	28.2	7.1
600	-0.3	28.5	7.5

Figure 5.32: Secant CTE $20-T$ °C of graphite and $\alpha\text{-MoC}_{1-x}$ in MG-6541Fc (from XRD).

5.3.3 Electrical conductivity

Superficial electrical conductivity measurements on MG-6541Fc are shown in Table 5.15. The variation in measuring frequency does not significantly alter the result, but there is a clear tendency to slightly higher values with increasing frequency f (lower penetration depth).

The average result from the IP tests is 1.04 MS m^{-1} at the highest available frequency. No tests with the 4-wire DC method were performed in this grade, therefore the TP direction conductivity is not characterised.

The TP-surface measurements reported in Table 5.15 consist of a 3D average value of TP and IP directions, due to the measurement technique used. They are hence not practical for the characterisation. However, it may be possible to infer from them the actual TP conductivity; unfortunately the attempts to do it were unsuccessful.

Table 5.15: Superficial electrical conductivity measurements on 10 specimens with size 12.5×10 (TP) $\times 125$ mm. Six measurement points per specimen. (*) See text.

Surface	f [kHz]	1	2	3	4	5	6	7	8	9	10	Average	σ_{RMS}
IP	60	1.12	0.94	1.03	1.16	1.00	0.93	0.95	0.98	1.02	1.07	1.02	0.08
IP	960	1.11	0.97	1.07	1.21	1.04	0.95	0.98	0.97			1.04	0.09
TP*	60	0.50	0.50	0.49	0.45	0.42	0.43	0.44	0.43	0.43	0.46	0.45	0.03

5.3.4 Thermophysical properties

The density at RT measured with the Archimede's method is 2.515 g cm^{-3} .

The thermal diffusivity (IP and TP) and the specific heat of MG-6541Fc are shown in Figures 5.33, 5.34 and 5.35 respectively. The mathematical functions that fit the experimental data are shown in the plots. The conductivity is calculated from the diffusivity and specific heat fitting curves, assuming constant density (2.515 g cm^{-3}), see Figure 5.36.

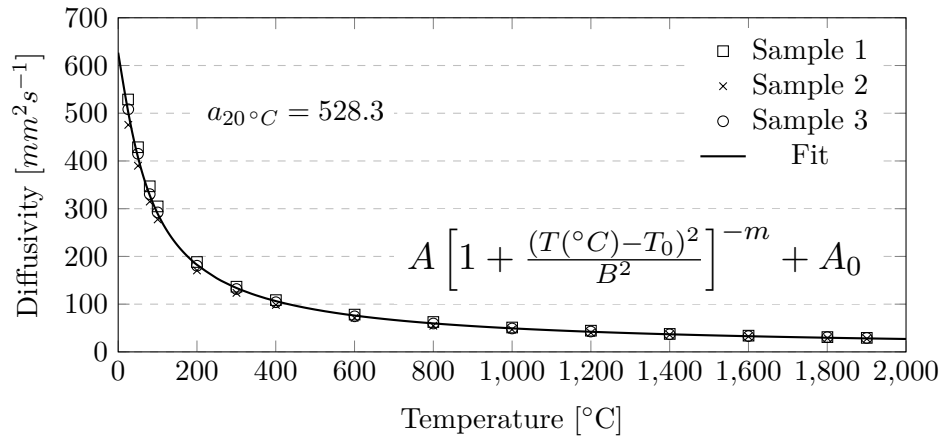


Figure 5.33: Thermal diffusivity of MG-6541Fc IP. Fitting equation constants: $A = 725.4$, $B = 55.69$, $T_0 = -34.86$, $m = 0.4819$ and $A_0 = 5.162$. All specimens with thickness $\approx 8 \text{ mm}$.

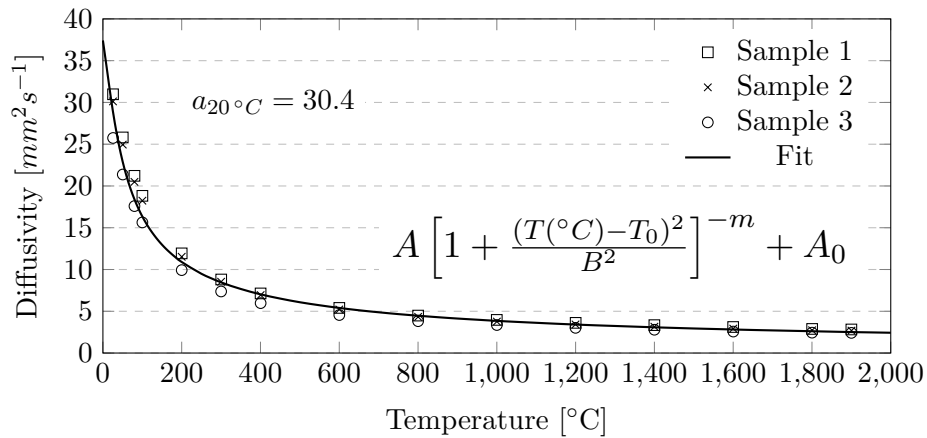


Figure 5.34: Thermal diffusivity of MG-6541Fc TP. Fitting equation constants: $A = 42.13$, $B = 62.65$, $T_0 = -43.71$, $m = 0.5325$ and $A_0 = 1.572$. All specimens with thickness $\approx 2 \text{ mm}$.

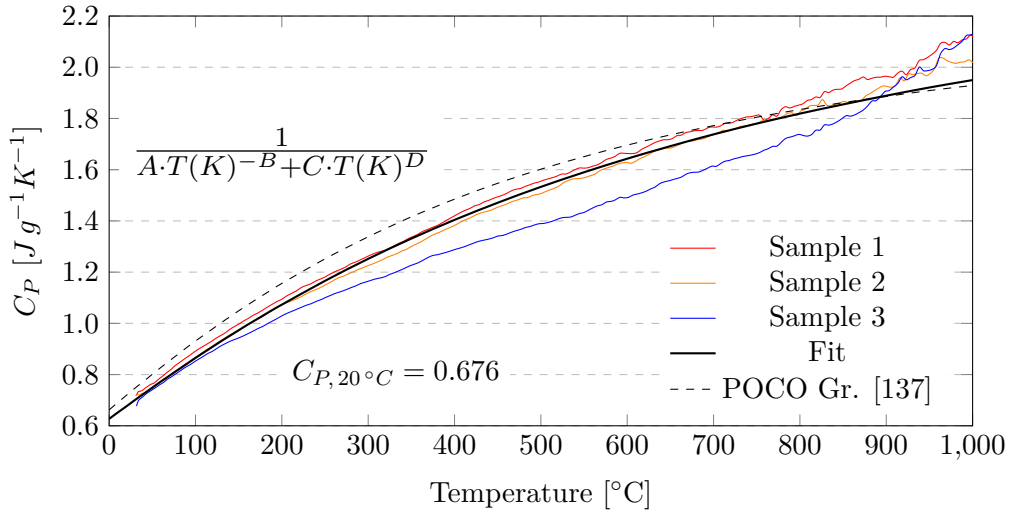


Figure 5.35: Specific heat of MG-6541Fc. Fitting equation constants: $A = 3.860$, $B = 1.437$, $C = 3.786\text{E-}4$ and $D = 3.779\text{E-}4$.

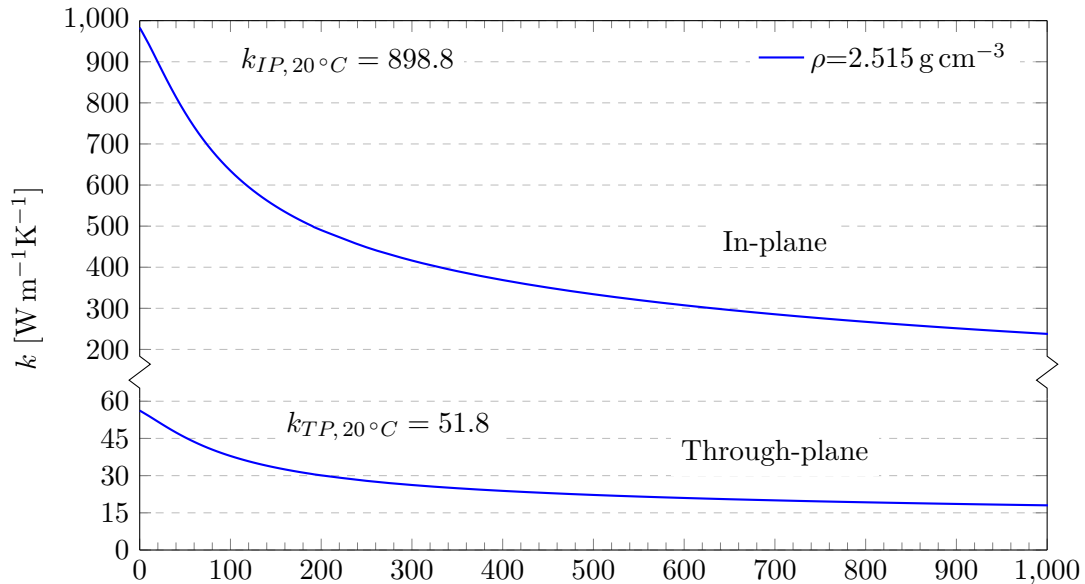


Figure 5.36: Thermal conductivity of MG-6541Fc in both directions. Calculated from constant density.

Thermal expansion measurements (IP and TP) are shown in Figures 5.37 and 5.38. None of the measurements shows abrupt changes in the thermal expansion behaviour, which could indicate phase transitions. Therefore the $\alpha\text{-MoC}_{1-x}$ carbide phase (stabilized by Ti) seems to be stable in the range of temperature investigated (20–1950 °C). This would be confirmed by XRD measurements heating up to those temperatures.

The dl/L_0 curves are fitted with a 8th degree polynomials, one for each orientation, in order to calculate the average CTE and to smooth out experimental errors close to room temperature. The differences between heating-up and cooling-down ramps could be due to accommodation of the specimen in the sample holder. The change in length of the TP specimens (0.173 %) is much larger than of the IP specimens (0.007 %, negligible), indicating relevant relaxation of internal stresses after the 20–1950–20 °C cycle. Positive residual strain parameters indicate that the specimens lengthen after the test. The comparison of

micrometre measurements before and after the test confirms this behaviour (in the IP, the change is in the order of $1\ \mu\text{m}$, therefore undetectable).

The IP cooling-down ramp shows a more constant CTE, with a value of $2.0 \times 10^{-6}\ \text{K}^{-1}$ in the range $20\text{--}1000\ ^\circ\text{C}$. On the other hand, the cooling-down TP value is $13.8 \times 10^{-6}\ \text{K}^{-1}$ in the same range of temperatures.

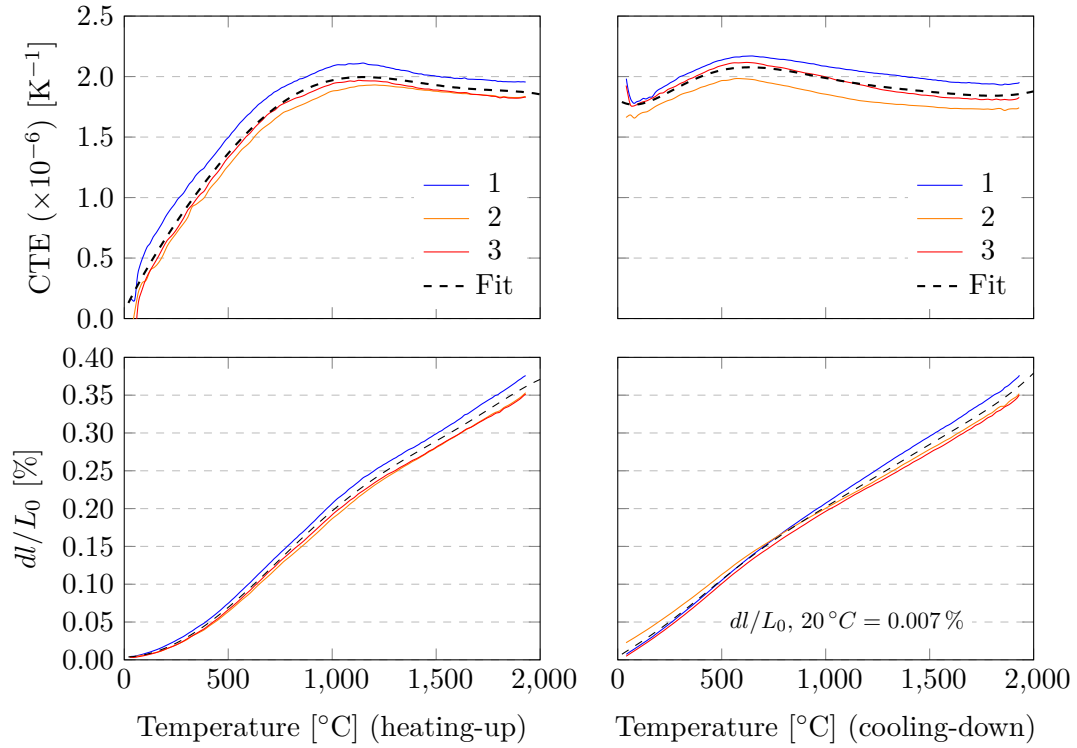
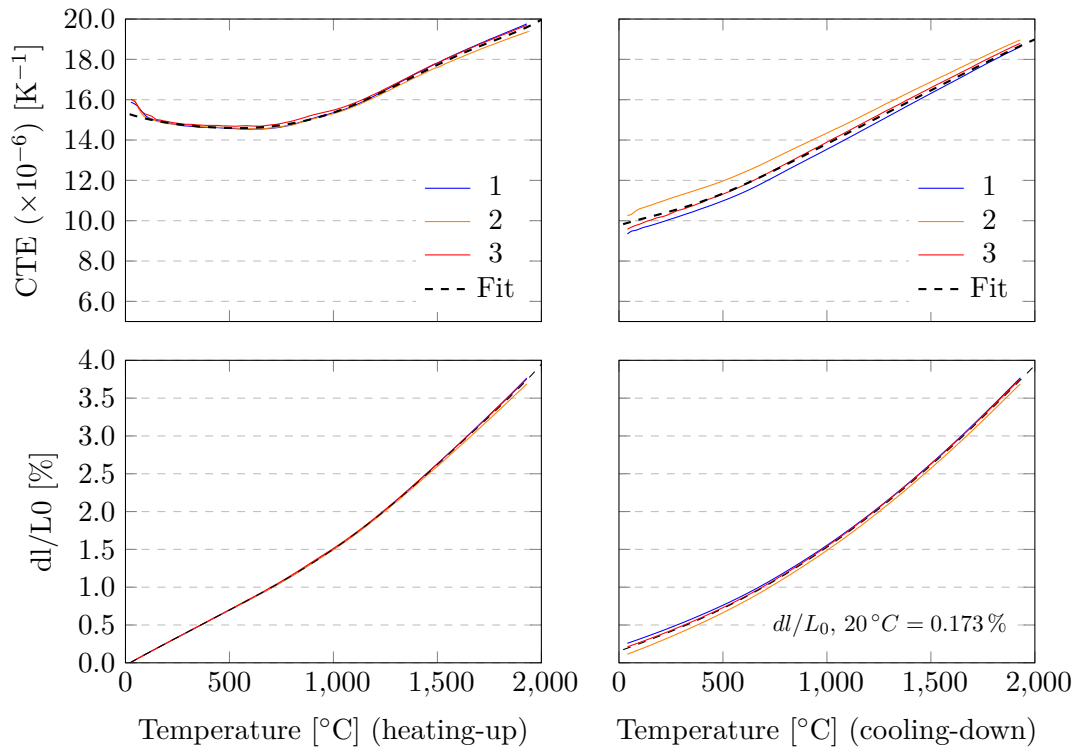


Figure 5.37: CTE MG-6541Fc IP. All specimens with length $\approx 10\ \text{mm}$.

Figure 5.38: CTE MG-6541Fc TP. All specimens with length ≈ 10 mm.

5.3.5 Mechanical properties

The bending test curves are shown in Figure 5.39. In the IP direction, the average maximum strength is 81.4 ± 4.2 MPa and the average strain to rupture is $1760 \pm 70 \mu\text{m m}^{-1}$. In the TP direction, the average maximum strength is 10.6 ± 1.0 MPa and the average strain to rupture is $4920 \pm 1080 \mu\text{m m}^{-1}$.

The nominal size of the specimens, the test jig span (L) and the loading span are listed below. All the test were made with four point configuration.

- IP1-IP4: $5 \times 10 \times 55$ mm, $L=50$ mm, loading span= $L/2$.
- TP1-TP5: $5 \times 10 \times 25$ mm, $L=20$ mm, loading span= $L/2$.

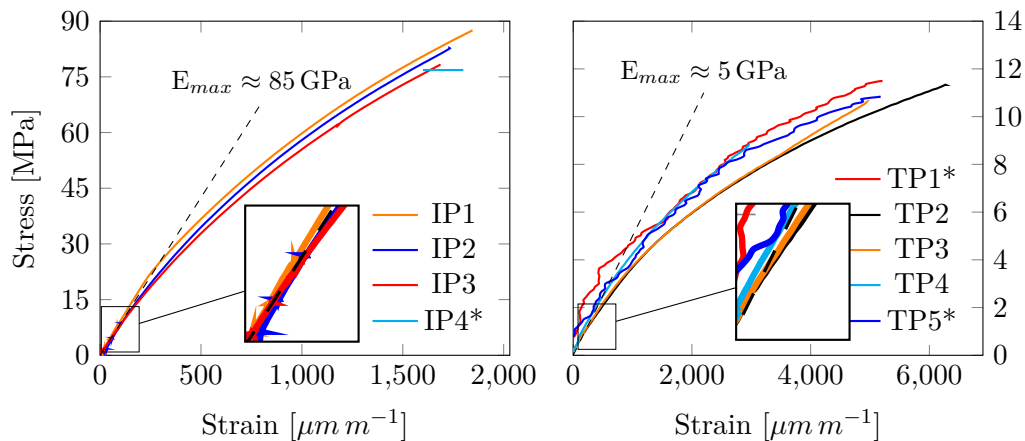


Figure 5.39: Flexural test MG-6541Fc. (*) Specimens IP4, TP1 and TP5 tested without strain gauge, specimens TP1 and TP5 tested with laser extensometer.

Impact Excitation Technique (IET) results are shown in Table 5.16. The flexural and torsional resonance frequencies were acquired. The results from the Finite Element Modeling (FEM) analysis are reported in Table 5.17. It is shown that the results from the analytical formula are deviated with respect to the FEM optimisation, and show in fact non-physical derived Poisson's ratio. The FEM method is more accurate, in accordance with the elastic properties theory.

The Poisson's ratios do not have relevant influence in the resonance frequencies, (see section E.5), hence they cannot be characterised with this method. For this reason, ν_{XY} and ν_{XZ} were set to 0.1 (not optimised), which is a reasonable value considering the composition of the material (see section E.6). ν_{YZ} is derived from E_Y and G_{YZ} , see equation E.8.

Table 5.16: IET test of MG-6541Fc, experimental resonance frequencies of IP and TP specimens. Frequencies resulted from the FEM optimisation. (ff: flexural, ft: torsional).

Specimen	m [g]	L [mm]	b [mm]	t [mm]	ff [kHz]	ft [kHz]
IP 1	6.57	54.94	10.04	4.70	8.500	-
IP 2	6.53	54.60	10.23	4.69	8.890	16.620
IP 3	6.71	54.75	10.25	4.80	8.770	16.300
IP 4	6.55	55.13	10.07	4.71	8.380	16.560
Average TP:		54.86	10.15	4.73	8.635	16.493
FEM optimisation:		(")	(")	(")	8.497	15.814
TP 1	3.181	25.03	10.06	5.08	10.184	18.764
TP 2	3.188	25.04	10.06	5.06	10.080	18.734
TP 3	3.183	25.04	10.06	5.03	10.272	18.952
TP 4	3.195	25.05	10.05	5.06	10.256	18.997
TP 5	3.143	25.04	10.07	5.00	9.977	18.522
Average TP:		25.04	10.06	5.05	10.154	18.794
FEM optimisation:		(")	(")	(")	10.263	18.916

Table 5.17: Elastic properties of MG-6541Fc resulted from the IET analysis.

	E_X	E_Y	E_Z	G_{XY}	G_{YZ}	G_{XZ}	ν_{YZ}	ν_{XY}	ν_{XZ}
FEM optimisation	4.7	84.1	84.1	4.1	37.4	4.1	0.123	0.1	0.1
Analytical ¹	4.8	75.2	75.2	4.0	16.2	4.0	1.32 ²	-	-

¹ From analytical formula (ASTM C1259-01), for comparison purposes.

² Non-physical, derived from E_Y and G_{YZ} , see equation E.8.

5.4 Chromium carbide - graphite CG-1100Ba

CG-1100Ba material belongs to the Chromium carbide - graphite family, a variation of the MoGr family (introduced in Section 1.3.3). It features the advantages described in Chapter 2; the main difference with respect to MoGr is the replacement of molybdenum by chromium. The material processing parameters are detailed in Section 4.6. The specimens used for characterisation are shown in Figure 5.40.

The characterisation results are presented below.

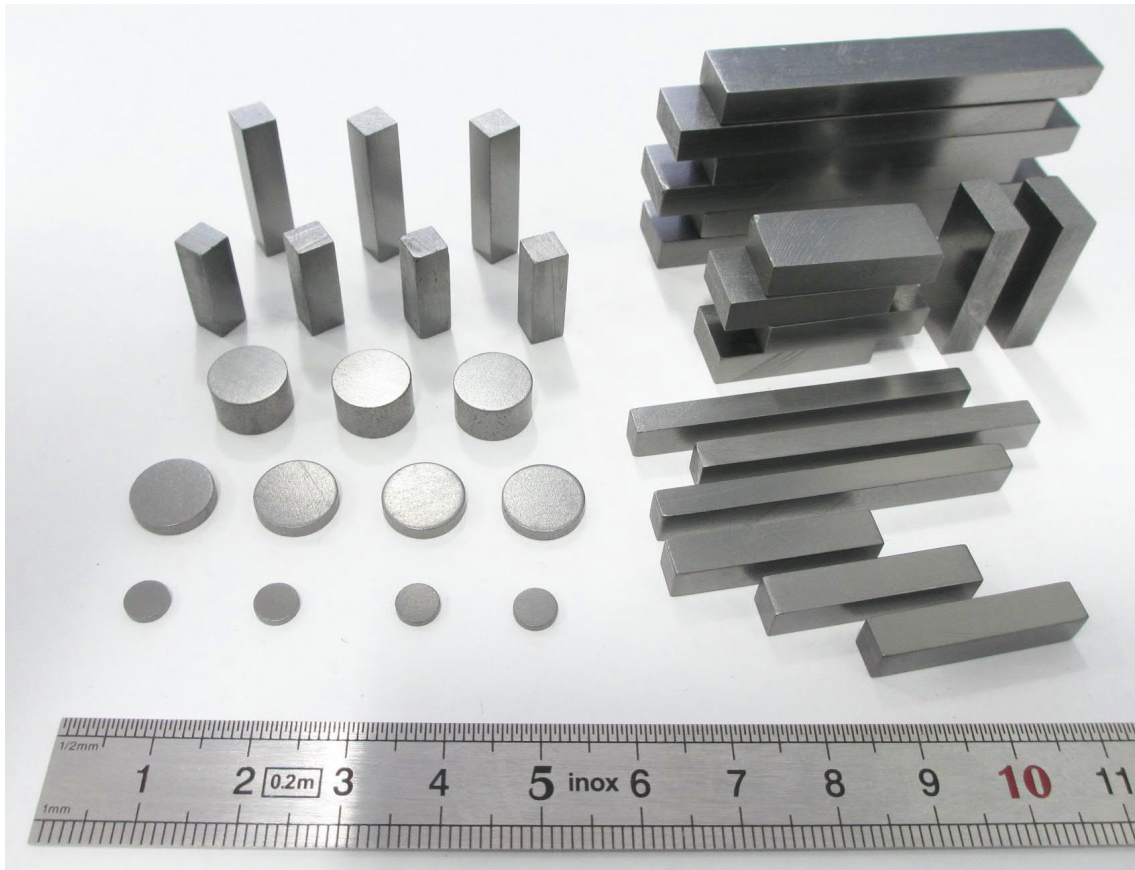


Figure 5.40: CG-1100Ba specimens for characterisation machined by Brevetti Bizz.

5.4.1 Microstructure

Figure 5.41 shows SEM observations of polished CG-1100Ba TP surfaces. The as-polished surfaces show a connected graphite matrix (dark) with chromium carbide particles (bright) having an average size of $10\ \mu\text{m}$, a small fraction of the particles have sizes smaller than $5\ \mu\text{m}$. It is possible to appreciate how some carbides tend to elongate in the direction orthogonal to the force (pressing force was vertical on figure 5.41), filling the voids between graphite flakes.

The contrast visible in the graphite matrix allows to identify the alignment of the graphite basal planes. The texture shows that it is not perfectly perpendicular to the pressing force (vertical), which helps in reducing anisotropy.

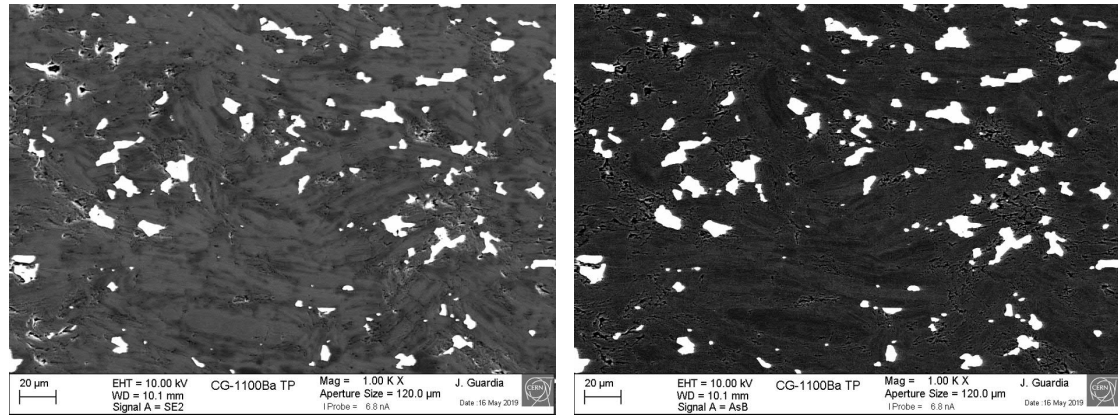


Figure 5.41: SEM observations of CG-1100Ba TP surface, pressing force was vertical. (Left) SE image. (Right) BE image. The SE image shows channeling effect in graphite, allowing identification of crystalline domains.

5.4.2 Crystallography and lattice expansion

Figure 5.42 shows the XRD analysis of CG-1100Ba, including IP and TP surfaces. The TP surface shows reduced intensity in the $00l$ peaks, such as (002).

The carbide phase is identified as a modification of Cr_3C_2 orthorhombic phase [139, 140]. This modified structure was found to exist with two chemical variations: one where some chromium is substituted by vanadium, Cr_2VC_2 , and another one where some carbon is replaced by nitrogen, $\text{Cr}_3(\text{C,N})_2$ [140]. Both of them exhibit the same orthorhombic structure and similar lattice parameters. The phase with V has slightly larger parameters than those of $\text{Cr}_3(\text{C,N})_2$ [140].

Vanadium is not used during the material's production and would be easily detectable with EDS analysis. EDS analyses on the final material have not shown detectable impurity content, including both V and N. However, due to the high detection limit of this technique, other analytical methods should be used to confirm the presence of trace amounts of these elements. Air contains 78 vol.% nitrogen, and could be put in contact with the carbide during the high-pressure compaction of the powders and subsequent sintering at Cr-C liquid phase temperature (2000 °C). For this reason, the stabilizing agent is likely to be nitrogen. The atomic ratio Cr-C measured by EDS in the carbide particles of CG-1100B0 is 58.3-41.7, a bit richer in C than Cr_3C_2 (60-40). This small difference could be due to the surrounding graphite matrix being partially detected as well.

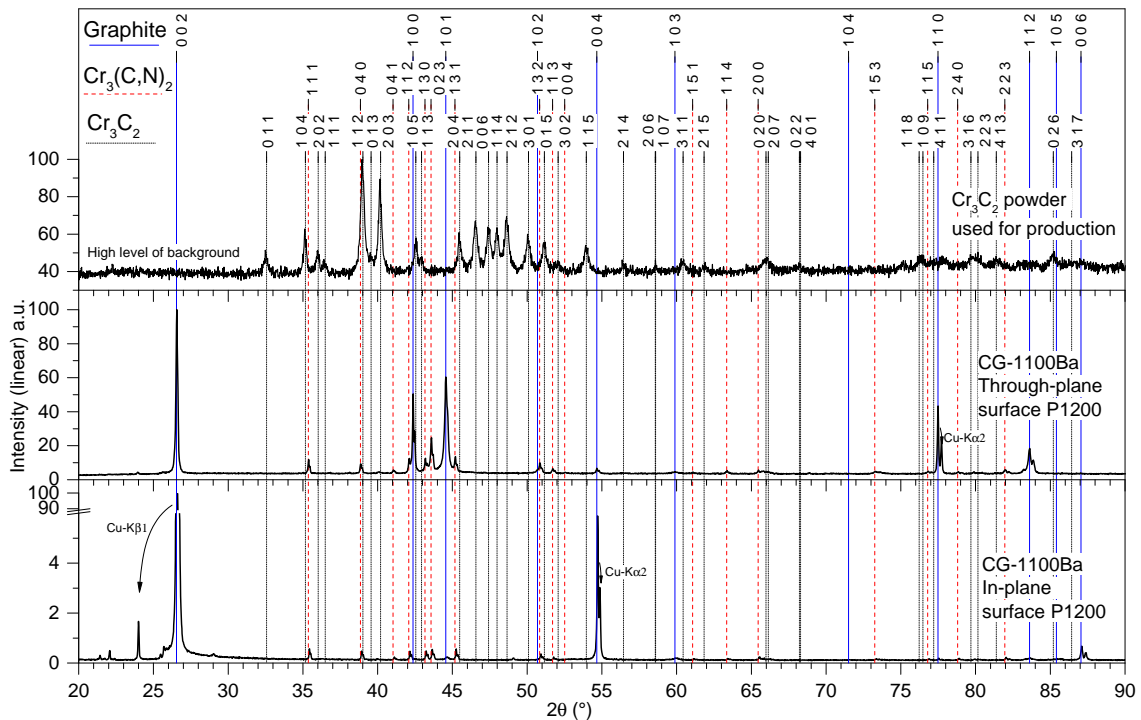


Figure 5.42: CG-1100Ba IP and TP XRD patterns.

Some molten material coming out from the plate was also analysed with XRD, and surprisingly the chromium carbide phase was different than inside the material, see Figure 5.43. Two pieces of material were analysed, one coming from the first sintering cycle (CG-1100A0) and another from the second subsequent cycle to the same plate (CG-1100B0). Both of them showed the same carbide phase than in the original carbide powder, orthorhombic Cr_3C_2 (plus high quality graphite, precipitated from the Cr-C liquid phase). CG-1100A0 molten material shows larger relative graphite content with respect to CG-1100B0, seen in the relative intensity of the carbide peaks. More details of these molten material are shown in section 6.6.

This could be explained by the release of nitrogen when the molten spill is depressurised outside of the mould. The molten phase do not necessary cool down immediately when leaking from the mould, as the latter is expected to be at similar temperatures than the inner sintered plate. Therefore, there is likely time for diffusion processes to take place.

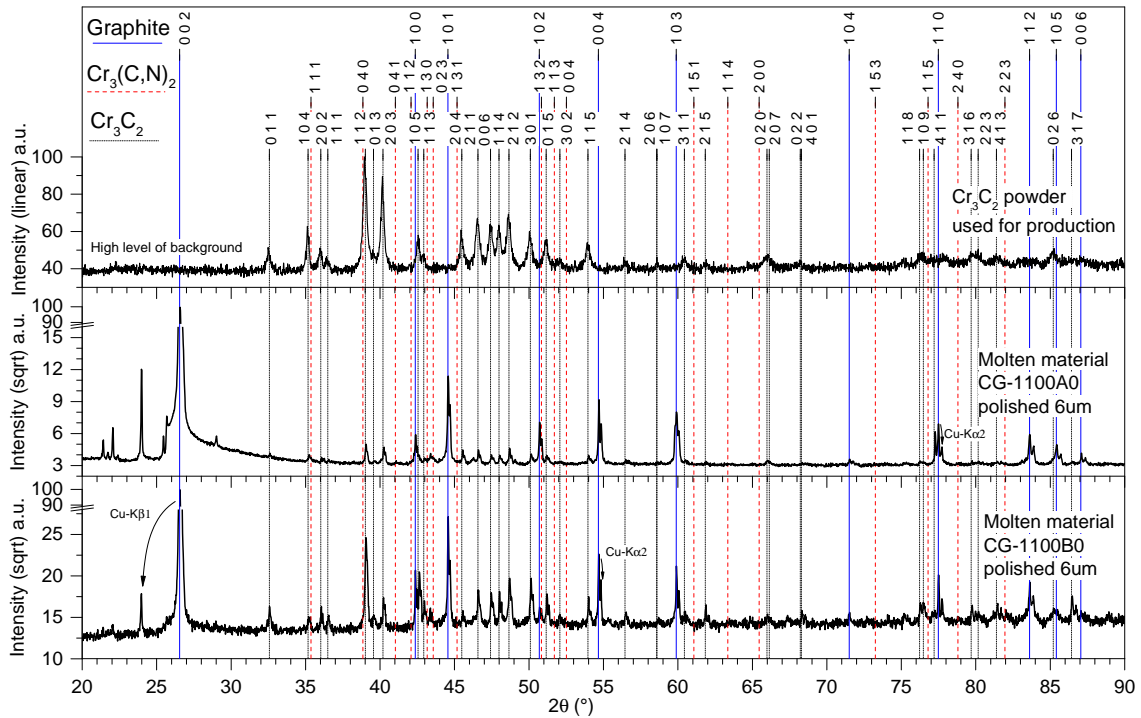


Figure 5.43: Cr-C molten phase XRD patterns, compared with Cr_3C_2 powder.

Figure 5.44 shows the high temperature patterns on the CG-1100Ba TP sample. The TP surface was sanded with P1200 sandpaper. The test shows that no new peaks due to oxidation, even at the highest investigated temperature (600 °C). This is interesting, considering that the atmosphere is air. The intensity of the (002) peak decreases after the stay at high temperature. On the other hand, the intensity of the (110) peak slightly increases. This is most likely caused by the removal of superficial bent flakes on the TP surface, by combustion in air. This removal exposes more the inner TP surface, and the $hk0$ planes produce stronger reflections. Indeed, the graphite (110) peak does not change in intensity upon cooling down. The shifting differences of the peaks are related to the different thermal expansion behaviour.

As explained above, the carbide phase is identified as $\text{Cr}_3(\text{C,N})_2$, a modification of Cr_3C_2 structure.

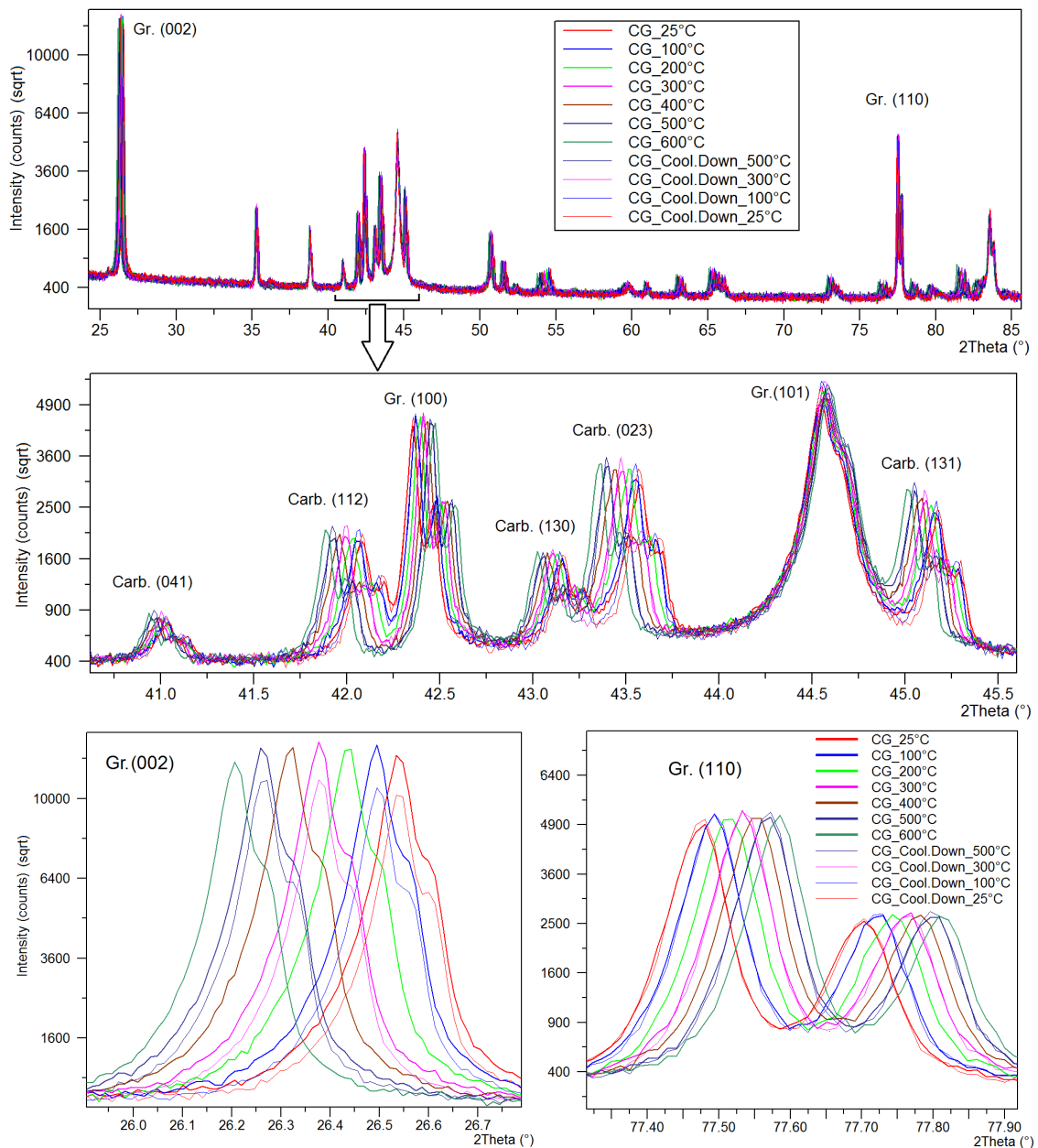


Figure 5.44: CG-1100Ba TP experimental XRD patterns.

Tables G.3 and G.4 (Appendix G) list the corrected peak positions and the results of the lattice parameters of graphite and $\text{Cr}_3(\text{C,N})_2$ orthorhombic carbide. The specimen displacement correction s is calculated as explained in section 3.5.2. The matching between heating-up and cooling-down ramps is virtually perfect, confirming that the process is fully reversible for these temperatures.

Second degree polynomials are fitted to the data, see Table 5.18. Figures 5.45 and 5.46 show the experimental lattice parameters of graphite and $\text{Cr}_3(\text{C,N})_2$ in CG-1100Ba, both the measurements and the fitting curve. The graphite parameters from the literature are also reported for comparison, indicating complete graphitisation.

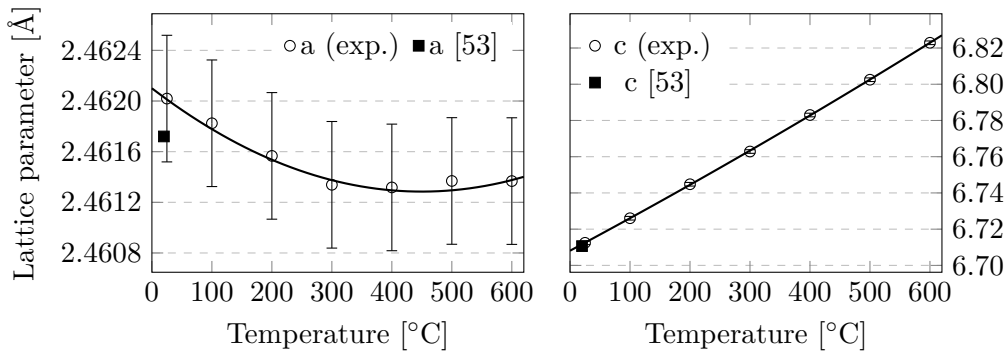
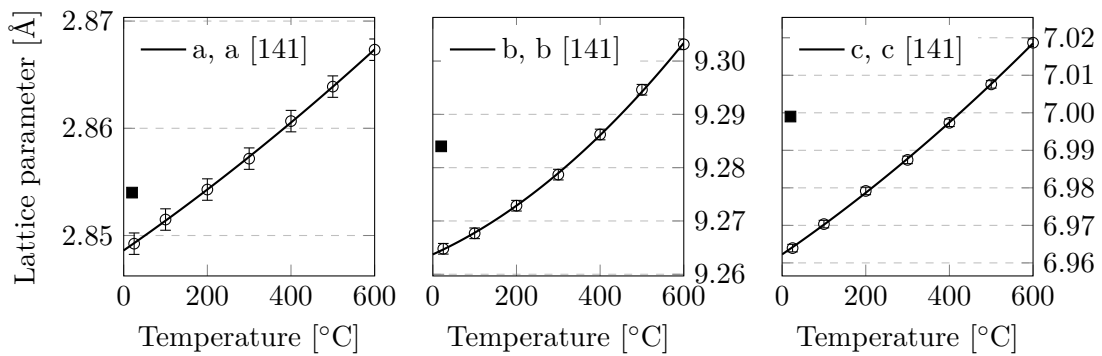


Figure 5.45: Lattice parameters versus temperature of graphite in CG-1100Ba.

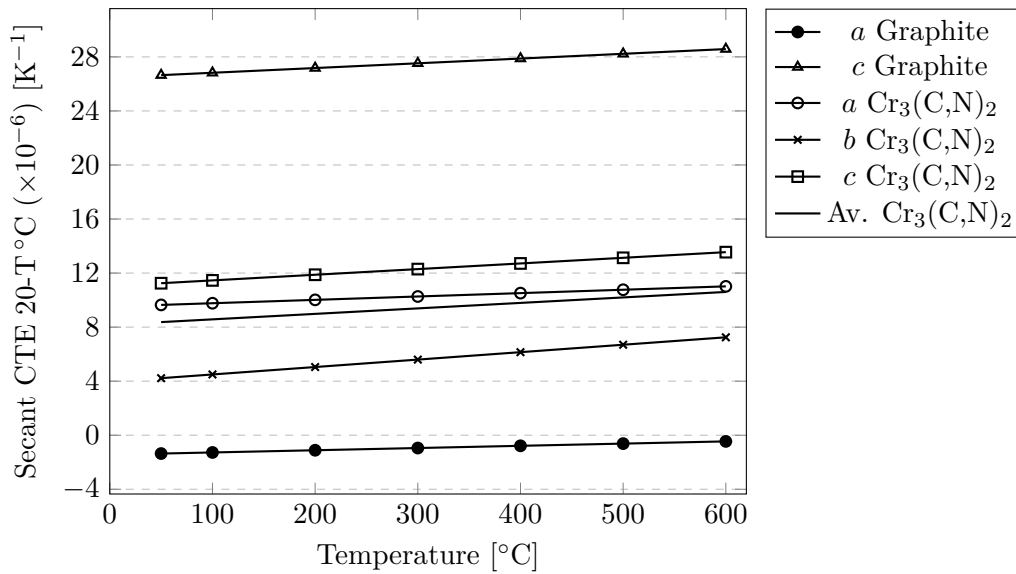
Figure 5.46: Lattice parameters versus temperature of $\text{Cr}_3(\text{C,N})_2$ in CG-1100Ba. Isostructural phase Cr_2VC_2 parameters are reported for comparison [141].Table 5.18: Fitting equation for the lattice parameters variation ($d = AT^2 + BT + C$, T in $^\circ\text{C}$, d in \AA) in CG-1100Ba. From the heating-up curves.

	A	B	C	Value at 20 $^\circ\text{C}$ [\AA]
a Gr	$4.0313 \cdot 10^{-9}$	$-3.6267 \cdot 10^{-6}$	2.4621	2.462(0)
c Gr	$2.3545 \cdot 10^{-8}$	$1.7721 \cdot 10^{-4}$	6.7081	6.712
a $\text{Cr}_3(\text{C,N})_2$	$7.1101 \cdot 10^{-9}$	$2.6977 \cdot 10^{-5}$	2.8486	2.849
b $\text{Cr}_3(\text{C,N})_2$	$5.0948 \cdot 10^{-8}$	$3.5542 \cdot 10^{-5}$	9.2637	9.264
c $\text{Cr}_3(\text{C,N})_2$	$2.9104 \cdot 10^{-8}$	$7.6300 \cdot 10^{-5}$	6.9623	6.964

The CTE is calculated from the fitting curves, the results are shown in Table 5.19 and Figure 5.47.

Table 5.19: Result of the secant CTE 20-T °C of graphite and Cr₃(C,N)₂ in CG-1100Ba ($\times 10^{-6} m^{-1} K^{-1}$). Heating-up ramp.

T [°C]	Graphite		Cr ₃ (C,N) ₂			
	<i>a</i>	<i>c</i>	<i>a</i>	<i>b</i>	<i>c</i>	Av.
50	-1.4	26.6	9.6	4.2	11.2	8.4
100	-1.3	26.8	9.8	4.5	11.5	8.6
200	-1.1	27.2	10.0	5.0	11.9	9.0
300	-0.9	27.5	10.3	5.6	12.3	9.4
400	-0.8	27.9	10.5	6.1	12.7	9.8
500	-0.6	28.2	10.8	6.7	13.1	10.2
600	-0.5	28.6	11.0	7.2	13.5	10.6

Figure 5.47: Secant CTE 20-T °C of graphite and Cr₃(C,N)₂ in CG-1100Ba (from XRD).

5.4.3 Electrical properties

Electrical conductivity measurements were performed with two methods: 4-wire DC and superficial eddy-current techniques (sigmatest), see section 3.4. The results are presented in figure 5.48, which depicts the average values and their σ_{RMS} , represented by the error bars. Unfortunately, the initial position inside the sintered plate could not be tracked to understand these variations.

The superficial measurements were performed with the 4 different frequencies that can be set in the measuring device, at the same locations to track their individual variation, both before and after a polishing process with fine sandpaper (P1200). The reasoning behind the test after polishing is that it can remove the superficial damage caused by machining, expected to be $\sim 10 \mu m$, see section 6.1.3. The results are taken from 34 different measured points on the two faces of 6 specimens for bending test, therefore with good statistical coverage.

The best individual surface shows $1.01 \pm 0.07 MS m^{-1}$ at 960 kHz ($0.88 \pm 0.03 MS m^{-1}$ at 60 kHz). It has been observed that the two in-plane surfaces of the sintered plates show slightly higher conductivity values with respect to the inner volume. This could be the

reason of the variation between different specimens.

The DC 4-wire value ($0.74 \pm 0.07 \text{MS m}^{-1}$) is the average value of 6 specimens, the best specimen shows $0.83 \pm 0.02 \text{MS m}^{-1}$.

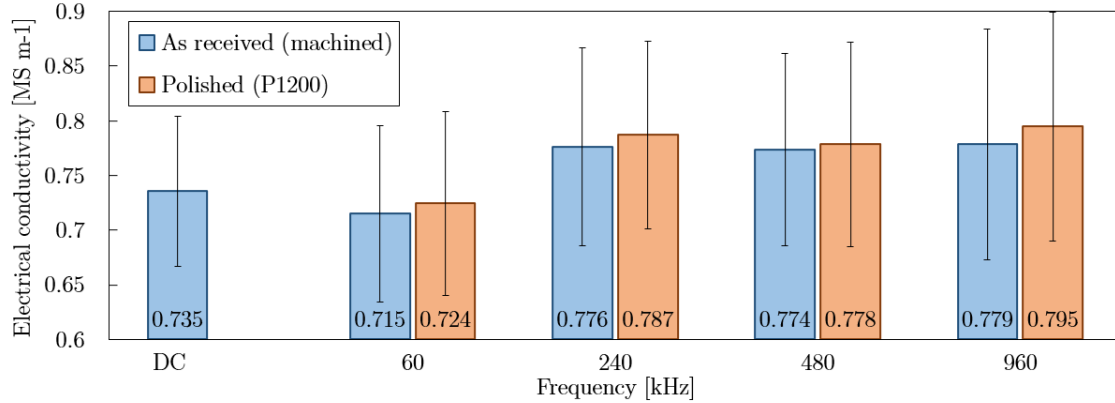


Figure 5.48: Electrical conductivity measurements on CG-1100Ba IP direction. DC 4-wire bulk and eddy-current superficial tests.

The variation in the frequency produces similar differences in all the measured points. Figure 5.49 shows the average variation with respect to the average DC value. Table 5.20 shows the variations with respect to the 60 kHz measurement. The variations show similar numbers for the as-received and polished surfaces.

The results show a big increase when moving from 60 to 240 kHz, and then they show almost no change at 480 and 960 kHz. This do not have proportionality to the skin depth, which would justify a physical reason. The manual of the device recommends that the materials are 3 times thicker than the skin depth to avoid errors in the measurement. At 60 kHz, the recommended specimen thickness is more than 6 mm (see Table 5.22), while the actual thickness was only 5 mm. It is therefore reasonable to assume that the error at 60 kHz is due to the specimen thickness, and the differences between 240-960 kHz are within the device experimental error.

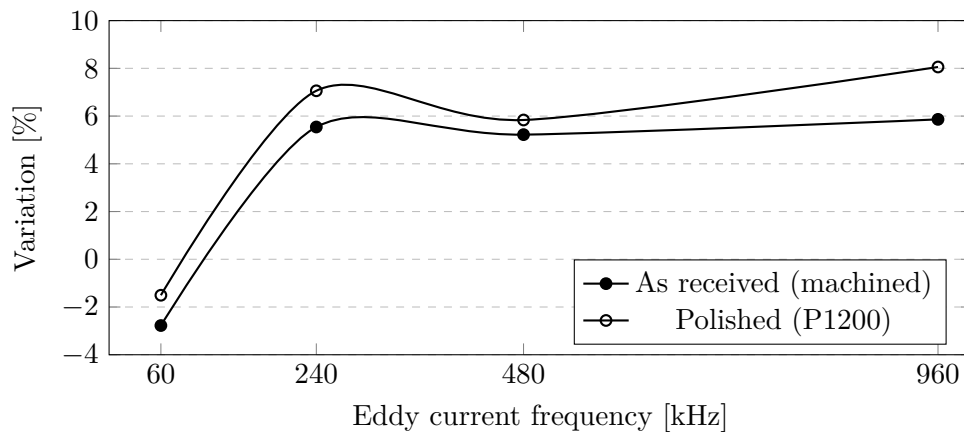


Figure 5.49: Superficial electrical conductivity on CG-1100Ba (IP), measured with different frequencies. Variation with respect to the 4-wire DC bulk value.

The average variation on the surface after polishing is always positive, see Table 5.21, around +0.5% overall. However, the standard deviation is very large, in the order of 3.8%

Table 5.20: Average superficial γ_e variation at each individual point with respect to 60 kHz test [%].

	240	480	960 [kHz]
As-received	8.7±6.5	8.4±5.0	8.8±5.8
Polished	8.9±4.0	7.5±4.8	9.6±6.2
Both	8.8±5.4	8.0±4.9	9.2±6.0

overall, which eliminates the validity of this 0.5 % increase.

Table 5.21: Average superficial γ_e variation at each individual point after polishing [%].

60	240	480	960 [kHz]
0.2±2.4	0.8±5.4	0.1±3.2	1.1±3.5

The penetration depth at all frequencies, see Table 5.22 is much larger than the damage expected by the machining ($\sim 10 \mu\text{m}$, see Section 6.1.3). This implies that even if the polishing process removes the superficial damage, it would have a negligible effect on the result.

Table 5.22: Skin depth [mm] of materials having 0.74 and 0.8 MS m^{-1} , at frequencies between 60 and 960 kHz (equation 3.15).

	60	240	480	960 [kHz]
0.74 MS m^{-1}	2.39	1.19	0.84	0.60 [mm]
0.8 MS m^{-1}	2.30	1.15	0.81	0.57 [mm]

5.4.4 Thermophysical properties

The average density at RT measured on the IET specimens (weight and dimensions) is 2.15 g cm^{-3} .

The thermal diffusivity (IP and TP) and the specific heat of CG-1100Ba are shown in Figures 5.50, 5.51 and 5.52 respectively. The mathematical functions that fit the experimental data are shown in the plots. The conductivity is calculated from the diffusivity and specific heat fitting curves, assuming constant density (2.15 g cm^{-3}), see Figure 5.53.

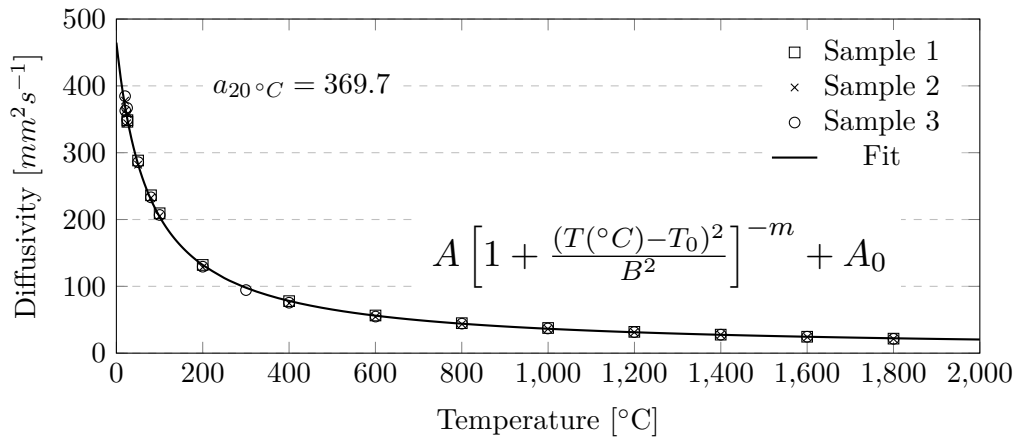


Figure 5.50: Thermal diffusivity of MG-1100Ba IP. Fitting equation constants: $A = 3502$, $B = 9.628$, $T_0 = -74.75$, $m = 0.4922$ and $A_0 = 2.751$. All specimens with thickness ≈ 6 mm.

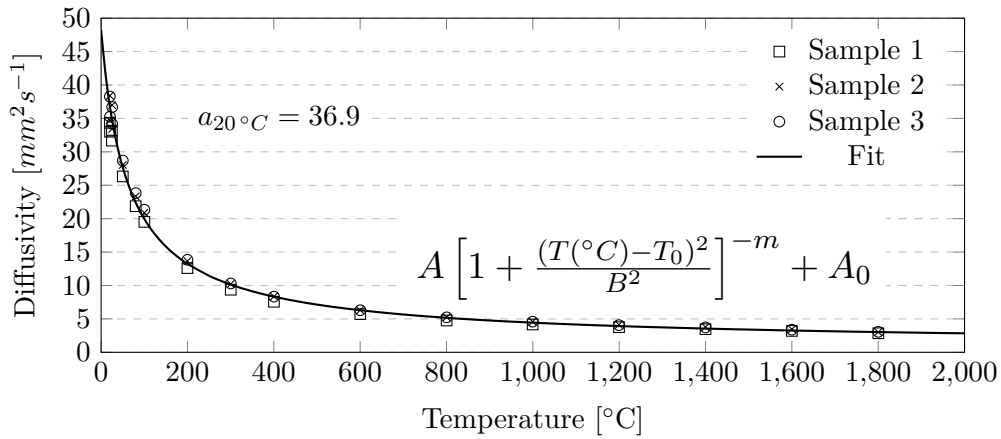


Figure 5.51: Thermal diffusivity of MG-1100Ba TP. Fitting equation constants: $A = 288.5$, $B = 6.530$, $T_0 = -52.99$, $m = 0.4295$ and $A_0 = 0.7727$. All specimens with thickness ≈ 2 mm.

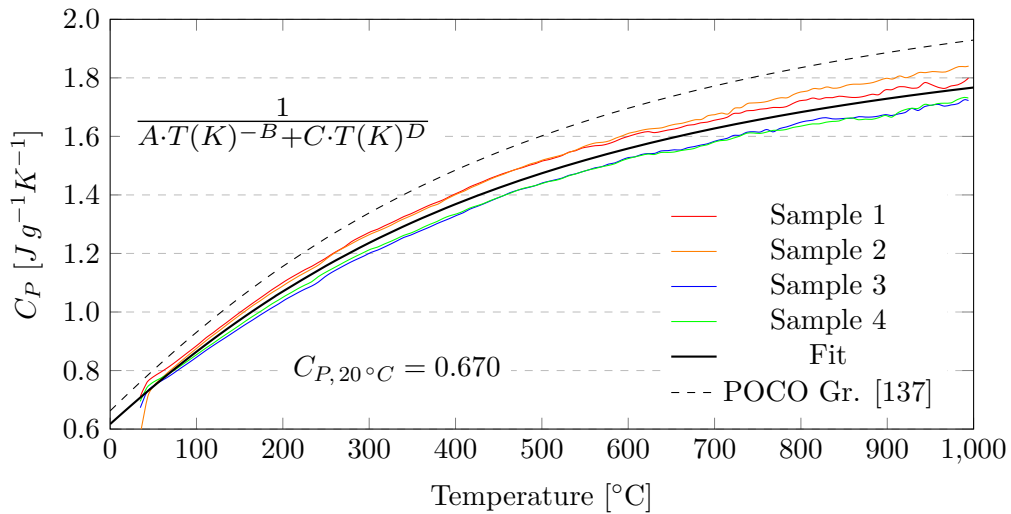


Figure 5.52: Specific heat of MG-1100Ba. Fitting equation constants: $A = 11.77$, $B = 1.644$, $C = 4.047E-4$ and $D = 0.02191$.

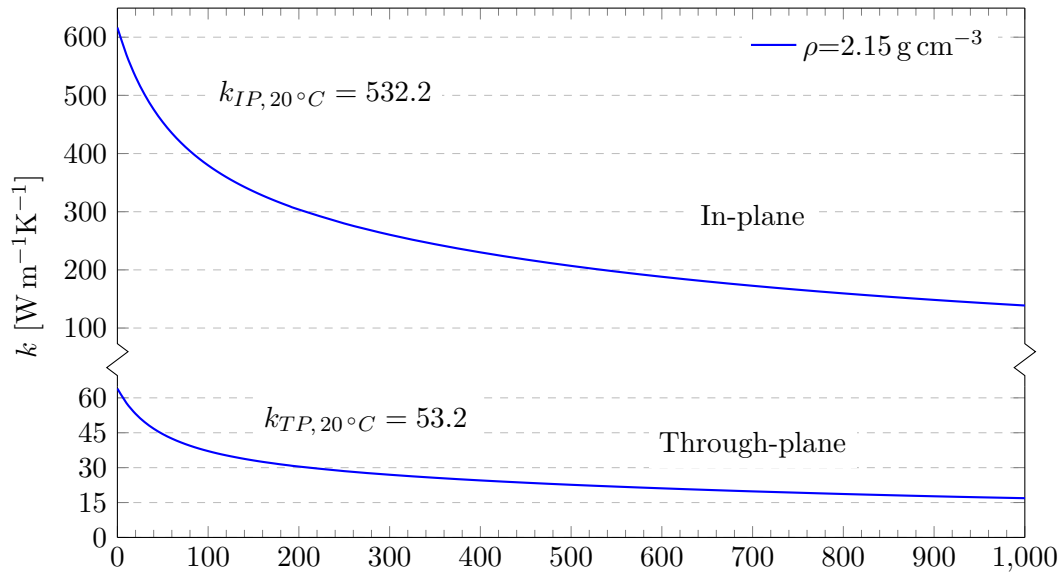


Figure 5.53: Thermal conductivity of CG-1100Ba in both directions. Calculated from constant density.

Thermal expansion measurements (IP and TP) are shown in Figures 5.54 and 5.55. The tests were performed in the range 20–1700 °C, to prevent melting of chromium carbide.

The dl/L_0 curves were not fitted with polynomials due to the presence of abrupt slope changes. In the IP direction, the difference of CTE between heating-up and cooling-down ramps is very subtle, indicating good stability to the thermal cycle applied. There is a change in slope of the dl/L_0 curves at around 1000 °C.

The artefacts at the beginning of the heating-up curves (under ~ 100 °C), in both directions, are typically due to sample accommodation in the sample holder, confirmed by the absence of this behaviour in the cooling down ramp.

The change in length (residual strain) of the specimens was measured with a micrometer, being only 0.03 % in the IP specimens, but 0.73 % in the TP specimens, see Table 5.23. The dl/L_0 curves confirm this behaviour. The relaxation of internal stresses in the IP direction is very small, while in the TP is relevant. In the TP specimens, there is an abrupt change in the dl/L_0 slope at ~ 1680 °C (heating-up) and at 1600–1640 °C (cooling-down). According to the phase diagram (Figure 2.17), the stability limit of the Cr_{23}C_6 Cr-rich carbide is 1849 K (1576 °C), besides, there is an eutectic reaction between the Cr_7C_3 and Cr_3C_2 phases at 2000 K (1727 °C). It would be expected, due to the presence of carbon (graphite) in excess around the carbide particles, that the carbides do not tend to the Cr-rich side of the diagram. This behaviour observed in the dilatometer, and the high residual strain observed after the cooling-down ramp, would be explained by a phase transition to a lower density carbide phase. The density of the $\text{Cr}_3(\text{C,N})_2$ depends on the relative content of C and N; with 10% of the carbon atoms substituted by nitrogen, the theoretical density is 6.466 g cm^{-3} . On the other hand, the rest of carbide phases have larger densities: Cr_{23}C_6 6.97 g cm^{-3} , Cr_7C_3 has 6.92 g cm^{-3} , and Cr_3C_2 has 6.68 g cm^{-3} [30]. It is therefore not clear the reason of this behaviour.

This event needs further verification, for example by performing XRD on the specimens after the dilatometry test.

The IP cooling-down CTE is $2.4 \times 10^{-6} \text{ K}^{-1}$ in the range 20–1000 °C. On the other

hand, the TP direction shows $11.2 \times 10^{-6} \text{ K}^{-1}$ in the same range of temperatures.

Table 5.23: Length of the CG-1100Ba specimens before and after the dilatometer measurement, measured with a micrometer (mm).

	In-plane			Through-plane		
	L_0	L_{final}	Var. [%]	L_0	L_{final}	Var. [%]
Sample 1	25.054	25.054	0.0000	15.033	15.144	0.738
Sample 2	25.037	25.038	0.0040	15.028	15.117	0.592
Sample 3	25.038	25.058	0.0799	15.005	15.135	0.866
Sample 4				15.01	15.118	0.720
Average			0.03			0.73

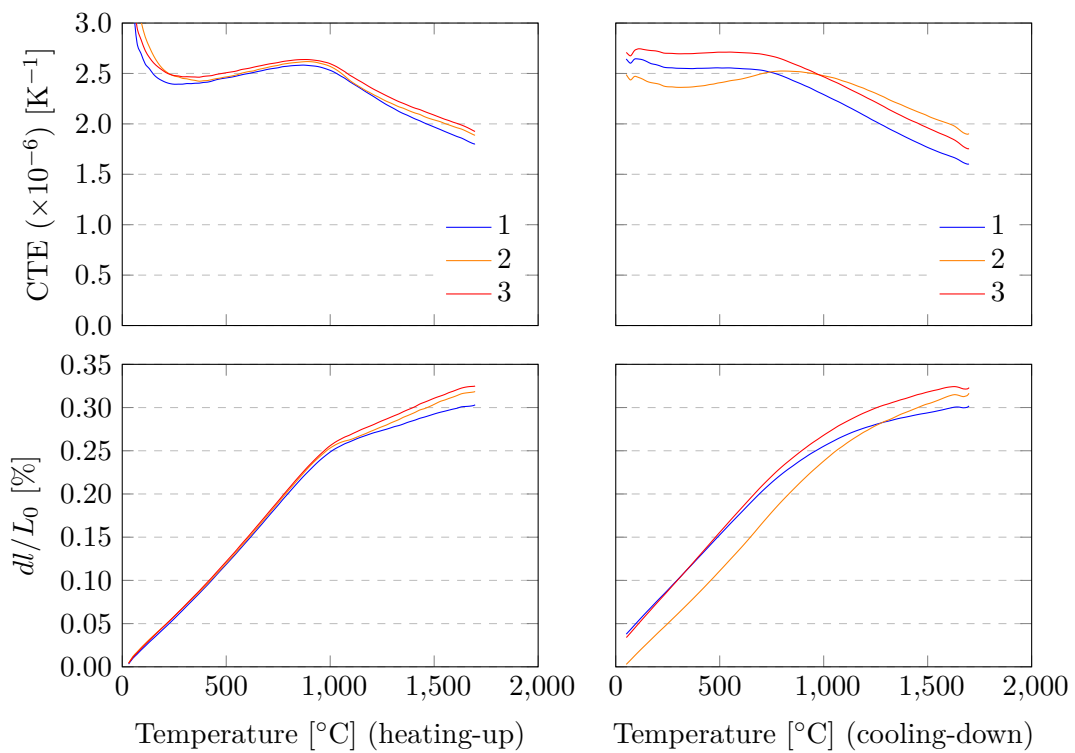
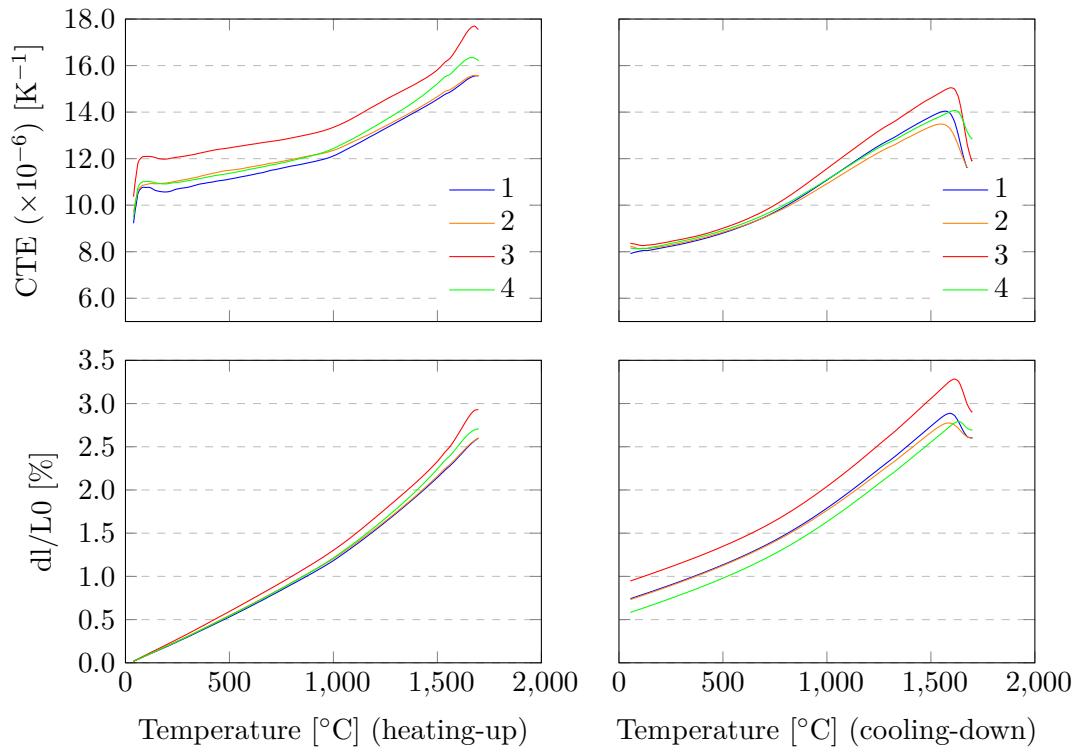


Figure 5.54: CTE CG-1100Ba IP. All specimens with length ≈ 25 mm.

Figure 5.55: CTE CG-1100Ba TP. All specimens with length ≈ 15 mm.

5.4.5 Mechanical properties

The bending test curves are shown in Figure 5.56. In the IP direction, the average maximum strength is 26.2 ± 1.5 MPa and the average strain to rupture is $1210 \pm 200 \mu\text{m m}^{-1}$. In the TP direction, the average maximum strength is 5.5 ± 0.6 MPa and the average strain to rupture is $4200 \pm 560 \mu\text{m m}^{-1}$.

The nominal size of the specimens, the test jig span (L) and the loading span are listed below. All the test were made with four point configuration.

- IP1-IP5: $5 \times 10 \times 55$ mm, $L=50$ mm, loading span= $L/2$.
- TP1-TP5: $5 \times 10 \times 25$ mm, $L=20$ mm, loading span= $L/2$.

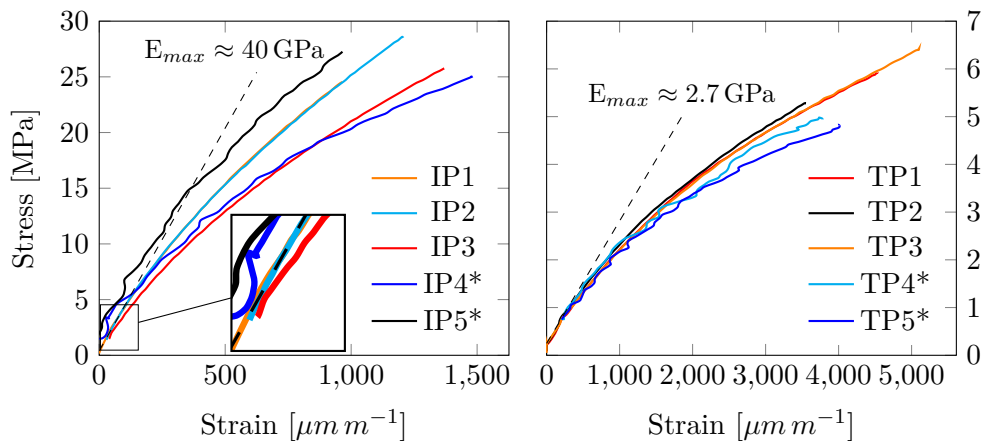


Figure 5.56: Flexural test CG-1100Ba. (*) Specimens IP4-5 and TP4-5 tested with laser extensometer.

Impact Excitation Technique (IET) results are shown in Table 5.24. The flexural and torsional resonance frequencies were acquired. The results from the Finite Element Modeling (FEM) analysis are reported in Table 5.25. It is shown that the results from the analytical formula are deviated with respect to the FEM optimisation, showing in fact non-physical derived Poisson's ratio. The FEM method is more accurate, in accordance with the elastic properties theory.

The Poisson's ratios do not have relevant influence in the resonance frequencies, (see section E.5), hence cannot be characterised with this method. For this reason, ν_{XY} and ν_{XZ} were set to 0.1 (not optimised), which is a reasonable value considering the composition of the material (see section E.6). ν_{YZ} is derived from E_Y and G_{YZ} , see equation E.8.

Table 5.24: IET test of CG-1100Ba, experimental resonance frequencies of IP and TP specimens. Frequencies resulted from the FEM optimisation. (ff: flexural, ft: torsional).

Specimen	m [g]	L [mm]	b [mm]	t [mm]	ff [kHz]	ft [kHz]
IP1	5.807	54.86	10.02	5.01	6.930	13.105
IP2	5.917	54.85	10.03	5.02	6.870	13.340
IP3	5.648	54.85	10.03	4.88	6.344	12.630
IP4	5.819	54.85	10.03	5.00	6.038	13.517
IP5	5.790	54.86	10.01	4.88	6.443	13.128
Average IP:		54.86	10.02	4.95	6.647	13.051
FEM optimisation:		(")	(")	(")	6.647	13.119
T1	2.479	22.44	10.04	5.03	9.533	-
T2	2.465	22.44	10.00	5.04	9.681	18.607
T3	2.412	22.44	10.01	4.94	9.582	18.672
T4	2.433	22.44	10.02	4.96	9.558	18.705
T5	2.416	22.45	10.00	5.04	9.697	18.836
Average TP:		22.44	10.01	5.00	9.610	18.705
FEM optimisation:		(")	(")	(")	9.604	18.697

Table 5.25: Elastic properties of CG-1100Ba resulted from the IET analysis.

	E_X	E_Y	E_Z	G_{XY}	G_{YZ}	G_{XZ}	ν_{YZ}	ν_{XY}	ν_{XZ}
FEM optimisation	2.4	38.7	38.7	2.8	15.9	2.8	0.215	0.1	0.1
Analytical ¹	2.6	33.3	33.3	2.8	8.1	2.8	1.06 ²	-	-

¹ From analytical formula (ASTM C1259-01), for comparison purposes.

² Non-physical, derived from E_Y and G_{YZ} , see equation E.8.

5.5 Chromium carbide - graphite CG-1100A0

CG-1100A0 material belongs to the Chromium carbide - graphite family, similarly to CG-1100Ba (section 5.4). The material CG-1100A0 it is in fact a cylinder cut from the plate CG-1100Ba just after the first sintering cycle, without second sintering cycle nor post-sintering cycle. The comparison of processing parameters is shown in section 4.6. The cylinder of material had only $\text{Ø}12.5 \times 19.2$ mm, see Figure 5.57, therefore a limited number

of samples, most of them with exceptionally small sizes, were extracted for characterisation:

- Dilatometer IP: 2 specimens $3 \times 3 \times 10$ mm.
- Dilatometer TP: 2 specimens $3 \times 3 \times 10$ mm.
- LFA IP: 2 specimens $\text{Ø}6 \times 5.5$ mm.
- LFA TP: 2 specimens $\text{Ø}12.5 \times 1.6$ mm.
- DSC: 2 specimens $\sim 5 \times 5 \times 1$ mm.

The characterisation results are presented below.

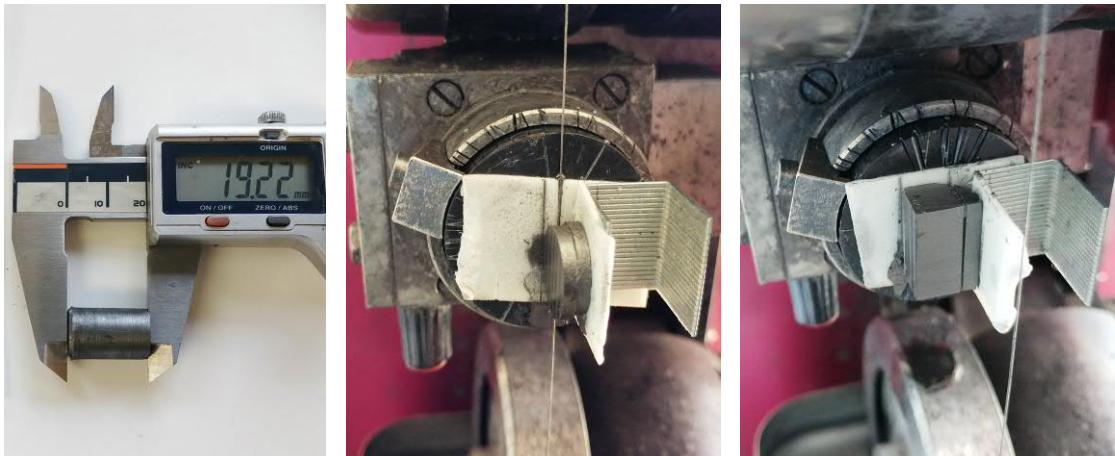


Figure 5.57: (Left) Original piece of CG-1100A0. (Center and right) Slicing process with diamond wire saw (black sample holder is $\text{Ø}30$ mm).

5.5.1 Microstructure

Figure 5.58 shows SEM observations of polished CG-1100A0 TP surfaces (pressing force was vertical). The as-polished surfaces show a connected graphite matrix (dark) with chromium carbide particles (bright) having an average size of $5 \mu\text{m}$.

The contrast visible in the graphite matrix (BE image) allows to identify the alignment of the graphite basal planes. The texture shows that it is not perfectly perpendicular to the pressing force (vertical), which helps in reducing anisotropy.

In contrast with CG-1100Ba grade (Figure 5.41) these images show moderately large content of voids, caused by lack of compaction. This material was sintered for only half of the time than CG-1100Ba grade, which justifies the different compactness.

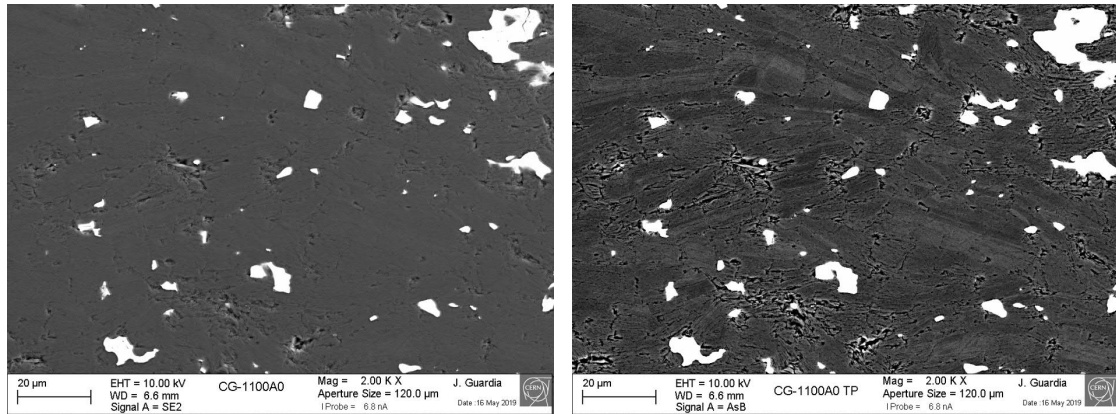


Figure 5.58: SEM observations of CG-1100A0 TP surface, pressing force was vertical. (Left) SE image. (Right) BE image. The BE image shows channeling effect in graphite, allowing identification of crystalline domains.

5.5.2 Crystallography

Figure 5.59 shows the XRD analysis of CG-1100A0, including IP and TP surfaces. The TP surface shows reduced intensity in the $00l$ peaks, such as (002).

The carbide phase identified in grade CG-1100Ba ($\text{Cr}_3(\text{C},\text{N})_2$) also appears in this case, but the Cr_3C_2 phase is present as well. The relative amounts are difficult to quantify, as the texture has a big influence in the peak intensity, however, by looking at the overall peak heights, both phases are present in relevant amount.

In the TP test, the (200) peak from $\text{Cr}_3(\text{C},\text{N})_2$ is very intense. The same phase in the CG-1100Ba TP pattern, shows (023) as its highest peak, indicating different texture. The intense (200) peak is due to a large total area of carbide particle(s) oriented with a perpendicular to the surface. In the IP pattern, the graphite 001 peaks are very large, due to the preferred orientation, therefore all the carbide peaks appear very small.

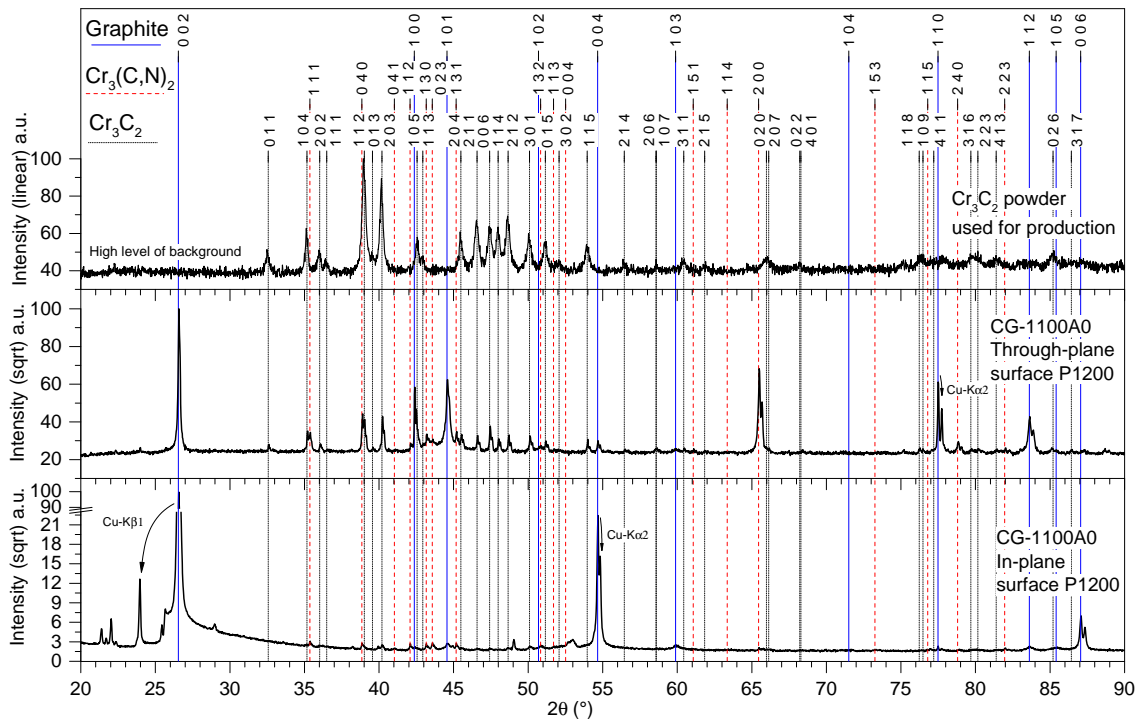


Figure 5.59: CG-1100A0 IP and TP XRD patterns.

5.5.3 Thermophysical properties

The average density at RT measured on with the Archimede's method is 2.31 g cm^{-3} .

The thermal diffusivity (IP and TP) and the specific heat of CG-1100A0 are shown in Figures 5.60, 5.61 and 5.62 respectively. The mathematical functions that fit the experimental data are shown in the plots. The conductivity is calculated from the diffusivity and specific heat fitting curves, assuming constant density (2.31 g cm^{-3}), see Figure 5.63.

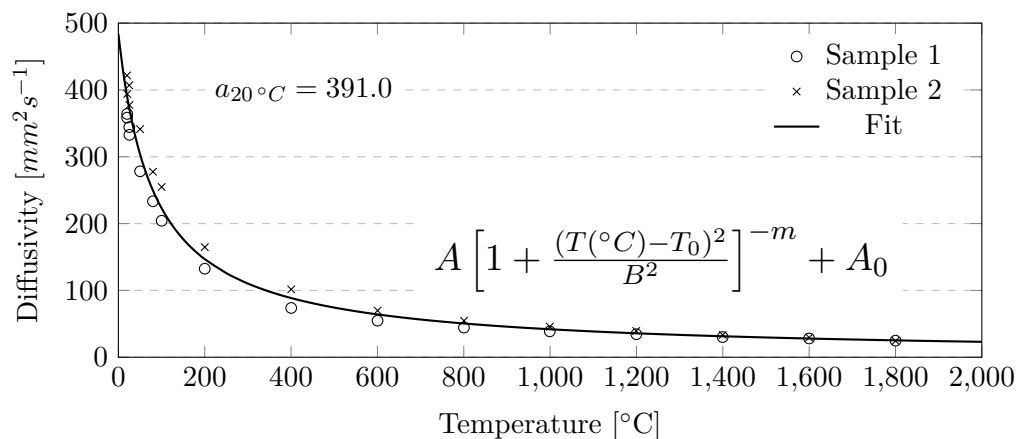


Figure 5.60: Thermal diffusivity of MG-1100A0 IP. Fitting equation constants: $A = 1788$, $B = 18.50$, $T_0 = -73.36$, $m = 0.4647$ and $A_0 = 0.823$. All specimens with thickness $\approx 5.5 \text{ mm}$.

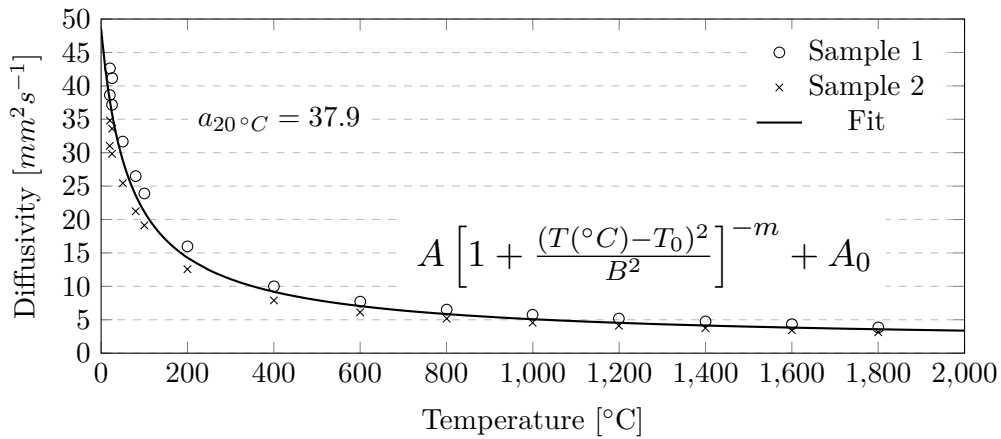


Figure 5.61: Thermal diffusivity of MG-1100A0 TP. Fitting equation constants: $A = 297.2$, $B = 6.633$, $T_0 = -56.68$, $m = 0.4264$ and $A_0 = 1.143$. All specimens with thickness ≈ 2 mm.

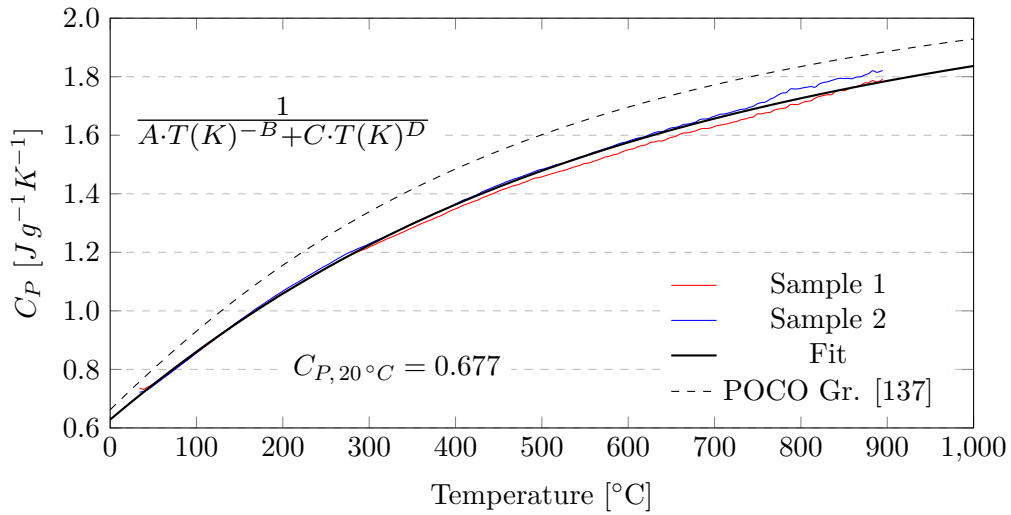


Figure 5.62: Specific heat of MG-1100A0. Fitting equation constants: $A = 4.284$, $B = 1.462$, $C = 4.098E-4$ and $D = 3.748E-3$.

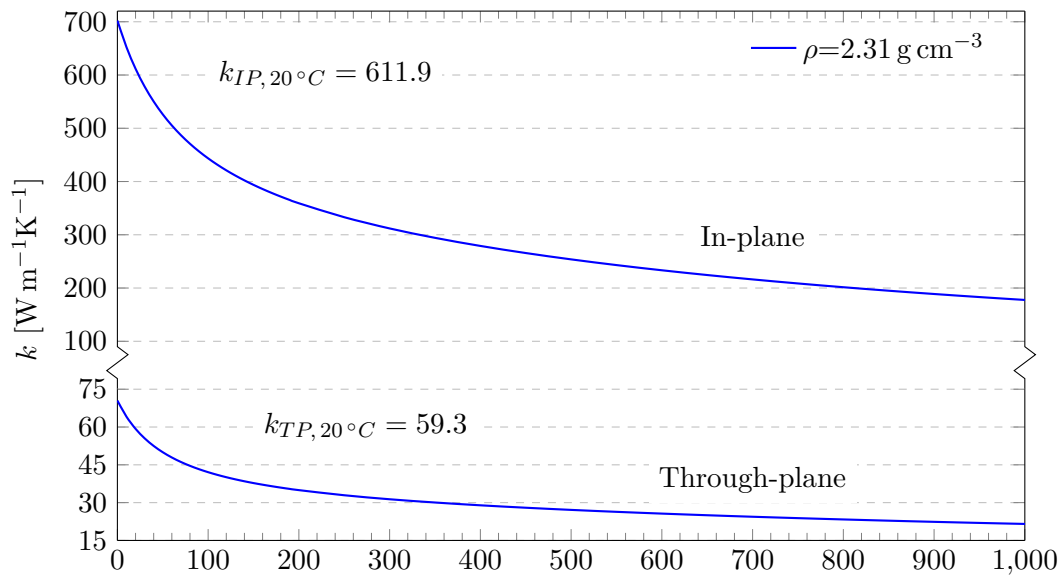


Figure 5.63: Thermal conductivity of CG-1100A0 in both directions. Calculated from constant density.

Thermal expansion measurements (IP and TP) are shown in Figures 5.64 and 5.65. The tests were performed in the range 20–900 °C.

The IP dl/L_0 curves were not fitted with polynomials due to the presence of abrupt slope changes that impeded good fitting. In the IP direction, the difference of CTE between heating-up and cooling-down ramps is not very large, indicating good stability to the thermal cycle applied.

Fifth degree polynomials were fitted to the dl/L_0 curves, which helps to smooth out experimental errors.

The artefacts at the beginning of the heating-up curves (under ~ 100 °C), in both directions, are typically due to sample accommodation in the sample holder, confirmed by the absence of this behaviour in the cooling down ramp.

The change in length (residual strain) of the specimens was measured with a micrometer, being only 0.02% in the IP specimens and 0.31% in the TP specimens, see Table 5.26. The dl/L_0 curves confirm this behaviour. The relaxation of internal stresses in the IP direction is very small, while in the TP is moderately high. This behaviour is observed in MoGr materials as well, see section 5.3.

The IP cooling-down CTE is $\sim 4.5 \times 10^{-6} \text{ K}^{-1}$ in the range 20–1000 °C. On the other hand, the TP direction shows $12.1 \times 10^{-6} \text{ K}^{-1}$ in the same range of temperatures. There is a relevant difference in TP CTE between the two ramps, as the heating-up ramp shows values around $3 \times 10^{-6} \text{ K}^{-1}$ higher.

Table 5.26: Length of the CG-1100A0 specimens before and after the dilatometer measurement, measured with a micrometer (mm).

	In-plane			Through-plane		
	L_0	L_{final}	Var. [%]	L_0	L_{final}	Var. [%]
Sample 1	9.910	9.909	0.010	10.443	10.475	0.306
Sample 2	9.916	9.918	0.020			
Average			0.02			0.31

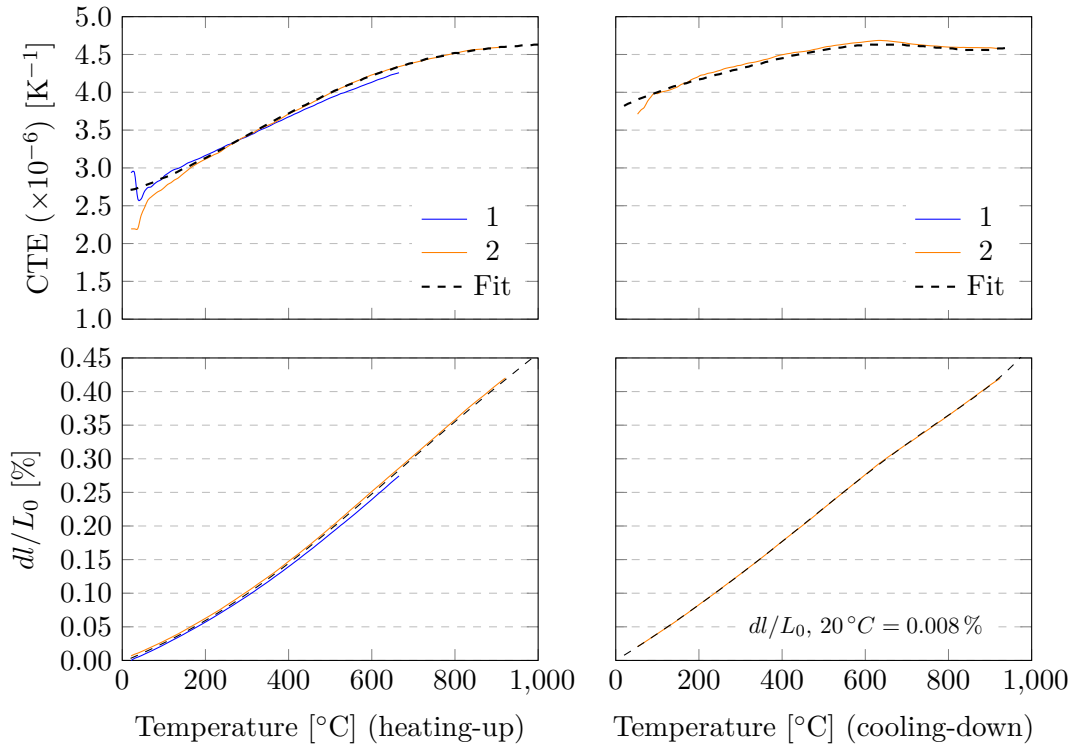


Figure 5.64: CTE CG-1100A0 IP. All specimens with length ≈ 10 mm.

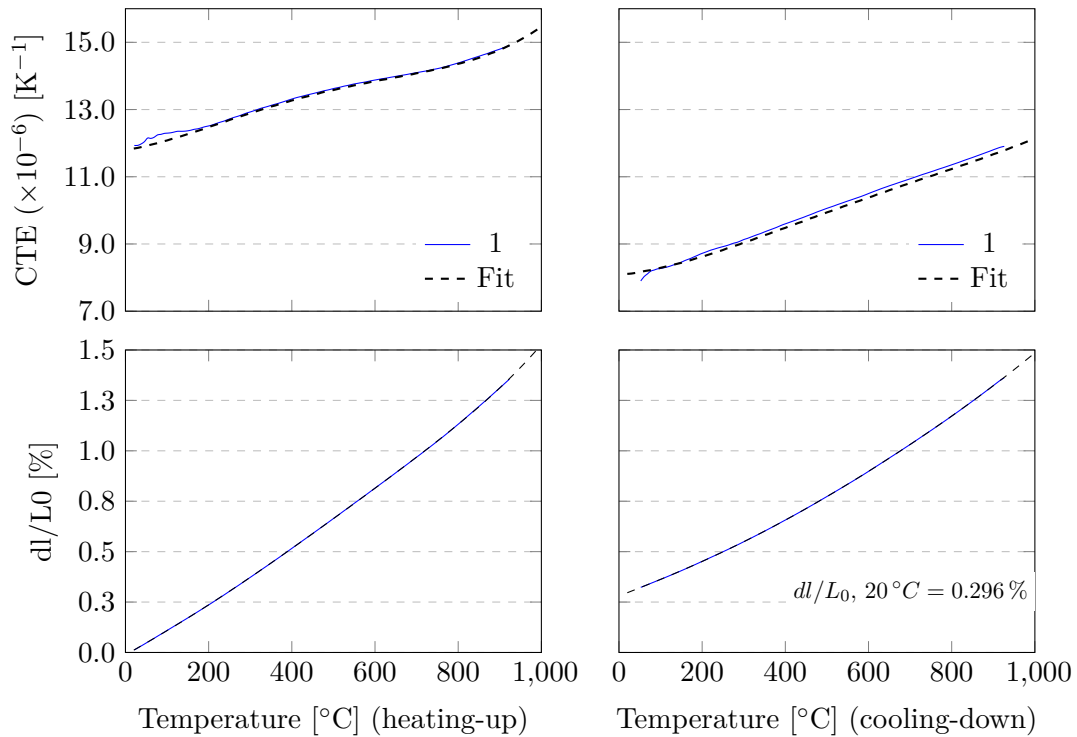


Figure 5.65: CTE CG-1100A0 TP. All specimens with length ≈ 10 mm.

5.6 Chromium carbide - graphite CG-1100B0

CG-1100B0 material belongs to the Chromium carbide - graphite family, similarly to CG-1100Ba (section 5.4). The material CG-1100B0 it is in fact half of the sintered plate, which was cut prior to the post-sintering cycle, see Figures 5.66 and 5.67. The comparison of processing parameters is shown in section 4.6.

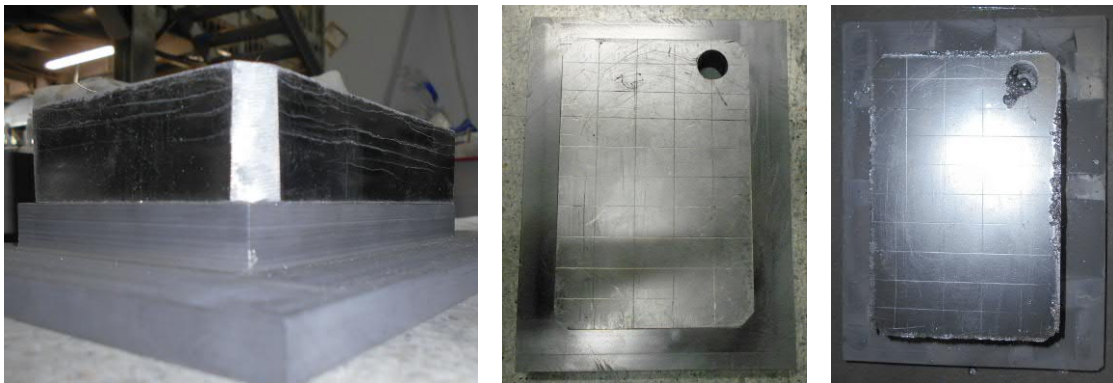


Figure 5.66: Production steps of CG-1100B0 material, from left to right: Green body compaction, first sintering cycle + machining, second sintering cycle. The hole is due to the extraction of CG-1100A0 material. Note how the molten material spilled inside the hole comes mainly from the direction towards the centre of the plate.

The location of the CG-1100B0 specimens inside the plate is illustrated in Figures 5.67 and 5.68.

The characterisation results are presented below.

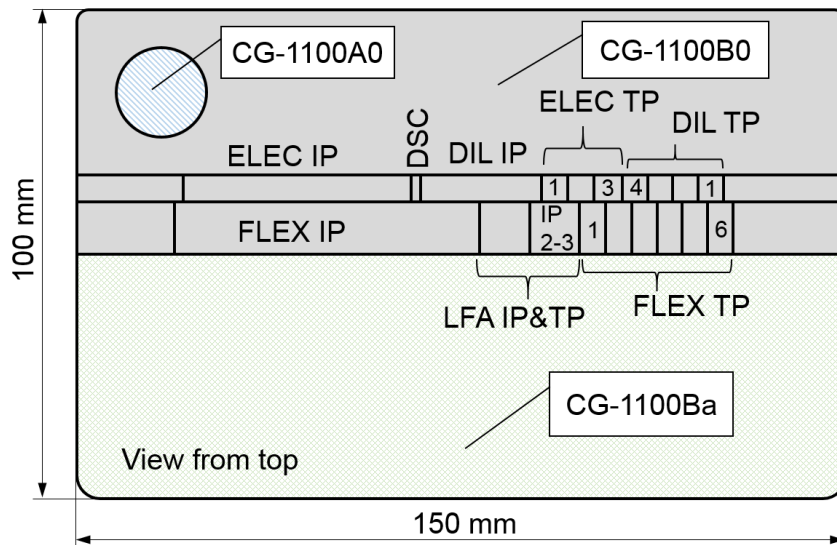


Figure 5.67: Schematic of the provenance of the A0, B0 and Ba materials, from CG-1100 plate. The positions of all specimens from CG-1100B0 grade are shown (view from top). The full plate size is 150 × 100 × ~ 23 mm. The pressing direction is parallel to the short side.

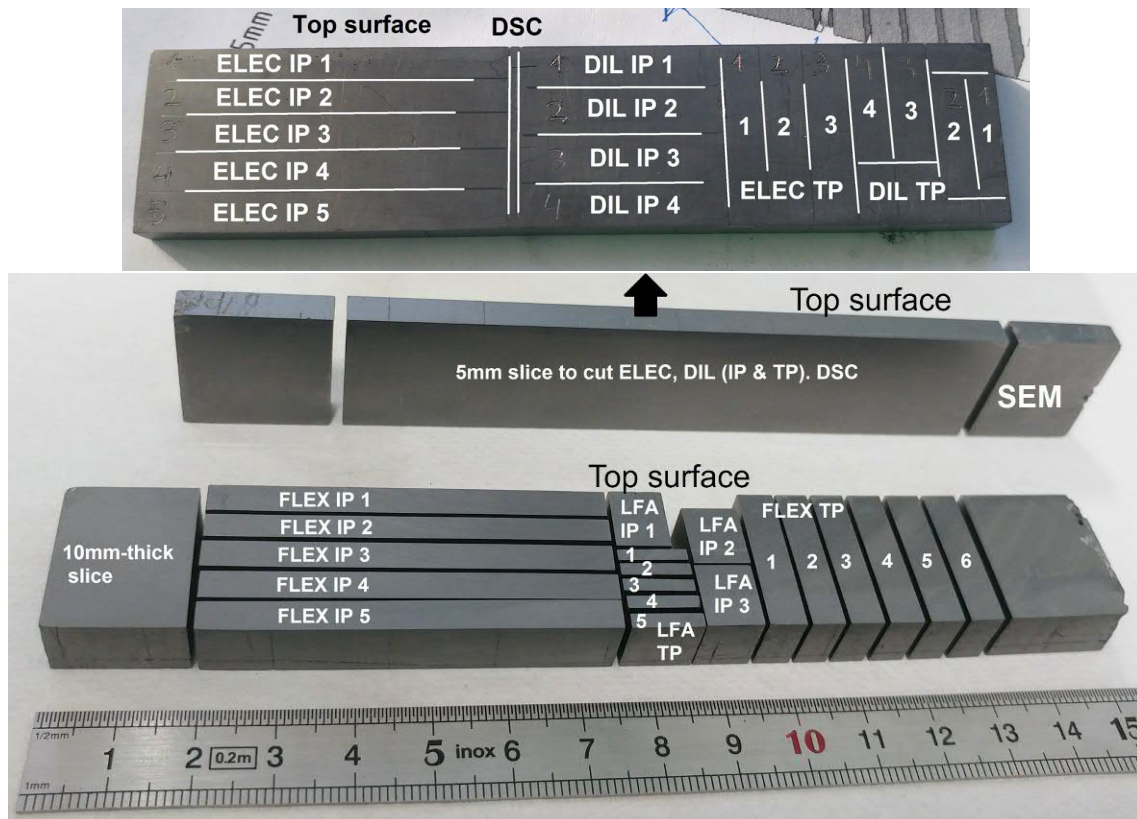


Figure 5.68: Plate location of all CG-1100B0 specimens, cut with diamond wire saw.

5.6.1 Microstructure

SEM observations of polished CG-1100B0 TP surfaces (pressing force was vertical) are presented below. The piece observed is the one at the top right side of Figure 5.68 ($\sim 22.9 \times 20 \times \sim 5$ mm), the exact same face shown there. All the SEM images are oriented with the plate top surface at the top and the right plate edge at the right side.

Figure 5.69 represents the average microstructure of CG-1100B0, taken from the mid-thickness of the plate, at around 15 mm from the lateral edge. It shows a connected graphite matrix (dark) with chromium carbide particles (bright) having an average size of $10 \mu\text{m}$.

There is little contrast visible in the graphite matrix (BE image), but the alignment of the graphite basal planes can be reconstructed. The texture is analogous to the other CG-1100 materials, not perfectly perpendicular to the pressing force (vertical), which helps in reducing anisotropy.

These images show similar content of voids than in CG-1100Ba grade (Figure 5.41). The sintering cycles in this material were identical than in CG-1100Ba, but the latter had a further post-sintering pressure-less step.

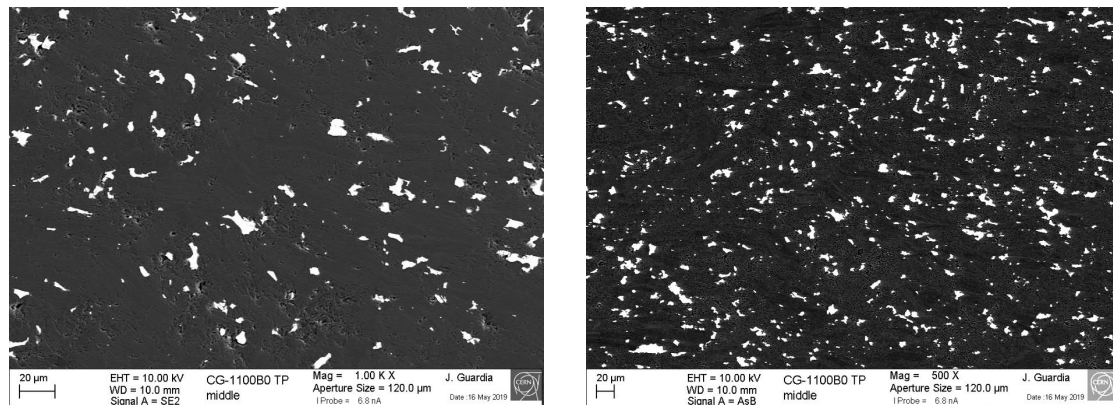


Figure 5.69: SEM observations of CG-1100B0 TP surface, pressing force was vertical. (Left) SE image. (Right) BE image. The BE image shows weak channeling effect in graphite, helping to identify the texture.

Figure 5.70 shows the lateral plate edge of CG-1100B0. The outer lateral 2-4 mm shows agglomeration of carbides. On the other hand, the top and bottom surface edges do not. This could be due to more easiness to spill material in the parallel-to-basal-planes direction. The SEM images of the agglomerations (Figure 5.71) show big graphite flakes grown from the dissolution-precipitation mechanism. Those flakes have sizes up to $50 \mu\text{m}$ in the c-axis direction and up to $300 \mu\text{m}$ in the basal-plane direction. They tend to be aligned as the parent graphite matrix, but many flakes are not and show random orientations.

Apart from those features around the plate lateral edge, the microstructure of the material is homogeneous, analogous to Figure 5.69.

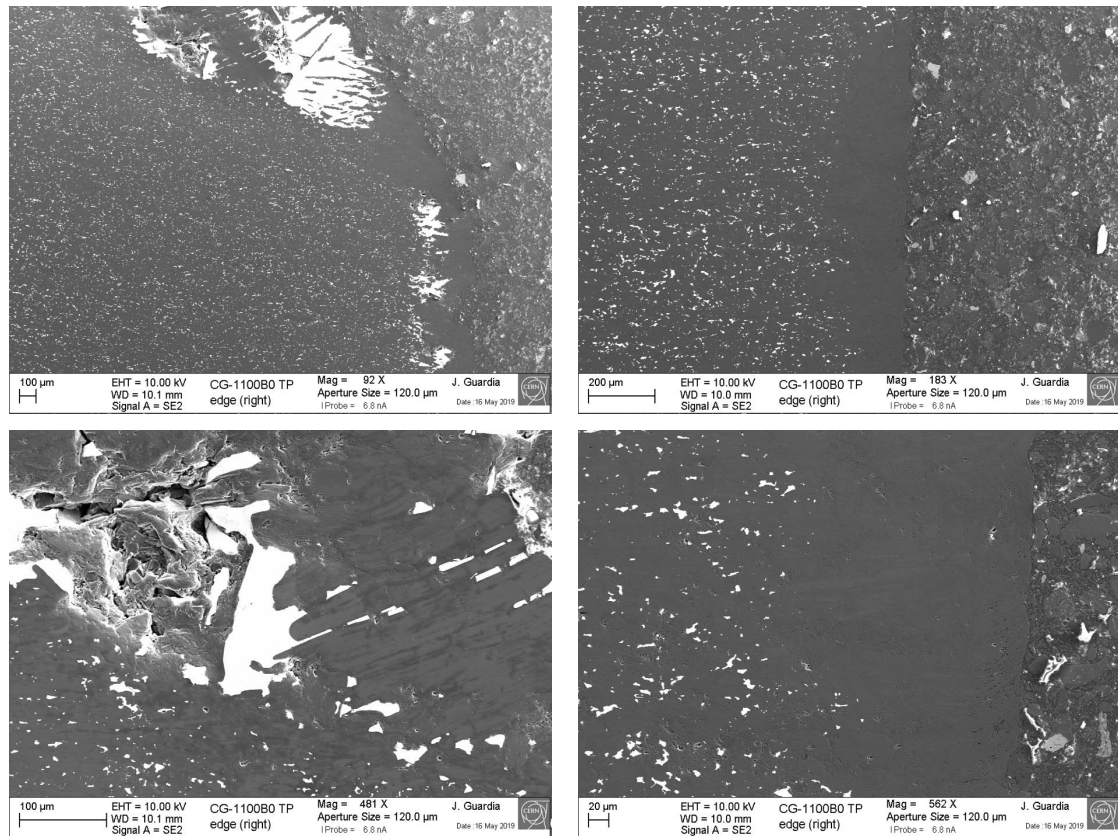


Figure 5.70: SEM SE observations of CG-1100B0 lateral plate edge, pressing force was vertical. Right side of the images corresponds to the sample mounting resin. (Left) top-lateral corner showing carbide agglomeration. (Right) lateral edge showing absence of carbides. Bottom images show close-up views of the same points.

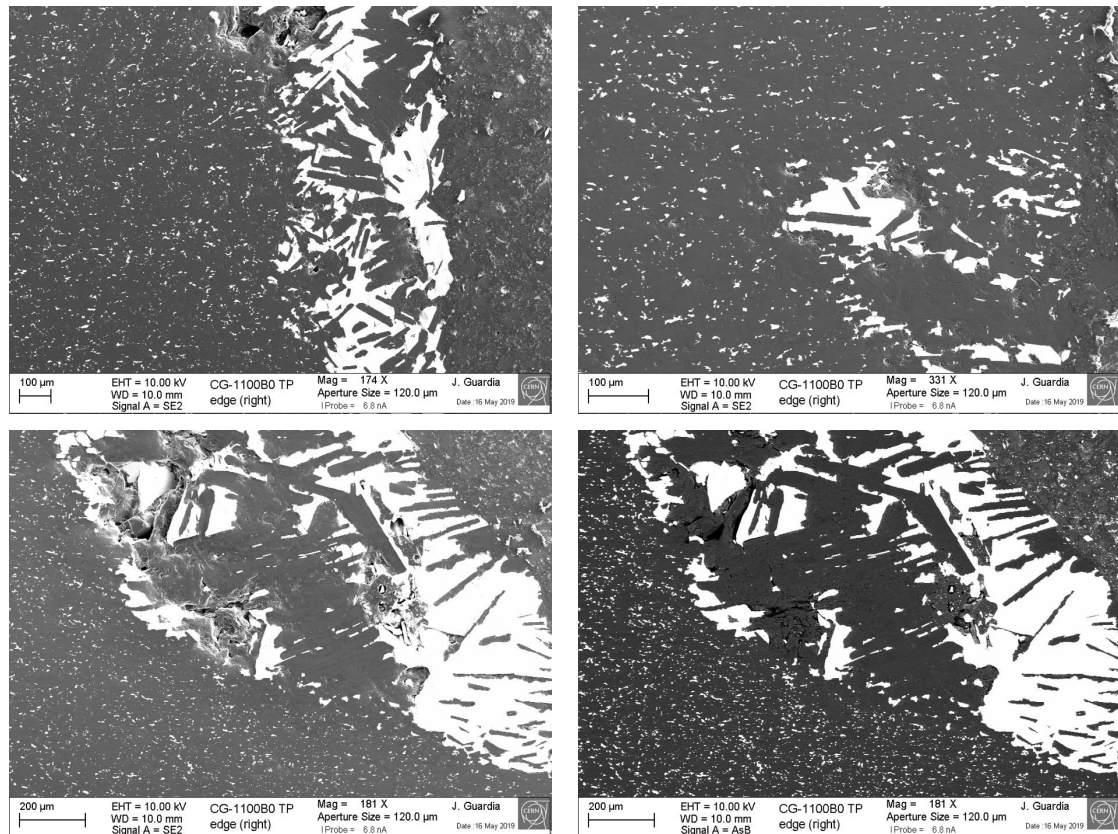


Figure 5.71: SEM observations of the carbide agglomerations at the lateral plate edge. All SE images except bottom-right (BE).

5.6.2 Crystallography

Figure 5.72 shows the XRD analysis of CG-1100B0, including TP surface and the molten material spilt during the its last sintering cycle. The carbide phase identified in grade CG-1100Ba ($\text{Cr}_3(\text{C},\text{N})_2$) also appears in this case, and is the only carbide phase present in this grade. The preferred orientation of the carbide particles is slightly different, as here the highest peak is (130), while in CG-1100Ba, (023) was the most intense one.

The molten phase shows a completely different pattern, as it does not show the $\text{Cr}_3(\text{C},\text{N})_2$ peaks, but it clearly shows the Cr_3C_2 ones. This could be due to the pressure release when leaking out from the mould, which helps eliminating the nitrogen stabilizing agent. The molten material is expected to have much bigger grains than the particles inside the composite, see SEM observations in Section 6.6. This difference in size could play a role in the phase stability.

The molten material contains high quality graphite, produced by the dissolution-precipitation mechanism.

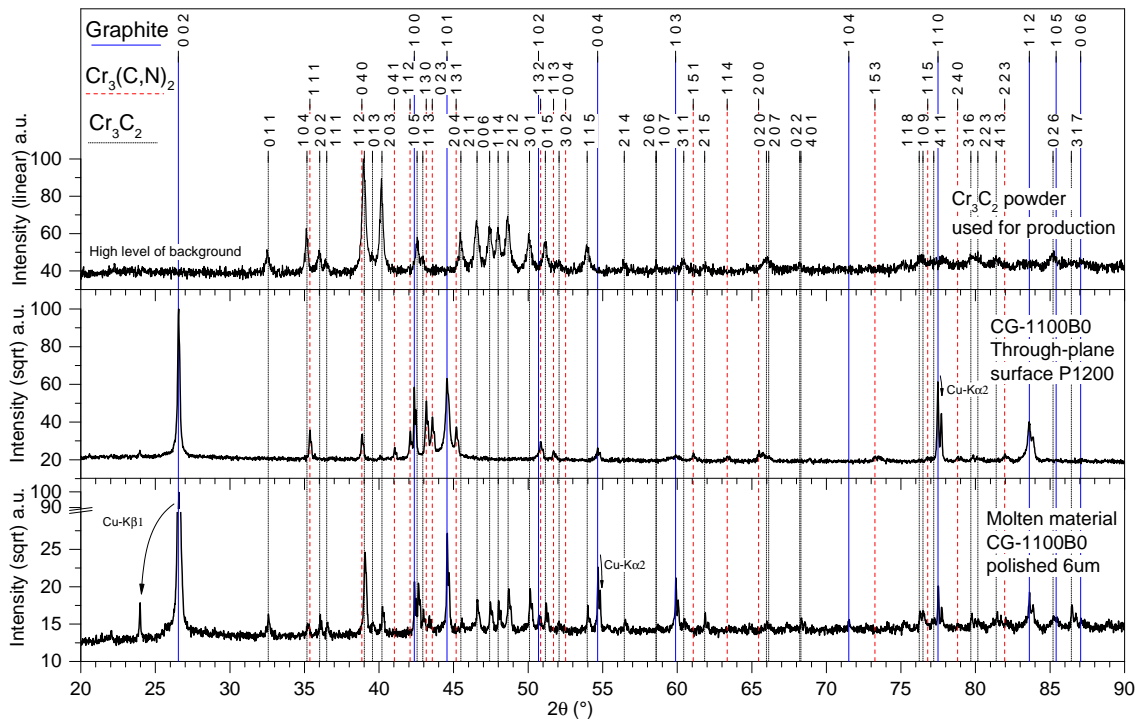


Figure 5.72: CG-1100B0 TP and molten material XRD patterns.

5.6.3 Electrical properties

In-plane electrical conductivity measurements were performed with two methods: 4-wire DC and superficial eddy-current techniques (Sigmatest), see section 3.4. The specimens measured were position-tracked along the plate thickness to understand possible conductivity variations.

The results on the IP direction are presented in figure 5.73, which depicts the variation along the plate thickness. The specimens tested were those called "ELEC IP" in Figure 5.68 (DC 4-wire method) and "FLEX IP" (Eddy-current method at 960 kHz, on the two faces). The values consist of the average of three tests on each surface or bulk specimen. It is evident that the inner volume of the plate has slightly lower electrical conductivity than the outer surfaces. The plate surfaces reach $1.00 \pm 0.02 \text{ MS m}^{-1}$ (top) and $0.93 \pm 0.10 \text{ MS m}^{-1}$ (bottom), while the inner part shows around 0.75 MS m^{-1} .

The DC test on the best specimen (the one closest to the top face) results in an electrical conductivity of $0.88 \pm 0.03 \text{ MS m}^{-1}$. The average of all 5 bulk specimens is $0.78 \pm 0.07 \text{ MS m}^{-1}$.

It is important to note, as explained in section 1.2, that the collimator materials require high electrical conductivity only at the surface. For this reason, one can take advantage of this particular material inhomogeneity.

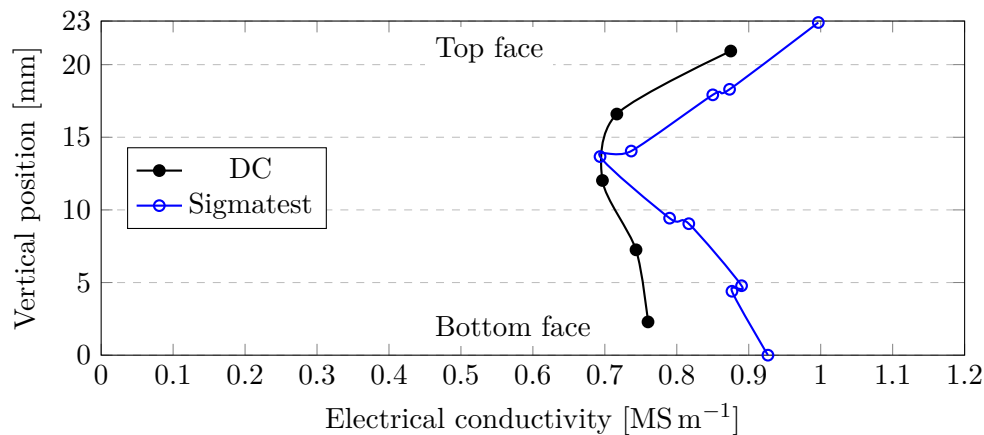


Figure 5.73: Electrical conductivity measurements on CG-1100B0 (IP), measured along plate thickness (thickness=22.9 mm).

5.6.4 Thermophysical properties

The average density at RT measured on the IET specimens (weight and dimensions) is 2.21 g cm^{-3} . The variation of density measured on several specimens along plate thickness is shown in Figure 5.74, the specimens are shown in Figure 5.68. There is no clear trend, with all values within the range $2.21 \pm 2\% \text{ g cm}^{-3}$, which is in the order of the measurement uncertainty. With these results, the trend observed on the electrical conductivity (Figure 5.73) needs further investigation.

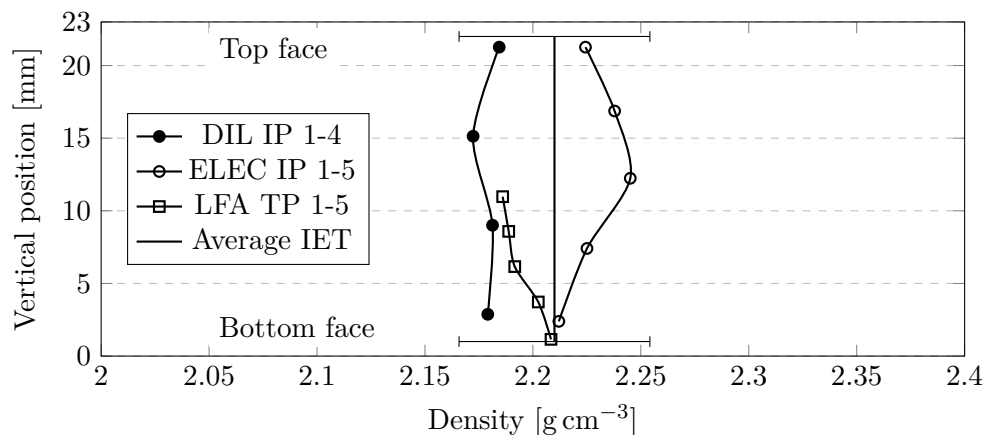


Figure 5.74: Density (Archimede's) measurements on CG-1100B0, measured along plate thickness (thickness=22.9 mm). Error bar represent a $\pm 2\%$ error.

The thermal diffusivity (IP and TP) and the specific heat of CG-1100B0 are shown in Figures 5.75, 5.76 and 5.77 respectively. The mathematical functions that fit the experimental data are shown in the plots. The conductivity is calculated from the diffusivity and specific heat fitting curves, assuming constant density (2.21 g cm^{-3}), see Figure 5.78.

In the IP direction the position of the specimens along the plate thickness does not play a significant role, the 3 specimens have similar diffusivity values. This could be because the specimen dimensions are almost as big as half of the plate thickness ($10 \times 10 \times 8.5 \text{ mm}$, see Figure 5.68), averaging the result over that volume.

However, in the TP direction, the specimens show a specific trend along the plate thickness, see Figure 5.79. The variation shows a diffusivity maximum at around the mid-

thickness of the plate, decreasing towards the bottom surface, and increasing again just below it. This behaviour is expected to be approximately symmetric on the top side of the plate. This trend is different with respect to the IP electrical conductivity (Figure 5.73).

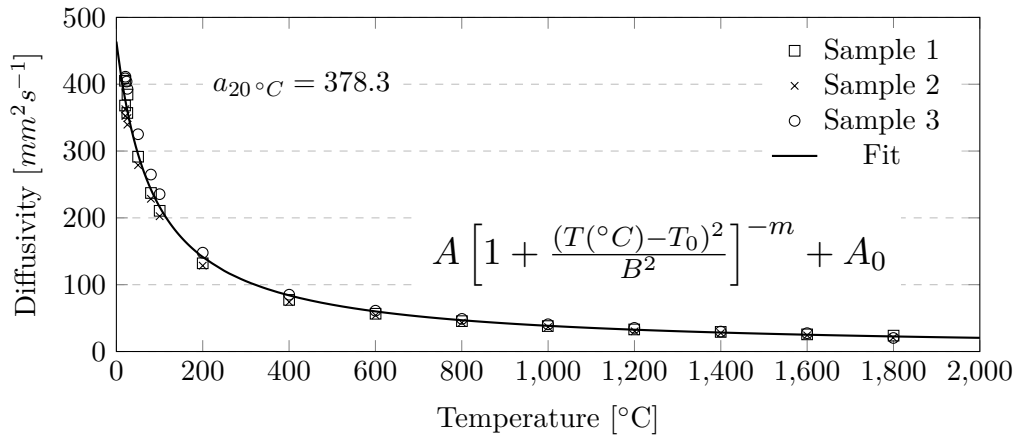


Figure 5.75: Thermal diffusivity of CG-1100B0 IP. Fitting equation constants: $A = 1268$, $B = 28.08$, $T_0 = -75.07$, $m = 0.4794$ and $A_0 = 0$. All specimens with thickness ≈ 8.5 mm.

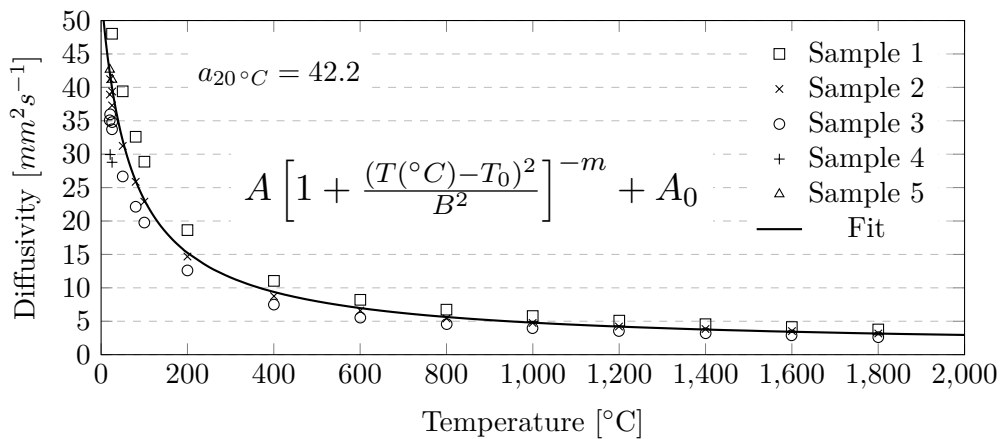


Figure 5.76: Thermal diffusivity of CG-1100B0 TP. Fitting equation constants: $A = 350.3$, $B = 7.975$, $T_0 = -62.57$, $m = 0.4555$ and $A_0 = 0.7255$. All specimens with thickness ≈ 2 mm.

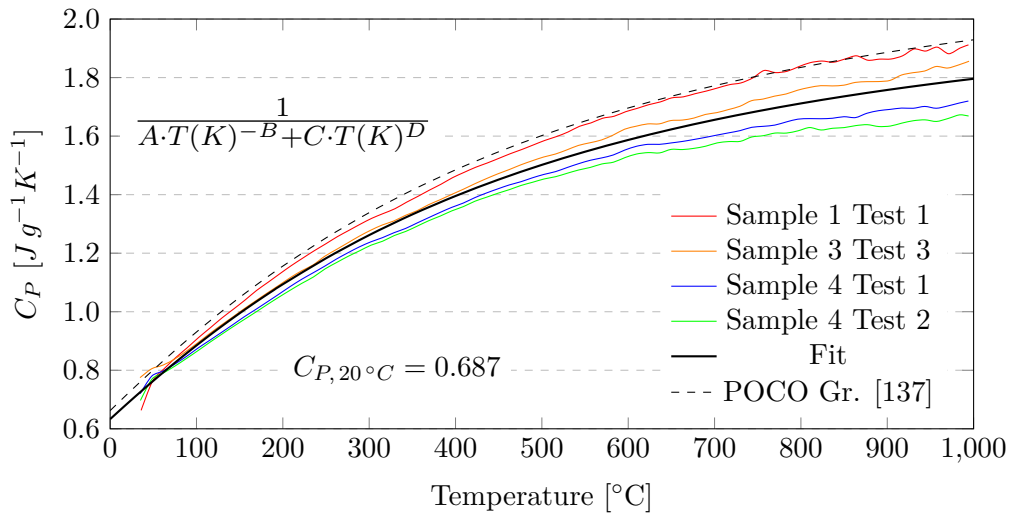


Figure 5.77: Specific heat of CG-1100B0. Fitting equation constants: $A = 11.42$, $B = 1.644$, $C = 3.993E-4$ and $D = 0.02191$.

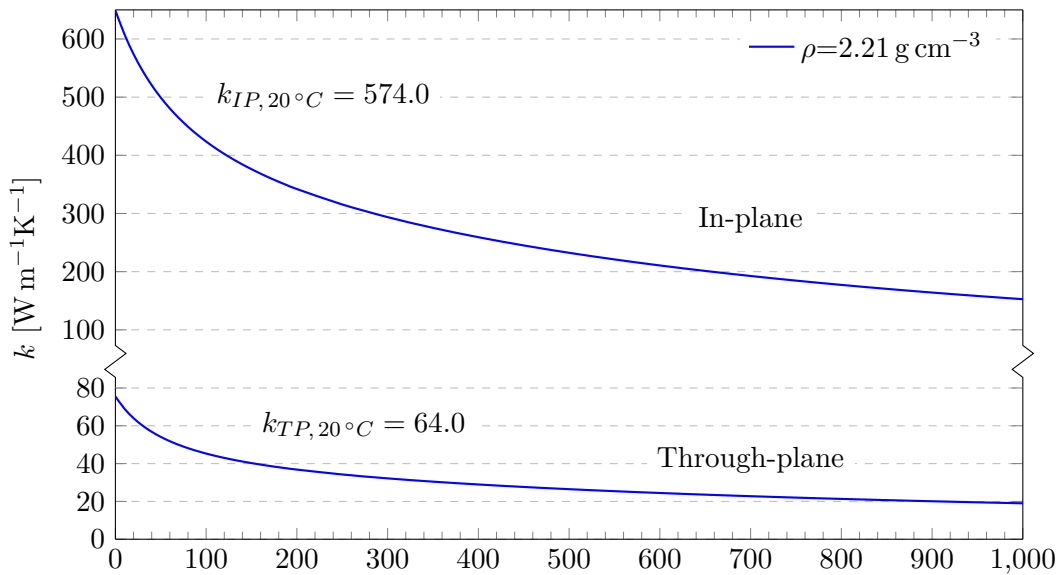


Figure 5.78: Thermal conductivity of CG-1100B0 in both directions. Calculated from constant density.

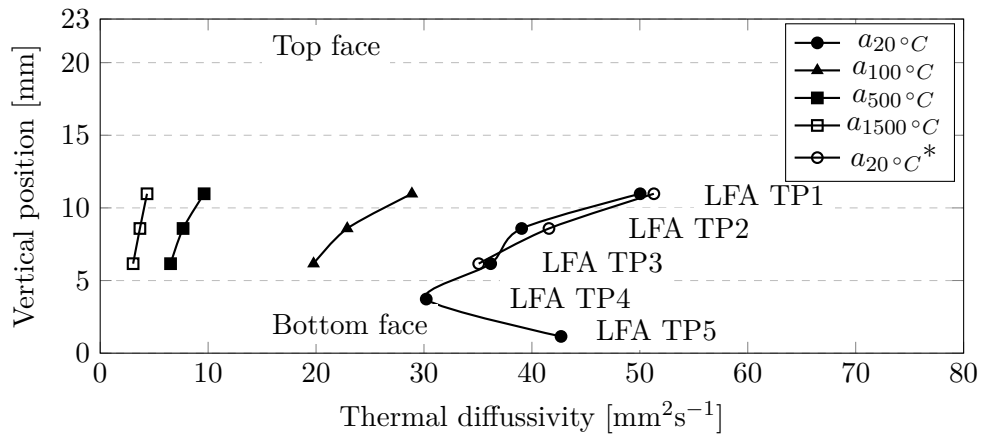


Figure 5.79: Thermal diffusivity measurements on CG-1100B0 (TP), measured along plate thickness (thickness=22.9 mm). Specimens shown in Figure 5.68. (*) Tested after cooling down 1800–20 °C.

Thermal expansion measurements (IP and TP) are shown in Figures 5.80 and 5.81. The tests were performed in the range RT–1700 °C, to prevent melting of chromium carbide.

The dl/L_0 TP curves were not fitted with polynomials due to the presence of abrupt slope changes. In the IP direction, the difference of CTE between heating-up and cooling-down ramps is very subtle, indicating good stability to the thermal cycle applied. Samples IP1-2 have slightly different heating-up dl/L_0 curves than IP3-4, noting that 1-2 specimens were cut from the top half and 3-4 from the bottom-half of the plate, see 5.68.

There are no relevant differences between the 4 TP specimens, even if 1-2 were cut from at mid-thickness and 3-4 at the top side of the plate, see 5.68. The dashed black line in Figure 5.80 represents the fit to all relevant specimens.

The artefacts at the extremities of the dl/L_0 curves, amplified in the CTE curves, are typically due to unsteady heating/cooling rate. They are more common in the heating up ramp up to ~ 100 °C.

The change in length (residual strain) of the specimens was measured with a micrometer, being only 0.05 % in the IP specimens, but 1.14 % in the TP specimens, see Table 5.27. The dl/L_0 curves confirm this behaviour. The relaxation of internal stresses in the IP direction is very small, while in the TP is large. In the TP specimens, there is an abrupt change in the dl/L_0 slope at ~ 1680 °C (heating-up) and at 1600 °C (cooling-down). According to the phase diagram (Figure 2.17), the stability limit of the Cr_{23}C_6 Cr-rich carbide is 1849 K (1576 °C), besides, there is an eutectic reaction between the Cr_7C_3 and Cr_3C_2 phases at 2000 K (1727 °C). It would be expected, due to the presence of carbon (graphite) in excess around the carbide particles, that the carbides do not tend to the Cr-rich side of the diagram. This behaviour observed in the dilatometer, and the high residual strain observed after the cooling-down ramp, would be explained by a phase transition to a lower density carbide phase. The density of the $\text{Cr}_3(\text{C,N})_2$ depends on the relative content of C and N; with 10% of the carbon atoms substituted by nitrogen, the theoretical density is 6.466 g cm^{-3} . On the other hand, the rest of carbide phases have larger densities: Cr_{23}C_6 6.97 g cm^{-3} , Cr_7C_3 has 6.92 g cm^{-3} , and Cr_3C_2 has 6.68 g cm^{-3} [30]. It is therefore not clear the reason of this behaviour.

This event needs further verification, for example by performing XRD on the specimens after the dilatometry test.

The IP cooling-down CTE is $2.8 \times 10^{-6} \text{ K}^{-1}$ in the range 20–1000 °C. On the other hand, the TP direction shows $11.0 \times 10^{-6} \text{ K}^{-1}$ in the same range of temperatures.

Table 5.27: Length of the CG-1100B0 specimens before and after the dilatometer measurement, measured with a micrometer (mm).

	In-plane			Through-plane		
	L_0	L_{final}	Var. [%]	L_0	L_{final}	Var. [%]
Sample 1	25.060	25.078	0.072	15.551	15.744	1.241
Sample 2	25.068	25.069	0.004	15.568	15.747	1.150
Sample 3	25.078	25.095	0.068	15.267	15.439	1.127
Sample 4	25.089	25.104	0.060	15.252	15.411	1.042
Average			0.05			1.14

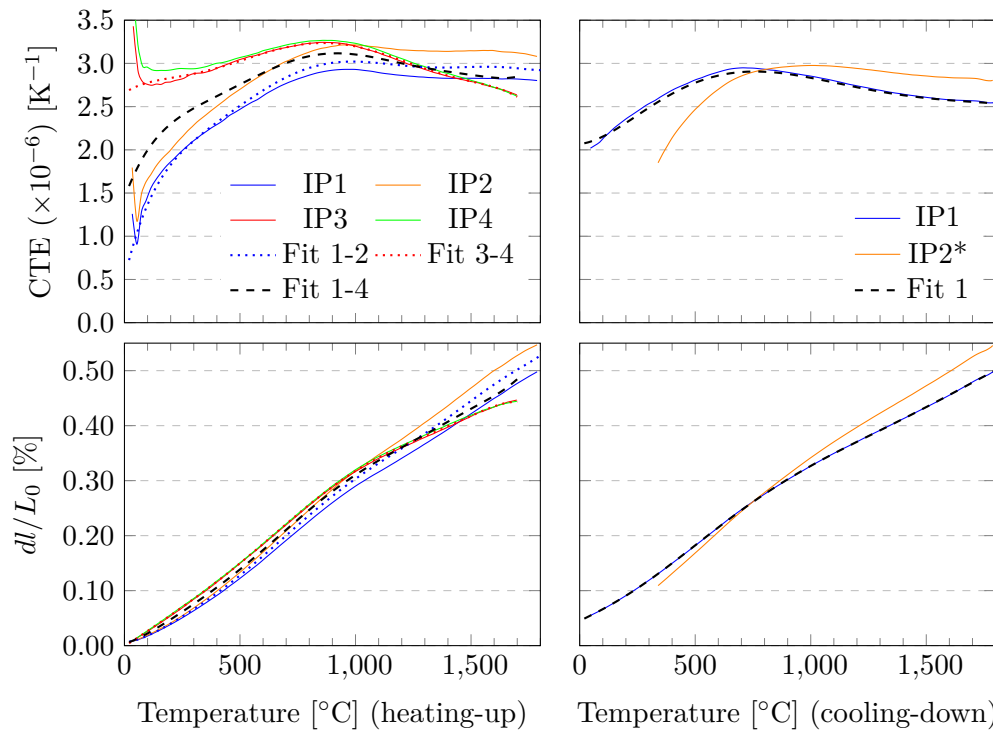
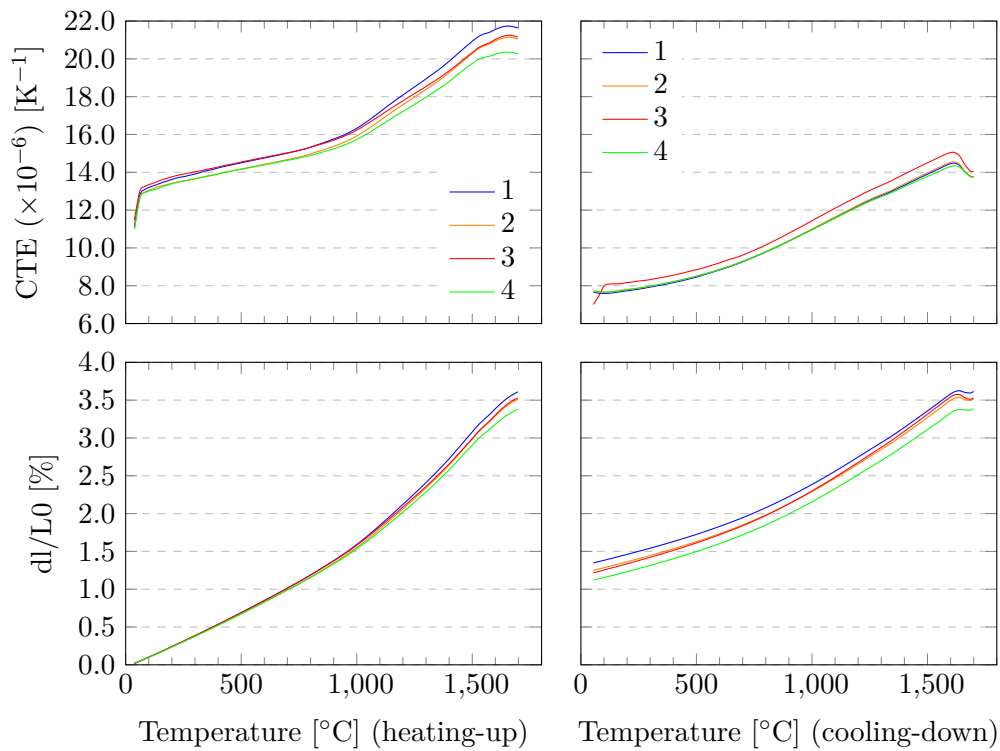


Figure 5.80: CTE CG-1100B0 IP. All specimens with length ≈ 25 mm. Fitting polynomials: IP1-2 up and IP1-4 up 9th degree, IP3-4 up and IP1 down 7th degree. (*) IP2-4 specimens suffered a data acquisition problem during cooling-down, only IP1 test is valid.

Figure 5.81: CTE CG-1100B0 TP. All specimens with length ≈ 15 mm.

5.6.5 Mechanical properties

The bending test curves are shown in Figure 5.82. In the IP direction, the average maximum strength is 31.2 ± 4.9 MPa and the average strain to rupture is $1640 \pm 560 \mu\text{m m}^{-1}$. In the TP direction, the average maximum strength is 6.6 ± 1.2 MPa and the average strain to rupture is $4240 \pm 780 \mu\text{m m}^{-1}$.

The nominal size of the specimens, the test jig span (L) and the loading span are listed below. All the test were made with four point configuration.

- IP1-IP5: $4 \times 10 \times 55$ mm, $L=50$ mm, loading span= $L/2$.
- TP1-TP6: $5 \times 10 \times 25$ mm, $L=20$ mm, loading span= $L/2$.

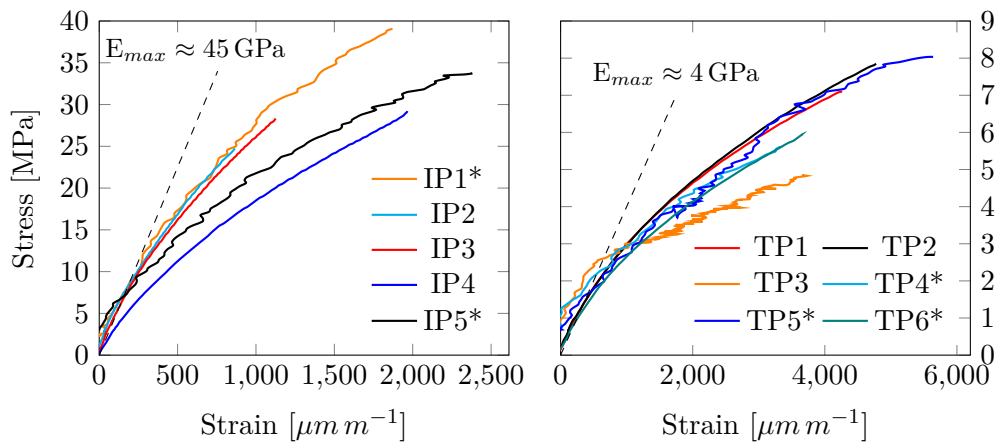


Figure 5.82: Flexural test CG-1100B0. (*) Specimens tested with laser extensometer.

Impact Excitation Technique (IET) results are shown in Table 5.28. The flexural and torsional resonance frequencies were acquired. The results from the Finite Element Modeling (FEM) analysis are reported in Table 5.29. It is shown that the results from the analytical formula are deviated with respect to the FEM optimisation, and show in fact non-physical derived Poisson's ratio. The FEM method is more accurate, in accordance with the elastic properties theory. The torsional frequency acquired in most of the IP specimens was actually other resonance mode, as there is a big mismatch with the FEM results. Apart from the usual IP and TP specimens, the 5 mm-thick plate shown in image 5.68 was tested with the IET method prior to cutting (named TP7 in Table 5.28). TP7 parallelepiped specimen provided extra information for the FEM optimisation, and due to its large size the density of CG-1100B0 grade was calculated from its dimensions with small uncertainty.

The Poisson's ratios do not have relevant influence in the resonance frequencies, (see section E.5), hence cannot be characterised with this method. For this reason, ν_{XY} and ν_{XZ} were set to 0.1 (not optimised), which is a reasonable value considering the composition of the material (see section E.6). ν_{YZ} is derived from E_Y and G_{YZ} , see equation E.8.

Table 5.28: IET test of CG-1100B0, experimental resonance frequencies of IP and TP specimens. Frequencies resulted from the FEM optimisation. (ff: flexural, ft: torsional). ρ calculated from mass and dimensions.

Specimen	m [g]	L [mm]	b [mm]	t [mm]	ρ [g cm ⁻³]	ff [kHz]	ft [kHz]
IP1	5.614	56.15	9.83	4.60	2.21	6.600	15.700
IP2	4.723	56.06	9.86	3.87	2.21	5.168	12.414
IP3	5.180	56.00	9.88	4.24	2.21	5.661	13.679
IP4	5.214	55.91	9.90	4.27	2.21	5.870	14.668
IP5	5.348	55.84	9.90	4.40	2.20	5.729	15.135
Average IP:		55.992	9.874	4.276	2.21	5.806	14.319
FEM optimisation:		(")	(")	(")	(")	5.864	12.963
TP1	2.765	22.97	9.98	5.46	2.21	12.326	21.000
TP2	2.504	22.96	9.98	4.93	2.22	11.200	19.990
TP3	2.612	22.96	9.99	5.14	2.22	11.600	20.385
TP4	2.714	22.96	10.00	5.32	2.22	12.080	21.252
TP5	2.748	22.95	10.01	5.38	2.22	12.090	21.290
TP6	2.774	22.95	10.01	5.39	2.24	12.090	21.325
Average TP:		22.958	9.995	5.270	2.22	11.898	20.874
FEM optimisation:		(")	(")	(")	(2.21)	12.016	20.954
TP7	28.663	105.81	22.94	5.34	2.21	2.140	5.900
FEM optimisation:		(")	(")	(")	(")	2.147	5.812*

(*)2nd torsional mode. 2nd flexural mode: 5.860 kHz. 1st tors.: 2.683 kHz.

Table 5.29: Elastic properties of CG-1100B0 resulted from the IET analysis.

	E_X	E_Y	E_Z	G_{XY}	G_{YZ}	G_{XZ}	ν_{YZ}	ν_{XY}	ν_{XZ}
FEM optimisation	3.8	42.8	42.8	3.5	18.1	3.5	0.184	0.1	0.1
Analytical ¹	4.0	39.3	39.3	3.5	12.3	3.5	0.600 ²	-	-

¹ From analytical formula (ASTM C1259-01), for comparison purposes.

² Non-physical, derived from E_Y and G_{YZ} , see equation E.8.

5.7 Chromium carbide - graphite CG-1240X

CG-1240X material belongs to the Chromium carbide - graphite family, similarly to CG-1100Ba (section 5.4). The material CG-1240X production parameters are shown in section 4.6, the main novelty in this grade is the use of very large graphite flakes (Asbury 3763 grade, see section 4.1.2).

Unfortunately the production process failed due to the breakage of the graphite mould around the plate, which caused also the partial rupture of the sintered plate and the sudden stop of the cycle, see Figure 5.83. The mould breakage is discussed in section 6.6. However, due to reason of time, another production attempt was not possible, and it was decided to characterise the ruptured plate because of the relevance of this new composition. The pieces used for obtaining of the samples were the biggest ones available, coming from the plate edge.



Figure 5.83: Sintering failure of plate CG-1240X. Plate surface is 150×100 mm.

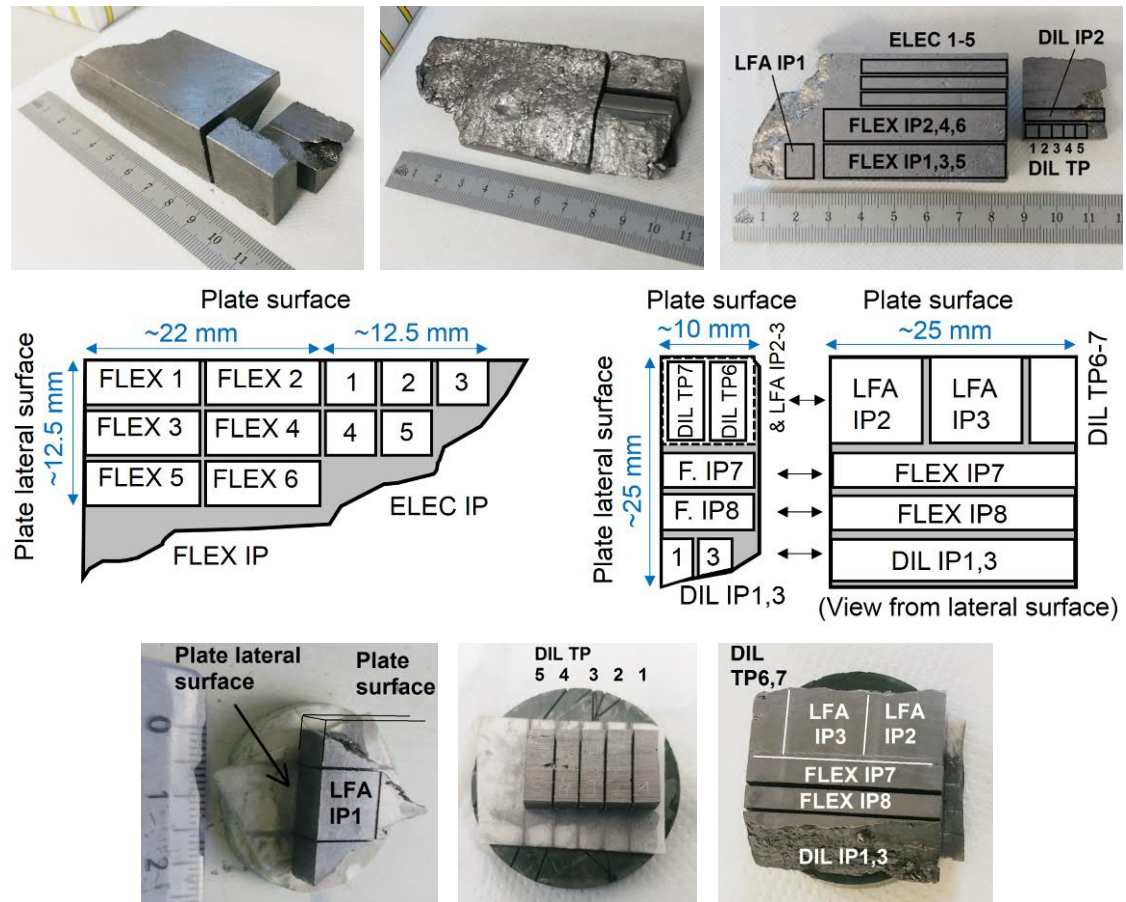


Figure 5.84: Specimens for characterisation obtained from CG-1240X plate.

5.7.1 Microstructure

Figures 5.85 and 5.86 show SEM observations of polished CG-1240X TP surfaces (pressing force was vertical). The observation area is ~ 15 mm far from the lateral plate surface, at around mid-thickness of the plate, therefore representing the bulk material.

The images show a connected graphite matrix (dark) with chromium carbide particles (bright). The electron channelling in the backscattered electron (BE) images allow identification of graphite domains. The domains are large, with a -axis dimension around $700\text{--}800\ \mu\text{m}$ and c -axis dimensions around $30\ \mu\text{m}$, similarly to the parent graphite powder (see Section 4.1.2). The texture of these domains is not perfectly perpendicular to the pressing force, showing some waviness in the flakes, which helps in reducing anisotropy. The matrix shows moderate content of voids, which are probably produced during the mould breakage event.

The carbide particles are clearly elongated between the graphite domains, with size ranging from 2 to around $20\ \mu\text{m}$, the average being in the order of $10\ \mu\text{m}$.

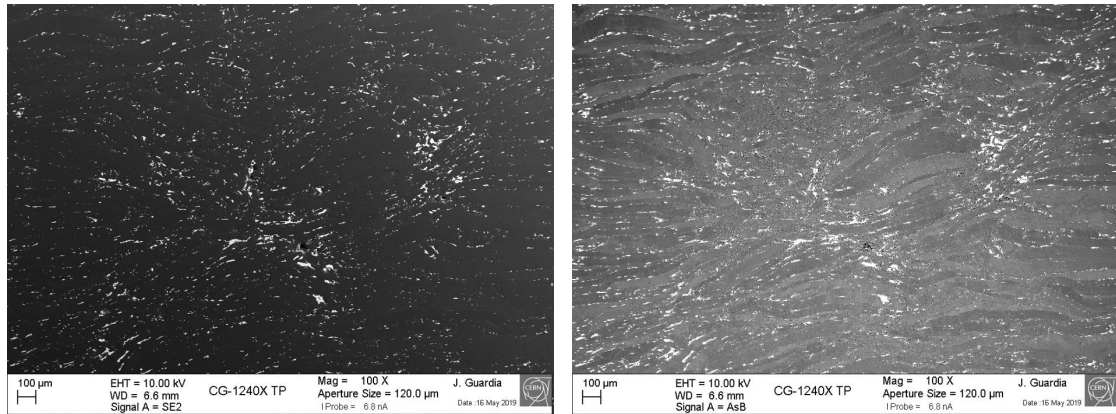


Figure 5.85: SEM observations of CG-1240X TP surface, pressing force was vertical. (Left) SE image. (Right) BE image. The BE image shows channeling effect in graphite, allowing identification of crystalline domains.

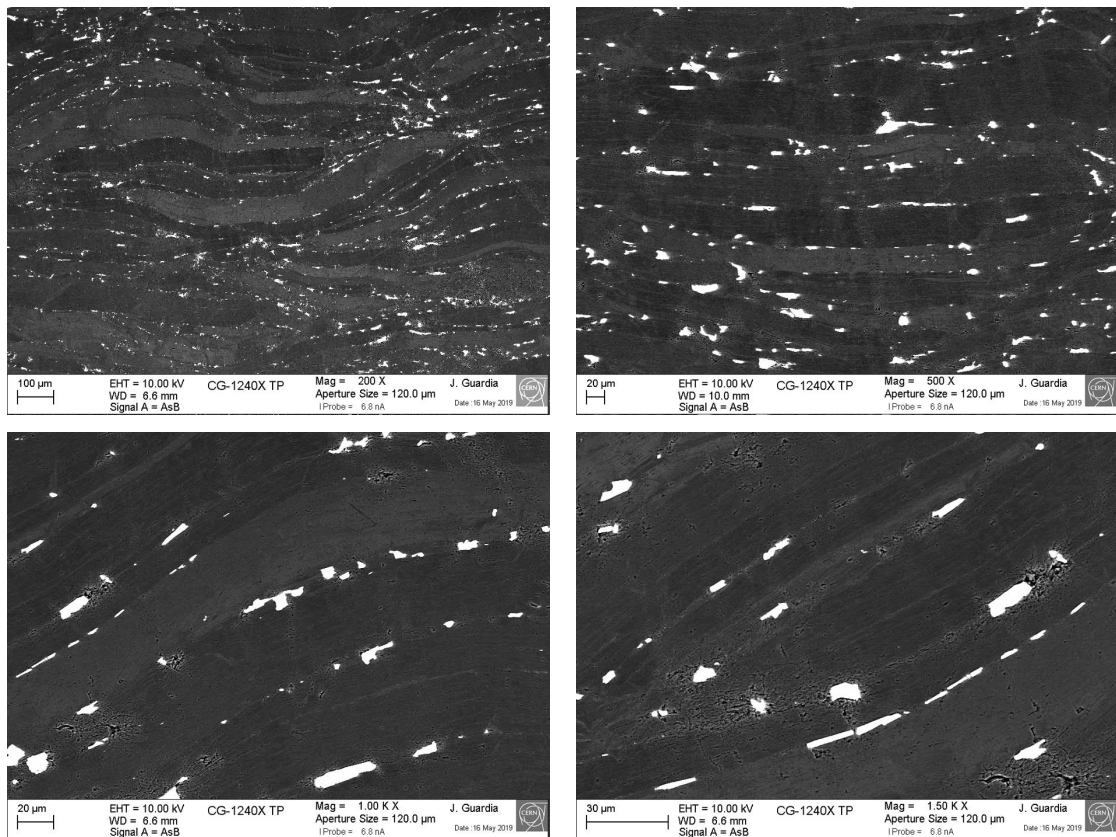


Figure 5.86: SEM observations of CG-1240X TP surface at high magnifications, pressing force was vertical. All BE images, showing channeling effect in graphite, which allows identification of crystalline domains.

5.7.2 Crystallography and lattice thermal expansion

Figure 5.87 shows the acquired patterns on the CG-1240X TP sample. The TP surface was sanded with P1200 sandpaper. The test shows that no new peaks due to oxidation. The intensity of the (002) peak decreases after the stay at high temperature. On the other hand, the intensity of the (110) slightly increases. This is most likely caused by the removal of superficial bent flakes on the TP surface, by combustion in air. The removal

exposes more the inner TP surface, and the $hk0$ planes produce stronger reflections. Note the differences in shifting of the peaks, related to different thermal expansion behaviour.

In this grade, differing from CG-1100Ba, there are two chromium carbide phases. The Cr_3C_2 phase is present, but also the $\text{Cr}_3(\text{C,N})_2$ modification of the latter. In CG-1100Ba only the modified structure was present.

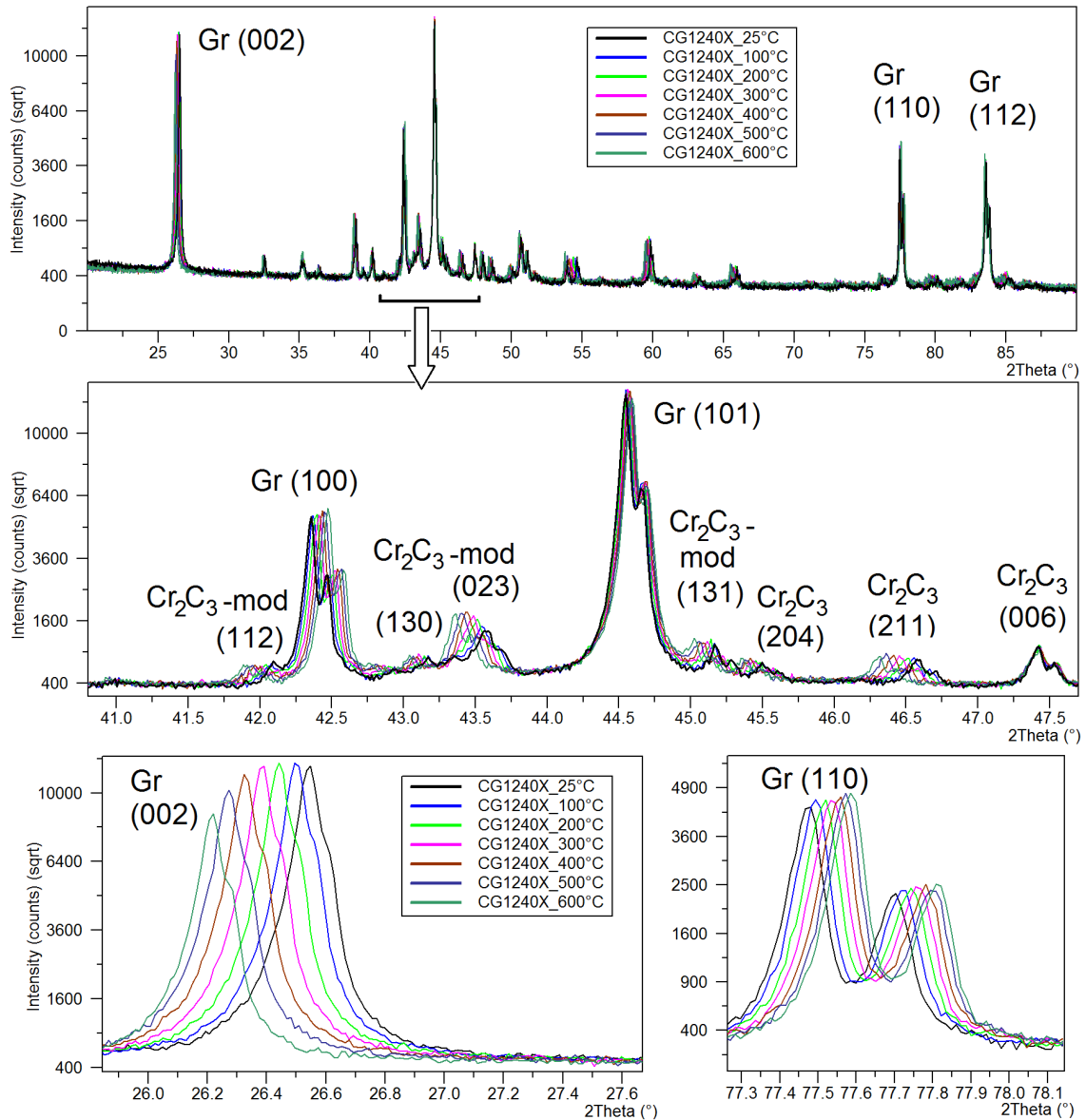


Figure 5.87: CG-1240X TP experimental XRD patterns.

Tables G.5, G.6 and G.7 (Appendix G) list the corrected peak positions and the results of the lattice parameters of graphite and the two carbide phases. The specimen displacement correction s is calculated as explained in section 3.5.2.

Second degree polynomials are fitted to the data, see Table 5.30. Figures 5.88, 5.89 and 5.90 show the experimental lattice parameters of all phases present in CG-1240X, both the measurements and the fitting curve. The graphite parameters from the literature are also reported for comparison, indicating complete graphitisation.

Table 5.30: Lattice parameter 2nd degree polynomial fitting equation (heating-up curves)

	A	B	C	Value at 20°C [Å]
a Gr.	$3.5605 \cdot 10^{-9}$	$-3.1379 \cdot 10^{-6}$	2.4622	2.4621
c Gr.	$2.1211 \cdot 10^{-8}$	$1.7933 \cdot 10^{-4}$	6.7069	6.710
a Cr ₂ C ₃	$6.1980 \cdot 10^{-9}$	$7.1972 \cdot 10^{-5}$	5.5250	5.526
b Cr ₂ C ₃	$1.2807 \cdot 10^{-8}$	$3.1407 \cdot 10^{-5}$	2.8283	2.829
c Cr ₂ C ₃	$3.9589 \cdot 10^{-8}$	$2.2640 \cdot 10^{-5}$	11.4920	11.493
a Cr ₃ (C,N) ₂	$4.0023 \cdot 10^{-9}$	$3.1088 \cdot 10^{-5}$	2.8473	2.848
b Cr ₃ (C,N) ₂	$2.9379 \cdot 10^{-8}$	$4.1927 \cdot 10^{-5}$	9.2640	9.265
c Cr ₃ (C,N) ₂	$2.6985 \cdot 10^{-8}$	$7.6957 \cdot 10^{-5}$	6.9620	6.964

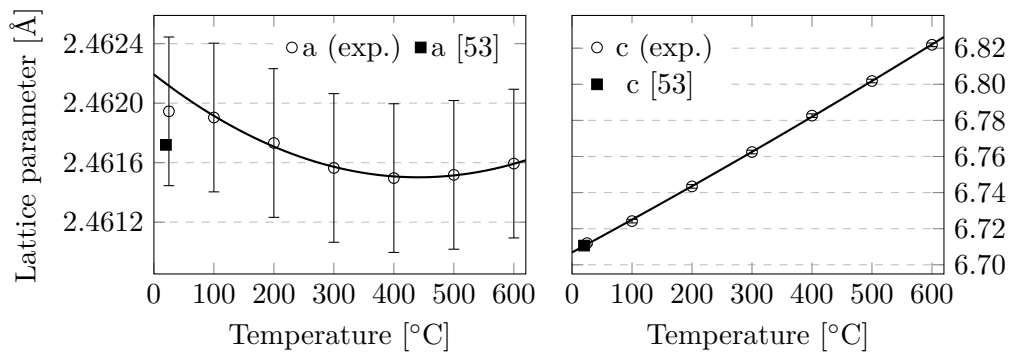
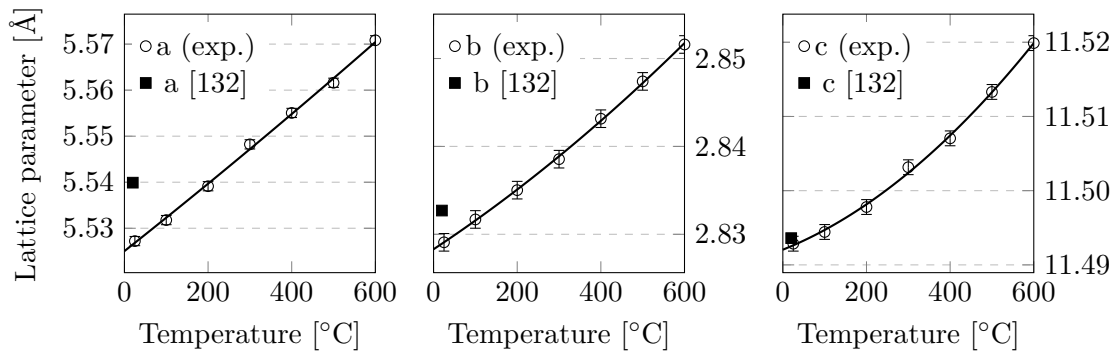
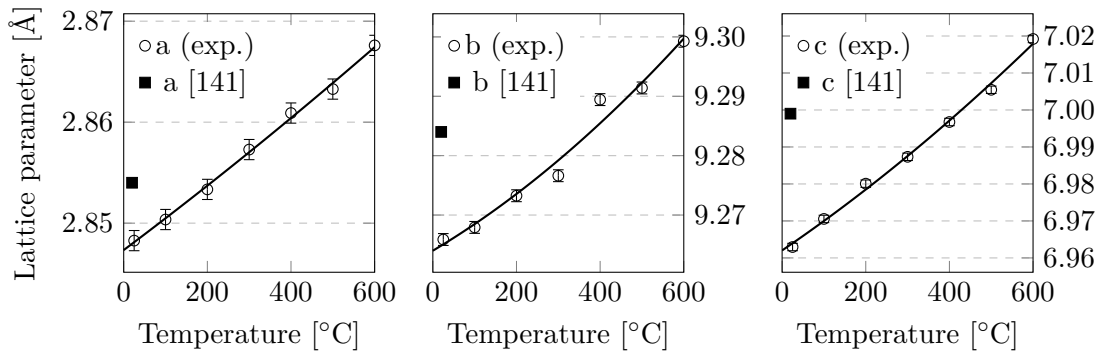


Figure 5.88: Lattice parameters versus temperature of graphite in CG-1240X.

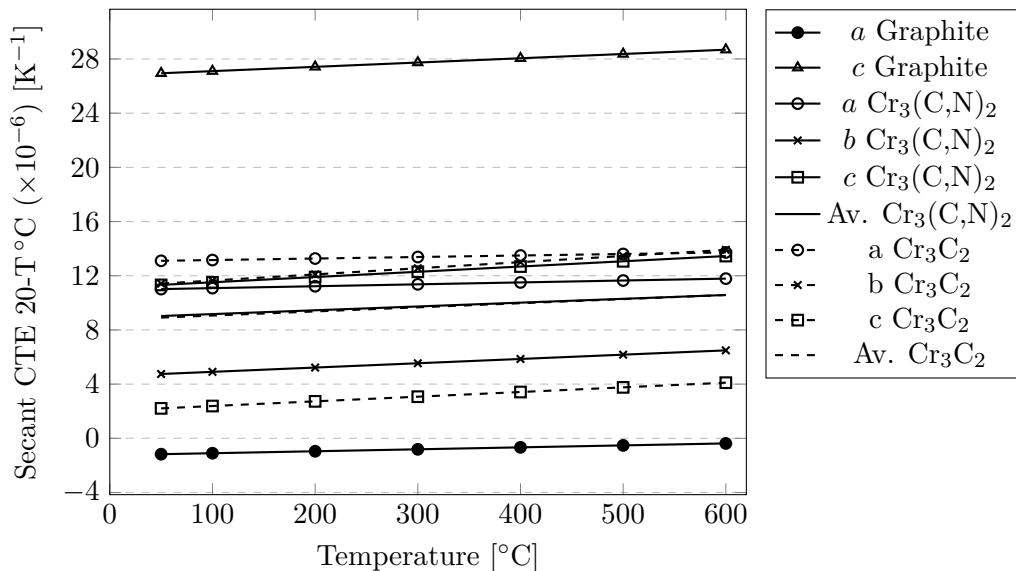
Figure 5.89: Lattice parameters versus temperature of Cr₃C₂ in CG-1240X.

Figure 5.90: Lattice parameters versus temperature of $\text{Cr}_3(\text{C,N})_2$ in CG-1240X.

The CTE is calculated from the fitting curves, the results are shown in Table 5.31 and Figure 5.91.

Table 5.31: Result of the secant CTE 20-T °C of graphite and $\alpha\text{-MoC}_{1-x}$ in CG-1240X TP ($\times 10^{-6} \text{ m}^{-1} \text{ K}^{-1}$). Heating-up ramp.

T [°C]	Graphite		Cr_2C_3				$\text{Cr}_3(\text{C,N})_2$			
	a	c	a	b	c	Av.	a	b	c	Av.
50	-1.2	26.9	13.1	11.4	2.2	8.9	11.0	4.7	11.3	9.0
100	-1.1	27.1	13.2	11.6	2.4	9.1	11.1	4.9	11.5	9.2
200	-1.0	27.4	13.3	12.1	2.7	9.4	11.2	5.2	11.9	9.5
300	-0.8	27.7	13.4	12.6	3.1	9.7	11.4	5.5	12.3	9.7
400	-0.7	28.1	13.5	13.0	3.4	10.0	11.5	5.9	12.7	10.0
500	-0.5	28.4	13.6	13.5	3.8	10.3	11.6	6.2	13.1	10.3
600	-0.4	28.7	13.7	13.9	4.1	10.6	11.8	6.5	13.5	10.6

Figure 5.91: Secant CTE 20-T °C of graphite, Cr_3C_2 and $\text{Cr}_3(\text{C,N})_2$ in CG-1240X (from XRD).

5.7.3 Electrical conductivity

Bulk electrical conductivity measurements on CG-1240X grade, IP direction, are shown in Table 5.32. The 5 specimens shown in the schematic of Figure 5.84 were measured, giving an average resistivity of $0.95 \mu\Omega \text{ m}$ or conductivity 1.06 MS m^{-1} , the best specimen (No 3) resulted in 1.15 MS m^{-1} .

Table 5.32: 4-wire DC method electrical measurements on CG-1240X, see section 3.4.

	Sample 1	Sample 2	Sample 3	Sample 4	Sample 5	Average
d_1 [mm]	3.78	3.76	3.81	3.74	3.48	
d_2 [mm]	4.03	3.70	3.60	3.91	3.88	
d_3 [mm]	~ 45	~ 45	~ 45	~ 45	~ 45	
L [mm]	30.0	30.0	30.0	30.0	30.0	
Current [mA]	1000	1000	1000	1000	1000	
Av. Voltage [μV]	2000	2120	1900	1950	2070	
ρ_e [$\mu\Omega \text{ m}$]	1.02	0.98	0.87	0.95	0.93	0.95
γ_e [MS m^{-1}]	0.98	1.02	1.15	1.05	1.07	1.06

The superficial eddy-current electrical conductivity test (960 kHz) was performed on the specimens from bending test, see Figure 5.84. The results are shown in Figure 5.92 ($1.02 \pm 0.16 \text{ MS m}^{-1}$).

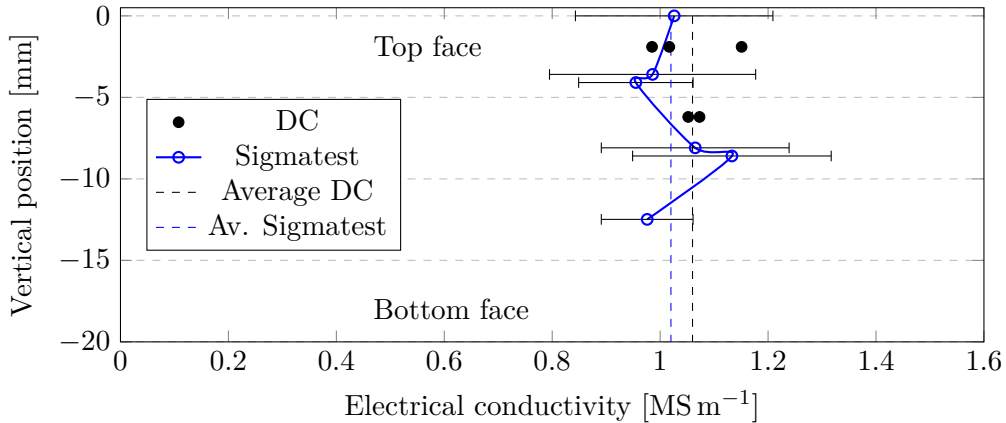


Figure 5.92: Electrical conductivity measurements on CG-1240X (IP), measured along plate thickness. Error bars represent the standard deviation.

There is not a clear variation along the plate thickness. However, the dispersion of the results is large, with maximum values of 1.13 MS m^{-1} (eddy-current test) and 1.15 MS m^{-1} (DC).

5.7.4 Thermophysical properties

The average density at RT measured on all FLEX IP, DIL TP and ELEC IP specimens (Archimede's method) is $2.26 \pm 0.03 \text{ g cm}^{-3}$. During the liquid immersion weighting, the value was slightly increasing with time due to absorption of ethanol and release of air. This is due to the presence of voids or cracks. The density value reported is measured quickly after the first immersion, to take into account the open porosity.

The IP thermal diffusivity and the specific heat of CG-1240X are shown in Figures 5.93 and 5.95 respectively. The mathematical functions that fit the experimental data are shown in the plots. The conductivity is calculated from the diffusivity and specific heat fitting curves, assuming constant density (2.26 g cm^{-3}), see Figure 5.96.

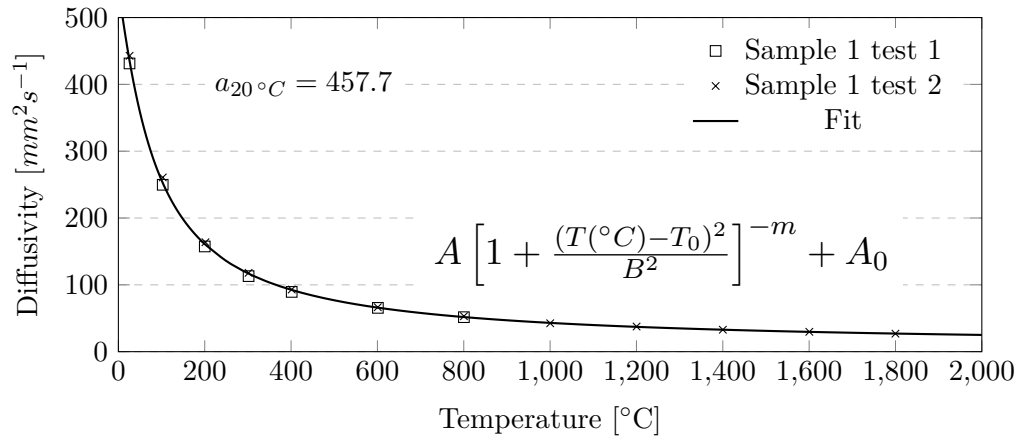


Figure 5.93: Thermal diffusivity of CG-1240X IP. Fitting equation constants: $A = 698.7$, $B = 57.52$, $T_0 = -47.20$, $m = 0.5085$ and $A_0 = 6.581$. All specimens with thickness $\approx 7.5 \text{ mm}$.

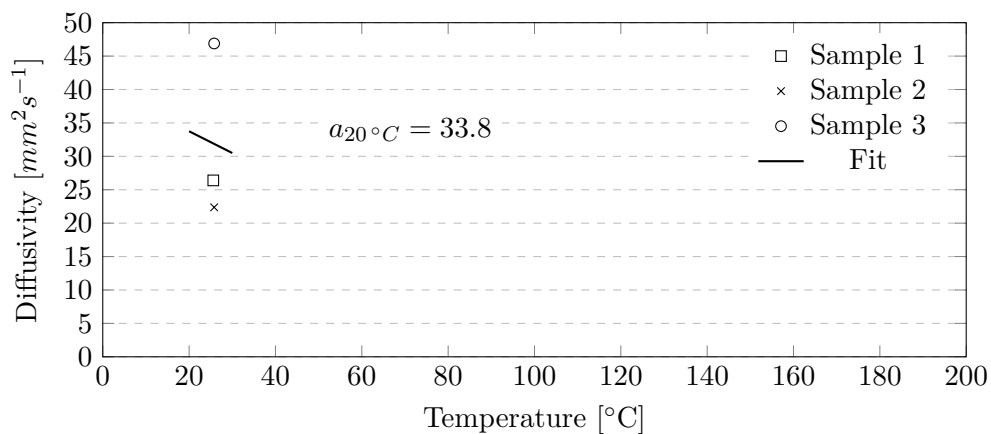


Figure 5.94: Thermal diffusivity of CG-1240X TP. All specimens with thickness $\approx 2 \text{ mm}$. Only measurements at RT are available; the fit is obtained from the average value, using the slope of $a_{CG-1100B0 \text{ TP}}$.

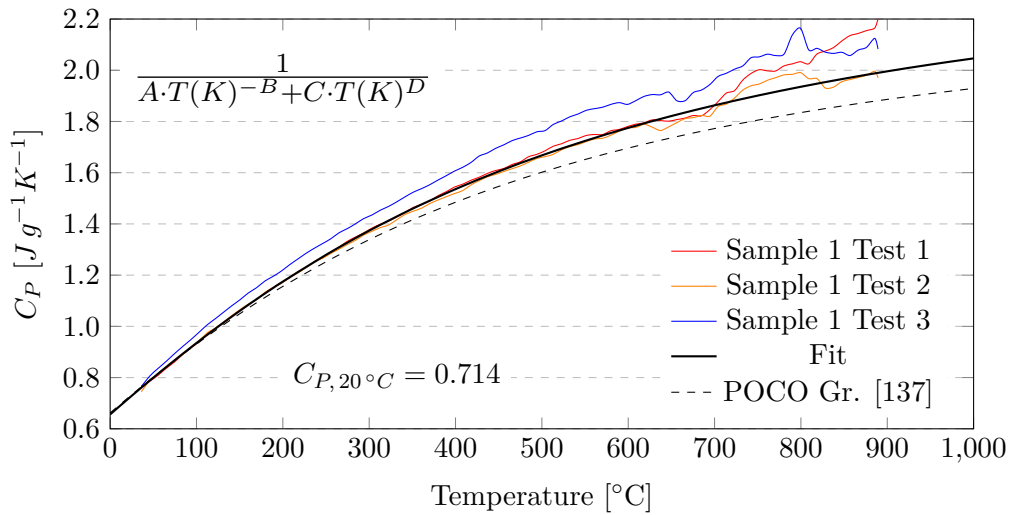


Figure 5.95: Specific heat of CG-1240X. Fitting equation constants: $A = 11.54$, $B = 1.644$, $C = 3.403\text{E-}4$ and $D = 0.02191$.

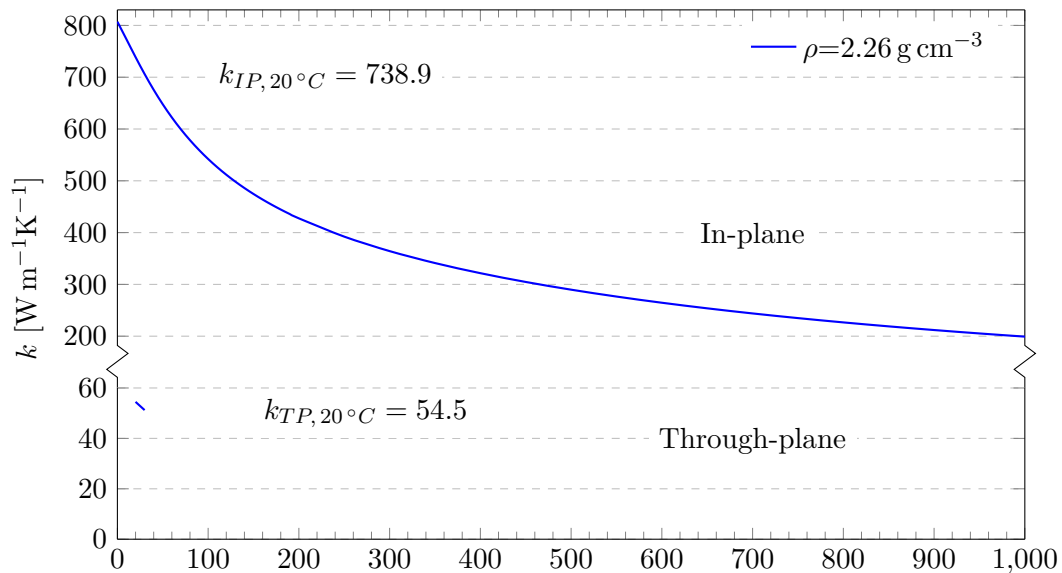


Figure 5.96: Thermal conductivity of CG-1240X in both directions. TP direction was characterised only at RT. Calculated from constant density.

Thermal expansion measurements (IP and TP) are shown in Figures 5.97 and 5.98. The tests were performed in the range RT–700 °C.

The dl/L_0 TP curves were not fitted with polynomials due to the big differences between samples. In the IP direction, the difference of CTE between heating-up and cooling-down ramps is very subtle, indicating good stability to the thermal cycle applied. The dashed black line in Figure 5.97 represents the fitting curve.

Specimens TP6 and TP7 were cut from positions less than 10 mm far from the lateral plate edge, while TP1 and TP3 are representing the bulk material, see Figure 5.84. The specimens closer to the surface show lower CTE values, possibly corresponding to slightly higher carbide content. They also show larger residual deformation than specimens TP1 and TP3.

The artefacts at the extremities of the dl/L_0 curves, amplified in the CTE curves, are typically due to unsteady heating/cooling rate. They are more common in the heating up ramp up to $\sim 100^\circ\text{C}$. The fitting curve smooths out this experimental error.

The change in length (residual strain) of the specimens was measured with a micrometer, being only -0.01% in the IP specimens, and 0.07% in the TP specimens, see Table 5.33. The dl/L_0 curves confirm this behaviour. The relaxation of internal stresses in both directions is very small, compared to other grades. This is possibly due to the low maximum temperature reached in the dilatometry test ($\sim 700^\circ\text{C}$), compared with other grades which reached $\sim 1800^\circ\text{C}$.

The IP cooling-down CTE (extrapolated) is $2.3 \times 10^{-6} \text{ K}^{-1}$ in the range $20\text{--}1000^\circ\text{C}$.

Table 5.33: Length of the CG-1240X specimens before and after the dilatometer measurement, measured with a micrometer (mm).

	In-plane			Through-plane			
	L_0	L_{final}	Var. [%]	L_0	L_{final}	Var. [%]	
IP1	24.585	24.584	-0.004	TP1	10.237	10.236	-0.010
IP2	24.609	24.604	-0.020	TP3	10.253	10.253	0.000
IP3	24.569	24.571	0.008	TP6	9.729	9.746	0.175
				TP7	9.681	9.693	0.124
Average			-0.01			0.07	

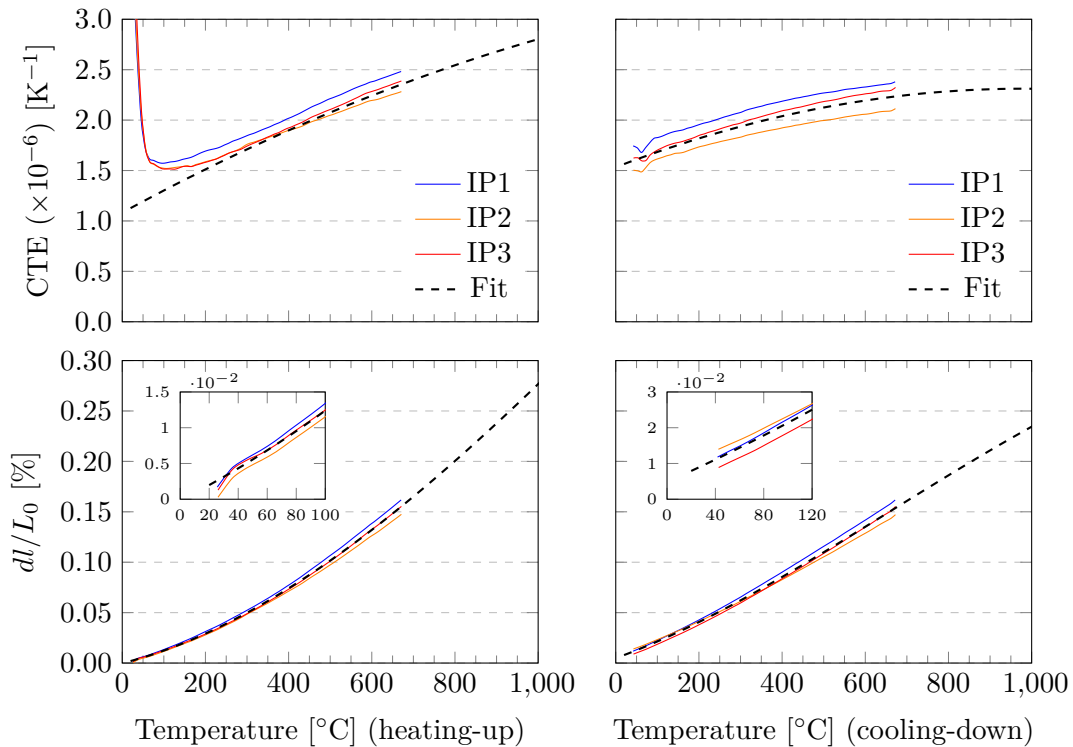


Figure 5.97: CTE CG-1240X IP. All specimens with length ≈ 25 mm. Fitting polynomials are all 3th degree.

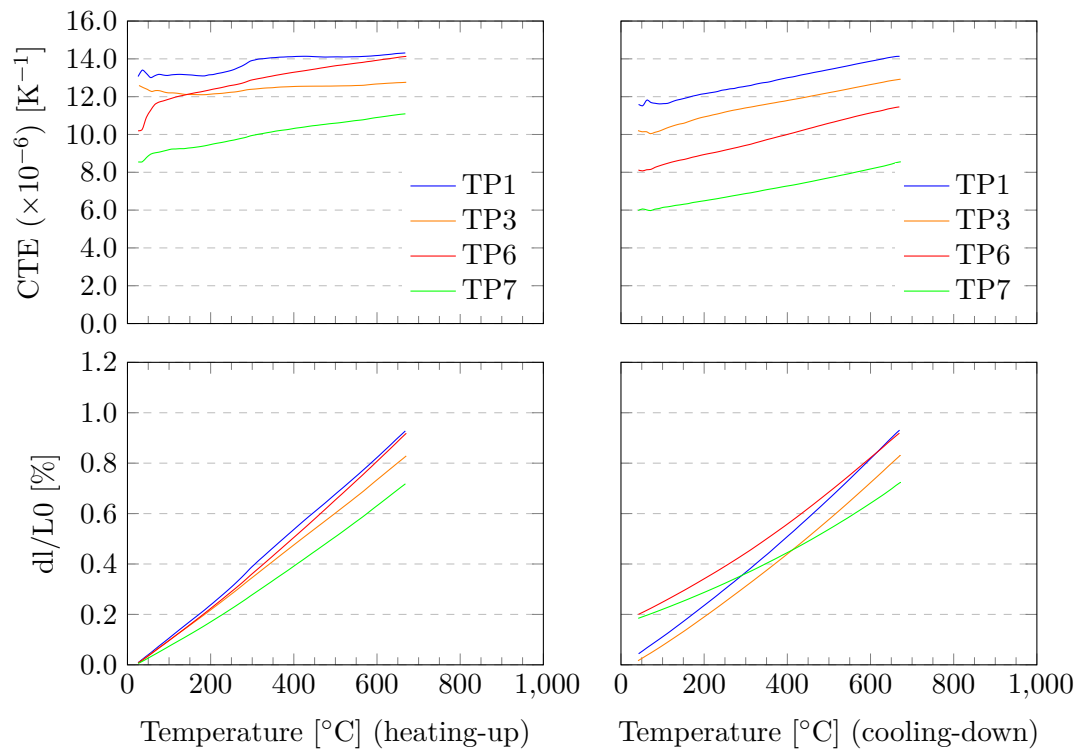


Figure 5.98: CTE CG-1240X TP. All specimens with length ≈ 10 mm.

5.7.5 Mechanical properties

The bending test curves are shown in Figure 5.99. In the IP direction, the average maximum strength is 15.0 ± 2.7 MPa and the average strain to rupture is $2370 \pm 1020 \mu\text{m m}^{-1}$.

Note how the smaller specimens (7 and 8) show better strength and strain to rupture, with average values of 18.6 ± 0.2 MPa and $3680 \pm 10 \mu\text{m m}^{-1}$. This is due to the relevance of cracks in the strength of these brittle materials. The smaller volume under stress results in lower failure probability (crack propagation), due to the smaller amount of cracks.

The Impact Excitation Technique (IET) was not performed on this grade due to the difficulties to obtain TP specimens from the available material. The slope in the elastic domain of the bending test plot shows a maximum Young's modulus of around 20 GPa. Specimen IP5 shows a different, more stiffer behaviour than the others.

The nominal size of the specimens, the test jig span (L) and the loading span are listed below. All the test were made with four point configuration.

- IP1-IP6: $4 \times 11 \times 55$ mm, L=50 mm, loading span=L/2.
- IP7-IP8: $3 \times 11 \times 25$ mm, L=20 mm, loading span=L/2.

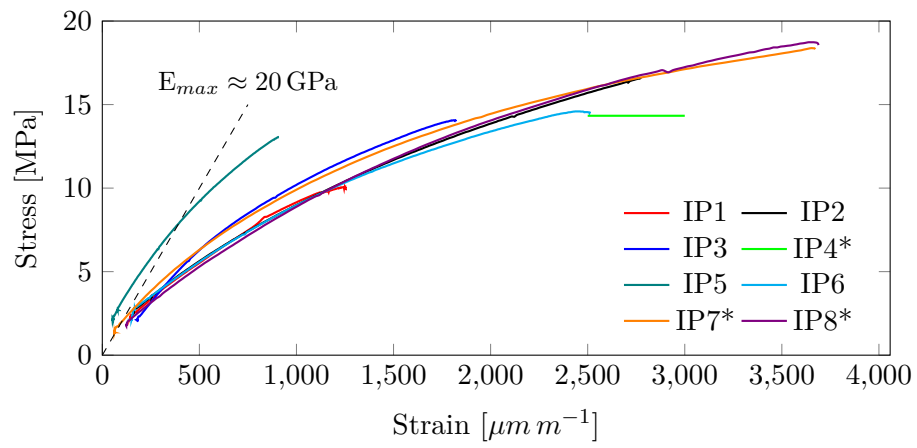


Figure 5.99: IP bending test of CG-1240X grade. (*) IP4 specimen not instrumented with strain gauge, IP7-8 specimens are of different size, see below.

6 | Discussion

This chapter contains the discussion of results from all investigated materials, which were presented in chapter 5. The knowledge acquired from the different comparisons between materials is reported.

The structure of this chapter is as follows. First, the microstructure of the graphite matrix and carbide particles is discussed. Second, the effects of some important production parameters are detailed. Then, the summarized results of the thermo-physical characterisation are reported for all the investigated materials. At the end of the chapter, the catalytic graphitisation effect of chromium and molybdenum liquid phases are discussed.

6.1 Microstructure

6.1.1 Carbide particles

Chromium carbide phases

The carbide phase identified in grades CG-1100B0 and CG-1100Ba ($\text{Cr}_3(\text{C,N})_2$) is a modification of Cr_3C_2 orthorhombic structure [140]. This phase is probably stabilized by nitrogen from air trapped in the sintered body during the compaction processes. More details have been reported in Section 5.4.2.

However, in grade CG-1100A0, sintered for half of the time than the other two materials (see Table 4.14), the Cr_3C_2 phase appears as well (Figure 5.59). It is interesting that the high temperature pressure-less heat treatment performed to CG-1100Ba grade did not affect to the phase $\text{Cr}_3(\text{C,N})_2$. It would be expected that nitrogen could be released by diffusion processes to the primary vacuum at the treatment chamber. The solidified LP that spilled out from the mould into the furnace chamber shows only the Cr_3C_2 phase (shown in Figure 5.43).

These results indicate that the lower level of internal compaction (grade CG-1100A0) prevents the complete process that diffuses nitrogen in the carbide structure to stabilise the $\text{Cr}_3(\text{C,N})_2$ phase. Once the material reaches higher compaction state, this phase remains stable, even after the thermal treatment at liquid-phase temperature ($\sim 2000^\circ\text{C}$). However, when the Cr-C(-N) LP spills out from the mould, the nitrogen is released, changing phase to the original Cr_3C_2 .

The reason of the stabilization of $\text{Cr}_3(\text{C,N})_2$ needs further investigation. The behaviour observed in the dilatometry measurements may indicate phase transitions. For this reason, the presence of only Cr_3C_2 phase in the composites may be preferable.

Molybdenum carbide phases

The undoped molybdenum carbides, formed upon solidification of the eutectic mixture, experience three changes of phase until complete cool-down at RT, as shown in the Mo-C binary diagram (Figure 2.14). Several phase changes were detectable in the dilatometer measurements, due to the change in density of the carbide phases [37].

The FCC carbides of molybdenum ($\alpha\text{-MoC}_{1-x}$) and titanium (TiC) exhibit completely solid solubility between them, resulting in a carbide phase $(Ti_{1-x}, Mo_x)_{1-y}C_y$, labelled δ in the ternary diagram, which is stable over a wide range of temperatures and stoichiometries [37]. The effect of small quantities of titanium in MoGr, around one titanium atom every 10 molybdenum atoms, appears to be sufficient to turn all molybdenum carbide into the FCC phase ($\alpha\text{-MoC}_{1-x}$), over the full range of temperatures of interest.

XRD analyses performed in grades with titanium revealed the absence of hexagonal or orthorhombic molybdenum carbides and the presence of a FCC phase, with $a = 4.264 \text{ \AA}$, except a trace amount of $\eta\text{-MoC}_{1-x}$ in grade MG-6403Fc, probably due to the change in thermal treatment (Figure 6.1). According to the phase diagram Mo-C (Figure 2.14), the cubic $\alpha\text{-MoC}_{1-x}$ phase is stable only above 1960°C , thus it is being stabilized down to RT with the Ti addition.

The absence of phase changes in the material is believed to be beneficial during beam impact scenarios, which could locally raise the temperature of collimator absorber materials to thousands of degrees.

Apart from graphite peaks, grade MG-6530Aa containing no titanium shows multiple peaks matching those of dimolybdenum carbide Mo_2C and of hexagonal $\eta\text{-MoC}_{1-x}$ phases. According to the phase diagram, the hexagonal $\eta\text{-MoC}_{1-x}$ is only stable above 1655°C , while here it is found at RT; this was also observed by Matthews [60] and was explained by that phase being easily retained during furnace cooling. Dimolybdenum carbide Mo_2C phase suffers a transition between the orthorhombic $\zeta\text{-Fe}_2\text{N-type}$ "low temperature" phase and the hexagonal $\epsilon\text{-Fe}_2\text{N-type}$ based "middle temperature" phase at $\sim 1350^\circ\text{C}$, and then an order-disorder transition into a $L'3\text{-type}$ structure at around $\sim 1960^\circ\text{C}$ [142, 143]. Due to the negligible X-ray scattering factor of carbon compared with molybdenum, the orthorhombic $\zeta\text{-Mo}_2\text{C}$ phase shows only peaks from the hexagonal partial structure of the molybdenum atoms. Parthé and Sadagopan [144] showed that neutron diffraction is a more appropriate technique for the Mo_2C phase identification. The relationship between the orthorhombic structure and the hexagonal molybdenum sublattice is given by: $a_{orth} = c_{hex}$, $b_{orth} = 2 \cdot a_{hex}$ and $c_{orth} = \sqrt{3} \cdot a_{hex}$. The detected dimolybdenum carbide Mo_2C phase corresponds to orthorhombic $\zeta\text{-Mo}_2\text{C}$, but Figure 6.1 shows only the peaks corresponding to its hexagonal molybdenum partial structure. More details about the molybdenum carbide phases can be found in reference [37].

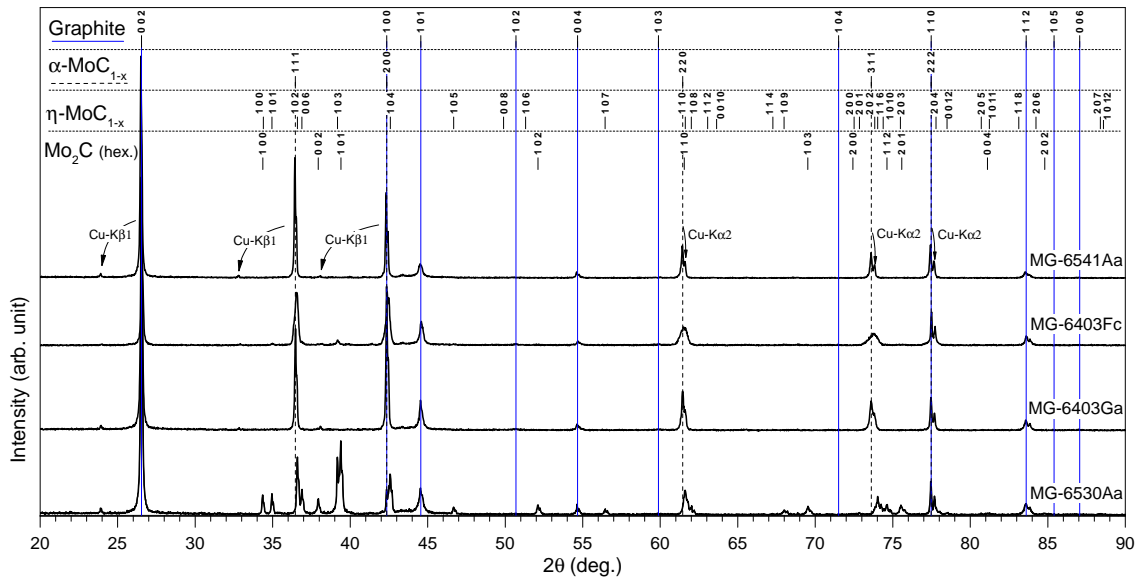


Figure 6.1: XRD comparison of four MoGr grades.

Nanoindentation tests on Molybdenum carbides

Nanoindentation tests were performed on 13-15 different carbide particles of each of four MoGr grades. Only the loading part of the test was acquired, therefore the Young's modulus measurement is not available. Either the small size of the particles, in the order of $5\ \mu\text{m}$, or the relatively low rigidity of the graphite matrix, led to many non-valid tests.

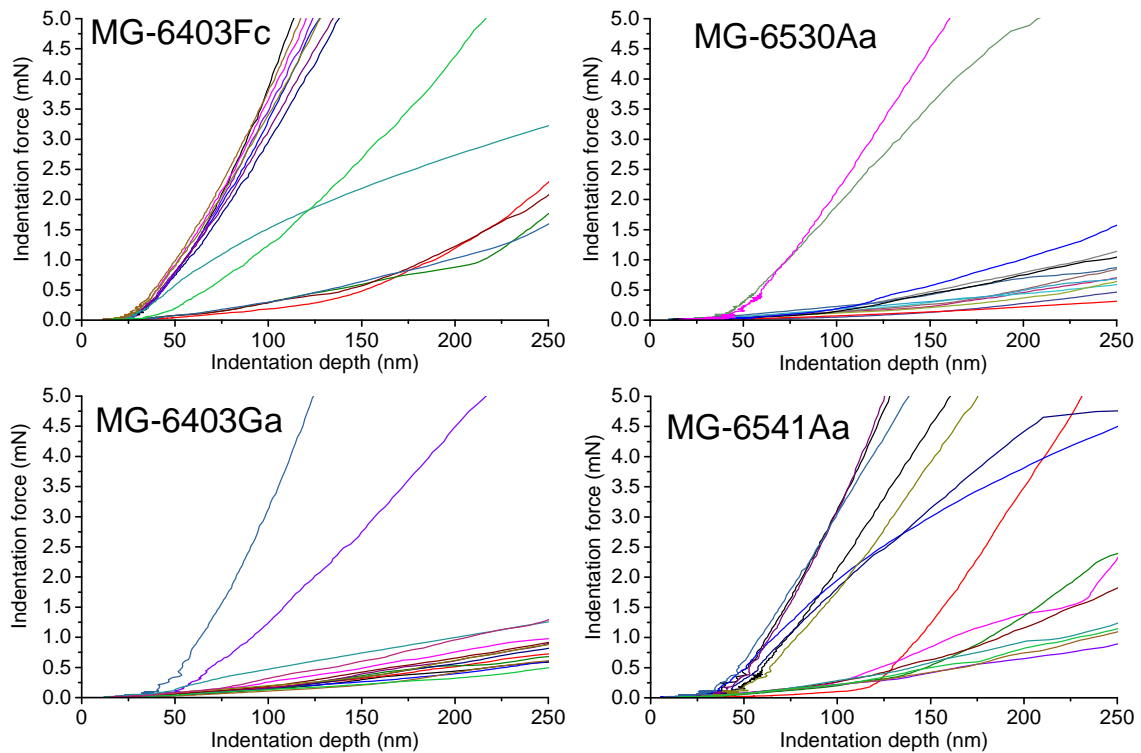


Figure 6.2: Nanoindentation tests on carbide particles. Force versus indentation depth.

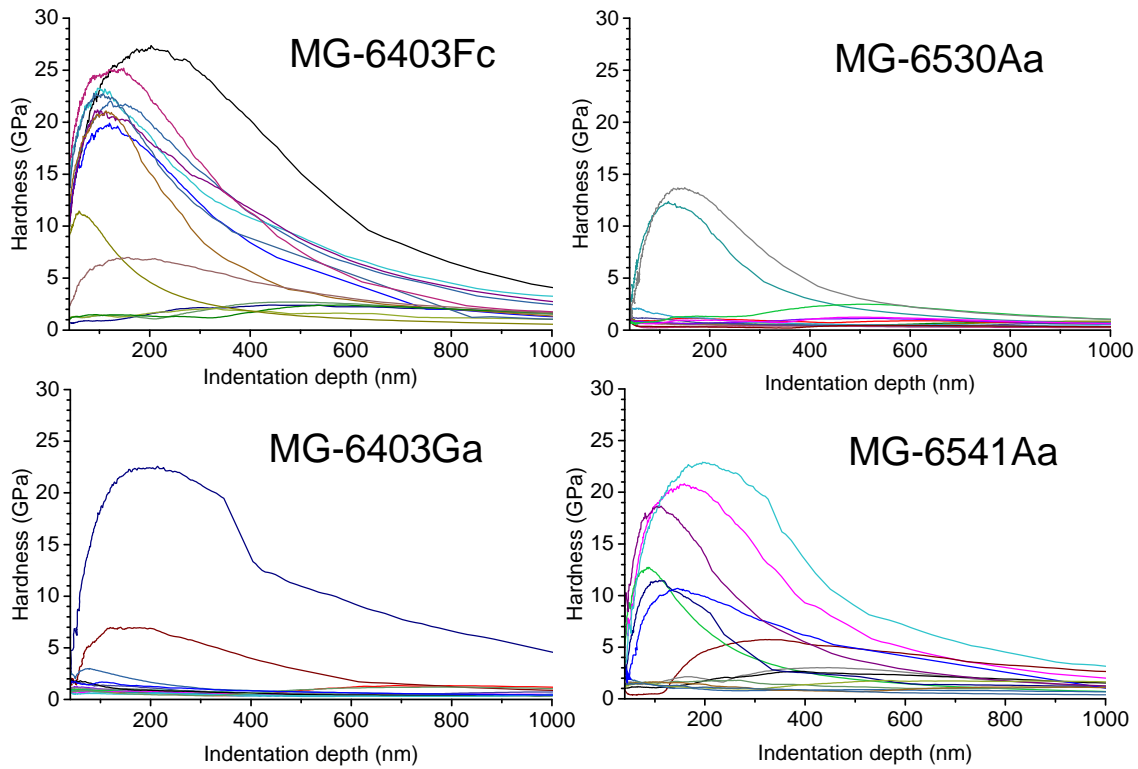


Figure 6.3: Nanoindentation tests on carbide particles. Hardness versus indentation depth.

Table 6.1 lists the values of hardness obtained from the hardness-penetration relevant curves. From the 4 grades tested, only MG-6530Aa had no Ti addition, therefore not containing the FCC $\alpha\text{-MoC}_{1-x}$ carbide phase. The other 3 materials, as shown in Figure 6.1, contain almost exclusively the FCC carbide [37]. Results presented in Table 6.1 show that the FCC carbide is slightly harder than the hexagonal/orthorhombic carbides present in MG-6530Aa. As described above, this statement is only preliminary due to the low repeatability and experimental difficulties when measuring these small carbide particles embedded in a soft graphite matrix.

Table 6.1: Hardness results [GPa] from nanoindentation tests, peak values. Only tests showing values within 30% of the maximum value are reported.

Test	MG-6403Fc	MG-6403Ga	MG-6541Aa	MG-6530Aa
1	27.1	22.4	22.8	13.6
2	25.1		20.8	12.3
3	23.1		18.7	
4	22.7			
5	21.6			
6	21.1			
7	21			
8	19.7			
Average	22.7	22.4	20.8	13.0
Standard dev.	2.4	-	2.1	0.9

Lattice thermal expansion of the carbide particles

Lattice parameters of the two Chromium carbide phases identified in the investigated materials are shown in Figures 6.4 and 6.5. Their coefficients of thermal expansion (CTE, α) in all crystallographic orientations, calculated as shown in Section 3.5.2, are shown in Figure 6.6.

The comparison of the average CTE's of all Cr and Mo carbides identified in the investigated materials is shown in Figure 6.7. These average CTE's are calculated as the sum of the three orthogonal CTE's divided by three.

Several conclusions are extracted from these results:

- Cr_3C_2 phase behaves similarly in the initial powder than in grade CG-1240X. Their average CTE is almost identical. The measured lattice parameters at RT are matching closely those reported in the literature [132].
- $\text{Cr}_3(\text{C,N})_2$ phase behaves similarly in grades CG-1100Ba and CG-1240X, with the biggest difference in α_a . The measured lattice parameters at RT are slightly smaller than those reported in the literature for the isostructural phase Cr_2VC_2 [141]. Slightly larger lattice parameters in Cr_2VC_2 compared with $\text{Cr}_3(\text{C,N})_2$ phase were observed also in reference [140].
- Cr_3C_2 and $\text{Cr}_3(\text{C,N})_2$ phases have almost identical average CTE, as shown in Figure 6.6. The values range from $8.5\text{--}9 \times 10^{-6} \text{ K}^{-1}$ at 50°C to $\sim 10.5 \times 10^{-6} \text{ K}^{-1}$ at 600°C
- FCC $\alpha\text{-MoC}_{1-x}$ carbide, stabilised by the Ti addition, has similar average CTE (equal to a CTE) than $\eta\text{-MoC}_{1-x}$ (hexagonal) carbide. $\zeta\text{-Mo}_2\text{C}$ (orthorhombic) carbide shows slightly lower values than these two. The naming of the molybdenum carbides is defined as in reference [37].
- The two carbide families, those composed of Cr and of Mo, have significant differences in their thermal expansion behaviour, in terms of the average CTE. The chromium carbides have $\alpha_{average}$ larger by a factor 3 in the investigated range of temperatures, see Figure 6.7.

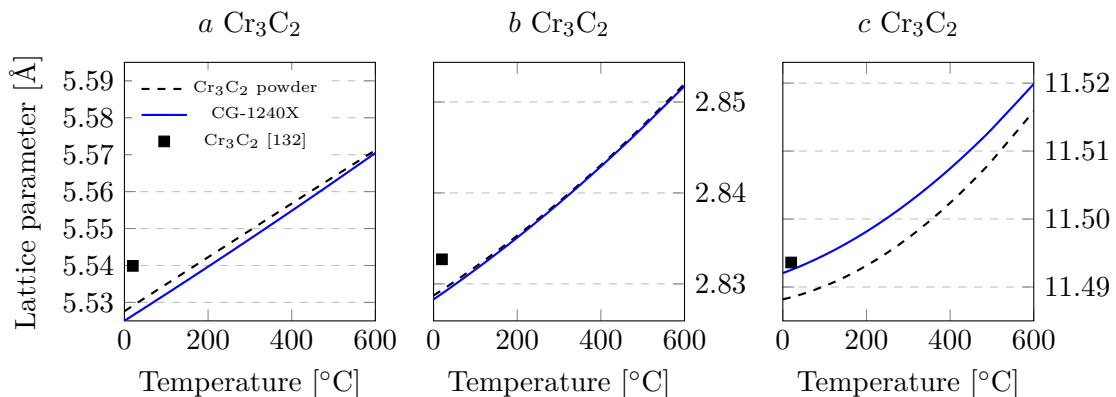


Figure 6.4: Lattice parameters versus temperature of Cr_3C_2 .

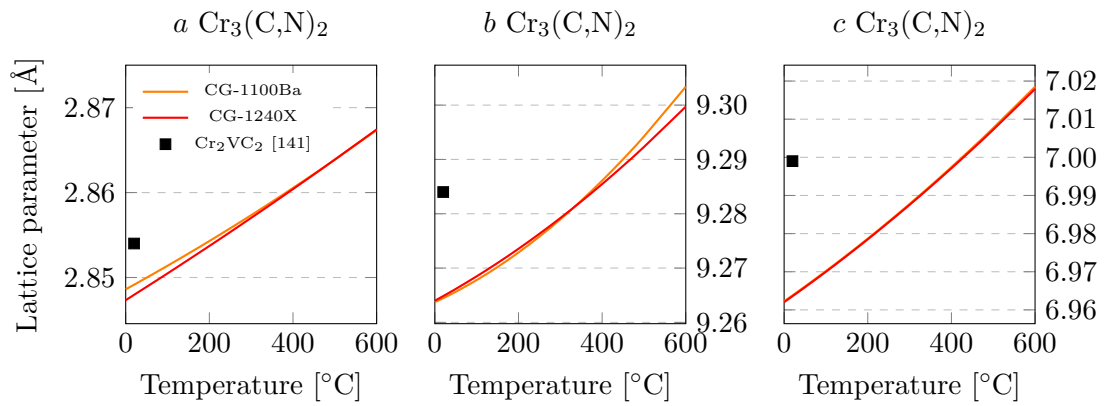


Figure 6.5: Lattice parameters versus temperature of $\text{Cr}_3(\text{C,N})_2$. Isostructural phase Cr_2VC_2 parameters are reported for comparison.

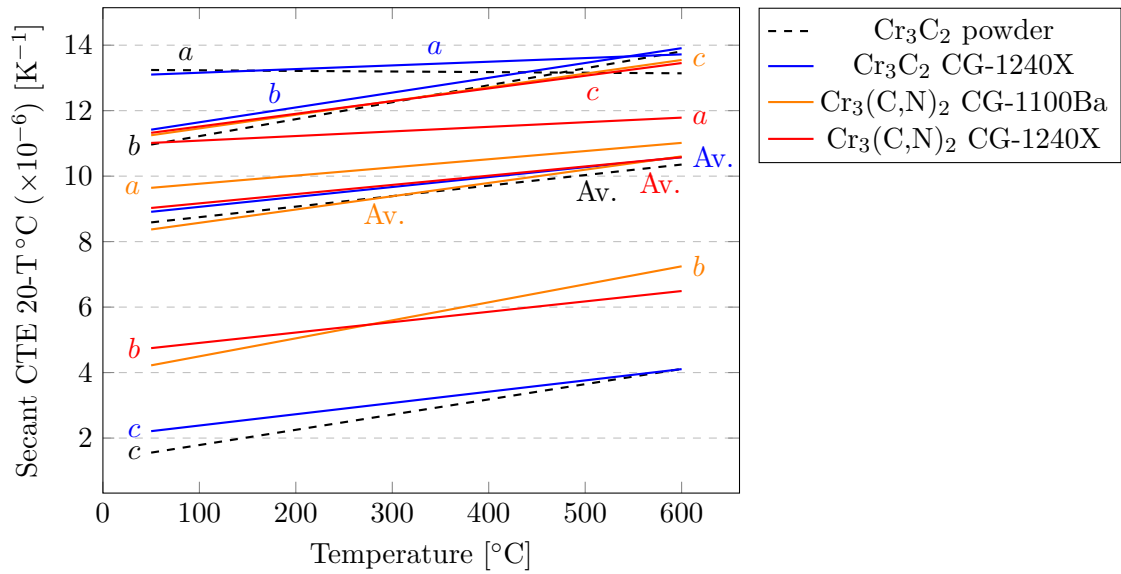


Figure 6.6: Comparison of secant CTE 20-T °C of chromium carbides. The plot includes the 3 crystallographic orientations (orthorhombic crystals) and the average between them.

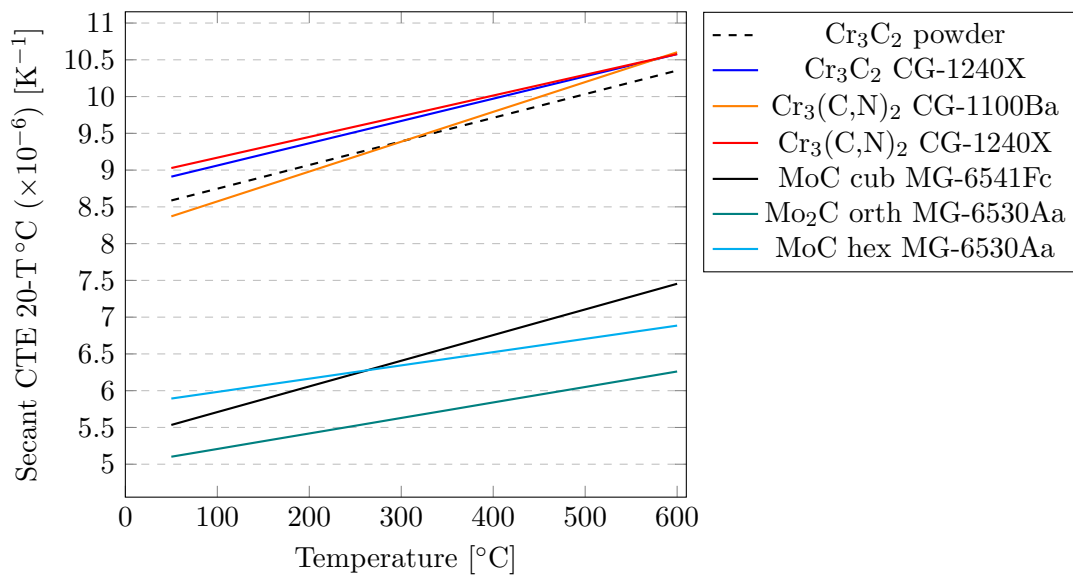


Figure 6.7: Secant CTE 20-T °C of chromium and molybdenum carbides, directional average.

The results show, as it was expected, that there is a mismatch between thermal expansion coefficients of carbides and graphite. This mismatch produces stresses at the interface, which may produce cracks or may limit the mechanical performance of the composites. The smaller the particles, the lesser the stresses are, due to the smaller contact length. However, for a precise analysis, a Finite Element Modelling (FEM) study could be performed to assess this aspect of the composites.

6.1.2 Graphite

The graphite matrix is expected to play a major role in the macroscopic thermo-physical properties of the composites, as they contain graphite in volume fractions larger than 90%.

However, relevant differences between grades have not been identified in the SEM microstructural observations in the grades using Asbury 3260 (section 4.1.1). On the other hand, the CG-1240X grade, produced with Asbury 3763 powder (section 4.1.2) shows a different microstructure, with much larger grains (Section 5.7).

Nanostructure

Representative low and medium magnification STEM images of a FIB lamella (grade MG-6403Fc) are shown in Figure 6.8. The technique is described in Section 3.6.3.

The graphite flakes as well as one molybdenum carbide particle are seen in these micrographs. The latter shows micrometric size, and it is well bonded to the graphite matrix. Some cracks parallel to the graphite basal planes are visible in the graphite matrix.

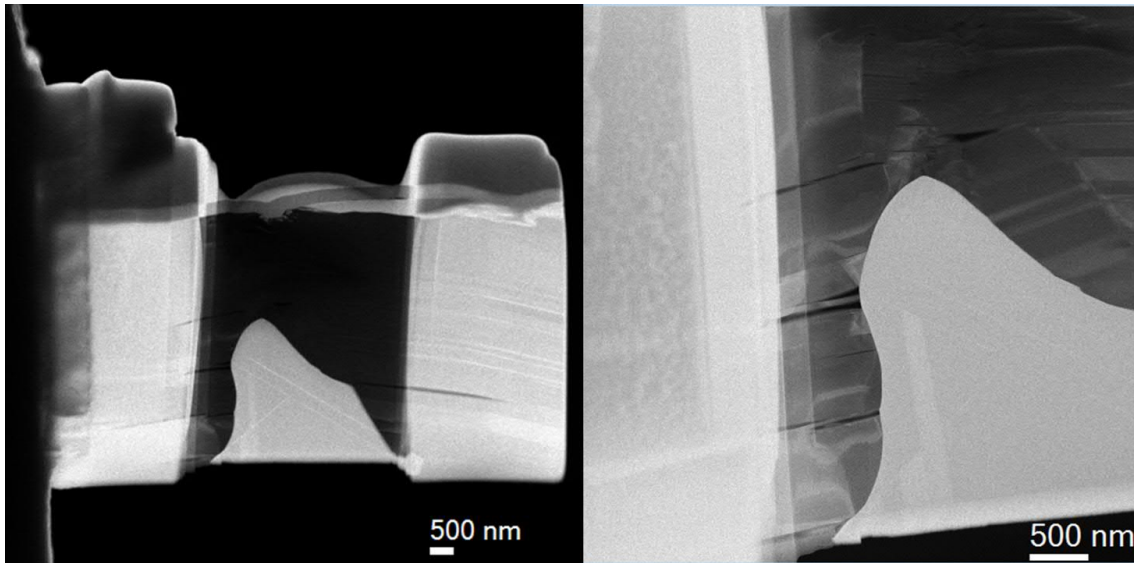


Figure 6.8: Low and medium magnification HAADF-STEM micrographs recorded on the lamella prepared from MG-6403Fc grade.

Higher magnification images were acquired for better visualization of these structures, Figure 6.9. The graphenic flakes are clearly observed in the three micrographs. In two of them (left and right) the carbide grains are also well resolved.

The graphite structure shows grains with different orientations, as expected in a polycrystalline material. The individual graphite domains show a small degree of basal plane corrugation, seen in the right micrograph.

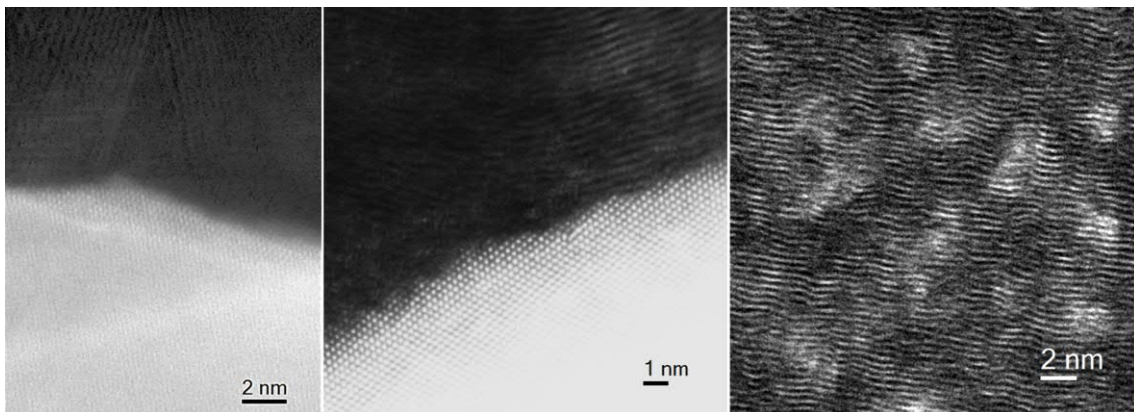


Figure 6.9: High magnification HAADF-STEM micrographs recorded on the lamella prepared from MG-6403Fc grade.

Lattice thermal expansion

The comparison of high-temperature XRD results of the graphite phase in the different materials is shown in Figures 6.10 and 6.11. These measurements allow to characterise the thermal expansion of the phase in all crystallographic directions. Full details are reported in Chapters 4 (initial Asbury 3260 graphite powder) and 5.

The lattice parameter versus temperature plot shows that all the composites have the same interplanar distance (c) than that of the best quality graphite. This is also true for TPG material and for the initial Asbury 3260 graphite powder. However, isotropic

graphite R4550 material shows larger interplanar distance, corresponding to lower graphitisation level. In the a -direction, there is some dispersion, because in this direction, graphite does not change in length much, therefore the experimental errors are critical. As detailed in section 3.5.2, the estimated uncertainty of the method used is 0.002 \AA in the worst conditions, which is as large as the range of variation of a in the plot. Nevertheless the curvature of the plots matches the expected behaviour, and the results of Asbury 3260 and TPG at RT match closely the absolute value reported in reference [53] (high quality crystalline graphite). The lowest-graphitised material studied (R4550) has not only larger c but presumably also slightly larger a than the others.

The slope in the curves from Figure 6.10 defines the thermal expansion behavior, as explained in Section 3.5.2. The results shown in Figure 6.11 show that the pure graphites having high quality (TPG and Asbury 3260 powder) have slightly larger CTE in the c -axis direction. Therefore, the carbide particles present in the composites may keep the planes together at the carbide-graphite contact points, applying compressive stresses to the graphite due to the differential thermal expansion. This effect is however very weak, compared with the measured macroscopic CTE. Isotropic graphite R4550 also shows lower CTE in the c -direction compared with the high quality pure graphites.

In the a -direction the differences are probably due to the experimental error made because of the small variation of the a parameter in graphite.

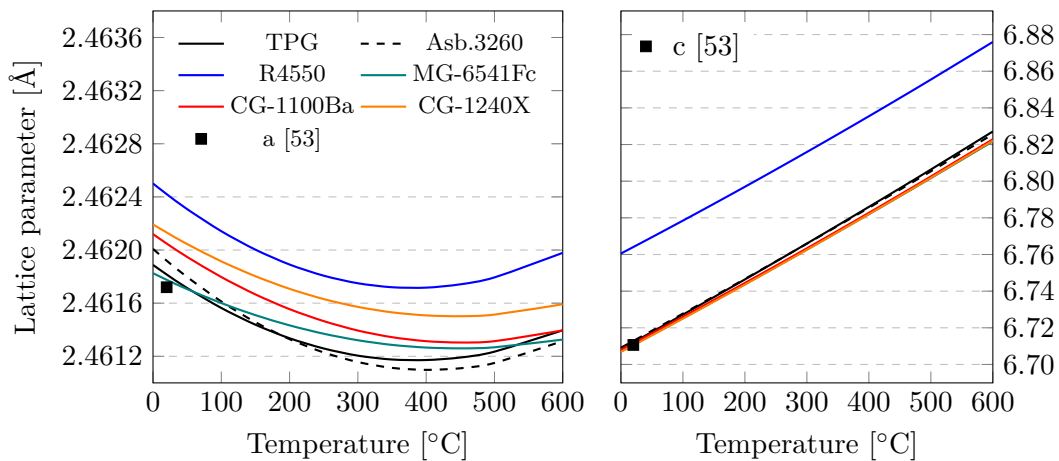


Figure 6.10: Graphite lattice parameters versus temperature: a (left), c (right).

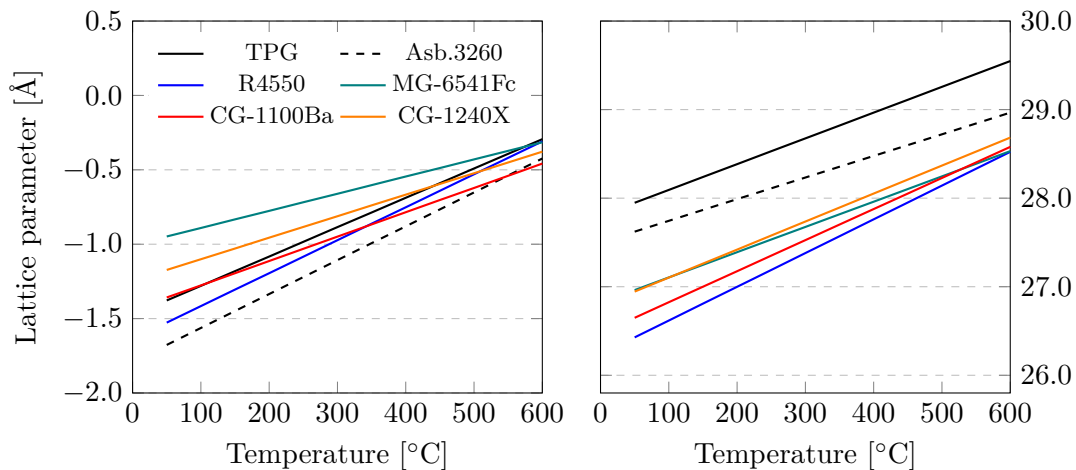


Figure 6.11: Result of the secant CTE $20-T$ °C of graphite ($\times 10^{-6} m^{-1} K^{-1}$): a (left), c (right).

6.1.3 Superficial features of the graphite-based materials

Machining superficial effects

Graphite crystallites on the surface tend to orient parallel to it, independently from their initial orientation, if shear forces are applied to the surface. For example, these forces occur when machining or mechanically polishing the materials. This effect is demonstrated by XRD measurements in section 5.1.2, on the TP surface of TPG material. It is mainly affecting TP surfaces, as in IP surfaces the flakes are already oriented parallel to the surface. This effect has also been observed in the investigated composites.

The three possible cases to study are shown in Figure 6.12. The sketch shows a milling insert machining the red surface, but the effect is analogous in mechanical polishing or sanding processes. Several MoGr (MG-6403Fc) specimens having surfaces machined with conventional milling were observed after ion-polishing, in order to reveal the damage at the cross-section. The SEM observations are shown in Figures 6.13 and 6.13. The results show a depth of around $10 \mu m$ with larger porosity content than the bulk, due to microcracks between graphite basal planes and around the carbide particles. The images show clear aligning of the flakes that are vertical in the bulk material and become horizontal (parallel to the surface machined) after the milling process. As demonstrated in section 5.4.3, this layer is too small to show changes in the superficial electrical conductivity, at least at frequencies in the order of 1 MHz.

It is expected that the damage produced by conventional milling is deeper than by mechanical sanding/polishing processes with small abrasive particles. The damage caused by abrasive particles should be proportional to their size. This local bending of the graphite basal-planes poses difficulties in observing the actual porosity of the composites after conventional mechanical polishing. For this reason, if the small pore features need to be characterised, ion-polishing technique is much more appropriate technique to prepare the samples for observation.

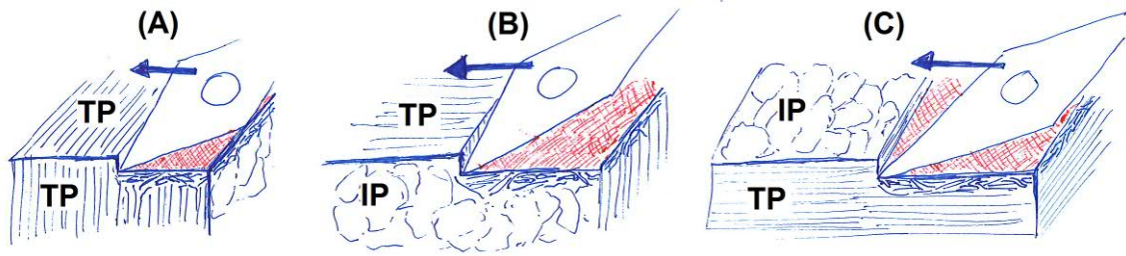


Figure 6.12: The 3 possibilities to observe machining superficial damage (red color) in a transversely isotropic material: (A) TP surface with vertical basal planes, top TP surface machined, (B) IP surface machined on the top TP surface and (C) TP surface with horizontal basal planes, top IP surface machined.

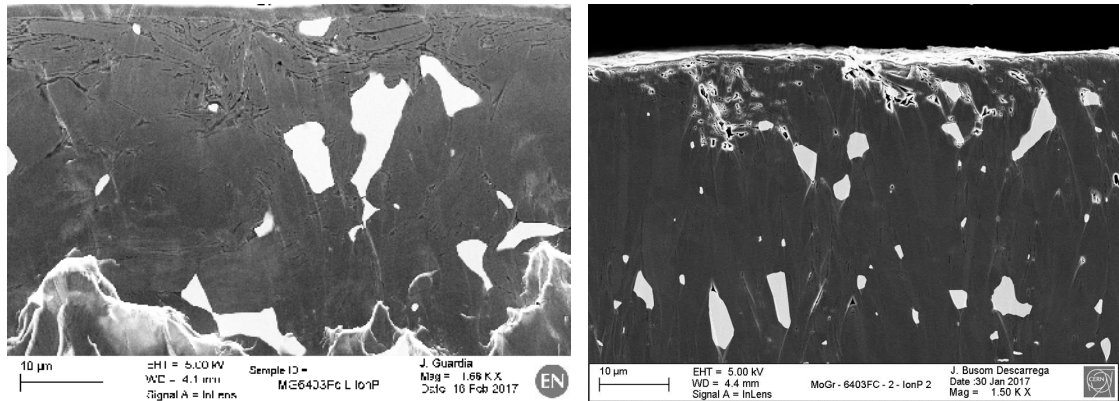


Figure 6.13: Low magnification SEM observations of ion-polished MG-6403Fc. (Left) case B and (right) case A from Figure 6.12.

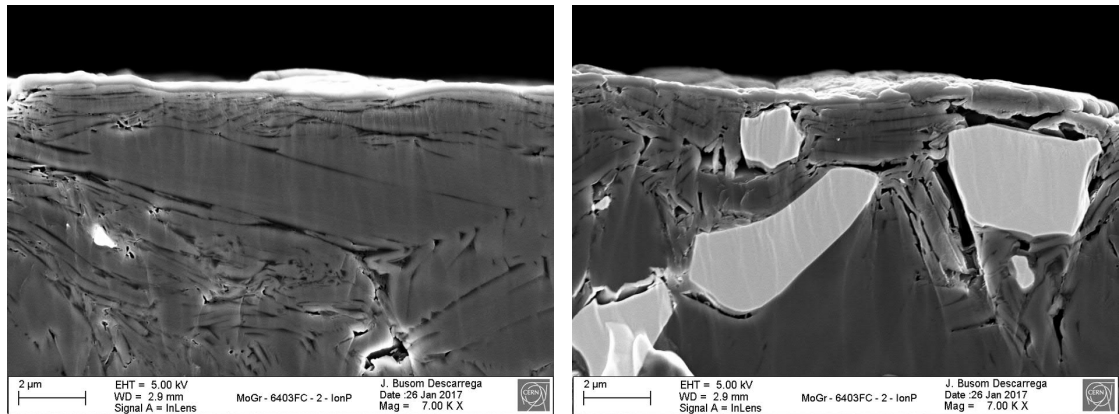


Figure 6.14: High magnification SEM observations of ion-polished MG-6403Fc. Both correspond to case A from Figure 6.12.

Case C shown in Figure 6.12 was not analysed. This case is relevant when the IP composite surface needs to be machined and coated with a thin film, as the substrate strength close to the surface may be negatively affected by the milling.

Sonication superficial effects

Differences in light reflectivity and/or scattering of the polished samples were observed in the two different orientations of the MoGr material after applying the same polishing

process (Figure 6.15). The preferred orientation of the graphite matrix allows flatter surfaces perpendicular to graphite basal planes compared with in-plane surfaces.

Both polished surfaces were also submitted to ultrasonic bath in ethanol at RT during 15 minutes. Sonication is an efficient method to remove dust from the surface prior to microscopical observations, but this treatment was found to change the visual appearance of MoGr, especially in one of the two orientations. The quality of the mirror surface was worsened after sonication, in particular in the in-plane surfaces (Figure 6.15).

Some of the graphite crystallites were removed from the surface during the ultrasonic bath. The SEM observations comparing the same surfaces, before and after sonications are shown in Figures 6.16 and 6.17. On perpendicular surfaces, the removal is much less severe. Due to its anisotropic sp^2 hybridization, C-C bond in graphite is much weaker between basal planes than inside them (7 kJ/mol and 524 kJ/mol respectively [57]), resulting in an easier removal of flakes attached only to basal-plane surfaces. Furthermore, carbides can only form a strong bond with the edges of graphite planes [61]. These effects allow weakly bonded graphite flakes to be removed by ultrasonic bath if they are exposed at the surface. Since not all graphite crystallites stay in the preferred orientation, there are intact zones of in-plane surfaces after sonication and, conversely, removal of some particles in the perpendicular surfaces.

In other MoGr grades, the effects of sonication are analogous to the observations reported in Figures 6.17 and 6.16.

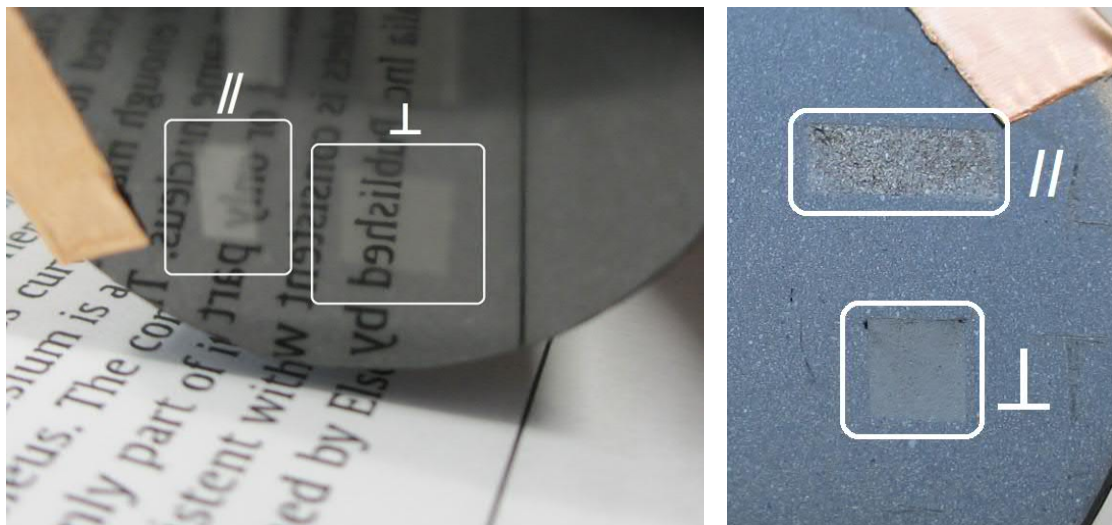


Figure 6.15: (Left) Molybdenum graphite samples embedded in a black resin cylinder and polished for SEM observation, showing differences in light reflectivity/scattering between in-plane and perpendicular surfaces. (Right) the same after ultrasonic bath treatment.

On graphite and CFC, the sonication treatment does not remove bulk material. This could be due to the presence of strong bonding between the initial filler graphite particles which is provoked by the pitch impregnation and subsequent carbonization and graphitisation processes. The production details for typical artificial graphites and CFC's can be found in reference [57]. These materials contain relatively large pores; the pores exposed to the surface tend to be filled with the dust produced during machining. As it is clearly visible at the beginning of ultrasound bath cleaning, this dust is removed into the liquid, exposing the actual porous structure of the materials.

In addition, the sonication has another interesting effect on graphite and CFC. The flakes unstick from themselves, lifting from the surface and changing slightly their super-

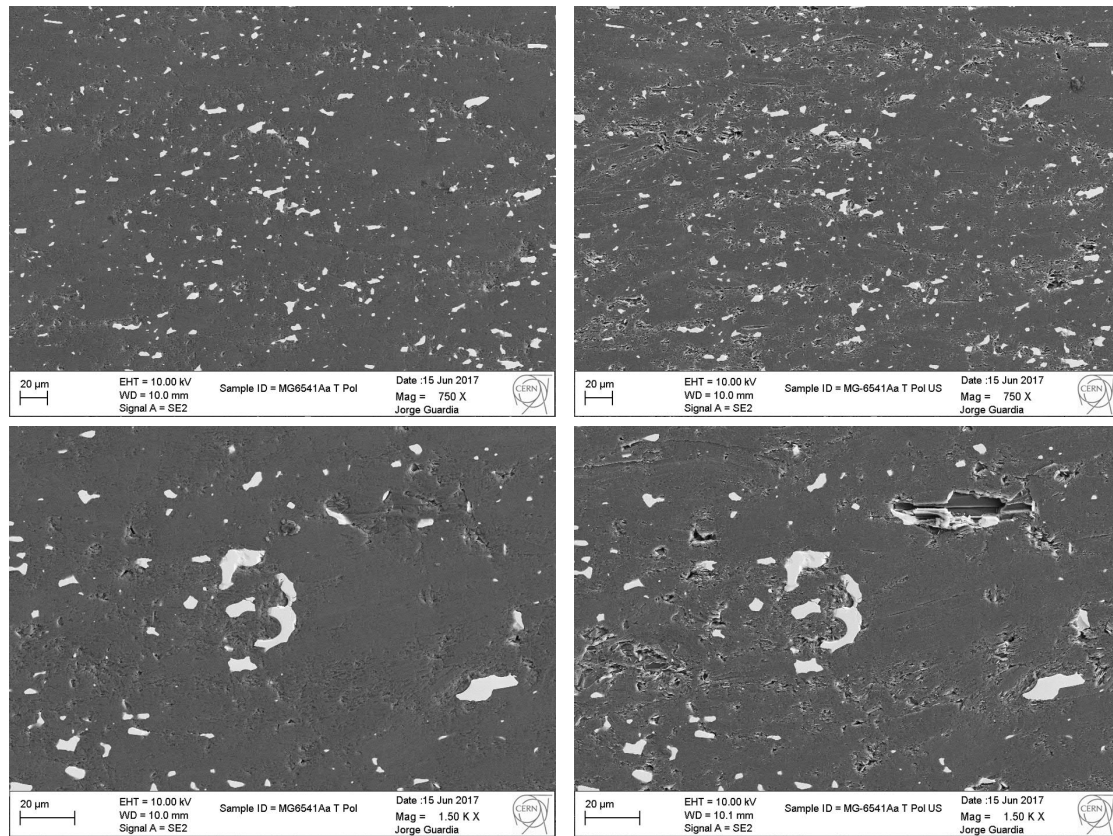


Figure 6.16: SEM observations of a through-plane MG-6541Aa polished surface, before (left) and after (right) sonication.

facial exposure (Figures 6.19 and 6.18). This lifting effect produces changes in the visual appearance. The flakes are lifted, changing their orientation. As demonstrated above, the shear forces can align these flakes again in the direction parallel to the surface. In fact, it is just enough to rub anything along the surface, such as a paper tissue, to change again the visual appearance due to the new alignment.

We can conclude that sonication is therefore an efficient method to remove loosen superficial flakes in the composites and to lift the superficial flakes on materials produced from standard carbonization-graphitisation processes. This can be exploited if thin-film deposition techniques are foreseen, as the adhesion forces can be enhanced in the sonicated surfaces.

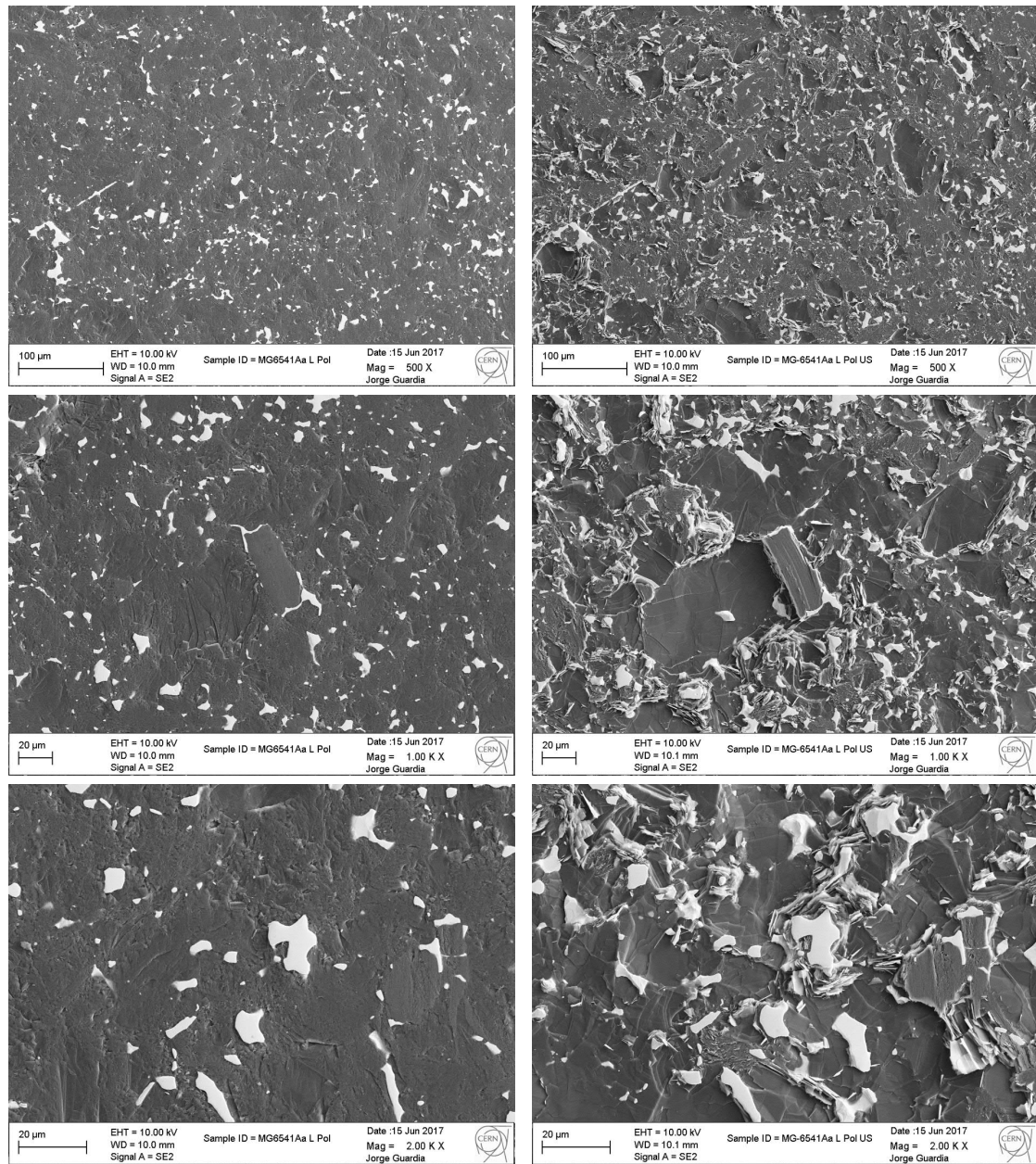


Figure 6.17: SEM observations of in-plane MG-6541Aa polished surfaces, before (left) and after (right) sonication.

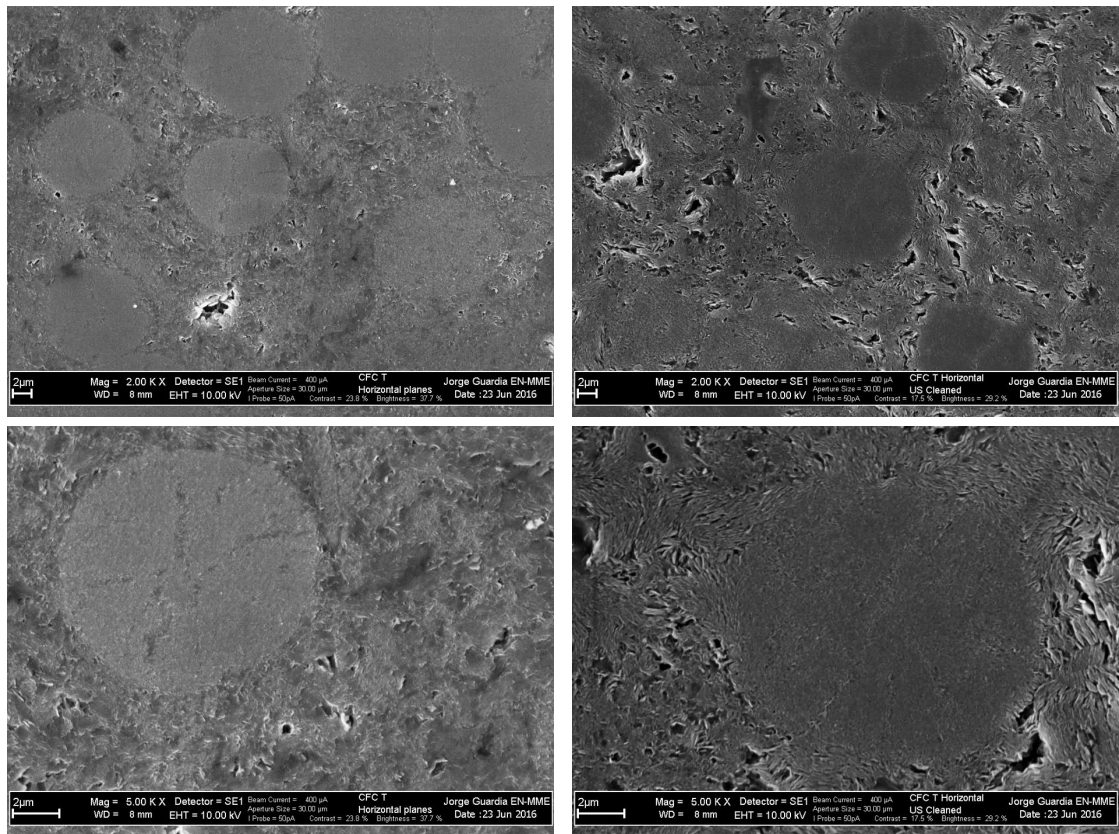


Figure 6.18: SEM observations of through-plane CFC AC150K polished surfaces, before (left) and after (right) sonication.

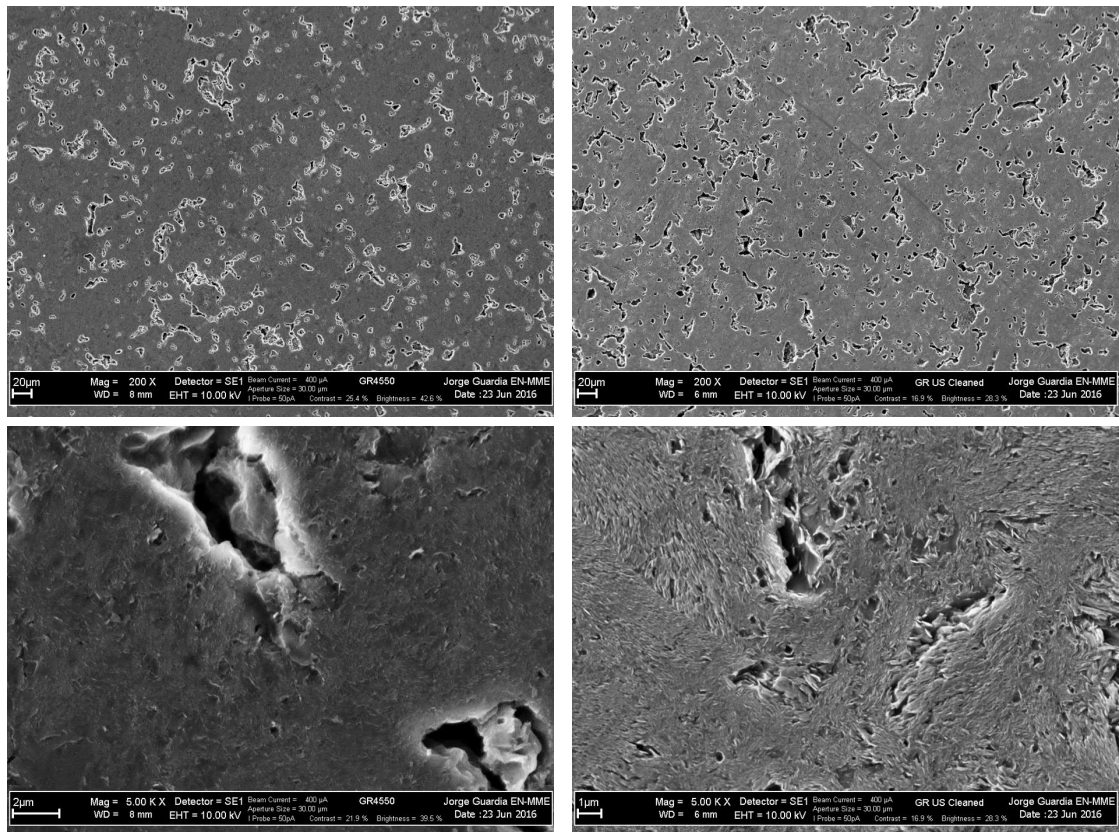


Figure 6.19: SEM observations of a graphite R4550 polished surface, before (left) and after (right) sonication.

6.2 Macroscopic properties

6.2.1 Thermal conductivity

Figures 6.20, 6.21 and 6.23 show the thermal conductivities k (IP and TP) and the specific heats C_P of the investigated materials. The curves correspond to the fitting equations that best match the experimental data, described in Chapter 5. TPG k data shown includes the real variation of density with temperature, while the k of the rest of materials do not. As shown in Figure 5.14 the error made by this assumption in TPG is negligible up to at least 1000 °C.

The k of pure aluminium and copper are included for comparison purposes. The C_P of two relevant carbides (Cr_3C_2 and Mo_2C) present in the composites are also reported.

Only TPG material approaches k_{IP} of HOPG ($\sim 1840 \text{ W m}^{-1} \text{ K}^{-1}$ at 300 K), as shown in table 1.6. MG-6541Fc has the highest k_{IP} among all investigated composites.

Chromium-graphite materials are ranked with CG-1240X in the first place, CG-1100A0 in the second place and CG-1100B0 in the third place of best thermal conductors (IP). However, the two latter ones are very similar. It is clear that the post-sintering cycle performed to CG-1100Ba grade is worsening the IP k .

With respect to the two most used metals for thermal transfer applications (Cu and Al), the composites show better k around RT. The two metals exhibit quasi-constant conductivity as temperature increases, while graphite has a steep decrease in k . This due to the different thermal transport mechanisms, discussed in section 1.4. At RT, the composites exhibit K_{IP} exceeding twice of that of copper. Below RT their k_{IP} is expected to increase, for comparison, HOPG exhibits a peak of $\sim 5000 \text{ W m}^{-1} \text{ K}^{-1}$ at 123 K [145].

It is interesting that CrGr materials have slightly better TP k than MoGr, see Figure 6.21. This is probably due to the absence of thermal graphitisation during the sintering cycle (see section 2.1.1), which tends to orient the graphite in the direction perpendicular to the applied force. CrGr composites are therefore less anisotropic than MoGr. Figure 6.22 plots the k_{IP}/k_{TP} ratio of the different materials. TPG has the largest ratio, exceeding 200 at RT, while MoGr is in the order of 17 and CrGr around 10. Isotropic graphite R4550 has an advantage over the rest of anisotropic materials as its k surpasses the k_{TP} of all the others.

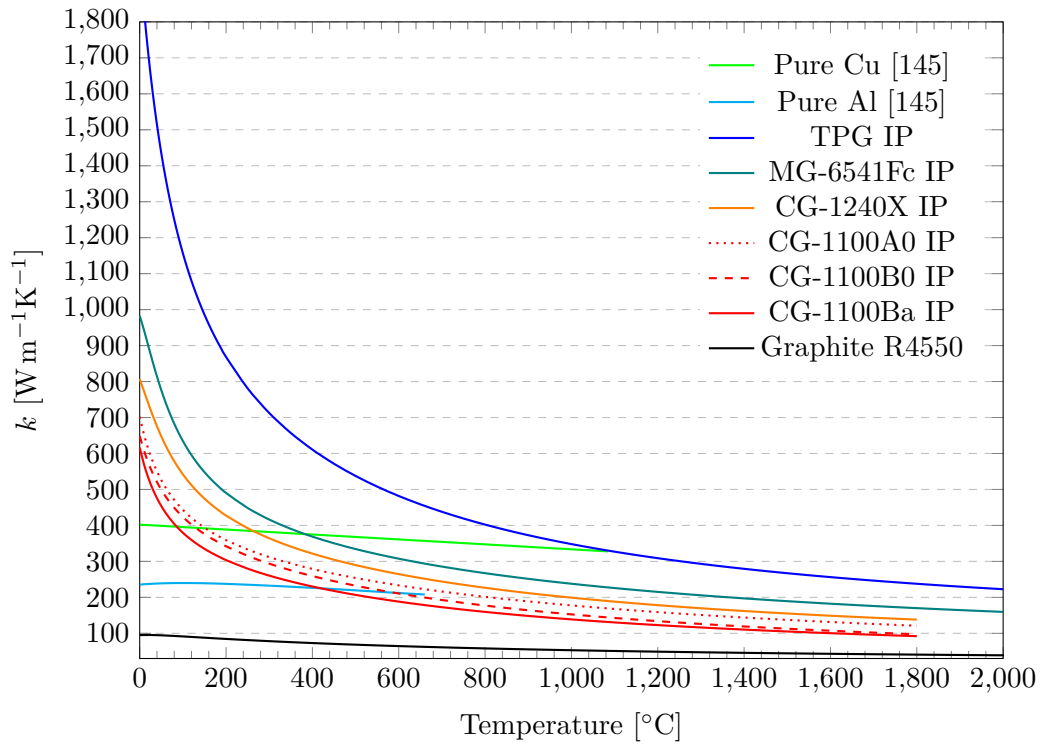


Figure 6.20: In-plane thermal conductivity of the investigated materials.

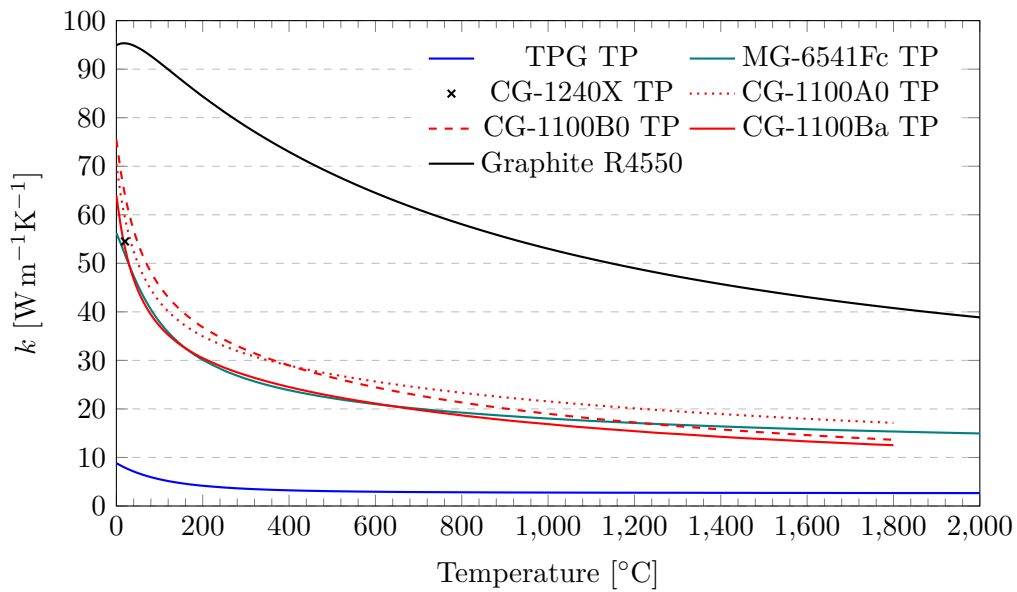


Figure 6.21: Through-plane thermal conductivity of the investigated materials.

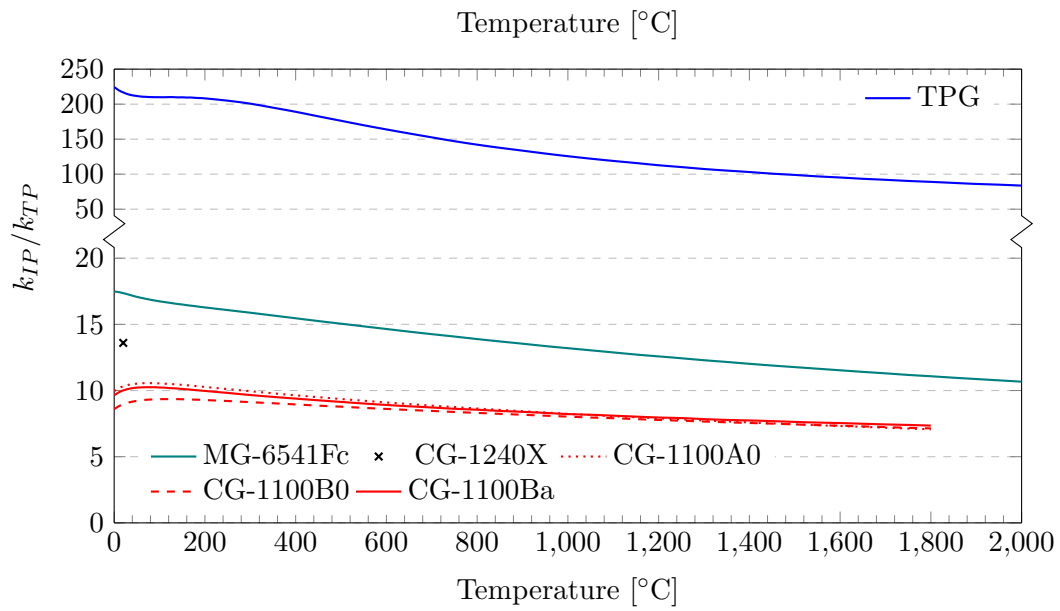


Figure 6.22: Ratio between IP and TP thermal conductivities. Calculated from the fitting curves.

6.2.2 Specific heat

The C_P of materials exclusively composed of graphite match closely the C_P curve of POCO graphite reported in reference [137]. The measurement's accuracy, as detailed in Section 3.1, is in the order of 5%.

All composites have slightly lower C_P than pure graphite, as they contain carbides with lower C_P , see Figure 6.23. Grade CG-1240X shows higher C_P than pure graphite above around 100°C, but the difference is within the measurement accuracy. The final C_P is defined by the mass content of each component. As explained in section 4.4, the fact of some liquid phase escaping the mould entails difficulties to calculate the actual compaction and the final composition, preventing precise estimation of the theoretical composite C_P .

Chromium-graphite composites (red curves) have all similar behaviour, with lower C_P than pure graphite. This difference is due to the presence of chromium carbide which has lower C_P than graphite

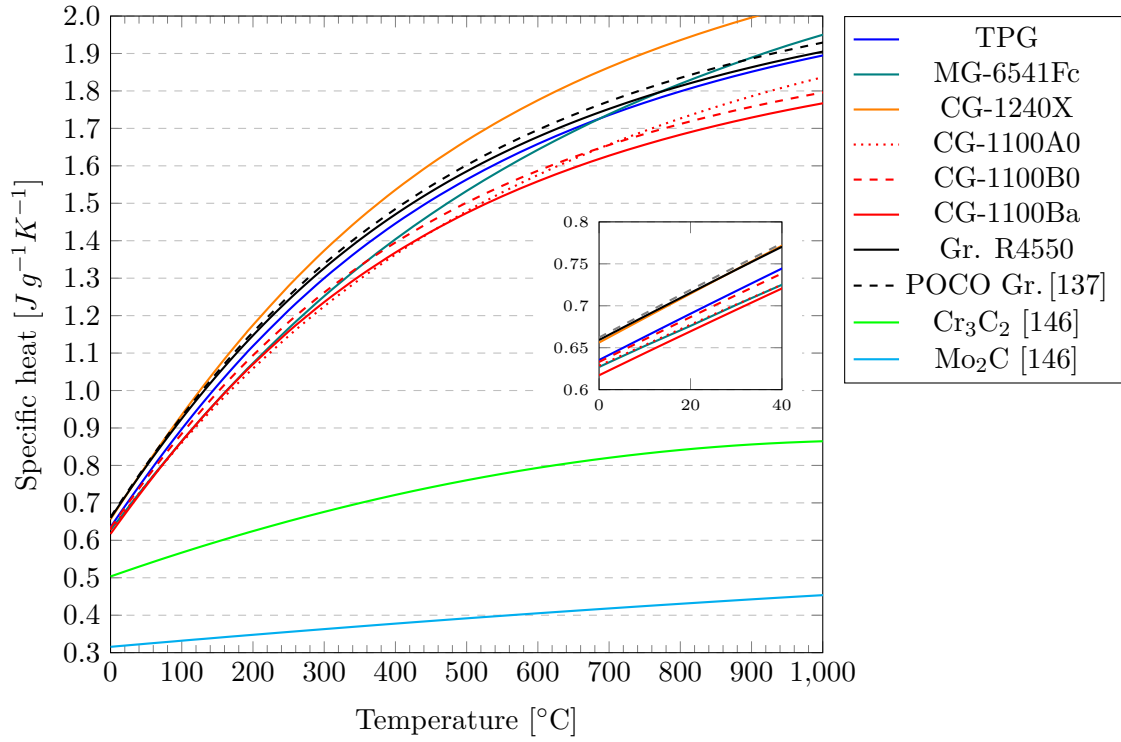


Figure 6.23: Specific heat of the investigated materials.

6.2.3 Mechanical properties

Highly oriented pyrolytic graphite (HOPG) is the closest real material to ideal graphite crystals, and a reference material for the investigated materials.

The compliance matrix S of HOPG was determined in reference [147] (isotropic 12-plane):

$$S_{HOPG} = \begin{bmatrix} 9.75 \cdot 10^{-7} & -1.61 \cdot 10^{-7} & -3.35 \cdot 10^{-7} & 0 & 0 & 0 \\ -1.61 \cdot 10^{-7} & 9.75 \cdot 10^{-7} & -3.35 \cdot 10^{-7} & 0 & 0 & 0 \\ -3.35 \cdot 10^{-7} & -3.35 \cdot 10^{-7} & 2.77 \cdot 10^{-5} & 0 & 0 & 0 \\ 0 & 0 & 0 & 3.77 \cdot 10^{-3} & 0 & 0 \\ 0 & 0 & 0 & 0 & 3.77 \cdot 10^{-3} & 0 \\ 0 & 0 & 0 & 0 & 0 & 2.27 \cdot 10^{-6} \end{bmatrix} \text{mm}^2 \text{N}^{-1} \quad (6.1)$$

The engineering elastic constants are obtained with the formulas E.6. A rotation of the axes can be made to use the same axes convention than for the rest of materials of the thesis (isotropic 23-plane). To do the Cartesian axes rotation, 3 becomes 1, 1 becomes 2 and 2 becomes 3. The results are shown in Table 6.2.

TPG material shows an IP Young modulus at RT of only 65 GPa (Section 5.1.5), compared with the value reported above of 1025 GPa. The investigated composites exhibit similar values to TPG, reaching 84 GPa in MG-6541Fc grade.

Pyrolytic graphites show increasing modulus with decreasing deposition temperature. The higher moduli from low heat treatment temperatures reflect the non-graphitic character and possibly show influences from strong boundary restraint effects [148]. The low values in the more graphitic materials arise from the increasing influence of the shear modulus in misaligned lamellar regions [148]. The crack morphology and distribution

Table 6.2: Elastic constants of HOPG obtained from its compliance matrix 6.1

Isotropic 12-plane			Isotropic 23-plane		
E_1	1025	GPa	E_2	1025	GPa
E_2	1025	GPa	E_3	1025	GPa
E_3	36.1	GPa	E_1	36.1	GPa
G_{12}	0.27	GPa	G_{23}	0.27	GPa
G_{13}	0.27	GPa	G_{12}	0.27	GPa
G_{23}	440	GPa	G_{13}	440	GPa
ν_{12}	0.165		ν_{32}	0.165	
ν_{13}	0.012		ν_{12}	0.012	
ν_{32}	0.012		ν_{13}	0.012	

changes the stress distribution in the body and hence the stresses experienced by the individual crystallites [148]. The presence of porosity of wide size and shape distribution lowers the modulus. In fact, Jenkins suggested that microcracks aligned with the basal planes contribute 50% to the RT modulus, as they can accommodate strains and change the stress distribution within the polycrystalline aggregate [148].

Basal plane shear within crystallites is the source of the non-linearity and hysteresis effects observed in all of the stress-strain curves of polycrystalline graphites 6.1. Besides, this poses additional difficulties in the characterisation of polycrystalline graphite-based materials, as the elastic-properties are actually strain dependent [148].

Graphite-based materials fall into the general class of brittle materials. The fracture stress is therefore controlled by flaws in the material and the fracture energy. At temperatures above 2000 °C, when plastic flow at crack tips becomes much easier, the work of fracture shows a very sharp increase. Theoretical predictions of ideal strength on single-walled nanotubes show values of strength approaching 100 GPa [148]. However, high quality graphite filaments produced by Bacon (1960) displayed strengths up to 20 GPa and a strain to failure of 2.5% [148]. Apart from porosity and flaws, the same limiting factor described above for the Young's modulus apply also to the strength in the real materials: basal plane shear in misaligned crystallites.

The effect of increasing temperature is generally to increase the strength of the graphite to an extent much greater than that shown by the elastic modulus. This is mainly due to closure of microcracks by the effect of the large c-axis expansion.

These factors are expected to limit the modulus and most importantly the strength to rupture in the investigated materials. As described in section 1.2, materials showing low elastic modulus are beneficial for being used as collimator materials, however maximizing strength and strain to rupture is of paramount importance.

The presence carbide particles in MoGr materials mitigates the effects of basal plane shear and delamination, improving the strength to rupture with respect to purely oriented graphites. This is particularly important in the TP direction, where the strength of the graphite crystallites is negligible as a consequence of the weak Van der Waals forces between the atomic layers.

Harada [95] reported that substantial improvements in the mechanical strength and densification of the composites are attained when using finer starting metal/carbide particles. CrGr materials are produced with finer carbide particles than MoGr (1.6 versus

5 μm). This parameter alone is not significantly affecting to the strength of the final material.

CrGr does not show large strengths to rupture even in the IP direction. An analysis of the dust produced when machining specimens with the diamond wire saw reveals that the graphite particles are comparable in size and morphology to the initial graphite flakes, see Figure 6.24. Most of the initial flakes, such as the one shown in Figure 6.24 (right), are in fact agglomerations of smaller flakes, which show the same size than the graphite dust (5–10 μm). This indicates that the bonding between these flakes is the weakest link after the sintering process. A similar test on MoGr material is not available. However, the IP strength of MoGr materials is considerably larger than in CrGr materials. It is important to note that MoGr materials are sintered at 2600°C, which is much above the thermal graphitisation threshold, $\sim 2000^\circ\text{C}$ (section 2.1.1). However CrGr materials are not. Above this threshold, carbon atoms are mobile enough to start bonding adjacent graphite particles.

The catalytic effect of the metal-carbon liquid phase may not reach all the graphite-graphite interfaces, leading to limited cohesion. It is expected that the presence of thermal graphitisation allows better bonding where the catalytic agents do not manage to dissolve and reprecipitate carbon atoms.

It would be expected that if graphite crystallites are not strongly bonded, the IP transport properties (thermal and electrical conductivities) would be low. However, CrGr materials exhibit moderately large IP transport properties, which are still lower than MoGr ones, but this difference is smaller with respect to the difference in strength. This could be due to the different fundamental physical mechanisms that rule the transport properties, see section 1.4.

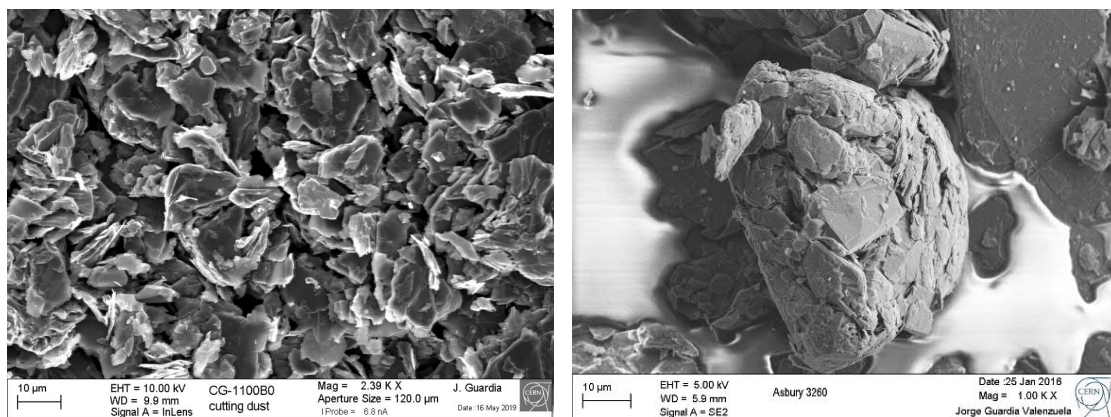


Figure 6.24: Comparison between the morphology of machining dust from CG-1100B0 (left) and the initial Asbury 3260 graphite (right). Both SEM images have comparable scale.

6.2.4 Overall comparison

The complete list of MoGr and CrGr characterisation results is shown in Tables 6.3 and 6.4. Table 6.5 shows the characterisation results of the investigated commercial materials made of pure carbon. Symbol ”-” represents not-determined values. The characterisation techniques are described in Chapter 3.

Residual deformation or residual strain (RD) in CrGr materials are influenced by the different maximum temperatures reached in their dilatometer measurements: 900 $^\circ\text{C}$ in

Table 6.3: MoGr thermo-mechanical characterisation results at room temperature

Direction ¹	MG-6530Aa		MG-6541Aa		MG-6403Ga		MG-6403Fc		MG-6541Fc	
		⊥		⊥		⊥		⊥		⊥
ρ ($g\ cm^{-3}$)	2.51		2.49		2.49		2.55		2.52	
c_p ($J\ g^{-1}\ K^{-1}$)	0.60		0.64		0.60		0.62		0.68	
γ_e ($MS\ m^{-1}$)	0.82*	0.05	0.98*	0.06	0.88*	0.08	0.95*	0.07	1.04*	-
a ($mm^2\ s^{-1}$)	0.88		1.01		0.93		1.01		-	-
k ($W\ m^{-1}\ K^{-1}$)	469	31	490	28	430	37	466	31	528	30
α RT-200°C ²	706	47	781	45	647	56	740	50	899	52
α RT-1000°C ²	1.7	11.6	2.3	10.0	2.0	9.3	2.7	7.9	1.8	10.3
RD (%)	1.7	15.3	2.3	13.6	2.2	12.5	2.8	11.0	2.0	13.8
R_M (MPa)	0.04	0.17	0.02	0.14	0.02	0.18	0.00	0.12	0.01	0.17
ε_{adm} (MPa)	70.9±3	12±0	79.5±4	12.4±1	73.5±7	11.6±0	58.1±8	10±1	81.4±4	10.6±1
E_{y-z}, E_x (GPa)	.25±.05	.72±.18	.19±.01	.71±.11	.26±.03	.44±.03	.24±.05	.49±.07	.18±.01	.49±.11
G_{yz}, G_{xy-xz} (")	76.7	4.7	85.8	4.5	74.2	3.8	60.4	4.0	84.1	4.7
	33.0	3.8	36.9	4.7	32.1	4.7	26.3	3.7	37.4	4.1

¹ In-plane (||) and through-plane (⊥) directions, see Figure 4.32.

² ($10^{-6}\ K^{-1}$).

* By eddy-current method, otherwise by four-wire method

Table 6.4: CrGr thermo-mechanical characterisation results at room temperature

Direction ¹	CG-1100A0		CG-1100B0		CG-1100Ba		CG-1240X	
		⊥		⊥		⊥		⊥
ρ ($g\ cm^{-3}$)	2.31		2.21		2.15		2.26	
c_p ($J\ g^{-1}\ K^{-1}$)	0.677		0.687		0.670		0.714	
γ_e ($MS\ m^{-1}$)	0.84*	-	1.00*	0.08	1.01*	0.08	1.06*	-
a ($mm^2\ s^{-1}$)	-	-	0.78		0.74		1.02	-
k ($W\ m^{-1}\ K^{-1}$)	391	38	378	42	370	37	458	-
α RT-200°C ²	612	59	574	64	532	53	739	-
α RT-1000°C ²	4.2	8.6	2.3	7.9	2.6	8.3	1.8	~11.5
RD (%)	4.6	12.1	2.8	11.2	2.4	11.2	2.3	~15.0
R_M (MPa)	0.02	0.31	0.05	1.14	0.03	0.73	-0.01	0.07
ε_{adm} %	-	-	31.2±4.9	6.6±1.2	26.2±1.5	5.5±0.6	15.0±2.7	-
E_{y-z}, E_x (GPa)	-	-	0.16±.06	0.42±.08	0.12±.02	0.42±.06	0.24±.10	-
G_{yz}, G_{xy-xz} (")	-	-	42.8	3.8	38.7	2.4	~20	-
	-	-	18.1	3.5	15.9	2.8	-	-

¹ In-plane (||) and through-plane (⊥) directions, see Figure 4.32.

² ($10^{-6}\ K^{-1}$).

* By eddy-current method on the plate surface, otherwise by four-wire method (average).

CG-1100A0, 1700°C in CG-1100B0, 1700°C in CG-1100Ba, and 700°C in CG-1240X. This effect is discussed in the dilatometry measurements section of each grade (Chapter 5).

Concerning values shown in Table 6.5 for the materials made of pure carbon, it is worth noting that all the dilatometry tests were performed up to $\sim 2000^\circ\text{C}$, except in TPG TP direction (600°C). Therefore the RD value in the latter is optimistic in the comparison.

Chromium carbide - graphite materials show transport properties comparable with those of Molybdenum carbide - graphite materials. However, CrGr show relevant differences in their mechanical properties, with R_M values much lower than in MoGr materials.

Table 6.5: Thermo-mechanical characterisation results of the investigated commercial materials made of pure carbon.

Direction ¹	Gr. R4550	PG (TPG)		CFC (AC150K), orthotropic		
	Isotropic		⊥	Z	Y	X
ρ ($g\ cm^{-3}$)	1.83	2.26		1.89		
c_p ($J\ g^{-1}\ K^{-1}$)	0.715	0.69		0.712		
γ_e ($MS\ m^{-1}$)	0.08	2.5*	0.0009	0.24	0.18	0.03
a ($mm^2\ s^{-1}$)	73	1095	5	227	174	40
k ($W\ m^{-1}\ K^{-1}$)	95	1710	8	304	233	54
α RT–200°C ²	4.2	-0.9	29.3 ³	-0.4	-0.2	10.7
α RT–1000°C ²	5	~0.4	~29.5 ³	0.5	0.5	11.4
RD (%)	-0.01	-0.02	0.01 ³	0.001	0.002	0.07
R_M (MPa)	61.2±3	25.5±0.4	-	139.6±1	104.2±3	10.3±3
ε_{adm}	0.72±0.04	0.08±0	-	0.14±0.01	0.20±0.04	0.43±0.03
E (GPa)	11.5	~65	-	110.2	75.4	3.1
G (GPa)	4.6	-	-	21.5	4.3	3.3

¹ In-plane (||)/through-plane (⊥) or Cartesian directions, see Figures 4.32 and 1.17a.

² ($10^{-6}\ K^{-1}$).

³ From specimen TP4, measured only up to 600 °C. α RT–1000°C is extrapolated.

* By eddy-current method on the surface, otherwise by four-wire method (average).

Table 6.6 shows different ratios and indicators extracted from the material properties, in order to benchmark the anisotropy and the relationship between electrical and thermal conductivities.

MG-6530Aa shows the largest anisotropy in the CTE amongst all composites, while CG-1100B0 shows the lowest.

The average CTE values are quite similar in all composites, but MG-6530Aa maintains the worst position, and this time CG-1100Ba shows the optimum (lowest) value. The presence of Ti in all MoGr grades except MG-6530Aa could be the reason of this difference. FCC phase α - MoC_{1-x} stabilised by the Ti addition should be more isotropic than the other types of molybdenum carbides.

MG-6541Fc grade exhibits the largest k_{av} , with $616\ W\ m^{-1}\ K^{-1}$. CG-1240X and MG-6403Fc are in second place in terms of k_{av} .

However, CG-1240X shows the lowest anisotropy ratio among these three materials, indicating larger k_{TP} than the others. In general, the anisotropy of the composites in the electrical conductivity tends to be slightly larger than in the thermal conductivity. PG material shows an extremely high ratio IP/TP of γ_e , approaching 3000, while for k , the ratio is around 200.

The last two rows of Table 6.6 indicate the difference between the thermal and electrical conductivities of the materials and those of HOPG. These values show that these two properties do not share the same trend. As explained in Section 1.4, this is due to the different transport mechanisms of thermal and electrical conduction in graphitic materials.

Within CrGr materials, CG-1100A0 material shows the largest IP CTE, and similar TP CTE to the others. For these reasons, its overall properties are not very advantageous in collimators.

CG-1100B0 and CG-1100Ba have similar thermal and electrical properties, and their CTE are quite close as well. There is a clear reduction of the strength to rupture after the pressure-less heat treatment. However, E decreases as well, which is an advantage for thermal shock scenarios and strain-imposed loads. This change in mechanical properties

after post-sintering treatment is visible also between grades MG-6403Ga and MG-6403Fc (see production parameters in section 4.6) and should be further investigated.

Grade CG-1240X shows the largest IP transport properties among all investigated CrGr materials, while keeping its k_{TP} around the same level than the other grades. Unfortunately, as explained in section 5.7, the production process failed, and some properties (such as mechanical properties) may show detrimental effects from the mould breakage. The sudden release of pressure might have caused internal cracks in the material.

Table 6.6: Comparison of anisotropy ratios and other indicators.

	PG (TPG)	MG-6530Aa	MG-6541Aa	MG-6403Ga	MG-6403Fc	MG-6541Fc	CG-1100B0	CG-1100Ba	CG-1240X
α_{av} RT–1000°C ($10^{-6} K^{-1}$)	10.1	6.3	6.0	5.7	5.5	5.9	5.6	5.3	6.5
Ratio TP/IP of α RT–1000°C	-	8.8	6.0	5.6	3.9	6.9	4.0	4.7	6.5
Ratio IP/TP of R_M	-	5.9	6.4	6.3	5.8	7.7	4.7	4.8	-
Ratio IP/TP of E	-	16.3	19.1	19.5	15.1	17.9	11.3	16.1	-
k_{av} ($W m^{-1} K^{-1}$)	1143	342	353	383	510	616	404	372	511
Ratio IP/TP of k	213.8	10.4	11.3	9.8	14.9	17.4	9.0	10.0	13.6
Ratio IP/TP of γ_e	2778	16.6	16.3	11.0	13.0	-	12.5	12.6	-
$\gamma_{e,IP}$ (% of that of HOPG)	100	33.2	39.2	35.2	36.4	41.6	40.0	40.4	42.4
k_{IP} (% of that of HOPG)	92.9	26.6	27.6	29.7	40.2	48.8	31.2	28.9	40.2

HOPG IP values: $k = 1840 W m^{-1} K^{-1}$ and $\gamma_e = 2.5 MS m^{-1}$ (Section 1.4).

Homogeneity of the properties within the sintered volume

It is well known that one-sided uniaxial compaction of powders creates different distributions of stresses in the two faces of the plate [135]. This is the most probable cause of the small γ_e differences observed between the two sides of the same sintered plate. These differences in pressure could give slightly different preferred orientations to the graphite crystallites, resulting in these small variations in electrical conductivity. In the radial direction of the plates, significant differences in the properties have not been detected.

6.3 Carbon fibres

Carbon fibres (CF) were added with the purpose of improving the mechanical strength. Some influence in the thermal properties could also be expected due to the highly ordered nature of the pitch-based CFs.

Careful Scanning Electron Microscopy (SEM) examination of the fracture surfaces of bending test specimens revealed no visible trace of CFs. The diameter of the CFs ($10 \mu m$) is probably small enough to be dissolved and re-precipitated by the molten Mo-C phase. A similar effect was observed but in solid nickel at $1100^\circ C$ in [77], where the dissolution-precipitation mechanism managed to completely dissolve and recrystallize CFs. In early MoGr grades, which were processed below the eutectic temperature, the CFs were not dissolved and were clearly visible in the microstructural examinations as bundles of agglomerated CFs [29].

The strengthening effect of the CFs on the mechanical properties has not been demonstrated [37]; on the other hand, short CFs seem to have a beneficial role on thermo-physical properties (grade MG-6541Aa). For this reason, it was decided to maintain this addition for grade MG-6541Fc.

The dissolution of the carbon fibres confirms the carbon-solvent performance of the liquid phase. XRD diffraction confirmed lower graphitisation levels in the fibres than in the rest of initial graphite powders. For this reason, they are the least thermodynamically stable carbon solids in the initial mixture, hence dissolved in first place. However, the use of other carbon sources containing pure carbon but with low graphitisation level, such as carbon black, may provide the same effect and be more cost-efficient.

6.4 Titanium addition to molybdenum carbide

The undoped molybdenum carbides, formed upon solidification of the eutectic mixture, experience three changes of phase until complete cool-down at RT, as shown in the Mo-C binary diagram (Figure 2.14). The phase changes occurring at 1475 and 1655°C in the binary system are detectable in the dilatometer measurements of perpendicular CTE, only in grade MG-6530Aa (without Ti), due to the change in density of the carbide phases [37]. The phase changes are not visible in the in-plane measurements, either because of the texture of the carbide phases in the material or simply because the measured CTE is lower, leading to lower sensitivity to small variations of length.

The FCC carbides of molybdenum ($\alpha\text{-MoC}_{1-x}$) and titanium (TiC) exhibit completely solid solubility between them, resulting in a carbide phase $(Ti_{1-x}, Mo_x)_{1-y}C_y$, labelled δ in the ternary diagram, which is stable over a wide range of temperatures and stoichiometries [149]. The effect of small quantities of titanium in MoGr, around one titanium atom every 10 molybdenum atoms, appears to be sufficient to turn all molybdenum carbide into the FCC phase ($\alpha\text{-MoC}_{1-x}$), over the full range of temperatures of interest.

XRD analyses performed in grades with titanium revealed the absence of hexagonal or orthorhombic molybdenum carbides and the presence of a FCC phase, with $a = 4.264 \text{ \AA}$, except a trace amount of $\eta\text{-MoC}_{1-x}$ in grade MG-6403Fc, probably due to the change in thermal treatment. According to the phase diagram Mo-C (Figure 2.14), the cubic $\alpha\text{-MoC}_{1-x}$ phase is stable only above 1960°C, thus it is being stabilized down to RT with the Ti addition.

The absence of phase changes in the material is believed to be beneficial during beam impact scenarios, which could locally raise the temperature of collimator absorber materials to thousands of degrees. The presence of strongly stabilized phases usually improves the radiation resistance.

Despite the eutectic in equilibrium with carbon (graphite) moving from 2584°C in Mo-C system (45at.% C) to 2777°C in Ti-C system (65at.% C) [37], the small addition of titanium should negligibly raise the eutectic temperature. In fact, a relevant difference in the melting temperature of the carbides was not observed with the sintering system used. The hot pressing strain seems to occur at a faster speed in the grades with Ti, which could be related with a better mobility of the LP Mo-Ti-C. The higher affinity of Ti for carbon with respect to Mo, as seen in the standard enthalpies of formation of the carbides ($TiC -231$, $Mo_2C -46$ and $MoC -10 \text{ kJ mol}^{-1}$ [130]), could accelerate the catalytic graphitisation process. Another difference observed is that the grades doped with Ti behave during machining as a harder material.

6.5 Processing temperature and outgassing behaviour

Collimators must operate in ultra-high vacuum (down to 10^{-10} mbar) to avoid undesired collisions between beam particles and gas molecules. This level of vacuum requires that collimator materials have outgassing rates lower than 10^{-12} mbar l s⁻¹ cm⁻² at RT. Several MoGr grades produced exhibit outgassing rates 1 to 2 orders of magnitude above the specification, with gases from air as predominant species. Two sources are considered: the final surface of the blocks and gas trapped in the bulk. Concerning the former, tests are pointing to possible detrimental effects of the machining creating superficial micro-defects prone to gas trapping: this could be mitigated by applying surface treatments after production. As to the latter, special compaction techniques of the powders, changes in the sintering cycle and different thermal treatments under vacuum are being investigated.

To improve the outgassing behaviour, the temperature of the post-sintering cycle was increased in the grade MG-6403Fc in order to exceed again the eutectic point, to help the diffusion and outgassing of gas trapped inside the material, possibly coming from the first stages of pressing.

The higher post-sintering treatment temperature of grade MG-6403Fc increased the thermal expansion coefficient in the in-plane direction and decreased it in the perpendicular direction, pointing to a higher degree of isotropy. The fact that the electrical conductivity is similar in grades MG-6403Ga and MG-6403Fc, while the strength in the latter slightly decreases ($\sim 20\%$), should be further investigated. Similar strength decrease is observed in CG-1100Ba with respect to CG-1100B0 (not thermally treated). A possible explanation is that the post-sintering treatment produces micro-cracks by relaxing internal stresses without breaking the conduction path. The high residual deformation in CG-1100B0, specially in the TP direction, needs further investigation. However, CG-1100Ba grade was thermally treated and also exhibits significant residual deformation.

The re-melting of the carbide inclusions in a pressure-free state in grade MG-6403Fc, is certainly releasing internal stresses, and it could also help to orient some graphite crystallites in a more efficient arrangement for an improved thermal conductance.

The reason of the excessive outgassing rates observed in MoGr is not yet clear and intensive investigations are being performed to address the issue.

6.6 Catalytic graphitisation

Part of the molten liquid phase escapes the mould during the sintering process, reaching the furnace chamber. This spilled liquid phase material was analysed with optical and scanning electron microscopy techniques. Figures 6.26 and 6.27 show the LP spill material from MoGr grades. Figures 6.28 and 6.29 show the LP spill from CrGr materials.

Molten chromium-carbon liquid phase (LP) is an effective medium for the carbon dissolution-precipitation mechanism, which allows production of graphite with presumably the best crystalline quality, see Chapter 2. Flakes as big as 800 μm have been detected in Cr-C droplets spilled out of the mould, see Figure 6.30. In similar droplets coming from MoGr materials the largest observed flake diameter is 1200 μm , see Figure 6.27.

The ability of Cr-C liquid phase to dissolve carbon was the cause of the mould breakage of plate CG-1240X. Figure 6.25 shows the upper graphite punch with major damage due to the dissolution by the LP. Similar damage occurred to the lateral die, producing its failure probably because of the cross-section reduction.



Figure 6.25: Upper graphite punch used to sinter CG-1240X plate, showing extensive dissolution by the Cr-C liquid phase.

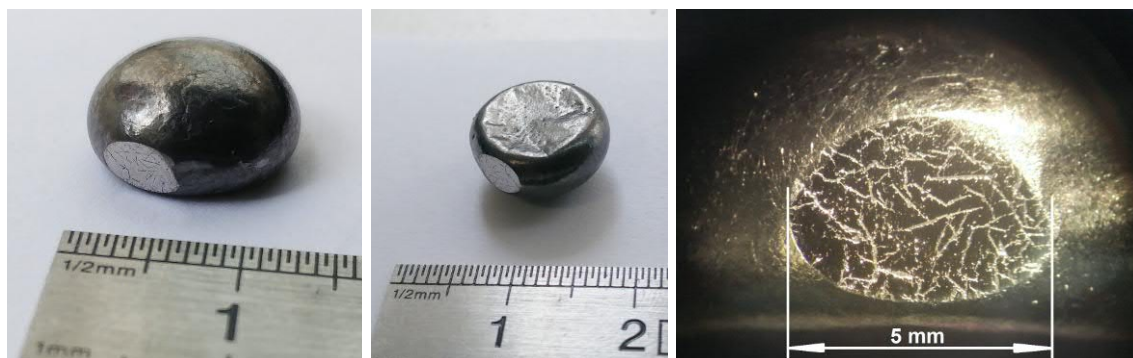


Figure 6.26: Mo-C(-Ti) LP spill material from MG-6403Fc plate. A small surface was polished to reveal its internal structure, which shows grown graphite flakes visible with optical microscopy (right).

Another LP sample, from a failed sintering test with the same initial composition is shown in Figure 6.27

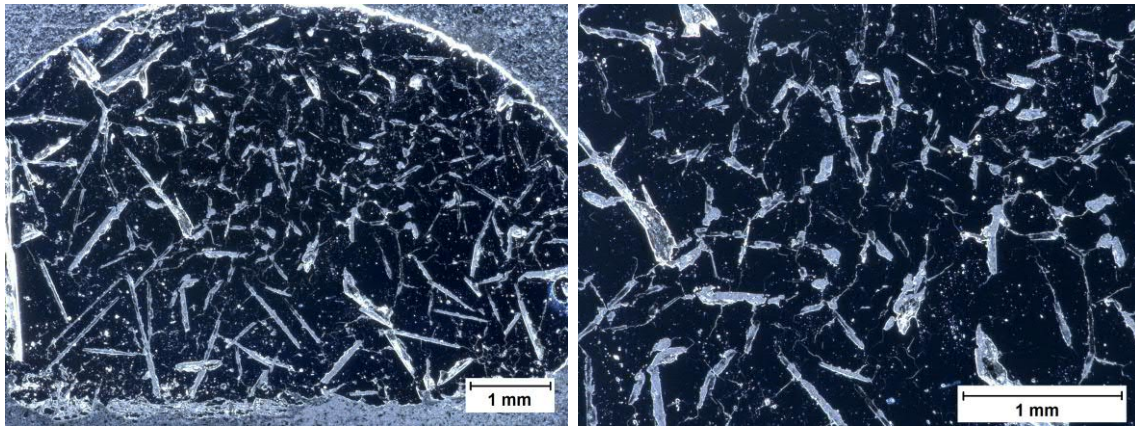


Figure 6.27: Mo-C(-Ti) LP spill material from MG-6403Fc failed sintering test, observed with optical microscopy. The darker areas are in this case the most reflective mirror-like surfaces (polished carbide), while the acicular flakes are made of graphite.

The actual time and temperature at which the LP was producing these graphite flakes is not known. It is reasonable to assume temperatures slightly lower than the sintering dwell and holding times also similar to the sintering duration at most. As shown in section 4.6, for CrGr materials it is < 2400 s and < 2000 °C, and for MoGr materials it is < 2400 s and < 2600 °C.



Figure 6.28: Cr-C LP spill material from CG-1100A0 plate. One surface was polished to reveal its internal structure.



Figure 6.29: Cr-C LP spill material from CG-1100B0 plate. One surface was polished to reveal its internal structure, which shows visible grown graphite flakes (left).

Some of flakes grown in the surface of Cr-C droplets show no metal or carbide bonded to their surface, see Figures 6.32 to Figure 6.36. This could indicate that the liquid phase,

when saturated with carbon, does not wet the graphitic surfaces as detailed in section 2.1.5. Other possibility could be the evaporation of Cr due to the vacuum atmosphere.

The density of the material coming from the first sintering cycle shows less carbide content and therefore more graphite, visible in the low magnification observations in Figure 6.30. In fact, the density is lower in CG-1100A0 molten phase material, see Table 6.7.

Table 6.7: Density measurements (g cm^{-3}) on solid LP pieces. Specimen 1 is the one analysed by SEM and XRD techniques.

Piece	Cycle 1 (A0)	Cycle 2 (B0)
1	1.838	4.237
2	1.647	3.310
3	1.702	3.430
4		3.551
Average	1.73	3.63

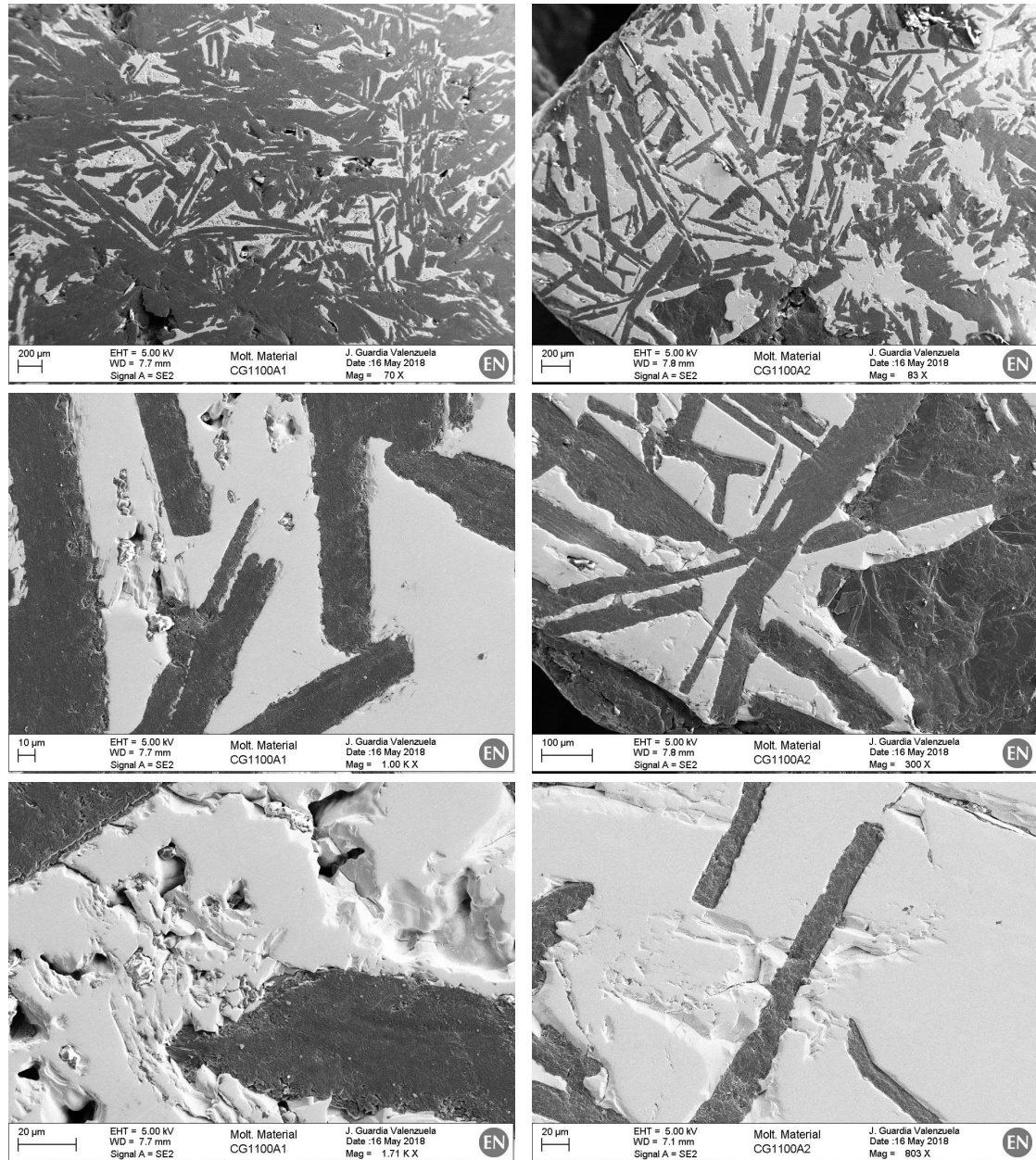


Figure 6.30: SEM observations of the LP spill. (Left) From CG-1100A0 cycle. (Right) From CG-1100B0 cycle (second subsequent cycle to CG-1100A0).

Figure 6.31 demonstrates that the flakes grow in random orientations, visible with the difference of contrast due to electron channeling. In that image, a flake seems to be parallel to the polished surface.

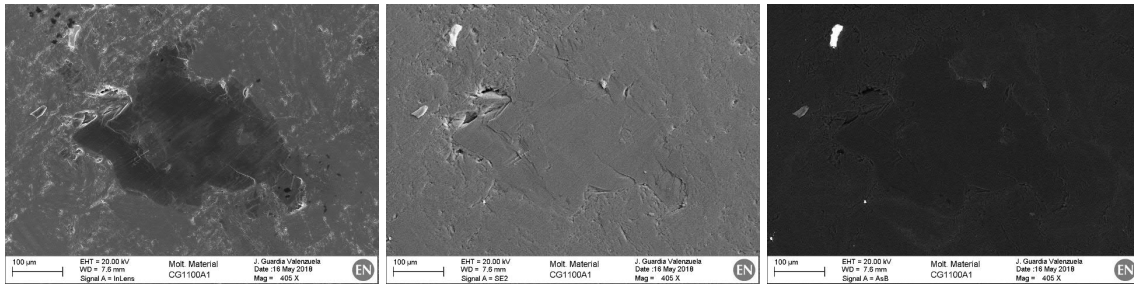


Figure 6.31: SEM observations of a graphite flake in the LP spill from CG-1100A0 cycle oriented parallel to the surface. From left to right: SE, SE and BE detector images.

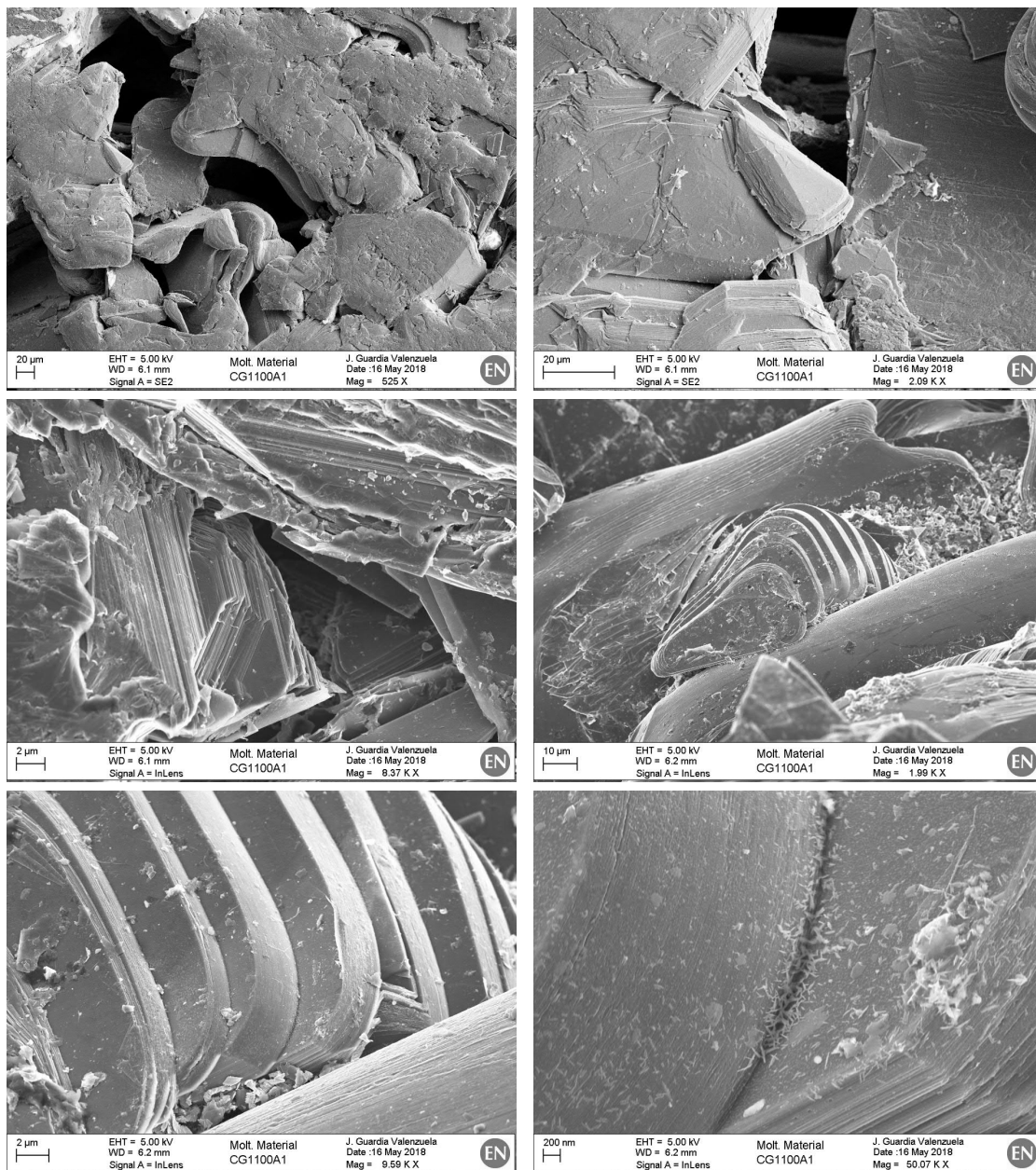


Figure 6.32: SEM observations of the LP spill from CG-1100A0 cycle showing exposed flakes produced by the dissolution-precipitation mechanism. The area observed is the external surface of the droplet (not-polished).

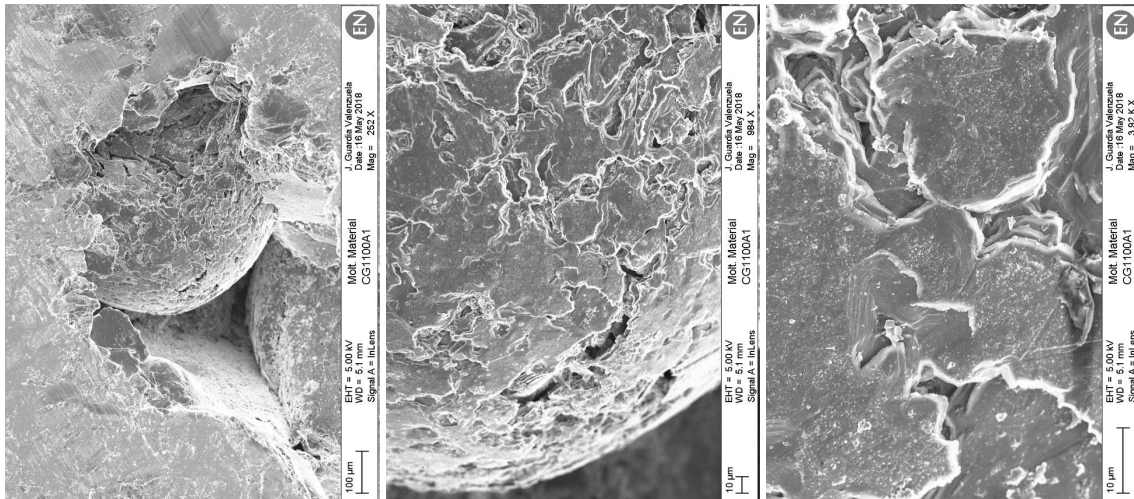


Figure 6.33: SEM observations of a graphite sphere in the LP spill from CG-1100A0 cycle. These images are taken at a pore visible on the polished surface.

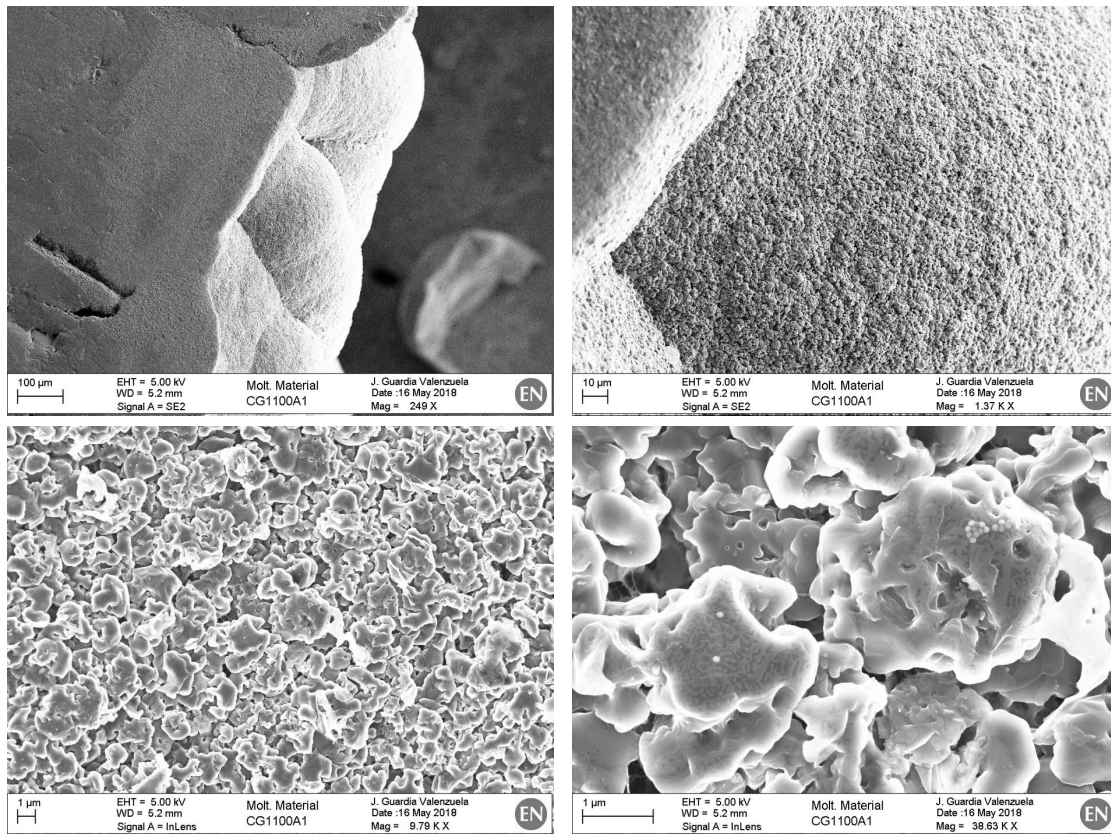


Figure 6.34: SEM observations of the LP spill from CG-1100A0 cycle. The images correspond to the external surface of the droplet (not polished). No relevant Cr content appears in these areas, as demonstrated in Figure 6.35.

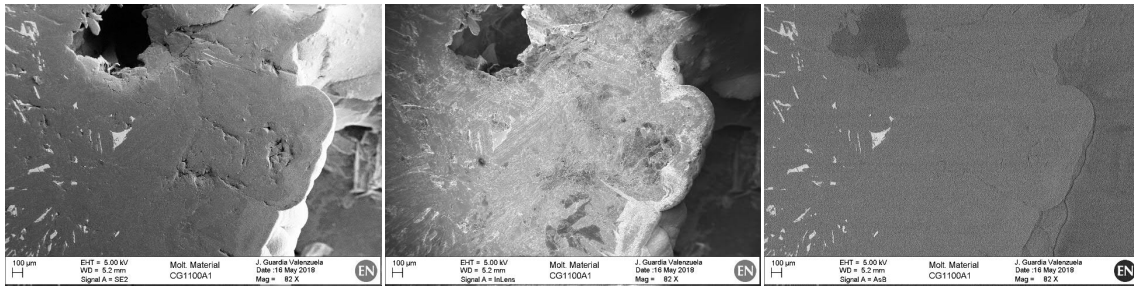


Figure 6.35: SEM observations of the LP spill from CG-1100A0 cycle. The images correspond to the polished surface, but the external droplet surface is also visible at the bottom right area of the three images. From left to right: SE, SE and BE detector images. Note how the BE image does not show carbide content at the droplet external surface.

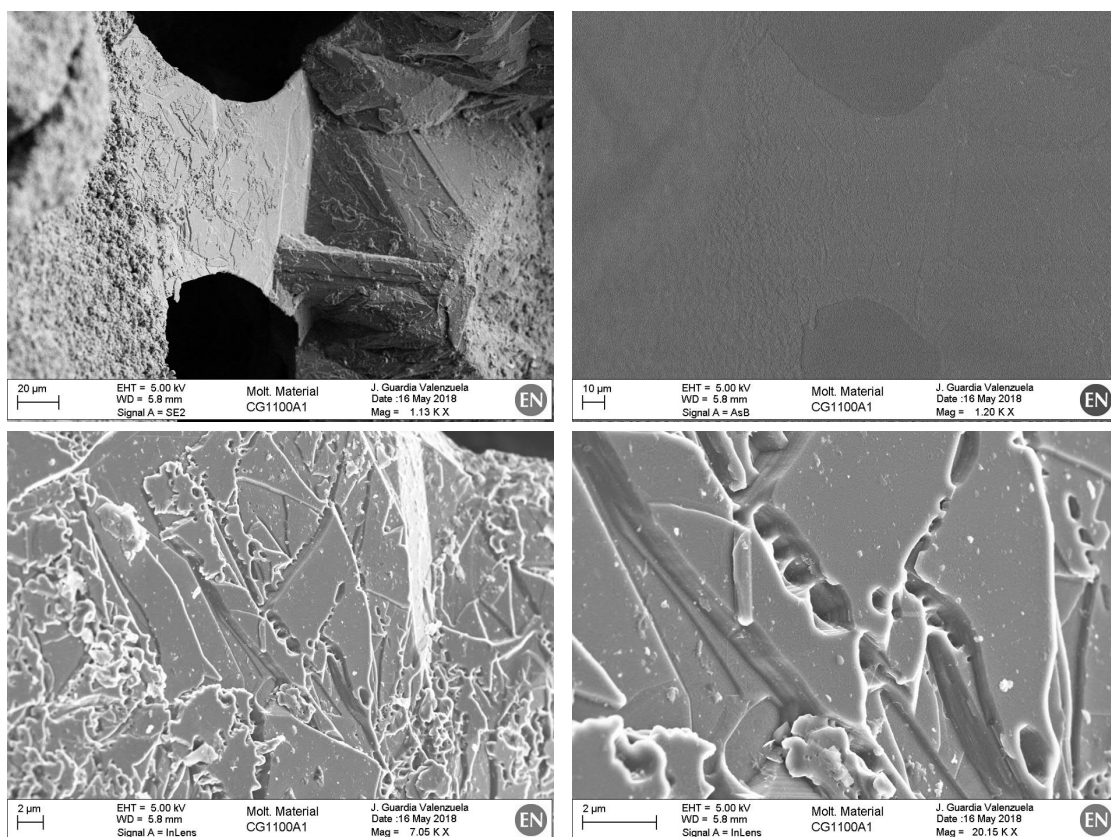


Figure 6.36: SEM observations of the LP spill from CG-1100A0 cycle. The area observed correspond to the external part of the droplet (not polished). Carbon structures were built by the dissolution-precipitation mechanism. The top right image (BE) demonstrates that there is no significant carbide content in these structures.

Cr-C system, unlike Mo-C, does not feature carbon precipitation from the solid carbides during cooling down. The effect of carbon precipitation from solid carbides in the composites need further verification. In fact, carbon dissolution-precipitation processes in liquid phase are expected to play a major role in the production of these materials.

These observations demonstrate the efficiency of Cr-C LP in carbon dissolution processes. Catalytic graphitisation by the dissolution-precipitation mechanism has been confirmed both in Cr-C and Mo-C liquid phases.

7 | Conclusions and perspectives

A family of graphite-matrix composite materials containing molybdenum carbide particles (MoGr), has been successfully developed for CERN future HL-LHC collimators. MoGr material is produced at temperatures $\sim 2600^\circ\text{C}$ by spark plasma sintering, comprising molten metal-carbon liquid phase (LP). The last developments are reported by J.Guardia-Valenzuela et al. [37], constituting the basis of this thesis.

The investigated carbide-graphite composites are mainly composed of oriented graphite, therefore they exhibit a transversely isotropic behaviour with in-plane properties comparable to those of pure ordered graphites. However, unlike the latter, which are extremely anisotropic, the composites keep reasonable thermo-physical and mechanical properties also in the direction perpendicular to the basal planes. Furthermore, the material can be produced in sizes compatible with industrial requirements and machined to the desired shape by conventional milling methods.

Besides high energy physics, the combination of properties of these carbide - graphite composites is appealing for a broad range of thermal management applications, particularly in aerospace and electronics, where reduced thermal expansion and low density are required along with high thermal conductivity.

The research in this thesis aimed at significantly extending the knowledge of the physical mechanisms — such as catalytic graphitisation — that govern the behaviour of these materials (Chapter 2). Given this understanding, similar properties can, in theory, be achieved with other catalysts than molybdenum. The efficiency of the liquid phase to dissolve carbon was identified as the most important parameter. This, together with the temperature at which the aforementioned LP is formed, define the basis for the survey. One of the main goals of this research was to find new production routes reducing the material cost and facilitating the sintering control, therefore increasing the market dissemination potential. A broad spectrum of candidate elements to replace molybdenum has been explored. Chromium was selected for the study because of (I) its ability to form a LP at relatively low temperature compared with molybdenum, (II) the ability of this LP to dissolve a large amount of carbon, almost identical to that of molybdenum, (III) the stability of the solidified chromium carbides, and (IV) the availability and reasonable cost of small particle size Cr_3C_2 powder (Section 2.3.6).

Four chromium carbide - graphite (CrGr) grades were produced and extensively characterised. These materials, unlike MoGr, can be sintered at temperatures lower than 2000°C maintaining the advantages of the liquid phase sintering. One of the advantages is that at these temperatures the graphite parts of the sintering set-up should not suffer creep.

In the direction of graphite basal-planes, at room temperature, CrGr features thermal conductivities of $530\text{--}740\text{ W m}^{-1}\text{K}^{-1}$ and electrical conductivity of around 1 MS m^{-1} . This is close enough to MoGr, which shows k approaching $900\text{ W m}^{-1}\text{K}^{-1}$ and similar γ_e . Their coefficient of thermal expansion (secant) between room temperature and 1000°C is $2\text{--}3 \times 10^{-6}\text{ K}^{-1}$. Densities of CrGr range between $2.1\text{--}2.3\text{ g cm}^{-3}$ while those of MoGr between $2.5\text{--}2.6\text{ g cm}^{-3}$.

However, mechanical properties are considerably lower than MoGr. These differences are currently being investigated. Some preliminary findings (Section 6.2.3) indicate that this is due to weak bonding between the initial graphite flakes. The sintering temperatures are under the threshold of thermal graphitisation, hence the catalytic graphitisation process is the sole responsible to ensure good matrix cohesion.

The characteristics of CrGr materials are close to the requirements for collimator absorbers. Beam-impact experiments on MoGr have shown adequate resistance to the typical loads in collimators. Similar tests on CrGr materials are required to assess their behaviour under real beam-impact scenarios.

Characterisation results have been presented for all the grades produced. Microstructural and phase analysis have been performed. The thermal expansion behaviour and stability of all relevant phases have been characterised by in-situ X-ray diffraction (XRD) up to 600 °C. The results have been compared with two high quality commercial graphites: pyrolytic graphite (PG) and fine-grained nuclear isotropic graphite.

Microscopic observations confirm the effectiveness of chromium-carbon LP for the carbon dissolution-precipitation mechanism, which allows production of graphite with presumably the best crystalline quality (Chapter 2). In fact, graphite flakes as big as 800 µm have been detected in Cr-C droplets spilled out of the mould. This size is close to that of flakes detected in droplets coming from MoGr materials (1200 µm).

Besides, carbon fibres (CFs) seem to be dissolved and reprecipitated as graphite by the liquid phase, confirming the carbon-solvent performance of the investigated liquid phases. Despite of the CFs dissolution, effects on thermo-physical properties may still be attributed to their inclusion. XRD diffraction confirmed lower graphitisation levels in the fibres than in the rest of initial graphite powders. For this reason, they are the least stable carbon solid in the initial mixture, hence dissolved in first place. The use of other carbon sources instead of CFs such as highly pure carbon black, may provide the same effect and be more cost-efficient (Section 6.3).

Some of the flakes grown in the Cr-C droplets by the dissolution-precipitation mechanism appear with no metal or carbide bonded to their surface. This could indicate that the liquid phase, when saturated with carbon, does not wet the graphitic surfaces.

Cr-C system, unlike Mo-C, do not feature carbon precipitation from the solid carbides during cooling down. The effect of carbon precipitation from solid carbides in the composites need further verification. In any case, carbon dissolution-precipitation processes in liquid phase are expected to play a major role in the production of these materials.

XRD and SEM tests revealed that superficial graphite crystallites from all graphite-based materials bend to align parallel to the surface, when mechanical processes such as machining or sanding are used (Section 6.1.3).

Besides, ultrasonic bath cleaning has been found to modify the surface of the carbide-graphite composites by removal of some graphite particles. This effect is more acute in surfaces parallel to graphite-basal planes. On the other hand, in commercial graphite or

carbon fibre-carbon (CFC) materials no flakes are removed, but there are other surface changes at the micro-scale: the flakes lift from the surface and change slightly their superficial exposure. These effects of sonication (Section 6.1.3), can be of interest for bonding applications such as thin-film deposition.

Perspectives

One aspect that remains for future investigation is the assessment of the compaction of the materials. SEM observations have shown that the level compaction is large, with little visible porosity. However, as shown in Section 6.1.3, ion-milling techniques are required for precise assessment of the porosity. Another possibility, would be to measure the volume content of the carbides by image analysis in order to infer the level of compaction and the porosity content. However, some uncertainties may arise due to unknown precise carbide density (stoichiometry), and due to potentially anisotropic dimensions of the carbides.

The characterisation results of grade CG-1240X have shown interesting properties, as it surpasses the other CrGr materials in IP transport properties while keeping similar TP properties. A second sintering test, in order to obtain the final material is therefore of interest.

In order to address the issue of limited graphite-matrix cohesion, we are considering the use of small quantity of carbon pitch together with carbonisation-graphitisation heat treatments. Pitch releases volatile hydrocarbon molecules which can build up gas pressure inside the material and cause cracks. However, if the gas quantity is small enough and no cracks are produced during the heating-up ramp, the volatiles may be able to decompose into solid carbon and gaseous hydrogen, with the latter being able to diffuse out of the mould.

The in-situ XRD analyses provided useful information to characterise the mismatch between thermal expansion coefficients of carbides and graphite, which produces stresses at the interface. These stresses may lead to cracks or may limit the mechanical performance of the composites. The smaller the particles, the less important the stresses are, due to the smaller contact length. The CTE mismatch is probably less relevant than the limitations of the bond between the graphite particles themselves. However, for a detailed analysis, a Finite Element Modelling (FEM) study could be performed to assess this aspect of the composites.

At present, one important aspect that requires characterisation is the outgassing behaviour of CrGr materials. This aspect needs to be addressed in order to satisfy ultra-high vacuum requirements and qualify its potential use in particle accelerators.

Conclusiones y perspectivas

Una familia de materiales compuestos de matriz grafitica con partículas de carburo de molibdeno (MoGr), ha sido satisfactoriamente desarrollada para los colimadores del futuro acelerador HL-LHC del CERN. El material MoGr se produce por sinterización por descarga de plasma a temperaturas de $\sim 2600^\circ\text{C}$, integrando fase líquida (FL) de metal-carbono. Los últimos desarrollos están publicados por J. Guardia-Valenzuela et al. [37], constituyendo la base de esta tesis.

Los composites de carburo-grafito investigados están mayoritariamente compuestos de grafito orientado, por lo que muestran un comportamiento transversalmente isótropo con propiedades en la dirección de los planos basales comparables a las de grafitos orientados puros. Sin embargo, a diferencia de éstos últimos, que son extremadamente anisotrópicos, los composites mantienen propiedades termofísicas y mecánicas razonables en la dirección perpendicular a los planos basales (TP). El material puede producirse en tamaños compatibles con los requisitos industriales y mecanizarse con métodos convencionales.

Además de en física de altas energías, la combinación de propiedades de estos composites es atractiva para un amplio catálogo de aplicaciones de transferencia de calor, particularmente aeroespaciales y electrónicas, donde se necesitan bajos coeficientes de expansión, bajas densidades y altas conductividades térmicas.

Esta tesis busca ampliar significativamente el conocimiento de los mecanismos físicos — como la grafitización catalizada — que controlan el comportamiento de estos materiales (Capítulo 2). Estos conocimientos indican que se pueden conseguir propiedades similares con otros catalizadores diferentes al molibdeno. La eficacia de la FL disolviendo carbono se identificó como el parámetro más importante. Esto, junto con la temperatura a la que la susodicha FL se forma, definen la base de los criterios de selección. Uno de los objetivos principales de esta investigación es encontrar nuevas rutas de producción que reduzcan el coste y faciliten el control del sinterizado, por lo tanto que consigan aumentar su aplicación y uso en el mercado. Un gran abanico de elementos han sido explorados. El cromo fue seleccionado para este estudio por (I) su capacidad de formar una FL a una temperatura relativamente baja comparada con el molibdeno, (II) la capacidad de esta FL de disolver una gran cantidad de carbono, casi la misma que el molibdeno, (III) la estabilidad de los carburos de cromo sólidos, y (IV) la disponibilidad y coste razonable del polvo de Cr_3C_2 de pequeño tamaño de partícula.

Cuatro grados de material carburo de cromo - grafito (CrGr) fueron producidos y extensivamente caracterizados. Estos materiales, a diferencia del MoGr, se pueden sinterizar a temperaturas por debajo de 2000°C , manteniendo las ventajas del sinterizado con fase líquida. Una de las ventajas es que, a esas temperaturas, los útiles de sinterizado de grafito no sufren termofluencia.

En la dirección de los planos basales, a temperatura ambiente, el CrGr muestra conductividades térmicas de $530\text{--}740\text{ W m}^{-1}\text{K}^{-1}$ y conductividades eléctricas de alrededor de 1 MS m^{-1} . Éstas se acercan bastante a las del MoGr, que muestra k de casi $900\text{ W m}^{-1}\text{K}^{-1}$ y γ_e similar. Sus coeficientes de expansión (secante) entre temperatura ambiente y 1000°C es de $2\text{--}3 \times 10^{-6}\text{ K}^{-1}$. La densidad del CrGr esta entre $2.1\text{--}2.3\text{ g cm}^{-3}$, mientras que la del MoGr es de $2.5\text{--}2.6\text{ g cm}^{-3}$.

Sin embargo, las propiedades mecánicas son considerablemente más bajas que las del MoGr. Estas diferencias están siendo actualmente investigadas. Los resultados preliminares (Sección 6.2.3) indican que esto es debido a un enlace débil entre partículas de grafito. La temperatura de sinterizado está por debajo del umbral de grafitización térmica, por lo que la grafitización catalizada es la única responsable de asegurar buena cohesión en la matriz.

Las características del CrGr se acercan a los requisitos para absorbentes de colimadores. Experimentos de impacto de haz de partículas en el MoGr han demostrado la adecuada resistencia a las sollicitaciones típicas en colimadores. Se tendrían que hacer ensayos similares en el CrGr para evaluar el comportamiento ante impactos reales.

Se han presentado resultados de la caracterización de todos los grados desarrollados. Los ensayos incluyen caracterización de la microestructura e identificación de las fases cristalinas. Los coeficientes de expansión térmica y la estabilidad de las fases se han caracterizado con difracción de rayos X in-situ hasta $600\text{ }^{\circ}\text{C}$. Los resultados se han comparado con dos grados comerciales de grafito también caracterizados: grafito pirolítico y grafito isotrópico de grano fino (grado nuclear).

Las observaciones microscópicas confirman la efectividad de la FL cromo-carbono para el mecanismo de disolución-precipitación, que permite producir grafito de presumiblemente la mejor calidad cristalina (Capítulo 2). De hecho, se han detectado partículas laminares de grafito de hasta $800\text{ }\mu\text{m}$ en gotas de Cr-C derramadas del molde. Estas dimensiones se acercan a las partículas detectadas en gotas del MoGr ($1200\text{ }\mu\text{m}$).

Además, parece que las fibras de carbono se disuelven y reprecipitan en forma de grafito, confirmando la capacidad de disolver carbono de las FL investigadas. A pesar de su disolución, se pueden atribuir efectos en las propiedades termofísicas a su inclusión. Los ensayos de difracción de rayos X muestran los niveles más bajos de grafitización en las fibras de todos los componentes iniciales. Por ello, las fibras son los sólidos carbonosos menos estables y se disolverán en primer lugar. El uso de otras fuentes de carbono como negro de carbono en vez de fibras, podría dar los mismos resultados con un menor coste (Sección 6.3).

Algunas de los copos de grafito que crecen en las gotas de Cr-C mediante el mecanismo de disolución-precipitación aparecen sin nada de metal o carburo adherido a su superficie. Esto podría indicar que la FL, cuando está saturada de carbono, no impregna las superficies gráficas.

El sistema binario Cr-C, al contrario que el de Mo-C, no muestra precipitación de carbono desde los carburos en estado sólido durante el enfriamiento. El efecto de la precipitación de carbono desde los carburos sólidos necesita ser investigado con más detalle. En cualquier caso, se espera que los procesos de disolución-precipitación en FL tengan un rol principal en la producción de estos materiales.

Ensayos XRD y SEM han revelado que los granos superficiales de grafito en todos los materiales gráfiticos se doblan y alinean paralelamente a la superficie, en caso de aplicación de procesos mecánicos como el mecanizado o el lijado (Sección 6.1.3).

Además, se ha hallado que la limpieza con ultrasonidos modifica la superficie de los composites carburo-grafito, arrancando algunas partículas de grafito. Este efecto se agudiza en las superficies paralelas a los planos basales. Por otra parte, en los grafitos y composites carbono-fibras de carbono (CFC) comerciales, no se arrancan partículas, pero hay otros cambios superficiales: las partículas se levantan de la superficie y cambian ligeramente su exposición superficial. Estos efectos de los ultrasonidos (Sección 6.1.3) podrían ser interesantes para preparar la superficie cuando se requiera buena adherencia (deposición de capas delgadas).

Perspectivas

Un aspecto que queda para una futura investigación es la evaluación de la compactación de los materiales. Las observaciones SEM muestran que el nivel de compactación es alto, con poca porosidad. Sin embargo, como se muestra en la sección 6.1.3, se necesitan procesos de pulido con haz de iones para estimar con precisión la porosidad. Otra posibilidad sería la medición del volumen de carburos por análisis de imagen para deducir la porosidad. Sin embargo, hay algunas incertidumbres debido al desconocimiento de la densidad de forma precisa de los carburos (estequiometría), y debido a que pueden presentar anisotropía en las dimensiones de los mismos.

Los resultados de caracterización del grado CG-1240X han mostrado interesantes propiedades, ya que sobrepasa a los otros grados de CrGr en las propiedades de transporte en el plano sin empeorar notablemente en la dirección perpendicular al plano. Una segunda prueba de sinterizado sería de interés para obtener el material sin defectos.

Para solucionar el problema de la limitada cohesión en la matriz gráfitica, se está considerando el uso de pequeñas cantidades de brea junto con los tratamientos térmicos de carbonización-grafitización. La brea produce hidrocarburos volátiles que pueden generar sobrepresión y causar grietas. Sin embargo, si la cantidad de gas es suficientemente pequeña y no se producen grietas durante la rampa de calentamiento, los volátiles podrían descomponerse en carbono sólido e hidrógeno gaseoso, siendo el último capaz de difundir fuera del material.

Los datos de los ensayos XRD in-situ sirven para caracterizar la diferencia entre coeficientes de expansión del grafito y los carburos, que genera tensiones en la interfaz. Estas tensiones podrían provocar grietas o limitar el desempeño mecánico del material. Seguramente, las diferencias de expansión no son tan relevantes como la cohesión entre las partículas de grafito. Sin embargo, un estudio detallado con simulaciones de elementos finitos (FEM) podría desarrollarse para evaluar este aspecto de los composites.

Actualmente, un aspecto importante que requiere caracterización es el degaseado de los materiales CrGr. Esto necesita ser evaluado para cumplir con los requisitos de compatibilidad con ultra alto vacío, y validar su uso en el acelerador de partículas.

APPENDICES

A | LHC operation and some of its engineering challenges

In this section, the basic principles of operation of the LHC and some of the faced engineering challenges are presented.

Injection

LHC can work accelerating either protons or lead ions. Lead ions are obtained from an isotopically pure lead sample (around 10 k€ for 10 grams) heated up to 800 °C.

In the case of protons, they are extracted from a hydrogen gas bottle. One LHC beam of 2808 bunches of 1.15×10^{11} protons contains the same protons than a sphere of $\varnothing = 0.23 \text{ mm}$ containing hydrogen at NTP (20 °C and 1 atm).

Once hydrogen gas is ionized (hydrogen nucleus is composed of just one proton), the resulting protons are accelerated, first by a linear accelerator and then by several circular accelerators with increasing size (BOOSTER, PS and SPS), up to the injection in the LHC. This process typically takes a bit more than 1h [150]. Figure A.1 shows the schematic of the accelerators and the experiments built at CERN, most of them are in underground tunnels (such as the 27km-long LHC, at an average depth of 100m).

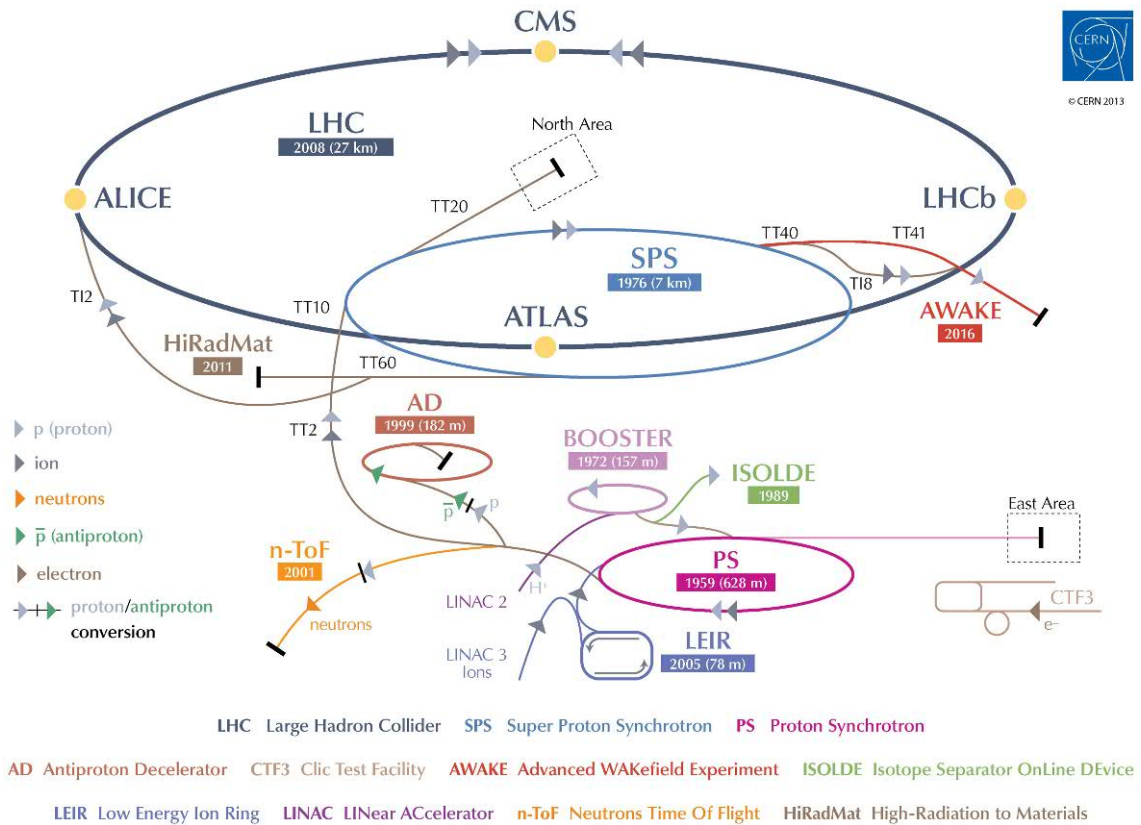


Figure A.1: CERN accelerator complex

Beam acceleration and structure

The technology used for accelerating particles is based on electrostatic linear acceleration by superconducting (4.5K) resonant radio-frequency (RF) cavities, picture A.3a. The working principle of the RF cavities is similar to the device which generates microwaves in microwave ovens, with a different purpose. The alternating electrostatic field is used to accelerate charged particles. The advantage of a circular accelerator over a linear one is that does not require a large set of RF cavities, because the particles can pass through them multiple times to reach the top energy.

Each cavity can achieve a maximum voltage of 2 MV (5.3 MV/m) at 400 MHz, with a total of eight cavities per beam line. It takes around 20 min from the injection to reach LHC top energy [150].

The ideally timed particles, with exactly the right energy, will see zero accelerating voltage when the LHC is at full energy. Particles with slightly different energies arriving earlier or later will be accelerated or decelerated. This is why the beam is not a continuous flow, instead, is sorted in discrete packets called "bunches".

The cavities oscillation frequency of 400.79 MHz (period 2.495 ns) produces, in the 26659 m of the ring, 35640 "buckets" or places where the bunches can accommodate [151]. The bunch spacing is fixed at 24.95 ns (7.48 m), meaning that between two consecutive bunches there are 9 empty buckets. Therefore, the "bunch clock" frequency is defined by a division 1:10 of the RF frequency. This scheme defines a total of 3564 possible bunch positions in the ring [151]. Each bunch (around 7.5 cm long) passes in less than 1 ns.

The maximum number of bunches (2808) leaves some empty positions which sum 18.9 μ s (5.7 km) of the 88.9 μ s lap time, allowing to include several gaps in the pattern of bunches for practical reasons. These gaps allow time for example to accommodate the rise times of the various injection kicker magnets (200 ns, 1 μ s) and the rise time of the beam dump kicker (3 μ s) [152].

The SPS can circulate and inject to the LHC a maximum of 4 batches of 72 bunches each (288 bunches), so it has to inject several synchronized times into the LHC in order to create the full beam. The typical bunch disposition of the LHC with the pattern of batches "234 334 334 334" is shown in Figure A.2.

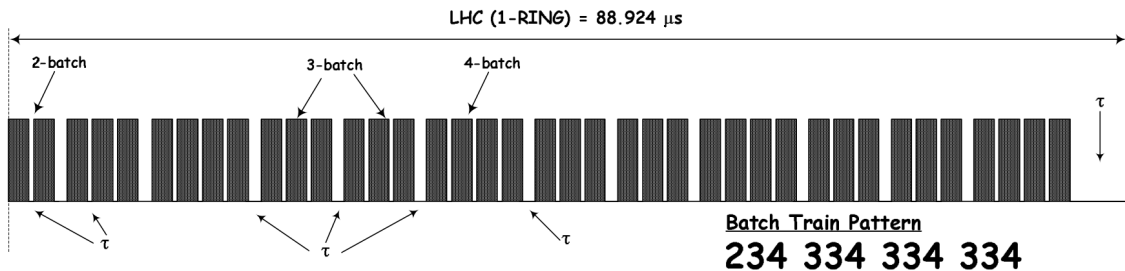
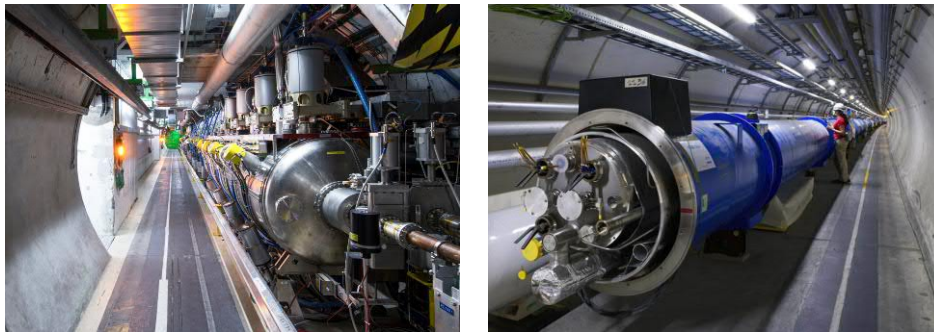


Figure A.2: Schematic of the bunch disposition around a LHC ring for the 25ns filling scheme. Each of the 39 batches is made of 72 bunches ($39 \times 72 = 2808$) [152].

All in all, the average bunch crossing rate at the collision points is equal to number of bunches N_b multiplied by revolution frequency f : $2808 \times 11245 = 31.6 MHz$.

Figure A.3: LHC devices



(a) Radio-Frequency cavities in point 4

(b) Dipole showing its connections

Dipole magnets and cryogenics

Magnets are required to bend the trajectory of the proton beam. Without the correct field, the beam of particles would not turn the angle required to continue inside the beam pipe of the circular accelerator. Therefore, most of the 27km of the ring are taken up by superconducting dipole magnets (1232 units) generating 8.33 T , see picture A.3b.

The superconducting dipoles operate at 1.9 K , maintained with a complex liquid helium cooling system. The LHC's cryogenic system requires 40 MW of electric power and 120 tonnes of liquid helium to cool down around $36,000\text{ tonnes}$ of magnet cold masses distributed over the 27km ring. Below 2.17 K , liquid helium passes to superfluid state, having nil viscosity and high thermal conductivity. The cooling process uses some $10,000\text{ tonnes}$ of liquid nitrogen to bring the temperature of helium down to 80 K . The helium is then cooled down to 4.5 K and then to 1.9 K .

The large electric current ($11,850\text{ A}$) required to produce the magnetic field is supplied to the magnet coils from power converters operating at room temperature. The conductor from the converter is a large piece of copper ($\approx 2000\text{ mm}^2$) which cannot be connected directly with the superconducting cable due to the huge amount of heat that would be otherwise transferred to the cryostat. The current leads connecting to the superconducting cables in the cryostat are a critical device for the LHC. They have a nominal operating current of 13kA while transferring a heat load into the liquid helium of less than 1.5 W/lead [153]. To achieve this value they require $\leq 0.85\text{ g/s}$ of 20 K helium cooling gas, available in the LHC cryogenic system. The interesting design of the current lead uses tapes of Bi-2223 high-temperature superconductor (HTS) as thermal barrier (low thermal conductivity), and a fin-type cooling system working with 20 K helium gas [154], see Figure A.4.

There are two parallel beam pipes where the two beams travel in opposite directions. The design of the dipoles allows to share the same magnetic field for the two beam pipes, in a way that they see it in opposite directions, therefore turning to the same side. In picture A.3b it is possible to see the connections of the two beam pipes in a dipole magnet.

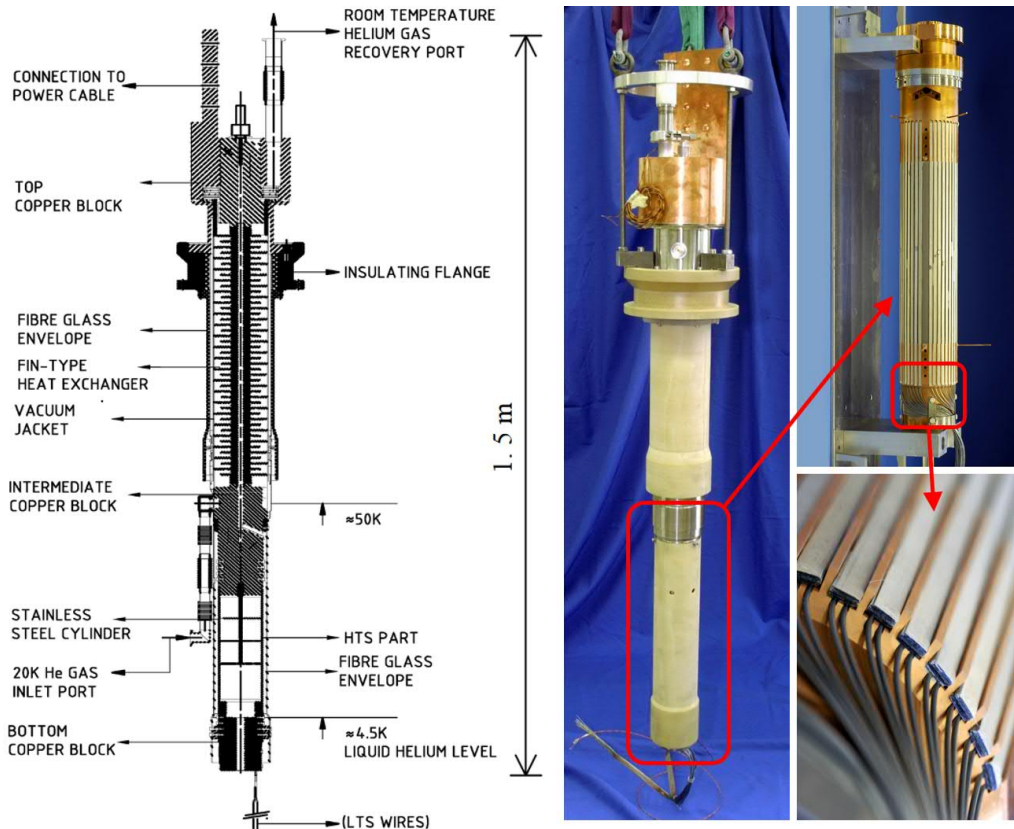


Figure A.4: 13000 A lead schematic and prototype [154]. Note the size of the copper conductor at the top compared with the superconducting cable at the bottom.

Collisions and detectors

Once the top energy is achieved, the two beams travelling in opposite directions are intersected to collide at the experiment points, where the detectors are located. ATLAS (Figure A.5), CMS, ALICE and LHCb are the four experiments that use head-on collisions, all located in underground caverns.

There are three more experiments at the LHC and many more experiments that use the beam from the accelerators that inject into the LHC. For example, there are several experiments ongoing that use antiprotons obtained from the Antiproton Decelerator (AD), see Figure A.1. The antiprotons are produced by colliding the PS beam into a metallic target, then they are decelerated in order to perform measurements on them.

Currently, the LHC operates with the parameters shown in table 1.2, producing around 800 million collisions per second, see Equation 1.6. Each time two opposite travelling bunches cross (2 times 1.15×10^{11} protons), only about 25 of them collide, see Equation 1.7. The accelerator operates full time, the maximum possible number of days per year in order to maximize the production of interesting events.

Collisions produce many sub-atomic particles that are detected, tracked and characterised with the aid of magnetic fields, calorimeters, pixel detectors, gas ionization tubes, etc. For instance, most detectors work with an internal fixed magnetic field; tracking the curved trajectory of charged particles in these detectors allows deducing their mass.

Each of the four detectors has around 40 million sensors, like a 40 mega-pixel camera,

but taking more than 30 million pictures per second. The data flow of each of the 4 detectors in the LHC is around 1GB/s after the filtering process (total of around 50.000 TB or 50 PB per year). Only the interesting information from the detectors is stored for future analysis. The data is archived to long-term magnetic tape storage. While tapes may sound like an outdated mode of storage, they are actually the most reliable and cost-effective technology for large-scale archiving of data [155]. The filtering hardware and algorithms are extremely important, as the LHC produces 40,000 GB/s of raw information ($\approx 1\text{ Mb/event}$). Information technologies (IT) are therefore fundamental at CERN.

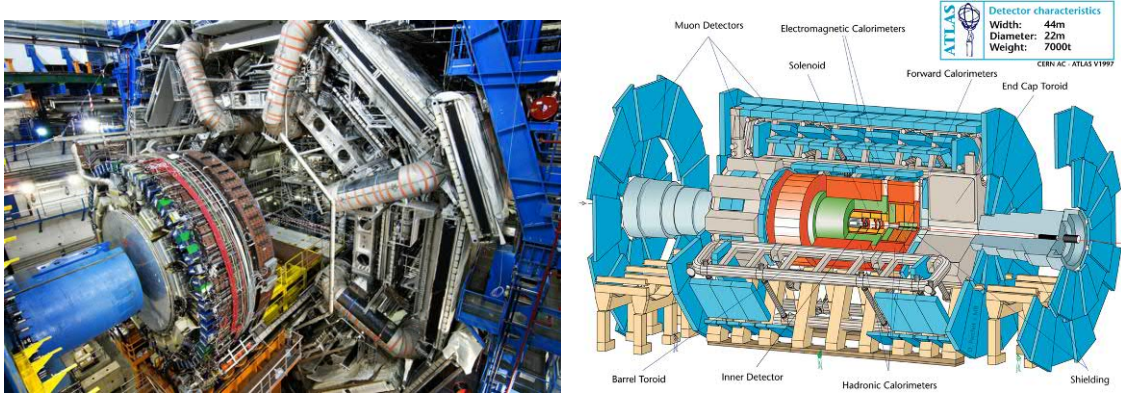


Figure A.5: ATLAS detector ($\varnothing 22\text{ m} \times 44\text{ m}$).

Every turn, the beam intensity decreases due to particle losses, mainly in the collimation system and in the collision points [156]. The remaining part of the beam continue circulating in the ring and colliding at the interaction points. To maintain adequate levels of luminosity, after around 10h, the beams are dumped and new ones are injected.

LHC dump

For each of the two LHC beam lines there is a beam dump device "TDE" designed to receive 2×10^4 full beam aborts at 7 TeV during an operational lifetime of 20 years. This device belongs to the *Beam Intercepting Devices* (BID) family. The beam dump is not only used in emergencies. After around 10h of physics experiments with stable beams circulating, the luminosity decreases too much and the beams have to be disposed in the dumps.

Carbon materials were chosen as the most suitable absorbing material for the beam dump core, with the highest melting (sublimation) temperature and the best thermal shock resistance of the investigated materials [153].

The beam dump core is made of 4420kg of graphite with a total length of 7.7m and a diameter of 0.7m. Two grades are used: polycrystalline isotropic graphite with a density of 1.73 g/cm^3 and stacked flexible graphite plates with a density of 1.1 g/cm^3 . The structure is as shown in Figure A.6. This is followed by 1 m of aluminium and 2 m of iron at the end.

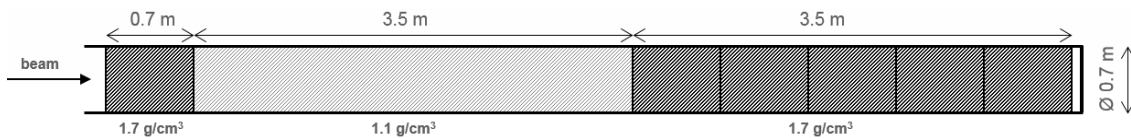


Figure A.6: Dump core structure with two different grades of graphite.

The graphite core is shrink-fitted in a 12 mm-wall stainless-steel pressure vessel, filled with 1.2 bar of N_2 to prevent reaction of the graphite with air. The maximum temperature increase is limited to 1250 °C; the vessel incorporates welded tubes for cooling water. The dump is separated from the vacuum at the LHC beam pipe by a Ø600 mm window made of carbon composite (thickness 15 mm) and a 0.2 mm foil of stainless steel. The window is designed to withstand the differential pressure and to have a maximum temperature increase of 42 K for nominal beam impacts [157]. The beam core vessel is surrounded by about 900 ton of radiation shielding blocks, made with recycled magnet yokes from the decommissioned Intercepting Storage Rings (ISR), see Figure A.7. The window and the dump core are only sufficiently robust to full energy impacts with the beam dilution system [157] [158]. A set of vertical and horizontal dilution kicker magnets is installed in the extraction channel, to sweep the beam onto the beam dump block in a "e" shape, see Figure A.8. The purpose of this is that not all bunches end up on the same spot.

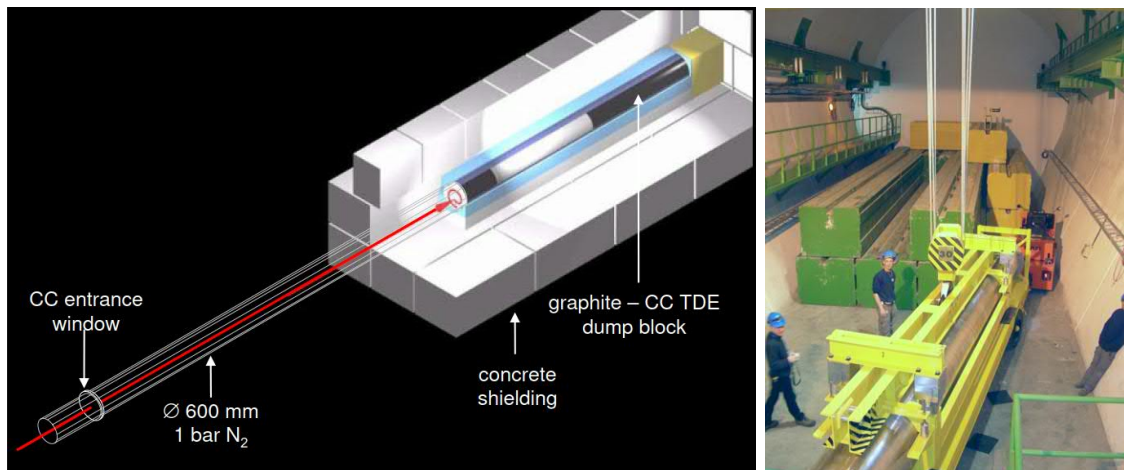


Figure A.7: LHC Beam dump schematic [157] and picture of the dump core installation.

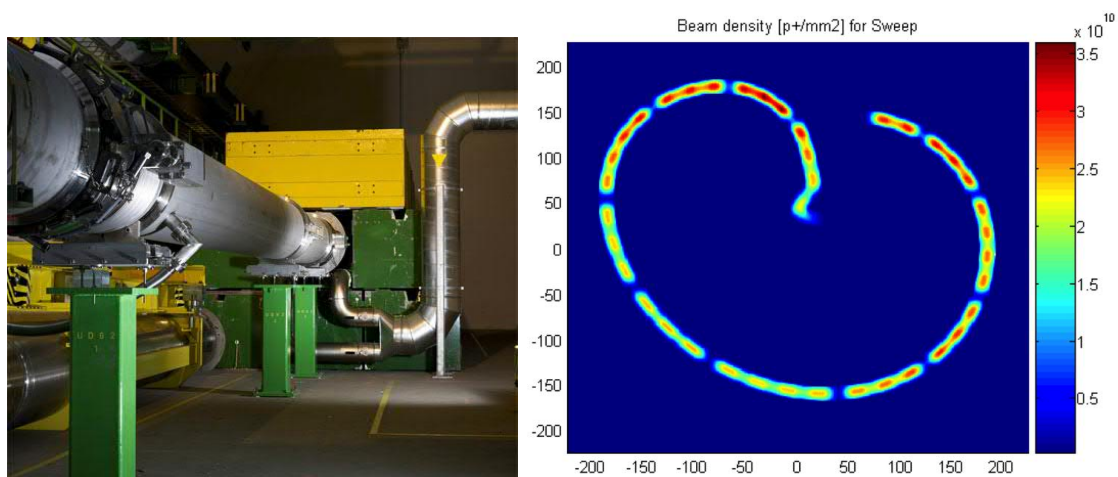


Figure A.8: (Left) LHC Beam dump. (Right) Simulated beam density on the dump window with the dilution system [157], note the bunch disposition from Figure A.2.

Some nuclear safety concerns were expressed before the first LHC run in 2008. The possibility of a chain reaction from nuclear fusion of carbon in the dump, due to the LHC beam impacts was analysed and excluded in a technical memorandum [159].

B | Knowledge Transfer at CERN

Knowledge transfer (KT) is the process whereby knowledge, technology, expertise, discoveries, move from CERN to society. CERN has a well-established tradition of collaboration with companies and research institutes, with the objective to generate technological results having a potential for commercial exploitation.

The mandate of the Knowledge Transfer group is to transfer CERN technologies, via licensing for instance, or using them to create new technologies for applications in research domains other than Particle Physics or for commercial exploitation, on the basis of a written agreement [160]. Some of its missions are: evaluate invention disclosures, protect intellectual property, negotiate licensing and contractual agreements, promote technologies, and provide legal advice on intellectual property issues [160]. Figure B.1 shows the Start-Up and Spin-Off companies that have been created involving CERN technology and know-how.

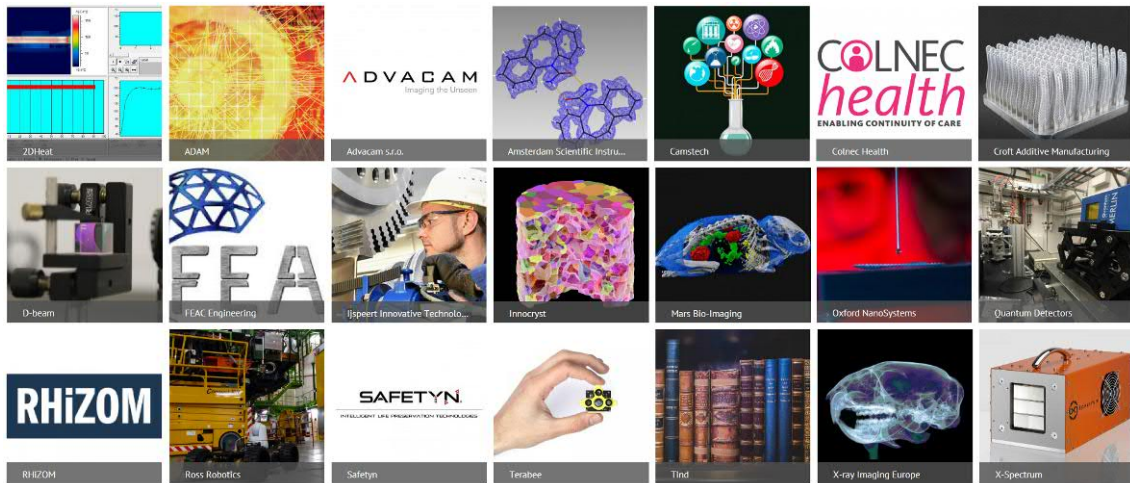


Figure B.1: Current (2018) Start-Ups & Spin-Offs Using CERN Technology & Know-How [160]

Registering a patent usually is not an easy task and it has relevant costs. Costs of filing a patent are divided between patent attorney fees (including drafting and translation) and the official fees and taxes that must be paid to file and maintain the patent in the national or regional patent offices. The costs vary mainly depending on the number and countries in which the patent is filed and how long it is maintained; it can cost over its total lifecycle between CHF 5000 and CHF 200000 [160] ($1\text{€}\approx 1.1\text{CHF}$).

There have been a lot of non-existent technologies required at CERN in vacuum applications, cryogenics, informatics, sensors, control systems, etc. that have been developed initially for the accelerators or detectors, and now industries or consumers are using them every day.

In 1973, Bent Stumpe developed at CERN the first capacitive touch screen [161]. It was necessary to reduce the size of the knobs, switches and oscilloscopes panels for the control room of the coming new Super Proton Synchrotron. Before that, individual cables from each control were linking directly to the actual devices, but in that new 7km circumference machine, it would be unfeasible. After the invention, one complete room of control racks

was substituted by a touch-screen computer with the appropriate software. Figure B.2 shows the 628m long PS control room without touch-screen technology and the 10-times bigger SPS (7km long) control room with the technology. The technology developed for the capacitive touch screen was immediately transferred to industry, in particular to the Danish firm *Ferroperm*. This is one example of Knowledge Transfer.

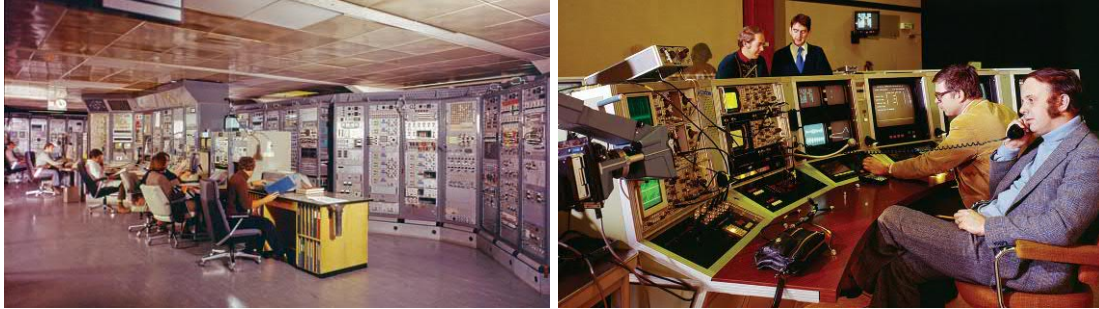


Figure B.2: (Left) PS (628m) control room in 1974. (Right) SPS (7km) control room in 1977.

Nowadays, the use of particle beams for cancer therapy is being exploited more and more. Particle accelerators have shown advantages with respect to standard radiotherapy techniques, see Figure B.3, and are used in hospitals for cancer treatment. At present (April 2019), there are 94 particle therapy facilities in clinical operation all over the world [162]. The energy of particle beams can be deposited in the region of the tumour with much less damage to the healthy tissues. CERN is actively collaborating with its know-how in particle accelerators for developing medical equipment.

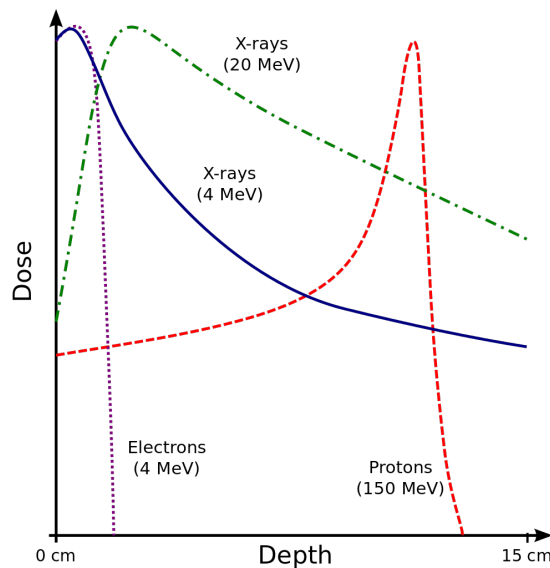


Figure B.3: Energy deposition profiles (Bragg peak) of different radiation types. Unlike electrons or X-rays, the dose from protons to tissue is maximum just over the last few millimetres of the particle's range, depending on the energy. Image by Cepheiden / CC BY-SA 3.0

Besides, accelerators are used in many other domains, such as sterilization of food (food preservation and safety) or medical equipment, ion-implantation for electronic devices and for surface hardening, electron-beam welding, focused ion-beam (FIB) milling, electron-beam polymer cross-linking, etc.

In fact, KT group is actively promoting the use of collimator materials developed at CERN for thermal management applications.

C | Advanced collimation techniques

Besides collimators relying on direct impacts on matter, there are two advanced techniques that are currently being studied for the collimators of the future. Their advantage over standard collimators is that the absorbers can be placed at a larger distance from the beam, thus minimizing impedance and beam instability issues.

Hollow Electron Beam Collimation (HEBC)

The collimation effect of hollow electron beam is based on the interaction between the transverse field of proton and electron beams.

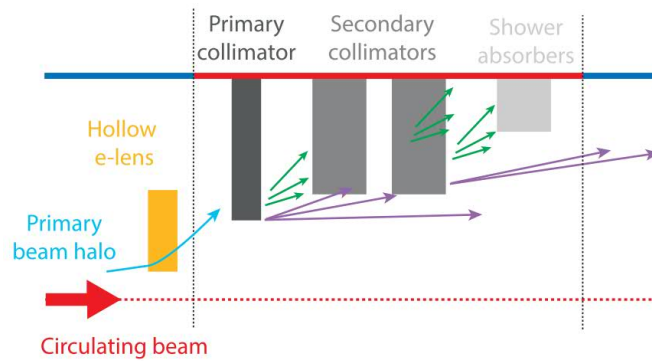


Figure C.1: Schematic of HEBC [16].

An electron gun with appropriate geometry produces a hollow electron beam that is guided by strong magnetic fields into the proton beam pipe. The electron beam overlaps with the proton beam over a given distance, and is afterwards extracted and dumped into an electron collector.

A schematic of the Tevatron Electron Lens 2 (TEL2) is shown in Figure C.2.

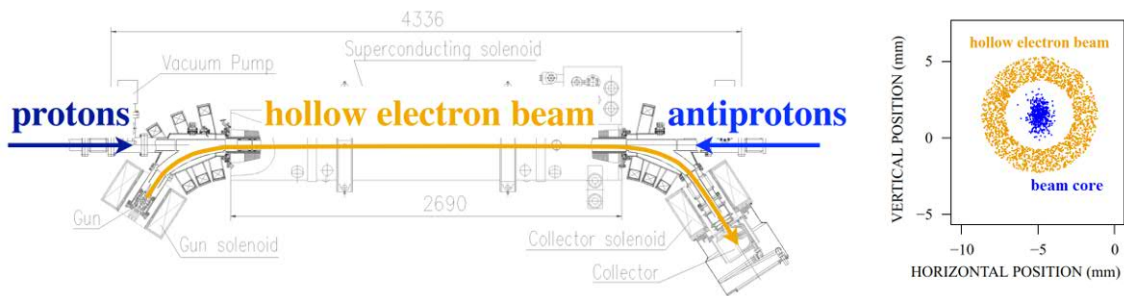


Figure C.2: Technical drawing of the TEL2 set-up and in-plane view of the hollow electron beam

The hollow electron beam has zero electric field inside, so is not affecting particles travelling inside. On the other hand, particles travelling outside or along the electron beam are deviated towards absorbers.

Bent-crystal collimation

Bent crystals can be used to steer high-energy particles by the channelling effect, see Figure C.3.

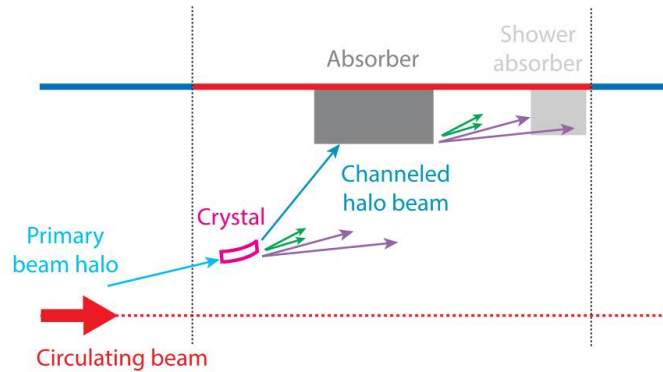


Figure C.3: Schematic of crystal collimation [16].

The ordered structure in a perfect crystal makes some orientations more favourable for charged particles to be gone through than others, see Figure C.4. This is the channelling effect. Many physical phenomena are involved in the channelling effect, such as elastic scattering (Rutherford scattering), inelastic energy-loss processes, secondary-electron emission, electromagnetic radiation, nuclear reactions, etc.

Positively charged particles like protons are repelled from the nuclei, and after entering the space between two neighbouring planes, they will tend to follow that space, at the largest possible distance from the nuclei. Therefore, the positively charged particles have a low probability of interacting with the nuclei and electrons of the planes (small "de-channelling" effect) and so they can travel long distances.

This technology has been tested in the LHC up to 6.5 TeV with promising results [163].

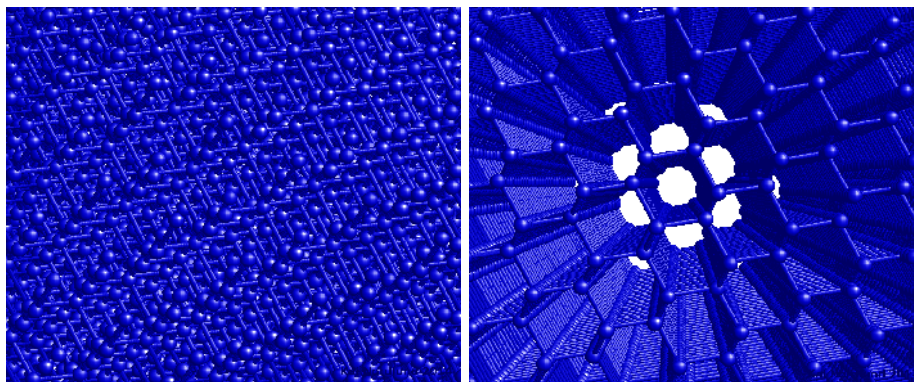


Figure C.4: 12 nm thick Si crystal: (Left) Random direction. (Right) Oriented along the 110 direction to illustrate channelling. Original by Knordlun / CC-BY-SA-3.0.

D | Radiation damage

There are three mechanisms by which particles or radiation lose energy when penetrating matter. These mechanisms can damage the lattice structure of the material and disturb its normal behaviour [164]:

- **Electronic excitations/ionization**
- **Elastic interactions**
- **Inelastic interactions**













The first mechanism is caused by charged particles that remove electrons via the Coulomb interaction, or by ionizing radiation. Excitation is the process where an electron from a low-energy orbit is shifted to a outer shell; this process can also lead to ionization. In elastic and inelastic interactions, energy and momentum are transferred from particles to the nucleus. Particle radiation, such as α , β , proton and neutron radiation produce these interactions. Particle radiation is generated by nuclear reactions, such as fission, fusion and radioactive decay, by cosmic rays and by particle accelerators.

Ionizing radiation

The name "radiation" is given to several forms of energy emitted or transmitted in the form of waves or particles. Ionizing radiation interacts strongly with matter, removing electrons from the atoms and dissipating the excess energy as heat. Some forms of ionizing radiation are listed here:

- **Photons** are the elementary particles responsible of electromagnetic fields, including electromagnetic radiation. The light and heat from an incandescent lamp are forms of electromagnetic radiation, but in this case they are not *ionizing*. The lowest first ionization energy of all elements is 3.89 eV, for caesium (Cs); photons with more energy than that are considered *ionizing*. Ionizing radiation starts in the ultraviolet (UV) rays, continuing with X-rays and gamma rays in the electromagnetic spectrum, see Table D.1.

Table D.1: Electromagnetic spectrum

		Wavelength		Frequency	Photon Energy
Gamma rays		<6pm		>50EHz	>200keV
X-rays		6pm-8.8nm		34PHz-50EHz	141eV-200keV
UV		8.8-390nm		769THz-34PHz	3.18-141eV
Visible	Violet	390-455nm		659-769THz	2.72-3.18eV
	Blue	455-491nm		611-659THz	2.53-2.72eV
	Green	491-577nm		520-611THz	2.15-2.53eV
	Yellow	577-600nm		500-520THz	2.07-2.15eV
	Orange	600-625nm		478-500THz	1.98-2.07eV
	Red	625-789nm		380-478THz	1.57-1.98eV
Infrared		789nm-1mm		300GHz-380THz	1.24meV-1.57eV
Microwave		1mm-30cm		10GHz-300GHz	4.1μeV-1.24meV
Radio		>30cm		<10GHz	<4.1μeV

Even though photons are electrically neutral, they can ionize atoms directly through the photoelectric effect and the Compton effect. Either of those interactions will cause the ejection of an electron from an atom at relativistic speeds, turning that electron into a beta particle (secondary beta particle) that will ionize many other atoms. For this reason, photons are called indirectly ionizing radiation.

- **Alpha particles** consist of two protons and two neutrons, the nucleus of an Helium atom. They are strong ionizing particles, as they have a +2 charge. When they take two electrons from the nearest atom they become an helium atom.

Alpha particles from radioactive decay have low penetration capability; due to their low energy and relatively large mass and charge, they interact strongly with matter. Elements emitting alpha radiation are the most efficient ones to produce localised heat, so they are used in *radioisotope thermoelectric generators* (RTG). RTG use the heat generated by the radioactive decay to produce electricity with thermoelectric devices, mainly for aerospace applications. For example, Cassini spacecraft launched in 1997 used 3 RTGs, each of them containing around 8 kg of plutonium-238, producing 4410 W of heat which was converted into 285 W of electric power [165]. The decay of Pu-238 makes the power to decrease with time, but only about 0.8% each year, making it ideal for decades of operation [165]. Voyager 1 and 2 spacecrafts, also powered by Pu-238 RTGs, launched in 1977, continue operating in 2018 after 41 years, and they are expected to continue until 2025 when their RTGs will no longer supply enough electric power. This is partly due to radiation damage in the thermoelectric materials.

- **Charged nuclei, including protons** are positive charges able to remove electrons, like alpha particles.
- **Beta particles** are high-energy electrons. High-energy beta particles produce X-rays known as bremsstrahlung ("braking radiation") or secondary electrons (delta ray) as they pass through matter. Both of these can cause an indirect ionization effect. Bremsstrahlung effect is greater when penetrating high atomic number materials.
- **Positrons or antielectrons** are the antimatter counterpart of the electron. When they collide with an electron, annihilation occurs, resulting in the conversion into gamma ray photons (energy).

Electrical effects of ionization

The charged nature of ionized materials makes them to have temporarily high electrical conductivity. This effect is exploited for example in radiation detectors such as the Geiger-Muller counter. On the other hand, this effect poses problems for example in electronic devices, where the semiconductors can suffer current peaks that induce operation errors of even permanent damage. Ionizing radiation is known to be the cause of Single Event Upsets (SEU), a change of state in a logic element such as a memory bit.

Devices intended for operating in high radiation environments may be made radiation

hard to resist such effects through appropriate design, material selection, and fabrication methods. Sensors used to monitor collimators and any other device installed around the accelerator are subjected to this artefacts.

Chemical effects of ionization

Ionizing radiation can break chemical bonds in molecules and crystal lattices (radiolysis). This process forms of highly reactive free radicals that then may react chemically with neighbouring materials.

In metals or ceramics, the disruption of the crystal lattices, causes them to become amorphous, to relax stresses with consequent swelling and creep. These changes in the atomic lattice are translated into macroscopic property changes such as embrittlement. Ionizing radiation contributes to the activation energy of certain reactions such as polymerization and corrosion.

One way to avoid chemical effects of ionizing radiation is to use mono-atomic fluids, such as inert gases or molten elements, as they have no chemical bonds to break and no crystal lattice to disturb.

Elastic interactions

All forms of particle radiation can transfer energy to the nuclei of the irradiated matter in the form of recoil momentum.

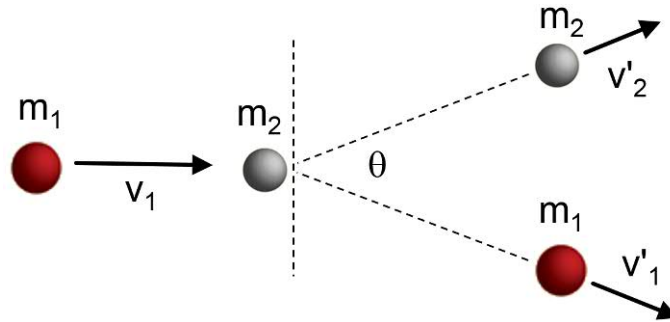


Figure D.1: Schematic of elastic collision.

Elastic collisions, by definition, show both conservation of kinetic energy and conservation of momentum: $E_{k1i} + E_{k2i} = E_{k1f} + E_{k2f}$ and $p_{1i} + p_{2i} = p_{1f} + p_{2f}$. All of the kinetic energy of the particles before the collision is still in the form of kinetic energy afterwards, see Figure D.1.

$$\frac{1}{2}m_1v_{1i}^2 + \frac{1}{2}m_2v_{2i}^2 = \frac{1}{2}m_1v_{1f}^2 + \frac{1}{2}m_2v_{2f}^2 \quad (\text{D.1})$$

$$m_1v_{1i} + m_2v_{2i} = m_1v_{1f} + m_2v_{2f} \quad (\text{D.2})$$

These two equations determine the final velocities:

$$v_{1f} = \frac{m_1 - m_2}{m_1 + m_2}v_{1i} + \frac{2m_2}{m_1 + m_2}v_{2i} \quad (\text{D.3})$$

$$v_{2f} = \frac{2m_1}{m_1 + m_2}v_{1i} - \frac{m_1 - m_2}{m_1 + m_2}v_{2i} \quad (\text{D.4})$$

Note several interesting cases when the particle 2 is initially at rest ($v_2 = 0$), for perfectly elastic collisions:

- If $m_1 = m_2$, $v_{1f} = 0$ and $v_{2f} = v_1$ (this is demonstrated in the Newton's cradle).
- If $m_1 \ll m_2$, v_{1f} tends to $-v_1$ and v_{2f} tends to zero.
- If $m_1 \gg m_2$, v_{1f} tends to v_1 and v_{2f} tends to $2v_1$.

This demonstrates that radiation made of heavy particles, such as ions or alpha particles, transfers more energy to the atoms in the lattice than light particles such as electrons.

In the case of elastic interactions the hit nucleus remains the same, just gains recoil momentum. The first hit atom is called Primary Knocked-on Atom (PKA). The energy and momentum are transferred to the nucleus and not to its electrons, so the atom moves in a partly ionized state through the lattice. The gained energy is lost mainly by Coulomb interactions (ionization and excitation) and is again dissipated as heat. If the energy is large enough, the PKA can knock on other atoms, which again leave their site. As a result, many atoms can be moved from their original lattice position. This process is comparable to billiard balls colliding. In the atomic lattice, it produces defects such as interstitial atoms and vacancies. Defects make the lattice less flexible against strain, due to impeded movement of dislocations, which manifests in an increase in hardness.

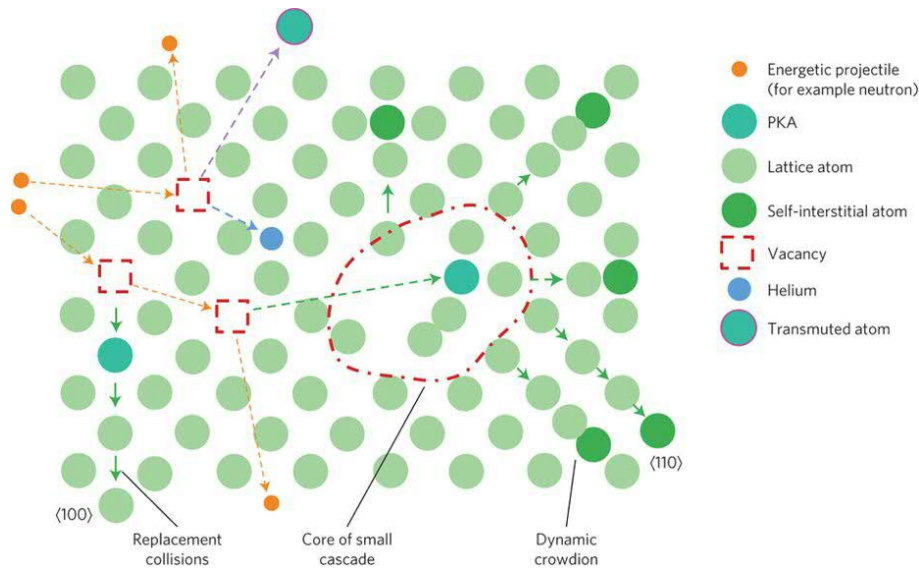


Figure D.2: Schematic of radiation damage, showing both elastic and inelastic (transmutation) interactions [166].

The term Displacement per atom (DPA) is the quantification of how many positions have moved the atoms on average in the lattice, proportional to the radiation damage. DPA is typically calculated by Monte Carlo simulations. Most of the defects heal out by different processes, including thermal annealing. DPA cannot be measured because most of the defects created heal out within 50 ps. However, some of the defects can be visualized with TEM.

Inelastic interactions

Inelastic interactions are defined as those in which part of the kinetic energy is transformed into some other form of energy in the collision. The momentum is conserved in inelastic collisions though: $E_{k1i} + E_{k2i} > E_{k1f} + E_{k2f}$ and $p_{1i} + p_{2i} = p_{1f} + p_{2f}$.

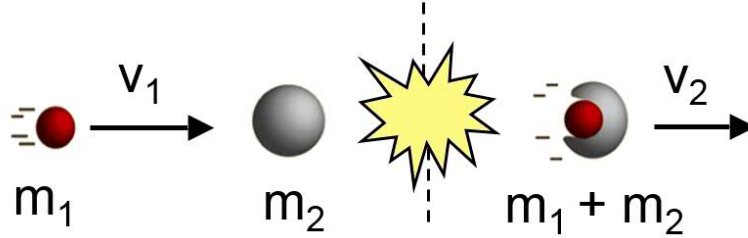


Figure D.3: Schematic of inelastic collision.

In a perfectly inelastic collision, both particles have the same velocity after the collision: $v_{1f} = v_{2f}$, remaining attached together, see Figure D.3. In the case of the particle 2 being at rest before the collision ($v_2 = 0$):

$$m_1 v_{1i} = (m_1 + m_2) v_f \quad (\text{D.5})$$

Developing the equations of kinetic energy and momentum, the kinetic energy lost is obtained:

$$E_{k\text{lost}} = E_{ki} \frac{m_2}{m_1 + m_2} \quad (\text{D.6})$$

The fraction of kinetic energy lost depends on the ratio between the masses. Inelastic interactions lead to nuclear transmutation, which can produce unstable nuclei (radioactive), see Figure D.4. The radioactive decay of these unstable nucleus, produces particle radiation, which in turn lead to accelerated radiation damage. Regardless of whether it is unstable or not, the transmuted atom becomes an impurity inside the original lattice, which modifies its macroscopic properties. These impurities reduce the thermal and electrical conductivities and change the mechanical properties, typically increasing the hardness.

Usually, the damage done to the lattice by the elastic recoils is much larger than that due to the impurities. However, is not the case when large amounts of helium and hydrogen are produced due to nuclear reactions [164].

Phase transformations induced by radiation

In general, the significant amount of energy deposited by the energetic particles as they travel through the solid can bring phase transformations. In the absence of irradiation, the thermodynamic driving forces determine the relative stability of phases; and thermally-driven kinetics (associated, for example, with point defect migration), determine the rates of phase transformations. The energetic particle flux present under irradiation can alter both the stability of phases and the kinetics of phase transformations. Therefore, phases that do not occur in the absence of irradiation can be produced. These alterations in phase stability have profound consequences for materials behaviour under irradiation.

For example, diamond nanometric particles have been obtained by irradiating graphite with 350 MeV krypton ions, at room temperature [167].

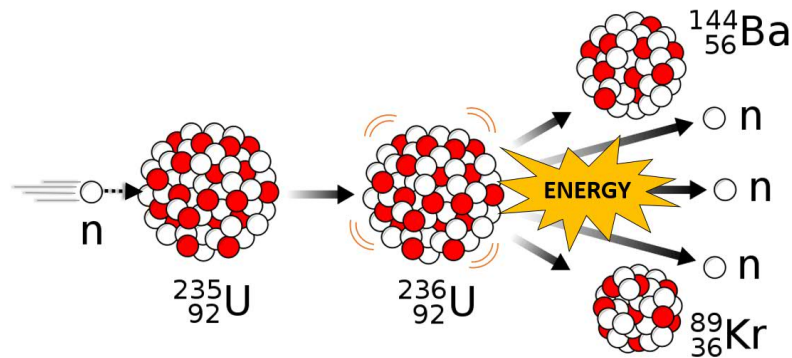


Figure D.4: Example of inelastic nuclear interaction between a ^{235}U atom impacted by a neutron. The interaction produces the transmutation of the uranium atom into ^{236}U unstable atom, followed by its radioactive decay. This is the typical fission reaction in nuclear power plants. By MikeRun / CC-BY-SA-4.0 / modified from original.

Summary of macroscopic radiation damage effects

- **Hardening/embrittlement:** The defects created in the atomic lattice by the different mechanisms described above inhibit the movement of dislocations, leading to an increase in hardness. Although hardening produces stronger materials (resist more stress before failing or yielding), they are more brittle (fracture with very little deformation) and have less fracture toughness (need less energy to grow a crack).
- **Decrease of certain physical properties:** Because of those defects, thermal and electrical conductivities decrease.
- **Swelling** which lead to dimensional changes of components and can also induce additional mechanical stress and fracture. Components under stress suffer creep, i.e. bolts and springs release their elastic preload.
- **Increased corrosion rates:** Ionizing radiation accelerates chemical reactions like corrosion, in particular in contact with fluids.
- **Radiolysis:** It is the dissociation of molecules by ionizing radiation. In particular, produces degradation of organic compounds such as polymers, greases, etc. that become hard and brittle, therefore stop behaving as intended.
- **Phase transformations:** As explained above, radiation produce phase changes which lead to changes in mechanical and physical properties. Changes to phases with different density lead to changes in volume which can produce cracks.
- **Thermal fatigue:** Part of the energy deposited by the radiation is dissipated as heat, see section 1.3.1. Therefore, pulsed radiation can produce thermal fatigue. Fatigue can be accelerated by the embrittlement due to radiation damage.

E | Elastic constants derivation

This Appendix describes the method used to derive the elastic constants of anisotropic materials from the experimental natural frequencies. In particular, the procedure is focused in transversely isotropic materials, but it is applicable to other types as well.

As explained in section 3.3.1, it is not possible to analytically calculate the elastic properties from the natural frequencies of anisotropic bodies. Therefore, the formulae from the standard method ASTM C1259-01, which allow to obtain the elastic properties from the resonant frequencies, cannot be used.

Instead, a finite element analysis optimisation algorithm is performed to derive the elastic constants by reverse engineering. ANSYS software, in this case version 17.2, was used as FEM code.

At the end of the appendix, the limitations of the method are detailed.

E.1 Elastic compliance matrix and elastic (engineering) constants

A solid is described as ideally elastic (or simply elastic) when it recovers its initial stress- and strain-free configuration upon removal of the applied loads or temperature field. In that case, a unique mathematical relationship between the stresses and strains that act within the loaded solid exists. The concept of elastic deformation or elastic strain was introduced by Robert Hooke in 1676, who developed a constitutive law for elastic and isotropic solids.

The generalization of Hooke's law to anisotropic materials is attributed to Augustin-Louis Cauchy (1829). It postulates that every component of the stress tensor is coupled linearly with every component of the strain tensor through the compliance matrix S . In indicial notation this is expressed by $\varepsilon_{ij} = S_{ijkl}\sigma_{kl}$, simplified to $\varepsilon_{ij} = S_{ij}\sigma_{ij}$. J.M.C. Duhamel and F.E. Neumann in the 19th century included the effects of temperature, by adding the strain contribution caused by free thermal expansion. Thus, the total strain at a point of a solid subjected to thermomechanical loading is $\varepsilon_{ij} = S_{ij}\sigma_{ij} + \alpha_{ij}[T - T_{ref}]$, with T_{ref} the temperature at which the solid is deemed stress and strain free, typically RT.

$$\begin{bmatrix} \varepsilon_{11} \\ \varepsilon_{22} \\ \varepsilon_{33} \\ 2\varepsilon_{23} \\ 2\varepsilon_{13} \\ 2\varepsilon_{12} \end{bmatrix} = \begin{bmatrix} S_{11} & S_{12} & S_{13} & S_{14} & S_{15} & S_{16} \\ S_{21} & S_{22} & S_{23} & S_{24} & S_{25} & S_{26} \\ S_{31} & S_{32} & S_{33} & S_{34} & S_{35} & S_{36} \\ S_{41} & S_{42} & S_{43} & S_{44} & S_{45} & S_{46} \\ S_{51} & S_{52} & S_{53} & S_{54} & S_{55} & S_{56} \\ S_{61} & S_{62} & S_{63} & S_{64} & S_{65} & S_{66} \end{bmatrix} \begin{bmatrix} \sigma_{11} \\ \sigma_{22} \\ \sigma_{33} \\ \sigma_{23} \\ \sigma_{13} \\ \sigma_{12} \end{bmatrix} + \begin{bmatrix} \alpha_{11} \\ \alpha_{22} \\ \alpha_{33} \\ 2\alpha_{23} \\ 2\alpha_{13} \\ 2\alpha_{12} \end{bmatrix} [T - T_{ref}] \quad (\text{E.1})$$

In order to predict the elastic behaviour of materials under any mechanical load, it is required to know all the constants of the compliance matrix. These predictions are fundamental for the design and engineering studies of components for any application, such as collimator devices for particle accelerators.

Orthotropic materials

Orthotropic materials are a subset of anisotropic materials having properties that differ along three mutually-orthogonal axes. In such a case equation E.1 becomes:

$$\begin{bmatrix} \varepsilon_{11} \\ \varepsilon_{22} \\ \varepsilon_{33} \\ 2\varepsilon_{23} \\ 2\varepsilon_{13} \\ 2\varepsilon_{12} \end{bmatrix} = \begin{bmatrix} S_{11} & S_{12} & S_{13} & 0 & 0 & 0 \\ S_{21} & S_{22} & S_{23} & 0 & 0 & 0 \\ S_{31} & S_{32} & S_{33} & 0 & 0 & 0 \\ 0 & 0 & 0 & S_{44} & 0 & 0 \\ 0 & 0 & 0 & 0 & S_{55} & 0 \\ 0 & 0 & 0 & 0 & 0 & S_{66} \end{bmatrix} \begin{bmatrix} \sigma_{11} \\ \sigma_{22} \\ \sigma_{33} \\ \sigma_{23} \\ \sigma_{13} \\ \sigma_{12} \end{bmatrix} + \begin{bmatrix} \alpha_{11} \\ \alpha_{22} \\ \alpha_{33} \\ 0 \\ 0 \\ 0 \end{bmatrix} [T - T_{ref}] \quad (\text{E.2})$$

The factor 2 multiplying ε_{23} , ε_{13} and ε_{12} results from the different ways shear strain and engineering shear strain are defined:

$$\gamma_{23} = \varepsilon_{23} + \varepsilon_{32} = 2\varepsilon_{23} \quad \gamma_{13} = \varepsilon_{13} + \varepsilon_{31} = 2\varepsilon_{13} \quad \gamma_{12} = \varepsilon_{12} + \varepsilon_{21} = 2\varepsilon_{12} \quad (\text{E.3})$$

Those engineering shear strains result in $\varepsilon_{23} = \frac{S_{44}}{2}\sigma_{23}$, $\varepsilon_{13} = \frac{S_{55}}{2}\sigma_{13}$ and $\varepsilon_{12} = \frac{S_{66}}{2}\sigma_{12}$.

The constitutive equations are usually expressed in terms of engineering constants when practical applications are under consideration. The engineering constants of an orthotropic material (9 independent) are given by:

$$\begin{aligned} E_1 &= \frac{1}{S_{11}} & \nu_{12} &= -\frac{S_{12}}{S_{11}} & G_{23} &= \frac{1}{S_{44}} \\ E_2 &= \frac{1}{S_{22}} & \nu_{13} &= -\frac{S_{13}}{S_{11}} & G_{13} &= \frac{1}{S_{55}} \\ E_3 &= \frac{1}{S_{33}} & \nu_{23} &= -\frac{S_{23}}{S_{22}} & G_{12} &= \frac{1}{S_{66}} \end{aligned} \quad (\text{E.4})$$

Transversely-isotropic materials

Transversely isotropic materials possess physical properties that are symmetric about an axis. In the plane normal to such axis, the material properties are the same in all directions. Taking 12 as the plane of isotropy, the constitutive law becomes:

$$\begin{bmatrix} \varepsilon_{11} \\ \varepsilon_{22} \\ \varepsilon_{33} \\ 2\varepsilon_{23} \\ 2\varepsilon_{13} \\ 2\varepsilon_{12} \end{bmatrix} = \begin{bmatrix} S_{11} & S_{12} & S_{13} & 0 & 0 & 0 \\ S_{12} & S_{11} & S_{13} & 0 & 0 & 0 \\ S_{13} & S_{13} & S_{33} & 0 & 0 & 0 \\ 0 & 0 & 0 & S_{44} & 0 & 0 \\ 0 & 0 & 0 & 0 & S_{44} & 0 \\ 0 & 0 & 0 & 0 & 0 & 2(S_{11} - S_{12}) \end{bmatrix} \begin{bmatrix} \sigma_{11} \\ \sigma_{22} \\ \sigma_{33} \\ \sigma_{23} \\ \sigma_{13} \\ \sigma_{12} \end{bmatrix} + \begin{bmatrix} \alpha_{11} \\ \alpha_{11} \\ \alpha_{33} \\ 0 \\ 0 \\ 0 \end{bmatrix} [T - T_{ref}] \quad (\text{E.5})$$

The engineering constants of a transversely isotropic material (5 independent), 12 being the plane of isotropy, are given by:

$$\begin{aligned} E_1 &= E_2 = \frac{1}{S_{11}} & \nu_{12} &= -\frac{S_{12}}{S_{11}} & G_{13} &= G_{23} = \frac{1}{S_{44}} \\ E_3 &= \frac{1}{S_{33}} & \nu_{13} &= \nu_{23} = -\frac{S_{13}}{S_{11}} & G_{12} &= \frac{E_1}{2(1+\nu_{12})} \end{aligned} \quad (\text{E.6})$$

In the case of the plane of isotropy is 23, the constitutive relationship becomes:

$$\begin{bmatrix} \varepsilon_{11} \\ \varepsilon_{22} \\ \varepsilon_{33} \\ 2\varepsilon_{23} \\ 2\varepsilon_{13} \\ 2\varepsilon_{12} \end{bmatrix} = \begin{bmatrix} S_{11} & S_{12} & S_{12} & 0 & 0 & 0 \\ S_{12} & S_{22} & S_{23} & 0 & 0 & 0 \\ S_{12} & S_{23} & S_{22} & 0 & 0 & 0 \\ 0 & 0 & 0 & 2(S_{22} - S_{23}) & 0 & 0 \\ 0 & 0 & 0 & 0 & S_{55} & 0 \\ 0 & 0 & 0 & 0 & 0 & S_{55} \end{bmatrix} \begin{bmatrix} \sigma_{11} \\ \sigma_{22} \\ \sigma_{33} \\ \sigma_{23} \\ \sigma_{13} \\ \sigma_{12} \end{bmatrix} + \begin{bmatrix} \alpha_{11} \\ \alpha_{22} \\ \alpha_{22} \\ 0 \\ 0 \\ 0 \end{bmatrix} [T - T_{ref}] \quad (\text{E.7})$$

In such a case, the five engineering constants become:

$$\begin{aligned} E_1 &= \frac{1}{S_{11}} & \nu_{12} &= \nu_{13} = -\frac{S_{12}}{S_{11}} & G_{23} &= \frac{E_2}{2(1+\nu_{23})} \\ E_2 &= E_3 = \frac{1}{S_{22}} & \nu_{23} &= -\frac{S_{23}}{S_{22}} & G_{12} &= G_{13} = \frac{1}{S_{55}} \end{aligned} \quad (\text{E.8})$$

Isotropic materials

For isotropic materials, the constitutive law is further simplified, resulting in:

$$\begin{bmatrix} \varepsilon_{11} \\ \varepsilon_{22} \\ \varepsilon_{33} \\ 2\varepsilon_{23} \\ 2\varepsilon_{13} \\ 2\varepsilon_{12} \end{bmatrix} = \begin{bmatrix} S_{11} & S_{12} & S_{12} & 0 & 0 & 0 \\ S_{12} & S_{11} & S_{12} & 0 & 0 & 0 \\ S_{12} & S_{12} & S_{11} & 0 & 0 & 0 \\ 0 & 0 & 0 & 2(S_{11} - S_{12}) & 0 & 0 \\ 0 & 0 & 0 & 0 & 2(S_{11} - S_{12}) & 0 \\ 0 & 0 & 0 & 0 & 0 & 2(S_{11} - S_{12}) \end{bmatrix} \begin{bmatrix} \sigma_{11} \\ \sigma_{22} \\ \sigma_{33} \\ \sigma_{23} \\ \sigma_{13} \\ \sigma_{12} \end{bmatrix} + \begin{bmatrix} \alpha_{11} \\ \alpha_{11} \\ \alpha_{11} \\ 0 \\ 0 \\ 0 \end{bmatrix} [T - T_{ref}] \quad (\text{E.9})$$

The engineering constants of an isotropic material (2 independent) are :

$$\begin{aligned} E_1 &= E_2 = E_3 = E & \nu_{12} &= \nu_{13} = \nu_{23} = \nu & G_{12} &= G_{13} = G_{23} = G \\ E &= \frac{1}{S_{11}} & \nu &= -\frac{S_{12}}{S_{11}} & G &= \frac{E}{2(1+\nu)} \end{aligned} \quad (\text{E.10})$$

E.2 Numerical derivation of the elastic constants

The algorithm for the computation of the elastic constants is based on a numerical modal analysis, which calculates the resonance frequencies of a defined geometry with defined elastic properties and density. To perform the optimisation loop, arbitrary elastic properties together with the measured density are introduced. The finite element code can then perform an optimisation process to obtain the elastic properties that best match the measured resonant frequencies.

Four modal analysis systems (B, C, D and E) are created, corresponding to the flexural and torsional modes of the IP and TP specimens. The material properties (Engineering Data) are shared with all the systems.

E. Elastic constants derivation

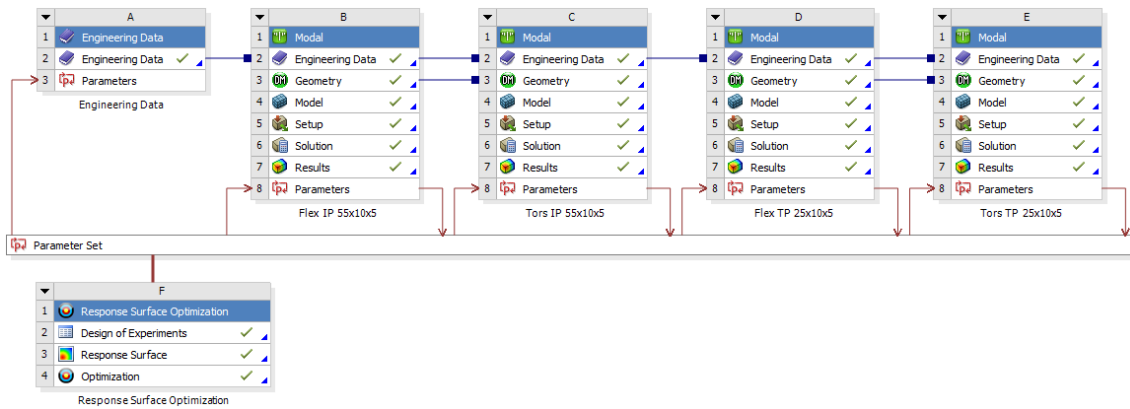


Figure E.1: Project schematic in ANSYS 17.2 version

The dimensions of the specimens are set in the geometry section. As several specimens are measured and only one is simulated, the average values are taken.

ANSYS cannot identify the types of the resonance mode. It calculates all of them, ordered from the lowest to highest frequency. This method requires to precisely know which mode is being simulated in every modal analysis system. To do that, the geometry is divided in eight sub-blocks (Figure E.2). This allows to define several internal lines and surfaces, that are required to force a particular resonance mode, described in Section E.3.

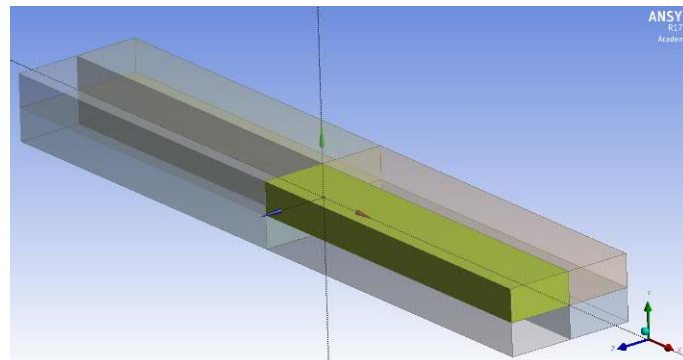


Figure E.2: Specimen geometry

A new material is added to the "engineering data". The properties "density" (Physical) and "orthotropic elasticity" (Linear Elastic) are added to the material, see Figure E.4. As shown in section 3.3.1, the density value is very important because all the results from the modal analysis simulation depend on it. The density is determined experimentally, see Section 3.1. With the rest of variables constant, equations 3.9 and 3.13 show that a denser specimen will vibrate at lower frequency, due to its larger mass. The elastic properties values can be arbitrary but must assume realistic values, and within the range of the expected ones.

Inside each of the four systems, the model has to be properly set-up. First the correct material and orientation (coordinate system) is assigned to the 8 sub-blocks of each specimen. Creating a new "coordinate system of the piece" is convenient.

The standard homogeneous structural SOLID186 element was adopted for structural

E. Elastic constants derivation

modelling in ANSYS. SOLID186 is a higher order 3-D 20-node solid element that exhibits quadratic displacement behaviour. Optimized discretisation of the geometry provides accurate results while preserving short computing times, which are important due to the parametric nature of the conducted analyses and the available computing power. The typical element size and spatial distribution are shown in Figure E.3. Mesh convergence study confirmed proper discretisation of the geometry; increasing degrees of freedom does not change representative results.

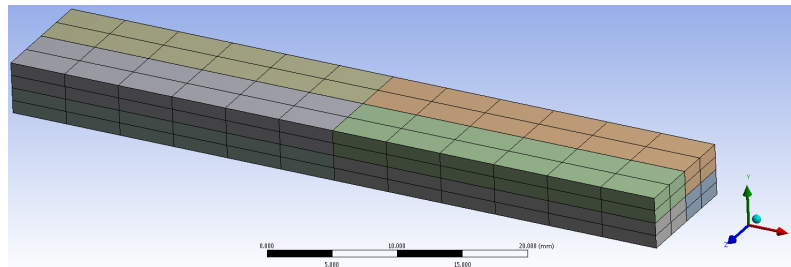


Figure E.3: Specimen mesh

	A	B	C	D	E
1	Contents of Engineering Data		Source	Description	
2	Material				
3	MoGr				
4	Structural Steel				
* Click here to add a new material					
Properties of Outline Row 3: MoGr					
	A	B	C	D	E
1	Property		Value	Unit	
2	Density	2540		kg m^-3	
3	Orthotropic Elasticity				
4	Young's Modulus X direction	4.11E+09	Pa		<input checked="" type="checkbox"/>
5	Young's Modulus Y direction	6.08E+10	Pa		<input checked="" type="checkbox"/>
6	Young's Modulus Z direction	6.08E+10	Pa		<input checked="" type="checkbox"/>
7	Poisson's Ratio XY	0.1			<input checked="" type="checkbox"/>
8	Poisson's Ratio YZ	0.12667			<input checked="" type="checkbox"/>
9	Poisson's Ratio XZ	0.1			<input checked="" type="checkbox"/>
10	Shear Modulus XY	3.8E+09	Pa		<input checked="" type="checkbox"/>
11	Shear Modulus YZ	2.7E+10	Pa		<input checked="" type="checkbox"/>
12	Shear Modulus XZ	3.8E+09	Pa		<input checked="" type="checkbox"/>

Figure E.4: Engineering data

E.3 Vibration modes

Torsional mode

In order to force the torsional mode, the two central lines crossing the sample are defined as a "fixed support" (displacement equal to zero), see Figure E.5. This blocks all the 6 degrees of freedom, so the resulting mode to check is the first one. Besides blocking that lines, in order to have the natural torsional behaviour, it is required to include a constrain equation so that the opposite faces in the long side of the specimen rotate in opposite directions. The two opposite faces are defined as remote points, see Figure E.6. Then the constraint equation $0 = 1 * Rotation X(Rem.point 1) + 1 * Rotation X(Rem.point 2)$

E. Elastic constants derivation

is defined, with X the direction of the long side in the global coordinate system (the one showed in the ANSYS screen-shots), see Figure E.7.

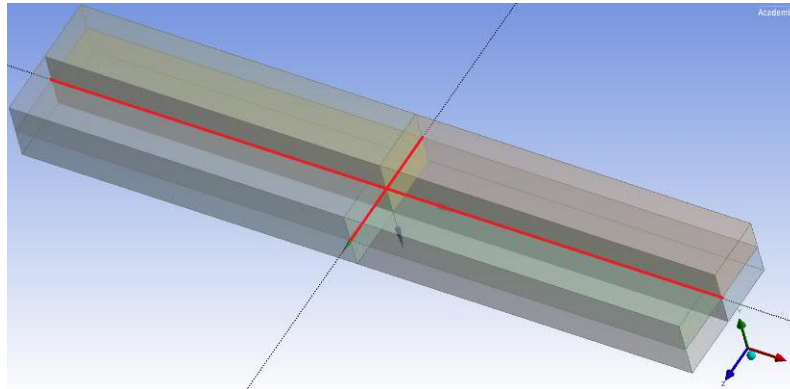


Figure E.5: Torsional mode block

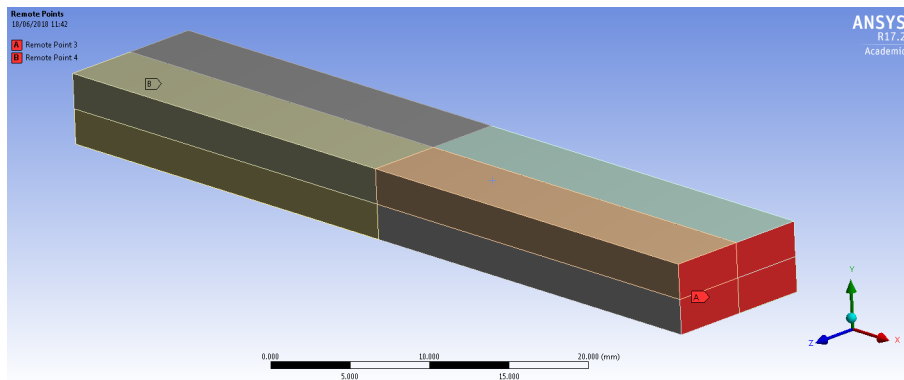


Figure E.6: Torsional mode block

Outline

Filter: Graphics Visible Bodies

Project

- Model (C4)
 - Geometry
 - Coordinate Systems
 - Remote Points
 - Remote Point 3
 - Remote Point 4
 - Connections
 - Mesh
- Modal (C5)
 - Pre-Stress (None)
 - Analysis Settings
 - Fixed Support 2
 - Constraint Equation
 - Solution (C6)
 - Solution Information
 - Total Deformation Tors L 55x10x5

Worksheet

Constraint Equation

$0 = 1 (1/^\circ) * \text{Remote Point 3(Rotation X)} + 1 (1/^\circ) * \text{Remote Point 4(Rotation X)}$

Coefficient	Units	Remote Point	DOF Selection
1	1/°	Remote Point 3	Rotation X
1	1/°	Remote Point 4	Rotation X

Figure E.7: Torsional mode block

Flexural mode

In a free-standing specimen, there are 6 degrees of freedom (3-axis displacement and 3-axis rotation). Typically the flexural mode is the one with the lowest frequency, so the mode to check is thus the seventh. The problem of leaving no supports is that, depending on the properties, the orientation and the geometry, a not desired mode can have the lowest

frequency. This is critical because this situation may change in different design points of the optimisation algorithm, complicating the convergence to a solution, or leading to a wrong one. For this reason, in some cases the flexural mode must be forced so that the mode in the desired direction is obtained.

The flexural mode is difficult to force in a way that does not disturb the frequency result. This is because the points that remain stationary are difficult to locate. A way to force it is to define the central plane (Figure E.8) as a "frictionless support" (allows to freely move those points within the plane direction, but blocks their movement in the perpendicular direction). This blocks 3 out of 6 degrees of freedom and thus the flexural mode will be the fourth mode. The fifth mode in this case will probably be the second flexural mode.

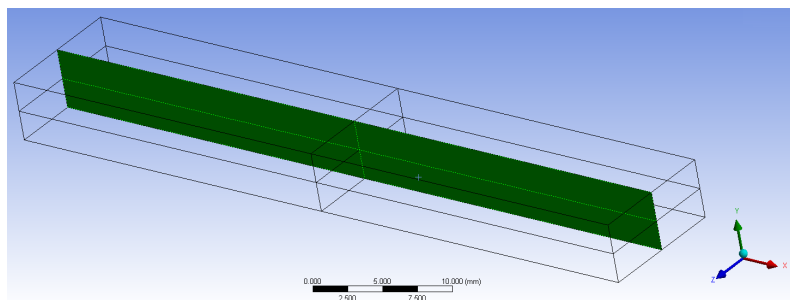


Figure E.8: Flexural mode block

Mode verification

The boundary conditions, such as supports, influence the result of the modal analysis. The simulation of the free-standing specimen is useful to check all the resonance modes and their frequencies.

When doing experimentally the test, the operator detects and measures resonance frequencies, but cannot easily know to which mode they correspond. If doubts arise, a FEM simulation with estimated properties, of the free-standing specimen, can be performed for clarification. In the example below of a free-standing specimen (Figures E.9 to E.13), the torsional mode frequency is almost the same as that of a non desired flexural mode, making difficult the test. The results are visualized in terms of total deformation; the color scale ranges between blue (minimum deformation) to red (maximum deformation). This allows to visualize the type of resonance mode. Deformation absolute values given by the simulation are not relevant.



Figure E.9: Plot of the frequencies of the first 10 modes of an IP free-standing specimen. The first 6 modes with $F \approx 0 Hz$ are the degrees of freedom.

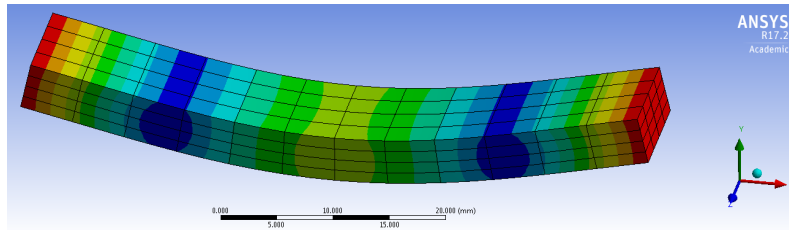


Figure E.10: First flexural mode (mode 7, 5864 Hz).

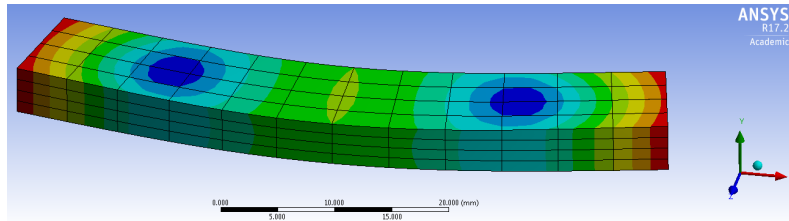


Figure E.11: First flexural mode in a non desired orientation (mode 8, 12963 Hz).

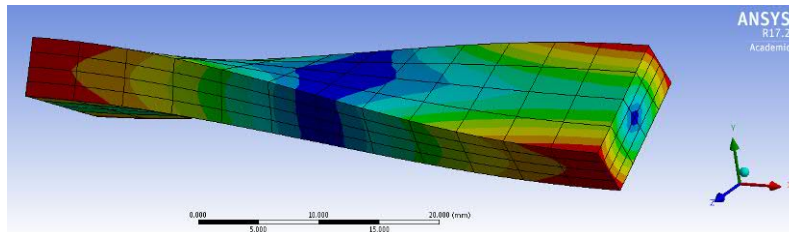


Figure E.12: First torsional mode (mode 9, 13125 Hz).

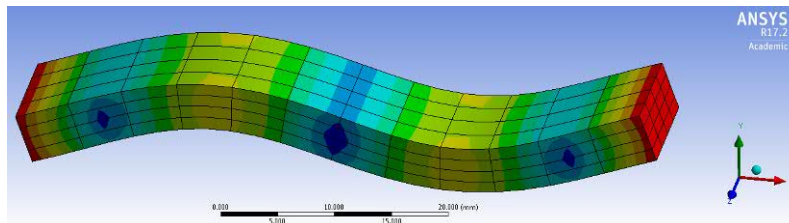


Figure E.13: Second flexural mode (mode 10, 14583 Hz).

E.4 Optimisation set-up and results

In order to perform optimisation algorithm, the frequency result has to be a parameter. This is selected by inserting "total deformation" probes in the Solution section. Inside them, the frequency can be parametrized, see Figure E.14.

E. Elastic constants derivation

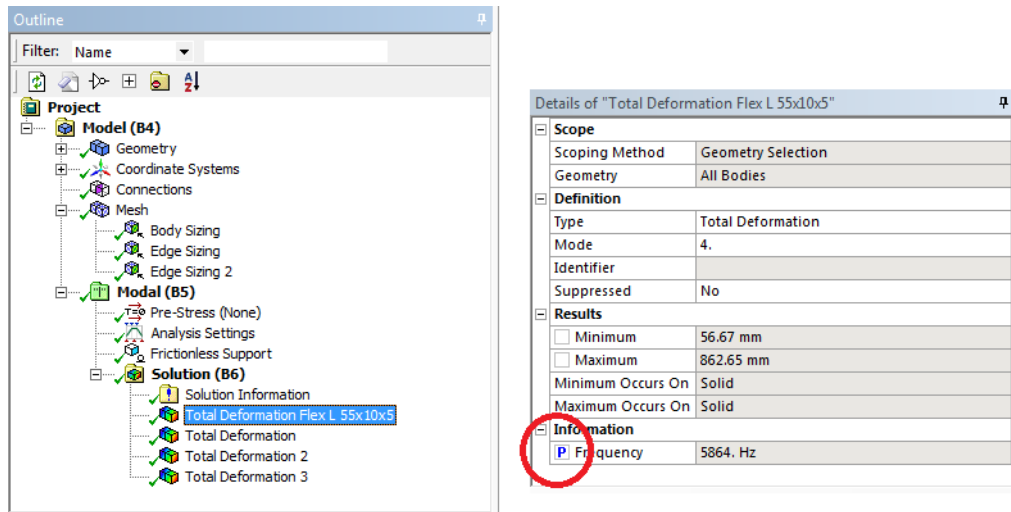


Figure E.14: Frequency result set as parameter.

The parameter set shows the configuration of all the parameters, see Figure E.15. As the investigated graphite-matrix composites are typically transversely orthotropic, there are 5 independent elastic constants. The TP direction is defined as the X and the IP directions are Y and Z. In this scenario, $E_Y = E_Z$, so P3 is defined as an expression "P2". $G_{XY} = G_{XZ}$, so P7 is defined as the expression "P5". $\nu_{XY} = \nu_{XZ}$, so P16 is defined as "P15". Lastly, the equation $G_{YZ} = \frac{E_Y}{2(1+\nu_{YZ})}$ is used to define ν_{YZ} (P13) as the expression "(P2/2 * P6) - 1". The Poisson's ratio is defined instead of the shear modulus, because in this way it can be easily restricted within the physical range. As it will be demonstrated in section E.5, the resonant frequencies are very little sensitive to the Poisson's ratios, so this optimisation process cannot identify appropriate values. A reasonable value for the investigated material is thus fixed ($\nu_{XY} = 0.1$). Then, due to the parameter relationships set, ν_{XZ} also changes automatically to the same value.

Outline of All Parameters				
	A	B	C	D
1	ID	Parameter Name	Value	Unit
2	Input Parameters			
3	Engineering Data (A1)			
4	P1	Young's Modulus X direction	4.8608E+09	Pa
5	P2	Young's Modulus Y direction	8.5186E+10	Pa
6	P3	Young's Modulus Z direction	8.5186E+10	Pa
7	P5	Shear Modulus XY	4.901E+09	Pa
8	P6	Shear Modulus YZ	3.5098E+10	Pa
9	P7	Shear Modulus XZ	4.901E+09	Pa
10	P13	Poisson's Ratio YZ	0.21354	
11	P15	Poisson's Ratio XY	0.1	
12	P16	Poisson's Ratio XZ	0.1	
*	New input parameter	New name	New expression	
14	Output Parameters			
15	Tors L 55x10x5 (C1)			
16	P18	Total Deformation Tors L 55x10x5 Reported Frequency	16474	Hz
17	Flex L 55x10x5 (B1)			

Properties of Outline A4: P1		
	A	B
1	Property	Value
2	General	
3	Expression	4860810651.4803295 [Pa]
4	Usage	Input
5	Description	
6	Error Message	
7	Expression Type	Constant
8	Quantity Name	Stress

Properties of Outline A10: P13		
	A	B
1	Property	Value
2	General	
3	Expression	(P2/(2*P6))-1
4	Usage	Input
5	Description	
6	Error Message	
7	Expression Type	Derived
8	Quantity Name	

Figure E.15: Parameter set

Now, the design of experiments can be configured to define the different design points (DP) that allow the response surface to be calculated. The configuration is set to "central

E. Elastic constants derivation

composite design” and ”auto defined”.The ν_{XY} can be ticked off (disabled) and set it as fix. The more parameters have to be studied, the more design points will be created and the optimisation will be more complex. In this case there will be 4 parameters to optimize. Here the ranges where the values of each parameter are expected to be are defined. If the ranges are too wide or too narrow, the solution may not be found. In particular, too wide ranges can produce issues due to changes in the type of resonance mode. For the materials investigated in this thesis, based on experience, these ranges are appropriate:

- E_X between 1 and 10 GPa
- E_Y between 20 and 100 GPa
- G_{XY} between 2 and 7.5 GPa
- G_{YZ} between 10 and 40 GPa
- ν_{XY} 0.1 (fix)

This will create different DP that can be solved afterwards. The solution calculation process of around 50 design points takes around 2 hours of computing time. If the combination of inputs of a particular DP is not physically possible, the simulation will fail, sometimes crashing ANSYS and preventing to continue, see Figure E.16.

1	A	B	C	D	E	F	G	H	I	J	K	L	M	P20
	Name	Update Order	P1 - Young's Modulus X direction (Pa)	P2 - Young's Modulus Y direction (Pa)	P5 - Shear Modulus XY (Pa)	P6 - Shear Modulus YZ (Pa)	P16 - Poisson's Ratio XZ	P3 - Young's Modulus Z direction (Pa)	P7 - Shear Modulus XZ (Pa)	P13 - Poisson's Ratio YZ	P17 - Total Deformation Flex L 55x10x5 Reported Frequency (Hz)	P18 - Total Deformation Tors L 25x10x5 Reported Frequency (Hz)	P19 - Total Deformation Flex T 25x10x5 Reported Frequency (Hz)	
2	2 DP 63	1	2E+09	7E+10	4.75E+09	2.5415E+10	0.1	7E+10	4.75E+09	0.37714				
3	10 DP 64	2	3.1832E+09	4.8874E+10	2.8134E+09	1.6905E+10	0.1	4.8874E+10	2.8134E+09	0.44557	6550.1	12033	8449.7	155
4	18 DP 65	3	3.1832E+09	4.8874E+10	2.8134E+09	3.3925E+10	0.1	4.8874E+10	2.8134E+09	-0.27969	6548.7	13659	8449.6	156
5	14 DP 66	4	3.1832E+09	4.8874E+10	6.6866E+09	1.6905E+10	0.1	4.8874E+10	6.6866E+09	0.44557	6816.6	14724	8559	239
6	22 DP 67	5	3.1832E+09	4.8874E+10	6.6866E+09	3.3925E+10	0.1	4.8874E+10	6.6866E+09	-0.27969	6813.4	17840	8558.9	239
7	12 DP 68	6	3.1832E+09	9.1126E+10	2.8134E+09	1.6905E+10	0.1	9.1126E+10	2.8134E+09	1.6953				
8	20 DP 69	7	3.1832E+09	9.1126E+10	2.8134E+09	3.3925E+10	0.1	9.1126E+10	2.8134E+09	0.34304	8484.9	13677	8450	156
9	16 DP 70	8	3.1832E+09	9.1126E+10	6.6866E+09	1.6905E+10	0.1	9.1126E+10	6.6866E+09	1.6953				
10	24 DP 71	9	3.1832E+09	9.1126E+10	6.6866E+09	3.3925E+10	0.1	9.1126E+10	6.6866E+09	0.34304	9086.6	17842	8560.2	239
11	4 DP 72	10	6E+09	4E+10	4.75E+09	2.5415E+10	0.1	4E+10	4.75E+09	-0.21306	6128.4	15229	11572	202
12	6 DP 73	11	6E+09	7E+10	2E+09	2.5415E+10	0.1	7E+10	2E+09	0.37714	7359.3	11629	11224	132
13	8 DP 74	12	6E+09	7E+10	4.75E+09	1.333E+10	0.1	7E+10	4.75E+09	1.6257				
14	1 DP 75	13	6E+09	7E+10	4.75E+09	2.5415E+10	0.1	7E+10	4.75E+09	0.37714	7914.2	15232	11572	202
15	9 DP 76	14	6E+09	7E+10	4.75E+09	3.79E+10	0.1	7E+10	4.75E+09	-0.066667	7911.7	16528	11572	202
16	7 DP 77	15	6E+09	7E+10	7.5E+09	2.5415E+10	0.1	7E+10	7.5E+09	0.37714	8085	17018	11673	254
17	5 DP 78	16	6E+09	1E+11	4.75E+09	2.5415E+10	0.1	1E+11	4.75E+09	0.96734				
18	11 DP 79	17	8.8168E+09	4.8874E+10	2.8134E+09	1.6905E+10	0.1	4.8874E+10	2.8134E+09	0.44557	6542.7	12036	13575	156
19	19 DP 80	18	8.8168E+09	4.8874E+10	2.8134E+09	3.3925E+10	0.1	4.8874E+10	2.8134E+09	-0.27969	6541.3	13663	13575	157

Figure E.16: Solved design points (created by the algorithm). Some of them failed.

In this case the analysis is set to ”custom” and the failed DP are deleted, see Figure E.17. In ”custom” type is possible to manually add DP. Once all present DP are solved the design of experiments is completed. This window allows to export the table with all the calculated frequencies as a CSV format.

1	A	B	C
	Property	Value	Unit
2	Design Points		
3	Preserve Design Points After DX Run	<input checked="" type="checkbox"/>	
4	Retain Data for Each Preserved Design Point	<input checked="" type="checkbox"/>	
5	Failed Design Points Management		
6	Number of Retries	1	
7	Retry Delay	30	s
8	Design of Experiments		
9	Design of Experiments Type	Custom	

Figure E.17: Custom type

E. Elastic constants derivation

The response surface relates the mutual effects of different parameters. It can be calculated in the next ANSYS subsystem. A genetic aggregation algorithm is selected [168]. In this window, one can check the quality of the set of DP, the maximum predicted error of each frequency. A refinement process that creates new DP to diminish this error can be performed there.

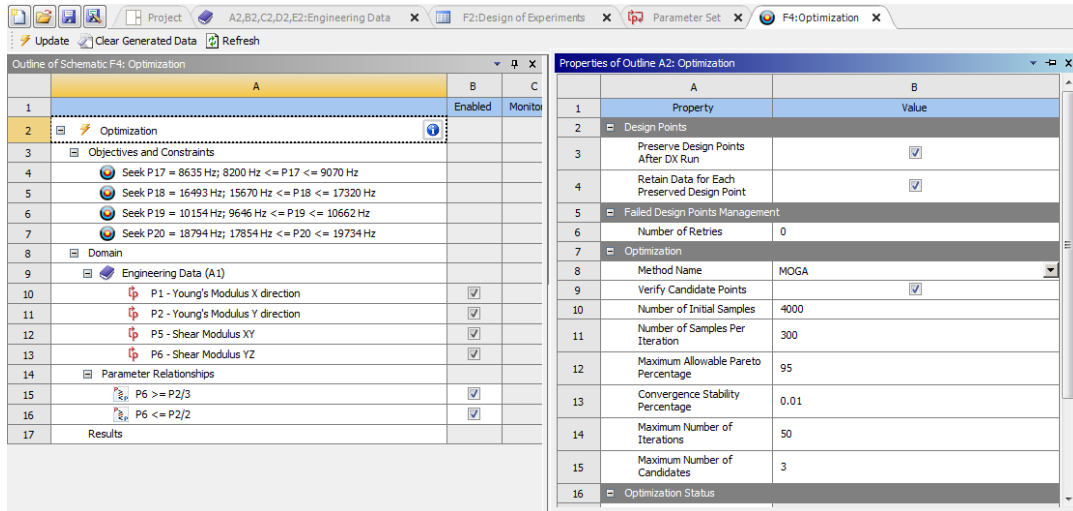


Figure E.18: Optimisation

The optimisation to find the elastic properties of the specimens can be performed now, see Figure E.18. The average frequency of the measured specimens is used. In order to allow possible experimental errors, a $\pm 5\%$ range of the average frequency is set to constraint the seeking process. The ν_{YZ} is calculated from the transversely orthotropic relationship, and it has to be within the physical range (0 to 0.5). For this reason the parameters involved in that relationship are constrained:

- $G_{YZ} \geq E_Y/3$
- $G_{YZ} \leq E_Y/2$

The optimisation process is launched, with the configuration shown in Figure E.18. The algorithm tries to find three candidate combinations of input parameters (elastic properties) that have all the output parameters (resonance frequencies) within the defined ranges, see Figure E.19. If the process is successful, three candidates are proposed and verified (simulated). Those points are saved in the parameter set. They can be added to the design of experiments (custom) to quickly repeat the optimisation process, including those DP that should be very close to the best solution.

E. Elastic constants derivation

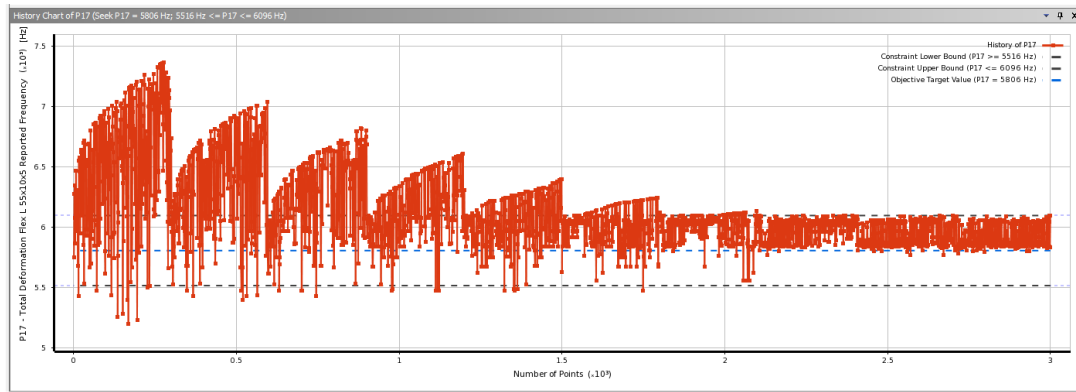


Figure E.19: Optimisation progress of one of the natural frequencies.

Candidate Points							
	Candidate Point 1	Candidate Point 1 (verified) DP 75	Candidate Point 2	Candidate Point 2 (verified) DP 76	Candidate Point 3	Candidate Point 3 (verified) DP 77	
P1 - Young's Modulus X direction (Pa)	3.8387E+09		3.7305E+09		3.7036E+09		
P2 - Young's Modulus Y direction (Pa)	4.2424E+10		4.2806E+10		4.1522E+10		
P5 - Shear Modulus XY (Pa)	3.5321E+09		3.5183E+09		3.5135E+09		
P6 - Shear Modulus YZ (Pa)	2.1023E+10		2.1191E+10		2.0309E+10		
P17 - Total Deformation Flex L 55x10x5 Reported Frequency (Hz)	★ ★ 5841.4	★ ★ 5841.7	★ ★ 5864.9	★ ★ 5865.4	★ ★ 5782.9	★ ★ 5782.9	
P18 - Total Deformation Tors L 55x10x5 Reported Frequency (Hz)	★ 13771	★ 13771	★ 13782	★ 13782	— 13639	— 13639	
P19 - Total Deformation Flex T 25x10x5 Reported Frequency (Hz)	★ ★ 12033	★ ★ 12033	★ ★ 11870	★ ★ 11869	★ ★ 11828	★ ★ 11828	
P20 - Total Deformation Tors T 25x10x5 Reported Frequency (Hz)	★ ★ 21021	★ ★ 21021	★ ★ 20978	★ ★ 20979	★ ★ 20961	★ ★ 20962	

Figure E.20: Optimisation results.

The candidate points are inspected; if necessary, a manual DP is added and calculated. It is important to select the final candidate DP (solved) as "current" in the "parameter set" and check the four simulation systems. The vibration modes have to be verified so that they are the expected ones. If all the processes are successful, the optimized elastic properties values are finally obtained.

If the seeking process to approach the desired frequency is not able to converge, it could be due to a too narrow range of expected elastic properties. Another cause could be that one experimental frequency value does not correspond to the expected vibration mode. In this case one can perform a mode verification (section E.3) with the most likely elastic properties to identify the approximate frequencies. Afterwards, another experimental test to measure the frequencies can be performed to look for the appropriate vibration mode.

E.5 Parameters correlation

A parameter correlation study can be included in the ANSYS project to understand which elastic properties affect which vibration mode.

An example performed with CG-1100B0 material (see chapter 4) is presented here. In order to prevent non-physical combination of properties, small ranges of values near the optimized elastic properties are used: E_X 20-50GPa, E_Y 38-48 GPa, G_{XY} 2-8GPa, ν_{XY} 0.1, G_{YZ} 15-21GPa. The results are shown below.

The "local sensitivity plot" is interesting, as it shows the relationships between properties and resonance modes, see Figure E.21.

E. Elastic constants derivation

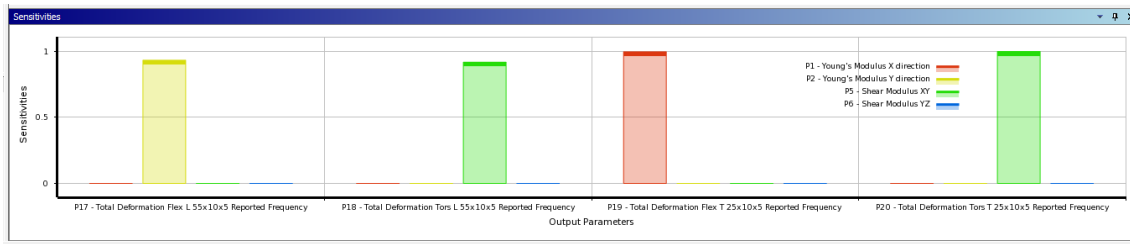


Figure E.21: Sensitivity plot

The sensitivity plot shows the following conclusions:

- $F_{flexural}$ of IP specimen is influenced by E_Y .
- $F_{torsional}$ of IP specimen is influenced by G_{XY} .
- $F_{flexural}$ of TP specimen is influenced by E_X .
- $F_{torsional}$ of TP specimen is influenced by G_{XY} .

Neglecting the anisotropy of the material properties, the elastic constants E and G affect to the resonance modes as shown in equations 3.9 and 3.13.

The correlations between the elastic constants and the resonance frequencies are shown in Figures E.22 to E.27. Red and blue lines are the linear and quadratic trendlines. The vertical axis is the frequency and the horizontal is the elastic constant. Those figures are shown only for visualizing the dependence between the parameters.

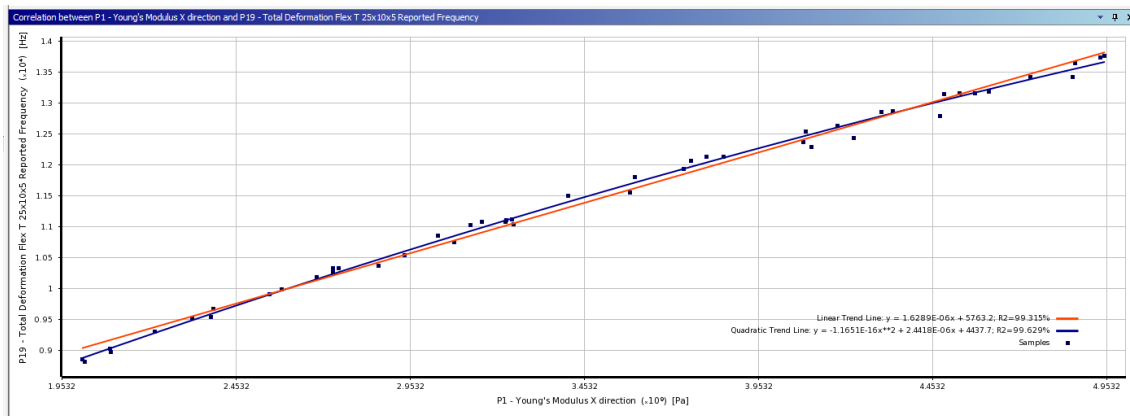


Figure E.22: Correlation between E_X and $F_{flexural}$ of TP specimen

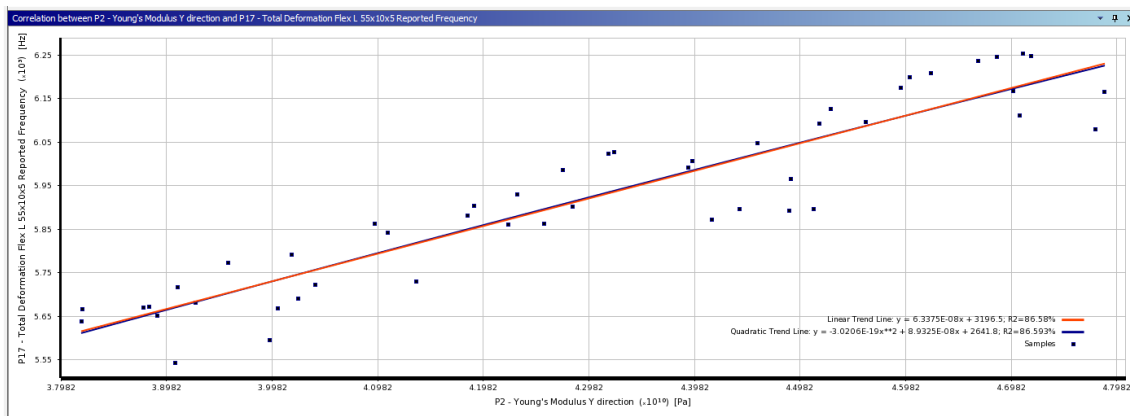


Figure E.23: Correlation between E_Y and $F_{flexural}$ of IP specimen

E. Elastic constants derivation

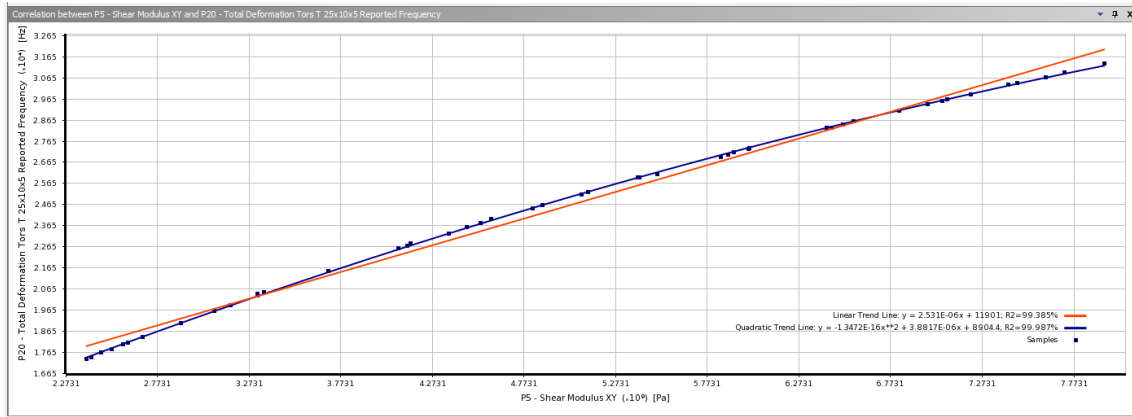


Figure E.24: Correlation between G_{XY} and $F_{torsional}$ of TP specimen

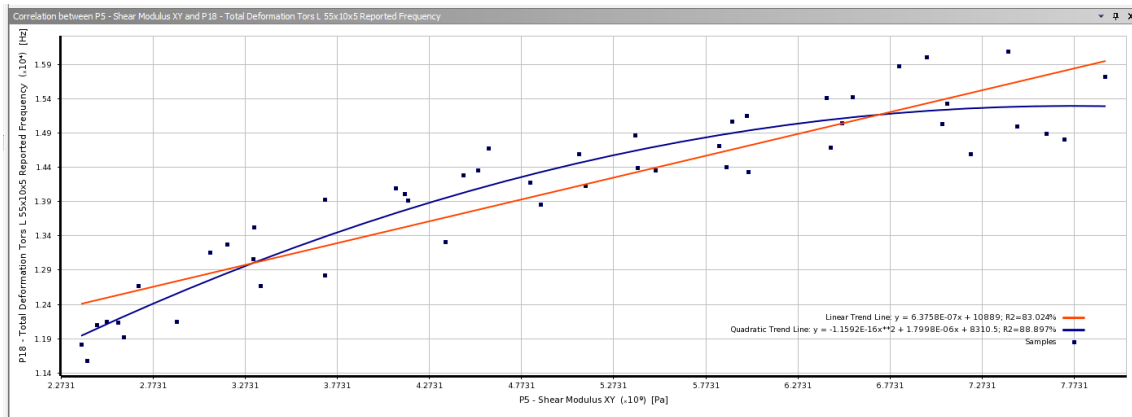


Figure E.25: Correlation between G_{XY} and $F_{torsional}$ of IP specimen

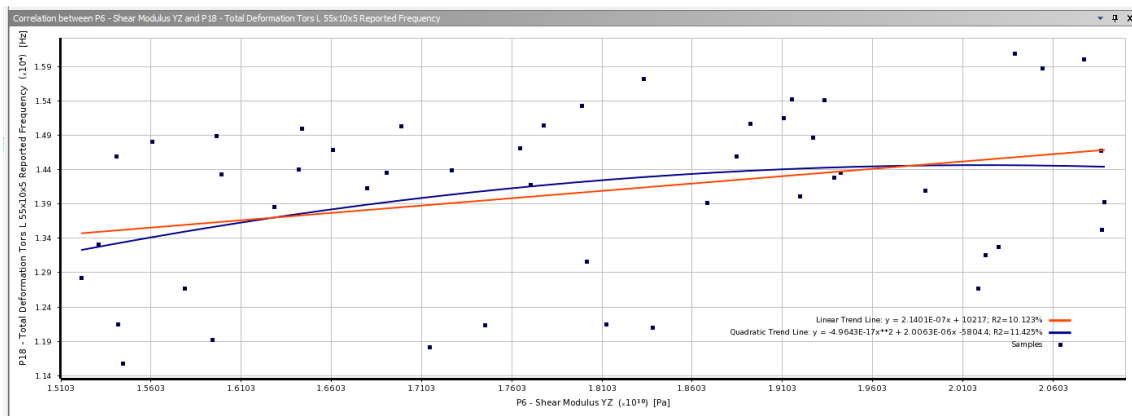


Figure E.26: Correlation between G_{YZ} and $F_{torsional}$ of IP specimen (no clear dependence)

E. Elastic constants derivation

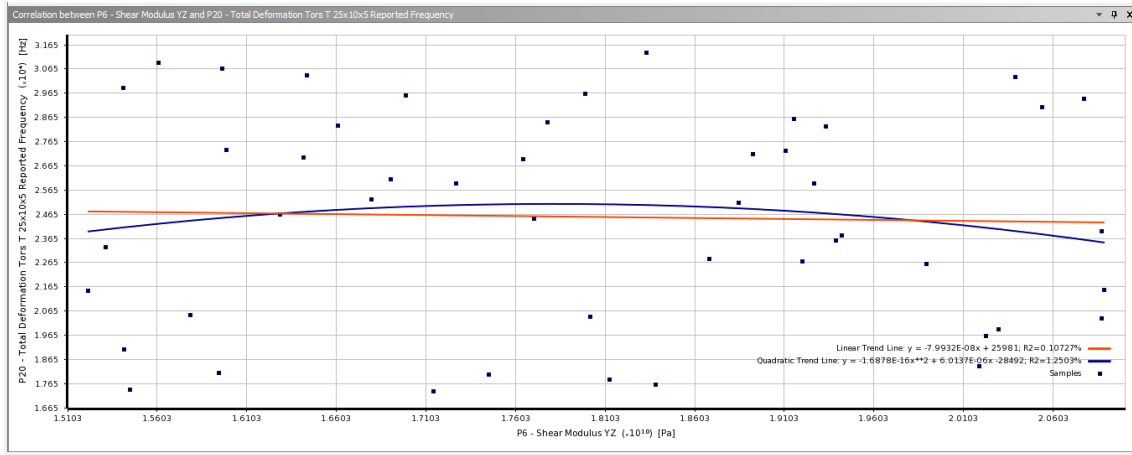


Figure E.27: Correlation between G_{YZ} and $F_{torsional}$ of TP specimen (no clear dependence)

As shown in Figures E.26 and E.27, G_{YZ} is not clearly defining a trend in any of the resonance modes. According to the orientation of the tested specimens, it would be expected that the $F_{torsional}$ of IP specimen is dependent on G_{YZ} . It is not the case, probably due to the geometry of the specimen, which is not ideal to apply shear in the YZ plane when vibrating in torsional mode.

Figures E.24 and E.25 show that G_{XY} influences the $F_{torsional}$ of both IP and TP specimens, but the trend is more clear in the TP specimen.

ν_{YZ} is derived from on E_Y and G_{YZ} , see equation E.8. As explained before, G_{YZ} does not clearly influence the resonance frequencies, therefore this method cannot be used to obtain precise values of ν_{YZ} .

Another parameter correlation analysis was performed in CG-1100B0 material, this time to see the influence of ν_{XY} . ν_{XY} was set as variable in the range 0.05-0.15, and the rest of constants were set as the optimized ones: $E_X = 4 \text{ GPa}$, $E_Y = 43 \text{ GPa}$, $G_{XY} = 3.5 \text{ GPa}$ and $G_{YZ} = 18 \text{ GPa}$. The correlation plots are shown in Figures E.28 and E.29.

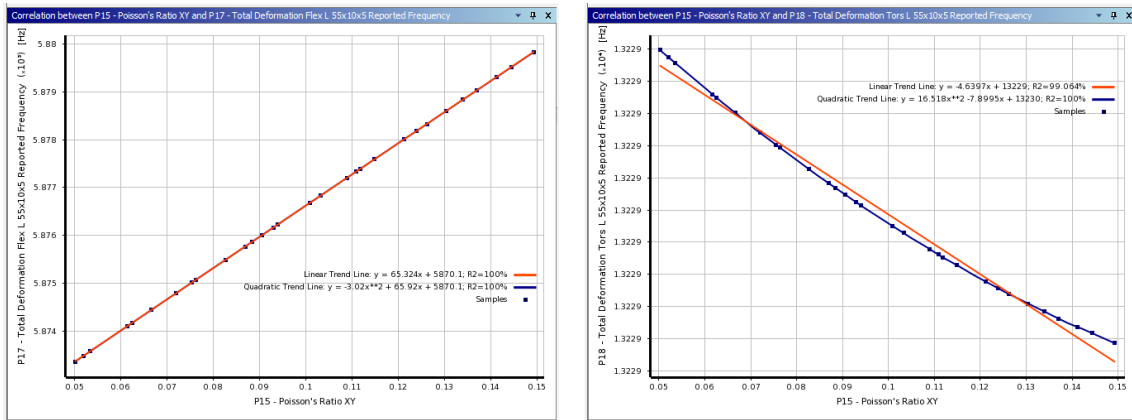


Figure E.28: Correlation between ν_{XY} (0.05-0.15) and $F_{flexural}$ (left) or $F_{torsional}$ (right) of IP specimen.

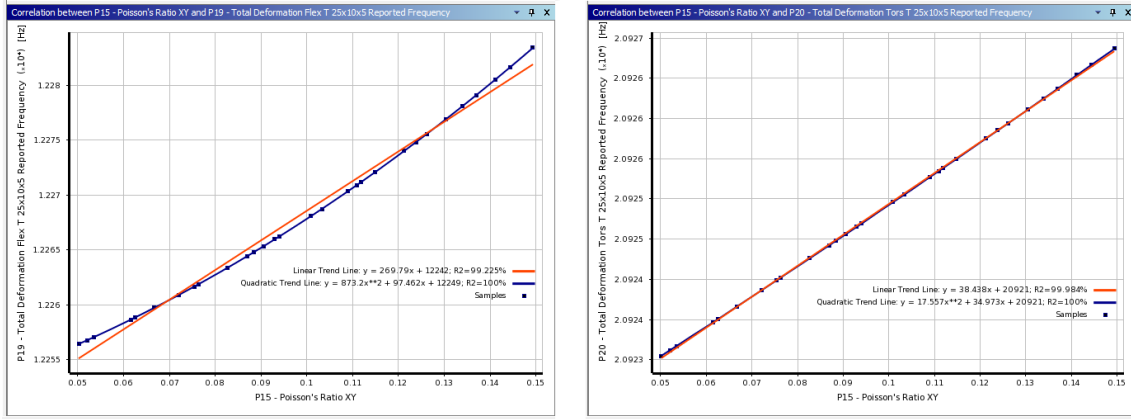


Figure E.29: Correlation between ν_{XY} (0.05-0.15) and $F_{flexural}$ (left) or $F_{torsional}$ (right) of TP specimen

The plots show a clear dependence between ν_{XY} and the resonant frequencies, but the effect in the frequency is negligible: in the best case it changes the frequency by 6 Hz. This effect is not relevant enough to be used experimentally to obtain ν_{XY} .

E.6 Important considerations of the method

The conclusion drawn from previous section E.5 is that the IET+optimisation method presented here, for the investigated materials, is able to obtain precisely only the following constants:

- E_X
- E_Y and thus E_Z
- G_{XY} and thus G_{XZ}

The rest of constants G_{YZ} , ν_{XY} , ν_{XZ} and ν_{YZ} , which consist in 2 independent ones (see equation E.6), have to be characterised with other means.

Other tests to measure the Poisson's ratios can be performed. For example traction and bending tests in the elastic region, with strain gauges placed to measure lateral deformations.

Ultrasound test to measure the speed of sound in different directions can be used to obtain the Poisson's ratios. This was tried by the author, but excessive damping of the materials in the TP direction makes those measurements not practicable.

The solution adopted is to use the rule of mixtures for the Poisson's coefficients. In this way, one can approximate these constants for the carbide-graphite composites, therefore knowing all of the independent elastic constants. Assuming that HOPG has $\nu_{XY} = 0.01$ and $\nu_{YZ} = 0.17$ (Table 6.2), and carbides have approximately isotropic $\nu = 0.19$ [86], the target ν_{YZ} for the composites should be between 0.17 and 0.19 (≈ 0.2). Also, taking into account that the graphite grains inside the composites have certain degree of misalignment, and that there are carbide particles inside the material with higher ν , ν_{XY} was set to 0.1, slightly higher than in HOPG.

F | Uncertainty calculation for the electrical conductivity measurements

The uncertainty of a measurement is a parameter, associated with the result of a measurement, that characterises the dispersion of the values that could reasonably be attributed to the measurand. A measurand is a particular quantity subject to measurement.

The uncertainty is an important parameter of any measurement, often overlook, that gives information about the range in which the true value could be. This is particularly relevant when comparing measurements on different samples, as it is required to understand if the true values are comparable or not.

The standard uncertainty for electrical conductivity measurements is calculated with the principle of propagation of uncertainty [169]. This allows to know the combined standard uncertainty knowing the individual uncertainties of each of the measured parameters. Formula F.1 corresponds to the function used to calculate the electrical conductivity (see section 3.4).

$$\gamma_e = \frac{I \cdot L}{V \cdot d_1 \cdot d_2} \quad (\text{F.1})$$

In this case the all input quantities are uncorrelated or independent. The combined standard uncertainty $u_c(y)$ of the measured value y is the positive square root of the combined variance $u_c^2(y)$, which is given by:

$$u_c^2(y) = \sum_{i=1}^N [c_i^2 u^2(x_i)] \quad (\text{F.2})$$

The sensitivity coefficients c_i are evaluated (units in SI) at the expectations X_i of each parameter x_i .

$$c_i = \frac{\partial f}{\partial x_i} = \frac{\partial f}{\partial X_i} \quad (\text{F.3})$$

The standard uncertainty of each parameter ($u(x_i)$) is obtained from:

$$u(x_i) = a/\sqrt{3} \quad u(x_i) = a/\sqrt{6} \quad u(x_i) = \sigma_{RMS} \quad (\text{F.4})$$

For rectangular (with width $\pm a$), triangular (with width $\pm a$) and normal (with standard deviation σ_{RMS}) distributions respectively.

In the case of the function f being γ_e (equation F.1):

$$\frac{\partial \gamma_e}{\partial I} = \frac{L}{V \cdot d_1 \cdot d_2} \quad (\text{F.5})$$

$$\frac{\partial \gamma_e}{\partial L} = \frac{I}{V \cdot d_1 \cdot d_2} \quad (\text{F.6})$$

$$\frac{\partial \gamma_e}{\partial V} = -\frac{I \cdot L}{V^2 \cdot d_1 \cdot d_2} \quad (\text{F.7})$$

$$\frac{\partial \gamma_e}{\partial d_1} = -\frac{I \cdot L}{V \cdot d_1^2 \cdot d_2} \quad (\text{F.8})$$

$$\frac{\partial \gamma_e}{\partial d_2} = - \frac{I \cdot L}{V \cdot d_1 \cdot d_2^2} \quad (\text{F.9})$$

The convolved distribution of parameters characterised by normal distributions will also be normal. However, even if the distributions of the parameters are not normal, the convolved distribution may often be approximated by a normal distribution because of the Central Limit Theorem [169].

The convolution of the five non-normal distributions (rectangular and triangular) of each parameter of equation F.1 is thus assumed normal. Therefore, the standard uncertainty (normal distribution) corresponds to a level of confidence p of 68.3%. The extended uncertainty is calculated by multiplying it by a coverage factor k_p , (Table G.1 of reference [169]). If a coverage factor of 2.58 is used, the level of confidence is 99%. The uncertainty of the electrical conductivity measurement is calculated with $p = 99\%$.

Example of a MoGr sample

A sample of MoGr is measured with the current supply fixed at 1000 mA, and the spacing L fixed to 29,5 mm. The sample is measured with a digital caliper and is tested in the test bench. Table F.1 shows the individual uncertainties. The resulting individual variables are: $d_1 = 3.97 \text{ mm}$, $d_2 = 5.12 \text{ mm}$, $L = 29.5 \text{ mm}$, $I = 1000 \text{ mA}$ and $V = 1580 \text{ } \mu\text{V}$.

Table F.1: Individual parameters of the measurement. Their uncertainties are the resolution of the devices, which correspond to the width " $\pm a$ " of the rectangular and triangular distributions.

	Uncertainty	Units	Distribution type
I	1	mA	Rectangular
V	10	μV	Rectangular
d_1	0.01	mm	Rectangular
d_2	0.01	mm	Rectangular
L	0.5	mm	Triangular

All the digital devices used for measurements (the caliper for d_1 and d_2 , the ammeter for I, the voltmeter for V) provide measurements with rectangular distributions. This is because the digit rounding produce this kind of distribution. For example, a caliper measurement of 4.42 mm corresponds to a true value that could be in a range 4.415 to 4.424, all values in between having equal probability.

On the other hand, the measurement of the distance L between voltmeter probes is done visually on top of a ruler with grooves separated 0.5 mm. With this method, the probability that the true value is close to the measured one is greater than that of values that are further away from it. For this reason its distribution is assumed to be triangular.

The conductivity of this sample results in 0.92 MS/m (equation F.1). The calculation of standard uncertainty of the example measurement results in $7.4 \cdot 10^3 \text{ S/m}$, thus 0.8% of the value. The expanded uncertainty with level of confidence 99% is $1.9 \cdot 10^4 \text{ S/m}$, thus 2.1% of the value. This is specific for this particular measurement case, however, the uncertainty of measurements with similar parameters should not vary much. A measurement with this uncertainty, performed with calibrated equipment, is considered very reliable.

The uncertainties of other thermo-physical measurements done at CERN and presented in this thesis are known to be always within 5%. For the sake of simplicity and to be conservative, the same 5% value is adopted for the uncertainty of the 4-wire electrical conductivity measurements.

G | High temperature X-ray diffraction data tables

This annex contains the data tables of the X-ray diffraction (XRD) measurements performed at high temperature. The results extracted from these analyses are presented in Chapter 5.

Table G.1: Graphite 2θ corrected peak positions [$^{\circ}$] in MG-6541Fc TP test. Resulting lattice parameters.

	T [$^{\circ}$ C]	s [mm]	(002)	(100)*	(101)	(004)	(110)*	(112)	a [\AA]	c [\AA]
Heating up	25	-0.001	26.540		44.556	54.673	77.479	83.604	2.461(8)	6.712
	100	-0.029	26.485		44.550	54.543	77.483	83.588	2.461(6)	6.725
	200	-0.064	26.410		44.539	54.377	77.491	83.559	2.461(5)	6.744
	300	-0.095	26.337		44.531	54.213	77.501	83.537	2.461(3)	6.762
	400	-0.137	26.260		44.520	54.041	77.502	83.497	2.461(2)	6.782
	500	-0.190	26.179		44.504	53.870	77.500	83.464	2.461(3)	6.802
	600	-0.232	26.105	42.371	44.492	53.726	77.498	83.427	2.461(3)	6.821
Cooling d.	500	-0.167	26.188	42.375	44.509	53.903	77.507	83.470	2.461(1)	6.800
	300	-0.078	26.340		44.536	54.206	77.507	83.533	2.461(1)	6.762
	100	-0.034	26.478		44.545	54.534	77.480	83.583	2.461(8)	6.727
	25	0.009	26.538		44.551	54.651	77.476	83.598	2.461(9)	6.712

*Gr.(100) overlaps with α -MoC $_{1-x}$ (200), Gr.(110) overlaps with α -MoC $_{1-x}$ (222).

Table G.2: α -MoC $_{1-x}$ 2θ corrected peak positions [$^{\circ}$] in MG-6541Fc TP test. Resulting lattice parameters.

	T [$^{\circ}$ C]	s [mm]	(111)	(200)*	(220)	(311)	(222)*	a [\AA]
Heating up	25	-0.001	36.470	42.358	61.455	73.621		4.264
	100	-0.029	36.462	42.354	61.431	73.591		4.266
	200	-0.064	36.454	42.339	61.403	73.547		4.269
	300	-0.095	36.444	42.322	61.372	73.502		4.272
	400	-0.137	36.436	42.308	61.341	73.456	77.301	4.275
	500	-0.190	36.427	42.292	61.302	73.403	77.238	4.278
	600	-0.232	36.412	42.269	61.254	73.336	77.175	4.282
Cooling d.	500	-0.167	36.341	42.207	61.221	73.326	77.174	4.278
	300	-0.078	36.396	42.272	61.319	73.448	77.312	4.272
	100	-0.034	36.432	42.329	61.390	73.547		4.268
	25	0.009	36.456	42.350	61.433	73.597		4.265

*Gr.(100) overlaps with α -MoC $_{1-x}$ (200), Gr.(110) overlaps with α -MoC $_{1-x}$ (222).

G. High temperature X-ray diffraction data tables

Table G.3: Graphite 2θ corrected peak positions [$^{\circ}$] in CG-1100Ba TP test. Resulting lattice parameters.

	T [$^{\circ}$ C]	s [mm]	(002)	(100)	(101)	(004)	(110)	(112)	a [\AA]	c [\AA]
Heating up	25	0.002	26.535	42.357	44.548	54.658	77.474	83.597	2.4620	6.712
	100	-0.027	26.481	42.361	44.542	54.531	77.482	83.580	2.4618	6.726
	200	-0.061	26.407	42.365	44.535	54.363	77.490	83.557	2.4616	6.745
	300	-0.088	26.335	42.370	44.527	54.206	77.500	83.532	2.4613	6.763
	400	-0.135	26.255	42.370	44.515	54.032	77.501	83.493	2.4613	6.783
	500	-0.181	26.178	42.369	44.501	53.873	77.500	83.463	2.4614	6.802
Cooling d.	600	-0.231	26.098	42.368	44.491	53.696	77.497	83.427	2.4614	6.823
	500	-0.185	26.179	42.370	44.502	53.867	77.500	83.461	2.4613	6.802
	300	-0.094	26.335	42.369	44.527	54.205	77.499	83.527	2.4614	6.763
	100	-0.020	26.487	42.363	44.547	54.533	77.487	83.585	2.4617	6.725
	25	0.002	26.539	42.357	44.551	54.659	77.474	83.599	2.4620	6.712

Table G.4: $\text{Cr}_3(\text{C,N})_2$ 2θ corrected peak positions [$^{\circ}$] in CG-1100Ba TP test. Resulting lattice parameters.

	T [$^{\circ}$ C]	s [mm]	(111)	(040)	(041)	(112)	(130)	(023)	(131)	(132)
Heating up	25	0.002	35.359	38.847	41.035	42.080	43.163	43.574	45.175	50.832
	100	-0.027	35.331	38.838	41.015	42.046	43.134	43.536	45.148	50.800
	200	-0.061	35.294	38.813	40.991	41.999	43.102	43.488	45.107	50.753
	300	-0.088	35.259	38.788	40.961	41.955	43.066	43.437	45.067	50.698
	400	-0.135	35.214	38.752	40.927	41.898	43.018	43.378	45.019	50.640
	500	-0.181	35.172	38.719	40.881	41.842	42.969	43.318	44.969	50.580
Cooling d.	600	-0.231	35.128	38.682	40.840	41.788	42.922	43.253	44.912	50.513
	500	-0.185	35.172	38.720	40.882	41.843	42.970	43.315	44.966	50.577
	300	-0.094	35.258	38.786	40.962	41.951	43.063	43.431	45.063	50.696
	100	-0.020	35.331	38.839	41.022	42.050	43.140	43.537	45.150	50.804
	25	0.002	35.358	38.853	41.037	42.080	43.164	43.571	45.176	50.836

	T [$^{\circ}$ C]	(113)	(114)	(153)	(240)	(223)	a [\AA]	b [\AA]	c [\AA]
Heating up	25	51.699	63.355	73.276	78.825	81.975	2.849	9.265	6.964
	100	51.653	63.294	73.227	78.757	81.902	2.851	9.268	6.970
	200	51.596	63.194	73.134	78.674	81.796	2.854	9.273	6.979
	300	51.531	63.134	73.054	78.579	81.685	2.857	9.279	6.987
	400	51.460	63.027	72.972	78.468	81.570	2.861	9.286	6.997
	500	51.384	62.936	72.877	78.389	81.445	2.864	9.295	7.008
Cooling d.	600	51.304	62.831	72.785	78.286	81.320	2.867	9.303	7.019
	500	51.388	62.933	72.876	78.385	81.443	2.864	9.295	7.008
	300	51.524	63.123	73.067	78.587	81.679	2.857	9.279	6.988
	100	51.656	63.292	73.213	78.761	81.898	2.851	9.267	6.970
	25	51.700	63.354	73.272	78.817	81.966	2.849	9.264	6.964

G. High temperature X-ray diffraction data tables

Table G.5: Graphite 2θ corrected peak positions [$^\circ$] in CG-1240X TP test. Resulting lattice parameters.

	T [$^\circ$ C]	s [mm]	(002)	(100)	(101)	(004)	(103)	(110)	(112)	a [\AA]	c [\AA]
Heating up	25	0.009	26.546	42.358	44.548	54.651	59.875	77.476	83.601	2.462	6.712
	100	-0.020	26.490	42.360	44.541	54.540	59.810	77.485	83.583	2.462	6.724
	200	-0.058	26.413	42.362	44.530	54.367	59.730	77.491	83.557	2.462	6.743
	300	-0.098	26.337	42.365	44.522	54.201	59.646	77.499	83.530	2.462	6.762
	400	-0.146	26.257	42.367	44.509	54.032	59.555	77.498	83.494	2.461	6.783
	500	-0.191	26.182	42.366	44.497	53.866	59.463	77.497	83.460	2.462	6.802
	600	-0.241	26.103	42.366	44.484	53.683	59.371	77.492	83.420	2.462	6.822

Table G.6: Cr_2C_3 2θ corrected peak positions [$^\circ$] in CG-1240X TP test. Resulting lattice parameters.

	T [$^\circ$ C]	s [mm]	(011)	(112)	(203)	(204)	(211)	(006)	(114)
Heating up	25	0.009	32.563	39.021	40.198	45.499	46.583	47.421	48.006
	100	-0.020	32.534	38.987	40.169	45.483	46.543	47.415	47.975
	200	-0.058	32.497	38.944	40.134	45.439	46.480	47.400	47.932
	300	-0.098	32.459	38.897	40.077	45.393	46.415	47.377	47.886
	400	-0.146	32.403	38.845	40.040	45.351	46.342	47.357	47.838
	500	-0.191	32.358	38.792	40.005	45.303	46.276	47.334	47.782
	600	-0.241	32.314	38.735	39.953	45.251	46.199	47.311	47.726

	T [$^\circ$ C]	(212)	(015)	(115)	(020)	a [\AA]	b [\AA]	c [\AA]
Heating up	25	48.670	51.166	53.965	65.989	5.527	2.829	11.493
	100	48.628	51.142	53.931	65.930	5.532	2.832	11.494
	200	48.564	51.102	53.899	65.846	5.539	2.835	11.498
	300	48.494	51.062	53.839	65.732	5.548	2.839	11.503
	400	48.430	51.019	53.790	65.633	5.555	2.843	11.507
	500	48.368	50.968	53.730	65.513	5.562	2.847	11.513
	600	48.291	50.915	53.656	65.406	5.571	2.852	11.520

Table G.7: $\text{Cr}_3(\text{C,N})_2$ 2θ corrected peak positions [$^\circ$] in CG-1240X TP test. Resulting lattice parameters.

	T [$^\circ$ C]	s [mm]	(112)	(130)	(023)	(131)	a [\AA]	b [\AA]	c [\AA]
Heating up	25	0.009	42.098	43.176	43.579	45.176	2.848	9.266	6.963
	100	-0.020	42.061	43.150	43.537	45.152	2.850	9.268	6.971
	200	-0.058	42.012	43.114	43.483	45.111	2.853	9.273	6.980
	300	-0.098	41.954	43.063	43.437	45.070	2.857	9.277	6.987
	400	-0.146	41.897	42.997	43.374	45.015	2.861	9.289	6.997
	500	-0.191	41.851	42.976	43.323	44.971	2.863	9.291	7.005
	600	-0.241	41.788	42.931	43.253	44.919	2.868	9.299	7.019

Bibliography

- [1] CERN Website, 2018. URL <https://home.cern/about>.
- [2] CERN Council Website, 2018. URL <http://council.web.cern.ch/council/en/governance/convention.html>.
- [3] CERN Document Server: Final Budget of the Organization for the Sixty-Third Financial Year, 2017. URL <https://cds.cern.ch/record/2240771>.
- [4] CERN Document Server: CERN Annual Personnel Statistics, 2017. URL <https://cds.cern.ch/record/2317058>.
- [5] LHC Guide, Mar 2017. URL <http://cds.cern.ch/record/2255762>.
- [6] W. Herr and B. Muratori. Concept of luminosity. *CAS - CERN Accelerator School: Intermediate Course on Accelerator Physics*, 2006. URL <https://cds.cern.ch/record/941318>.
- [7] Prafulla Behera. Minimum bias physics at the LHC with the ATLAS detector. *ATLAS e-News*, 2011. URL http://atlas-service-eneews.web.cern.ch/atlas-service-eneews/2009/features_09/features_minibias.php.
- [8] G. Antchev, P. Aspell, I. Atanassov, V. Avati, J. Baechler, C. Baldenegro Barrera, et al. First measurement of elastic, inelastic and total cross-section at $\sqrt{s}=13$ TeV by TOTEM and overview of cross-section data at LHC energies. *The European Physical Journal C*, 79(2):103, Feb 2019. doi: 10.1140/epjc/s10052-019-6567-0.
- [9] Nikolai Mokhov. Interactions of particles with matter. The CERN Accelerator School, 2018. URL https://indico.cern.ch/event/643268/contributions/2610612/attachments/1600992/2557182/CAS2018_Mokhov_Particle-Matter_Int.pdf. 21 February - 6 March 2018, Zurich, Switzerland.
- [10] S Heinemeyer, C Mariotti, G Passarino, R Tanaka, J R Andersen, P Artoisenet, et al. Handbook of LHC Higgs Cross Sections: 3. Higgs Properties: Report of the LHC Higgs Cross Section Working Group. Technical report, CERN, 2013. URL <https://cds.cern.ch/record/1559921>.
- [11] G. Apollinari, I. Béjar Alonso, O. Brüning, M. Lamont, and L. Rossi. *High-Luminosity Large Hadron Collider (HL-LHC): Preliminary Design Report*. CERN Yellow Reports: Monographs. CERN, Geneva, 2015. ISBN 9789290834236. doi: 10.5170/CERN-2015-005.
- [12] Michael Benedikt and Frank Zimmermann. Towards future circular colliders. *J. Korean Phys. Soc.*, 69(6):893–902, 2016. doi: 10.3938/jkps.69.893.
- [13] Frank Zimmermann. HE-LHC baseline parameters, FCC Week 2017, Berlin, 2017. URL <https://indico.cern.ch/event/556692/contributions/2590826/attachments/1469360/2272924/HE-LHC-Baseline-Parameters.pdf>.
- [14] P Odier, M Ludwig, and S Thoulet. The DCCT for the LHC Beam Intensity Measurement. Technical Report CERN-BE-2009-019, CERN, Geneva, May 2009. URL <https://cds.cern.ch/record/1183400>.

- [15] Oscar Frasciello. *Wake Fields and Impedance Calculations of LHC Collimators' Real Structures*. Warsaw University of Technology Publishing House, 07 2016. ISBN 978-83-7814-539-4. URL <https://cds.cern.ch/record/2202972>.
- [16] S. Redaelli. Beam cleaning and collimation systems. *CERN Yellow Reports*, 2(0): 403, 2016. doi: 10.5170/CERN-2016-002.403.
- [17] J B Jeanneret, D Leroy, L R Oberli, and T Trenkler. Quench levels and transient beam losses in LHC magnets. Technical Report CERN-LHC-Project-Report-44, CERN, Geneva, May 1996. URL <https://cds.cern.ch/record/308241>.
- [18] Alessandro Bertarelli et al. The mechanical design for the LHC collimators. In *Proceedings, 9th European Particle Accelerator Conference (EPAC): Lucerne, Switzerland*, 2004. URL <https://cds.cern.ch/record/794628>.
- [19] Alessandro Dallochio, G Belingardi, T Kurtyka, and A Bertarelli. *Study of Thermo-Mechanical Effects Induced in Solids by High Energy Particle Beams: Analytical and Numerical Methods*. PhD thesis, Turin Polytechnic, 2008. URL <https://cds.cern.ch/record/1314219>.
- [20] Federico Carra, Alessandro Bertarelli, Alessandro Dallochio, Luca Gentini, Paolo Gradassi, et al. Mechanical Engineering and Design of Novel Collimators for HL-LHC. In *Proceedings, 5th International Particle Accelerator Conference (IPAC): Dresden, Germany, 2014*. URL <https://cds.cern.ch/record/1748367>.
- [21] Elena Quaranta, Alessandro Bertarelli, R Bruce, Federico Carra, Francesco Cerutti, A Lechner, Stefano Redaelli, E Skordis, and P Gradassi. Modeling of beam-induced damage of the LHC tertiary collimators. *Physical Review Accelerators and Beams*, 2017. doi: 10.1103/PhysRevAccelBeams.20.091002.
- [22] C. Bracco. Injection: Hadron Beams. In *Proceedings of the CAS-CERN Accelerator School: Beam Injection, Extraction and Transfer, Erice, Italy,*, 2017. doi: 10.23730/CYRSP-2018-005.131.
- [23] Federico Carra. *Thermomechanical Response of Advanced Materials under Quasi-Instantaneous Heating*. PhD thesis, Turin Polytechnic, 2017. doi: 10.5281/zenodo.1240450.
- [24] A. Bertarelli, E. Berthome, V. Boccone, F. Carra, F. Cerutti, N. Charitonidis, et al. An experiment to test advanced materials impacted by intense proton pulses at CERN HiRadMat facility. *Nuclear Instruments and Methods in Physics Research Section B: Beam Interactions with Materials and Atoms*, 308:88 – 99, 2013. doi: 10.1016/j.nimb.2013.05.007.
- [25] Nicolas Mounet. *The LHC Transverse Coupled-Bunch Instability*. PhD thesis, Ecole Polytechnique, Lausanne, 2012. URL <https://cds.cern.ch/record/1451296>.
- [26] Carlotta Accettura, Alessandro Bertarelli, et al. Ultra-high vacuum characterization of molybdenum-carbide graphite for HL-LHC collimators. In *Proceedings, 10th International Particle Accelerator Conference (IPAC): Melbourne, Australia, 2019*. doi: 10.18429/JACoW-IPAC2019-MOPTS093.
- [27] A. Bertarelli. Beam-induced damage mechanisms and their calculation. *CERN Yellow Reports*, 2(0):159, 2016. doi: 10.5170/CERN-2016-002.159.

- [28] I Efthymiopoulos, C Hessler, H Gaillard, D Grenier, M Meddahi, P Trilhe, et al. HiRadMat: A new irradiation facility for material testing at CERN. In *Proceedings, 2nd International Particle Accelerator Conference (IPAC): San Sebastian, Spain*, 2011. URL <https://cds.cern.ch/record/1403043>.
- [29] Nicola Mariani. *Development of novel, advanced molybdenum-based composites for high energy physics applications*. PhD thesis, Milan Polytechnic, 2014. URL <https://cds.cern.ch/record/2133098>.
- [30] G. Samsonov and I. M. Vinitiskii. *Handbook of Refractory Compounds*. IFI/Plenum, 1980. ISBN 0-306-65181-5. Translated from Russian by Kenneth Shaw.
- [31] A. Bertarelli, C. Accettura, E. Berthomé, L. Bianchi, P. Bolz, F. Carra, C. Fichera, M. Frankl, T. Furness, G. Gobbi, P. Grosclaude, J. Guardia-Valenzuela, M. Guinchard, et al. Dynamic Testing and Characterization of Advanced Materials in a New Experiment at CERN HiRadMat Facility. In *Proceedings, 9th International Particle Accelerator Conference (IPAC): Vancouver, Canada*, 2018. doi: 10.18429/JACoW-IPAC2018-WEPMF071.
- [32] M Ohler, J Baruchel, and P Galez. An x-ray diffraction topographic study of highly oriented pyrolytic graphite. *Journal of Physics D: Applied Physics*, 28(4A):A78, 1995. URL <http://stacks.iop.org/0022-3727/28/i=4A/a=015>.
- [33] A. Tuffanelli, M. Sanchez del Rio, G. Pareschi, M. Gambaccini, A. Taibi, A. Fantini, and M. Ohler. A comparative characterization of highly oriented pyrolytic graphite by means of diffraction topography. *Proceedings of SPIE - The International Society for Optical Engineering*, 1999. doi: 10.1117/12.370091. URL http://www.esrf.eu/computing/scientific/people/srio/publications/spie99_mosaics.pdf.
- [34] A. W. Moore. *Chemistry and physics of carbon vol 11. p. 69*, volume 11. Marcel Dekker INC., 1973.
- [35] Elias Métral. Beam intensity limitations. HiLumi LHC FP7 High Luminosity Large Hadron Collider Design Study Deliverable Report, CERN, Nov 2014. URL <https://cds.cern.ch/record/1972601>.
- [36] Alessandro Bertarelli and Stefano Bizzaro. International patent application WO 2015062657, 2015.
- [37] Jorge Guardia-Valenzuela, Alessandro Bertarelli, Federico Carra, Nicola Mariani, Stefano Bizzaro, and Raul Arenal. Development and properties of high thermal conductivity molybdenum carbide - graphite composites. *Carbon*, 135:72 – 84, 2018. doi: 10.1016/j.carbon.2018.04.010.
- [38] Elena Quaranta, Alessandro Bertarelli, Nicolo Biancacci, Roderik Bruce, Federico Carra, Elias Métral, et al. Towards optimum material choices for the HL-LHC collimator upgrade. In *Proceedings, 7th International Particle Accelerator Conference (IPAC): Busan, Korea*, 2016. doi: 10.18429/JACoW-IPAC2016-WEPMW031.
- [39] Jean-Paul Issi. Thermal and electrical properties of carbons relationship to structure, 2001.

- [40] J.G. Lavin, D.R. Boyington, J Lahijani, Bernard Nysten, and Jean-Paul Issi. The correlation of thermal conductivity with electrical resistivity in mesophase pitch-based carbon fiber. *Carbon*, 31:1001–1002, 12 1993. doi: 10.1016/0008-6223(93)90207-Q.
- [41] Y. Iye. 1.10 - electronic states and transport properties of carbon crystalline: Graphene, nanotube, and graphite. In Pallab Bhattacharya, Roberto Fornari, and Hiroshi Kamimura, editors, *Comprehensive Semiconductor Science and Technology*, pages 359 – 382. Elsevier, 2011. ISBN 978-0-444-53153-7. doi: 10.1016/B978-0-44-453153-7.00068-7.
- [42] S. Mizushima. Various aspects of interaction between electrons and phonons in graphite. *Carbon*, 17(3):187 – 193, 1979. doi: 10.1016/0008-6223(79)90078-2.
- [43] A Arndt, Detlef Spoddig, P Esquinazi, J Barzola-Quiquia, Srujana Dusari, and T Butz. Electric carrier concentration in graphite: Dependence of electrical resistivity and magnetoresistance on defect concentration. *Physical Review B*, 80:195402, 11 2009. doi: 10.1103/PhysRevB.80.195402.
- [44] L. A. Pendry, C. Zeller, and F. L. Vogel. Electrical transport properties of natural and synthetic graphite. *Journal of Materials Science*, 15(8):2103–2112, 1980. doi: 10.1007/BF00550638.
- [45] Jian-Hao Chen, Chaun Jang, Shudong Xiao, Masa Ishigami, and Michael S. Fuhrer. Intrinsic and extrinsic performance limits of graphene devices on SiO_2 . *Nature Nanotechnology*, 3:206–209, 2008. doi: 10.1038/nnano.2008.58.
- [46] R.O. Dillon, I.L. Spain, J.A. Woollam, and W.H. Lowrey. Galvanomagnetic effects in graphite-i: Low field data and the densities of free carriers. *Journal of Physics and Chemistry of Solids*, 39(9):907 – 922, 1978. doi: 10.1016/0022-3697(78)90104-X.
- [47] K.I. Bolotin, K.J. Sikes, Z. Jiang, M. Klima, G. Fudenberg, J. Hone, P. Kim, and H.L. Stormer. Ultrahigh electron mobility in suspended graphene. *Solid State Communications*, 146(9):351 – 355, 2008. doi: 10.1016/j.ssc.2008.02.024.
- [48] Yoshihiro Hishiyama and Yutaka Kaburagi. Electrical resistivity of highly crystallized kish graphite. *Carbon*, 30(3):483 – 486, 1992. doi: 10.1016/0008-6223(92)90047-Z.
- [49] P.G. Klemens and D.F. Pedraza. Thermal conductivity of graphite in the basal plane. *Carbon*, 32(4):735 – 741, 1994. doi: 10.1016/0008-6223(94)90096-5.
- [50] M.R. Null, W.W. Lozier, and A.W. Moore. Thermal diffusivity and thermal conductivity of pyrolytic graphite from 300 to 2700 K. *Carbon*, 11(2):81 – 87, 1973. doi: 10.1016/0008-6223(73)90058-4.
- [51] Giorgia Fugallo, Andrea Cepellotti, Lorenzo Paulatto, Michele Lazzeri, Nicola Marzari, and Francesco Mauri. Thermal conductivity of graphene and graphite: Collective excitations and mean free paths. *Nano Letters*, 14(11):6109–6114, 2014. doi: 10.1021/nl502059f.
- [52] D.F. Pedraza and P.G. Klemens. Effective conductivity of polycrystalline graphite. *Carbon*, 31(6):951 – 956, 1993. doi: 10.1016/0008-6223(93)90197-I.

- [53] J. Y. Howe, C. J. Rawn, L. E. Jones, and H. Ow. Improved crystallographic data for graphite. *Powder Diffraction*, 18(2):150–154, 2003. doi: 10.1154/1.1536926.
- [54] J.M. Zazula. On Graphite Transformations at High Temperature and Pressure Induced By Absorption of the LHC Beam. Technical Report LHC-Project-Note-78, CERN, Geneva, Jan 1997. URL <http://cds.cern.ch/record/691793>.
- [55] A. Öya and H. Marsh. Phenomena of catalytic graphitization. *Journal of Materials Science*, 17(2):309–322, 1982. doi: 10.1007/BF00591464.
- [56] Philippe Ouzilleau, Aimen E. Gheribi, and Patrice Chartrand. The graphitization temperature threshold analyzed through a second-order structural transformation. *Carbon*, 109:896 – 908, 2016. doi: 10.1016/j.carbon.2016.08.041.
- [57] Hugh O. Pierson. *Handbook of Carbon, Graphite, Diamonds and Fullerenes*. Noyes Publications, 1993. ISBN 978-0-8155-1339-1.
- [58] Edward Goodrich Acheson. 492,767 (1893), 568,323 (1896), 617,979 (1899), 645,285 (1900), 711,031 (1902). U.S. Patents.
- [59] H. L. Riley. Amorphous carbon and graphite. *Q. Rev. Chem. Soc.*, 1:59–72, 1947. doi: 10.1039/QR9470100059.
- [60] R.B. Matthews. *Deformation and strengthening in molybdenum carbide - natural graphite composite materials*. PhD thesis, University of Wales, 1970.
- [61] R. B. Matthews and G. M. Jenkins. The high temperature interaction between molybdenum and graphite. *Journal of Materials Science*, 10(11):1976–1990, Nov 1975. doi: 10.1007/BF00754489.
- [62] C. Baraniecki, P.H. Pinchbeck, and F.B. Pickering. Some aspects of graphitization induced by iron and ferro-silicon additions. *Carbon*, 7(2):213–224, 1969. doi: 10.1016/0008-6223(69)90104-3.
- [63] William D. Callister. *Materials Science and Engineering An Introduction*. John Wiley & Sons, v edition, 2000.
- [64] C. H. Xu, C. L. Fu, and D. F. Pedraza. Simulations of point-defect properties in graphite by a tight-binding-force model. *Phys. Rev. B*, 48:13273–13279, Nov 1993. doi: 10.1103/PhysRevB.48.13273.
- [65] Prof. Helmut Föll. Iron, Steel and Swords website, 2019. URL <https://www.tf.uni-kiel.de/matwis/amat/iss/index.html>.
- [66] V. N. Eremenko, Ya. V. Natanzon, and V. P. Titov. Dissolution kinetics and diffusion coefficients of iron, cobalt, and nickel in molten aluminum. *Soviet materials science : a transl. of Fiziko-khimicheskaya mekhanika materialov / Academy of Sciences of the Ukrainian SSR*, 14(6):579–584, Nov 1978. doi: 10.1007/BF01159987.
- [67] Tunezo Saito, Yasuji Kawai, Kazuo Maruya, and Michiyoshi Maki. Diffusion of some alloying elements in liquid iron. *The Research Institute of Mineral Dressing and Metallurgy*, 11:401–410, 1959. doi: 10.1007/00102165.

- [68] Ana C. F. Ribeiro, Ornella Ortona, Susana M. N. Simões, Cecília I. A. V. Santos, Pedro M. R. A. Prazeres, et al. Binary Mutual Diffusion Coefficients of Aqueous Solutions of Sucrose, Lactose, Glucose, and Fructose in the Temperature Range from (298.15 to 328.15) K. *Journal of Chemical & Engineering Data*, 51(5):1836–1840, 2006. doi: 10.1021/je0602061.
- [69] David R Lide and Henry V Kehiaian. *CRC handbook of thermophysical and thermochemical data*. CRC Press, Boca Raton, FL, 1994.
- [70] A. Einstein. Über die von der molekularkinetischen theorie der wärme geforderte bewegung von in ruhenden flüssigkeiten suspendierten teilchen. *Annalen der Physik*, 322(8):549–560, 1905. doi: 10.1002/andp.19053220806.
- [71] A. D. LeClaire. 8.2 Diffusion tables for C, N, and O in metals: Datasheet from Landolt-Börnstein - Group III Condensed Matter · Volume 26: “Diffusion in Solid Metals and Alloys” in SpringerMaterials. Springer-Verlag Berlin Heidelberg, 1990. doi: 10.1007/10390457_90.
- [72] M. H. Hon and R. F. Davis. Self-diffusion of 14c in polycrystalline β -sic. *Journal of Materials Science*, 14(10):2411–2421, 1979. doi: 10.1007/BF00737031.
- [73] W. Mayr, W. Lengauer, P. Ettmayer, D. Rafaja, J. Baue, and M. Bohr. Phase equilibria and multiphase reaction diffusion in the cr-c and cr-n systems. *Journal of Phase Equilibria*, 20(1):35, Jan 1999. doi: 10.1361/105497199770335929. URL <https://doi.org/10.1361/105497199770335929>.
- [74] J.L. White and J.M. Pontelandolfo. Graphite-carbide materials prepared by hot-working with the carbide phase in the liquid state. *Nature*, 209:1018 – 1019, March 1966. doi: 10.1038/2091018a0.
- [75] Zoltán Weltsch, Antal Lovas, János Takács, Ágnes Cziráki, Attila Toth, and George Kaptay. Measurement and modelling of the wettability of graphite by a silver-tin (ag-sn) liquid alloy. *Applied Surface Science*, 268:52 – 60, 2013. doi: <https://doi.org/10.1016/j.apsusc.2012.11.150>.
- [76] A.E.B. Presland F.J. Derbyshire and D.L. Trimm. Graphite formation by the dissolution-precipitation of carbon in cobalt, nickel and iron. *Carbon*, 13:111–113, 1975. doi: 10.1016/0008-6223(75)90267-5.
- [77] P. W. Jackson and J. R. Marjoram. Compatibility studies of carbon fibres with nickel and cobalt. *Journal of Materials Science*, 5(1):9–23, 1970. doi: 10.1007/BF02427179.
- [78] R.A. Munson. Surface energies of liquid metal interfaces with carbon. *Carbon*, 5(5): 471 – 474, 1967. doi: [https://doi.org/10.1016/0008-6223\(67\)90023-1](https://doi.org/10.1016/0008-6223(67)90023-1).
- [79] Yu. V. Naidich and G. A. Kolesnichenko. Investigation of the Wetting of and Adhesion to Graphite and Diamond by Liquid Metals. In A. I. Belyaev, editor, *Surface Phenomena in Metallurgical Processes*, pages 218–223. Springer New York, Boston, MA, 1965. ISBN 978-1-4757-0076-3. doi: 10.1007/978-1-4757-0076-3_29. The original Russian text was published by Metallurgizdat in Moscow in 1963.
- [80] Yu. V. Naidich and G. A. Kolesnichenko. Investigation of the wetting of diamond and graphite by molten metals and alloys III. The wetting of diamond crystals. *Soviet Powder Metallurgy and Metal Ceramics*, 3(3):191–195, 1965. doi: 10.1007/BF00773947.

- [81] Yu. V. Naidich, I. A. Lavrinenko, G. A. Kolesnichenko, G. P. Volk, and V. P. Uman-skii. Diamond and cubic boron nitride composites with a metallic binder: Their production and application. *Powder Metallurgy and Metal Ceramics*, 32(6):476–479, Jun 1993. doi: 10.1007/BF00560722.
- [82] Auren Ferguson, Andrew Harvey, Ian J Godwin, Shane D Bergin, and Jonathan N Coleman. The dependence of the measured surface energy of graphene on nanosheet size. *2D Materials*, 4(1):015040, dec 2016. doi: 10.1088/2053-1583/aa50c0.
- [83] A.J. Kinloch. *Adhesion & Adhesives - Science & Technology*. Chapman & Hall, 1987.
- [84] Jian-Min Zhang, Fei Ma, and Ke-Wei Xu. Calculation of the surface energy of bcc metals by using the modified embedded-atom method. *Surface and Interface Analysis*, 35(8), 2003. doi: 10.1002/sia.1587.
- [85] Nicolas Eustathopoulos, Michael G. Nicolas, and Béatrice Drevet, editors. *Chapter 8 Wetting properties of metal/carbon systems*, volume 3 of *Pergamon Materials Series*. Pergamon, 1999. doi: [https://doi.org/10.1016/S1470-1804\(99\)80010-8](https://doi.org/10.1016/S1470-1804(99)80010-8).
- [86] Hugh O Pierson. *Handbook of refractory carbides and nitrides: properties, characteristics, processing and applications*. Noyes Publications, Park Ridge, NJ, 1996. ISBN 978-0-8155-1392-6.
- [87] N. Subramanian W. Weisweiler and B. Terwiesch. Catalytic influence of metal melts of the graphitization of monolithic glasslike carbon. *Carbon*, 9:755–761, 1971.
- [88] B. Predel. Au-C (Gold-Carbon): Datasheet from Landolt-Börnstein - Group IV Physical Chemistry · Volume 5A: "Ac-Au – Au-Zr" in SpringerMaterials, 1991. doi: 10.1007/10000866_264.
- [89] Yu. V. Naidich, V. M. Perevertailo, and G. M. Nevodnik. Wetting of graphite by nickel as affected by the liquid-phase dissolution process of carbon. *Soviet Powder Metallurgy and Metal Ceramics*, 10(1):45–47, 1971. doi: 10.1007/BF00798047.
- [90] Michael Humenik, D.W. Hall, and R.L. Van Alsten. Graphite-base cermets: a new material for bearing, electrical and high-temperature applications. *Material Progress in Powder Metallurgy*, page 101, April 1962.
- [91] Yu. V. Naidich and G. A. Kolesnichenko. Investigation of the wetting of diamond and graphite by molten metals and alloys V. Carbide-formation kinetics at the graphite/metallic melt interface. *Soviet Powder Metallurgy and Metal Ceramics*, 7(2):139–141, 1968. doi: 10.1007/BF00774308.
- [92] W. D. Kingery, J. M. Woulbroun, and F. R. Charvat. Effects of applied pressure on densification during sintering in the presence of a liquid phase. *Journal of the American Ceramic Society*, 46(8):391–395, 1963. doi: 10.1111/j.1151-2916.1963.tb11758.x.
- [93] M. Humenik and R.L. Van Alsten. 2,983,034, 1961. U.S. Patent.
- [94] J.L. White and J.M. Pontelandolfo. Graphite-carbide materials prepared by hot-working with a dispersed liquid-carbide phase. *Carbon*, 4(3):305 – 314, 1966. doi: 10.1016/0008-6223(66)90043-1.

- [95] Y. Harada. Graphite-metal carbide composites. Technical Report NASA-CR-507, Illinois Institute of Technology (IIT), Chicago, June 1966. URL <https://ntrs.nasa.gov/archive/nasa/casi.ntrs.nasa.gov/19660019930.pdf>.
- [96] J L. White and K Koyama. Graphitic materials hot-worked with a dispersed liquid carbide: Thermal and electrical conductivity. *Journal of the American Ceramic Society*, 51:394–398, 1968. doi: 10.1111/j.1151-2916.1968.tb11901.x.
- [97] D. John and G. M. Jenkins. Hot-working and strengthening in metal carbide-graphite composites. *Journal of Materials Science*, 21(8):2941–2958, 1986. doi: 10.1007/BF00551515.
- [98] Kazutoshi Yamada, Teruo Takahashi, Muneyuki Motoyama, and Hiroshi Nagai. X-ray spectroscopic analysis of solid state reaction during mechanical alloying of molybdenum and graphite powder mixture. *Materials Transactions*, 43(9):2292–2296, 2002. URL <https://www.jim.or.jp/journal/e/43/09/2292.html>.
- [99] J.-C. Zhao, editor. *Methods for Phase Diagram Determination*. Elsevier Science Ltd, Oxford, 2007. ISBN 978-0-08-044629-5. doi: 10.1016/B978-0-08-044629-5.X5000-9.
- [100] B. Predel. C-Mo (Carbon-Molybdenum): Datasheet from Landolt-Börnstein - Group IV Physical Chemistry · Volume 5B: "B-Ba – C-Zr" in SpringerMaterials, 1992. doi: 10.1007/10040476_643.
- [101] H. Kleykamp and G. Shumacher. The constitution of the silicon-carbon system. *Physical Chemistry Chemical Physics*, 97(06):799–804, 1993. doi: 10.1002/bbpc.19930970609.
- [102] SpringerMaterials Website. Landolt-Börnstein Series materials science databases.
- [103] B. Predel. C-Cr (Carbon-Chromium): Datasheet from Landolt-Börnstein - Group IV Physical Chemistry · Volume 5B: "B-Ba – C-Zr" in SpringerMaterials, 1992. doi: 10.1007/10040476_624.
- [104] H. Nowotny. *Alloy chemistry of transition element borides, carbides, nitrides, aluminides, and silicides, in "Electronic structure and alloy chemistry of the transition elements"*. Wiley (Interscience), 1963.
- [105] Commodity Closing Prices. <http://www.infomine.com/investment/>, 2019.
- [106] Jorge Guardia Valenzuela. Development and Characterization of a Novel Graphite-matrix Composite Material for Thermal Management Applications. Master's thesis, University of Zaragoza, 2015. URL <https://cds.cern.ch/record/2221106>.
- [107] CERN ActiWiz Website. <http://actiwiz.web.cern.ch/>, 2019.
- [108] Laura Bianchi. Thermophysical and mechanical characterization of advanced materials for the LHC collimation system. Master's thesis, Università di Pisa, 2017. URL <https://cds.cern.ch/record/2265824>.
- [109] Oscar Sacristan-de-Frutos, Alessandro Bertarelli, Laura Bianchi, Federico Carra, et al. Thermo-Physical and Mechanical Characterisation of Novel Materials under Development for HL-LHC Beam Intercepting Devices. In *Proceedings, 8th International Particle Accelerator Conference (IPAC): Copenhagen, Denmark*, 2017. doi: 10.18429/JACoW-IPAC2017-WEPVA113.

- [110] Eleftherios Iakovakis. Thermophysical and mechanical characterization of novel advanced materials for the LHC collimation system. Master's thesis, Aristotle University of Thessaloniki, 2015.
- [111] L. Bianchi. Challenges of Laser Flash Analysis in high thermal diffusivity materials, April 2017. <https://edms.cern.ch/document/1606182/1>.
- [112] Sophia Katrina Leiva. Oxidation of Graphitic Materials at High Temperatures in Differential Scanning Calorimetry. Bachelor's thesis, Western Norway University of Applied Sciences, 2018.
- [113] G. R. Cowper. The shear coefficient in timoshenko's beam theory. *Journal of Applied Mechanics*, 33:335–340, 1966. doi: 10.1115/1.3625046.
- [114] L. Lutterotti and P. Scardi. Simultaneous structure and size-strain refinement by the Rietveld method. *Journal of Applied Crystallography*, 1990. doi: 10.1107/S0021889890002382.
- [115] Luca Lutterotti, Siegfried Matthies, and Hans Rudolf Wenk. MAUD: a friendly Java program for Material Analysis Using Diffraction. *International Union of Crystallography: Newsletter of the Commission on Powder Diffraction*, 21:14–15, 1999. URL <https://www.fkf.mpg.de/4112013/cpd21.pdf>.
- [116] Adriana Daskevic, Andrius Merkys, Armel Le Bail, Daniel Chateigner, Luca Lutterotti, Miguel Quiros, Nadezhda R. Serebryanaya, Peter Moeck, Robert T. Downs, and Saulius Grazulis. Crystallography Open Database (COD): an open-access collection of crystal structures and platform for world-wide collaboration. *Nucleic Acids Research*, 40(D1):D420–D427, 2011. doi: 10.1093/nar/gkr900.
- [117] C. Suryanarayana and M. Grant Norton. *X-Ray Diffraction. A Practical Approach*. Springer, 1998.
- [118] D. Chateigner, L. Lutterotti, M. Morales, Y. El Mendili, P. Boullay, and S. Gascoin. Combined Analysis: Probing the crystallite sizes by XRD down to nm, together with structure, texture, phases, residual stresses, complemented by XRF, GiXRF and electron diffraction, 2018. URL http://www.ecole.ensicaen.fr/~chateign/danielc/slides/Chateigner_slides_Nanoday2018.pdf. Nanoday, Caen, 8th Feb. 2018.
- [119] T.G. Fawcett, S.N. Kabbekodu, J. Faber, F. Needham, and F. Mcclune. Evaluating experimental methods and techniques in X-ray diffraction using 280,000 data sets in the powder diffraction file. International Centre for Diffraction Data (ICDD), 2003. URL http://www.icdd.com/assets/support/Fawcett-EVALUATING_EXPERIMENTAL_METHODS.pdf.
- [120] S. Walsh and D. Diamond. Non-linear curve fitting using Microsoft Excel solver. *Talanta*, 42(4):561 – 572, 1995. doi: [https://doi.org/10.1016/0039-9140\(95\)01446-I](https://doi.org/10.1016/0039-9140(95)01446-I).
- [121] M. E. Straumanis and S. Zyszczyński. Lattice parameters, thermal expansion coefficients and densities of Nb, and of solid solutions Nb-O and Nb-N-O and their defect structure. *Journal of Applied Crystallography*, 3(1), 1970. doi: 10.1107/S002188987000554X.
- [122] D.B. Williams and B.C. Carter. *Transmission electron microscopy*. Springer, 1996.

- [123] L. Reimer and H. Kohl. *Transmission electron microscopy*. Springer, 2008.
- [124] S.J. Pennycook and P.D. Nellist. *Scanning Transmission Electron Microscopy: Imaging and Analysis*. Springer, 2011.
- [125] F.L. Deepak, A. Mayoral, and R. Arenal. *Advanced Transmission Electron Microscopy: Applications to Nanomaterials*. Springer, 2015.
- [126] L.A. Giannuzzi and F.A. Stevie. *Introduction to Focused Ion Beams: Instrumentation, Theory, Techniques and Practice*. Springer, 2005.
- [127] Michio Inagaki. Chapter 2.1 - advanced carbon materials. In Shigeyuki Somiya, editor, *Handbook of Advanced Ceramics (Second Edition)*, pages 25 – 60. Academic Press, Oxford, second edition edition, 2013. ISBN 978-0-12-385469-8. doi: <https://doi.org/10.1016/B978-0-12-385469-8.00002-2>.
- [128] Harry Marsh and Francisco Rodríguez-Reinoso. Chapter 9 - Production and Reference Material. In Harry Marsh and Francisco Rodríguez-Reinoso, editors, *Activated Carbon*, pages 454 – 508. Elsevier Science Ltd, Oxford, 2006. ISBN 978-0-08-044463-5. doi: <https://doi.org/10.1016/B978-008044463-5/50023-6>.
- [129] Hugh O. Pierson. *Handbook of Carbon, Graphite, Diamond and Fullerenes: Properties, Processing and Applications*. Noyes Publications, 1993.
- [130] G. V. Samsonov, editor. *Handbook of the physicochemical properties of the elements*. Plenum, 1968.
- [131] R.E. Taylor et al. *Thermal expansion of solids. IV. Series: CINDAS data series on material properties.: v I-4*. ASM International, 1998. ISBN 0-87170-623-7.
- [132] J. Glaser, R. Schmitt, and H.J. Meyer. Neue Strukturverfeinerung und Eigenschaften von Cr_3C_2 . *Zeitschrift fuer Naturforschung, Teil B. Anorganische Chemie, Organische Chemie*, 58:929–933, 2003. URL <http://www.crystallography.net/cod/7222489.html>.
- [133] Salvatore Grasso, Yoshio Sakka, and Giovanni Maizza. Electric current activated/assisted sintering (ECAS): a review of patents 1906-2008. *Science and Technology of Advanced Materials*, 10(5):053001, 2009. doi: 10.1088/1468-6996/10/5/053001.
- [134] T. Noda. Graphitization of carbon under high pressure. *Carbon*, 6(2):125 – 133, 1968. doi: 10.1016/0008-6223(68)90297-2.
- [135] S. Strijbos, P.J. Rankin, R.J. Klein Wassink, J. Bannink, and G.J. Oudemans. Stresses occurring during one-sided die compaction of powders. *Powder Technology*, 18(2):187 – 200, 1977. doi: [https://doi.org/10.1016/0032-5910\(77\)80008-9](https://doi.org/10.1016/0032-5910(77)80008-9).
- [136] R.D. Cope and J.C. Brown. An investigation of electrical discharge machining of graphite/epoxy composites. *Composites Manufacturing*, 1:167 – 171, 1990. doi: 10.1016/0956-7143(90)90164-R.
- [137] T.D. Burchell. *Comprehensive Nuclear Materials*, chapter 2.10 Graphite: Properties and Characteristics, pages 285–305. Elsevier, 2012. URL <http://cds.cern.ch/record/1474075>.

- [138] M.O. Marlowe. Elastic properties of three grades of fine grained graphite to 2000 °c. Technical Report NASA-CR-66933, Nucleonics Laboratory - General Electric Company, Pleasanton, California, 1970. URL <https://ntrs.nasa.gov/archive/nasa/casi.ntrs.nasa.gov/19700032783.pdf>.
- [139] Walter Steurer, Peter Rogl, Herbert Boller, Barnabas Kunsch, and Hans Nowotny. A neutron powder diffraction study of $(V, Cr)_3C_{2-x}$. *Journal of the Less Common Metals*, 76(1):145 – 151, 1980. doi: 10.1016/0022-5088(80)90018-1.
- [140] P. Ettmayer, G. Vinek, and H. Rassaerts. Die Kristallstruktur von $Cr_3(C, N)_2$ und Cr_2VC_2 . *Monatshefte für Chemie und verwandte Teile anderer Wissenschaften*, 97(4):1258–1262, 1966. doi: 10.1007/BF00903577.
- [141] V.S. Telegus, Yu.B. Kuzma, and P.I. Kripyakevich. The crystal structure of the compound VCr_2C_2 . *Dopovidi Akademii Nauk Ukrain's'koi RSR, Seriya A: Fiziko-Tekhnichni ta Matematichni Nauki*, pages 545–546, 1967. URL <http://www.crystallography.net/cod/1530865.html>.
- [142] J Dubois, T Epicier, C Esnouf, G Fantozzi, and P Convert. Neutron powder diffraction studies of transition metal hemicarbides M_2C_{1-x} – I. motivation for a study on W_2C and Mo_2C and experimental background for an in situ investigation at elevated temperature. *Acta Metallurgica*, 36(8):1891 – 1901, 1988. doi: 10.1016/0001-6160(88)90292-1.
- [143] T Epicier, J Dubois, C Esnouf, G Fantozzi, and P Convert. Neutron powder diffraction studies of transition metal hemicarbides M_2C_{1-x} – II. in situ high temperature study on W_2C_{1-x} and Mo_2C_{1-x} . *Acta Metallurgica*, 36(8):1903 – 1921, 1988. doi: 10.1016/0001-6160(88)90293-3.
- [144] E. Parthé and V. Sadagopan. The structure of dimolybdenum carbide by neutron diffraction technique. *Acta Crystallographica*, 16(3):202–205, Mar 1963. doi: 10.1107/S0365110X63000487.
- [145] C.Y. Ho, R.W. Powell, and P.E. Liley. Thermal conductivity of the elements: A comprehensive review. *Journal of Physical and Chemical Reference Data*, 3, 1974. URL <https://srd.nist.gov/JPCRD/jpcrdS1Vo13.pdf>. Supplement No.1.
- [146] James F. Lynch. Engineering Property Data on Selected Ceramics. Volume II. Carbides. Technical Report ADA087519, Metals and Ceramics Information Center. Columbus Laboratories, Ohio, 1979.
- [147] O. L. Blakslee, D. G. Proctor, E. J. Seldin, G. B. Spence, and T. Weng. Elastic Constants of Compression-Annealed Pyrolytic Graphite. *Journal of Applied Physics*, 41(8):3373–3382, 1970. doi: 10.1063/1.1659428.
- [148] Pierre Delhaès, editor. *Graphite and Precursors*. Gordon and Breach Science Publishers, 2001.
- [149] Ales Kroupa and Andy Watson. Carbon-Molybdenum-Titanium. Landolt-Börnstein - Group IV Physical Chemistry 11E2 (refractory metal systems), 2010. Copyright 2010 Springer-Verlag Berlin Heidelberg.
- [150] M Solfaroli Camillocci. LHC nominal cycle. *6th Evian Workshop on LHC beam operation, Evian Les Bains, France*, pages 45–48. 4 p, 2016. URL <https://cds.cern.ch/record/2294513>.

- [151] F Alessio, Z Guzik, and R Jacobsson. LHCb Global Timing and Monitoring of the LHC Filling Scheme. Technical Report LHCb-PUB-2011-004. CERN-LHCb-PUB-2011-004, CERN, Geneva, Jan 2011. URL <http://cds.cern.ch/record/1323826>.
- [152] R Bailey and Paul Collier. Standard Filling Schemes for Various LHC Operation Modes. Technical Report LHC-PROJECT-NOTE-323, CERN, Geneva, Sep 2003. URL <https://cds.cern.ch/record/691782>.
- [153] Oliver Sim Brüning, Paul Collier, P Lebrun, Stephen Myers, Ranko Ostojic, John Poole, et al. *LHC Design Report*. CERN Yellow Reports: Monographs. CERN, Geneva, 2004. doi: 10.5170/CERN-2004-003-V-1.
- [154] A Ballarino, S Mathot, and D Milani. 13000 A HTS Current Leads for the LHC Accelerator: From Conceptual Design to Prototype Validation. Technical Report LHC-Project-Report-696. CERN-LHC-Project-Report-696, CERN, Geneva, Mar 2004. URL <https://cds.cern.ch/record/729433>.
- [155] Breaking data records bit by bit, 2017. URL <https://home.cern/news/news/computing/breaking-data-records-bit-bit>.
- [156] G Papotti, A Gorzawski, M Hostettler, R Schmidt Cern, Geneva, and Switzerland. Beam losses through the cycle. *4th Evian Workshop on LHC beam operation, Evian-les-Bains, France, 17 - 20 Dec 2012*, pages 83–86. 4 p, 2012. URL <https://cds.cern.ch/record/2302425>.
- [157] R Veness, B Goddard, L Massidda, S J Mathot, and A Presland. Design of the LHC Beam Dump Entrance Window. *CERN-LHC-Project-Report-965*, page 4 p, Aug 2006. URL <https://cds.cern.ch/record/977787>.
- [158] V Kain. Beam Transfer and Machine Protection. *2014 Joint International Accelerator School: Beam Loss and Accelerator Protection, Newport Beach, CA, USA*, pages 137–158. 22 p, Aug 2016. URL <https://cds.cern.ch/record/2206779>. Comments: 22 pages, contribution to the 2014 Joint International Accelerator School: Beam Loss and Accelerator Protection, Newport Beach, CA, USA , 5-14 Nov 2014.
- [159] R.Assmann, A.Ferrari, B.Goddard, R.Schmidt, and N.A.Tahir. Interaction of the CERN Large Hadron Collider (LHC) beam with the beam dump block. Technical report, CERN, July 2008. URL <http://lsag.web.cern.ch/lsag/BeamdumpInteraction.pdf>.
- [160] CERN Knowledge Transfer Website, 2018. URL <http://kt.cern/>.
- [161] Bent Stumpe and Christine Sutton. The first capacitive touch screens at CERN. *CERN Courier*, 2010. URL <https://cerncourier.com/the-first-capacitive-touch-screens-at-cern/>. Video: The first touch-screen used at CERN <https://www.youtube.com/watch?v=tQe5dlzScwU>.
- [162] Particle Therapy Co-operative Group, 2019. URL <https://www.ptcog.ch/index.php/facilities-in-operation>.
- [163] Roberto Rossi, Oliver Aberle, Odd Andreassen, Mark Butcher, Cristovao Andre Dionisio Barreto, Francesca Galluccio, Iñigo Lamas Garcia, et al. Status of Crystal Collimation Studies at the LHC. In *Proceedings, 8th International Particle Accelerator Conference (IPAC): Copenhagen, Denmark, 2017*. URL <http://cds.cern.ch/record/2289710>.

- [164] D.C. Kiselev, R.M. Bergmann, R. Sobbia, V. Talanov, and M. Wohlmuther. Radiation Damage of Components in the Environment of High-Power Proton Accelerators. In *Proc. of International Conference on Cyclotrons and Their Applications (Cyclotrons'16), Zurich, Switzerland, September 11-16, 2016*, 2017. URL <http://jacow.org/cyclotrons2016/papers/moc01.pdf>.
- [165] Gary Bennett, James J Lombardo, Richard J Hemler, Gil Silverman, C W Whitmore, Wayne R Amos, et al. Mission of Daring: The General-Purpose Heat Source Radioisotope Thermoelectric Generator. *4th IECEC, AIAA.*, 2006. doi: 10.2514/6.2006-4096.
- [166] A. Moeslang J. Knaster and T. Muroga. Materials research for fusion. *Nature Physics*, 12:424–434, 2016. doi: 10.1038/nphys3735.
- [167] T.L. Daulton, M.A. Kirk, R.S. Lewis, and L.E. Rehn. Production of nanodiamonds by high-energy ion irradiation of graphite at room temperature. *Nuclear Instruments and Methods in Physics Research Section B: Beam Interactions with Materials and Atoms*, 175-177:12 – 20, 2001. doi: [https://doi.org/10.1016/S0168-583X\(00\)00603-0](https://doi.org/10.1016/S0168-583X(00)00603-0). Twelfth International Conference of Ion Beam Modification of Materials.
- [168] Miryea Borg. Numerical Modelling and Experimental Testing of Novel Materials for LHC Collimators. Master's thesis, University of Malta, 2015.
- [169] Joint Committee for Guides in Metrology. JCGM 100:2008, Evaluation of measurement data - Guide to the expression of uncertainty in measurement, 2008. URL https://www.bipm.org/utis/common/documents/jcgm/JCGM_100_2008_E.pdf.

Abbreviations

AR As-received	IET Impact Excitation Technique
BCC Body Centred Cubic	IP In-plane
BE Backscattered electron	LFA Laser Flash Analysis
CERN European Organization for Nuclear Research	LHC Large Hadron Collider
CFC Carbon Fibre-reinforced Carbon	LP Liquid phase
CFs Carbon Fibres	MoGr Molybdenum carbide - graphite
CrGr Chromium carbide - graphite	MS Mosaic spread (c-axis misalignment)
CTE Coefficient of Thermal Expansion	PG Pyrolytic Graphite
DSC Differential Scanning Calorimetry	ppm Particle per million ($1/10^6$)
EDS Energy Dispersive X-ray Spectroscopy	RD Residual Deformation
FCC Face Centred Cubic	RRR Residual Resistivity Ratio
FEM Finite Element Method	RT Room Temperature
FIB Focused Ion Beam	SE Secondary electron
GB Grain boundaries	SEM Scanning Electron Microscopy
HL-LHC High Luminosity Large Hadron Collider	STEM Scanning Transmission Electron Microscopy
HOPG Highly Oriented Pyrolytic Graphite	TEM Transmission Electron Microscopy
	TP Through-plane
	XRD X-Ray Diffraction

Nomenclature

a Thermal diffusivity	k Thermal conductivity
α Coefficient of Thermal Expansion	k_B Boltzmann constant
c_p Specific heat	ρ Density
E Young's modulus	ρ_e Electrical resistivity
ε_{adm} Strain to failure	R_M Failure strength
G Shear modulus	σ_{RMS} Standard deviation
γ_e Electrical conductivity	T_m Melting temperature